Annual Research Briefs – 2001

Center for Turbulence Research

December 2001

CONTENTS

Preface 1

Large-eddy simulation of gas turbines combustors. K. MAHESH, G. CONSTANTINESCU, S. APTE, G. IACCARINO and P. MOIN 3

Consistent boundary conditions for integrated LES/RANS simulations: LES outflow conditions. J. U. SCHLÜTER and H. PITSCH 19

Explicit filtering and subgrid-scale models in turbulent channel flow. J. GULLBRAND 31

Prediction of high Reynolds number flow over a circular cylinder using LES with wall modeling. M. WANG, P. CATALANO and G. IACCARINO 45

An experimental and computational investigation of flow past cacti. S. TALLEY, G. IACCARINO, G. MUNGAL and N. N. MANSOUR 51

Interacting flamelet model for non-premixed turbulent combustion with local extinction and re-ignition. H. PITSCH, S. FEDOTOV and C. M. CHA 65

Transported PDF modeling of turbulent nonpremixed combustion. C. M. CHA 79

Higher-order singly-conditional moment closure modeling approaches to turbulent combustion. C. M. CHA and H. PITSCH 87

Progress in large eddy simulation of premixed and partially premixed turbulent combustion. L. DUCHAMP DE LAGENESTE and H. PITSCH 97

Generalized symmetries of the G-equation without underlying flow field. M. OBERLACK 109

Large-eddy simulations of combustion instability suppression by static turbulence control. J. U. SCHLÜTER 119

Combustion instability due to the nonlinear interaction between sound and flame. X. WU, M. WANG and P. MOIN 131

DNS of transition in hypersonic boundary-layer flows including high-temperature gas effects. C. STEMMER and N. N. MANSOUR 143

Temperature-fluctuation scaling in reacting boundary layers. M. P. MARTIN and G. V. CANDLER 151

Preliminary LES over a hypersonic elliptical cross-section cone. M. P. MARTIN, M. WRIGHT, G. V. CANDLER, U. PIOMELLI, G. WEIRS and H. JOHNSON 163

Stochastic sub-grid modeling of drop breakup for LES of atomizing spray. M. GOROKHOVSKI and S. APTE 169

Study of the turbulence modulation in particle-laden flows using LES. J. GARCÍA 177

A formulation for fast computations of rigid particulate flows. N. A. PATANKAR 185

Direct numerical simulation of polymer flow. Y. DUBIEF and S. K. LELE 197

Structure and evolution of circumstellar disks during the early phase of accretion from a parent cloud. O. C. IDOWU 209

Modeling blood flow in a porcine aorta bypass graft: realization of physiological conditions. V. FAVIER and C. A. TAYLOR 219

An evolutionary algorithm for multi-objective optimization of combustion processes. D. BÜCHE, P. STOLL and P. KOUMOUTSAKOS 231

Shape optimization for aerodynamic noise control. A. L. MARSDEN, M. WANG and B. MOHAMMADI 241

Incomplete sensitivities in design and control of fluidic channels. B. MOHAMMADI, R. BHARAWAJ, J. I. MOLDHO and J. SANTIAGO 249

Efficient Fast Multipole Method for low frequency scattering. E. DARVE 259

Calculating free energies using average force. E. DARVE and A. POHORILLE 271

Buckyballs in water: structural characteristics and energetics. E. M. KOTSALIS, R. L. JAFFE, J. H. WALTHER, T. WERDER and P. KOUMOUTSAKOS 283

Instability of Blasius boundary layer in the presence of steady streaks. X. WU and J. LUO 293

Effects of long-wavelength Klebanoff modes on boundary-layer instability. X. WU and M. CHOUDHARI 305

The large-scale organization of autonomous turbulent wall regions. J. JIMÉNEZ, O. FLORES and M. GARCÍA-VILLALBA 317

Direct numerical simulation of the very large anisotropic scales in a turbulent channel. J. C. DEL ÁLAMO and J. JIMÉNEZ 329

CFD analysis of flow in an open-jet aeroacoustic experiment. S. MOREAU, G. IACCARINO, M. ROGER and M. WANG 343

RANS solver with adaptive structured boundary non-conforming grids. S. MAJUMDAR, G. IACCARINO and P. Durbin 353

Modeling the "rapid" part of the velocity/pressure-gradient correlation inhomogeneous turbulence. S. V. POROSEVA 367

Simulating separated flows using the $k-\varepsilon$ model. S. V. POROSEVA and G. IACCARINO 375

Wall corrections in modeling rotating pipe flow. S. V. POROSEVA 385

Appendix: Center for Turbulence Research 2000 Roster 397

Preface

This report contains the 2001 Annual Progress Reports of the postdoctoral fellows and visiting scholars of the Center for Turbulence Research. In 2001 CTR sponsored 15 resident Postdoctoral Fellows, 7 Research Associates and 3 Senior Research Fellows, hosted 7 visiting scholars and many shorter-term visitors, and supported 6 doctoral students. Most of the doctoral students engaged in turbulence research at CTR are supported by the U.S Office of Naval Research or the Air Force Office of Scientific Research.

CTR is closely associated with the Stanford multidepartmental Center for Integrated Turbulence Simulations (CITS), funded by the Department of Energy's Accelerated Strategic Computing Initiative (ASCI). The aim of the CITS program is to compute the complete flow through an aircraft gas turbine engine. The combustion chamber is the most critical region: it is typically of very complicated geometrical shape, and the fuel is introduced as a spray of droplets which must disperse and vaporize before burning. The first paper in this volume describes large-eddy simulation of the air flow in a real aircraft gas turbine combustor, and there are several papers relevant to the crucial problem of spray combustion.

The two most noticeable features of this year's reports are the application of large-eddy simulation (LES) to a wide range of practical problems, and the continued broadening of the Center's interests, especially in natural phenomena: the Center's alphabet could start with Astrophysics, Buckyballs and Cacti. The diversification of interests has brought with it an increasing number of contacts with industry and with other branches of the natural sciences and life sciences.

The papers fall into seven groups: in order, these are: large-eddy simulation; combustion and hypersonics; sprays and particles; control and optimization; molecular dynamics; instability, acoustics and turbulence structure; and Reynolds-averaged turbulence models (RANS models). Many papers could be included in more than one group, so the groups are not explicitly labeled in the Contents. The common theme, of course, is that these are computer-intensive problems.

As is recognized in the aircraft-engine industry, large-eddy simulation is becoming a powerful engineering tool for predicting internal flows and mixing in real propulsion systems, where Reynolds numbers are low (compared to those in external aerodynamics) and the flow can be separated and highly unsteady. These flow conditions are difficult to capture with RANS models, but can be accurately predicted by LES because they are dominated by large-scale motions. The problem of economically computing high-Reynolds-number attached or separating flows remains. Here all eddies are small, and if the LES is carried right down to the surface then either the mesh has to be so fine that the calculation reduces to DNS, or the sub-grid-scale model has to carry most of the Reynolds stresses and the calculation effectively reduces to RANS. The first one is impossibly expensive and the other is likely to compromise accuracy. Since the day of widespread industrial use of LES has not yet arrived, CTR continues to support work on Reynolds- averaged models.

Combustion is a long-standing interest at CTR, and the work has received a boost from the appointment of Prof. Norbert Peters to the Department of Mechanical Engineering. Much of our work is supported by NASA's Ultra Efficient Engine Technology (UEET) Program. Hypersonic flow with real-gas effects shares many of the problems of combustion, and is also an ongoing interest of NASA.

The importance of spray dynamics in combustion of liquid fuels has been mentioned above: the behavior of particle- laden flows in general is of very wide engineering interest. A special case of particle-laden flow is the long-standing mystery of liquid flow with a suspension of long-chain polymer molecules: spectacular reductions in flow resistance can be achieved but the mechanism is still controversial.

Control and optimization, of turbulent flow or of other systems, is another long-standing interest at CTR, and again is relevant to many branches of engineering.

Molecular dynamics, far though it is from CTR's original interests, is a fast-developing field involving very intensive computing.

Instability problems are closely related to control problems, notably in the case of combustion. Instability of laminar flows is yet another problem that is yielding to intensive computing in the form of DNS. The phenomenological relation between the earlier stages hydrodynamic instability and final, fully-developed turbulence may not be very close, but the computational problems are virtually identical. Aeroacoustics and turbulence structure are the original interests of CTR, and basic research on these topics is still the foundation of improved models, whether the sub-grid-scale models of LES or the traditional RANS models used in industry.

We are grateful to Professor Peter Bradshaw for his thorough technical editing of the reports in this volume. We welcome Peter's participation in CTR in this capacity and his increased interactions with the CTR research staff.

Parviz Moin
William C. Reynolds
Nagi N. Mansour

This volume, like other CTR progress-report volumes, is available as a .pdf file on the Web at http://ctr.stanford.edu

Large-eddy simulation of gas turbine combustors

By Krishnan Mahesh †, George Constantinescu, Sourabh Apte, Gianluca Iaccarino AND Parviz Moin

1. Motivation and objectives

This report discusses our progress towards developing a numerical algorithm, and solver capable of performing large-eddy simulation in geometries as complex as the combustor of a gas-turbine engine. LES is considered a particularly attractive approach for combustor simulation because of its demonstrated superiority over RANS in predicting mixing. A working combustor – the PW6000 – is chosen to develop and demonstrate LES capability.

As discussed in previous reports (Mahesh *et al.* 1999, 2000), an algorithm and LES solver for unstructured grids are under development.

2. Accomplishments

Our progress in the last year is as follows:

- A new formulation was derived that is discretely energy-conserving for arbitrary grids. This was found essential to perform simulations at high Reynolds numbers, and on 'bad' grids encountered in complex geometries such as the Pratt & Whitney combustor.
- Turbulent validations were performed for the swirling flow in a coaxial combustor geometry, flow over a cylinder and turbulent channel flow.
- Turbulent simulations were initiated in the complex Pratt & Whitney combustor. Also simulations were performed in a test rig geometry used by Pratt & Whitney for which experimental data is available.
- A spray module was integrated with the gas-phase solver. Validation simulations in a swiring coaxial combustor geometry Sommerfeld & Qiu (1991) were performed. Spray simulations in the Pratt & Whitney combustor were initiated.

3. Algorithm improvements

3.1. *Base algorithm*

Recall that the algorithm described at the end of last year's report stored pressure at the centroids of the elements, and velocity at their faces. As shown in figure 1, only the normal component of velocity was stored and advanced in time; the other two components were reconstructed. The velocity component v_n satisfied,

$$\frac{\partial v_n}{\partial t} - (\vec{u} \times \vec{\omega}) \cdot \vec{n} + \frac{\partial}{\partial n}\left(\frac{\vec{u} \cdot \vec{u}}{2}\right) = -\frac{1}{\rho}\frac{\partial p}{\partial n} + \nu \left(\nabla^2 \vec{u}\right) \cdot \vec{n}. \tag{3.1}$$

The convection term was written in terms of velocity and vorticity, and the pressure-projection approach was used to ensure that the velocity field was discretely divergence-free. As shown in last year's report, good results were obtained for laminar unsteady flows, and low Reynolds number turbulent flows in complex geometries.

† Aerospace Engineering and Mechanics, University of Minnesota

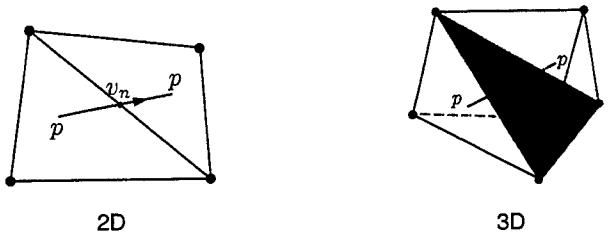

FIGURE 1. Positioning of variables in staggered algorithm.

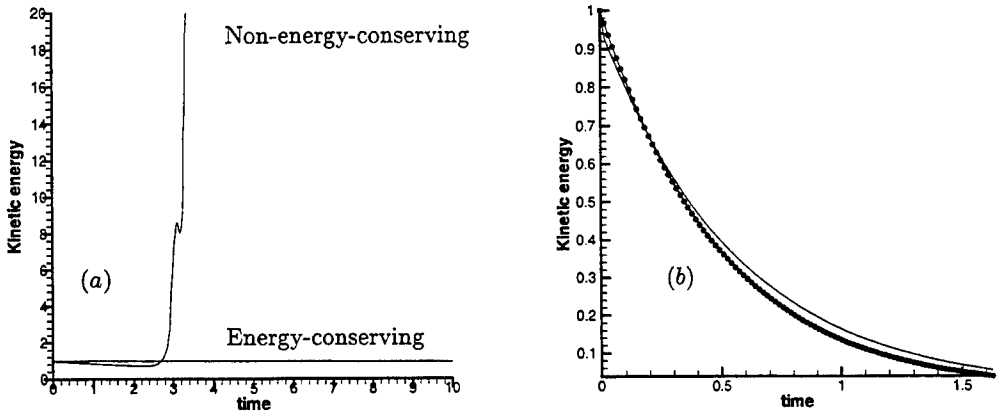

FIGURE 2. Illustration of the importance of discretely conserving kinetic energy. The kinetic energy is plotted against time for the Taylor problem at (*a*): $Re = 10^9$, and (*b*): $Re = 1$. At the lower Reynolds number, both schemes are stable. At higher Reynolds number, only the energy-conserving scheme is stable. The solid circles in (*b*) denote the analytical solution; the energy-conserving formulation passes through them.

However, problems with robustness were experienced this year when the simulations were extended to high Reynolds number, and to 'bad' grid elements that are inevitable in complex geometries such as the combustor geometry provided by Pratt & Whitney. It was established that the robustness problems were caused by the fact that the algorithm only conserved momentum, and not kinetic energy, on arbitrary grids with highly skewed elements.

An alternative formulation was derived, in which the convection term discretely conserves kinetic energy for arbitrary grids. Recall that discrete energy conservation refers to the fact that for incompressible flow, the convection term in the kinetic energy equation is expressible in divergence form, i.e. $\partial/\partial x_j\,(u_j u_i u_i/2)$. Conservation of momentum and the continuity equation ensure kinetic energy conservation for the continuous equations; however the same is not true for the discrete equations, where momentum conservation does not imply energy conservation. It is readily seen that kinetic energy conservation is a desirable feature for the algorithm since it implies that the L_2 norm is bounded.

The basic idea behind the new formulation is as follows. The traditional fractional-step algorithm on structured grids stores the face-normal velocity component on all faces. Control volumes are then identified around the faces, and the momentum equation for the velocity component is advanced in time. The primary reason for staggering is that

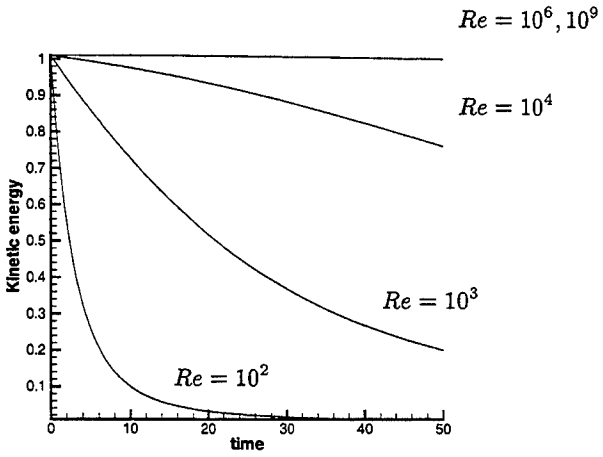

FIGURE 3. Kinetic energy of isotropic turbulence is plotted against time at varying Reynolds numbers. The Reynolds number is increased from $10^2, 10^3, 10^4, 10^6$ and 10^9 respectively. Note that the scheme is robust even at the highest Reynolds numbers.

the pressure equation does not suffer from odd-even decoupling. However, solution of the momentum equation requires that the velocity components tangential to the face be known. These are obtained through interpolation. The interpolant has to be carefully constructed such that the resulting momentum equation implies conservation of kinetic energy. There are two problems with extending this approach to arbitrary unstructured grids: (i) defining control volumes around the faces in three-dimensions is complicated; furthermore, skewed elements yield highly skewed control volumes. (ii) the resulting interpolation for the tangential velocities is unacceptably inaccurate if discrete energy conservation is required. We base these statements on actual computations performed using an energy-conserving formulation that we derived from a fully staggered formulation. The resulting formulation yielded acceptable results for Cartesian grids but was unacceptably inaccurate for the complex Pratt & Whitney combustor geometry.

An alternative formulation was therefore derived. Velocity and pressure are now stored at the centroids of the *volumes*. The cell-centered velocities are advanced in the predictor step such that kinetic energy conservation is ensured for the predictor step. These predicted velocities are then interpolated to the faces and then projected. Both interpolation and projection are robust procedures since they do not add energy to the solution (when the computational stencil uses local neighbors). Projection yields the pressure potential at the cell-centers, and the pressure gradient is used to correct the cell velocities. A straightforward use of the gradient theorem yields very good results on smooth grids, but is found unacceptable for highly skewed or very rapidly varying grids. This lack of robustness can be explained from an energy-conservation point of view. A novel discretization for the pressure gradient was derived. This formulation of the algorithm has been found to yield very good results for both 'simple' problems (Taylor problem, isotropic turbulence, channel, cylinder, coaxial combustor) as well as the exceedingly complex geometry of the Pratt & Whitney combustor.

The importance of discrete energy conservation is illustrated in Fig. 2, which shows the evolution of kinetic energy in the Taylor problem – an analytical solution, which describes counter-rotating vortices that decay in time. Our energy-conserving formulation is com-

Gas Phase (Air)		*Particle Phase (Glass)*	
Flow rate in primary jet, g/s	9.9	Loading Ratio in Primary Jet	0.034
Flow rate in secondary jet, g/s	38.3	Flow rate, g/s	0.34
Inlet Reynolds number	26200	Density ratio, ρ_p/ρ_f	2152
Swirl number	0.47		

TABLE 1. Flow conditions and particle properties used in the Sommerfeld & Qiu (1991) experiments.

pared to a non-dissipative formulation that only conserves momentum. Both formulations have the same computational stencil. At low Reynolds numbers, where the dissipative scales are resolved, both formulations are stable, although the energy-conserving formulation shows better agreement with the analytical result. However, at very high Reynolds numbers where the dissipative scales are not resolved, the formulation that does not conserve kinetic energy becomes unstable after some time, while the energy conserving formulation is seen to maintain its initial kinetic energy as required by the analytical solution. Figure 3 shows the decay of turbulent kinetic energy of isotropic turbulence when computed on a coarse grid (32^3). The Reynolds number is increased from 100 to 10^9. No subgrid model is used. Even the lowest Reynolds number is not completely resolved at this resolution. Note however that the solution does not become numerically unstable; instead it exhibits the proper Reynolds number sensitivity (reduced decay rate with increasing Reynolds number). It is this robustness that makes accurate LES of high Reynolds number flows possible.

3.2. *Integration with spray modules*

The gas-phase solver was extended to include the effect of liquid droplets. The droplets are modeled as point particles which satisfy Lagrangian equations. They influence the gas phase through source terms in the gas-phase equations. As the particles move, their position is located and each particle is assigned to a control volume of the gas-phase grid. The gas-phase properties are interpolated to the particle location and the particle equations are solved. The particles are then relocated, particles that cross interprocessor boundaries in our parallel computaton are duly transferred, source terms in the gas-phase equation are computed, and the computation is further advanced. Spray integration involves the following key issues: (i) Efficient search and location of droplets on an unstructured grid (ii) Interpolation of gas-phase properties to the droplet location for arbitrarily shaped control volumes (iii) inter-processor droplet transfer.

3.2.1. *Locating particles in elements of arbitrary shape*

Locating particles in a generalized-coordinate structured code is straightforward, since the physical coordinates can be transformed into a uniform computational space. However, this is not the case for unstructured grids. Westermann (1992) describes several

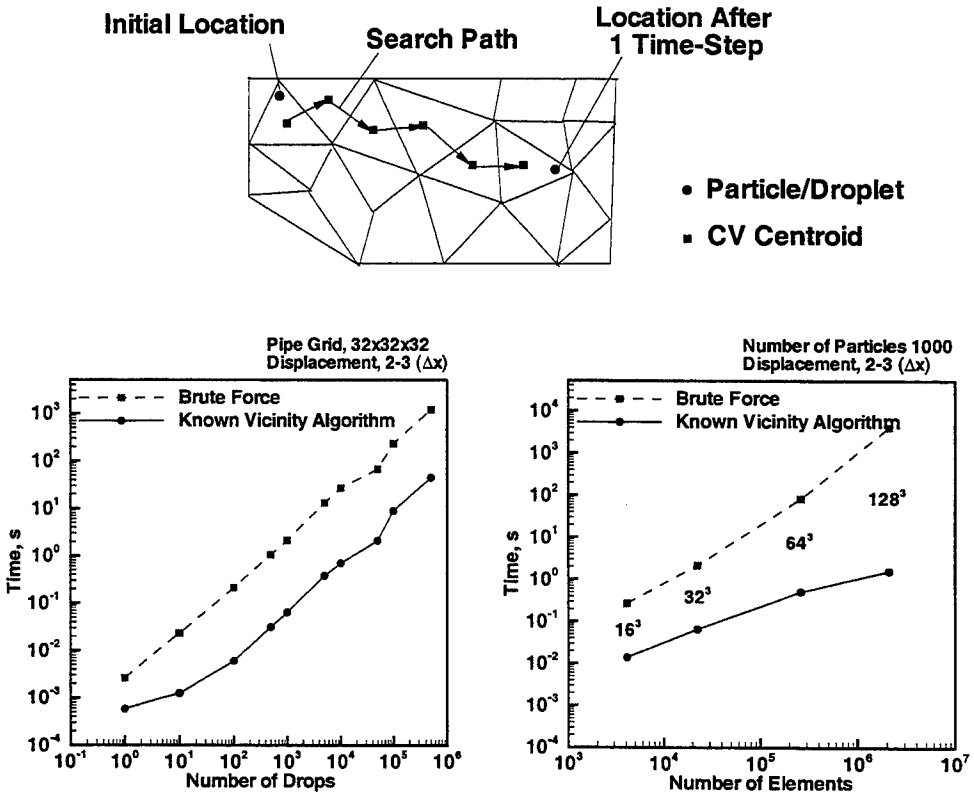

FIGURE 4. (*a*) Schematic of the known-vicinity algorithm to track particle positions on unstructured grids. (*b*) Comparison of the brute force and known vicinity search algorithms.

approaches to locate particles in particle-in-cell codes. Two such techniques are implemented in the unstructured code, and are described below.

One approach to determining whether a particle lies inside a control volume is based on the calculation of partial volumes. The nodes of the control volume are joined to the particle location, and the volumes of the resulting sub-cells are compared to that of the control volume. If the particle lies inside the control volume, the sum of the sub-cell volumes will be equal to the total volume. The advantage of this method is that it can be applied to all control volumes simultaneously and a separate search algorithm for particle location is not required. However, the method is slow since it involves computations of partial volumes for each cell. Also, it was found to fail drastically for highly skewed meshes due to inaccuracies in the computation of partial volumes.

The second approach projects the particle location onto the faces of the control volume and compares these vectors with outward face-normals for all faces. If the particle lies within the cell, the projected vectors point the same way as the outward face-normals. This technique, although more accurate, requires a search algorithm to select the control volume to which the criterion is applied.

3.2.2. *Search algorithms for particles on unstructured grids*

Three approaches were examined and are termed the brute-force, modified-brute-force and known-vicinity approaches respectively. The brute-force approach simply loops over

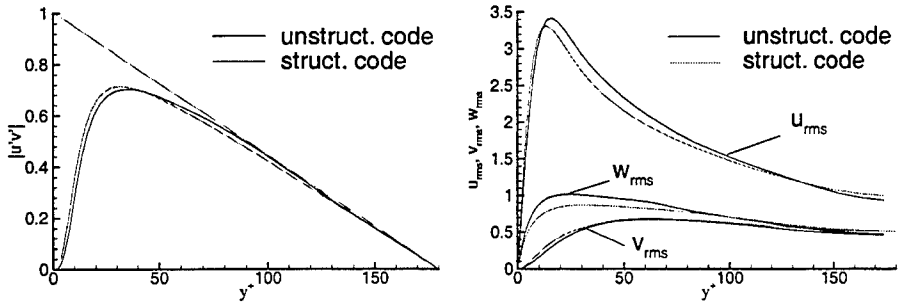

FIGURE 5. Comparison of the unstructured solver to a structured solver using the same grid. Results correspond to turbulent Reynolds stresses in a turbulent channel at $Re_\tau = 180$ on a coarse ($32 \times 64 \times 32$) grid. The structured grid results were kindly provided by Dr. Bill Cabot, Lawrence Livermore National Laboratory.

all the elements of the grid and applies the localization criterion described above. As expected, it is extremely slow when particles number about a million, as is the case even for coarse LES. The modified-brute-force approach evaluates the closest point of the mesh to the particle location and only considers the elements surrounding that point. Should this attempt (which in general is very successful) fail, the elements surrounding all the close points are considered. If this also fails for some pathological cases Lohner (1995), the search region is enlarged or the brute-force method is applied. This modified approach is found effective to initialize particles, and as a fall-back position for more refined algorithms.

Given a good initial guess for a particle location, the known-vicinity algorithm outperforms all others Lohner (1995). Particle location at earlier time-steps provide a very good initial guess in LES. Knowing the initial and final location of the particle, this algorithm searches in the direction of the particle motion until it is relocated (Fig. 4). The neighbor-to-neighbor search is extremely efficient if the particle is located within 10-15 attempts, which is usually the case for 90% of the particles in present simulations. If this algorithm fails, we fall back to the 'modified-brute-force' method to locate the particle. A combination of these two algorithms is found highly efficient and robust for complex geometries and hybrid meshes encountered in realistic combustor geometries.

The known-vicinity algorithm is compared to the modified-brute-force method in Fig. 4. Two cases are considered: (i) domain size is fixed, and the particles are displaced for 2-3 cell-sizes in all three coordinate directions, (ii) the number of particles is kept fixed (1000 particles) and the element size per processor is increased. The known-vicinity approach is seen to be noticeably better than the modified-brute-force approach. Note that these comparisons were performed on a single processor of an Origin 2000.

Least-squares interpolation is used to interpolate gas-phase properties linearly each to particle location. Also particles that cross interprocessor boundaries are assigned to the ghost control volumes of the gas-phase solver, and then passed across processors.

4. Validation

The gas-phase solver was validated for a variety of benchmark flows: Taylor problem, isotropic turbulence, turbulent channel flow, flow over a cylinder, and the turbulent flow in a coaxial combustor. The simulations in the coaxial combustor geometry also included

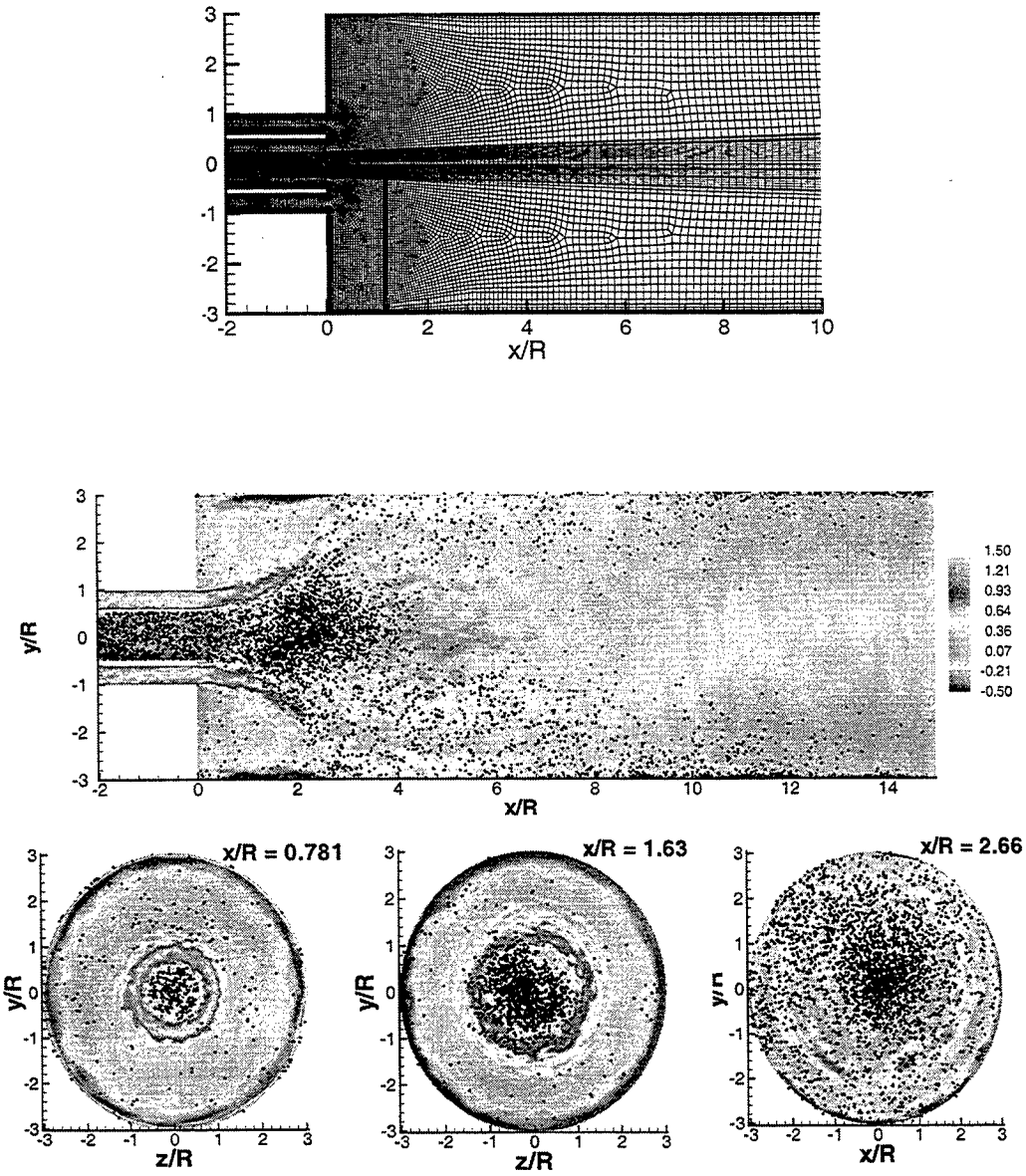

FIGURE 6. Cross-section of the grid and particles superposed on contours of instantaneous axial velocity in LES of the flow in a coaxial combustor geometry. Conditions correspond to an experiment by Sommerfeld & Qiu (1991). Only part of the computational domain is shown for clarity.

particles. The purpose of these validation studies was to establish that the algorithm can accurately simulate turbulence, is robust at high Reynolds numbers and on 'bad' grids, and has accuracy is comparable to that of structured grid solvers that use the same grid and computational stencil. Some of these validation cases are reported below.

Figure 5 shows results from computations of turbulent channel flow at $Re_\tau = 180$ on a very coarse grid ($32 \times 64 \times 32$). No subgrid model was used. Despite its simplicity, channel flow is known to be very sensitive to errors arising from the non-linear terms. On very

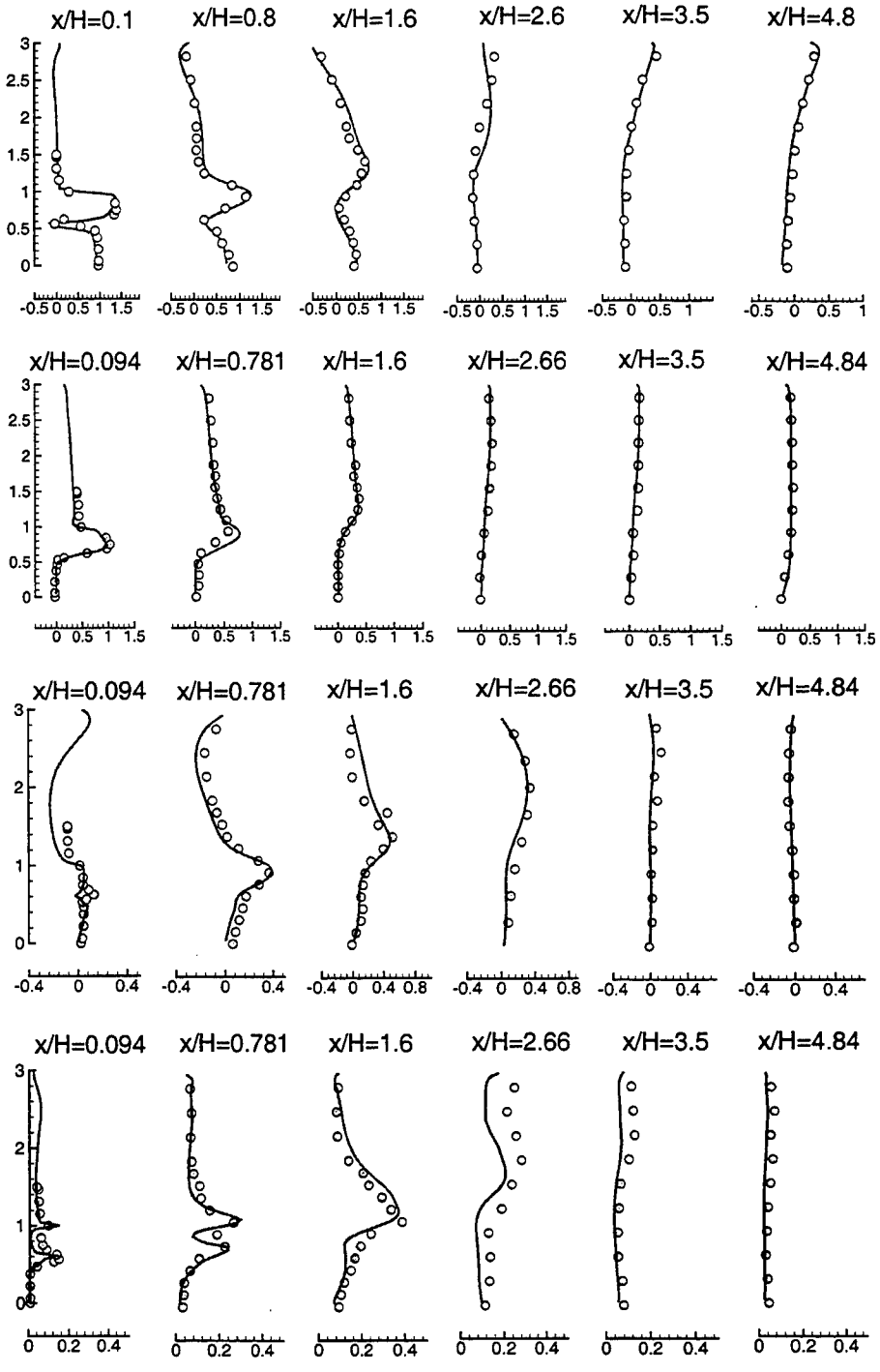

FIGURE 7. Comparison between LES (———) and experiment (∘), Sommerfeld & Qiu (1991) for the gas-phase of particle-laden swirling flow in a coaxial combustor. (*a*): mean axial velocity, (*b*): mean swirl velocity, (*c*): mean radial velocity, (*d*) turbulent kinetic energy.

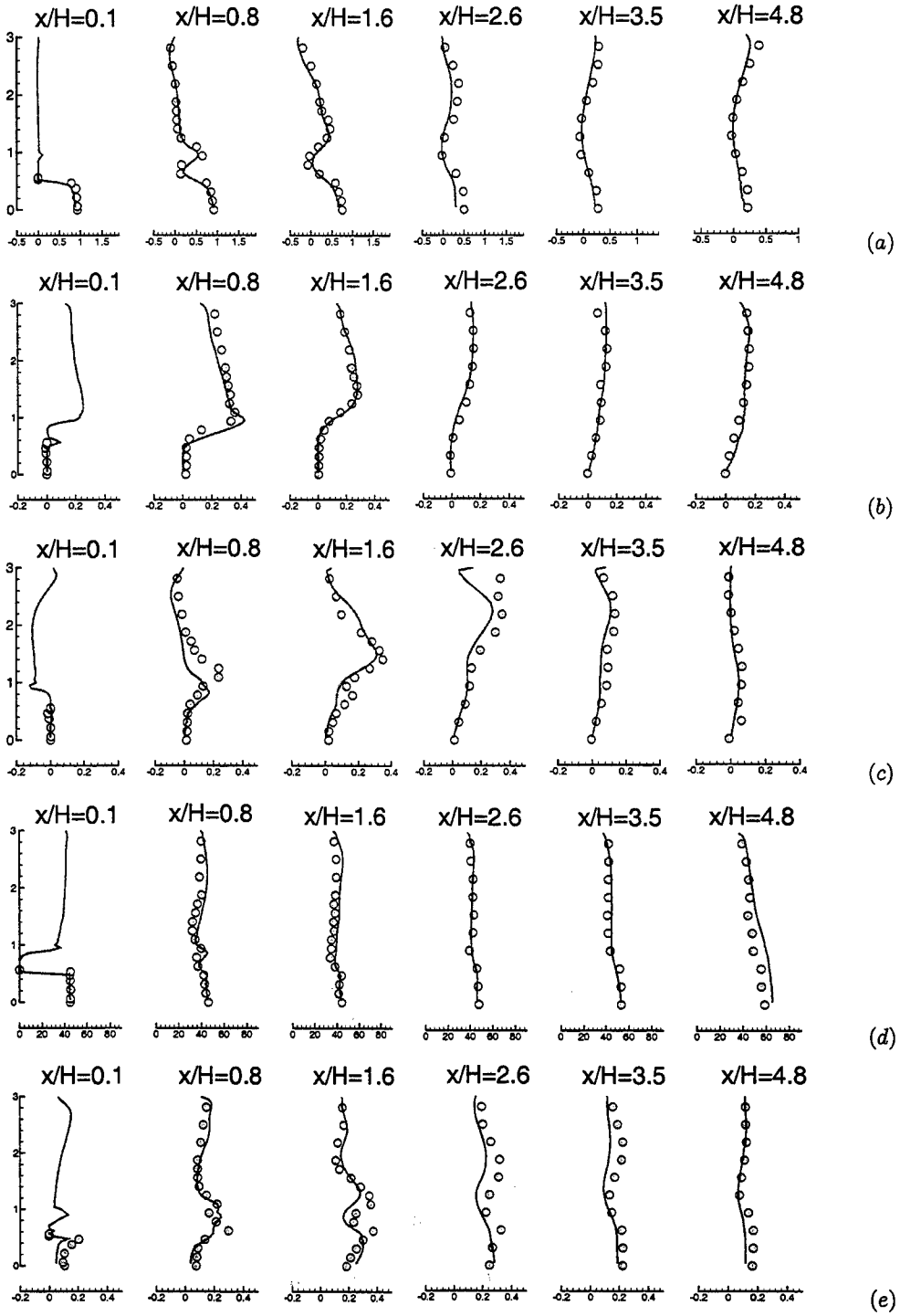

FIGURE 8. Comparison between LES (———) and experiment (o), Sommerfeld & Qiu (1991) for the particle-phase of swirling flow in a coaxial combustor. (*a*): mean particle axial velocity, (*b*): mean particle swirl velocity, (*c*): mean particle radial velocity, (*d*) mean particle diameter, (*e*) rms of particle axial velocity.

coarse grids, the turbulence in the channel can either decay or the entire solution can blow-up depending upon the numerical algorithm used. We compare our results to those provided by Dr. Bill Cabot (Lawrence Livermore National Laboratory) from a structured solver using the second-order staggered grid and fractional step approach on the same grid. The comparison shows that the accuracy of the unstructured algorithm is nearly the same as a structured solver for structured grids.

The flow in a swirl-stabilized coaxial combustor represents an important validation case. Sommerfeld & Qiu (1991) provide detailed measurements of this flow, which tests both the gas-phase solver and the spray module. A cross-section of the geometry and the unstructured mesh used for simulating this particle-laden flow is shown in Fig. 6. The flow is from left to right, and consists of a primary jet issuing out of the core, and a swirling jet issuing out of the annulus. The primary jet is laden with glass beads whose diameter varies from 20 microns to 80 microns. Detailed flow conditions and particle properties are summarized in Table 1. As a result of the swirl, the streamlines diverge as they exit into the dump region, and a recirculation region is set up (Fig. 6). The computations used an unstructured grid composed of approximately 2 million hexahedral elements. Turbulent fluctuations from a separate calculation are specified at the inflow and convective boundary conditions are imposed at the exit. The dynamic subgrid model was used. At the time of writing, flow statistics for the gas- and particle-phases have been computed. Figure 7 compares computed profiles of mean and turbulent gas-phase velocities with experiment, while Fig. 8 compares the corresponding particle statistics. In addition, variation of mean particle diameter is also compared. Good agreement is observed.

5. Simulations in Pratt & Whitney combustor

Validation calculations are being performed in the combustor of the PW6000 engine. These calculations are seen as a prerequisite to integrating the unstructured solver with the turbomachinery code. As shown in Fig. 9, the geometry of the PW6000 combustor is exceedingly complex, and poses serious challenges to both grid-generation and the solver. These simulations are being performed in two steps: (i) mixing of a passive scalar by cold flow (ii) introduction of heat release. The cold flow calculation is in progress, and results are reported below. Validation data is available for bulk quantities such as mass-splits and pressure drops for this case. Cold flow simulations are also being performed in a simpler configuration, termed the front-end validation model. This geometry has exactly the same fuel injector and combustion chamber as the PW6000 combustor, but is fed by a cylindrical plenum and does not have dilution holes (Fig. 13). It is being simulated because detailed LDV measurements are available from Pratt & Whitney. Note that the injector is the most geometrically complex component of the entire combustor. Quantitative validation for the front-end model will therefore establish considerable confidence in the results obtained for the PW6000 combustor.

5.1. *Grid generation*

A commercial grid generator (GAMBIT, Fluent Corporation) was used for grid generation. Both geometries (the PW6000 combustor and front-end validation model) were received from Pratt & Whitney as IGES files. The PW6000 geometry contained more than 9000 entities (surfaces, edges, vertices) which were cleaned up and reduced to 1200 entities. As shown in Fig. 9, the combustor chamber is fed by three coaxial swirlers and several dilution holes. The inlet air passes through the pre-diffuser and follows two

paths; the main stream flows through the swirlers and enters the chamber, while the secondary stream is diverted to the outer diffusers and enters the combustor through the dilution holes. Diversion of the outer diffuser air to secondary systems, and transpiration air through the liners of the main combustor, were not considered in the computations reported here; they are currently being included. The computational domain was divided into about 100 volumes for grid-generation; hexahedral meshes were generated over about 85% of the volumes. Tetrahedral meshes were generated for the swirlers, and pyramids were used to connect tetrahedral and hexahedral elements. An initial coarse grid has been generated; it contains about 1.3M elements (0.6M tetrahedra, 0.65M hexahedra). Figure 9 shows the grid. The level of geometrical complexity is obvious. Also note that the coarse grid consists of highly-skewed elements with rapid variations in element size and type. Figure 13 shows a schematic of the grid generated for the front-end validation model. The procedure described above was used to generate two grids: coarse (2.2M elements) and fine (4.5M elements).

5.2. *Results*

The flow conditions for the PW6000 combustor simulations are as follows. The flow into the pre-diffuser of the PW6000 is at a bulk Reynolds number of 500,000, which corresponds to a Reynolds number of approximately 150,000 in the main swirler, based on the diameter and flow rate through the swirler. Turbulent fluctuations from a separate computation in a pipe sector are specified at the inflow, and convective boundary conditions are specified at the exit. The flow in the domain was initialized to be at rest. Statistics were gathered after initial transients exited the domain.

The first computation performed in this geometry was at a very low Reynolds number of 1000, and did not include a subgrid model. Its objective was to assess the ability of the algorithm to handle a geometry with this level of complexity, and a mesh with extreme variations in size and element skewness. It was found that while geometrical complexity was adequately handled, 'bad' regions of the mesh posed severe problems. These problems were explained from energy-conservation principles, and the above-mentioned novel discretization was derived for the pressure gradient. This fundamental change in the algorithm has proven to be extremely successful in terms of its ability to handle complex geometries, high Reynolds numbers, and bad grids.

Figure 10 shows contour plots of both instantaneous and mean flow-fields in the PW6000 combustor. The flow in the diffuser is seen to be attached, it then passes smoothly through regions where the mesh rapidly changes, swirl is generated by the swirlers, and the flow in the dump region is determined by the interaction between the swirling primary jets and the dilution jets. Also shown in Fig. 11 are velocity contours from a computation on the same grid at the significantly lower inlet Reynolds number of 1000. No subgrid model was used in the low Reynolds number computations, while the high Reynolds number computations used the Smagorinsky model. The results at low Reynolds number are seen to be strikingly different, in that no recirculation region is seen downstream of the injector; instead the primary flow is jet-like. This behavior can be explained on physical grounds; the swirl that is generated by the swirler decays in the channel downstream of the swirler before the flow exits into the dump region. The decay rate of swirl is determined by the viscosity. At low Reynolds number, the decay of swirl

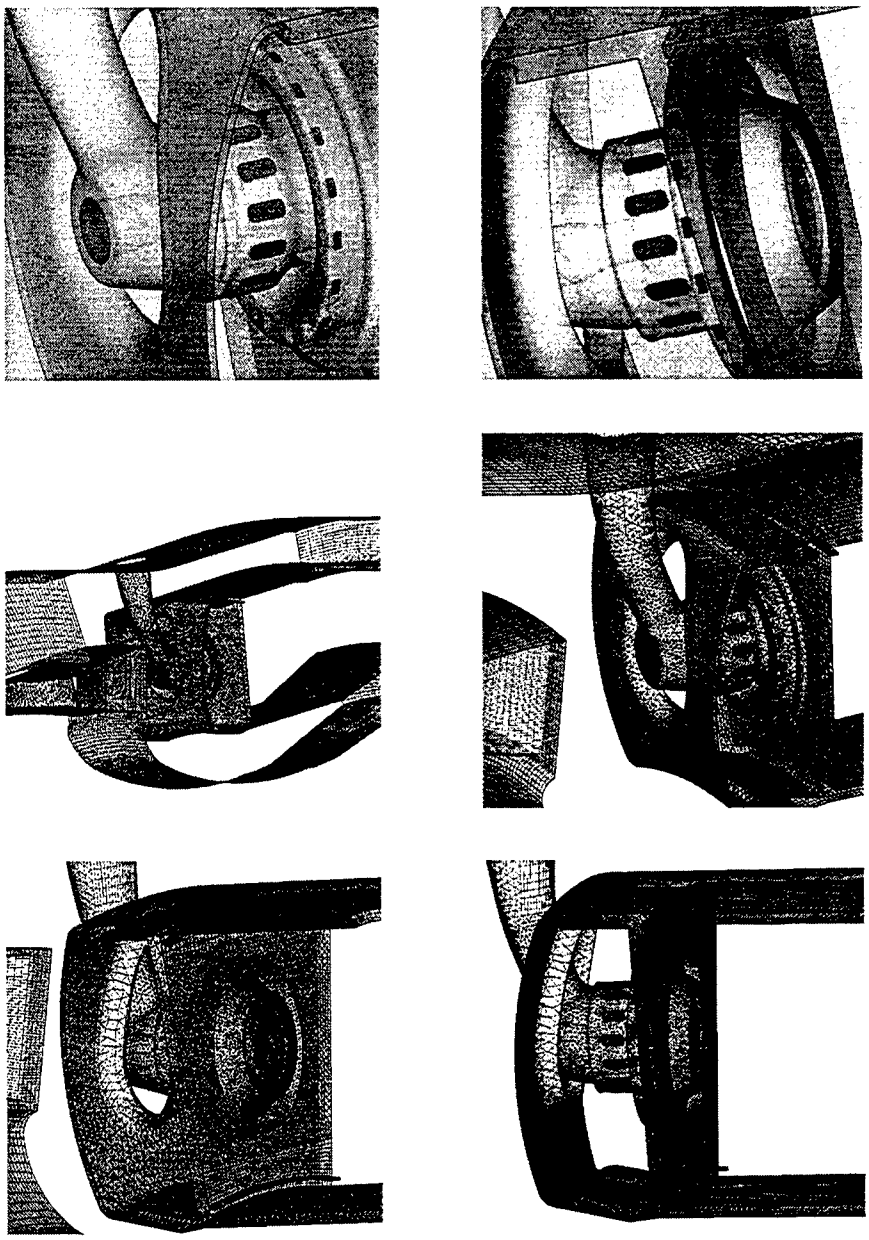

FIGURE 9. Illustration of the geometry and surface mesh in the PW6000 combustor geometry.

is significant enough that the exiting jet has negligible levels of swirl, and as a result no recirculation region is formed. On the other hand, at high Reynolds number the swirl velocity does not decay very much in the channel and, as a result, the exiting swirling jets diverge and a recirculation region is formed. This Reynolds-number sensitivity observed on a coarse grid is very encouraging, and reinforces the importance of having an algorithm that is robust without being dissipative.

The computations in the PW6000 geometry did not include the effect of outer-diffuser air being diverted to secondary systems, and transpiration air through the liner of the

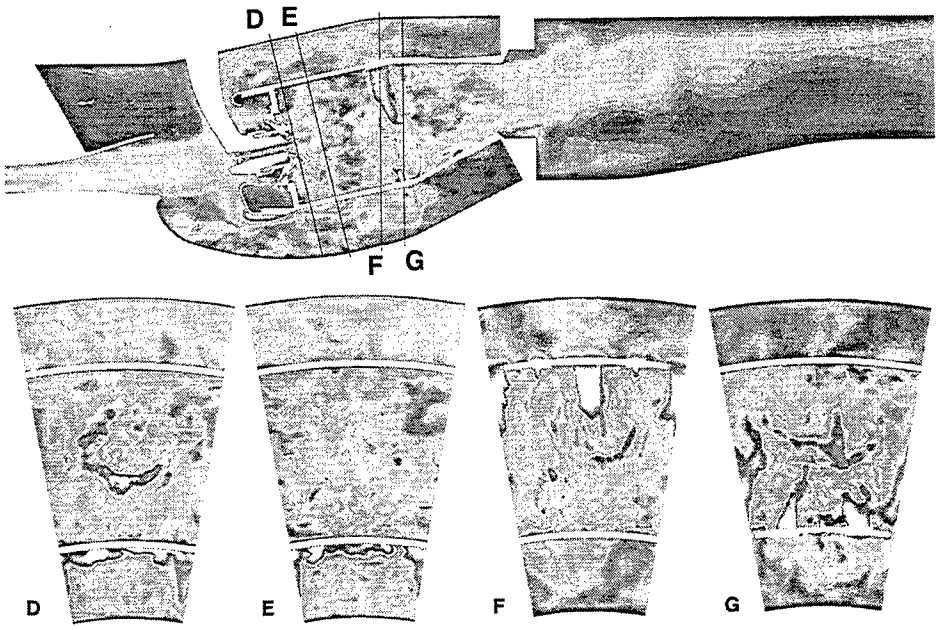

FIGURE 10. Contours of instantaneous velocity magnitude in LES of flow in the PW6000 combustor geometry.

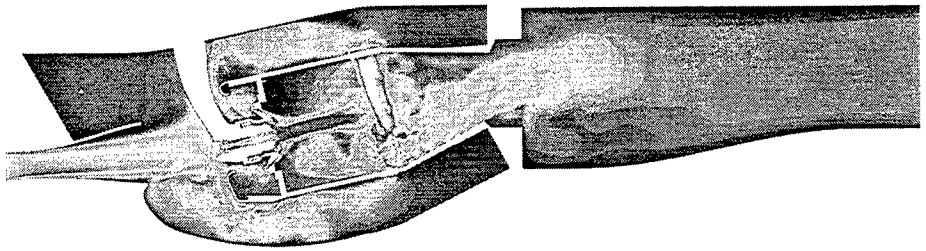

FIGURE 11. Contours of instantaneous velocity magnitude in the PW6000 combustor at a low inlet Reynolds number of 1000. Notice that flow downstream of the injector is jet-like instead of showing recirculation as in the high Reynolds number results shown above.

combustor. These effects have now been included, and a computation on the same grid is in progress. These results will be compared to bulk data like mass flow splits and mean pressure drops that will be made available by Pratt & Whitney. Also, computations are underway with particles; an instantaneous snapshot is shown in Fig. 12.

The front-end validation model is an important validation case because it uses the same injector as the PW6000 simulation. LDV data is available at three stations downstream of the injector. The Reynolds number in the main injector is approximately 100,000 in these computations. Figure 13 shows a schematic of the grid and contours of the velocity field. Two grids were generated: coarse (2.2M elements) and fine (4.5M elements). Simulations on the coarse grid have been performed, and used to initialize the fine grid computation which is underway. Statistics are being gathered on the fine grid at the time of writing. The mean pressure drop across the injector has converged, and shows very

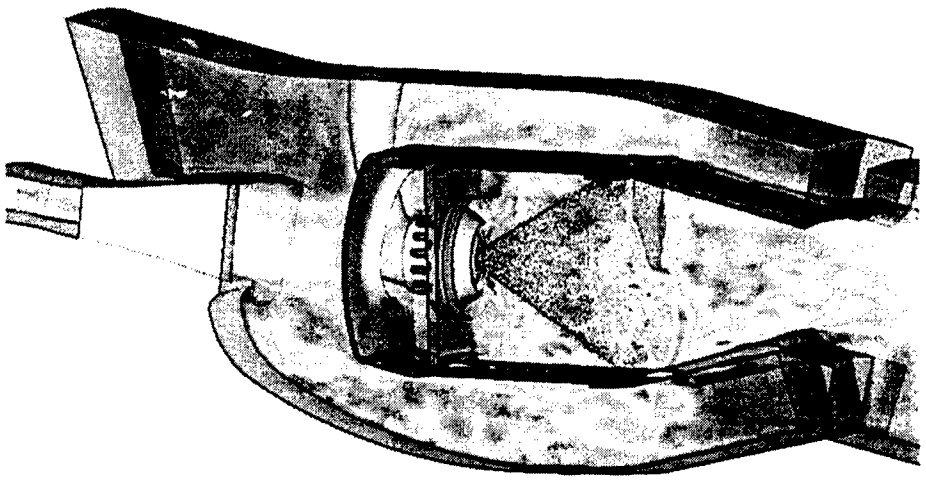

FIGURE 12. Instantaneous snapshot of particles superposed on velocity contours in PW6000 combustor geometry.

good agreement with experiment (4588 Pa as compared to 4500 Pa). In contrast, a RANS computation was performed on the same grid and found to yield a much higher drop of 5660 Pa. More detailed comparison will be performed once all quantities are converged.

6. Summary and future plans

Our progress in the last year is as follows:

- A new formulation was derived that is discretely energy-conserving for arbitrary grids. This was found essential for performing simulations at high Reynolds number simulations, and on the 'bad' grids found in complex geometries such as the Pratt & Whitney combustor.
- Turbulent validations were performed for the swirling flow in a coaxial combustor geometry, flow over a cylinder and turbulent channel flow.
- Turbulent simulations were initiated in the complex Pratt & Whitney combustor. Also, simulations were performed in a test rig geometry used by Pratt & Whitney for which experimental data is available.
- A spray module was integrated with the gas-phase solver. Validation simulations in a swiring coaxial combustor geometry Sommerfeld & Qiu (1991) were performed. Spray simulations in the Pratt & Whitney combustor were initiated.

Our plans for the next year are as follows:

- Complete validation in the front-end model.
- Complete validated simulations, including transpiration and secondary flows, in the PW6000 geometry.
- Perform reacting flow simulations in the PW6000 geometry.
- Extend the spray models to include droplet evaporation and spray-sheet break-up.

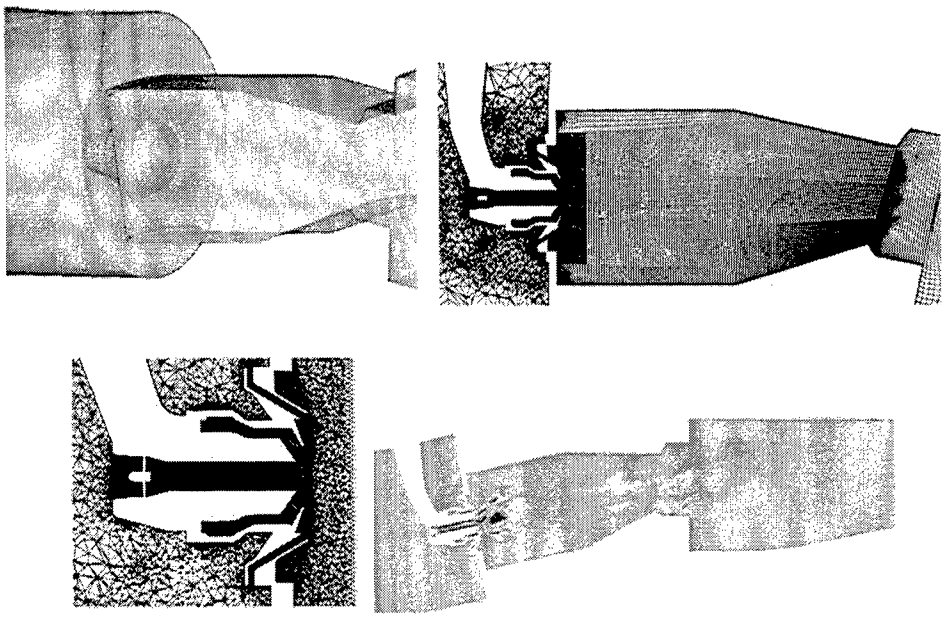

FIGURE 13. Illustration of the front-end validation model geometry, the grid, and instantaneous contours of streamwise velocity.

Acknowledgments

We would like to acknowledge Dr. Joseph C. Oefelein for his generous help in providing the spray modules developed for structured grids. Financial support for this work is provided by the Department of Energy's ASCI program.

REFERENCES

LOHNER, R. 1995 Robust, vectorized search algorithms for interpolation on unstructured grids. *J. Comp. Phys.* **101**, 307-313.

PIERCE, C. & MOIN, P. 2001 The progress variable approach for large eddy simulation of turbulent combustion. *Report TF-80*, Mech. Engg. Dept., Stanford Univ.

SOMMERFELD, M. & QIU, H. H. 1991 Detailed measurements in a swirling particulate two-phase flow by a phase-Doppler anemometer. *Int. J. Heat and Fluid Flow* **12**, 20-28.

WESTERMANN, T. 1992 Localization schemes in 2D boundary-fitted grids. *J. Comp. Phys.* **101**, 307-313.

Consistent boundary conditions for integrated LES/RANS simulations: LES outflow conditions

By J. U. Schlüter and H. Pitsch

1. Motivation

Numerical simulations of complex large-scale flow systems must capture a variety of physical phenomena in order to predict the flow accurately. Currently, many flow solvers are specialized to simulate one part of a flow system effectively, but are either inadequate or too expensive to be applied to a generic problem.

As an example, the flow through a gas turbine can be considered. In the compressor and the turbine section, the flow solver has to be able to handle the moving blades, model the wall turbulence, and predict the pressure and density distribution properly. This can be done by a flow solver based on the Reynolds-Averaged Navier-Stokes (RANS) approach. On the other hand, the flow in the combustion chamber is governed by large scale turbulence, chemical reactions, and the presence of fuel spray. Experience shows that these phenomena require an unsteady approach (Veynante & Poinsot, 1996). Hence, the use of a Large-Eddy Simulation (LES) flow solver is desirable.

While many design problems of a single flow passage can be addressed by separate computations, only the simultaneous computation of all parts can guarantee the proper prediction of multi-component phenomena, such as compressor/combustor instability and combustor/turbine hot-streak migration. Therefore, a promising strategy to perform full aero-thermal simulations of gas-turbine engines is the use of a RANS flow solver for the compressor sections, an LES flow solver for the combustor, and again a RANS flow solver for the turbine section (Fig. 1).

2. Interface Treatment

The simultaneous computation of the flow in all parts of a gas turbine with different flow solvers requires an exchange of information at the interfaces of the computational domains of each part. The necessity for information exchange in the flow direction from the upstream to the downstream flow solver is self-explanatory: the flow in a passage is strongly dependent on mass flux, velocity vectors, and temperature at the inlet of the domain. However, since the Navier-Stokes equations are elliptic in subsonic flow, the downstream flow conditions can have a substantial influence on the upstream flow development. This can easily be imagined by considering that, for instance, a flow blockage in the turbine section of the gas turbine can affect and even stop the flow through the entire engine. This means that the information exchange at each interface has to go in both, downstream *and* upstream, directions.

Considering an LES flow solver computing the flow in the combustor, information on the flow field has to be provided to the RANS flow solver computing the turbine as well as to the RANS flow solver computing the compressor, while at the same time, the LES solver has to obtain flow information from both RANS flow solvers (Fig. 2). The coupling can be done using overlapping computational domains for the LES and RANS

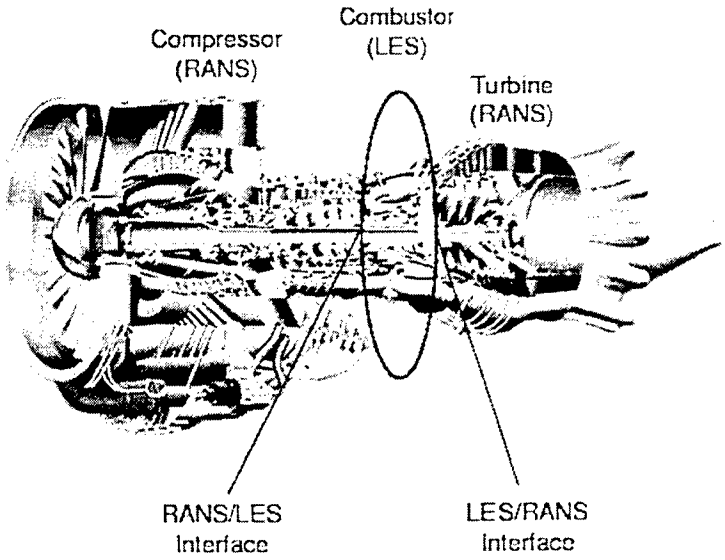

FIGURE 1. Gas turbine engine

simulations. For the example of the combustor/turbine interface this would imply that inflow conditions for RANS will be determined from the LES solution at the beginning of the overlap region, and correspondingly the outflow conditions for LES are determined from the RANS solution inside the overlap region.

However, the different mathematical approaches of the different flow solvers make the coupling of the flow solvers challenging. Since LES resolves large-scale turbulence in space and time, the time step between two iterations is relatively small. RANS flow solvers average all turbulent motions over time and predict ensemble averages of the flow. Even when a so-called unsteady RANS approach is used, the time step used by the RANS flow solver is still much larger than that for an LES flow solver.

The specification of boundary conditions for RANS from LES data is relatively straightforward. The LES data can be averaged over time and used as boundary condition for the RANS solver. The problem of specifying inflow conditions for LES from upstream RANS data is similar to specifying LES inflow conditions from experimental data, which is usually given in time averaged form, and has therefore been investigated in some detail. A method that has been successfully applied in the past, is, for instance, to generate a time-dependent database for inflow velocity profiles by performing a separate LES simulation, in which virtual body forces are applied to achieve the required time-averaged solution (Pierce & Moin, 1998b).

In the present study the remaining flux of information from a downstream RANS computation to an upstream LES computation is investigated. LES computations have already shown that the flow can be sensitive to the outflow conditions (Moin, 1997, Pierce & Moin, 1998a). The outflow conditions for LES have to be specified such that the time-averaged mean values of all computed quantities match the RANS solution at a given plane, but the instantaneous solution at the outflow still preserves the turbulent fluctuations.

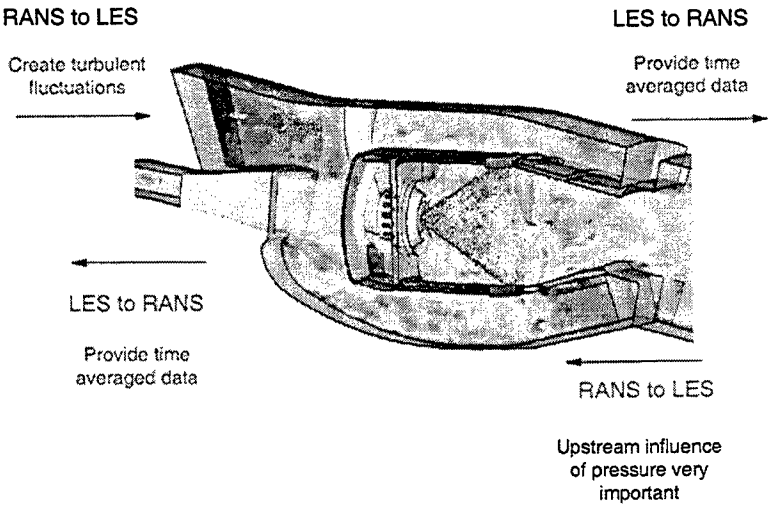

FIGURE 2. Gas turbine combustor with interfaces

3. Formulation of the outflow boundary treatment

Modern LES flow solvers are often based on a low-Mach-number formulation. With this approximation, acoustic pressure fluctuations are neglected and the hydrodynamic pressure variations are determined by a Poisson equation. This formulation makes it impossible to prescribe the pressure at the outlet of the LES domain directly. Instead, only the velocities or their derivatives can be specified as boundary conditions in the LES flow solver, and the pressure adjusts accordingly. The mean velocity profiles are enforced by adding a virtual body force to the right-hand side of the momentum equations inside the overlap region of the computational domains of the LES and the RANS flow solver. For a constant-density flow which is stationary in the mean, the body force is given by

$$F_i(\boldsymbol{x}) = \frac{1}{\tau_{\mathrm{F}}}(\bar{u}_{i,\mathrm{RANS}}(\boldsymbol{x}) - \bar{u}_{i,\mathrm{LES}}(\boldsymbol{x}))\,, \tag{3.1}$$

where $\bar{u}_{i,\mathrm{RANS}}$ is the vector of target velocities obtained from the RANS computation and $\bar{u}_{i,\mathrm{LES}}$ is the vector of time-averaged velocities from the LES computation. The forcing time scale τ_{F} can, to first order, be determined from the bulk velocity u_{B} and the length of the forcing region l_{F} as $\tau_{\mathrm{F}} = l_{\mathrm{F}}/u_{\mathrm{B}}$. Experience shows that the forcing time is usually much lower than this estimate, so that this can serve as an upper limit. For numerical purposes a convective boundary condition is applied at the outlet plane of the LES domain.

The forcing term in Eq. (3.1) involves only mean velocities, while the corresponding momentum equation is solved for the instantaneous velocities. Thus the mean velocities from the LES simulation are corrected without attenuating the resolved turbulent fluctuations. It will be shown later that, to achieve this goal, the averaging time for $\bar{u}_{i,\mathrm{LES}}$ needs to be longer than the characteristic times of the turbulence. Equation (3.1) also shows that the forcing term tends to zero if the actual mean velocity from the LES approaches the target velocity, which is a consistency requirement. Note also that the RANS velocities are prescribed not only in one plane, but in the entire overlap region.

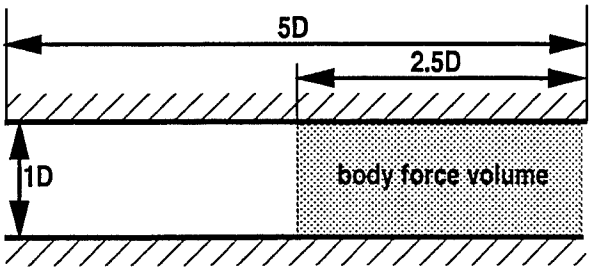

FIGURE 3. Geometry of the pipe geometry

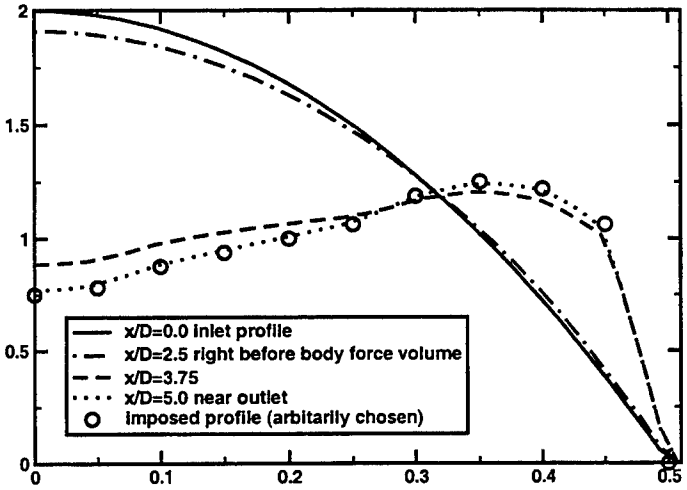

FIGURE 4. Laminar pipe flow: radial profiles of axial velocity component $\tilde{u}_x$

4. LES Flow Solver

For the current investigation, the LES flow solver developed at the Center for Turbulence Research (Pierce & Moin, 1998a) has been used. The flow solver solves the filtered momentum equations with a low-Mach-number assumption on an axisymmetric structured mesh. A second-order finite-volume scheme on a staggered grid is used (Akselvoll & Moin, 1996).

The subgrid stresses are approximated with an eddy-viscosity approach. The eddy viscosity is determined by a dynamic procedure (Germano *et al*, 1991; Moin *et al*, 1991).

5. Numerical experiment: pipe-flow geometry

In order to prove the feasibility and the well-posedness of this approach a pipe flow has been computed (Fig. 3). The pipe has a length of five times the diameter D and the virtual body force is applied in a volume of length $2.5\,D$ at the end of the pipe flow. The mesh consists of 128×32×64 cells.

As a first step, a laminar pipe flow at a Reynolds number Re=1000 is considered. Fig. 4 shows the resulting velocity profiles. The solid line shows the parabolic inlet profile corresponding to the solution of a fully-developed pipe flow. Without forcing, this would be the solution at any downstream location in the pipe. The circles denote an arbitrarily-chosen velocity profile, with the same mass flow rate as the inlet profile, which is to be

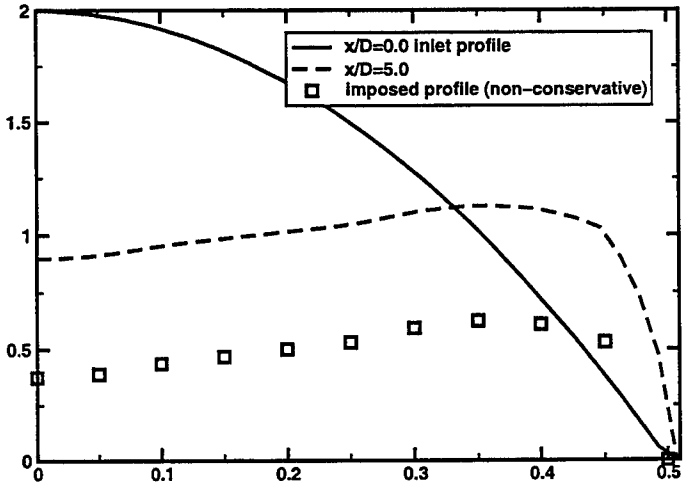

FIGURE 5. Laminar pipe flow with non-conservative velocity profile imposed

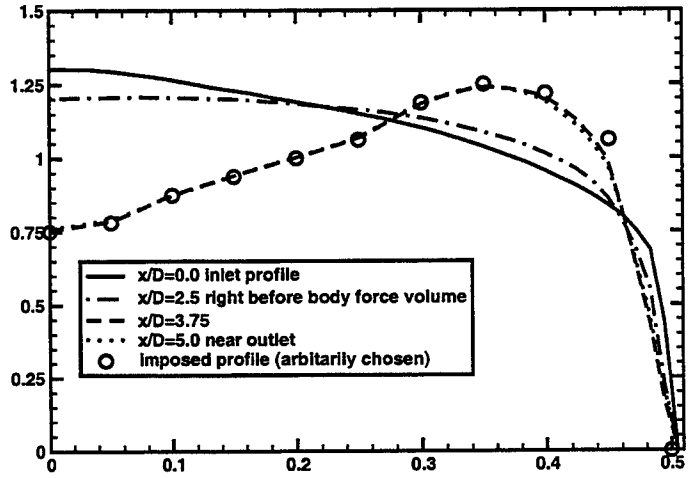

FIGURE 6. Turbulent pipe flow, radial profiles of axial velocity component $\bar{u}_x$

matched at the outlet. The dash-dotted line is a profile just upstream of the forcing region. The profile is different from the inflow solution, indicating that forcing influences the flow field even upstream of the forcing region. After applying the virtual body force, the computed velocity profile quickly converges towards the imposed velocity profile.

An important test for consistency and well-posedness is the enforcement of a velocity profile which does not conserve mass. The exchange of the velocity profiles between RANS and LES flow solver may introduce numerical errors, especially due to the interpolation between two different meshes, which could accumulate over time. In order to investigate the behavior of the proposed LES outflow conditions when encountering this problem, an additional computation was made, where a "non-conservative" velocity profile, with a different mass flow rate, was enforced. Fig. 5 shows the resulting velocity profiles. The squares denote the imposed velocity profile, which clearly underestimates the mass flux. However, the computed velocity profile at the end of the forcing region has the same

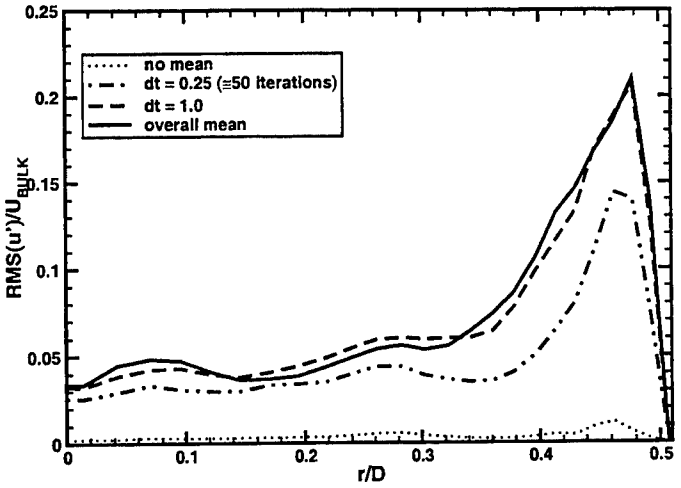

FIGURE 7. Turbulent pipe flow: radial profiles of axial velocity fluctuations $\sqrt{\overline{u'^2}}$ for different averaging time-span

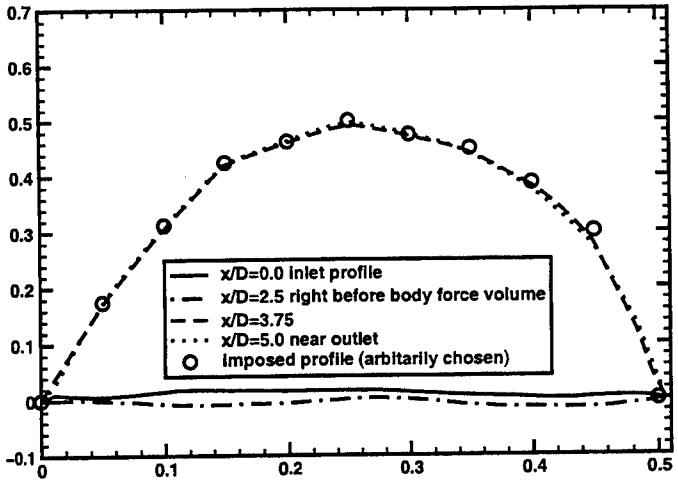

FIGURE 8. Turbulent pipe flow, radial profiles of azimuthal velocity component $\bar{u}_\phi$

mass flux as the inlet profile. This shows that the method is robust against inaccuracies resulting from the exchange of velocity profiles.

The next test case considered here is a turbulent pipe flow at a Reynolds number Re = 15000. Applying the proposed correction of the LES outflow by virtual body forces to this problem leads to the question of how to define the mean value $\bar{u}_{\text{LES}}$ of the LES computation. Several approaches have been tested:

(*a*) Using the actual velocity $\bar{u}_{\text{LES}} = u(t)$. This results in a strong damping of turbulent fluctuations, since fluctuations of the velocity obviously lead to a counteracting virtual body force.

(*b*) Using the overall mean value $\bar{u}_{\text{LES}} = \frac{1}{t-t_0}\int_{t_0}^{t} \bar{u}\, dt$. This ensures the least interference with turbulent fluctuations, but does not allow for unsteadiness in the mean profiles.

(*c*) Averaging over a trailing time window $\bar{u}_{\mathrm{LES}} = \frac{1}{\Delta t} \int_{t-\Delta t}^{t} \bar{u}\, dt$. Here it has to be ensured that Δt is long enough to average the turbulent fluctuations, but short enough to allow for unsteadiness of the mean profiles.

All approaches result in the same mean velocity field (Fig. 6). Since the turbulent velocity profile is already closer to the imposed profile than in the laminar case, the flow field converges faster towards the imposed profile. However, there are some remarkable differences in the turbulent fluctuations.

Fig. 7 shows the profiles of the axial velocity fluctuations for different averaging time-spans. Using approach (*a*) results in complete attenuation of the turbulence. Assuming that an overall mean value (approach (*b*)) preserves the turbulence, it can be seen that the averaging time has to be sufficiently long to prevent attenuation of the turbulence. Here, averaging over one non-dimensional time unit, given by the ratio of pipe diameter to bulk velocity, was found to be sufficient. This seems reasonable, since the abovementioned criteria require the averaging time to be of the order of the Eulerian integral time scale of the turbulence, which for a turbulent pipe flow is proportional to the ratio of pipe diameter to bulk velocity.

For a swirling flow the same procedure can also applied to the azimuthal velocity component. Fig. 8 shows the profiles of the azimuthal velocity component. Again, the inflow conditions correspond to a fully-developed turbulent pipe without swirl and the virtual body force is applied as shown in Fig. 3. At the end of the forcing region the target profile is matched perfectly.

The results of the pipe-flow investigation demonstrate that the proposed treatment of the LES outflow conditions with virtual body forces can be used to enforce a mean flow solution at the LES outflow, and that the enforced outflow conditions can indeed alter the upstream flow field.

6. Validation: swirl combustor geometry

In order to validate the proposed method for treating LES outflow conditions for an LES/RANS interface, the method will be applied to a more complex configuration. The test case chosen is that of a swirling flow inside a combustor geometry with a swirl number, $S = 0.38$, with S defined as:

$$S = \frac{1}{R} \frac{\int_0^R r^2 \bar{u}_x \bar{u}_\phi \, dr}{\int_0^R r \bar{u}_x^2 \, dr}, \tag{6.1}$$

where u_x is the axial velocity component, u_ϕ the azimuthal velocity component, and R the radius of the nozzle. This swirl number has been chosen because it is slightly above the critical limit at which a central recirculation zone develops, where the flow is believed to be most sensitive to outer influences such as the outflow boundary conditions (Gupta *et al*, 1984; Dellenback *et al*, 1988). Swirl flows are dominated by large-scale turbulence making these flows a field of application of LES *par excellence*. LES usually achieves high levels of accuracy in predicting swirl flows (Pierce & Moin, 1998a; Schlüter *et al.*, 2001).

In order to demonstrate the importance of LES outflow conditions and to prove the ability of the proposed LES outflow treatment with virtual body forces to prescribe outflow conditions correctly, three different outflow geometries have been considered:

(*a*) a swirl flow with a contraction near the outlet at $x/D = 3.0$ (Fig. 9);

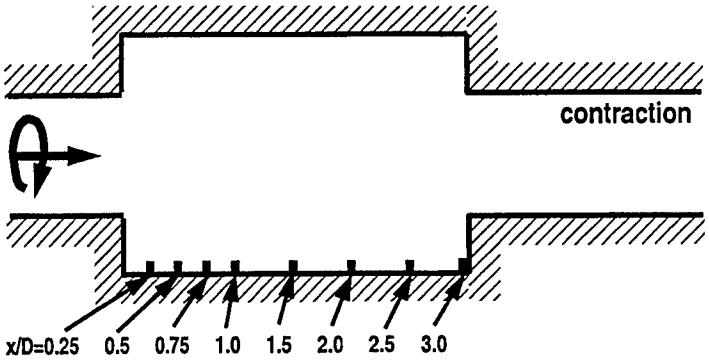

FIGURE 9. Swirl flow geometry with contraction

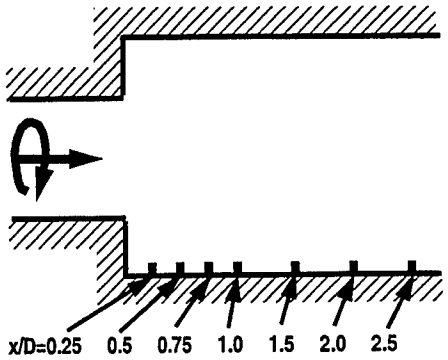

FIGURE 10. Reduced swirl flow geometry without virtual body force

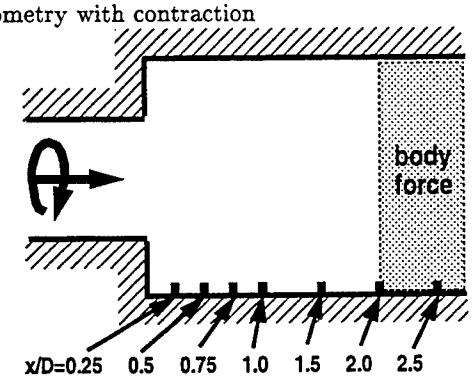

FIGURE 11. Reduced swirl flow geometry with virtual body force

(*b*) a swirl flow where the computational domain is cut off just upstream of the contraction of case (*a*) at $x/D = 2.75$ (Fig. 10);

(*c*) the same geometry as in case (*b*), but with the proposed boundary condition applied in order to simulate the effect of the contraction (Fig. 11).

The mesh size of geometry (*a*) consists of 384×64×64 cells while the mesh of cases (*b*) and *c*) consists of 256×64×64 cells. The point distribution of both meshes is the same, except for the contraction itself.

Case (*a*) will be considered as the reference case. Since the computational domain includes the contraction, its influence on the upstream flow will be correctly reflected in the LES solution. Assuming that the contraction is to be computed with a RANS code, in case (*b*) the computational domain has been reduced and the contraction is outside of the LES domain. Hence, its influence on the LES flow field is neglected in case (*b*).

Fig. 12 shows the mean velocity profiles in cases (*a*) and (*b*). It can be seen, that the velocity profiles of the computation with the reduced geometry (*b*) (dashed line) differ from the profiles of the computation of the full geometry (*a*) (solid line). Hence, it is apparent that the downstream geometry variation has a substantial influence on the entire domain, and that geometry (*b*) cannot be used to approximate the flow in geometry (*a*) without special boundary treatment.

In order to take the contraction outside of the computational domain into account, the proposed outflow boundary treatment is employed. The Reynolds-averaged velocity profiles from $x/D = 2.0 - 2.5$ from the LES computation of case (*a*) are imposed, with virtual body forces, on the reduced geometry. Fig. 12 shows the mean velocity profiles

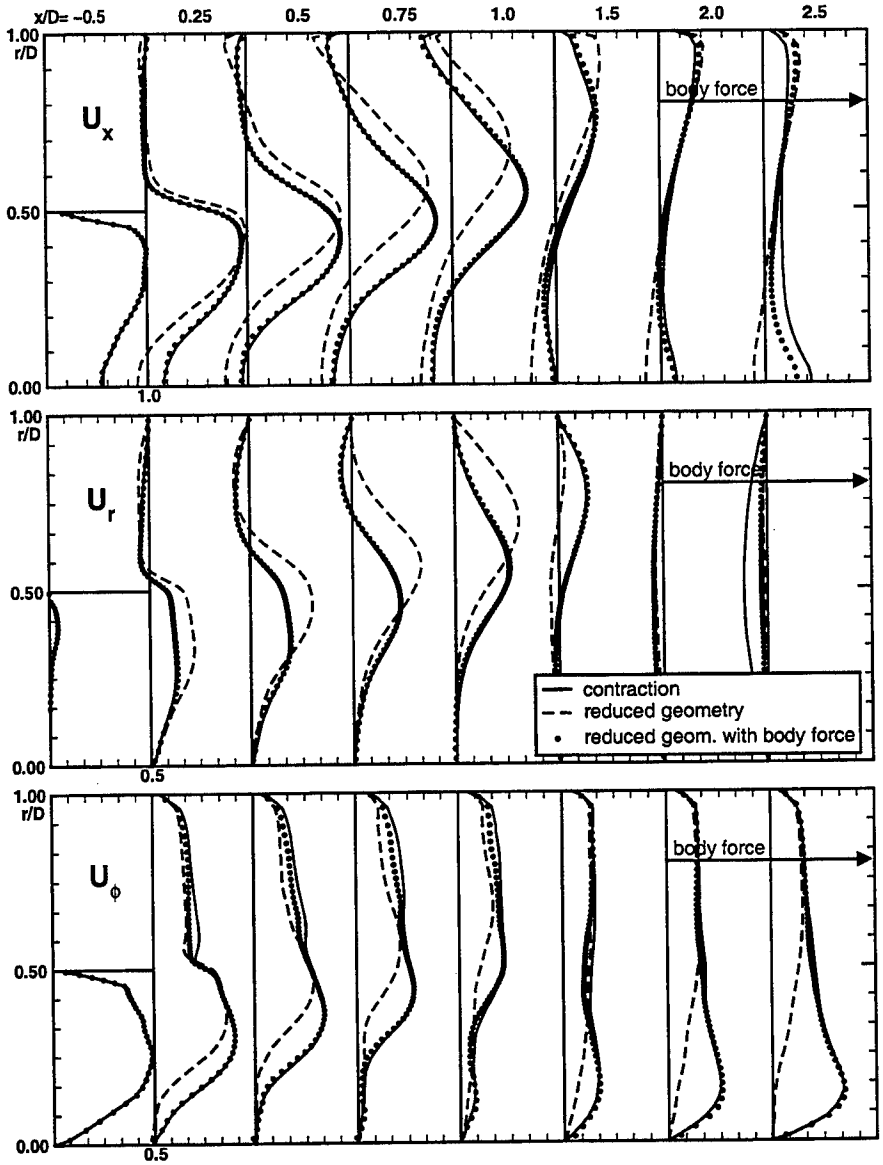

FIGURE 12. Velocity profiles for different axial locations; solid lines: contraction (case (*a*)); dashed lines: reduced geometry without virtual body force(case (*b*)); symbols: reduced geometry with virtual body force (case (*c*))

of case (*c*) (black dots). It can be seen that not only do the velocity profiles inside the virtual-body-force volume adjust, but so also do the velocity profiles upstream. The LES computation of the reduced geometry with the virtual body force delivers essentially the same prediction as the computation of the entire geometry.

The influence of the LES outflow condition on the velocity fluctuations is shown in Fig. 13. The different mean-velocity distribution due to the presence of a contraction results in a different turbulence distribution (compare solid line and dashed line in Fig. 13). The employment of the virtual body forces corrects not only the mean velocity field, but

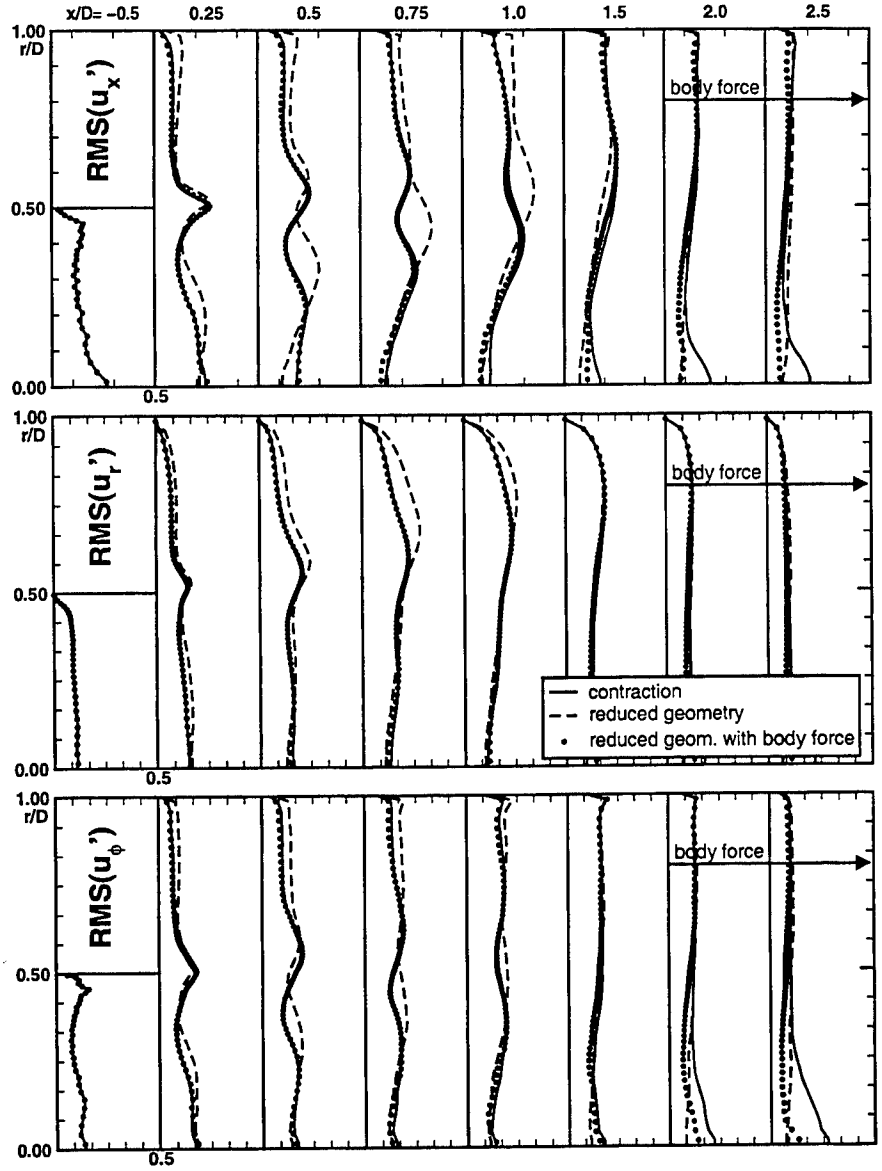

FIGURE 13. Profiles of velocity fluctuations for different axial locations; solid lines: contraction (case *(a)*); dashed lines: reduced geometry without virtual body force (case *(b)*); symbols: reduced geometry with virtual body force (case *(c)*)

also the turbulent quantities (compare solid line and filled circles in Fig. 13). The virtual body force results in an adjustment of the turbulent quantities so that the flow upstream of the body force volume is nearly indistinguishable from the complete computation with the contraction.

In Fig. 14, the axial pressure distribution on the axis is shown. Due to the variances in the flow fields of the cases *(a)* and *(b)*, especially in the extend and strength of the recirculation zone, the pressure distributions differ. Although the proposed outflow boundary adjustment by virtual body forces acts only on the velocity components and not

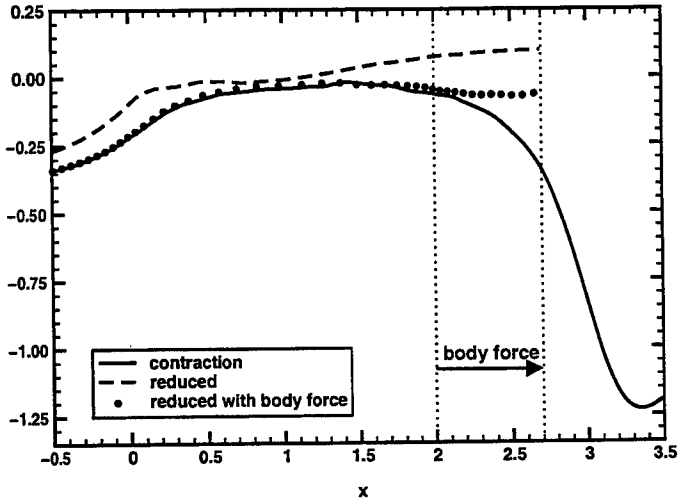

FIGURE 14. Axial pressure distribution on the axis; solid lines: contraction (case (*a*)); dashed lines: reduced geometry without virtual body force (case (*b*)); symbols: reduced geometry with virtual body force (case (*c*))

on the pressure itself, the pressure distribution adjusts to the modified outflow conditions. The pressure distributions in cases *(a)* and *(c)* are in agreement upstream of the body-force volume.

7. Conclusions

The results of this study show that the outflow conditions may have a major impact on the accuracy of LES computations. Hence, a proper description of the outflow conditions is mandatory.

To avoid the computation of the downstream geometry with LES a method has been proposed to correct the outflow conditions. This method ensures the adjustment of the LES flow field to the statistical data computed by a downstream RANS flow solver.

The adjustment of the LES outflow has an effect throughout the entire flow-field. The resulting prediction of the flow-field is nearly indistinguishable from an LES computation of the entire domain. This allows a drastic decrease in computational costs.

Future efforts will combine the LES flow solver with an actual RANS flow solver in a two-way-coupled LES/RANS simulations.

REFERENCES

AKSELVOLL, K., & MOIN, P. 1996 Large-eddy simulation of turbulent confined coannular jets. *J. Fluid Mech.* **315**, 387–411.

DELLENBACK, P. A., METZGER, D. E. & NEITZEL, G. P 1988 Measurements in turbulent swirling flow through an abrupt axisymmetric expansion. *AIAA J.* **26**, 669-681.

GERMANO, M., PIOMELLI, U., MOIN, P. & CABOT, W., 1991 A dynamic subgrid-scale eddy viscosity model. *Phys. Fluids A* **3**, 1760-1765.

GUPTA, A. K., LILLEY, D. G. & SYRED, N. 1984 *Swirl Flows.* Abacus Press.

MOIN, P., SQUIRES, K., CABOT, W. & LEE, S. 1991 A dynamic subgrid-scale model for compressible turbulence and scalar transport. *Phys. Fluids A* **3**, 2746-2757.

MOIN, P. 1997 Progress in large eddy simulation of turbulent flows. *AIAA* Paper 97-0749.

PIERCE, C. D. & MOIN, P. 1998A Large eddy simulation of a confined coaxial jet with swirl and heat release. *AIAA* Paper 98-2892.

PIERCE, C. D. & MOIN, P. 1998B Method for generating equilibrium swirling inflow conditions. *AIAA J.* **36**, 1325-1327.

SCHLÜTER, J., SCHÖNFELD, T., POINSOT, T., KREBS, W. & HOFFMANN, S. 2001 Characterization of confined swirl flows using large eddy simulations. *ASME* 2001-GT-0060

VEYNANTE, D. & POINSOT, T. 1996 Reynolds averaged and large eddy simulation modeling for turbulent combustion. In *New Tools in Turbulence Modeling*, Springer, 105–140.

Explicit filtering and subgrid-scale models in turbulent channel flow

By Jessica Gullbrand

1. Motivation and objectives

In large eddy simulation (LES), the large energy carrying length scales of turbulence are resolved and the small structures are modeled. The separation of large and small scales is done by applying a low-pass filter to the Navier-Stokes equations. The effect of the small-scale turbulence on the resolved scales is modeled using a subgrid-scale (SGS) model.

It is of great importance that the resolved length scales are captured accurately by the numerical scheme. Information from the smallest resolved length scales are commonly used to model the stresses of the unresolved scales in the SGS model. This requires that the numerical error of the scheme is sufficiently small. Therefore, high order numerical schemes are necessary in LES.

One approach is to use high-order finite-difference schemes. However, all finite-difference schemes have a truncation error that increases with the wavenumber (Lund & Kaltenbach 1995). To reduce the influence of this error, an explicit filtering can be applied that reduces or removes the small scales that otherwise would be largely affected by this error.

In using explicit filtering, it is a requirement that the filtering operation and the differentiation do commute. This is generally not the case in inhomogeneous flow fields where the required smallest resolved length scales vary throughout the flow fields. The varying filter width introduces a commutation error of $O(\Delta^2)$ where Δ represents the filter width (Ghosal 1996; Ghosal & Moin 1995). Therefore, most of the explicit filtering procedures that have been applied so far have been used in homogeneous flow fields or in homogeneous directions of more general flows. Explicit filtering in two dimensions has been studied by Lund & Kaltenbach (1995) and numerous filter functions by Piomelli *et al.* (1988) and Najjar & Tafti (1996).

The problem of lacking robust and straightforward filtering procedures that do commute was addressed by Vasilyev *et al.* (1998). They developed a general theory of discrete filtering for LES in complex geometries. A set of rules for constructing discrete filters, so that the filters commute to the desired order, was also proposed.

The ultimate goal of the explicit filtering procedure is to perform a "true" LES. In a true LES, the filtering procedure is decoupled from the computational grid. As the grid is refined while the explicit filter width is held fixed, the solution converges to a true LES. In the commonly-used approach to LES, the computational grid together with the low pass characteristics of the discrete differencing operators act as a filter and, as the grid is refined, the solution converges towards a direct numerical simulation (DNS) not an LES. However, before a true LES can be performed, the influence of the explicit filtering procedure on the SGS models need to be determined.

In this paper, explicit filtering is applied in three dimensions in a turbulent channel flow using the dynamic Smagorinsky model (DSM) (Germano *et al.* 1991) and the mixed model (MM) (Bardina *et al.* 1980; Zang *et al.* 1993) as SGS models. The turbulent

channel flow of Reynolds number $Re_\tau = 395$ is simulated using a conservative fourth-order finite-difference scheme (Vasilyev 2000). The influence of the three-dimensional filtering procedure on the DSM and the MM is investigated, as well as the influence of resolving the Leonard stress tensor. The results are compared to the DNS data by Moser *et al.* (1999).

2. Numerical method

2.1. *Governing equations*

In LES, the governing equations are filtered in space. The filter function G is applied to the flow variable f

$$\overline{f}(x,\Delta,t) = \int_{-\infty}^{\infty} G(x,x',\Delta) f(x',t) dx' \tag{2.1}$$

where Δ is the filter width.

The governing equations for incompressible flows are the filtered continuity and Navier-Stokes equations

$$\frac{\partial \overline{u}_i}{\partial x_i} = 0 \tag{2.2}$$

$$\frac{\partial \overline{u}_i}{\partial t} + \frac{\partial \overline{u}_i \overline{u}_j}{\partial x_j} = -\frac{\partial \overline{p}}{\partial x_i} + \frac{1}{Re_\tau} \frac{\partial^2 \overline{u}_i}{\partial x_j^2} - \frac{\partial \tau_{ij}}{\partial x_j} \tag{2.3}$$

where u_i denotes velocity vector and x_i the space coordinates. Re_τ is the Reynolds number, t is time, and p is pressure. The SGS stress tensor is defined as $\tau_{ij} = \overline{u_i u_j} - \overline{u}_i \overline{u}_j$. The equations are normalized with the friction velocity u_τ and the channel half width h.

The product $\overline{u}_i \overline{u}_j$ generates wavenumbers that cause aliasing errors and therefore an alternative to the above filtered Navier-Stokes equations is

$$\frac{\partial \overline{u}_i}{\partial t} + \frac{\partial \overline{\overline{u}_i \overline{u}_j}}{\partial x_j} = -\frac{\partial \overline{p}}{\partial x_i} + \frac{1}{Re_\tau} \frac{\partial^2 \overline{u}_i}{\partial x_j^2} - \frac{\partial \overline{\eta}_{ij}}{\partial x_j} \tag{2.4}$$

where $\overline{\eta}_{ij}$ is the SGS stress tensor defined as $\overline{\eta}_{ij} = \overline{u_i u_j} - \overline{\overline{u}_i \overline{u}_j}$. By explicitly filtering the non-linear terms, the wavenumber content of these terms is controlled (Lund 1997). In Eq. (2.4), all the terms of the Navier-Stokes equations contain the same wavenumbers.

The stress tensors τ_{ij} and η_{ij} describe the interaction between the large resolved Grid Scale (GS) and the small unresolved SGS. The stress tensors do not contain the same terms. If decomposition is applied to the velocity correlation $\overline{u_i u_j}$, τ_{ij} can be written as the sum of the Leonard stresses, L_{ij}, the cross stresses, C_{ij}, and the Reynolds stresses, R_{ij}, as $\tau_{ij} = L_{ij} + C_{ij} + R_{ij}$ (Clark *et al.* 1979). The expressions for the stresses are

$$L_{ij} = \overline{\overline{u}_i \overline{u}_j} - \overline{u}_i \overline{u}_j$$

$$C_{ij} = \overline{\overline{u}_i u'_j} + \overline{u'_i \overline{u}_j}$$

$$R_{ij} = \overline{u'_i u'_j}$$

where u_i' is the velocity fluctuation. The expliclit filtering of the convective terms in Eq. (2.4) results in a different expression of the SGS stress $\overline{\eta}_{ij}$. The interaction between the resolved scales, the Leonard stresses, is implicitly included in the convective terms. The stress tensor is described as the sum of the cross stresses and Reynolds stresses, $\overline{\eta}_{ij} = C_{ij} + R_{ij}$. The SGS stress tensors cannot be expressed in the resolved flow field variables and therefore, they have to be modeled.

2.2. *Subgrid-scale models*

Two widely-used SGS models are the scale similarity model (SSM) proposed by Bardina *et al.* (1980) and the DSM by Germano *et al.* (1991). It has been shown that the SSM does not dissipate enough energy and it is therefore most commonly used in a linear combination with a more-dissipative model such as the Smagorinsky model (Smagorinsky 1963) to form the MM. The model parameter in the Smagorinsky model can be either constant or calculated dynamically during the entire simulation. This is also the case when the Smagorinsky model is used in the MM. Bardina *et al.* (1980) used a constant model parameter while Zang *et al.* (1993) applied the dynamic approach. Both the SSM and the dynamic procedure of the DSM use the assumption that the behavior of the resolved and unresolved stresses is similar.

In the present investigation, τ_{ij} is modeled using the DSM while η_{ij} is modeled using either the DSM or the MM. The DSM models the Reynolds stresses in the SGS stress tensors. The influence of the Leonard stresses in τ_{ij} is investigated. For η_{ij}, the cross stresses are modeled by the SSM ($C_{ij} = \overline{u}_i\overline{u}_j - \overline{\overline{u}_i}\overline{\overline{u}_j}$) in the MM. By using the SSM, the possible drawback of Eq. (2.4) not being Galilean invariant is solved (Speziale 1985). An explicit filtering of η_{ij} is performed to ensure that the SGS terms contain only the desired wavenumbers. The model parameter in the DSM is calculated dynamically in all the simulations. The parameter is averaged in the homogeneous directions and calculated by the least square approximation by Lilly (1992).

3. Explicit filter

A general class of commutative discrete filters applied to nonuniform filter widths was proposed by Vasilyev *et al.* (1998). The procedure applies mapping of the nonuniform grid in physical space onto a uniform grid in computational space where the filtering is performed. The filters are constructed by applying a number of constraints to the filter weights to achieve both commutation and an acceptable filter shape. The filter weights are calculated by forcing the zeroth moment to be one and a number of higher moments to be zero. This determines the order of the commutation error. Other constraints can be added to adjust the filter shape.

In the simulations, two fourth-order commutative filters have been applied: one explicit filter and one test filter. The explicit filter is used when the convective terms and the SGS terms are explicitly filtered in Eq. (2.4). The test filter is used as the second filter in the dynamic procedure when calculating the model parameter in the DSM (Germano *et al.* 1991). The ratio between the test and the explicit filter widths is $\Delta_{test}/\Delta_{exp} = 2$. Between the explicit filter width and the computational cell size, the ratio is $\Delta_{exp}/\Delta_{grid} = 2$.

3.1. *Solution algorithm*

The space derivatives in the governing equations are discretized using a fourth-order finite-difference scheme on a staggered grid. The convective terms are discretized in a skew-symmetric form to ensure conservation of turbulent kinetic energy (Morinishi *et al.*

1998; Vasilyev 2000). The equations are solved with the third-order Runge-Kutta scheme described by Spalart *et al.* (1991). The diffusion term in the wall normal direction is treated implicitly with the Crank-Nicolson scheme to ease the constraint on the time step of the scheme. The splitting method of Dukowicz & Dvinsky (1992) is used to enforce the solenoidal condition. The resulting discrete Poisson equation for pressure is solved using a pentadiagonal direct matrix solver in the wall-normal direction and a discrete Fourier transform in the homogeneous/periodic directions. Periodic boundary conditions are applied in the streamwise and spanwise directions, while no-slip conditions are applied at the walls. A fixed mean pressure gradient is used in the streamwise direction. An evaluation of the fourth-order conservative scheme is reported in Gullbrand (2000).

4. Turbulent channel flow simulations

The Reynolds number is $Re_\tau = 395$ and the computational domain is $(2\pi h, 2h, \pi h)$ in (x, y, z), where x is the streamwise direction, y the wall normal direction, and z the spanwise direction. Two grid resolutions are used: a standard grid (36,37,36) and a fine grid (72,73,72). The computational grid is stretched in the wall normal direction by a hyperbolic tangent function (Vasilyev 2000). For the standard grid resolution, the streamwise grid size is $\Delta x^+ = 69$, the spanwise grid size $\Delta z^+ = 34$, and in the wall normal direction the grid size varies between $0.5 \leq \Delta y^+ \leq 56$. For the fine grid resolution, the values are $\Delta x^+ = 34$, $\Delta z^+ = 17$, and $0.25 \leq \Delta y^+ \leq 30$. A statistically stationary solution is obtained after 60 dimensionless time units and thereafter statistics are sampled during 30 time units. The time is normalized with the friction velocity and the channel half width.

5. Results

The results from using commutative explicit filtering in LES using the DSM and the MM are compared to the DNS data by Moser *et al.* (1999) for mean velocity, velocity fluctuations and energy spectra. The explicit filtering enters only into the equations through the calculation of the model parameter in the DSM, the second filtering of the velocity field used in the MM, and through the explicit filtering of the convective terms and SGS tensor in Eq. (2.4).

5.1. *Mean velocities*

The mean velocity profile predicted by using the explicit filtering and the DSM is overestimated in the log-law region when compared to the DNS data. The results are somewhat surprising, because the DSM is known to perform better (Gullbrand 2000). However, the model has not previously been applied in turbulent channel flow where three dimensional filtering is employed. The overestimation is not a result of the three dimensionality of the filter. This is shown in Fig. 1. When filtering only in the homogeneous directions is used, the overestimation in the log-law region increases. The overestimation is not an artifact of the relatively coarse resolution either. The fine grid resolution improves the results slightly, but the improvement is not good enough to explained the model behavior.

The explicit filtering of the convective terms and the SGS stress tensor in Eq. (2.4) show only a small influence on the results (Fig. 2). However, the slope in the log-law region is incorrect when explicit filtering are not performed of the previously mentioned terms. Eq. (2.4) produces the correct slope when using the DSM while Eq. (2.3) does not.

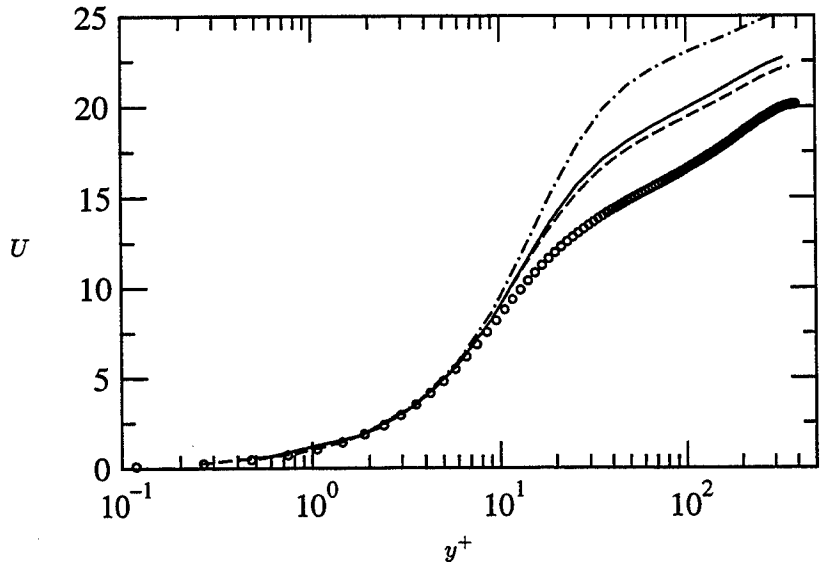

FIGURE 1. Mean velocity profile U as a function of the distance to the wall y^+. o: DNS, ——— : Eq. (2.4) with η_{ij} = DSM, - - - - : Eq. (2.4) with η_{ij} = DSM fine grid, and - · - : Eq. (2.4) with η_{ij} = DSM xz-filter.

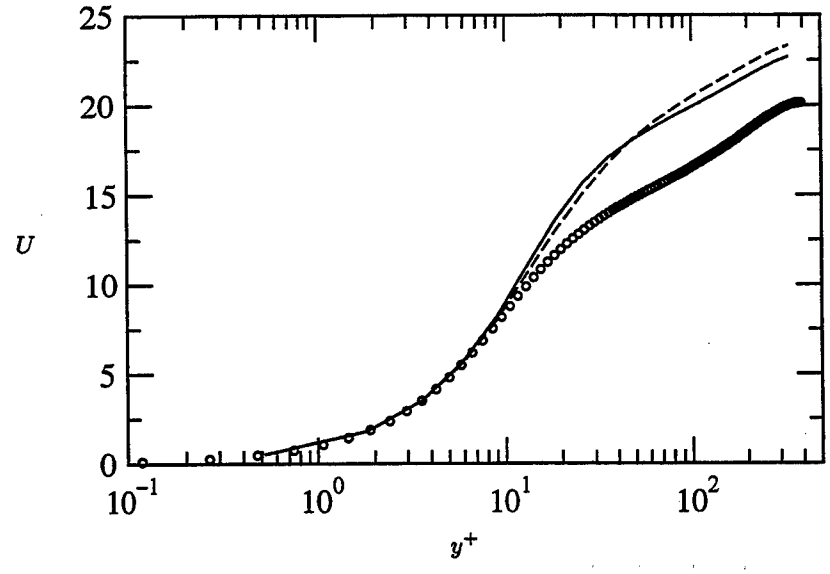

FIGURE 2. Mean velocity profile U as a function of the distance to the wall y^+. o: DNS, ——— : Eq. (2.4) with η_{ij} = DSM, and - - - - : Eq. (2.3) with τ_{ij} = DSM.

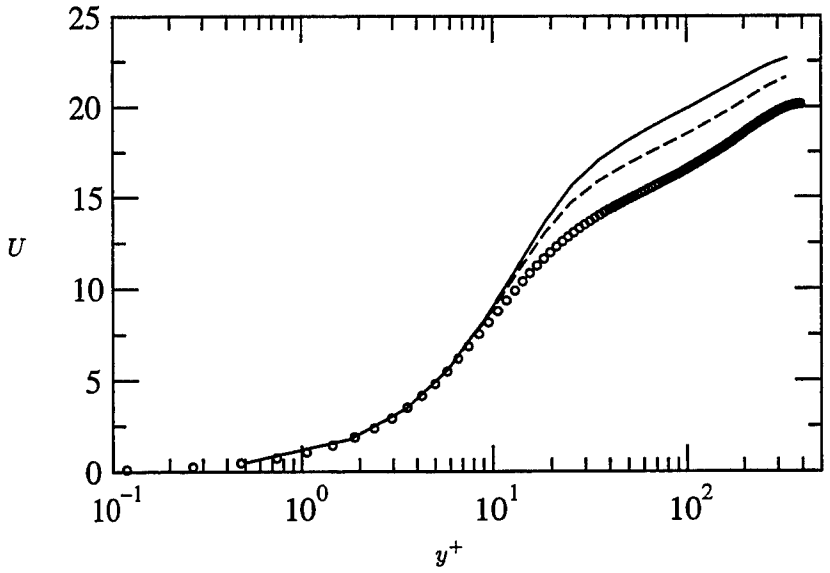

FIGURE 3. Mean velocity profile U as a function of the distance to the wall y^+. o: DNS, ——— : Eq. (2.4) with η_{ij} = DSM, and ---- : Eq. (2.4) with η_{ij} = MM.

The mean velocity profile improves when the MM is used instead of only the DSM in Eq. (2.4). However, the MM also overestimates the log-law region compared to the DNS data. The overestimation using the MM is about 7 % at the center of the channel while it is 13 % for the DSM. This is shown in Fig. 3.

5.2. *Velocity fluctuations*

The streamwise velocity fluctuation is overpredicted, while the wall normal and spanwise fluctuations are underpredicted when using explicit commutative filters on both the standard and fine computational grids. The difference between the LES and the DNS results is even larger when two dimensional filtering is applied. The predicted peak value in the streamwise direction is reduced on the finer grid (Fig. 4). Usually, the same trend with overprediction of the streamwise fluctuation and underprediction of the other two fluctuations is observed in the commonly used LES approach (Gullbrand 2000).

The velocity fluctuations using Eq. (2.4) are better predicted when compared to Eq. (2.3). The both equations predict equally high peak of the streamwise velocity fluctuation, but the wall normal and spanwise fluctuations are better captured by Eq. (2.4). This is shown in Fig. 5.

A lower peak value of the streamwise velocity fluctuation is predicted when the MM is compared to the DSM. Both results are calculated using Eq. 2.4. The MM results in an overprediction of the peak value of 16 % while it is 40 % for DSM. The wall normal and the spanwise fluctuations are better predicted with the DSM than the MM (Fig. 6).

5.3. *Energy spectra*

The resolved wavenumbers for the standard grid resolution and the fine grid can be seen in Fig. 7, where the energy spectra for each velocity correlation are shown as a function of the streamwise wavenumber. The increased resolution results in resolving

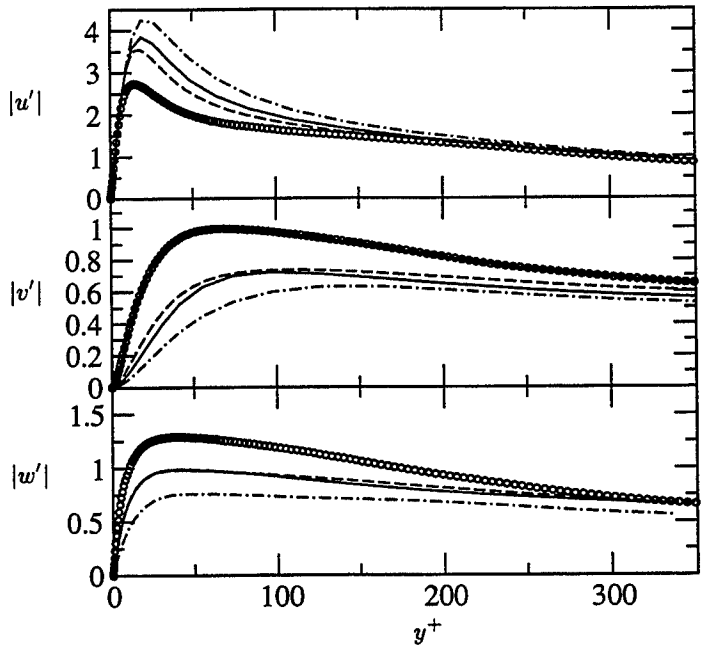

FIGURE 4. Velocity fluctuations in streamwise $|u'|$, wall normal $|v'|$ and spanwise $|w'|$ direction as a function of the distance to the wall y^+. o: DNS, ——— : Eq. (2.4) with η_{ij} = DSM, - - - - : Eq. (2.4) with η_{ij} = DSM fine grid, and - · - : Eq. (2.4) with η_{ij} = DSM xz-filter.

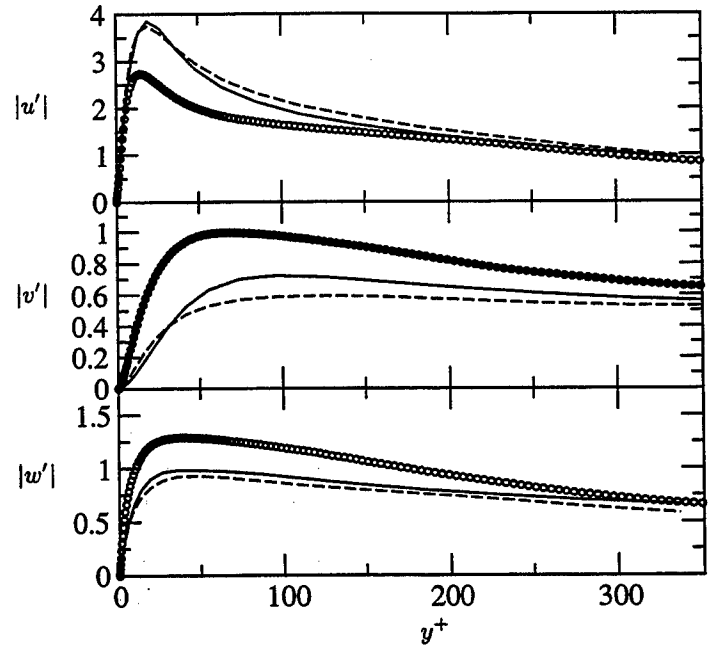

FIGURE 5. Velocity fluctuations in streamwise $|u'|$, wall normal $|v'|$ and spanwise $|w'|$ direction as a function of the distance to the wall y^+. o: DNS, ——— : Eq. (2.4) with η_{ij} = DSM, and - - - - : Eq. (2.3) with τ_{ij} = DSM.

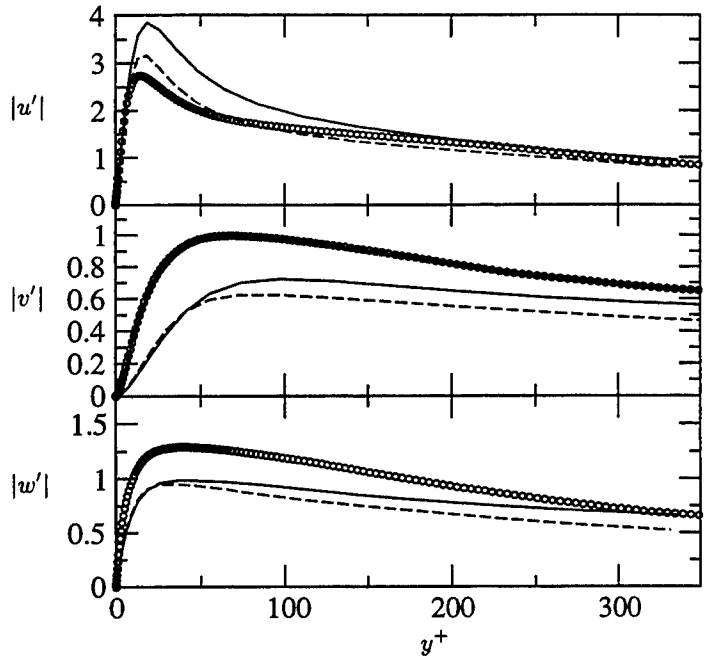

FIGURE 6. Velocity fluctuations in streamwise $|u'|$, wall normal $|v'|$ and spanwise $|w'|$ direction as a function of the distance to the wall y^+. o: DNS, ——— : Eq. (2.4) with η_{ij} = DSM, and - - - - : Eq. (2.4) with η_{ij} = MM.

higher wavenumbers. The filtering procedure in only the homogeneous directions does not include as broad spectra of resolved wavenumbers compared to filtering in all three dimensions. The fine grid resolution shows better resolution of the small wavenumbers when compared to the DNS results than the standard grid simulations do.

The energy spectra are different for using the DSM in Eq. (2.4) or in Eq. (2.3). Eq. (2.4) results in a higher energy content of the small wavenumbers, while the energy decays also in the small wavenumbers when Eq. (2.3) is employed (Fig. 8).

The MM captures the small wavenumbers better than the DSM. The MM also results in a small increase of the resolved wavenumbers. This is shown in Fig. 9.

The influence of the finite difference scheme on the wavenumbers is clearly seen in the figures. The steep slope at high wavenumbers is due to the modified wavenumber argument (Lund & Kaltenbach 1995).

6. Discussion and conclusions

Three dimensional explicit filtering in LES has been used for the DSM and the MM in turbulent channel flow. The simulations were performed using fourth order conservative finite difference schemes. The three dimensional explicit filter functions commute up to fourth order. The result of performing LES using the commutative filters is that the mean velocity profile is overestimated in the log-law region. The overestimation is not a result of the introduction of filtering in the wall normal direction. According to Fig. 1, the overestimation becomes even larger when filtering is applied only in the homogeneous directions.

The two formulations of the Navier-Stokes equations, Eq. (2.3) and Eq. (2.4), predict

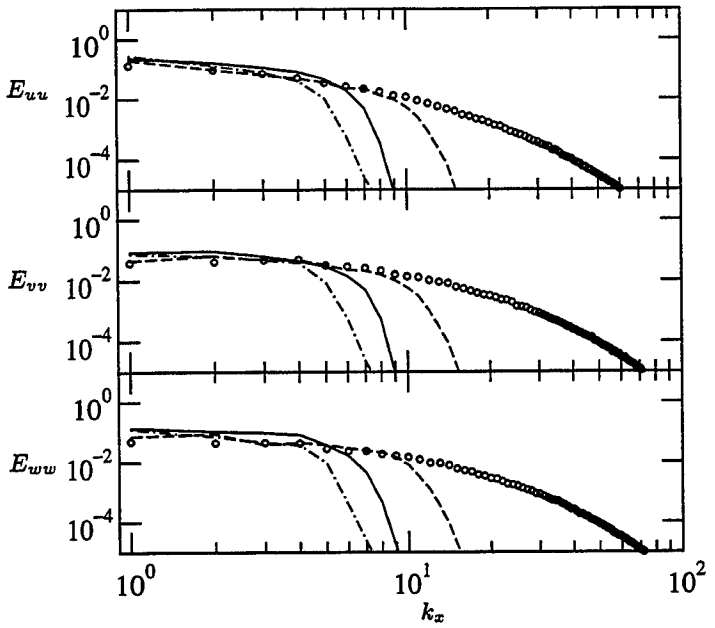

FIGURE 7. Energy spectrum of the streamwise E_{uu}, wall normal E_{vv} and spanwise E_{ww} velocity correlation as a function of the streamwise wavenumber k_x at $y^+ \approx 395$. o: DNS, ——— : Eq. (2.4) with η_{ij} = DSM, ---- : Eq. (2.4) with η_{ij} = DSM fine grid, and - · -: Eq. (2.4) with η_{ij} = DSM xz-filter.

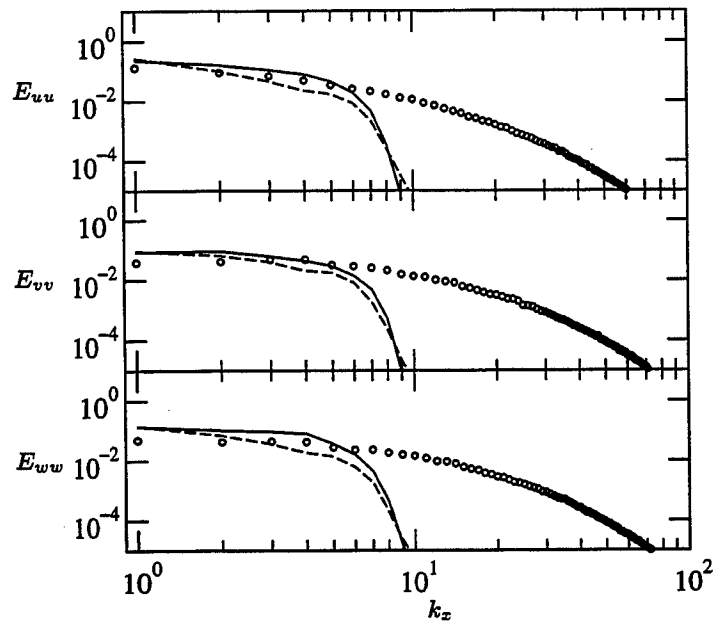

FIGURE 8. Energy spectrum of the streamwise E_{uu}, wall normal E_{vv} and spanwise E_{ww} velocity correlation as a function of the streamwise wavenumber k_x at $y^+ \approx 395$. o: DNS, ——— : Eq. (2.4) with η_{ij} = DSM, and ---- : Eq. (2.3) with τ_{ij} = DSM.

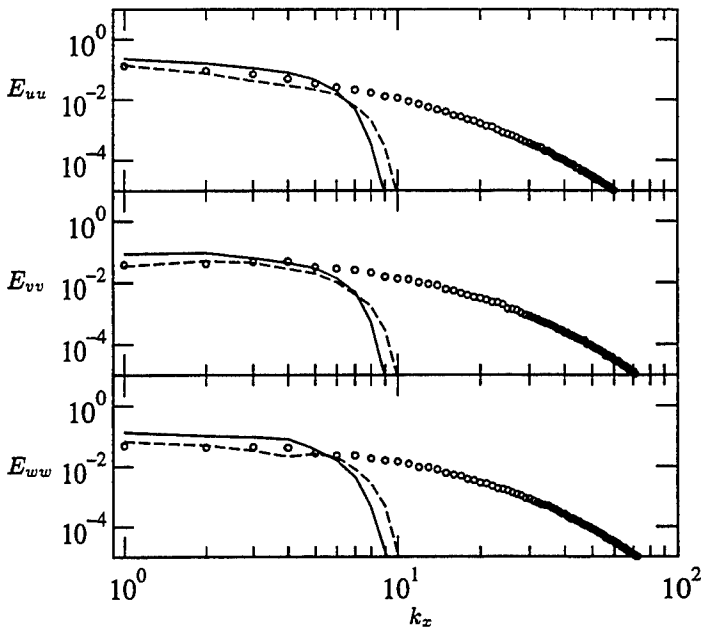

FIGURE 9. Energy spectrum of the streamwise E_{uu}, wall normal E_{vv} and spanwise E_{ww} velocity correlation as a function of the streamwise wavenumber k_x at $y^+ \approx 395$. o: DNS, ——— : Eq. (2.4) with η_{ij} = DSM, and ---- : Eq. (2.4) with η_{ij} = MM.

slightly different results. Eq. (2.4) has the best behavior and also the most consistent approach, with all the terms in the equation containing the same wavenumbers. This is achieved by explicitly filtering the convective terms and the SGS stress tensor. By filtering the convective terms, the Leonard stress term is accounted for in the equation. The difference in the calculated results between Eq. (2.3) and Eq. (2.4) is due to the influence of the Leonard stress tensor.

The MM captures the large scale behavior better that the DSM. This result depends upon the shape of the filter function. Most simulations with the DSM have been performed using the sharp cut-off filter in the homogeneous directions as the test filter. The developed commutative filters are Gaussian like filters. A study by Piomelli *et al.* (1988) showed that for two dimensional filtering, the best results are obtained by using the Gaussian filter with the MM and the cut-off filter with the Smagorinsky model. The Gaussian filter used in the Smagorinsky model resulted in an overprediction of the mean velocity profile in the log-law region. The over-prediction was about 17 % at the center of the channel for $Re_\tau = 180$. The findings by Piomelli *et al.* (1988) are confirmed in this study in Fig. 10. The commonly used LES approach without explicit filtering has been performed and two different test filters have been used: the commutative filter and the sharp cut-off filter. The standard grid resolution was used in the simulations. The filters are only employed in the homogeneous directions and the filter widths are twice the computational grid size. The test filters enter into the equations only through the calculation of the model parameter in the DSM. The mean velocity profiles are shown in Fig. 10. The velocity profile is highly overpredicted in the log-law region when using the commutative filter when compared to the results from using the sharp cut-off filter.

The contribution from the SGS model is increased in the explicitly filtered LES com-

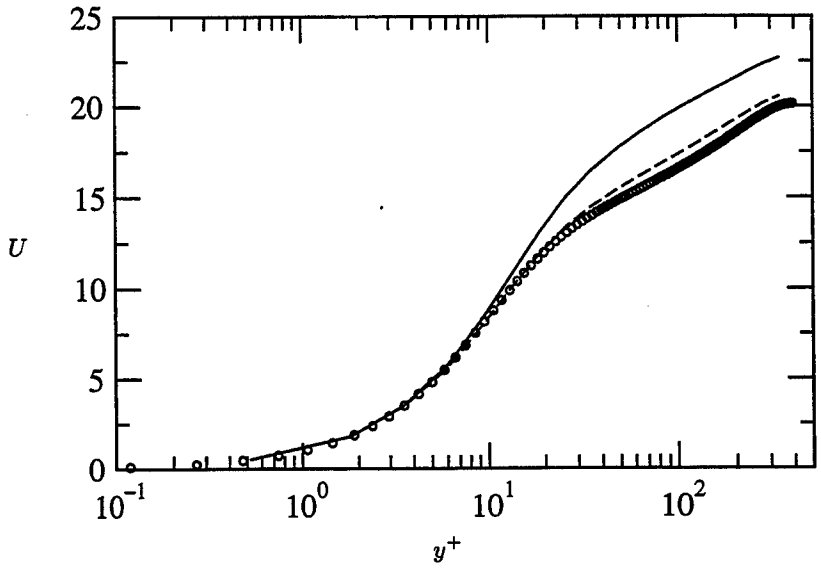

FIGURE 10. Mean velocity profile U as a function of the distance to the wall y^+. o: DNS, ——— : DSM 2-D commutative filter, and ---- : DSM 2-D sharp cut-off filter.

pared to the commonly used LES approach. The increase is expected, due to a reduction or an elimination of the high wavenumbers by the filtering procedure, causing the SGS model to model a larger range of wavenumbers. Therefore, the SGS model has a larger influence in the explicitly filtered LES.

7. Current work

In the current work, the true LES approach is investigated. The true LES is obtained by keeping the explicit filter width constant while the computational grid is refined. The solution converges to a true LES.

Different SGS models will also be investigated as well as the numerical error in the simulation. Two promising SGS models that have proven to perform well are the multi-scale model by Hughes *et al.* (2001) and the approximate deconvolution model by Stolz *et al.* (2001). The LES of turbulent channel flow in both papers have been performed using spectral methods. The models will be applied in the previously discussed fourth order finite difference code.

Acknowledgments

The author wishes to thank Prof. O. V. Vasilyev for providing the channel flow code and Prof. P. Moin for many helpful discussions. Discussions with Dr. Y. Dubief and Mr. G. Iaccarino are also gratefully acknowledged.

REFERENCES

BARDINA, J., FERZIGER, J. H. & REYNOLDS, W. C. 1980 Improved subgrid scale models for large eddy simulation. *AIAA-80-1357.*

CLARK, A., FERZIGER, J. H. & REYNOLDS, W. C. 1979 Evaluation of subgrid-scale models using an accurately simulated turbulent flow. *J. Fluid Mech.*, **91**, 1-16.

DUKOWICZ, J. K. & DVINSKY, A. S. 1992 Approximation as a higher order splitting for the implicit incompressible flow equations. *J. Comp. Phys.*, **102**, 336-347.

GERMANO, M., PIOMELLI, U., MOIN, P. & CABOT, W. H. 1991 A dynamic subgrid-scale eddy viscosity model. *Phys. Fluids A.* **3**, 1760-1765.

GHOSAL, S. 1995 An analysis of numerical errors in large-eddy simulations of turbulence. *J. Comp. Phys.* **125**, 187-206.

GHOSAL, S. & MOIN, P. 1995 The basic equations of the large eddy simulation of turbulent flows in complex geometry. *J. Comp. Phys.* **118**, 24-37.

GULLBRAND, J. 2000 An evaluation of a conservative fourth order DNS code in turbulent channel flow. *Annual Research Briefs*, Center for Turbulence Research, NASA Ames/Stanford Univ. 211-218.

HUGHES, T. J. R., OBERAI, A. A. AND MAZZEI, L. 2001 Large eddy simulation of turbulent chennel flows by the variational multiscale method. *Phys. Fluids*, **13**, 1784-1799.

LILLY, D. K. 1992 A proposed modification of the Germano subgrid-scale closure method. *Phys. Fluids A.* **4**, 633-635.

LUND, T. S. 1997 On the use of discrete filters for large eddy simulation. *Annual Research Briefs*, Center for Turbulence Research, NASA Ames/Stanford Univ. 83-95.

LUND, T. S. & KALTENBACH, H.-J. 1995 Experiments with explicit filtering for LES using a finite-difference method. *Center for Turbulence Research, Annual Research Briefs 1995*, 91-105.

MORINISHI, Y., LUND, T. S., VASILYEV, O. V. & MOIN, P. 1998 Fully conservative higher order finite difference schemes for incompressible flow. *J. Comp. Phys.* **143**, 90-124.

MOSER, R. D., KIM, J. & MANSOUR, N. N. 1999 Direct numerical simulation of turbulent channel flow up to Re_τ=590. *Phys. Fluids.* **11**, 943-945.

NAJJAR, F. M. & TAFTI, D. K. 1996 Study of discrete test filters and finite difference approximations for the dynamic subgrid-scale stress model. *Phys. Fluids.* **8**, 1076-1088.

PIOMELLI, U., MOIN, P. & FERZIGER, J. H. 1988 Model consistency in large eddy simulation of turbulent channel flows. *Phys. Fluids.* **31**, 1884-1891.

SMAGORINSKY, J. 1963 General circulation experiments with the primitive equations. *Mon. Weather Rev.* **91**, 99-152.

SPALART, P., MOSER, R. & ROGERS, M. 1991 Spectral methods for the Navier-Stokes equations with one infinite and two periodic directions. *J. Comp. Phys.* **96**, 297-324.

SPEZIALE, C. G. 1985 Galilean invariance of subgrid-scale stress models in the large-eddy simulation of turbulence. *J. Fluid Mech.* , 55-62.

STOLZ, S., ADAMS, N. A. & KLEISER, L. 2001 An approximate deconvolution model for large-eddy simulation with application to incompressible wall-bounded flows. *Phys. Fluids.* **13**, 997-1015.

VASILYEV, O. V. 2000 High order finite difference schemes on non-uniform meshes with good conservation properties. *J. Comp. Phys.* **157**, 746-761.

VASILYEV, O. V., LUND, T. S. & MOIN, P. 1998 A general class of commutative filters for LES in complex geometries. *J. Comp. Phys.* **146**, 82-104.

ZANG, Y., STREET, R. L. & KOSEFF, J. R. 1993 A dynamic mixed subgrid-scale model and its application to turbulent recirculating flows. *Phys. Fluids.* **5**, 3186-3196.

Prediction of high Reynolds number flow over a circular cylinder using LES with wall modeling

By Meng Wang, Pietro Catalano †, AND Gianluca Iaccarino

1. Motivation and objectives

The objective of this work is to assess the viability and accuracy of large-eddy simulation (LES) with wall modeling for high Reynolds number complex wall-bounded flows. It is well known that the conventional LES is extremely expensive at high Reynolds numbers due to the need to resolve the small but dynamically-important near-wall flow structures. As a practical alternative, LES can be coupled with a wall model which models these near-wall effects and provides the LES with a set of approximate boundary conditions, often in the form of wall shear stress (Cabot & Moin 2000).

In recent years, wall models based on turbulent boundary layer (TBL) equations and their simplified forms (Balaras, Benocci & Piomelli 1996; Cabot & Moin 2000) have received much attention. These models, used with a Reynolds-averaged Navier-Stokes (RANS) type of eddy viscosity, have shown promise for complex-flow predictions. For instance, Wang & Moin (2001) employed this approach to simulate the flow past the asymmetric trailing edge of an airfoil at chord Reynolds number of 2.15×10^6, and obtained very good agreement with solutions from the full LES (Wang & Moin 2000) at a small fraction of the computational cost.

The flow around a circular cylinder represents a canonical problem for validating new approaches in computational fluid dynamics. It is therefore reasonable or even necessary to subject the hybrid LES/wall-modeling methodology to the same "grand challenge". To take the best advantage of wall modeling, we concentrate on the super-critical flow regime in which the boundary layer on the cylinder becomes turbulent prior to separation. This is, to our knowledge, the first such attempt using LES, although a related method known as detached-eddy simulation (DES), in which the entire attached boundary layer is modeled, has been tested in this type of flow (Travin *et al.* 1999). Breuer (2000) recently conducted an LES study at a high sub-critical Reynolds number of $Re_D = 1.4 \times 10^5$, and showed fairly good comparison with experimental data in the near wake. In the present work, three simulations, at $Re_D = 5 \times 10^5$, 1×10^6, and 2×10^6, have been performed. Preliminary results and comparisons with experimental data are summarized in this article.

2. Numerical method and procedure

The same LES code and wall model implementation as used by Wang & Moin (2001) are used for the present calculations. The energy-conservative numerical scheme is of hybrid finite-difference/spectral type, written for a C-mesh (Mittal & Moin 1997). The time advancement is achieved by the fractional-step method, in combination with the Crank-Nicolson method for viscous terms and third-order Runge-Kutta scheme for convective terms. A multi-grid iterative procedure is used to solve the Poisson equation for

† Centro Italiano Ricerche Aerospaziali (CIRA), Italy

pressure. The subgrid-scale stress (SGS) tensor is modeled using the dynamic SGS model (Germano *et al.* 1991; Lilly 1992).

The computational domain has a spanwise size of $2D$ (D = cylinder diameter), over which the flow is assumed periodic and 48 grid points are distributed uniformly. In the planes perpendicular to the span, 401×120 grid points are used in the C-mesh, extending approximately $22D$ upstream of the cylinder, $17D$ downstream of the cylinder, and $24D$ into the far-field. Potential-flow solutions are imposed as boundary conditions in the far-field, and convective boundary conditions are used at the outflow boundary. Running at a maximum CFL number of 1.5, the non-dimensional time step $\Delta t U_\infty / D$ typically varies between 0.0030 and 0.0045. To obtain the results presented here, the simulations have advanced at least 150 dimensionless time units. The statistics are collected over the last 75 or so time units.

Approximate boundary conditions on the cylinder surface are imposed in terms of wall shear stress estimated from a wall model of the form

$$\frac{\partial}{\partial x_2}(\nu + \nu_t)\frac{\partial u_i}{\partial x_2} = \frac{1}{\rho}\frac{\partial p}{\partial x_i}, \qquad i = 1, 3 \tag{2.1}$$

This is a simpler variant of the TBL equation model (Cabot & Moin 2000) which allows for easier implementation and lower computational cost. Although Wang & Moin (2001) have shown that the full TBL equations (with dynamically adjusted ν_t) give better results in their trailing-edge flow, the discrepancy may be partly related to a surface curvature discontinuity which is absent from the cylinder surface. Since the pressure is taken from the LES at the edge of the wall layer, Eq. (2.1) can be integrated to the wall to obtain an algebraic model for the wall shear stress components (Wang 1999)

$$\tau_{wi} = \frac{\rho}{\int_0^\delta \frac{dy}{\nu+\nu_t}} \left\{ u_{\delta_i} - \frac{1}{\rho}\frac{\partial p}{\partial x_i}\int_0^\delta \frac{y dy}{\nu + \nu_t} \right\}, \tag{2.2}$$

where $u_{\delta i}$ denotes the tangential velocity components from LES at the first off-wall velocity nodes, at distance δ from the wall. In attached flows these nodes are generally placed within the lower edge of the logarithmic layer. In the present flow, however, δ^+ (in wall units) is found to vary from 0 to 100 depending on the local skin friction. The eddy viscosity is modeled by a damped mixing-length model: $\nu_t/\nu = \kappa y_w^+ \left(1 - e^{-y_w^+/A}\right)^2$, where $y_w^+ = y_w u_\tau / \nu$ is the distance to the wall in wall units, $\kappa = 0.4$, and $A = 19$.

3. Results and discussion

In Fig. 1, the contours of the vorticity magnitude at a given time instant and spanwise plane are plotted for $Re_D = 10^6$. Large coherent structures are visible in the wake, but they are not as well organized and periodic as in typical Kármán streets at lower (sub-critical) and higher (post-critical) Reynolds numbers. Compared to flows at lower Reynolds number (*e.g.* Kravchenko & Moin 2000; Breuer 2000), the boundary-layer separation is much delayed and the wake is narrower, resulting in a much smaller drag coefficient. Note that the rather thick layer seen along the cylinder surface consists mostly of vorticity contours of small magnitude. These levels are necessary for visualizing the wake structure, but are not representative of the boundary-layer thickness. The true boundary layer, with strong vorticity, is extremely thin in the attached region.

A comparison with two sets of experimental data of the mean pressure distribution

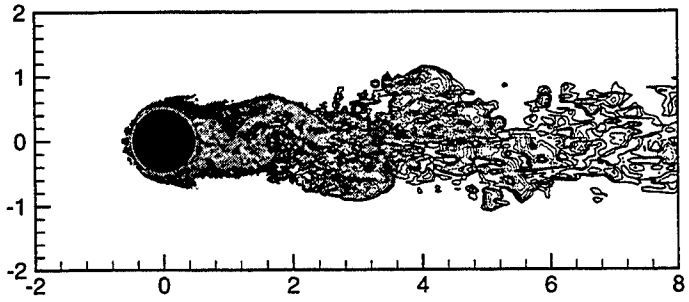

FIGURE 1. Instantaneous vorticity magnitude at a given spanwise cut for flow over a circular cylinder at $Re_D = 10^6$. 25 contour levels from $\omega D/U_\infty = 1$ to $\omega D/U_\infty = 575$ (exponential distribution) are plotted.

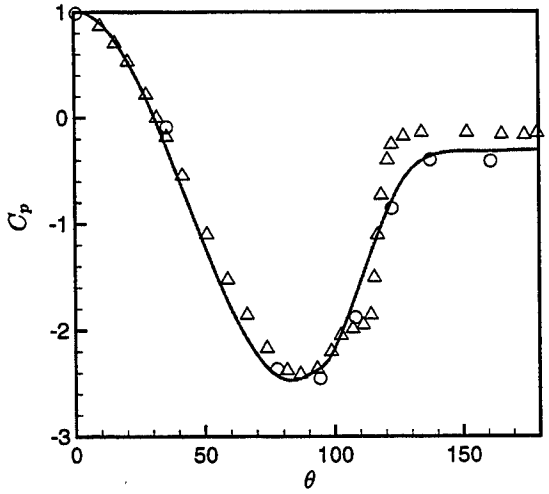

FIGURE 2. Mean pressure distribution on the circular cylinder. ——— Present LES at $Re_D = 10^6$; o Experiment of Warschauer & Leene (1971) at $Re_D = 1.26 \times 10^6$ (spanwise averaged); △ Experiment of Flachsbart (in Zdravkovich 1997) at $Re_D = 6.7 \times 10^5$.

on the cylinder surface is depicted in Fig. 2. Very good agreement is observed between the LES at $Re_D = 10^6$ and the experiment of Warschauer & Leene (1971) which was performed at $Re_D = 1.26 \times 10^6$. The original C_p data of Warschauer & Leene exhibit some spanwise variations; for the purpose of comparison the average value is plotted. Relative to the measurements of Flachsbart (see Zdravkovich 1997) at $Re_D = 6.7 \times 10^5$, the LES C_p shows smaller values in the base region. Note that Flachsbart's data contain a kink near $\theta = 110^o$, indicating the presence of a separation bubble. This type of separation bubble is characteristic of the critical regime, and is difficult to reproduce experimentally or numerically due to sensitivity to disturbances.

In Table 1, we compare the mean drag coefficient, the base pressure coefficient, and the Strouhal number from the LES at $Re_D = 10^6$ with the experimental values. The agreement with the measurements of Shih *et al.* (1993) is reasonably good. The LES somewhat overpredicts the drag coefficient compared with Shih *et al.* (1993), but underpredicts it relative to Achenbach (1968) (cf. Fig. 3). The Strouhal number of 0.22 from

	C_D	$-C_{p,base}$	St
LES	0.31	0.32	0.28
Exp. (Shih *et al.* 1993)	0.24	0.33	0.22
Exp. (Others, see Zdravkovich 1997)	0.17-0.40	-	0.18-0.50

TABLE 1. Drag, base pressure coefficient and Strouhal number for the flow around a circular cylinder at a Reynolds number of 10^6.

Shih *et al.* is for a rough-surface cylinder; no coherent vortex shedding was observed for smooth cylinders at Re_D larger than 4×10^5. Indeed, it is generally accepted that periodic vortex shedding does not exist in the super-critical regime of flow over a smooth cylinder (Zdravkovich 1997). From our simulation, a broad spectral peak of the unsteady lift centered at $St \approx 0.28$ is found. It can be argued that although the LES is performed for a smooth cylinder, the discretization of the cylinder surface and the numerical errors due to under-resolution may act as equivalent surface roughness, causing the flow field to acquire some rough-cylinder characteristics. The flow at high Reynolds number is very sensitive to surface roughness and to the level of free-stream turbulence, which contribute to the wide scatter of C_D and St among various experiments in the literature (Zdravkovich 1997), listed at the bottom of Table 1. Other factors causing the data scatter include wind-tunnel blockage and end-plate effects. Our simulation results fall easily within the experimental range. Generally speaking, there is a lack of detailed experimental data at super-critical Reynolds numbers. In particular, velocity and Reynolds-stress profile measurements are non-existent, making a more detailed comparison impossible.

To assess the robustness of the computational method, we have performed simulations at $Re_D = 5 \times 10^5$ and 2×10^6, in addition to the initial attempt at $Re_D = 1 \times 10^6$. The predicted mean drag coefficients are plotted in Fig. 3 along with the drag curve of Achenbach (1968). While the simulations predict C_D rather well at the two lower Reynolds numbers, the discrepancy becomes large at $Re_D = 2 \times 10^6$. More significantly, the LES solutions show relative insensitivity to the Reynolds number, in contrast to the experimental data which exhibit an increase in C_D with Reynolds number after the drag crisis. Similar Reynolds-number insensitivity has been observed for the other quantities shown previously. Poor grid resolution, which becomes increasingly severe as the Reynolds number increases, is the primary suspect.

Finally, the skin-friction coefficients predicted by the wall model in the LES calculations are plotted in Fig. 4 against the experimental data of Achenbach (1968) at $Re_D = 3.6 \times 10^6$. The levels are very different on the front half of the cylinder, but are in reasonable agreement on the back half. The boundary-layer separation and the recirculation region are captured rather well by the LES, indicating that they are not strongly affected by the upstream errors. The different Reynolds numbers in the LES and the experiment can account for only a small fraction of the discrepancy. Note that our computed C_f values are comparable to those reported by Travin *et al.* (2000) using DES. Travin *et al.* attribute the overprediction of C_f before separation to the largely-laminar boundary layer in the experiment, which has not been modeled adequately in either simulation. Grid resolution is another potential culprit in the present work. In addition, an overprediction of the skin

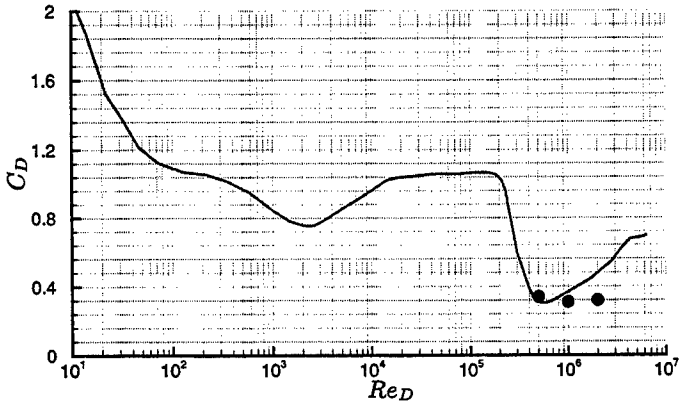

FIGURE 3. Drag coefficient as a function of Reynolds number. ——— Achenbach (1968); • Present LES.

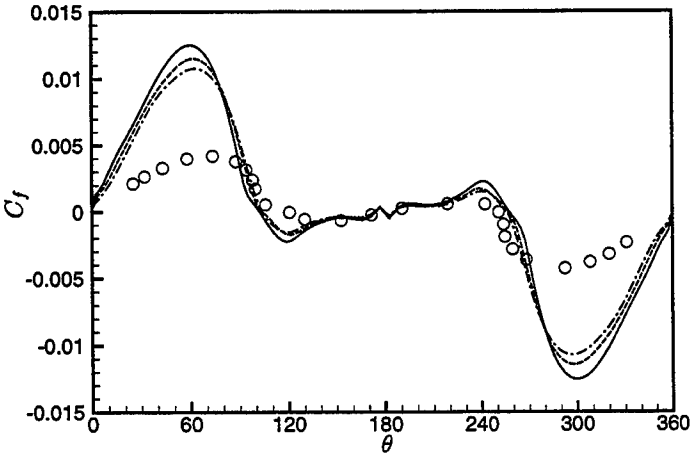

FIGURE 4. Skin friction distribution on the cylinder from LES: ——— $Re_D = 5 \times 10^5$; ---- $Re_D = 1 \times 10^6$; —·— $Re_D = 2 \times 10^6$. ○ Experiment of Achenbach (1968) at $Re_D = 3.6 \times 10^6$.

friction by the present wall model has also been observed by Wang & Moin (2001) in the acceleration region of the trailing-edge flow, suggesting that this simplified model may have difficulty with strong favorable pressure gradients. If this proves to be a major factor, the more general TBL equation model should provide a better alternative.

4. Concluding remarks

A bold numerical experiment has been carried out to compute the flow around a circular cylinder at supercritical Reynolds numbers using LES. The simulation is made possible by the use of a wall-layer model which alleviates the near-wall grid resolution requirements. Preliminary results are promising in the sense that they correctly predict the delayed boundary-layer separation and reduced drag coefficients consistent with measurements after the drag crisis. In quantitative terms, the mean pressure distributions

and overall drag coefficients are predicted reasonably well at $Re_D = 5 \times 10^5$ and 10^6. However, the computational solutions are inaccurate at higher Reynolds numbers, and the Reynolds-number dependence of the drag coefficient is not captured.

It must be emphasized that the results presented here are very preliminary. The grid used near the cylinder surface, particularly before separation, is quite coarse judged by the need to resolve the outer boundary-layer scales. The effect of the wall model under coarse grid resolution and in the laminar boundary layer is not clear. Evidently, a more systematic investigation is needed to separate the grid resolution and wall modeling effects, and to fully validate the numerical methodology in this challenging flow.

REFERENCES

ACHENBACH, E. 1968 Distribution of local pressure and skin friction around a circular cylinder in cross-flow up to $Re = 5 \times 10^6$. *J. Fluid Mech.* **34**, 625-639.

BALARAS, E., BENOCCI, C. & PIOMELLI, U. 1996 Two-layer approximate boundary conditions for large-eddy simulation. *AIAA J.* **34**, 1111-1119.

BREUER, M. 2000 A challenging test case for large eddy simulation: high Reynolds number circular cylinder flow. *Int. J. Heat Fluid Flow* **21**, 648-654.

CABOT, W. & MOIN, P. 2000 Approximate wall boundary conditions in the large-eddy simulation of high Reynolds number flow. *Flow Turb. Combust.* **63**, 269-291.

GERMANO, M., PIOMELLI, U., MOIN, P. & CABOT, W. H. 1991 A dynamic subgrid-scale eddy viscosity model. *Phys. Fluids A* **3**, 1760-1765.

KRAVCHENKO, A.G. & MOIN P. 2000 Numerical studies of flow over a circular cylinder at $Re_D = 3900$. *Phys. Fluids* **12**, 403-417.

LILLY D. K. 1992 A proposed modification of the Germano subgrid scale closure method. *Phys. Fluids A* **4**, 633-635.

MITTAL, R. & MOIN, P. 1997 Suitability of upwind-biased finite difference schemes for large-eddy simulation of turbulence flows. *AIAA J.* **35**, 1415-1417.

TRAVIN, A., SHUR, M., STRELETS, M. & SPALART, P. 1999 Detached-eddy simulations past a circular cylinder. *Flow Turb. Combust.* **63**, 269-291.

SHIH, W. C. L., WANG, C., COLES, D. & ROSHKO, A. 1993 Experiments on flow past rough circular cylinders at large Reynolds numbers. *J. Wind Engg and Industrial Aerodynamics* **49**, 351-368.

WANG, M. 1999 LES with wall models for trailing-edge aeroacoustics. *Annual Research Briefs*, Center for Turbulence Research, NASA Ames/Stanford Univ. 355-364.

WANG, M. & MOIN, P. 2000 Computation of trailing-edge flow and noise using large-eddy simulation. *AIAA J.* **38**, 2201-2209.

WANG, M. & MOIN, P. 2001 Wall modeling in LES of trailing-edge flow. *Proceedings of the Second International Symposium on Turbulence and Shear Flow Phenomena*, Stockholm, Sweden, **II**, 165-170.

WARSCHAUER, K. A. & LEENE, J. A. 1971 Experiments on mean and fluctuating pressures of circular cylinders at cross flow at very high Reynolds numbers. *Proc. Int. Conf. on Wind Effects on Buildings and Structures*, Saikon, Tokyo, 305-315 (see also Zdravkovich 1997).

ZDRAVKOVICH, M. M. 1997 *Flow Around Circular Cylinders. Vol. 1: Fundamentals.* Oxford University Press, Chap. 6.

An experimental and computational investigation of flow past cacti

By Sharon Talley, Gianluca Iaccarino, Godfrey Mungal AND Nagi N. Mansour

1. Motivation and objectives

This is an interdisciplinary study motivated by the saguaro cactus and other tall arborescent (treelike) succulents that withstand high wind velocities in their natural habitat. These desert plants have a cylindrical shape, modified by complex surface geometry. Typical diameters are of the order of 0.5 m, and at the highest wind speeds, when the cactus is in danger of being uprooted, the Reynolds number (Re) can be as large as 10^6. Because the shape of an object influences the surrounding airflow, natural selection may favor body morphologies that reduce forces exerted by wind gusts in their habitat. We hypothesize that the tall cacti morphology of longitudinal cavities and spines may function to reduce wind forces, including drag and also the fluctuating side-force caused by vortex shedding. We will address this hypothesis by experiments and numerical simulations.

The evolutionary process of random mutations followed by selection for or against those mutations is a continual shaping mechanism on organisms. Being products of their environment, organisms are equipped with adaptations that allow them to cope with the environmental stresses of their habitat. Longitudinal cavities and spines on succulent cylindrical plants evolved independently in two plant families: the Cactaceae of North and South America and the Euphorbiaceae of Southern Africa (Figs. 1a and 1b; Gibson & Nobel 1986). Thus, distantly related plant species living on different continents but in habitats with similar abiotic stresses have converged on a common body morphology. Convergent evolution to a common body shape provides compelling circumstantial evidence for the adaptive significance of this morphology in desert environments.

There has been much speculation on the function of cavities and spines on cacti, and the adaptive significance of the proposed functions is still open to speculation (Geller & Nobel 1984). Natural selection acts on the random mutations of existing structures (traits), resulting in improved structures, novel structures, and/or multiple-functionality of existing structures. Therefore, one function of a trait does not necessarily preclude other functions, and many traits may contribute to a common function. Given that the shape of an object affects the flow, it is surprising that no studies have examined how cavities and spines on desert succulents influence airflow.

Because there are many species of tall arborescent succulents, varying in body size, depth and number of cavities, and spine arrangement, we will focus on one of the most-studied of the tall arborescent succulents, the saguaro cactus, *Carnegiea gigantea* (Fig. 1b, 2, and 3). Saguaros are long-lived and slow to mature. They take 30 to 50 years to reach reproductive maturity and live up to 150 years of age. Adult saguaros have one main cylindrical stem ranging from 0.3 to 0.8 m in diameter (Benson 1981) and over 8 to 15 m in height (Hodge, 1991). Ten to 30 v-shaped cavities span the length of the stem (Hodge 1991). The number of cavities depends on the diameter of the stem, and new cavities can be added or deleted to maintain a cavity depth ratio (L/D – depth of the cavity divided by the diameter of the cylinder) of approximately 0.07 ± 0.0015 (Geller &

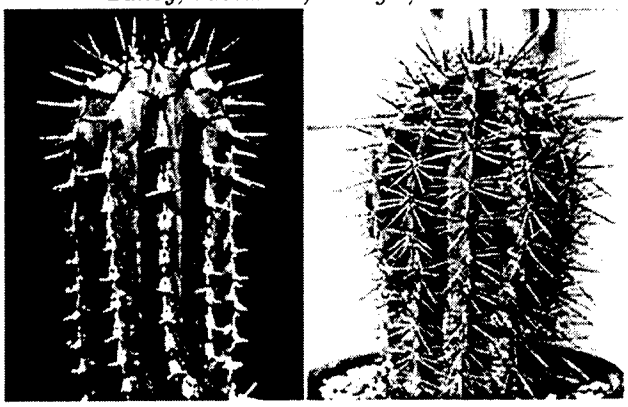

FIGURE 1. Convergence of the external morphology of desert succulents: (a) Euphorbia sp. (Euphorbiaceae) from Southern Africa and (b) young saguaro, *Carnegiea gigantea* (Cactaceae) from North America.

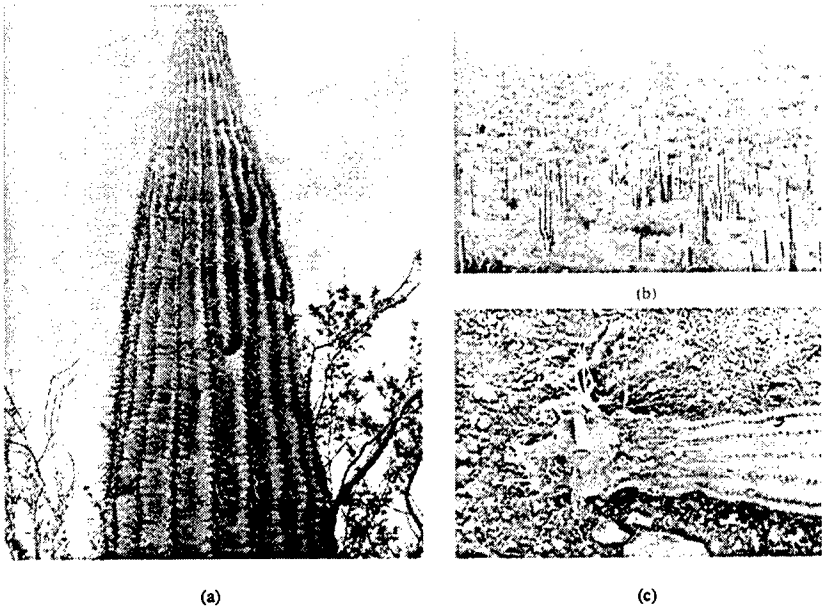

FIGURE 2. (a) Addition of cavities (ribs) on an adult saguaro trunk (b) Saguaro forest, and (c) Root system of a saguaro toppled by the wind.

Nobel 1984; Fig. 2a). Apices of the cavity junctures are adorned with whorls of 15 to 30 spines 2.5 to 7.6 cm long (Benson 1981).

In order for wind to be a selective agent on saguaros, high wind velocities must occur in saguaro habitats and they must affect their reproductive success. Within the distribution of saguaros, high wind velocities were recorded 15 m above the ground for a nine-year period (Bulk 1984). The maximum wind velocity recorded was 38 m/s, ($Re = 10^6$), and velocities exceeding 22 m/s ($Re = 7 \times 10^5$) occurred almost every month. Saguaro habitats contain less vegetation cover than other ecosystems and, consequently, have few if any other tall plants to shelter them from the wind (Fig. 2b). There is substantial circumstantial evidence that wind gusts exert enough force to topple saguaros, and thus, cause

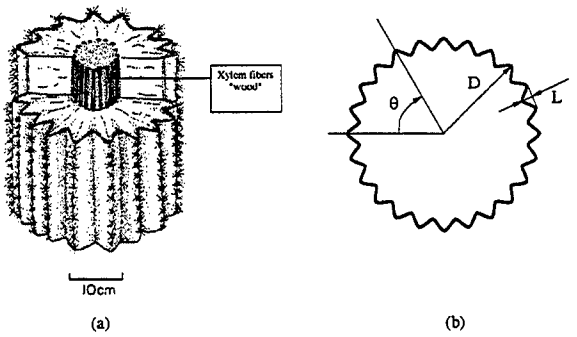

FIGURE 3. (a) Saguaro stem anatomy (Niklas & Buchman 1994). (b) Sketch of the cross-section

their premature mortality (Fig. 2c; Benson 1981; Alcock 1985; Pierson and Turner 1998), although information on the wind velocities required to topple large desert succulents is lacking. The natural-selection scenario would suggest that some saguaros are toppled by gusts (Fig. 2b), while many others remain standing. Considering that most tall cacti live for 150 years and take 30 to 50 years or more to reach reproduce maturity, strong gusts need only occur only every 30 to 50 years to be important in the natural selection of tall succulent morphology.

Another way stationary organisms can cope with high wind velocities is to increase their structural strength; however, investment in structural tissues has opportunity costs (Denny 1994). Saguaros have low investment in the structural tissues of the stem and even less in the roots. Succulent stems are 90 to 94% water (Gibson and Nobel 1986), and, therefore, use little structural tissue "wood" to support their massive structures. Saguaro wood is confined to the center of the stem (xylem fibers; Fig. 3a). The composite stem tissue has a density specific stiffness (ϵ/ρ) less than half of that for a solid wood stem (Niklas and Buchman 1994). The ratio of dry-weight investment in root mass to stem mass in cacti (0.08 to 0.14) is considerably less than most other plants forms (0.3 to 7.3), suggesting that saguaros invest comparatively little in root structural tissue (Nobel 1994). The saguaro root system is shallow, having a mean root depth of 25 cm and consisting of thin roots up to 2.5 cm in diameter (Fig. 2c). Their shallow root system, which provides poor root anchorage, has been noted to result in saguaro toppling when exposed to high wind velocities (Hodge 1991). The ability to dampen fluctuating side-force may also be particularly important in keeping these structures upright because large fluctuations in forces may break or dislodge roots. Because there are probably constraints on tissue strength, and evolution occurs by the natural selection of random mutations, it is conceivable that stationary organisms may evolve shapes that reduce drag and diminish fluctuating side-force.

At high Reynolds numbers ($Re > 10^4$) the drag coefficient (C_d) curves for spheres and cylinders have four distinct flow ranges, characterized by changes in drag caused by boundary-layer separation and by transition from laminar to turbulent flow (Fig. 4a; Roshko 1961; Achenbach 1977; Farell 1981). In the subcritical range, C_d is almost independent of Re (separation is laminar). Then, at the beginning of the critical range, C_d drops rapidly (boundary layer undergoes transition to turbulence). The lowest C_d on the curve is within the critical range, at what is referred to as the critical Re. The next range is the supercritical range, where C_d increases with increasing Re and continues to increase to the fully turbulent transcritical range.

When comparing C_d curves of uniformly rough and smooth cylinders, rough cylinders have C_d curves to the left of their smooth analogs and, therefore, experience the critical range at lower Re (Achenbach 1971). Roughness promotes transition, and, generally, the greater the roughness the greater the shift of the C_d curve to the left (the degree of surface roughness is quantified by the parameter k/D, the height of the roughness divided by the diameter of the cylinder). Although a greater degree of uniform surface roughness results in a lower critical Re, it is accompanied by a smaller drop in C_d and a smaller critical Re range. In addition, rough cylinders often have higher C_d in the postcritcal regime.

Experimental evidence shows that the shape of the C_d curve depends not only on the size but also on the shape and distribution of surface roughness. Cylinders with distributed strips of roughness have been shown to experience early transition without a rapid rise in C_d in the supercritical range (Fig. 4b; Nakamura and Tomonari 1982). Complex surface roughness, such as dimples on a golf ball (Bearman and Harvey 1976) and on a cylinder (Bearman and Harvey, 1993), also have a larger Re range of C_d reduction than cylinders with uniform roughness. Other surface modifications have been studied to passively reduce drag and fluctuating lift forces on circular cylinders; however, none have studied spanwise v-shaped cavities with $0.07L/D$.

This project addresses fundamental concepts in evolution by examining whether organisms are optimally shaped through natural selection to reduce drag and fluctuating lift. The fluid mechanics of cacti has not been examined experimentally or numerically. Such investigation would provide information on how longitudinal cavity depth and complex surface roughness can affect flow. There are surprisingly few studies on the fluid mechanics of biological organisms, especially terrestrial organisms with bluff bodies. There are no known bluff organisms that use surface roughness to reduce drag (Vogel 1981). Surface roughness has been argued to be an unlikely adaptation to control drag, because the reduction in C_d afforded by the surface roughness is accompanied by a dramatic increase in C_d at higher Re (Denny 1988 and Vogel 1981). However, if the increase in C_d occurs at Reynolds numbers that are rarely if ever experienced by the organism in question, it should have no effect on the organism's evolution.

2. Experimental study

2.1. *Wind tunnel*

Circular cylinders with diameter D of 9.98 cm were manufactured from Ren Shape 460 Modeling board. Five test cylinders are considered: a smooth cylinder, a uniformly rough cylinder ($k/D = 2.5 \times 10^{-3}$), and three cylinders differing in the depth of the vertical v-shaped cavities ($L/D = 0.035$, 0.07, and 0.105, see Fig. 3b). Each L/D cylinder had 24 cavities spanning 15°; bits were used to cut angles of 124°, 82.5° and 60° for the 0.035, 0.07, and 0.105 respectively. Roughness on the uniformly rough cylinder was provided by commercial 36 grit sandpaper (hydrodynamic roughness height, $k/D = 2.5 \times 10^{-3}$; Güven, Farell and Patel 1980). Sheets of sandpaper were cut and attached to the smooth cylinder with double-sided adhesive tape, and the thickness added to the cylinder was less than 2 mm.

Experimental measurements were performed at flow velocities from 13 to 29.5 m/s in a low-speed blower wind tunnel with a test section 1.18 m × 1.18 m in cross section. Cylinders were mounted vertically between two endplates attached to the roof and floor, giving an aspect ratio of 7.06 (h/D) and a geometric blockage (cylinder diameter divided by the width of the test section) of 13%. The endplates were $8D$ long by $7D$ wide, and

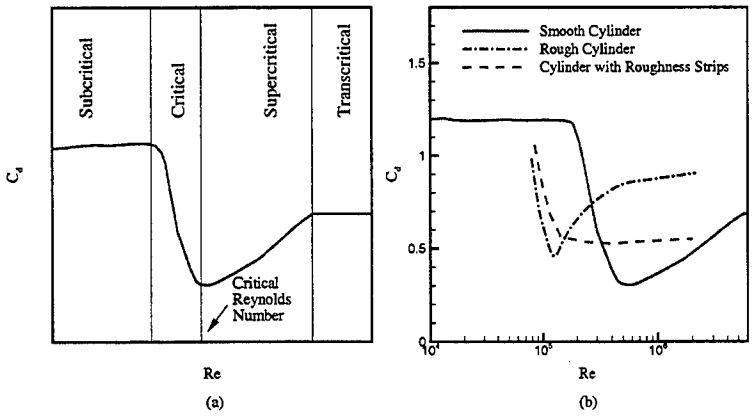

FIGURE 4. (a) C_d curve defining the regimes of flow around a smooth cylinder ($Re > 10^4$) and (b) Experimental C_d curves of smooth and rough cylinders cylinders. ——— : smooth surface (Achenbach 1971)); —·— : $k/D = 5.16 \times 10^{-3}$ (Nakamura & Tomonari 1982); – – – : smooth cylinder with strips of $k/D = 5.16 \times 10^{-3}$ at $\theta = 50$ degrees.

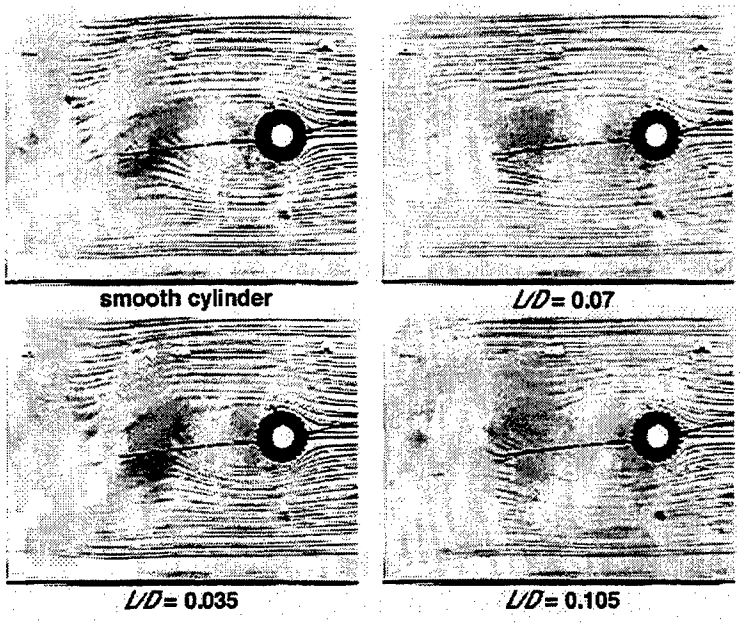

FIGURE 5. Smoke flow visualizations at Re =13,000. Flow is right to left (black line behind the cylinders is a fracture in the glass).

the distance between the cylinder axis and the leading edge was $3.5D$ (Szepessy 1994). The cylinder was rotated about its axis to place the cavities at different orientations to the flow, and then secured with supports.

Simple visualizations were performed using tufts of yarn attached to the cylinders, to a wand, and at the wire intersections of a fine framed grid. Flow was documented

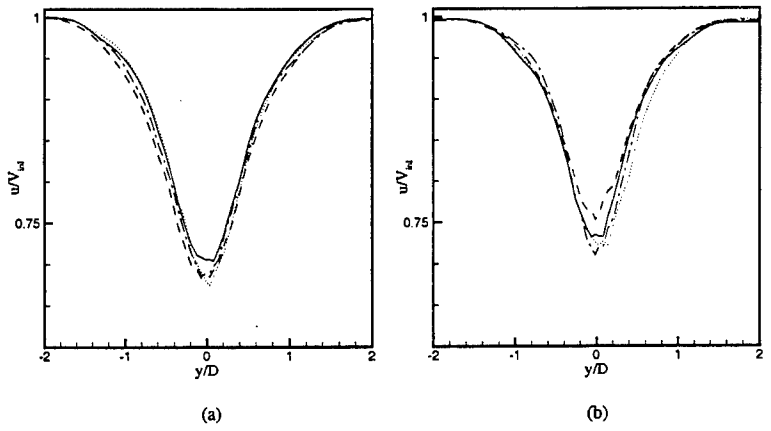

FIGURE 6. Velocity profiles at Re = 125,000 behind cylinders at different spanwise locations. Location of pitot-static probe from top endplate; L/D = ——— 0.5, – – – 2.3, —·— 3.5, and ····· 4.7. (a) Velocity profiles behind a smooth cylinder (b) Velocity profiles behind a cylinder with L/D 0.07.

using a Camcorder (Panasonic PV-L857). Visualization experiments were also carried out in a low-speed smoke tunnel (Collins model # 300; Collins Radio Co., Cedar Rapids, Iowa) with a test section 64.3 cm deep, 61 cm high, and 107 cm wide. Vortex streets at Re of approximately 13,000 were observed in all cases but the cylinder with a L/D of 0.07 (Fig. 5). The symmetric vortex shedding of the 0.07 L/D may be an artifact of the test cylinders not spanning the entire width of the test section. All test cylinders were examined in the same way.

Wake velocity profiles were measured with a Pitot-static tube supported by a motorized traversing mechanism. Profiles were measured at $3.2D$ behind the cylinder. The Pitot-static probe was traversed across the test section to a distance of about D from each wall. A total of 63 points were measured in the wake at a sampling rate 100 Hz for one minute (6000 samples/point).

2.2. *Data analysis*

In the Re range from 90,000 to 200,000, the cylinders with cavities and the one with uniform roughness had narrower wakes, with smaller velocity defect, than the smooth cylinder. On both counts, this suggests that the cylinders with cavities have a lower C_d than the smooth cylinder.

Velocity profiles were measured at different locations behind the cylinders to determine whether the flow was two-dimensional. Behind the smooth cylinder (Fig. 6a) the profiles are in very good agreement whereas larger discrepancies can be observed behind the cylinder with cavities (Fig. 6b), suggesting that longitudinal cavities may induce strong three-dimensional effects. Additional measurements and flow visulaization are required to clarify this issue.

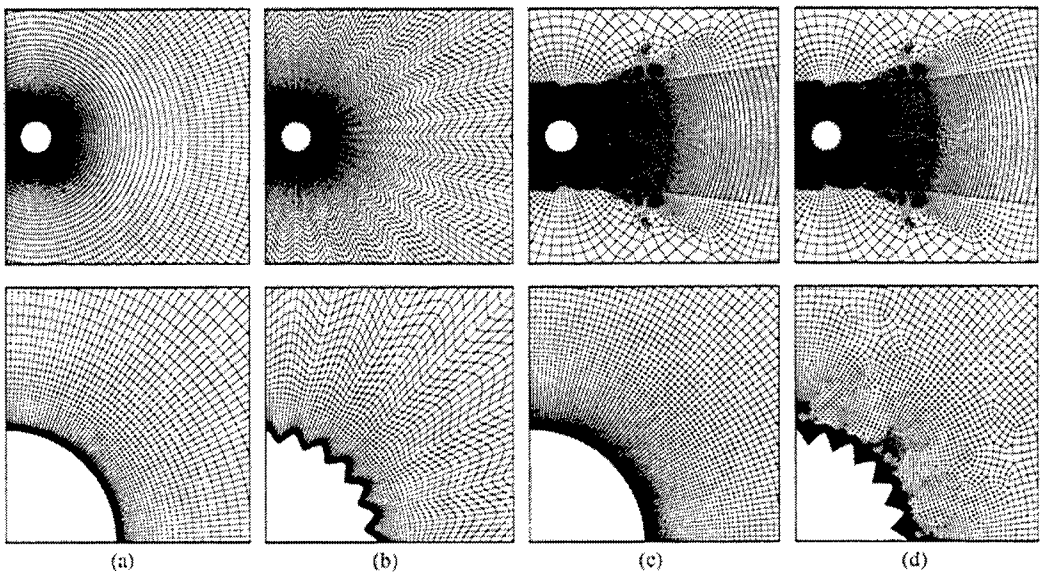

FIGURE 7. Example of the computational grids: (a-b) structured grids 241 × 100 elements; (c-d) unstructured grids ≈ 20,000 elements (a-c) $L/D = 0$ (b-d) $L/D = 0.07$. Lower set of figures is at about 7 times the scale of the upper set.

3. Numerical study

3.1. *Numerical method*

Preliminary simulations of the flow around a cactus section are carried out by solving the Navier-Stokes equations in two dimensions. Two codes are used: INS2D (Rogers & Kwak 1990) and Fluent (Fluent 1999). INS2D is an upwind based, third-order accurate code for structured (multiblock) grids; the artificial-compressibility approach is used for pressure-velocity coupling and the time integration is second-order accurate. Fluent is an unstructured-mesh solver based on second-order-accurate spatial and time discretization; the SIMPLE technique is used for pressure-velocity coupling. Turbulence modeling is based on the $v^2 - f$ model (Durbin 1995; Iaccarino 2001).

3.2. *Computational grids*

Cylinders with v-shaped cavities (with cavity ranging from $L/D = 0.0$ to $L/D = 0.105$) are considered. Several meshes have been generated to assess the sensitivity of the solution. In Fig. 7, examples of the grids are shown. Simulations using the structured grids (Fig. 7a and 7b) have been performed using both Fluent and INS2D. The structured grid is generated as an *O-type* mesh wrapped around the cylinder. The cavities are slightly smoothed to improve the orthogonality of the grid lines at the cylinder surface. The height of the first cell is adjusted according to Re; the distance from the far field boundary is $25D$ as used in Rogers & Kwak 1990. The unstructured meshes are generated using a quadrilateral paving technique (Blacker *et al.* 1991); this approach allows flexibility in clustering the grid cells in the wake region and close to the surface.

Table I shows results for the computations performed on different grids at a very low Reynolds number. The flow is unsteady and exhibits a periodic vortex shedding from the cylinder, but only the averaged drag coefficient is reported. Grid independence is achieved

for the smooth cylinder $L/D = 0$ using both the structured and the unstructured grids, and the corresponding values are extremely close.

The results for the flow around the cylinders with cavities show that grid independence is achieved only using the unstructured grids. An increase in cavity depth requires a finer resolution to capture accurately the in-cavity flow; in addition, the quality of the structured grid degrades as the cavity depth increases. It is worth noting that the results obtained using the finest structured grid (761 × 201) are in good agreement with the grid-independent results for the unstructured mesh.

In the following Sections only results computed using the unstructured grids are reported.

Grid	Elements	L/D 0	L/D 0.035	L/D 0.070	L/D 0.105
161 × 61	9,600	1.312	1.131	1.172	1.257
241 × 101	24,000	1.329	1.269	1.294	1.341
481 × 101	40,000	1.339	1.301	1.304	1.326
761 × 201	152,000	1.339	1.311	1.313	1.318

Structured grids

Elements	L/D 0	L/D 0.035	L/D 0.070	L/D 0.105
6,300	1.267	1.171	1.212	1.255
20,000	1.331	1.300	1.301	1.330
42,000	1.337	1.307	1.310	1.319
76,000	1.338	1.309	1.310	1.317

Unstructured grids

Table I. Computed time-averaged C_d for different computational grids – $Re = 100$

3.3. *Laminar simulations*

Flow simulations at low Reynolds number ($Re = 100$ and $Re = 200$) are carried out to evaluate the effect of cavity depth (and the accuracy of the predictions) without uncertainties related to the turbulence modeling. Two-dimensional simulations have been performed with unstructured grids using 6,000 to 42,000 elements (only the fine mesh results are presented). The calculations are carried out using a timestep $\Delta tU/D = 0.01$ (corresponding to approximately 35 time steps per vortex shedding period) and for a total time of $TU/D = 150$. The time history of drag and lift coefficients at $Re = 100$ are reported in Fig. 8a and 8b respectively. The statistics (time-averaged values, Strouhal number St etc.) are computed over a period $T_{av} = 50D/U$ and are reported in Table II: here C_l is the coefficient of fluctuating side force (peak values shown).

L/D	C_d	C_l	St
0	1.339 ± 0.010	± 0.330	0.160
0.035	1.304 ± 0.011	± 0.325	0.161
0.070	1.309 ± 0.010	± 0.334	0.162
0.105	1.318 ± 0.012	± 0.336	0.161

$Re = 100$

L/D	C_d	C_l	St
0	1.365 ± 0.037	± 0.664	0.175
0.035	1.361 ± 0.045	± 0.713	0.172
0.070	1.364 ± 0.057	± 0.742	0.172
0.105	1.381 ± 0.049	± 0.740	0.170

$Re = 200$

Table II. Statistics for low Reynolds number flow around cacti

The results indicate a small drag reduction ($\leq 10\%$) associated with the presence of the cavities. The cavity depth $L/D = 0.05$ is nearly optimal. The change in the unsteady side-force is also small, showing that the effect of the cavity is limited.

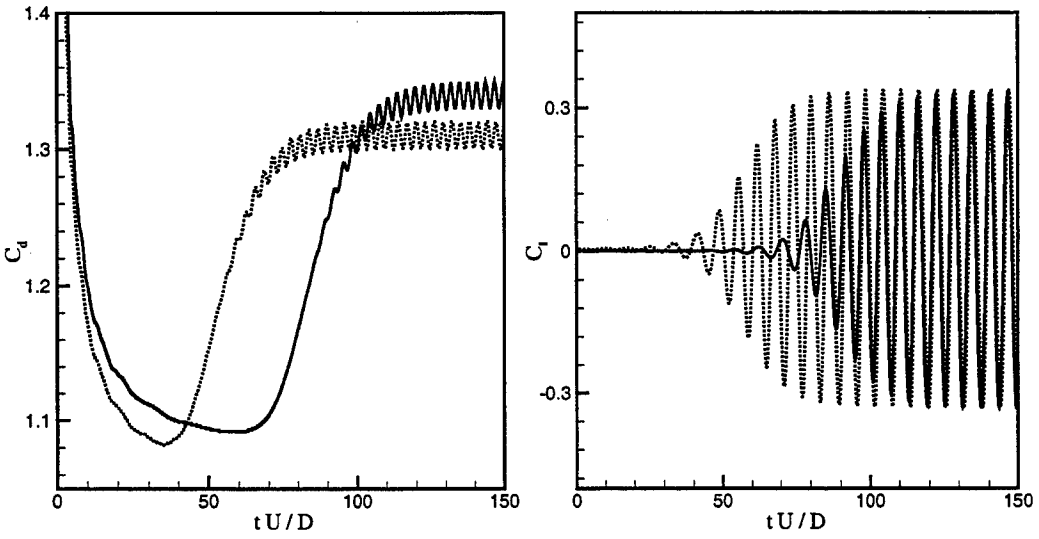

FIGURE 8. Time history of drag (a) and lift (b) coefficients. $Re = 100$. ——— : $L/D = 0$; ····· : $L/D = 0.07$

The results presented for the smooth cylinder at $Re = 200$ are in good agreement with the numerical simulations and the experimental data reported in Rogers & Kwak (1990). It is worth noting that $Re = 190$ represent the onset of three-dimensional flow in the wake of the cylinder.

3.4. *Turbulent simulations*

Calculations at $Re = 20,000$ and $Re = 100,000$ (subcritical regime, Fig. 4a) are performed using the $v^2 - f$ turbulence model. The time step, the simulated time and the averaging time are the same as before; the time history of lift and drag is shown in Fig. 9.

Compared to the results presented at low Re, the drag reduction is now larger ($\approx 25\%$). The strength of the unsteady motion is also greatly reduced, as seen in Table III.

L/D	C_d	C_l	St
0	1.683 ± 0.164	± 1.923	0.217
0.035	1.452 ± 0.076	± 1.562	0.221
0.070	1.419 ± 0.083	± 1.245	0.224
0.105	1.359 ± 0.052	± 0.987	0.223

$Re = 20,000$

L/D	C_d	C_l	St
0	1.644 ± 0.113	± 1.791	0.228
0.035	1.464 ± 0.120	± 1.462	0.224
0.070	1.401 ± 0.131	± 1.128	0.221
0.105	1.325 ± 0.079	± 0.864	0.221

$Re = 100,000$

Table III. Statistics for high Reynolds number flow around cacti

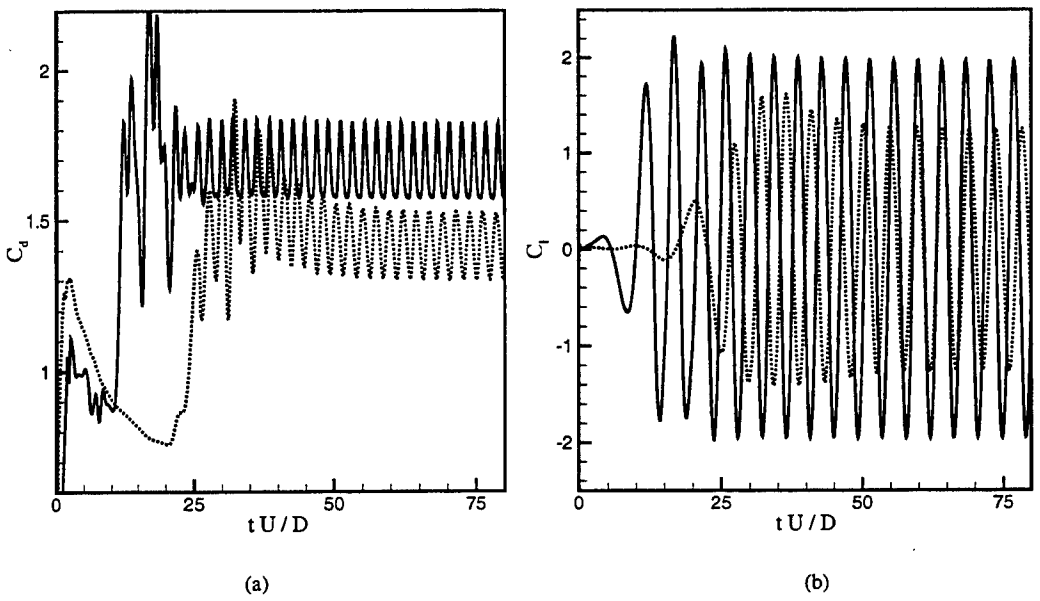

FIGURE 9. Time history of drag (a) and lift (b) coefficients. $Re = 20,000$. ——— : $L/D = 0$; ····· : $L/D = 0.07$

From the results presented in Table III, it appears that the cavity depth has a relatively strong effect on the drag and a substantial dampening effect on the unsteady motion.

The time averaged turbulent kinetic energy for the four geometries considered is reported in Fig. 10; the intensity very close to the cylinder decreases with the cavity depth, but higher values are observed in the near wake.

The comparison of the computed C_d with the experimental values for the smooth cylinder (Achenbach 1971) shows an overprediction of about 20%. The flow over the smooth cylinder in the subcritical regime is characterized by a laminar boundary layer separation; turbulence is generated in the separated shear layer and is sustained in the near wake. The smooth cylinder calculations ($L/D = 0$) are carried out with the $v^2 - f$ turbulence model switched off for $\theta \leq 90°$. This is necessary, especially at the higher Reynolds numbers, because turbulence models typically anticipate transition. The simulations with cavities are carried out with the model switched on from the stagnation point ($\theta = 0°$) because it is expected that transition occurs immediately after the first cavity. The exact location of transition has an impact on the accuracy of the drag calculation. In addition, in the subcritical range three-dimensional effects in the real-life wake are substantial.

Experimental and computed velocity profiles in the wake are compared in Fig. 11. The results for the smooth cylinder confirm that the calculation overestimate the drag (corresponding to the larger velocity defect in the wake); on the other hand, the data for the cylinder with cavities show remarkable agreement. It must be pointed out that the measurements exhibit three-dimensional effects that are not accounted for in the present two-dimensional simulations.

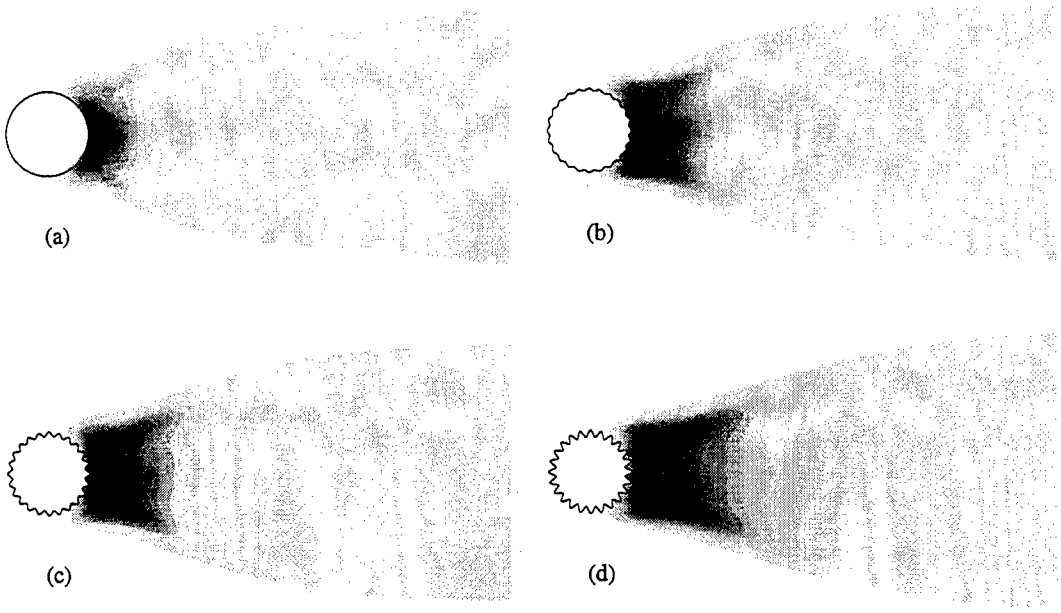

FIGURE 10. Time averaged turbulent kinetic energy: (a) $L/D = 0$; (b) $L/D = 0.035$; (c) $L/D = 0.070$; (d) $L/D = 0.105$

4. Conclusions and future plans

The preliminary numerical results presented suggest that the v-shaped cavities provide a damping effect of the fluctuating forces and a drag reduction. Further work is required to assess the effect of the cavities in the range of Re relevant for the cacti.

4.1. *Experimental work*

Future experiments should focus on obtaining C_d curves over a range of Re from 2×10^4 (for computational comparisons) to 10^6 (limit of wind velocities in the saguaro habitat). We will measure drag directly (using a multi-component force transducer - MC3A-X1000, Advanced Mechanical Technology, Inc, Watertown, MA), the pressure distribution around the test cylinders (using 16 static ports attached to a scanivalve), and vortex shedding frequency (using hot-wire anemometry). If there are interesting flow phenomena, the effect of spines on flow around the test cylinders will be evaluated (using 3-D PIV). Finally, experimental measurements will be performed on live cactus specimens.

4.2. *Numerical ccalculations*

Two-dimensional RANS calculations will be carried out up to $Re = 10^6$. The pressure and skin friction distributions on the surface will be examined for various cavity depth to evaluate the effect on the local flow characteristics.

The effect of the location of the laminar/turbulent transition must be investigated, together with the impact of the turbulence modeling.

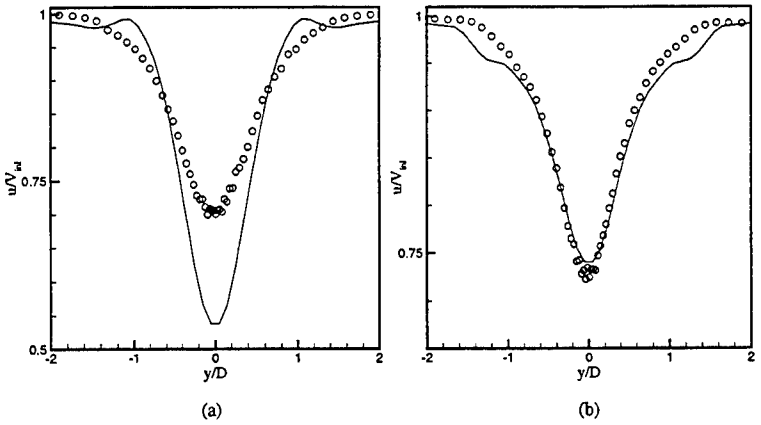

FIGURE 11. Velocity profiles in the wake of cylinders. ——— simulations (Re = 100,000); o experiments (Re = 125,000). (a) smooth cylinder (b) cylinder with L/D 0.07.

In addition, three-dimensional direct simulations will be required to perform a fair comparison with the experimental measurements in the subcritical and transcritical range.

Aknowledgements

We thank Profs. Peter Bradshaw, Rabindra Mehta, and John Eaton for advice and use of experimental equipment. We are grateful to Alex Hsu for help with laboratory work, Evangelos Kotsalis for help with numerical simulations, and Dr. Georgi Kalitzin for help with data analysis. We are especially thankful for technical support from graduate students Vijay Somandepalli, Simon Song, Paul Kodzwa, and Steve Solovitz. Additional thanks to Profs. Petros Koumoutsakos, Javier Jimenez and Haecheon Choi for suggestions.

REFERENCES

ACHENBACH, E. 1971 Influence of surface roughness on the cross-flow around a circular cylinder. *J. Fluid Mech.* **46**, 321-335.

ACHENBACH, E. 1977 The effects of surface roughness on the heat transfer from a circular cylinder to the cross flow of air. *International Journal of Heat and Mass Transfer* **20**, 359-362.

ALCOCK, J. 1985 *Sonaran Desert Spring*, The University of Chicago, Chicago.

BEARMAN, P. W., AND HARVEY, J. K. 1976 Golf ball aerodynamics. *Aeronautical Quarterly*, 112-122.

BEARMAN, P. W., AND HARVEY, J. K. 1993 Control of circular cylinder flow by the use of dimples. *AIAA J.* **31**, 1753-1756.

BENSON, L. 1981 *The Cacti of Arizona*, The University of Arizona Press, Tucson.

BLACKER T.D., M.B. STEPHENSON & S. CANANN 1991 Analysis automation with paving: A new quadrilateral meshing technique *Advances in Engineering Software*, **56**, pp.332-337.

DENNY, M. W. 1988 *Biology and the Mechanics of the Wave-Swept Environment*, Princeton University Press, New Jersey.

DENNY, M. W. 1994. Extreme drag forces and the survival of wind and water-swept organisms. *J. Exp. Biol.* **194**, 97-115.

DURBIN, P.A. 1995 Separated flow computations with the k-ϵ-v^2 model, *AIAA J.*, **33** pp.659-664.

FARELL, C. 1981 Flow around fixed circular cylinders: Fluctuating loads. *Proc. ASCE: J. Engg. Mech. Divn.* **107**, 565-573.

GELLER, G. N., & NOBEL, P. S. 1984. Cactus ribs: influence on PAR interception and CO_2 uptake. *Photosynthetica* **18**, 482-494.

GIBSON, A. C., & NOBEL, P. S. 1986 *The Cactus Primer*, Harvard University Press, Cambridge.

GUVEN, O., FARELL, C. & PATEL, V. C. 1978 Surface-roughness effects on mean flow. *J. Fluid Mech.* **98**, 673-701.

HODGE, C. 1991. *All About Saguaros*, Hugh Harelson-Publisheer, Phoenix.

IACCARINO, G. 2001 Predictions of a turbulent separated flow using commercial CFD codes, *J. Fluids Engg*, **123**, 1-10.

FLUENT INC. 1999 Fluent V5.3 User Manual.

NAKAMURA, Y., & TOMONARI, Y. 1982. Effects of surface roughness on the flow past circular cylinders at high Reynolds numbers. *J. Fluid Mech.* **123**, 363-378.

NIKLAS, K. J., & BUCHMAN, S. L. 1994. The allometry of saguaro height. *Amer. J. Botany* **81** 1161-1168.

NOBEL, P. S. 1994 *Remarkable Agaves and Cacti*, Oxford University Press, New York.

PIERSON, E. A., & TURNER, R. M. 1998 An 85-year study of saguaro (*Carnegiea gigantea*) demography. *Ecology* **79**, 2676-2693.

ROGERS, S. E. & KWAK, D. 1990 An upwind differencing scheme for the time accurate incompressible Navier-Stokes equations. *AIAA J.*, **28**, 253–262.

ROSHKO, A. 1961 Experiments on the flow past a circular cylinder at very high Reynolds number. *J. Fluid Mech.* **10**, 345-356.

SZEPESSY, S. 1994 On the spanwise correlation of vortex shedding from a circular cylinder at high Reynolds number. *Phys. Fluids* **6**, 2406-2416.

VOGEL, S. 1981 *Life in Moving Fluids*, Princeton University Press, Princeton.

Interacting flamelet model for non-premixed turbulent combustion with local extinction and re-ignition

By Heinz Pitsch, Chong M. Cha AND Sergei Fedotov

1. Motivation and objectives

The ability of unsteady laminar flamelet models to yield accurate predictions in non-premixed turbulent reacting flows has been investigated in many different studies. These include different geometries and flow situations, such as jet flames (Pitsch *et al.* 1998; Pitsch & Steiner 2000), diesel engines (Pitsch *et al.* 1996), and also show that even complex chemical processes such as the formation of NO_x and soot can be described with reasonable accuracy.

A particularly appealing feature of the model is that the local instantaneous scalar dissipation rate, which describes the rate of molecular mixing of fuel and oxidizer and is known to be the most important parameter in non-premixed combustion, appears explicitly as a parameter in the model. This permits the study of influence of this important quantity and simplifies the physical interpretation.

However, because of the simplifications made in the derivation of the flamelet equations, the model is not generally valid for arbitrary situations and fails, for instance, in predicting lifted flames or when local extinction and re-ignition events are important.

Local extinction and re-ignition has recently become one of the most prominent research topics in non-premixed turbulent combustion. Many studies have been devoted to this problem including; direct numerical simulations (DNS) (Sripakagorn *et al.* 2000, 2001); modeling studies using different approaches such as transported probability density function (pdf) methods (Xu & Pope 2000), and the one-dimensional turbulence model (Hewson & Kerstein 2001); and experiments (Barlow & Frank 1998). The Sandia flame series, investigated experimentally by Barlow & Frank (1998) consists of six flames with different Reynolds numbers and degrees of local extinction. These flames have become a benchmark data set for modeling studies.

Xu & Pope (2000) have presented predictions of three different Sandia flames, ranging from moderate to high degree of local extinction, with reasonable agreement with the experiments. In this study only the ensemble-averaged value of the scalar dissipation rate is used in the simulations, and fluctuations of this quantity are neglected.

The influence of the fluctuations of the scalar dissipation rate has been investigated by Pitsch & Fedotov (2001). In this work, the flamelet equations were used, with the scalar dissipation rate as a random variable. To describe the evolution of the scalar dissipation rate, a stochastic differential equation (SDE) was formulated. From these governing equations, a Fokker-Planck equation for the joint probability density function of the stoichiometric temperature and the scalar dissipation rate was derived. It has been shown that the fluctuations of the scalar dissipation rate can have a very strong effect, leading to local extinction even when the average scalar dissipation rate is below the extinction limit. However, because the study presented in Pitsch & Fedotov (2001) was

based on the flamelet equations, which cannot account for re-ignition, the real behavior of the physical system could not be investigated.

In the present work, an extension of the flamelet model is presented, which can account for re-ignition. The resulting modeled equations are solved numerically, and the mechanisms of extinction and re-ignition are investigated.

2. Governing equations

2.1. *Extended flamelet model*

To derive the extended flamelet equations, the equation for the temperature T is considered. The extended flamelet equations for other reactive scalars can be derived similarly. Since the model will subsequently be compared to the results of direct numerical simulations (DNS) we assume constant heat capacity c_p, and negligible temporal pressure change and radiative heat loss. The chemistry is described by a one-step reversible reaction with net reaction rate w. A more general formulation, accounting for the neglected terms and complex chemistry, is a trivial extension of the following derivation. In addition to the temperature equation, we will use the transport equation for the mixture fraction Z. If the Lewis number of the mixture fraction is assumed to be unity, the equations for mixture fraction $Z = Z(t, x_1, x_2, x_3)$ and temperature $T = T(t, x_1, x_2, x_3)$ can be written as

$$\rho \frac{\partial Z}{\partial t} + \rho \boldsymbol{v} \cdot \nabla Z - \nabla \cdot (\rho D \nabla Z) = 0 \tag{2.1}$$

$$\rho \frac{\partial T}{\partial t} + \rho \boldsymbol{v} \cdot \nabla T - \nabla \cdot (\rho D \nabla T) - \rho \frac{Q}{c_p} w = 0\,, \tag{2.2}$$

where t is the time, x_i are the spatial coordinates, ρ the density, $\boldsymbol{v}$ the velocity vector, D the diffusivity of the mixture fraction, and Q is the heat of reaction.

We now want to derive a flamelet equation which accounts for a burning state, but also for local extinction and re-ignition processes. In the derivation of the flamelet equations as proposed by Peters (1983, 1984), a coordinate transformation of the Crocco type is introduced into the governing equations, such that

$$(t, x_1, x_2, x_3) \longrightarrow (t, Z, Z_2, Z_3)\,, \tag{2.3}$$

in which the mixture fraction is introduced as a new independent coordinate. This implies that the new coordinate is locally attached to an iso-surface of the mixture fraction, say the stoichiometric mixture fraction Z_{st}, and the new coordinates Z_2, Z_3 lie in this surface. Then the transformation of the derivatives is given by

$$\frac{\partial}{\partial t} \longrightarrow \frac{\partial}{\partial t} + \frac{\partial Z}{\partial t}\frac{\partial}{\partial Z}\,, \qquad \nabla \longrightarrow \nabla Z \frac{\partial}{\partial Z} + \nabla_{Z\perp}\,, \qquad \text{with} \qquad \nabla_{Z\perp} = \begin{pmatrix} 0 \\ \partial/\partial Z_2 \\ \partial/\partial Z_3 \end{pmatrix}. \tag{2.4}$$

Introducing this into Eq. (2.2) and using Eq. (2.1), one obtains, for $T = T(t, Z, Z_2, Z_3)$,

$$\rho \frac{\partial T}{\partial t} - \frac{\rho \chi}{2}\frac{\partial^2 T}{\partial Z^2} - \rho \frac{Q}{c_p} w + \rho \boldsymbol{v} \cdot \nabla_{Z\perp} T - 2\nabla Z \cdot \frac{\partial}{\partial Z}(\rho D \nabla_{Z\perp} T)$$

$$- \nabla_{Z\perp} \cdot (\rho D \nabla_{Z\perp} T) - \nabla_{Z\perp} T \cdot \nabla Z \frac{\partial}{\partial Z}(\rho D) = 0\,. \tag{2.5}$$

Note that in Eqs. (2.2) and (2.5) there appear two derivatives with respect to time which

are associated with two different coordinate systems. In Eq. (2.2), $\partial T/\partial t$ is the rate of change of temperature as observed at a fixed point in space (x_1, x_2, x_3), whereas in Eq. (2.5) $\partial T/\partial t$ represents the rate of change of the temperature when moving with the iso-surface of the mixture fraction at fixed (Z, Z_2, Z_3).

In a subsequent asymptotic analysis, Peters (1983, 1984) shows that changes of the reactive scalars within surfaces of constant mixture fraction are small compared to changes in the direction normal to this surface, and can therefore be neglected. This leads to the flamelet equations,consisting of the first three terms in Eq. (2.5)

$$\rho\frac{\partial T}{\partial t} - \frac{\rho\chi}{2}\frac{\partial^2 T}{\partial Z^2} - \rho\frac{Q}{c_p}w = 0\,, \tag{2.6}$$

where the scalar dissipation rate, defined as

$$\chi = 2D\,(\nabla Z)^2 \tag{2.7}$$

appears as a new parameter. This equation has been analyzed in DNS of isotropic decaying turbulence with initially non-premixed reactants by Sripakagorn *et al.* (2000, 2001). It has been shown that Eq. (2.6) describes the extinction process very well, but obviously fails to predict re-ignition. At locations where local extinction has occurred, the scaling in Eq. (2.5) changes and the arguments leading to Eq. (2.6) are no longer true. Terms describing transport within surfaces of constant mixture fraction are then of leading order and therefore have to be considered. After extinction, the maximum flamelet temperature is small, so that changes in the direction normal to iso-surfaces of the mixture fraction can be neglected. If it is argued that re-ignition occurs by partially-premixed flame propagation along iso-surfaces of the mixture fraction, then an asymptotic analysis similar to that of Peters (1983) can be performed. Introducing a small parameter $\varepsilon = l_F\nabla Z$, where ε represents the ratio of length scales of order-unity temperature changes in direction normal to the direction along iso-mixture fraction surfaces, the coordinates Z_2 and Z_3 can be replaced by stretched coordinates such that $\xi_2 = Z_2/\varepsilon$ and $\xi_3 = Z_3/\varepsilon$. Then

$$\nabla_{\xi\perp} = \nabla_{Z\perp}/\varepsilon \quad \text{with} \quad \nabla_{\xi\perp} = \begin{pmatrix} 0 \\ \partial/\partial\xi_2 \\ \partial/\partial\xi_3 \end{pmatrix}. \tag{2.8}$$

Introducing Eq. (2.8) into Eq. (2.5) and keeping only leading-order terms, the equations describing the re-ignition process are obtained as

$$\rho\frac{\partial T}{\partial t} - \nabla_{Z\perp}\cdot(\rho D\nabla_{Z\perp}T) - \rho\frac{Q}{c_p}w = 0\,, \tag{2.9}$$

where the original coordinates Z_2 and Z_3 have been re-introduced. No scaling has been assumed for the time and the reaction term, but it is obvious that the accumulation and reaction terms are important for re-ignition, so these have been retained in the equation.

The leading-order equation which can describe both the extinction and re-ignition processes can now be obtained by combining Eqs. (2.6) and (2.9), yielding the extended flamelet equation as

$$\rho\frac{\partial T}{\partial t} - \frac{\rho\chi}{2}\frac{\partial^2 T}{\partial Z^2} - \nabla_{Z\perp}\cdot(\rho D\nabla_{Z\perp}T) - \rho\frac{Q}{c_p}w = 0\,. \tag{2.10}$$

In this equation the second term describes the flamelet-type diffusive transport, while the third term describes the interaction of different flamelets. The coordinates Z_2 and Z_3

still measure physical space while Z is the mixture fraction: note, however, that because Z, Z_2, and Z_3 form an orthogonal coordinate system, the partial derivatives with respect to Z_2 and Z_3 have to be evaluated at constant Z.

2.2. *Modeled extended flamelet equation*

To apply Eq. (2.10) in a numerical simulation, the newly-appearing diffusion term has to be modeled. A simple modeling approach is to represent this term by a molecular-mixing model frequently used in transported pdf modeling. Using for instance an Interaction by Exchange with the Mean (IEM) model, this term can be represented as

$$\frac{1}{\rho}\nabla_{Z\perp}\cdot(\rho D\nabla_{Z\perp}T) = -\frac{T-\langle T|Z\rangle}{T_{\rm IEM}}\,, \tag{2.11}$$

where $\langle T|Z\rangle$ is the average of the temperature conditioned on a given value of the mixture fraction, and $T_{\rm IEM}$ is the mixing time. The conditional average has been used here, since, as mentioned above, the diffusion term modeled in Eq. (2.11) describes only mixing at a given mixture fraction. It is well known that the application of IEM as a mixing model for reactive scalars creates problems if mixing occurs between states with different mixture fraction. It is interesting to note that in the current application of the IEM model, where mixing occurs only on surfaces of constant mixture fraction, this problem does not occur.

The modeled extended flamelet equation is then given by

$$\frac{\partial T}{\partial t} - \frac{\chi}{2}\frac{\partial^2 T}{\partial Z^2} + \frac{T-\langle T|Z\rangle}{T_{\rm IEM}} - \frac{Q}{c_p}w = 0\,. \tag{2.12}$$

The remaining modeling problem is now the determination of the mixing time $T_{\rm IEM}$. This can be done in different ways. A particularly appealing way is to make the assumption that all changes of the temperature along iso-surfaces of the mixture fraction are caused by changes in the scalar dissipation rate. The advantage of this assumption is that it incorporates the fact that extinction is caused by excessive scalar dissipation rate. Introduction of the scalar dissipation rate as a new independent coordinate seems reasonable since the scalar dissipation is the most important parameter in non-premixed combustion.

For the following derivation we first assume that the local instantaneous scalar dissipation rate can be described as a one-parameter function of the mixture fraction

$$\chi(t,x_1,x_2,x_3) = \chi_{\rm st}(t,x_1,x_2,x_3)f(Z)\,. \tag{2.13}$$

The exact form of the function $f(Z)$ is not important here, and can for instance be taken from a laminar counterflow configuration (Peters 1993), an unsteady mixing layer (Peters 1984), or a semi-infinite mixing layer (Pitsch *et al.* 1998). This assumption is valid at least within a small region around the reaction zone, which is assumed to be laminar, and has also been corroborated by the DNS data used for a validation of the present model (Sripakagorn *et al.* 2000, 2001), for the conditional mean quantities. A detailed discussion of this assumption in the context of this DNS data can be found in Cha *et al.* (2001). A transport equation for $\chi_{\rm st} = \chi_{\rm st}(t,x_1,x_2,x_3)$ has also been given by Cha *et al.* (2001) as

$$\rho\frac{\partial\chi_{\rm st}}{\partial t} + \rho\boldsymbol{v}\cdot\nabla\chi_{\rm st} - \nabla\cdot(\rho D\nabla\chi_{\rm st}) - F = 0\,, \tag{2.14}$$

where the source term F is given by

$$F = 2\frac{\rho D}{f(Z)}\frac{\partial f(Z)}{\partial Z}\nabla Z \cdot \nabla \chi_{\rm st} + \frac{1}{2}\rho\chi_{\rm st}^2\frac{\partial^2 f(Z)}{\partial Z^2} + \frac{G}{f(Z)}, \tag{2.15}$$

and G describes the production of scalar dissipation rate by strain-rate fluctuations and the dissipation by molecular diffusion.

With this assumption, an additional coordinate transformation $t, Z, Z_2, Z_3 \longrightarrow t, Z, \chi_{\rm st}$ can be used to replace the spatial coordinates Z_2 and Z_3 by the scalar dissipation rate, and an additional transport term in scalar-dissipation-rate space is obtained. The resulting equation is similar to the doubly-conditional moment-closure equations derived by Cha *et al.* (2001), but for local instantaneous quantities instead of conditionally-averaged ones.

It follows from Eq. (2.13) that $\chi_{\rm st}$ is not a function of Z, and therefore

$$\nabla_{Z\perp}\chi_{\rm st} = \nabla_Z \chi_{\rm st} \quad \text{with} \quad \nabla_Z = \begin{pmatrix} \partial/\partial Z_1 \\ \partial/\partial Z_2 \\ \partial/\partial Z_3 \end{pmatrix} \tag{2.16}$$

Then the transformation of the derivatives is given by

$$\frac{\partial}{\partial t} \longrightarrow \frac{\partial}{\partial t} + \frac{\partial \chi_{\rm st}}{\partial t}\frac{\partial}{\partial \chi_{\rm st}}, \qquad \nabla_{Z\perp} \longrightarrow \nabla\chi_{\rm st}\frac{\partial}{\partial \chi_{\rm st}}. \tag{2.17}$$

Introducing Eq. (2.17) into Eq. (2.10), and using Eq. (2.14) with the coordinates replaced by Eq. (2.4), one obtains the equation for $T = T(t, Z, \chi_{\rm st})$ as

$$\frac{\partial T}{\partial t} + F\frac{\partial T}{\partial \chi_{\rm st}} - \frac{\chi}{2}\frac{\partial^2 T}{\partial Z^2} - \frac{\gamma_{\rm st}}{2}\frac{\partial^2 T}{\partial \chi_{\rm st}^2} - \frac{Q}{c_p}w = 0, \tag{2.18}$$

where $\gamma_{\rm st}$ has been introduced as $\gamma_{\rm st} = 2D\left(\nabla\chi_{\rm st}\right)^2$. The convection term appearing in Eq. (2.18) from Eq. (2.14) can be neglected, by the same arguments as in the analysis that led to Eq. (2.9). Alternatively, the fourth term in Eq. (2.5) could be retained and would cancel with the convection term appearing here.

Equation (2.18) is generally very similar to the flamelet equations given by Peters (1984), but with two additional terms, a convection term in $\chi_{\rm st}$-space caused mainly by random production and dissipation of the scalar dissipation rate, and a diffusion term in $\chi_{\rm st}$-space with $\gamma_{\rm st}$ as the diffusion coefficient.

The solution of Eq. (2.18) describes the temperature evolution in a coordinate system attached to a point of constant mixture fraction and constant scalar dissipation rate. However, we are interested in the development of a flamelet, which is attached to a stoichiometric surface at the origin of the coordinate system introduced by Eq. (2.17). This is generally not at constant scalar dissipation rate. The $t, Z, \chi_{\rm st}$-coordinate system moves relative to this because of the production and dissipation of scalar dissipation rate F given by Eq. (2.15). We therefore introduce the concept of a "flamelet particle" and introduce a corresponding coordinate system. Let $\chi_{\rm st}(t)$ be the position of a flamelet particle in $\chi_{\rm st}$-space. By definition, this particle moves with the net production rate F such that

$$\frac{\partial \chi_{\rm st}}{\partial t} = F(t, Z, \chi_{\rm st}(t)). \tag{2.19}$$

Then Eq. (2.18) can be written as

$$\frac{\partial T}{\partial t} - \frac{\chi(t)}{2}\frac{\partial^2 T}{\partial Z^2} - \frac{\gamma_{\rm st}}{2}\frac{\partial^2 T}{\partial \chi_{\rm st}^2} - \frac{Q}{c_p}w = 0\,, \tag{2.20}$$

where the scalar dissipation rate $\chi_{\rm st}(t)$ is a random parameter determined by the solution of Eq. (2.19).

We now introduce the non-dimensional reaction source term ω, as defined in Pitsch & Fedotov (2001). and the non-dimensional temperature θ defined by

$$\theta = \frac{T - T_{{\rm st},u}}{T_{{\rm st},b} - T_{{\rm st},u}} \quad \text{with} \quad T_{{\rm st},u} = T_2 + (T_1 - T_2)\, Z_{\rm st} \tag{2.21}$$

where $T_{{\rm st},b}$ is the stoichiometric adiabatic flame temperature, also defined in Pitsch & Fedotov (2001). The non-dimensional time and scalar dissipation rate are defined as

$$\tau = \frac{\chi_{{\rm st},0}}{a}t \quad \text{and} \quad x = \frac{\chi}{\chi_{{\rm st},0}}\,, \tag{2.22}$$

where $a = \Delta Z Z_{\rm st}\,(1 - Z_{\rm st})$ and ΔZ is the reaction-zone thickness, and $\chi_{{\rm st},0}$ is a reference value, here chosen to be the stoichiometric scalar dissipation rate at extinction.

Equation (2.18) can then be written as

$$\frac{\partial \theta}{\partial \tau} - \frac{a x(\tau)}{2}\frac{\partial^2 \theta}{\partial Z^2} - \frac{\Upsilon_{\rm st}(\tau)}{2}\frac{\partial^2 \theta}{\partial x_{\rm st}^2} - \omega\,(\theta) = 0\,, \tag{2.23}$$

where $\Upsilon_{\rm st}$ is a dimensionless number representing the ratio of the time scales of the transport in the direction of $\chi_{\rm st}$ and the transport in the direction of Z, and is defined by

$$\Upsilon_{\rm st} = \frac{a\gamma_{\rm st}}{\chi_{{\rm st},0}^3}\,. \tag{2.24}$$

The transport term in the direction of Z always causes heat losses away from the reaction zone. In contrast to this, if a locally-extinguished spot is considered, the transport term in the x-direction leads to a gain of heat from hotter surrounding areas. Hence, $\Upsilon_{\rm st}$ characterizes the ability to re-ignite and will therefore be called the re-ignition parameter. Consequently, for $\Upsilon_{\rm st} = 0$ the flamelet equations as given in Pitsch & Fedotov (2001) are recovered.

Based on the assumption that temperature changes along iso-surfaces of the mixture fraction are caused only by changes in the scalar dissipation rate, we have now derived an equation similar to Eq. (2.12). However, the present form of the mixing term in $x_{\rm st}$ allows a straightforward physical modeling of the mixing time $T_{\rm IEM}$, if it is modeled in a manner similar to Eq. (2.11). Introducing the IEM-model for the diffusion term in the $x_{\rm st}$-direction in Eq. (2.23) we obtain

$$\frac{\partial \theta}{\partial \tau} - \frac{a x}{2}\frac{\partial^2 \theta}{\partial Z^2} + \frac{\Upsilon_{\rm st}}{2\,\langle x_{\rm st}\rangle^2}\frac{\theta - \langle \theta | Z, \Upsilon_{\rm st}\rangle}{C_{\rm IEM}} - \omega\,(\theta) = 0\,, \tag{2.25}$$

where $\langle T|Z, \Upsilon_{\rm st}\rangle$ is the mean temperature, conditioned on Z and $\Upsilon_{\rm st}$, of the system at a particular time τ. The mixing time $T_{\rm IEM}$ has been modeled as

$$T_{\rm IEM} = C_{\rm IEM}\frac{\langle \chi_{\rm st}\rangle^2}{\gamma_{\rm st}} \tag{2.26}$$

and the constant $C_{\rm IEM}$ is set to unity for subsequent numerical simulations.

2.3. *Stochastic differential equations for x_{st} and Υ_{st}*

In Eq. (2.25), x_{st} and Υ_{st} are fluctuating random quantities. In order to solve Eq. (2.25) we need to derive SDEs for both. This can be done according to the procedure outlined in Pitsch & Fedotov (2001). The resulting equations are

$$dx_{\mathrm{st}} = -\frac{x_{\mathrm{st}}}{\delta_x} \ln\left(\frac{x_{\mathrm{st}}}{\langle x_{\mathrm{st}}\rangle}\right) d\tau + \sigma_x \frac{2}{\sqrt{\delta_x}} x_{\mathrm{st}} \circ dW(\tau) \tag{2.27}$$

and

$$d\Upsilon_{\mathrm{st}} = -\frac{\Upsilon_{\mathrm{st}}}{\delta_\Upsilon} \ln\left(\frac{\Upsilon_{\mathrm{st}}}{\langle \Upsilon_{\mathrm{st}}\rangle}\right) d\tau + \sigma_\Upsilon \frac{2}{\sqrt{\delta_\Upsilon}} \Upsilon_{\mathrm{st}} \circ dW(\tau)\,, \tag{2.28}$$

where dW is a Wiener process. Here δ_x and δ_Υ represent the non-dimensional characteristic times for the probability density functions (pdf) of the respective quantities to reach a steady state, σ_x and σ_Υ are the variance parameters of the stationary log-normal pdf.

Equations (2.25), (2.27), and (2.28) denote a closed system of SDEs and can be solved numerically to obtain the joint pdf of the temperature, the scalar dissipation rate, and the re-ignition parameter in the form $p(\tau, \Theta_{\mathrm{st}}, x_{\mathrm{st}}, \Upsilon_{\mathrm{st}})$.

2.4. *Simplified model*

In Pitsch & Fedotov (2001) a Fokker-Planck equation for the joint pdf of temperature and the scalar dissipation rate was given and the corresponding system of SDEs for temperature and scalar dissipation rate was discussed. Here, this formulation has been extended to account for re-ignition, resulting in an additional SDE for the re-ignition parameter Υ_{st}. The solution of Eqs. (2.25), (2.27), and (2.28) is fairly straightforward, and the additional SDE significantly increases the computational cost. However, since the resulting pdf is three-dimensional, the computational requirements for achieving similar statistical convergence are substantially higher. For this reason we want to investigate a simplified model, where only the mean re-ignition parameter is considered in Eq. (2.25) and the SDE for this quantity does not have to be solved. This model will also be compared to the full model to assess the importance of the Υ_{st}-fluctuations.

Multiplying Eq. (2.25) with $p(\Upsilon_{\mathrm{st}}) = \delta(\Upsilon_{\mathrm{st}} - \langle \Upsilon_{\mathrm{st}}\rangle)$ and integrating over Υ_{st} yields

$$\frac{\partial \theta}{\partial \tau} - \frac{ax}{2}\frac{\partial^2 \theta}{\partial Z^2} + \frac{\langle \Upsilon_{\mathrm{st}}\rangle}{2\langle x_{\mathrm{st}}\rangle^2} \frac{\theta - \langle \theta | Z\rangle}{C_{\mathrm{IEM}}} - \omega(\theta) = 0\,. \tag{2.29}$$

This equation can be solved with Eq. (2.27) to obtain the joint pdf of temperature and scalar dissipation rate.

3. Results

3.1. *Analysis*

In order to analyze the influence of the additional term arising in the model, the transport term in Z will be modeled as described in Pitsch & Fedotov (2001), where also the necessary assumptions are discussed in detail. The equation can then be formulated at Z_{st} leading to

$$\frac{\partial \theta_{\mathrm{st}}}{\partial \tau} + x_{\mathrm{st}}\theta_{\mathrm{st}} + \frac{\Upsilon_{\mathrm{st}}}{2\langle x_{\mathrm{st}}\rangle^2} \frac{\theta_{\mathrm{st}} - \langle \theta_{\mathrm{st}} | \Upsilon_{\mathrm{st}}\rangle}{C_{\mathrm{IEM}}} - \omega(\theta_{\mathrm{st}}) = 0\,. \tag{3.1}$$

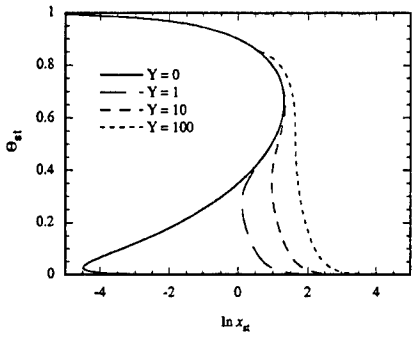

FIGURE 1. S-curves from steady state solutions of Eq. (3.1) for different values of $\Upsilon_{st,0}$

Assuming that Υ_{st} and x_{st} are constant, the steady-state solutions of Eq. (3.1) are easily computed. These solutions are shown in Fig. 1 for varying Υ_{st}. In the case $\Upsilon_{st} = 0$, the well-known S-shaped curve is recovered. It is indicated that in the region to the right of the curves, the temporal change of Θ_{st} is always negative; in the region left of the curves, always positive. Hence, if the scalar dissipation rate is increased beyond the value at the upper turning point, sudden extinction occurs. Re-ignition in this case can occur only if the scalar dissipation rate decreases to values lower than the lower turning point, where the temporal temperature change is always positive until the upper steady state is reached.

The influence of the diffusion term in χ-space becomes very obvious in the discussion of the steady-state solutions for non-zero $\langle\Upsilon_{st}\rangle$. For $\langle\Upsilon_{st}\rangle = 1$ this transport term leads to a heat flux from the hot surroundings to extinguished particles located on the lower steady branch. This additional term hence leads to a shift of the lower turning point to higher scalar dissipation rates. Extinguished particles can therefore re-ignite at much higher values of the scalar dissipation rate. This trend continues for increasing $\langle\Upsilon_{st}\rangle$. The higher the value of $\langle\Upsilon_{st}\rangle$, the higher the value of scalar dissipation rate, which allows for re-ignition. For very large values of $\langle\Upsilon_{st}\rangle$, as shown for $\langle\Upsilon_{st}\rangle = 100$, the turning points of the S-curve, and thereby also extinction as well as re-ignition events, disappear. Instead, all states on the steady curve are stable.

3.2. *Numerical simulation*

3.2.1. *Numerical method*

Monte-Carlo simulations are used to solve the system of equations (3.1), (2.27), and (2.28). N_p different realizations are used to represent the statistical behavior of these equations. The temperature equation is integrated using a second-order Runge-Kutta scheme. The equations for the SDEs for x_{st} and Υ_{st} are integrated with the second-order-accurate method of Milśhtein (1978). The solutions for these notional particles are then used to obtain the pdf.

3.2.2. *Influence of the re-ignition parameter* Υ_{st}

For the results presented in this section, the variance parameters σ and the time scale ratios δ appearing in Eqs. (2.27) and (2.28) are all chosen to be unity. For Eq. (2.27), this choice has been justified in Pitsch & Fedotov (2001). All other parameters, such as the Damköhler number and the heat release parameter, have been chosen as in Pitsch & Fedotov (2001). Three different cases will be shown: $\langle\Upsilon_{st}\rangle$ =1, 10, and 100. In addition, the case $\langle\Upsilon_{st}\rangle = 0$ is shown as a reference. This corresponds to the case studied in

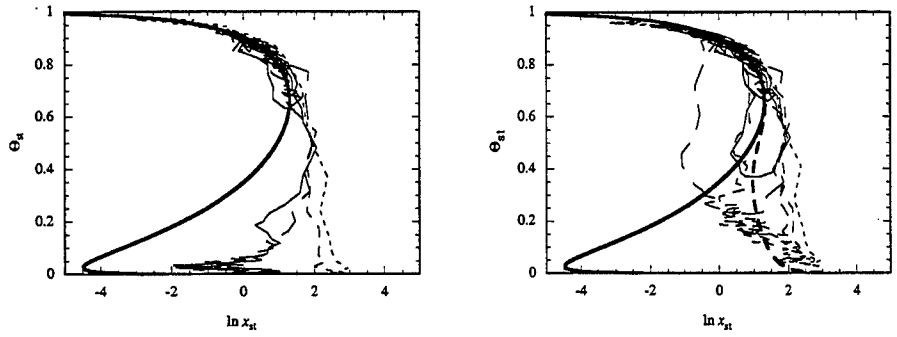

FIGURE 2. Temporal development of arbitrary extinguishing particles (thin lines). Thick lines are steady state solutions of Eq. (3.1) for $\langle \Upsilon_{st} \rangle = 0$ (solid line) and $\langle \Upsilon_{st} \rangle = 10$ (dashed line)

Pitsch & Fedotov (2001), where the transport in χ-space does not appear in the flamelet equations.

Numerical results for the system of SDEs are shown in the following Figures. In Fig. 2, it is demonstrated that the model presented here is capable of predicting re-ignition. In both Figures the paths of some extinguishing notional particles are shown. The left-hand Figure is for $\langle \Upsilon_{st} \rangle = 0$; the right-hand Figure shows particles with the same x_{st} history, but for $\langle \Upsilon_{st} \rangle = 10$. It has been discussed earlier that for $\langle \Upsilon_{st} \rangle = 0$, re-ignition cannot occur, which can clearly be seen in the left-hand Figure. However, in the right-hand Figure it is observed that the extinguishing particles undergo random changes of the scalar dissipation rate. If x_{st} becomes smaller than the correseponding steady solution, the temporal temperature change becomes positive, and the particle can re-ignite.

The pdfs $p(\Theta_{st}, x_{st})$ for $\langle \Upsilon_{st} \rangle = 0$, 1, 10, and 100 are given in Fig. 3. For $\langle \Upsilon_{st} \rangle = 0$ a large number of particles is extinguished, and this is seen in the Figure as a very narrow distribution at low Θ_{st}. For $\langle \Upsilon_{st} \rangle = 1$ the scalar dissipation rate where re-ignition can occur is already greatly increased. The pdf has a similar S-shape to the steady-solution curve, but is more pronounced. On the right-hand side of the steady-state curve, the probability of low temperature is still very high. The reason is that the probability for x_{st} to decrease below the re-ignition value is still very low. At $\langle \Upsilon_{st} \rangle = 10$, the pdf is very similar to the steady-state line, and the probability of low temperatures has strongly decreased. It should be noted that these S-shaped pdfs have also been found in DNS data (Sripakagorn *et al.* (2000, 2001)). At $\langle \Upsilon_{st} \rangle = 100$ extinction can hardly ever occur. Hence there is a very low probability of finding low temperatures.

3.2.3. *Application to DNS of non-premixed combustion in isotropic turbulence*

To further investigate and validate the proposed model it has been applied to the DNS experiment of Sripakagorn *et al.* (2000, 2001). This DNS has been specifically designed to investigate extinction and re-ignition. A one-step, reversible reaction between fuel and oxidizer evolves in isotropic, homogeneous, and decaying turbulence. Three different simulations, for different frequency coefficients of the global reaction, lead to low, moderate, and high levels of local extinction. These cases are referred to as cases A, B, and C, respectively. For case B, the maximum mean stoichiometric scalar dissipation rate is equal to the extinction value of scalar dissipation rate; for case A, the maximum mean scalar dissipation rate is much lower, and for case C much higher, than the extinction value. The numerical parameters used in these simulations are given in Cha & Pitsch (2001).

Here, we will present the results of two different models:

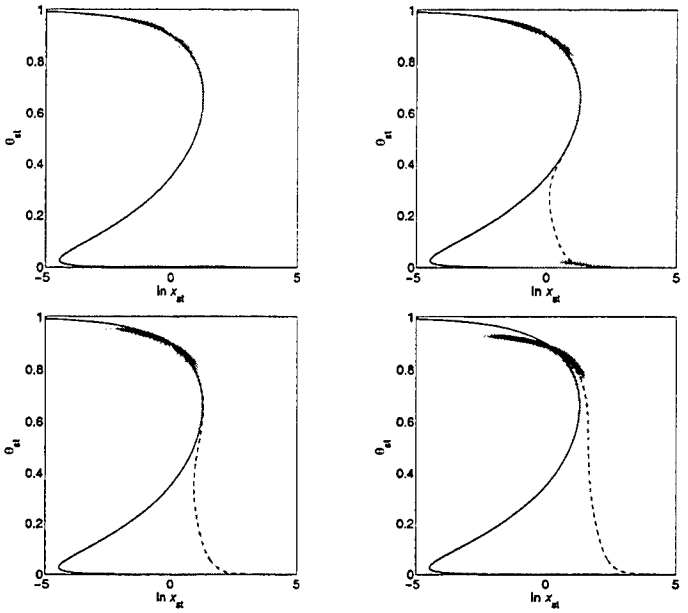

FIGURE 3. Joint pdfs $p(\Theta_{st}, x_{st})$ for $\langle \Upsilon_{st} \rangle = 0$ (upper left), $\langle \Upsilon_{st} \rangle = 1$ (upper right), $\langle \Upsilon_{st} \rangle = 10$ (lower left), $\langle \Upsilon_{st} \rangle = 100$ (lower right); lines are steady state solutions of Eq. (3.1) for $\langle \Upsilon_{st} \rangle = 0$ (solid) and $\langle \Upsilon_{st} \rangle = 10$ (dashed)

(*a*) The full model, solving Eqs. (2.25), (2.27), and (2.28). In this model the temperature Θ_{st}, the scalar dissipation rate x_{st}, and the re-ignition parameter Υ_{st} are treated as random variables; hence an SDE is solved for each of these quantities;

(*b*) The simplified model, given by the solution of Eqs. (2.29) and (2.27). In this model only the mean of the re-ignition parameter Υ_{st} is considered, and no SDE is solved for Υ_{st}.

The results of the Monte Carlo simulations are compared to DNS data in Fig. 4. Results are shown from left to right in order of increasing level of local extinction. Results of the full model are given in the upper row, results of the simplified model in the lower row. Numerical results are given by the lines, DNS data by the symbols. Closed symbols are the conditional mean temperature, open symbols represent the conditional fluctuations. In the DNS the mean scalar dissipation rate first increases up to approximately $t^* = 0.25$, where t^* is the time non-dimensionalized with the initial large-eddy turnover time, and afterwards decreases. Correspondingly, all cases show an extinction-dominated phase in the beginning at around $t^* = 0.5$. At later times, when the mean scalar dissipation rate becomes smaller, re-ignition becomes important, and the mean temperature increases again. This is also reflected in the conditional RMS values of the temperature. When the scalar dissipation rate increases and thereby the probability of finding local extinction increases, the pdf of the temperature becomes bimodal and hence the RMS becomes large. During the re-ignition period, extinguished pockets change to high temperature again, the pdf approaches a unimodal shape again, and the RMS values become smaller.

For case A, both models predict the conditional mean as well as the conditional variances very well. For moderate extinction (case B), the full model predicts a consistently lower temperature. The analysis shows that the reason for this is the overprediction of local extinction and is not necessarily related to the re-ignition model. Extinction has

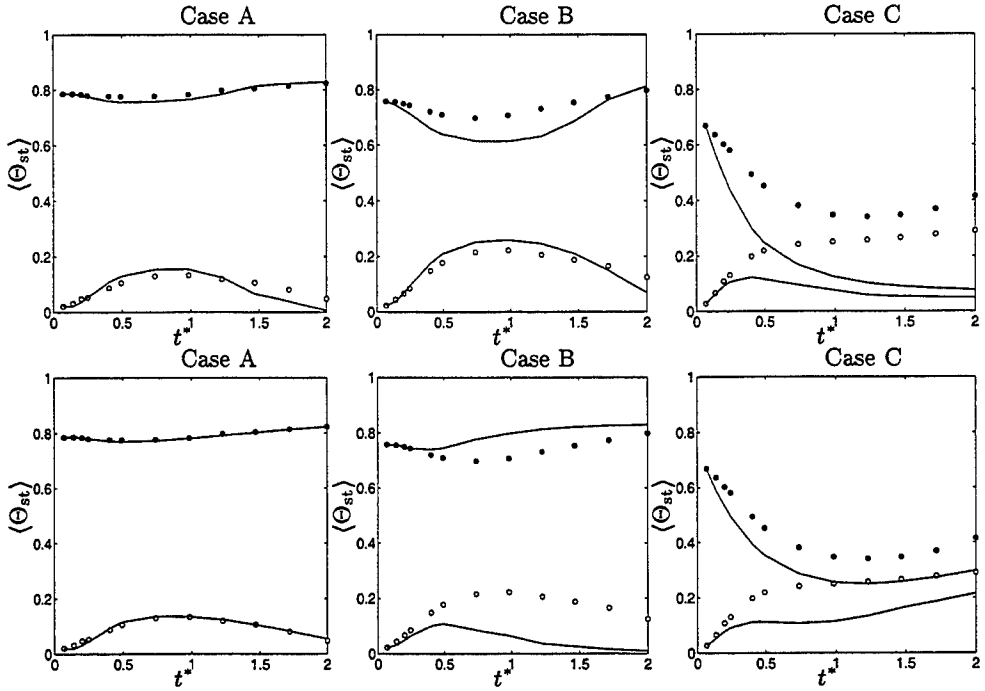

FIGURE 4. Modeling results (lines) for the full model (upper row) and simplified model (lower row) compared to DNS results (symbols). Closed symbols are the conditional mean temperature, open symbols the root mean squares.

been shown in Sripakagorn *et al.* (2000, 2001) to be very well predicted by the unsteady flamelet model, if the exact history of the scalar dissipation rate is known. Therefore, we are currently investigating the applicability of the SDE for the scalar dissipation to the current DNS data. The Reynolds number of the simulation might not be high enough to validate the assumption of a Markovian process to model fluctuations of scalar dissipation rate. It might be speculated that the DNS would be predicted well, if the initial amount of extinction was not too high. The simplified model predicts re-ignition to occur much earlier than the full model does. This also leads to the variance being underpredicted after the onset of the re-ignition process.

For case C, the full model predictions obviously tend to complete extinction. This can be seen from the fact that at low temperature the variance tends to zero, indicating that the pdf of temperature becomes unimodal at low temperatures. Note that the present flamelet-interaction model has the desirable feature that, if most of the system is extinguished, this model will accelerate extinction of the remaining, still-burning parcels. This underprediction of the temperature is again attributed to the overprediction of extinction at early times. Again, the simplified model predicts the onset of re-ignition much earlier. This leads to the interesting phenomenon that the simplified model correctly predicts re-ignition of the entire system, while the full model does not. However, as in the case of the full model, the amount of local extinction at early times is overpredicted by the simplified model, which seems to compensate for the fact that re-ignition is overestimated.

4. Conclusions

In this work, extinction and re-ignition in non-premixed turbulent combustion are investigated. A flamelet formulation accounting for transport within mixture-fraction iso-surfaces is developed. It is assumed that this transport is due only to changes of the local scalar dissipation rate. Space coordinates of the governing equations can then be replaced by the mixture fraction and the scalar dissipation rate, and so a new transport term appears in the flamelet equations. The "dissipation rate of the scalar dissipation rate", appearing as a diffusion coefficient of this term, is a new parameter of the problem. The resulting equations are simplified, and stochastic differential equations for the scalar dissipation rate and the new parameter are formulated. The system of equations is solved using a Monte Carlo method. The results show that the new transport term acts by increasing the scalar dissipation rate at the lower turning point of the S-shaped curve. The computed joint pdfs of temperature and scalar dissipation rate have shapes which are similar to those seen in DNS results. The model has been applied to the DNS of non-premixed combustion in isotropic decaying turbulence, showing good results for low and moderate levels of extinction. Currently, we are assessing the applicability of the developed SDE for scalar dissipation rate to the present DNS results.

Acknowledgements

The authors express gratitude to Paiboon Sripakagorn for making his DNS database available to us before publication.

REFERENCES

BARLOW, R. S. & FRANK, J. H. 1998 Effect of turbulence on species mass fractions in methane/air jet flames. *Proc. Comb. Inst.* **27**, 1087–1095.

CHA, C. M., KOSALY, G. & PITSCH, H. 2001 Modeling extinction and reignition in turbulent nonpremixed combustion using a doubly-conditional moment closure approach. *Phys. Fluids* Accepted.

CHA, C. M. & PITSCH, H. 2001 Higher-order singly-conditional moment closure modeling approaches to turbulent combustion. *Annual Research Briefs,* Center for Turbulence Research, NASA Ames/Stanford Univ. 83-91.

HEWSON, J. C. & KERSTEIN, A. R. 2001 Stochastic simulation of transport and chemical kinetics in turbulent $CO/H_2/N_2$ flames. *Comb. Theory Modelling* Submitted.

MILŚTEIN, G. N. 1978 A method of second-order accuracy integration of stochastic differential equations. *Theory Prob. Appl.* **23**, 396–401.

PETERS, N. 1983 Local quenching due to flame strech and non-premixed turbulent combustion. *Comb. Sci. Technol.* **30**, 1.

PETERS, N. 1983 Local quenching due to flame strech and non-premixed turbulent combustion. *Comb. Sci. Technol.* **30**, 1.

PETERS, N. 1984 Laminar diffusion flamelet models in non-premixed turbulent combustion. *Prog. Energy Comb. Sci.* **10**, 319–339.

PITSCH, H., BARTHS, H. & PETERS, N. 1996 Three-dimensional modeling of nox and soot formation in di-diesel engines using detailed chemistry based on the interactive flamelet approach. *SAE* Paper 962057.

PITSCH, H., CHEN, M. & PETERS, N. 1998 Unsteady flamelet modeling of turbulent hydrogen/air diffusion flames. *Proc. Comb. Inst.* **27**, 1057–1064.

PITSCH, H. & FEDOTOV, S. 2001 Investigation of scalar dissipation rate fluctuations in non-premixed turbulent combustion using a stochastic approach. *Comb. Theory Modelling* **5**, 41–57.

PITSCH, H. & STEINER, H. 2000 Large-eddy simulation of a turbulent piloted methane/air diffusion flame (Sandia flame D). *Phys. Fluids* **12**, 2541–2554.

SRIPAKAGORN, P., KOSÁLY, G. & PITSCH, H. 2000 Local extinction-reignition in turbulent nonpremixed combustion. *Annual Research Briefs,* Center for Turbulence Research, NASA Ames/Stanford Univ., 117–128.

SRIPAKAGORN, P., KOSÁLY, G. & PITSCH, H. 2001 Local extinction-reignition in turbulent nonpremixed combustion. *Comb. Flame* Submitted.

XU, J. & POPE, S. B. 2000 Pdf calculations of turbulent nonpremixed flames with local extinction. *Comb. Flame* **123**, 281–307.

Transported PDF modeling of turbulent nonpremixed combustion

By Chong M. Cha

1. Motivation and objectives

In moment methods of predicting turbulent combustion (Klimenko & Bilger 1999), closure of the nonlinear chemical source term presents the most difficult modeling challenge. In contrast, the products of the state-space variables pose no explicit closure problem in the transport equation for the joint PDF $p_{\psi\theta}$ of the reacting scalars, ψ, and the normalized temperature, θ (Dopazo 1994):

$$\frac{\partial}{\partial t}p_{\psi\theta}(\phi;t) = \sum_{j}^{N_s+1} \frac{\partial}{\partial \psi_j}\left[\dot{s}(\phi) - \langle \mathcal{D}\nabla^2\psi_j|\psi=\phi\rangle\right] p_{\psi\theta} \ , \tag{1.1}$$

where statistical homogeneity has been assumed for simplicity. Here, $\psi = (\psi_1, \ldots, \psi_{N_s})$ is a vector representing the concentrations of the N_s number of reacting species in the system; $\phi = (\phi_1, \ldots, \phi_{N_s}, \phi_{N_s+1})$ are the corresponding sample space variables for ψ and θ; $\mathcal{D}$ is the molecular diffusivity, assumed equal for all species; and $\dot{s}$ is the chemical source term, a known function of the ψ and θ sample space. The notation "$\langle A|B\rangle$" represents the average of A conditional on the event B. The transported PDF equation (1.1) is derived from the exact transport equations of $\psi(\boldsymbol{x},t)$ and $\theta(\boldsymbol{x},t)$ (O'Brien (1980) gives a good, detailed description of the derivation). Because no multi-point information exists at this single-point level, the molecular diffusion term in Eq. (1.1) must be modeled to obtain closure.

Due to the high-dimensionality of the transported PDF equation for practical engineering flows, where N_s can be large, Monte Carlo methods have been developed by Pope and co-workers (Pope 1990) to efficiently integrate Eq. (1.1). For closure, particle interaction mixing models are used to describe molecular diffusion by prescribing a mixing frequency between the notional particles of the Monte Carlo calculation. For example, in the simplest of these particle interaction models (Dopazo 1975),

$$(\mathcal{D}\nabla^2\psi_j)^{(i)} = -\frac{\phi_j^{(i)} - \frac{1}{N_p}\sum_{i=1}^{N_p}\phi_j^{(i)}}{T_j}$$

for the i-th notional particle of the j-th species. This model is termed "linear mean square estimation" (LMSE). N_p is the total number of particles in a computational volume. The mixing frequency, $1/T_j$, is usually taken as the inverse of the integral time scale of the turbulence, T_L, to within a multiplicative constant of order unity. This introduces two assumptions concerning the various ratios of the relevant time scales:

(a) The mixing frequency of a passive scalar, $1/T$, is proportional to the turbulence frequency, $T/T_L \sim \mathcal{O}(1)$;

(b) The mean mixing frequency is identical for all reacting species and proportional to that of a passive scalar, $T_j/T \sim \mathcal{O}(1)$.

The constant time scale ratio for the dissipation rate of scalar and velocity fluctuations is a turbulence modeling issue. The latter assumption is a combustion modeling issue and is the focus of the present paper.

Peters (2000) has pointed out the implicit assumption made in prescribing $T_j \sim T$. To review, for the passive scalar, ξ, T is the characteristic time for the dissipation of scalar energy:

$$\frac{1}{\langle \xi^2 \rangle} \frac{d\langle \xi^2 \rangle}{dt} = -\frac{\langle 2\mathcal{D}(\nabla \xi)^2 \rangle}{\langle \xi^2 \rangle} \equiv -\frac{1}{T}$$

with no change of the passive scalar mean. Defining the dissipation rate of ξ as $\chi \equiv 2\mathcal{D}(\nabla \xi)^2$, $T \equiv \langle \xi^2 \rangle / \langle \chi \rangle$. it follows that Equilibrium of developed turbulence implies that the cascade of turbulent kinetic energy produced at the large scales is in equilibrium with its dissipation occuring at the smallest scales. Thus, T can be represented by the integral scalar time scale. From assumption (a) above, the proportionality of T and the turbulence frequency gives $T \sim T_L \sim u'/L$. For a reacting scalar,

$$\frac{1}{\langle \psi_j^2 \rangle} \frac{d\langle \psi_j^2 \rangle}{dt} - \frac{\langle 2\psi_j \dot{s}_j \rangle}{\langle \psi_j^2 \rangle} = -\frac{\langle 2\mathcal{D}(\nabla \psi_j)^2 \rangle}{\langle \psi_j^2 \rangle} \equiv -\frac{1}{T_j} \ .$$

Defining $\chi_j \equiv 2\mathcal{D}(\nabla \psi_j)^2$, we have $T_j \equiv \langle \psi_j^2 \rangle / \langle \chi_j \rangle$. Clearly, $T_j = T$ is strictly valid only in the infinitely-fast and frozen-chemistry limits where $\dot{s} = 0$; is a good approximation for slow chemistry where the assumption of dissipation balancing production is sufficiently accurate; but would be poor for fast (but not infinitely fast) chemistry where chemical reaction is significant enough to modifiy the energy budget. Variations of the equilibrium assumption, like balance of production, dissipation, and reaction, have led to insight on the influence of chemistry on the T/T_j ratio, but for linear reaction (Peters 2000). In this paper, mapping closure (Chen *et al.* 1989; Pope 1991) is used to develop a model for T/T_j for realistic chemistry.

The paper is organized as follows: In the next section, the main ideas of mapping closure are summarized. A new model to prescribe the time-scale ratio of a passive-to-reactive scalar is formulated. The model is compared to results from DNS, where the exact time-scale ratio can be calculated. Finally, future applications are outlined to treat local extinction and reignition in the framework of transported PDF and moment closure methods.

2. Results and discussion

Very little work in applying mapping closure for turbulent reacting scalars has been done since its original conception by Chen *et al.* (1989) and generalization for multiple reactive scalars by Pope (1991). Gao, Jiang, and O'Brien have made many analytical developments for single (Gao 1991*b*,*a*; O'Brien & Jiang 1991) and multiple passive scalars (Gao & O'Brien 1991; Jiang *et al.* 1992). Girimaji (1993) has considered mapping(s) from time-evolving reference field(s), has made comparisons with a presumed beta pdf distribution of passive scalar mixing (Girimaji 1992*b*), and has pointed out problems with mapping closure of a passive scalar at very late stages of mixing (Girimaji 1992*a*). Although Valiño and co-workers applied a Monte Carlo method (Valiño *et al.* 1991) for a reacting case (Valiño & Gao 1992), the time scale of the reacting scalar was replaced by that of the passive scalar.

2.1. *Mapping closure revisited*

The main ideas behind mapping closure are reviewed. The normalized temperature is used as an illustrative example, but may be replaced by any reacting scalar in the summary to follow. Mapping closure introduces a mapping

$$\theta(x,t) = Y_{N_s+1}(z_0(z), z_1(z), \ldots, z_{N_s}(z), t) \ , \tag{2.1a}$$

where Y_{N_s+1} is a deterministic function and $(z_0, \ldots, z_{N_s})$ a vector of random variables. Then, the gradient of θ simply follows from application of the chain rule and can be written as

$$\nabla\theta = \sum_{j=0}^{N_s} \frac{\partial Y}{\partial z_j} \nabla z_j(J(t)x) \ , \tag{2.1b}$$

where $J(t)$ is the Jacobian of the coordinate transformation $z \to x$ accounting for advective stretching (Chen *et al.* 1989). For notational convenience, the sample space variable for z_j is also represented by "z_j". If the random variables $(z_0, \ldots, z_{N_s})$ are jointly Gaussian, then the transported PDF closure problem is addressed as multi-point information for z_j are known from their single-point statistics. An equally important motivation of choosing all z_j normally distributed is that it also allows conditional averages of θ to be related to its unconditional counterpart. More generally, it allows small-scale structure to be reconstructed from information at the integral scale.

Pope (1991) has derived the governing equations for the mapping functions of a general chemically reacting system. In the present notation, we have, for a reacting scalar,

$$\left[\frac{\partial}{\partial t} - \sum_{i=1}^{j} \langle \mathcal{D}_j (\nabla z_{i-1})^2 \rangle \left(\frac{\partial^2}{\partial z_{i-1}^2} - \frac{z_{i-1}}{\langle z_{i-1}^2 \rangle} \frac{\partial}{\partial z_{i-1}} \right) \right] Y_j = \dot{s}_j(Y_1, \ldots, Y_{N_s}, Y_{N_s+1}) \ . \tag{2.2a}$$

For a passive scalar, $\dot{s}_j \equiv 0$, and Y_j is written as "X_j". No general initial and boundary conditions exist. "External" information on the generally time-dependent evolution of the unconditional statistics of $|\nabla\psi_j|$ (or $|\nabla\xi_j|$ for X_j) must be prescribed.

Mapping closure is a self-contained turbulent combustion model. With the solution of Eq. (2.2*a*), the solution of Eq. (1.1) can be written directly as

$$p_{\psi\theta}(\phi_1, \ldots, \phi_{N_s+1}; t) = \left(\prod_{j=1}^{N_s+1} \left| \frac{\partial Y_j}{\partial z_{j-1}} \right| \right)^{-1} \prod_{i=1}^{N_s+1} p_{z_{i-1}}(z_{i-1}) \ , \tag{2.2b}$$

where p_{z_i} is normally distributed and Y_j is the solution of Eq. (2.2*a*). However, the mapping equations without simplification would be $N_s!$ times more expensive to integrate and therefore would not be computationally tractable for practical engineering flows where the number of species is usually large. Below, we simplify and solve the mapping equations in the flamelet regime.

2.2. *Dissipation rate of a passive scalar*

To illustrate past work on the application of mapping closure to the turbulent mixing of a passive scalar advected by Navier-Stokes turbulence, we consider the statistics of the mixture fraction of a simple one-step, second-order, reversible reaction: $\mathrm{F}+\nu\mathrm{O} \rightleftharpoons (1+\nu)\mathrm{P}$, where one mole of fuel (F) reacts with ν moles of oxidizer (O) to yield $(1+\nu)$ moles of product (P). The production rates for F, O, and P are $\dot{s}_\mathrm{F} = -\dot{s}$, $\dot{s}_\mathrm{O} = -\nu\dot{s}$, and

$\dot{s}_P = (1+\nu)\dot{s}$, respectively, where

$$\dot{s}(\psi_F, \psi_O, \psi_P, \theta) = A \exp\left(-\frac{Ze}{\alpha}\right)\left(\psi_F\psi_O - \frac{1}{K}\psi_P^2\right)\exp\left[-\frac{Ze(1-\theta)}{1-\alpha(1-\theta)}\right] .$$

Here, A is the frequency factor, α is the heat release parameter, and Ze is the Zeldovich number. The Schmidt number is 0.7 and Lewis numbers are unity. The molecular diffusivities and viscosity are independent of the temperature. The turbulent flow is incompressible, isotropic, homogeneous, and decaying (*cf.* Sripakagorn *et al.* (2000) for details of the simulation). The passive scalar for this binary mixing problem, the mixture fraction, is defined as

$$\xi = \frac{\nu\psi_F - \psi_O + 1}{\nu + 1}$$

which is then conserved under reaction.

The transport of $p_\xi(\eta, t)$, the PDF of ξ, is governed by (O'Brien 1980)

$$\frac{\partial}{\partial t}p_\xi(\eta,t) = -\frac{\partial}{\partial\eta}\langle\mathcal{D}\nabla^2\xi|\eta\rangle p_\xi = -\frac{\partial^2}{\partial\eta^2}\langle\mathcal{D}(\nabla\xi)^2|\eta\rangle p_\xi \ . \tag{2.3}$$

Spatial homogeneity has been assumed. To close Eq. (2.3), the mapping $\xi = X(z_0, t)$ is defined. Application of Eq. (2.2*a*), (2.1*b*), and (2.2*b*) gives

$$\frac{\partial}{\partial t}X(z_0,t) = \frac{\langle\mathcal{D}(\nabla\xi)^2\rangle}{\langle(\partial X/\partial z_0)^2\rangle}\left(\frac{\partial^2 X}{\partial z_0^2} - z_0\frac{\partial X}{\partial z_0}\right) \tag{2.4a}$$

$$\langle\mathcal{D}(\nabla\xi)^2|\xi=\eta\rangle = \langle\mathcal{D}(\nabla\xi)^2\rangle\frac{(\partial X/\partial z_0)^2}{\langle(\partial X/\partial z_0)^2\rangle} \tag{2.4b}$$

$$p_\xi(\eta,t) = \frac{1}{|\partial X/\partial z_0|}p_{z_0}(z_0) \ , \tag{2.4c}$$

respectively. The independence of z_0 and ∇z_0 (Chen *et al.* 1989) has been assumed. In Eq. (2.4*a*), the relation $\langle\mathcal{D}(\nabla\xi)^2\rangle/\langle(\partial X/\partial z_0)^2\rangle = \langle\mathcal{D}(\nabla z_0)^2\rangle$ has been used and hence knowledge of the Jacobian can be circumvented by knowledge of the effect of the turbulent velocity field on ξ directly. (Models for $\langle\mathcal{D}(\nabla\xi)^2\rangle \equiv \langle\chi\rangle/2$ are well known.) For this initially segregated system, boundary conditions are $X(-\infty,t) = 0$ and $X(+\infty,t) = 1$. Initial conditions are specified using an iterative approach such that the variance from $p_{z_0}/\left(|\partial X/\partial z_0|\right) = p_\xi$ gives the exact value of the DNS. The exact average dissipation rate from the DNS is used in integrating Eq. (2.4*a*). Figure 1 shows good agreement with the data for $\langle\mathcal{D}(\nabla\xi)^2|\eta\rangle$ and $p_\xi(\eta,t)$ calculated using Eq. (2.4*b*) and (2.4*c*) respectively, corroborating the previous work listed at the beginning of this section.

2.3. *Mapping function for a fast reacting scalar*

In the flamelet regime, ψ_j is governed by (Peters 2000)

$$\frac{\partial\psi_j}{\partial\tau} = \frac{\chi}{2}\frac{\partial^2\psi_j}{\partial\xi^2} + \dot{s}_j \ . \tag{2.5}$$

Correspondingly, the mapping Y_j in Eq. (2.2*a*) becomes a function of (z_0, t) only for all j and the mapping equations simplify to

$$\frac{\partial Y_j}{\partial t} = \frac{\langle\mathcal{D}(\nabla\xi)^2\rangle}{\langle(\partial X/\partial z_0)^2\rangle}\left(\frac{\partial^2 Y_j}{\partial z_0^2} - z_0\frac{\partial Y_j}{\partial z_0}\right) + \dot{s}_j(Y_1,\ldots,Y_{N_s+1}) \ . \tag{2.6}$$

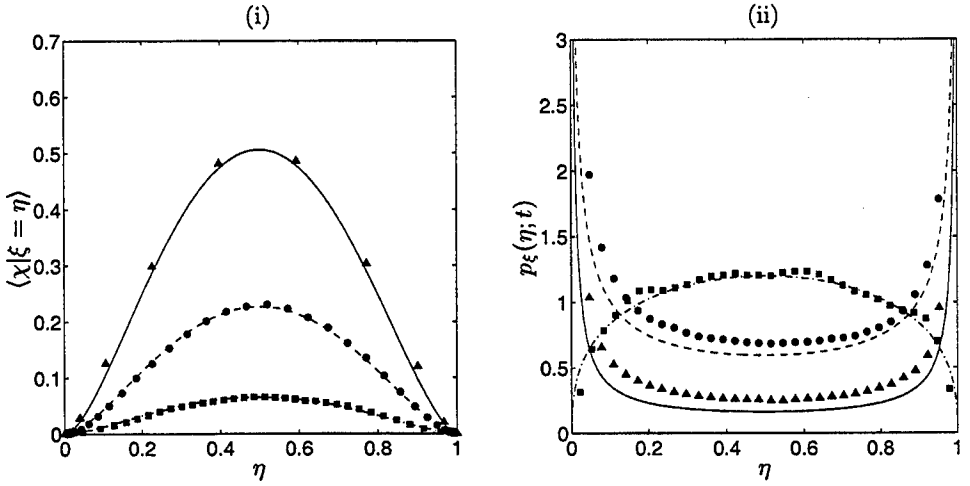

FIGURE 1. Passive scalar results. Comparison of mapping closure results with DNS data initially (triangles = DNS, solid line = mapping closure) and at times $t/\tau_{\text{eddy}} = 1$ (circles = DNS, dash-dash = mapping closure), and 2 (squares = DNS, dash-dot = mapping closure).

The mapping $\psi_j = Y_j(z_0, t)$ is not generally one-to-one. Initial conditions for Eq. (2.6) can be given by $Y_j = \psi_j(X(z_0, t_0), t_0)$, which is the steady-state solution of Eq. (2.5) with $\chi/2$ replaced by Eq. (2.4*b*). Boundary conditions for Eq. (2.6) are $Y_j(-\infty, t) = \psi_j(0, t)$ and $Y_j(+\infty, t) = \psi_j(1, t)$.

Given a solution for the mapping function Y_j, small scale processes for the reacting scalars can be described using the average dissipation rate of the passive scalar at the integral scale. In particular,

$$\langle \mathcal{D}(\nabla\psi_j)^2|\psi_j = \phi\rangle = \frac{\langle\chi\rangle}{2}\frac{(\partial Y_j/\partial z_0)^2}{\langle(\partial X/\partial z_0)^2\rangle} \tag{2.7a}$$

$$p_{\psi_j}(\phi, t) = \frac{1}{|\partial Y_j/\partial z_0|}p_{z_0}(z_0) \ . \tag{2.7b}$$

Using Eq. (2.7*a*) and Eq. (2.4*b*), the desired time-scale ratio for a passive-to-reactive scalar is then

$$\frac{T_j}{T} = \frac{\langle\psi_j^2\rangle/\langle(\partial Y/\partial z_0)^2\rangle}{\langle\xi^2\rangle/\langle(\partial X/\partial z_0)^2\rangle} \ . \tag{2.8}$$

Figure 2 shows good agreement with the DNS data for (i) $\langle 2\mathcal{D}(\nabla\psi_{\text{P}})^2|\psi_{\text{P}} = \phi\rangle \equiv \langle\chi_{\text{P}}|\psi_{\text{P}} = \phi\rangle$ and (ii) $p_{\psi_{\text{P}}}(\phi, t)$ calculated using Eq. (2.7*a*) and (2.7*b*) respectively. Figure 3 shows (i) the mean and standard deviation of ψ_{P} from Eq. (2.7*b*) and (ii) the time scale ratio calculated using Eq. (2.8). The figure shows that the relaxation time scale for a fast reacting scalar, T_j, can deviate significantly from T in the flamelet regime. Further, the mixing time scale is reduced in the presence of active chemistry ($T_j < T$).

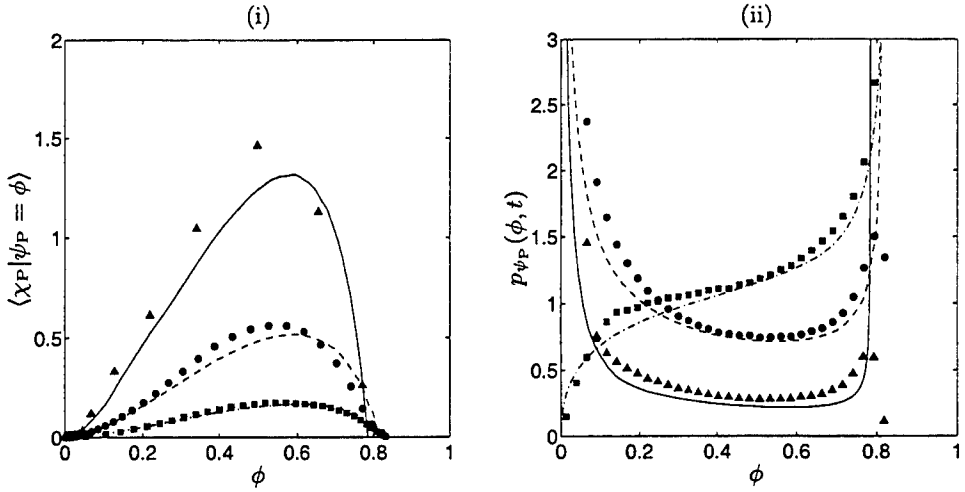

FIGURE 2. Reacting scalar results. Comparison of mapping closure results with DNS data initially (triangles = DNS, solid line = mapping closure) and at times $t/\tau_{\text{eddy}} = 1$ (circles = DNS, dash-dash = mapping closure), and 2 (squares = DNS, dash-dot = mapping closure).

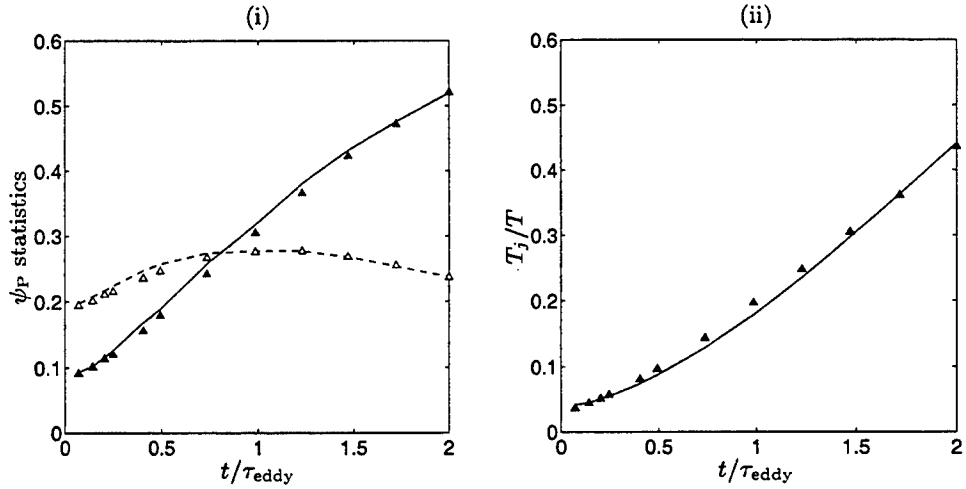

FIGURE 3. Prediction of time scale ratio by mapping closure in fast chemistry regime: (i) mean and rms and (ii) time scale ratio. Symbols are DNS data. Lines are modeling predictions.

3. Conclusions and future work

For sufficiently fast chemistry, the average time-scale ratio for a passive-to-reactive scalar was derived:

$$\frac{T_j}{T} \equiv \frac{\langle \psi_j^2 \rangle / \langle \chi_j \rangle}{\langle \xi^2 \rangle / \langle \chi \rangle} = \min \left\{ 1, \frac{\langle \psi_j^2 \rangle}{\langle \xi^2 \rangle} \frac{\langle (\partial X/\partial z_0)^2 \rangle}{\int_{-\infty}^{+\infty} (\partial \psi_j/\partial \xi)^2 (\partial X/\partial z_0)^2 p_{z_0} dz_0} \right\} , \tag{3.1}$$

where $\psi_j(\xi, t)$ is the solution of Eq. (2.5), the first or leading-order (un)steady flamelet equation. Equation (2.5) cannot describe reignition. Equation (3.1) can be directly applied to existing particle-interaction models for transported PDF closure modeling, which

can, in principle, describe global reignition. Equation (3.1) is not expected to describe the entire transition $T_j/T \to 1$ and the "min" function is required to properly bound the T_j/T ratio by the infinitely fast and frozen chemistry limits, where $T_j/T = 1$.

Ongoing/future work includes application to the extinction/reignition problem based on the following modeling approaches.

(*a*) Conditional moment closure modeling: Moment closure conditional on ξ represents the least computationally burdensome of turbulent combustion models. Application of Eq. (2.2*a*) may yield a description of the complex shapes of the conditional pdfs when extinction and reignition processes are significant. This is the subject of ongoing work (Cha & Pitsch 2001).

(*b*) Transported PDF modeling: To describe extinction/reignition using transported PDF modeling, more sophisticated particle interaction models are required where intermittency effects of the dissipation must be accounted for (Xu & Pope 2000). An accurate estimate of the overall mean mixing frequency is also essential in these local particle interaction models such as the extended LMSE model of Sabel'nikov & Gorokhovski (Sabel'nikov & Gorokhovski 2001).

In both these applications, a sound physical basis would be necessary to assign proper initial and boundary conditions to the more general mapping function equations, Eq. (2.2*a*) in this paper. Currently, the mapping closure approach is being developed for transported PDF modeling in large-eddy simulations (Cha & Trouillet 2001).

REFERENCES

CHA, C. M. & PITSCH, H. 2001 Higher-order conditional moment closure modeling of local extinction and reignition in turbulent combustion. *Combust. Theory Modelling* (submitted).

CHA, C. M. & TROUILLET, P. 2001 A model for the mixing time scale of a turbulent reacting scalar. *Bull. Amer. Phys. Soc.* **46** (10), 14.

CHEN, H., CHEN, S. & KRAICHNAN, R. H. 1989 Probability distribution of a stochastically advected scalar field. *Phys. Rev. Lett.* **63**, 2657–2660.

DOPAZO, C. 1975 Probability density function approach for a turbulent axisymmetric heated jet. Centerline evolution. *Phys. Fluids A* **18** (4), 397–404.

DOPAZO, C. 1994 Recent developments in PDF methods. In *Turbulent Reacting Flows* (ed. P. A. Libby & F. A. Williams), chap. 7, pp. 375–474. New York: Academic.

GAO, F. 1991*a* An analytical solution for the scalar probability density function in homogeneous turbulence. *Phys. Fluids A* **3**, 511–513.

GAO, F. 1991*b* Mapping closure and non-Guassianity of the scalar probability density functions in isotropic turbulence. *Phys. Fluids A* **3**, 2438–2444.

GAO, F. & O'BRIEN, E. E. 1991 A mapping closure for multispecies Fickian diffusion. *Phys. Fluids A* **3** , 956.

GIRIMAJI, S. S. 1992*a* A mapping closure for turbulent scalar mixing using a time-evolving reference field. *Phys. Fluids A* **4** , 2875–2886.

GIRIMAJI, S. S. 1992*b* On the modeling of scalar diffusion in isotropic turbulence. *Phys. Fluids A* **4** , 2529.

GIRIMAJI, S. S. 1993 A study of multiscalar mixing. *Phys. Fluids A* **5** , 1802.

JIANG, T.-L., GIVI, P. & GAO, F. 1992 Binary and trinary scalar mixing by Fickian diffusion—some mapping closure results. *Phys. Fluids A* **4**, 1028–1035.

KLIMENKO, A. Y. & BILGER, R. W. 1999 Conditional moment closure for turbulent combustion. *Prog. Energy Combust. Sci.* **25**, 595–687.

O'BRIEN, E. E. 1980 The probability density function (pdf) approach to reacting turbulent flows. In *Turbulent Reacting Flows* (ed. P. A. Libby & F. A. Williams), *Topics in Applied Physics* 44, chap. 5, pp. 185–218. Springer.

O'BRIEN, E. E. & JIANG, T. L. 1991 The conditional dissipation rate of an initially binary scalar in homogeneous turbulence. *Phys. Fluids A* **3**, 3121–3123.

PETERS, N. 2000 *Turbulent Combustion*. Cambridge: Cambridge University Press.

POPE, S. B. 1990 Computations of turbulent combustion: Progress and challenges. *Proc. Combust. Inst.* **23**, 591–612.

POPE, S. B. 1991 Mapping closures for turbulent mixing and reaction. *Theoret. Comput. Fluid Dynamics* **2**, 255–270.

SABEL'NIKOV, V. A. & GOROKHOVSKI, M. 2001 Extended LMSE and Langevin models of the scalar mixing in the turbulent flow. In *Second International Symposium on Turbulence and Shear Flow Phenomena*. Royal Institute of Technology (KTH), Stockholm, Sweden, June 27–29.

SRIPAKAGORN, P., KOSÁLY, G. & PITSCH, H. 2000 Local extinction-reignition in turbulent nonpremixed combustion. In *CTR Annual Research Briefs*, pp. 117–128. Stanford University / NASA Ames.

VALIÑO, L. & GAO, F. 1992 Monte Carlo implementation of a single-scalar mapping closure for diffusion in the presence of chemical reaction. *Phys. Fluids A* **4** (9), 2062.

VALIÑO, L., ROS, J. & DOPAZO, C. 1991 Monte Carlo implementation and analytic solution of an inert-scalar turbulent-mixing test problem using a mapping closure. *Phys. Fluids A* **3** (9), 2191.

XU, J. & POPE, S. B. 2000 PDF calculations of turbulent nonpremixed flames with local extinction. *Combust. Flame* **123**, 281–307.

Higher-order singly-conditional moment-closure modeling approaches to turbulent combustion

By Chong M. Cha AND Heinz Pitsch

1. Motivation and objectives

Currently, a fundamental closure approximation in conditional-moment-closure modeling (Klimenko & Bilger 1999) of turbulent, nonpremixed combustion is first-order closure of the average nonlinear chemical source terms, $\dot{w}$, conditioned on the mixture fraction, $\xi(t,x)$:

$$\langle \dot{w}(\boldsymbol{Y}(t,x),\theta(t,x),\rho(t,x))|\xi(t,x)\rangle \approx \dot{w}(\langle \boldsymbol{Y}|\xi\rangle,\langle\theta|\xi\rangle,\langle\rho|\xi\rangle) \ , \tag{1.1}$$

where $\boldsymbol{Y}$ is the vector of mass fractions of the reacting species and ρ is the density of the mixture. $\theta \equiv (T-T_\infty)/(T_f-T_\infty)$ is the reduced temperature, where T_f is the adiabatic flame temperature and T_∞ is the reference temperature. For convenience, the notation used here does not distinguish between the random variable and its corresponding sample space variable. The utility of first-order closure using conditional averaging is illustrated in Fig. 1, which shows in subplot (i) the reduced temperature θ as a function of ξ from the direct numerical simulation (DNS) of Sripakagorn *et al.* (2000). Subplot (ii) shows the probability density function (pdf) of θ conditioned on ξ within a given range of $\xi_{st} \pm \Delta\xi$, where ξ_{st} is the stoichiometric value of the mixture fraction, 0.5 for this case. $\Delta\xi$ decreases from the dash-dot line to the dash-dash line and finally to $\Delta\xi \approx 0$ for the solid line. Thus, the solid line is a representation of the conditional pdf of θ at ξ_{st}. The figure illustrates three points: (i) the inapplicability of first-moment closure under conventional (unconditional) averaging, which is well known; (ii) the much-improved representation of the pdf of θ by its mean value alone due to conditioning on ξ, helping to validate Eq. (1.1); and (iii) a negative skewness of the pdf due to the existence of local extinction and reignition events in this (numerical) experiment, which threatens the validity of Eq. (1.1). The extinction/reignition events, clearly visible in subplot (i) and evident in the pdfs at low values of θ_{st} in subplot (ii), are interpreted as fluctuations about the singly-conditional mean in the framework of singly-conditional moment-closure modeling.

Recently, modeling of the conditional variance has been proposed to improve closure of the conditional chemical source term (Swaminathan & Bilger 1998; Kronenburg *et al.* 1998; Mastorakos & Bilger 1998). The conditional variance can be used (Klimenko & Bilger 1999)

(*a*) in an additional, second-order correction to Eq. (1.1) or

(*b*) to construct a presumed pdf shape for one or more reactive scalars.

At present, we are investigating the feasibility of both these higher-order conditional-moment closure approaches for local extinction/reignition modeling. The DNS of Sripakagorn *et al.* (2000), specifically designed to investigate extinction/reignition, offers an ideal test case to investigate the merits and drawbacks of the higher-order conditional-moment closure strategies.

The paper is organized as follows: in the next section, the higher-order closure strategies

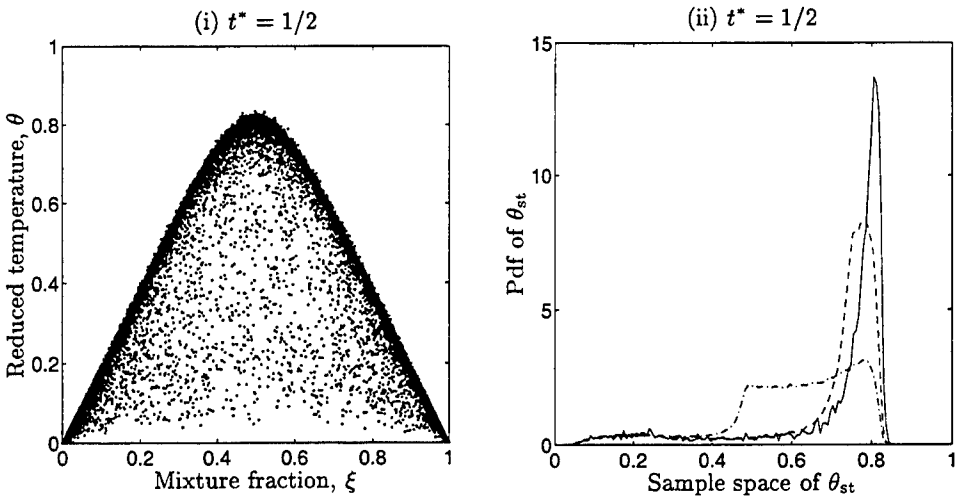

FIGURE 1. Motivation of the work. Subplot (i) is a scatter plot of the reduced temperature, θ, as a function of the local mixture fraction, ξ, at $t^* = 1/2$ (time has been nondimensionalized by the initial large-eddy turnover time) from the direct numerical simulation (DNS) experiment of Sripakagorn *et al.* (2000). (In the DNS, F + O $\leftrightarrow$ 2P evolves in decaying, homogeneous, isotropic turbulence with an initial $\mathrm{Re}_\lambda = 33$ on a 128^3 grid.) Subplot (ii) shows the conditional probability density function (pdf) of θ conditioned on ξ within a decreasing range of ξ values about $\xi_{st} = 0.5$, the stoichiometric value of the mixture fraction: The range decreases from the dash-dot line to the dash-dash line and finally to the pdf conditioned on $\xi \approx \xi_{st}$.

are described and governing equations given. In Sec. 3, *a priori* modeling comparisons are made with DNS experiments on a single-step, second-order, reversible reaction in grid turbulence. Finally, the two-conditional-moment closure modeling approaches for describing extinction/reignition are assessed and future directions outlined.

2. Combustion models

2.1. *DNS experiment*

The production rates for fuel (F), oxidizer (O), and product (P) for the present numerical experiment of F + O $\rightleftharpoons$ 2P evolving in isotropic, homogeneous, and decaying turbulence are $\dot{w}_\mathrm{F} = -\dot{w}$, $\dot{w}_\mathrm{O} = -\dot{w}$, and $\dot{w}_\mathrm{P} = 2\dot{w}$, respectively, where

$$\dot{w}(Y_\mathrm{F}, Y_\mathrm{O}, Y_\mathrm{P}, \theta) = A \exp\left(-\frac{\mathrm{Ze}}{\alpha}\right)\left(Y_\mathrm{F}Y_\mathrm{O} - \frac{1}{K}Y_\mathrm{P}^2\right)\exp\left[-\frac{\mathrm{Ze}(1-\theta)}{1-\alpha(1-\theta)}\right] \qquad (2.1)$$

is the reaction rate. Here, A is the frequency factor (multiplied by density and divided by molecular weight, assumed equal for all species), $\alpha \equiv (T_f - T_\infty)/T_f$ is the heat release parameter, and $\mathrm{Ze} \equiv \alpha T_a/T_f$ is the Zeldovich number. T_a is the activation temperature. The Schmidt number is 0.7 and Lewis numbers are unity. The turbulent flow is incompressible and the molecular diffusivities and viscosity are independent of the temperature (see Sripakagorn *et al.* (2000) for details of the simulation). Chemistry rate parameters are $\alpha = 0.87$, $\mathrm{Ze} = 4$, and $K = 100$. Two values of A define two different numerical experiments with moderate ($A = 8.0 \times 10^4$) and high ($A = 0.3 \times 10^4$) levels of local extinction. (These cases correspond to "Case B" and "Case C", respectively, in Cha *et al.* (2001).) Categorization of the level of local extinction by the terms "moderate" and "high" is described below.

2.2. *Higher-order conditional moment closure approaches*

The conditioned average of $\dot{w}$ as a function of all conditional moments can be obtained with: (i) a series expansion of the second exponential in Eq. (2.1) about $\epsilon \equiv \alpha\theta'/(1-\alpha(1-\langle\theta|\xi\rangle))$, where $\theta' \equiv \theta - \langle\theta|\xi\rangle$, valid for $|\epsilon| < \infty$; (ii) a series expansion for $(1+\epsilon)^{-1}$, valid for $|\epsilon| < 1$; and (iii) a decomposition of all species mass fractions about their conditional means, $Y = \langle Y|\xi\rangle + Y'$. Conditionally averaging the result yields, for the forward reaction rate,

$$\langle \dot{w}(Y_{\rm F}, Y_{\rm O}, Y_{\rm P}, \theta)|\xi\rangle = \dot{w}(\langle Y_{\rm F}|\xi\rangle, \langle Y_{\rm O}|\xi\rangle, \langle Y_{\rm P}|\xi\rangle, \langle\theta|\xi\rangle)(1 + \mathcal{B}' + \mathcal{C}' + \text{H.O.T.}) \tag{2.2}$$

$$\mathcal{B}' = \frac{\langle Y'_{\rm F} Y'_{\rm O}|\xi\rangle}{\langle Y_{\rm F}|\xi\rangle\langle Y'_{\rm O}|\xi\rangle} + \frac{\rm Ze}{[1-\alpha(1-\langle\theta|\xi\rangle)]^2}\left(\frac{\langle Y'_{\rm F}\theta'|\xi\rangle}{\langle Y_{\rm F}|\xi\rangle} + \frac{\langle Y'_{\rm O}\theta'|\xi\rangle}{\langle Y_{\rm O}|\xi\rangle}\right) + \left(\frac{\rm Ze/2}{1-\alpha(1-\langle\theta|\xi\rangle)} - \alpha\right)\frac{\langle\theta'^2|\xi\rangle}{[1-\alpha(1-\langle\theta|\xi\rangle)]^3}$$

$$\mathcal{C}' = \left(\frac{\rm Ze/2}{1-\alpha(1-\langle\theta|\xi\rangle)} - \alpha\right)\frac{\alpha^2/\rm Ze}{1-\alpha(1-\langle\theta|\xi\rangle)}\left(\frac{\langle Y'_{\rm F}\theta'^2|\xi\rangle}{\langle Y_{\rm F}|\xi\rangle} + \frac{\langle Y'_{\rm O}\theta'^2|\xi\rangle}{\langle Y_{\rm O}|\xi\rangle}\right) + \frac{\alpha}{1-\alpha(1-\langle\theta|\xi\rangle)}\frac{\langle Y'_{\rm F}Y'_{\rm O}\theta'|\xi\rangle}{\langle Y_{\rm F}|\xi\rangle\langle Y_{\rm O}|\xi\rangle} - \frac{\alpha^4/\rm Ze}{[1-\alpha(1-\langle\theta|\xi\rangle)]^2}\langle\theta'^3|\xi\rangle$$

valid for $|\epsilon| < 1$. The complete series is always convergent for $\alpha \leq 1$. For the present case of a single-step reaction, the conditional averages of all species and temperature can be obtained from the single equation for the average of θ conditioned on ξ:

$$\left(\frac{d}{dt} - \frac{\langle\chi|\xi\rangle}{2}\frac{\partial^2}{\partial\xi^2}\right)\langle\theta|\xi\rangle = 2\dot{w}(\langle Y_{\rm F}|\xi\rangle, \langle Y_{\rm O}|\xi\rangle, \langle Y_{\rm P}|\xi\rangle, \langle\theta|\xi\rangle)(1 + \mathcal{B} + \mathcal{C}) \ , \tag{2.3}$$

where $\mathcal{B}$ and $\mathcal{C}$ also contain the contributions of the backward reaction. $\langle\chi|\xi\rangle$ is the conditionally-averaged dissipation rate of ξ, specified directly from the DNS. e_Q and e_y closure has been invoked (Cha *et al.* 2001). For convenience, Eq. (2.3) is referred to as the `cmc3` model (third-order closure), as the `cmc2` model with $\mathcal{C} = 0$ (second-order closure), and as the `cmc1` model with both $\mathcal{B} = 0$ and $\mathcal{C} = 0$ (first-order closure). All double and triple conditional correlations are taken from the DNS.

2.3. *Presumed singly-conditional pdf approach*

The beta distribution, or β pdf, is a standard model to describe a random phenomenon whose set of all possible values lies in some finite interval (Ross 1984). The β pdf is a two-parameter distribution given by

$$p(\theta^*; a, b) = \begin{cases} \frac{1}{B(a,b)}\theta^{*a-1}(1-\theta^*)^{b-1} & 0 < \theta^* < 1 \\ 0 & \text{otherwise} \end{cases} \ , \tag{2.4}$$

where θ^* has been transformed (translated and normalized) onto the interval $[0, 1]$. The free parameters a and b enforce $\langle\theta^*\rangle(a,b)$ and $\langle\theta^{*2}\rangle(a,b)$, the first and second moments of θ^*, respectively, and $B(a,b)$ normalizes the pdf such that $\int p(\theta^*)d\theta^* = 1$. The presumed β pdf model for describing the mixing of a conserved scalar is described in Bilger (1980). For the present case of a single-step reaction, $p(\theta^*)$ models the conditional pdf of $\theta/\theta_{\rm eq}$, a reacting scalar, where $\theta_{\rm eq}$ is the equilibrium value of the reduced temperature at $\xi_{\rm st}$. Applying this definition to the conditional moment equations yields

$$\left(\frac{d}{dt} - \frac{\langle\chi|\xi\rangle}{2}\frac{\partial^2}{\partial\xi^2}\right)\langle\theta|\xi\rangle = 2\int \dot{w}(Y_{\rm F}, Y_{\rm O}, Y_{\rm P}, \theta)p(\theta|\xi; \langle\theta|\xi\rangle, \langle\theta'^2|\xi\rangle)d\theta^* \ , \tag{2.5}$$

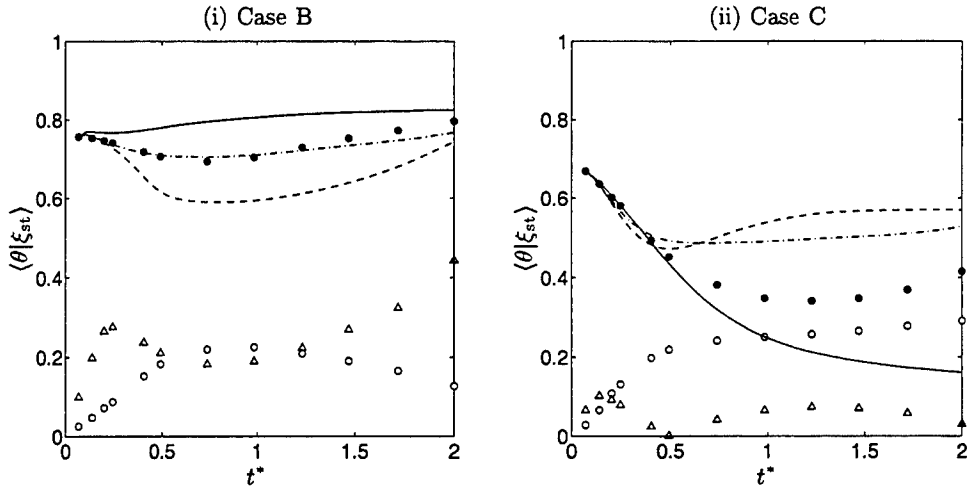

FIGURE 2. Comparison of higher-moment modeling results with DNS data. Solid circles = conditional average of the reduced temperature, $\langle\theta|\xi_{st}\rangle$, open circles = standard deviation about conditional means, $(\langle\theta'^2|\xi_{st}\rangle)^{1/2}$, open triangles = skewness, $|s|/10$. Solid line = first-order conditional moment closure results (cmc1), dash-dash line = second-order modeling results (cmc2), and dash-dot line = third-order predictions (cmc3). Subplot (i) = moderate extinction case (Case B) and subplot (ii) = high extinction case (Case C) from Cha *et al.* (2001).

where $\dot{w}(Y_F, Y_O, Y_P, \theta)$ is a known function of the ξ and θ sample space and $p(\theta|\xi)$ is a function of the conditional mean and variance of θ, $\langle\theta|\xi\rangle$ and $\langle\theta'^2|\xi\rangle$, respectively. Equation (2.5) is an integro-differential equation for $\langle\theta|\xi\rangle(t,\xi)$ and only $\langle\theta'^2|\xi\rangle$ is taken from the DNS to evaluate the right-hand side of Eq. (2.5) for the *a priori* study.

3. Results and discussion

Figure 2 compares the higher-moment modeling results (lines) to the DNS experimental data (symbols). Solid circles are the conditionally-averaged temperature at ξ_{st} taken directly from the numerical experiment. Subplot (i) is from the same case as was shown in Fig. 1. The deviation of $\langle\theta|\xi_{st}\rangle$ from the equilibrium value, $\theta_{eq} = 0.83$ at ξ_{st}, is due to the local extinction/reignition events that were seen in Fig. 1 (i). Only the frequency factor was decreased in the DNS for the case shown in Fig. 2 (ii); this results in increased extinction levels, and hence shows a larger deviation from θ_{eq} compared to the case in subplot (i). Open circles are the standard deviation about $\langle\theta|\xi_{st}\rangle$ and open triangles are the skewness, defined as

$$s = \frac{1}{\langle\theta'^2|\xi\rangle^{3/2}} \int (\theta - \langle\theta|\xi\rangle)^3 p(\theta|\xi) d\theta \ ,$$

where $p(\theta|\xi)$ is the conditional pdf. Note that s is a function of $\langle\theta^3|\xi\rangle$, a third-order term. In Fig. 2, solid lines are first-order modeling results (cmc1), dash-dash lines are second-order predictions (cmc2), and dash-dot lines are third-order modeling results (cmc3).

In Case B (subplot (i) in Fig. 2), second-order closure causes the mean to be underpredicted. Consideration up to the third-order terms in Eq. (2.3) evidently counteracts this effect and leads to good predictions of the data.

In Case C (subplot (ii) in Fig. 2), first-order closure is unable to predict the onset of reignition (in the mean). Both second- and third-order closures can predict the global

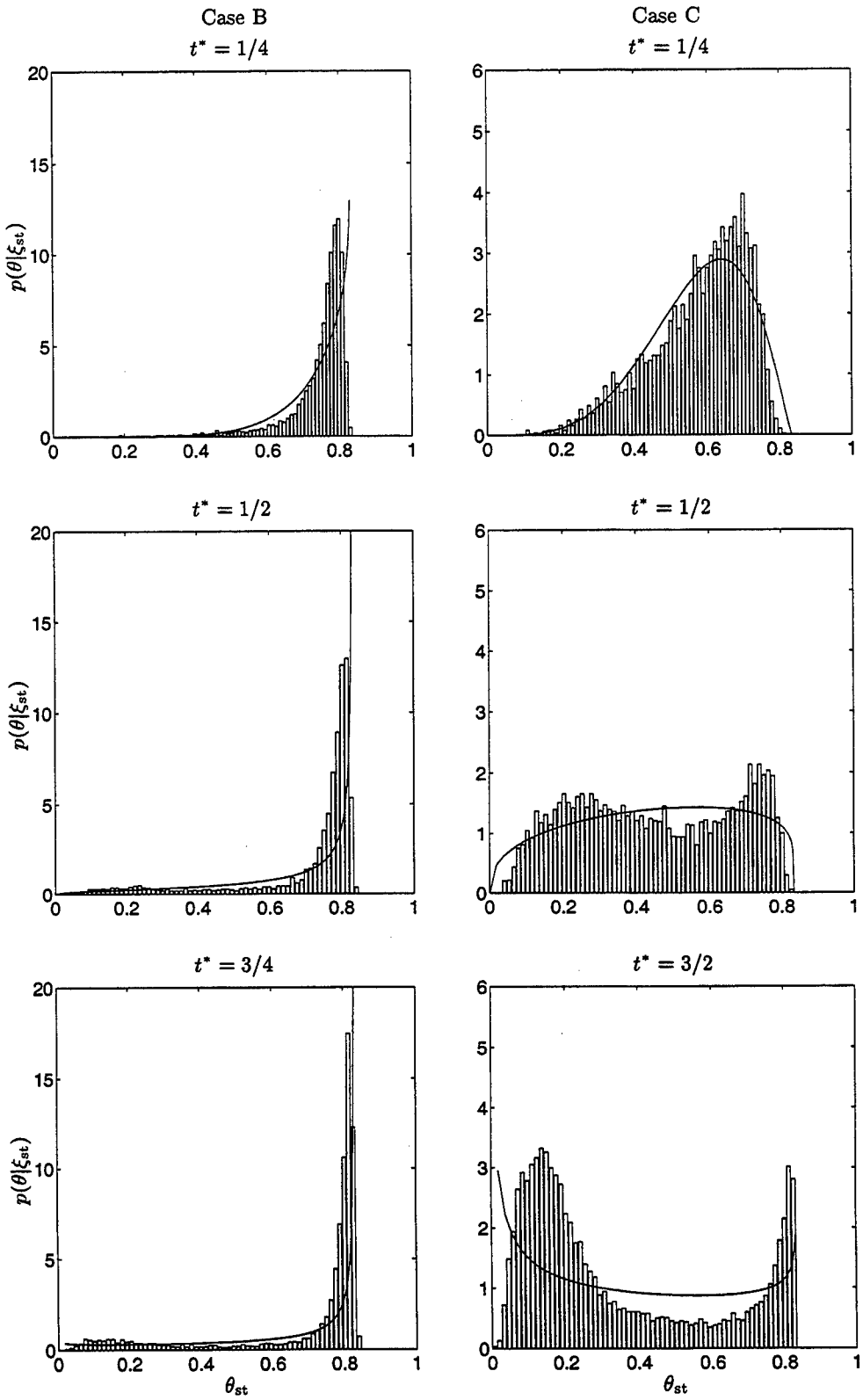

FIGURE 3. Conditional pdfs of θ at ξ_{st}, $p(\theta|\xi_{st})$, for Case B (left column) and Case C (right column). Solid lines are the presumed β pdf predictions using the exact conditional means and variances from the DNS.

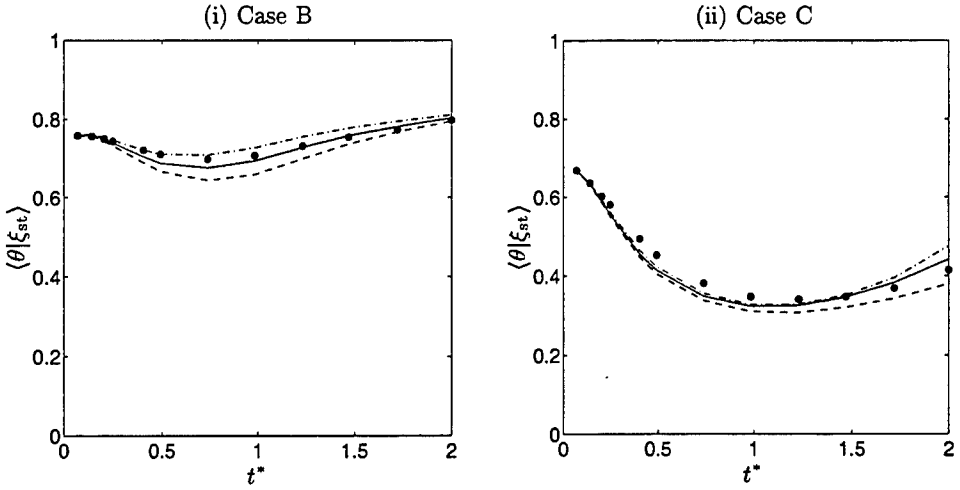

FIGURE 4. Comparison of presumed β pdf modeling results with DNS data. Symbols = DNS data of conditional average of the reduced temperature, $\langle\theta|\xi_{st}\rangle$ (solid circles). Lines = modeling results: Exact variance, $\langle\theta'^2|\xi\rangle$, from DNS used in the *a priori* modeling results (solid lines), $\pm 30\%$ relative errors added to the DNS variance (dash-dash lines). Subplot (i) = moderate extinction case (Case B) and subplot (ii) = high extinction case (Case C) from Cha *et al.* (2001).

reignition, but deviate from the data beyond $t^* \gtrsim 1/2$. Of note is that the skewness, $|s|$, decreases in the higher extinction case while the variance remains comparable.

Discussion of the modeling results in Fig. 2 centers on the conditional pdfs of θ at ξ_{st}, $p(\theta|\xi_{st})$, for representative times of interest. Figure 3 (left column) shows $p(\theta|\xi_{st})$ at $t^* = 1/4$, $1/2$, $3/4$, and $3/2$ for Case B. At early times ($t^* < 1/2$), the pdfs are unimodal—have a well-defined, single peak—with some negative skewness. The series expansion of the conditionally-averaged reaction rate, Eq. (2.2), does not contain details of the shape of the pdf. Evidently, skewness, or third-order information, and variance, or second-order information, are sufficient to correct first-moment closure, resulting in the good agreement with data that was seen in Fig. 2 (i). For larger times, $t^* \geq 1/2$, some bimodality begins to appear in the pdfs, but not enough to cause problems for the third-order closure, the `cmc3` model. For a general unimodal pdf, at least third-order moments are required to capture skewness. For this experimental case with moderate local extinction levels, the skewness is always negative for $p(\theta|\xi_{st})$ because the temperature can never exceed θ_{eq}. The implication is that in such a circumstance at least third-order information is required in the series expansion of $\langle\dot{w}|\xi\rangle$.

Figure 3 (right column) shows $p(\theta|\xi_{st})$ for Case C (corresponding to subplot (ii) in Fig. 2) at $t^* = 1/4$, $1/2$, $3/4$, and $3/2$. For $t^* \lesssim 1/4$, the standard deviation about the conditional average is comparable to Case B, but with reduced skewness (*cf.* Fig. 2), and second-order closure yields comparable results to the third-order closure predictions. For $t^* \gtrsim 1/2$, the pdfs become bimodal—have well-defined, double peaks—and thus the skewness can no longer characterize the shape of the pdfs. Third-order closure also breaks down. Bimodality becomes stronger for increasing times with comparable peak temperatures. The standard deviations in this case and in Case B (*cf.* Fig. 2) are comparable, because of the combined effect of the high extinction levels in the present case, which decrease $\langle\theta|\xi_{st}\rangle$, and the bimodality of the pdf. The reduction in skewness from Case B is due to the remarkable symmetry of the pdfs.

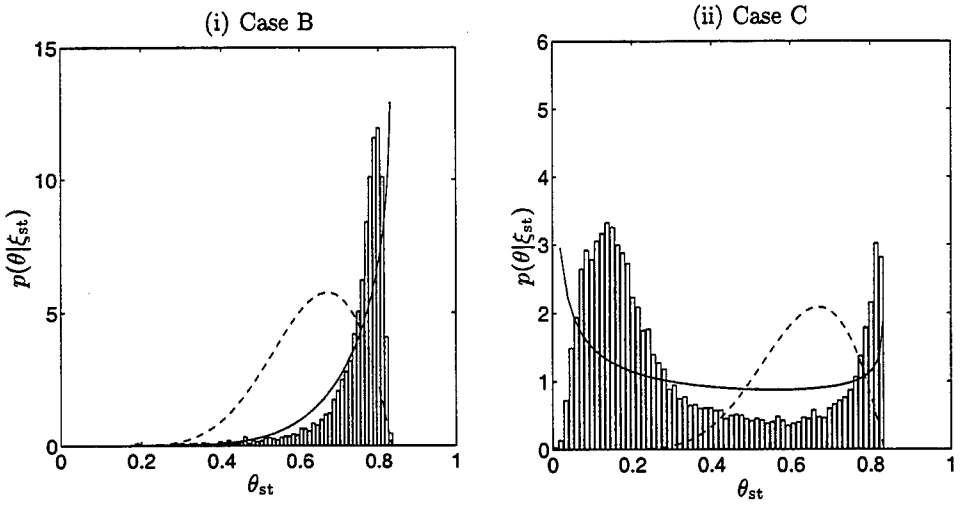

FIGURE 5. Why the presumed β pdf modeling works. Representative results reproduced from Fig. 3 with the chemical source term function (dash-dash lines) overlaid.

The skewed unimodal and bimodal pdf shapes in Fig. 3 are due to the realistic, Arrhenius kinetics which result in a bistable dynamic system (Pitsch & Fedotov 2001), as determined by the steady flamelet solution (Peters 1983). With low to moderate local extinction levels, the upper (stable) and middle (unstable) branches of the steady flamelet solution lead to negatively skewed pdf shapes, as was seen in the left-hand column of Fig. 3 (Case B). With moderate to high extinction levels, the upper and lower stable branches lead to bimodal pdf shapes, as was seen most dramatically in the right-hand column of Fig. 3 (Case C) for times $t^* > 1/2$. That the transitional probabilities always correspond to the minimum probability of the bimodal distributions is a direct result of the unsteady dynamics of the bistable system switching between the upper, high temperature ($\theta_{st} \sim \mathcal{O}(1)$) and lower, low temperature ($\theta_{st} \sim \mathcal{O}(0.1)$) stable branches (Pitsch *et al.* 2001). This switching is of course due to extinction and reignition.

Figure 3 also shows predictions of the conditional pdf shapes using the presumed β pdf model (solid lines). In this figure, both the conditional mean and the variance were taken directly from the DNS data. The success of the presumed β pdf model for passive scalar mixing is well known. Figure 3 shows that the presumed β pdf model does not have the flexibility to describe the variety of reactive scalar pdf shapes due to the modifications by reaction, more precisely the extinction/reignition dynamics which result from realistic, Arrhenius kinetics. In particular, the unimodal peaks are always underpredicted for Case B (left column). In Case C (right column), the presumed β pdf shape also underpredicts the twin peak densities of the bimodal pdfs, while the transitional probabilities between the extinguished and burning states are always overpredicted. However, in both cases, the overall unimodal or bimodal pdf shapes are generally well described.

In spite of the discrepancies in the presumed β pdf model's description of the unimodal and bimodal conditional pdf shapes of the reduced temperature, *a priori* modeling results of Eq. (2.5) show excellent agreement with the DNS. Figure 4 compares the results of the presumed β pdf model for $\langle\theta|\xi_{st}\rangle$ (lines) with the DNS data (symbols). Only the conditional variance, $\langle\theta'^2|\xi\rangle$, is taken from the DNS to evaluate the right-hand side of Eq. (2.5). Solid lines in Fig. 4 show results using the exact variance from the DNS, and dash-dash lines show results with $\pm 30\%$ relative errors added to the DNS variance. The

results suggest that even a crude estimate of the conditional variance is sufficient to predict the effects of local extinction and reignition on $\langle\theta|\xi\rangle$.

Discussion of the excellent agreement between the modelling results and the DNS data centers on the singly-conditional pdfs of Fig. 3. The right-hand side of Eq. (2.5) can be interpreted as the integral over the presumed β pdf shape, weighted by the nonlinear chemical source term. Figure 5 shows representative results reproduced from Fig. 3 with the chemical source term function (dash-dash lines) overlaid. The figure shows the relative weighting given to the discrepancies between the β pdf model and the true pdfs by the chemical source term. When the pdf is unimodal (Case B), the underprediction of the peak value made by the presumed β pdf model is reduced by the rapid decrease of the chemical source term as $\theta_{\rm st} \rightarrow \theta_{\rm eq}$. When the pdf is bimodal (Case C), only the transitional probabilities are significant and the discrepancies in the β pdf model results at the twin peak locations of the true pdf are no longer important. The strong nonlinearity of the chemical source term, due to the realistic, Arrhenius kinetic model, leads to a bistable system and the characteristic unimodal and bimodal pdf shapes, already described. The presumed β pdf shape can capture the overall unimodal and bimodal pdf shapes, with some discrepancies at the peak values of the true pdfs. Figure 5 shows that it is the strong nonlinearity of the chemical source term which diminishes the importance of these discrepancies in the modelling represented by Eq. (2.5). Hence, these types of discrepancies are also expected to be unimportant in reacting flows of practical interest, where Arrhenius kinetics are used.

4. Conclusions and future work

With moderate levels of local extinction, the conditional pdfs are unimodal (single-peaked). Information about the mean and variance alone in the series expansion of the conditional average of the chemical source term is insufficient to describe the influence of the fluctuations. That is, first- and second-order closures cannot describe the conditional means, and third-moments (or the skewness of the pdfs) are also required to obtain good predictions. With high levels of local extinction, the pdf can adopt a strong bimodal shape, and even third-order closure is insufficient to describe the conditional averages.

Information about the conditional second moment is sufficient to describe the effect of extinction/reignition on the conditional averages only if a presumed β pdf model is used. The presumed β pdf shape shows some discrepancies in describing the singly-conditional pdfs of a reacting scalar undergoing extinction/reignition, but the overall unimodal or bimodal pdf shapes are generally well described. The effects of the deviations are diminished by the strong nonlinearity of the chemical source term in a singly-conditional closure with a presumed β pdf shape, Eq. (2.5) in this paper, leading to excellent predictions of the conditional means. The insensitivity of the model to the conditional variance of the reacting scalar suggests the possibility of using the conditional variance which results from the fluctuations of the dissipation rate of the mixture fraction alone.

Acknowledgements

The authors express gratitude to Paiboon Sripakagorn for making his DNS database available to us before publication.

REFERENCES

BILGER, R. W. 1980 Turbulent flows with nonpremixed reactants. In *Turbulent Reacting Flows*, *Topics in Applied Physics* 44, Springer, 65–113.

CHA, C. M., KOSÁLY, G. & PITSCH, H. 2001 Modeling extinction and reignition in turbulent nonpremixed combustion using a doubly-conditional moment closure approach. *Phys. Fluids* (accepted).

KLIMENKO, A. Y. & BILGER, R. W. 1999 Conditional moment closure for turbulent combustion. *Prog. Energy Comb. Sci.* **25**, 595–687.

KRONENBURG, A., BILGER, R. W. & KENT, J. H. 1998 Second-order conditional moment closure for turbulent jet diffusion flames. *Proc. Comb. Inst.* **27**, 1097–1104.

MASTORAKOS, E. & BILGER, R. W. 1998 Second-order conditional moment closure for the autoignition of turbulent flows. *Phys. Fluids* **10** , 1246–1248.

PETERS, N. 1983 Local quenching due to flame stretch in non-premixed turbulent combustion. *Comb. Sci. and Tech.* **30**, 1–17.

PITSCH, H., CHA, C. M. & FEDOTOV, S. 2001 Flamelet modeling of non-premixed turbulent combustion with moderate local extinction and re-ignition. *Comb. Theory Modelling* (submitted).

PITSCH, H. & FEDOTOV, S. 2001 Investigation of scalar dissipation rate fluctuations in non-premixed turbulent combustion using a stochastic approach. *Comb. Theory Modelling* **5**, 41–57.

ROSS, S. 1984 *A First Course in Probability*, 2nd edn. Macmillan.

SRIPAKAGORN, P., KOSÁLY, G. & PITSCH, H. 2000 Local extinction-reignition in turbulent nonpremixed combustion. *Annual Research Briefs*, Center for Turbulence Research, NASA Ames/Stanford Univ. 117–128..

SWAMINATHAN, N. & BILGER, R. W. 1998 Conditional variance equation and its analysis. *Proc. Comb. Inst.* **27**, 1191–1198.

Progress in large-eddy simulation of premixed and partially-premixed turbulent combustion

By L. Duchamp de Lageneste AND H. Pitsch

1. Motivation and objectives

In many practical devices such as gas turbines and internal combustion engines, liquid fuel is injected as a spray and mixed with oxidizer as it vaporizes, so that combustion takes place in a partially-premixed regime. While partially-premixed flame propagation has been the subject of extensive experimental investigations (Su 2000; Muniz & Mungal 1997), its numerical simulation remains a challenging task. The mechanisms by which turbulence, chemical reactions, and heat release interact are still under investigation. Results by Veynante (1994) suggest the importance of premixed flame propagation in the process of flame stabilization. While DNS of turbulent premixed flames using realistic chemistry is still restricted to very simple geometries, classical RANS modeling of reacting flows is often considered to lack precision, especially when highly-unsteady problems are considered.

Different methods have been suggested to model turbulent premixed combustion in LES (Colin 2000; Kim & Menon 2000; Duchamp de Lageneste & Pitsch 2000). An approach based on a mixed level-set/diffusion-flamelet library applicable to premixed and partially-premixed combustion has been derived by Peters (1999) for RANS and validated by Herrmann (2000) showing good agreement with experimental data. Beside the fact that this method does not require solving any additional species transport equations or explicit modeling of chemical reaction rates, it also allows the use of arbitrarily complex chemistry without leading to prohibitive computational requirements.

The work presented here focuses on the implementation and validation of a similar approach in the LES context. First, the governing equations to be solved are presented together with the sub-grid models used, including an improved model for the turbulent burning velocity. Then we discuss the application of this approach to two different test cases; a turbulent Bunsen flame (Aachen flame F_3, (Chen 1996) and a lean, partially-premixed dump combustor, the so-called ORACLES geometry described in Besson (1999*a*) and Besson (1999*b*).

2. Governing equations

2.1. *Navier-Stokes equations*

We consider the low-Mach-number approximation to the Navier-Stokes equations (Williams 1985). In the LES context, these equations are written for the filtered variables $\overline{\rho}$, $\widetilde{\mathbf{u}}$ and $\overline{P}$ as:

Mass conservation

$$\frac{\partial \overline{\rho}}{\partial t} + \nabla \cdot (\overline{\rho}\widetilde{\mathbf{u}}) = 0\,, \tag{2.1}$$

Momentum conservation

$$\frac{\partial \overline{\rho}\widetilde{\mathbf{u}}}{\partial t} + \nabla \cdot (\overline{\rho}\widetilde{\mathbf{u}}\widetilde{\mathbf{u}}) = -\nabla \overline{P} + \nabla \cdot (\mu + \mu_t)\widetilde{\tau}\,, \tag{2.2}$$

where the Favre-filtered velocity vector is defined as $\widetilde{\mathbf{u}} = \overline{\rho\mathbf{u}}/\overline{\rho}$, $\widetilde{\tau}$ is the Reynolds stress tensor, and μ_t the turbulent sub-grid eddy viscosity, modeled using a dynamic approach (Moin 1991).

2.2. *G-equation*

In the level-set framework, the instantaneous flame-front location is given by an iso-surface G_0 of a continuous field G. The evolution of this iso-surface is described by the so-called G-equation (Kerstein 1988), valid only at G_0:

$$\frac{\partial G}{\partial t} + \mathbf{u} \cdot \nabla G = s_L |\nabla G|\,, \tag{2.3}$$

where s_L is the laminar burning velocity.

In the context of RANS, Peters (1999) has derived a model equation for the evolution of the mean flame-front location, valid in the corrugated flamelet and the thin reaction zones regime. Keeping in mind that in LES the reaction zone is still much smaller than the grid size, one can see that similar arguments can be used to propose a model equation describing the evolution of the filtered flame-front position. This equation reads

$$\overline{\rho}\frac{\partial \widetilde{G}}{\partial t} + \overline{\rho}\widetilde{\mathbf{u}} \cdot \nabla \widetilde{G} = \underbrace{\overline{\rho} s_T |\nabla \widetilde{G}|}_{Propagation} \underbrace{- \overline{\rho} D_t^G \widetilde{\kappa} |\nabla \widetilde{G}|}_{Curvature}\,, \tag{2.4}$$

where the turbulent burning velocity s_T as well as the scalar turbulent diffusivity D_t^G have to be modeled.

While a dynamic procedure (Moin 1991; Pierce & Moin 1998) is used to compute D_t^G, the turbulent burning velocity s_T requires further attention.

Peters (1999) derived the following model for s_T, which in addition to the turbulent velocity scales (u'/s_L) also takes the turbulent length scales (Δ_t/l_F) into account.

$$\frac{s_T - s_L}{s_L} = -\frac{a_4 b_3^2}{2b_1}\frac{\Delta_t}{l_F} + \left[\left(\frac{a_4 b_3^2}{2b_1}\frac{\Delta_t}{l_F}\right)^2 + a_4 b_3^2 \frac{u'\Delta_t}{s_L l_F}\right]^{\frac{1}{2}}, \tag{2.5}$$

where Δ_t is the turbulent integral length scale, l_F the laminar flame thickness, u' the turbulent velocity fluctuation and a_4, b_1, and b_3 are constants given in Peters (1999).

A similar expression can be proposed to model s_T in LES where Δ_t then stands for the filter size and u' is the sub-grid velocity fluctuation. The coefficients a_4, b_1, and b_3 also have to be adapted to LES.

As a first approximation, the results reported in Duchamp de Lageneste & Pitsch (2000) were obtained with b_1 and b_3 taken to be the RANS values while a_4 was re-evaluated to be 1.37. This new value was based on a turbulent sub-grid Schmidt number $\mathrm{Sc_t} = 0.4$ instead of 0.7 for RANS, as reported for a non-reacting scalar in a diffusion flame by Pitsch & Steiner (2000). Nevertheless, there is no evidence that the turbulent Schmidt number should remain constant in the case of the scalar $\widetilde{G}$. Consequently, this parameter is now computed locally as $a_4 = D_t^G/(u'\Delta_t)$ where u' and D_t^G are evaluated with a dynamic model.

As a final remark, it is important to note that in order to maintain sufficient regularity

for $\widetilde{G}$, a reinitialization procedure that constrains the $\widetilde{G}$ field to a distance function (such that $|\nabla\widetilde{G}| = 1$) has been implemented (Sethian 1996; Sussman & Fatemi 1999; Russo & Smereka 2000). A detailed description of the implementation of this method in our context can be found in Duchamp de Lageneste & Pitsch (2000).

2.3. *Temperature equation*

In the case of constant molecular properties, only the filtered density is needed in order to solve Eqs. (2.1) and (2.2). Nevertheless, if turbulent heat transport in the unburnt mixture is to be considered, it is necessary to introduce an equation for the filtered temperature $\widetilde{T}$:

$$\overline{\rho}\frac{\partial\widetilde{T}}{\partial t} + \overline{\rho}\widetilde{\mathbf{u}}\cdot\nabla\widetilde{T} = \nabla\cdot(\overline{\rho}D_t^T\nabla\widetilde{T}) + \overline{\rho}\widetilde{\omega}\,, \tag{2.6}$$

where D_t^T is the turbulent diffusivity of the temperature, obtained with a dynamic procedure. Here, $\widetilde{\omega}$ is not a chemical source term, but a volumetric heat source that is used to set $\widetilde{T}$ to the predicted flamelet library value in the burned gases.

Once the filtered temperature is known, the filtered density is recovered via the equation of state.

2.4. *Mixture fraction*

Modeling partial pre-mixing or dilution effects requires the introduction of a conserved scalar $\widetilde{Z}$, similar to the mixture fraction in non-premixed combustion. The burnt temperature is then pre-computed as a function of $\widetilde{Z}$ and its variance $\widetilde{Z''^2}$ by assuming a β-function pdf for this scalar.

In our case the values of $\widetilde{Z}$ range from 0 in pure air to 1 for a stoichiometric mixture, and are given by the solution of

$$\overline{\rho}\frac{\partial\widetilde{Z}}{\partial t} + \overline{\rho}\widetilde{\mathbf{u}}\cdot\nabla\widetilde{Z} = \nabla\cdot(\overline{\rho}D_t^Z\nabla\widetilde{Z})\,, \tag{2.7}$$

where D_t^Z is also computed dynamically.

In partially-premixed cases, where $\widetilde{Z}$ is fluctuating along the G_0 surface, one also has to compute the laminar burning velocity s_L and laminar flame thickness l_F appearing in Eq. (2.5) as functions of $\widetilde{Z}$.

2.5. *Total enthalpy*

If non-adiabatic effects, such as heat losses at boundaries, are to be included, one can also introduce the total enthalpy $\widetilde{H}$ as an additional parameter in the flamelet library. $\widetilde{H}$ is also a conserved scalar and obeys an equation similar to Eq. (2.7). In that case, one of the energy equations, total enthalpy or temperature, would actually be redundant. However, the enthalpy is only used in the burnt gas to determine the burnt temperature from the flamelet library. The volumetric heat source term in Eq. (2.6) is then used to enforce this temperature in the solution of the temperature equation which is then mainly used to describe the turbulent temperature transport in the unburnt gas.

2.6. *Numerical methods*

The code that was used in this study was developed at the Center for Turbulence Research by Pierce & Moin (1998). The filtered low-Mach-number approximation of the Navier-Stokes equations is solved in cylindrical or Cartesian coordinates on a structured staggered mesh that can be refined independently in the axial and radial directions. The

numerical method is a conservative, second-order finite-volume scheme. Second-order semi-implicit time advancement is used, which alleviates the CFL restriction in regions where the grid is refined. Details of the method can be found in Akselvoll & Moin (1996). The code has been thoroughly validated in various studies (Akselvoll 1996; Pierce & Moin 1998, 2001).

3. Large eddy simulation of a turbulent Bunsen flame

The experimental setup studied by Chen (1996) consists of a stoichiometric premixed methane-air flame, stabilized by a large pilot flame. Both incoming streams, the main jet and the pilot, have the same composition. The nozzle diameter D of the main stream is 12 mm. The pilot stream issues through a perforated plate (1175 holes of 1 mm in diameter) around the central nozzle, with an outer diameter of $5.67D$. The main stream is turbulent with a Reynolds number of $\mathrm{Re} = 23486$, based on the inner nozzle diameter and a bulk velocity of $U_0 = 30\,\mathrm{m/s}$.

3.1. *Grid and boundary conditions*

The computational domain extends to $20\,D$ downstream of the nozzle and $4\,D$ in the radial direction. The LES grid is $256 \times 96 \times 64$ corresponding to approximately 1.6 million cells. At the inflow boundary, instantaneous velocities extracted from a separate LES of a fully developed pipe flow are prescribed. Convective conditions (- Akselvoll & Moin 1996) are prescribed at the outflow boundary, while traction-free conditions (Boersma 1998) are imposed on the lateral boundary in order to allow entrainment of fluid into the domain.

3.2. *Results and discussion*

The mean radial profiles of temperature and axial velocity are shown in Fig. 1 for two different downstream locations: here $\overline{\theta}$ is the time-averaged non-dimensional temperature defined by $\overline{\theta} = \left(\overline{T} - T_u\right) / \left(T_b - T_u\right)$, and T_b and T_u are the adiabatic burned and unburned temperatures respectively. $\overline{U}_{ax}$ is the time-averaged axial velocity normalized by the bulk velocity U_0.

Comparison is made between experimental data (denoted by symbols), the LES results reported in Duchamp de Lageneste & Pitsch (2000) (dashed lines) and the actual simulation (solid lines).

The major discrepancies found between the results reported in Duchamp de Lageneste & Pitsch (2000) and the experimental data concerned an over-prediction of the mean temperature increase, leading to an over-prediction of the mean spreading rate of the jet. Chen (1996) noted that, while still in equilibrium, the gases in the pilot flame were found to be at a much lower temperature than the adiabatic temperature, due to heat losses to the burner surface. These heat losses were not taken into account in our previous simulation, and are now modeled by solving a transport equation for the total enthalpy, which appears as a parameter in the flamelet library. Prescribing a lower enthalpy in the pilot stream than in the main jet leads to a predicted maximum value of the mean temperature in good agreement with the experimental data, especially close to the burner (as shown in Fig. 1). As a consequence, the jet expansion due to heat release is now predicted with good accuracy.

While the evolution of the turbulent kinetic energy near the axis was generally well predicted in Duchamp de Lageneste & Pitsch (2000), the maximum value was over-predicted and the location of the peak was shifted toward the burnt side of the flame

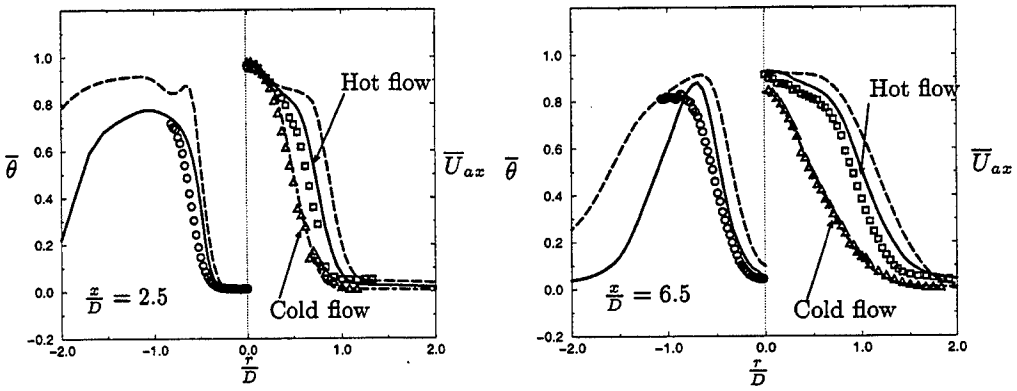

FIGURE 1. Radial profiles of the mean temperature and axial velocity at different axial positions. Symbols represent experimental data, lines LES results. Solid lines: non-adiabatic conditions, dashed lines: adiabatic conditions.

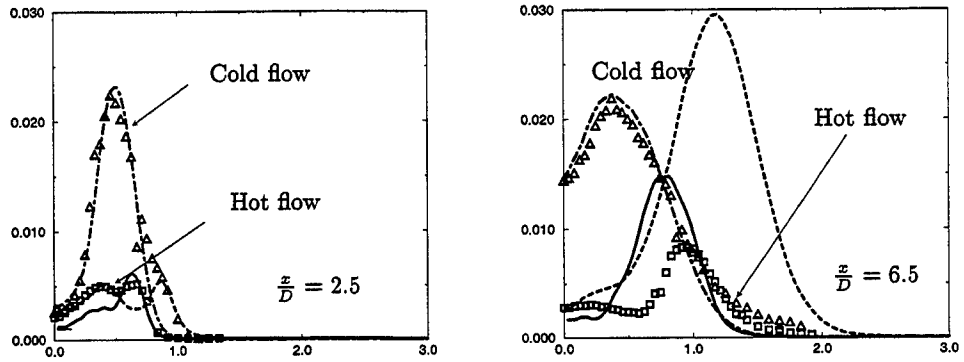

FIGURE 2. Radial profiles of the mean turbulent kinetic energy at different axial locations. Symbols represent experimental data, lines LES results. Solid lines: non-adiabatic conditions, dashed lines: adiabatic conditions.

(dashed lines in Fig. 2). The present simulation shows a clear improvement in both respects. At $x/D = 2.5$, both the location and the value of the peak are well predicted. At $x/D = 6.5$ the peak is well located and even though its value is still somewhat overestimated the agreement with the experimental data is considerably improved.

The intensity of the peak in turbulent kinetic energy located on the burnt side of the flame can be directly related to the development of the mixing layer between the hot burnt gases and the cold entrained air. From this viewpoint, the overestimation of the turbulent kinetic energy in Duchamp de Lageneste & Pitsch (2000), which they found to be growing with distance from the burner, is consistent with the overestimation of the burnt-gas temperature reported in that study. The non-adiabatic conditions used in the present simulation improve the prediction of the location of the heat release, and thereby lead to a much better estimation of the development of the mixing layer. Thus, the slight

over-prediction still observed in the temperature profiles further downstream could be responsible for the higher turbulence intensities found at these locations.

4. Large-eddy simulation of a lean, partially-premixed dump combustor

Constructed at the Laboratoire de Combustion et de Détonique (LCD) de l'ENSMA Poitiers (France) within the Brite-Euram project BE95-1953 (Besson 1999*b*), the test-rig ORACLES has been especially designed to provide accurate experimental data to assess the quality of different approaches in LES of turbulent premixed and partially-premixed combustion.

The experimental setup consists of two channel flows emerging into a wider combustion chamber which is shown in Fig. 3. For the reacting case, the flame is stabilized by the recirculation zones created behind each step. The channels are separated by a splitter plate which is recessed with respect to the expansion to avoid possible anchoring of the flame at the tip of the plate.

Special attention has been paid to providing suitable boundary conditions for LES. The two incoming channels are long enough ($\approx 100\,H$ where H is the step height) to ensure a fully-developed turbulent flow in each stream. In all the cases considered here, the mass flow rate is the same in both channels.

Several different cases have been studied experimentally (Besson 1999*a*). Here we will focus on two of these: the inert flow, used as a reference case, and a reacting case, where the equivalence ratio for the upper stream is 0.9, while it is 0.3 for the lower stream. The main reason for choosing the latter case is that it will provide the opportunity to test the ability of our method to handle partially-premixed turbulent combustion. It is also worth noting that the strong acoustic instabilities that have been detected in most cases with constant equivalence ratio are a problem which has been avoided here, to provide a basic validation of the combustion model.

4.1. *Grid and boundary conditions*

The computational domain extends to $20\,H$ downstream and $4\,H$ upstream of the expansion. The LES grid is $256 \times 128 \times 64$, corresponding to approximately 2.2 million cells. At the inflow boundary, instantaneous velocities obtained from a separate LES of two fully-developed channel flows are prescribed. Convective conditions (Akselvoll & Moin 1996) are used at the outflow boundary while adiabatic no-slip conditions are enforced on all walls.

4.2. *Results and discussion*

4.2.1. *Inert flow*

The basic features of inert flows behind a sudden expansion have been extensively studied both experimentally and numerically (Abbot & Kline 1962; Gagnon 1993).

For the major part of these studies, only one stream is considered, and Abbot & Kline (1962) have shown that the mean flow after a sudden expansion is asymmetrical if the ratio $A_r = (H_{\mathrm{channel}} + 2H_{\mathrm{step}})/H_{\mathrm{channel}}$ is greater than 1.5. For the present case, the area expansion ratio can be evaluated to be $A_r = 1.84$, predicting an asymmetrical mean flow. The experimental results corroborate this prediction, showing an upper mean recirculation zone much shorter than the lower one.

This important feature of the mean flow is captured by the LES, as can be seen on Fig. 3. Furthermore, Fig. 4 shows a comparison of the mean velocity profiles obtained at

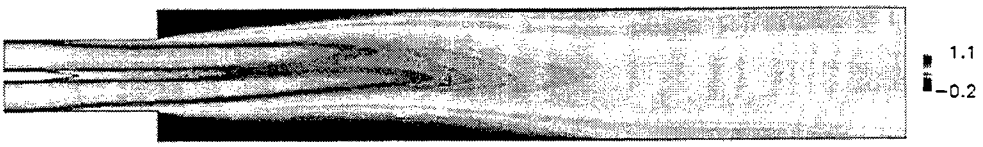

FIGURE 3. Cold flow simulation. Mean axial velocity.

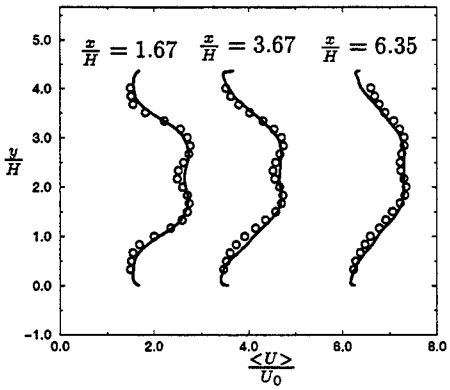

FIGURE 4. Cross-stream profiles of the mean axial velocity at different axial positions for the cold flow case. Symbols represent experimental data, lines LES results.

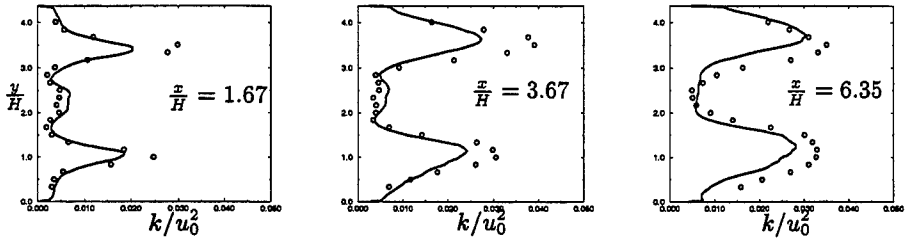

FIGURE 5. Cross-stream profiles of the mean turbulent kinetic energy at different axial positions for the cold flow case. Symbols represent experimental data, lines LES results.

different downstream locations in the inert case and confirms the very good quantitative agreement between the LES results and the experimental data.

Figure 5 shows vertical profiles of the turbulent kinetic energy for the axial positions shown in Fig. 4. The location and width of the peaks of turbulent kinetic energy downstream of each step are precisely predicted by the LES while the maximum intensity is slightly underestimated for the first stations. It can also be observed that the evolution of the local maximum around the symmetry axis created by the mixing layer between the two incoming streams is very well captured.

Since the intensity of the turbulent kinetic energy generated by the central mixing layer

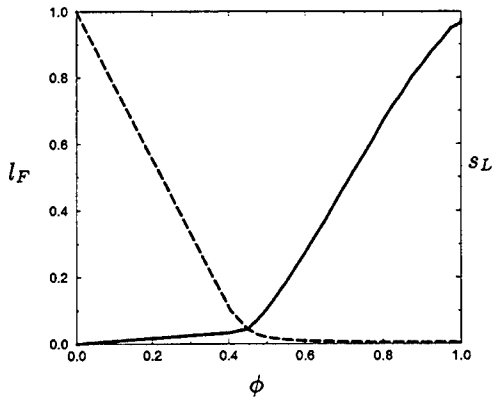

FIGURE 6. s_L (solid line) and l_F (dashed line) as functions of the equivalence ratio ϕ. Both are normalized by their maximum values.

FIGURE 7. Reacting case. Contours of mean axial velocity and of G_0.

is much lower than in the shear layers behind the steps, its influence on the stabilization of the flame can be expected to be small in the reacting case.

4.2.2. *Reacting flow*

In the cold-flow simulation, both inlet channels have the same chemical composition. For the reacting case, the upper channel has a mixture of propane and air at an equivalence ratio of $\phi_1 = 0.9$, while the equivalence ratio in the lower channel is $\phi_2 = 0.3$.

As ϕ will vary along the $\widetilde{G}_0$ surface, the laminar burning velocity s_L and the laminar flame thickness l_F appearing in Eq. (2.5) are now parameterized by ϕ. This dependence is shown in Fig. 6.

As can be seen in Fig. 6, the laminar burning velocity for $\phi = 0.3$ is much lower than for $\phi = 0.9$, while the laminar flame thickness follows the opposite trend. Consequently, the leanest branch of the flame can be expected to be close to the blow-off limit.

Indeed, the preliminary results reported below indicate that the leanest part of the flame barely propagates behind the lower step while the richest part propagates much faster, as shown in Fig. 7. Compared to the cold-flow case shown in Fig. 3, the reacting case exhibits a much shorter upper recirculation zone, due to the strong acceleration behind the richest flame branch. The lower recirculation zone is also shortened, but to a lesser extent.

Figure 8 shows the mean axial velocity profiles obtained at three different locations in the combustion chamber. The velocity increase in the upper part of the chamber due

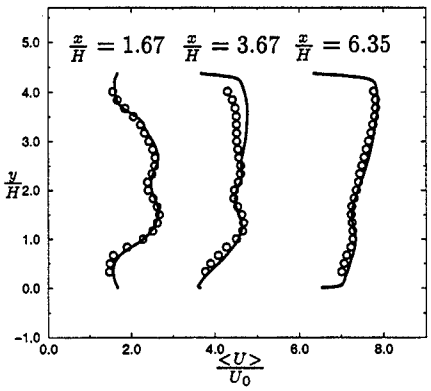

FIGURE 8. Cross-stream profiles of the mean axial velocity at different axial positions for the reacting flow case. Symbols represent experimental data, lines LES results.

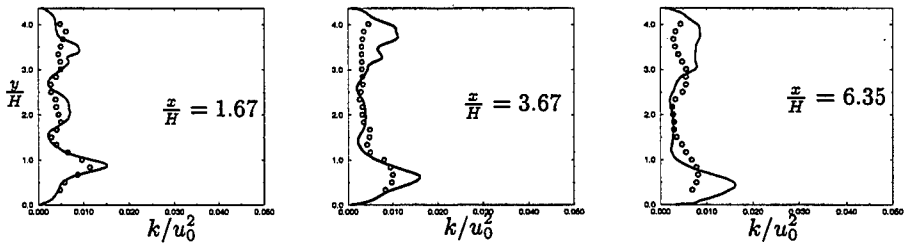

FIGURE 9. Cross-stream profiles of the mean turbulent kinetic energy at different axial positions for the reacting flow case. Symbols represent experimental data, lines LES results.

to heat release is well predicted except for a slight overestimation at $x/H = 3.67$. The corresponding profiles behind the lower step are also different from the cold-flow case. The mean velocity is increased moderately at $x/H = 3.67$, and even more at $x/H = 6.35$. Overall, the quantitative agreement with the experimental data is good.

Finally, Fig. 9 shows vertical profiles of turbulent kinetic energy for the same three axial locations. The agreement is reasonable for all three locations. However the simulation becomes less accurate for the downstream locations, which may indicate that the statistics are not fully converged. Nevertheless, the general trend of diminishing turbulent kinetic energy, especially in the richest part of the flame, is well reproduced. This is in contrast with the cold-flow case where, because of the converging shear layers, the turbulent kinetic energy increases with distance from the steps. In the reacting case, the strong heat release in the upper half of the domain prevents the upper shear layer frm spreading, while the smaller heat release in the bottom half is still sufficient to damp the turbulent fluctuations.

5. Conclusions and future plans

A mixed level-set/flamelet library formulation has been implemented as a suitable model for large-eddy simulation of turbulent premixed and partially-premixed flames.

The versatility of this approach has been demonstrated through its application to two very different cases.

The first study concerns the Aachen flame F_3, where the model has been shown to yield predictions in good agreement with the experimental data of Chen (1996). Two different simulations have been performed for this case. The first simulation uses adiabatic conditions. In the second approach, the total enthalpy is used as a parameter in the flamelet library to take heat losses near the burner exit into account. The latter refined model shows improved accuracy through a better physical description, with only a small computational overhead.

The second study presented in this report concerns the LES of a turbulent, partially-premixed lean dump combustor, the so-called ORACLES burner. Results are compared to the experimental data of Besson (1999*a*) for the non-reacting and reacting cases. The non-reacting case was found to exhibit recirculation zones which are asymmetric in the mean, typical of supercritical flows through sudden expansions. This behavior is well recovered by the LES, both qualitatively and quantitatively. The turbulent kinetic energy is also predicted with reasonable accuracy. Preliminary results for the reacting case are also presented showing very good agreement with experimental data for the time-averaged axial velocity. The turbulent kinetic energy is predicted less accurately than in the non-reacting case, although the overall agreement remains acceptable.

In the future we will focus on the derivation of a dynamic model for the turbulent burning velocity that will be tested against the present algebraic model. In addition the model will be applied to other ORACLES cases revealing combustion instabilities.

Acknowledgments

This work was supported in part by SNECMA Motors and the Department of Energy within the ASCI program.

REFERENCES

ABBOT, D. E. & KLINE, S. J. 1962 Experimental investigation of a subsonic turbulent flow over a single and double backward facing steps. *J. Basic Engg.* **84**, 317–325.

AKSELVOLL, K. 1996 An efficient method for temporal integration of the navier-stokes equations in confined axisymmetric geometrie. *J. Comp. Phys.* **125**, 454–463.

AKSELVOLL, K. & MOIN, P. 1996 Large-eddy simulation of turbulent confined co-annular jets. *J. Fluid Mech.* **31**, 387–411.

BESSON, M., BRUEL, P., CHAMPION, J. L. & DESHAIES, B. 1999*a* Inert and combusting flows developping over a plane symmetric expansion: experimental analysis of the main flow characteristics. In *AIAA* paper 99-0412.

BESSON, M., BRUEL, P. & DESHAIES, B. 1999*b* The contribution of ENSMA. Final Technical Report. *Tech. Rep.* BRITE EURAM-AERO BE95-1953.

BOERSMA, B., BRETHOUWER, G. & NIEUWSDAT, F. T. 1998 A numerical investigation on the effect of the inflow conditions on the self-similar region of a round jet. *Phys. Fluids* **10**, 899–909.

CHEN, Y. C., PETERS, N., SCHNEEMANN, G. A., WRUCK, N., RENZ, U. & MANSOUR,

M. S. 1996 The detailed flame structure of highly stretched turbulent premixed methane-air flames. *Comb. and Flame* **107**, 233–244.

COLIN, F., VEYNANTE, D. & POINSOT, T. 2000 A thickened flame model for large eddy simulation of premixed turbulent combustion. *Phys. Fluids* **12**, 1843–1863.

GAGNON, Y., GIOVANNINI, A. & HÉBRARD, P. 1993 Numerical simulation and physical analysis of high reynolds number recirculating flows behind sudden expansions. *Phys. Fluids* **5**, 2377–2389.

HERRMANN, M. 2000 Numerische Simulation vorgemischter und teilweise vorgemischter Turbulenten Flamen. PhD thesis, RWTH, Aachen.

KERSTEIN, A. R., ASHURST, W. T. & WILLIAMS, F. A. 1988 Equation for interface propagation in an unsteady homogeneous flow field. *Phys. Rev. A* **37**, 2728–2731.

KIM, W. W. & MENON, S. 2000 Numerical modeling of turbulent premixed flames in the thin-reaction zones regime. *Comb. Sci. Tech.* **26**, 1–32.

DUCHAMP DE LAGENESTE, L. & PITSCH, H. 2000 A level-set approach to large eddy simulation of premixed turbulent combustion. *Annual Research Briefs*, Center for Turbulence Research, NASA Ames/Stanford Univ. 105–116.

MOIN, P., SQUIRES, K., CABOT, W. & LEE, S. 1991 A dynamic subgrid-scale model for compressible turbulence and scalar transport. *Phys. Fluids* **A**, 2746–2757.

MUNIZ, L. & MUNGAL, G. 1997 Instantaneous flame stabilization velocities in lifted-jet diffusion flames. *Comb. and Flame* **111**, 16–31.

NILSSON, P. & BAI, X. S. 2000 Level-set flamelet library approach for premixed turbulent combustion. *Env. Therm. Fluid Sci.* **21**, 87–98.

PETERS, N. 1999 Turbulent burning velocity for large-scale and small-scale turbulence. *J. Fluid Mech.* **384**, 107–132.

PETERS, N. 2000 *Turbulent Combustion*. Cambridge University Pres.

PIERCE, C. D. & MOIN, P. 1998 Large eddy simulation of a confined jet with swirl and heat release. In *AIAA P.*, vol. 98-2892.

PIERCE, C. D. & MOIN, P. 2001 Progress-variable approach for large eddy simulation of turbulent combustion. *Tech. Rep.* TF-80. Dept. Mech. Eng., Stanford University.

PITSCH, H. & STEINER, H. 2000 Large eddy simulation of a turbulent piloted methane/air diffusion flame. *Phys. Fluids* **12**, 2541–2553.

RUSSO, G. & SMEREKA, P. 2000 A remark on computing distance functions. *J. Comp. Phys.* **163**, 51–67.

SETHIAN, J. A. 1996 *Level Set Methods : Evolving Interfaces in Geometry, Fluid Mechanics, Computer Vision and Material Science*. Cambridge University Press.

SU, L. K., HAN, D. & MUNGAL, G. 2000 Experimental results on the stabilization of lifted jet diffusion flames. *Annual Research Briefs*, Center for Turbulence Research, NASA Ames/Stanford Univ. 79–89.

SUSSMAN, M. & FATEMI, E. 1999 An efficient, interface-preserving level set re-distancing algorithm and its application to interfacial incompressible fluid flow. *SIAM Journ. Sci. Comp.* **20**, 1165–1191.

VEYNANTE, D., VERVISCH, L., POINSOT, T., LIÑAN, A. & RUETSCH, G. R. 1994 Triple flame structure and diffusion flame stabilization. *Proc. Summer Program*, Center for Turbulence Research, NASA Ames/Stanford Univ. 55–73.

WILLIAMS, F. A. 1985 Turbulent combustion. In *Math. of Comb.*, (J. Buckmaster, Ed.) 97–131.

Generalized symmetries of the G-equation without underlying flow field

By M. Oberlack †

It is shown that the admissible symmetries of the G-equation for flame fronts in premixed combustion depend essentially on whether the velocity of the underlying flow is zero or non-zero. The case of non-zero flow velocity has been exhaustively discussed by Oberlack, Wenzel & Peters (2001). If the flow velocity is zero a sixteen-dimensional Lie algebra of classical point symmetries exist. More importantly, an infinite series of generalized (Lie-Bäcklund) symmetries is derived, which includes as a special case the sixteen classical point symmetries.

1. Introduction

In recent years the G-equation, first derived by Williams (1985), has become the predominant approach for modeling premixed combustion in a very broad range of practical applications, such as spark-ignition engines and many others. A large amount of applied work has been dedicated to the G-equation. In order to make the G-equation amenable to numerical computations a diversity of numerical schemes have been derived, e.g. Adalsteinsson & Sethian (1999), Osher & Sethian (1988), Smiljanowski, Moser & Klein (1997), Sussman, Smereka & Osher (1994). Also, to make the G-approach applicable to turbulent premixed combustion a variety of model equations has been proposed, e.g. Im, Lund & Ferziger (1997), Peters (1992), Peters (1993), Ulitsky & Collins (1997), Weller, Tabor, Gosman & Fureby (1998) to name only a few.

In contrast, considerably less work has been dedicated to the mathematical properties of the G-equation. In particular, only recently have the important symmetry properties of the G-equation been explored, by Oberlack *et al.* (2001). Therein classical point symmetries of the G-equation in combination with the equations of fluid dynamics have been computed. It was shown that one particular symmetry, named "generalized scaling symmetry" by Oberlack *et al.* (2001), has important implications for the understanding and modelling of the G-equation in turbulent flows. New physically-sound modelling routes have been suggested. However, no generalized symmetries were investigated therein, since their derivation for the combined set of partial differential equations would have been formidable.

In the present approach we analyze a simplified version of the G-equation, where the flow velocity has been set to zero and the laminar burning velocity s_l is considered a constant. Physically speaking, this case describes the propagation of an infinitesimally-thin laminar flame sheet without flame-front advection due to an underlying flow field.

The G-equation with zero flow velocity is somewhat related to the eikonal equation. In Fushchich, Shtelen & Serov (1993) and Fushchich & Shtelen (1982) it is shown that the eikonal and related equations admit a wide class of symmetry transformations. Sub-

† Hydromechanics and Hydraulics Group, Darmstadt University of Technology, Petersenstraße 13, 64287 Darmstadt, Germany

sequently we prove that the set of classical point symmetries and generalized symmetries of the G-equation extend considerably if $\boldsymbol{u} = 0$ is imposed.

2. Symmetry groups of the G-equation

In Oberlack *et al.* (2001) the original form of the G-equation

$$\frac{\partial G}{\partial t} + u_k \frac{\partial G}{\partial x_k} = s_l \sqrt{\frac{\partial G}{\partial x_k}\frac{\partial G}{\partial x_k}}, \tag{2.1}$$

augmented by the equation of fluid dynamics, has been analyzed and discussed with respect to its classical point symmetries and the resulting physical consequences. Here $\boldsymbol{x}$ and t are space and time variables respectively, $\boldsymbol{u}$ is the velocity vector, s_l is the laminar burning velocity, and G denotes a scalar field quantity determining a instantaneous flame front at $G = G_0$. The G field has a physical meaning only at G_0.

During the derivation of the work in Oberlack *et al.* (2001) it became clear that it would be extremely difficult to extend this work to generalized symmetries as in Bluman & Kumei (1989). This task is usually considerably easier for scalar equations. For this reason the present work is limited to Eq. (2.1) where the flow velocity is set to zero

$$\frac{\partial G}{\partial t} = s_l \sqrt{\frac{\partial G}{\partial x_k}\frac{\partial G}{\partial x_k}}. \tag{2.2}$$

The latter equation has in fact close links to other equations known in mathematical physics. The first one is the eikonal equation which is the square of Eq. (2.2). In some models the squared version also contains an added constant. Though very similar in form, Eq. (2.2) and its squared version admit different reflection symmetries. Equation (2.2) admits only the reflection symmetries

$$t^* = t,\ \ x_i^* = -x_i,\ \ x_j^* = x_j,\ \ G^* = G,\ \ i = 1,2,3,\ \ j = 1,2,3/i \tag{2.3}$$

and

$$t^* = -t,\ \ x_i^* = x_i,\ \ G^* = -G,\ \ i = 1,2,3. \tag{2.4}$$

The squared version of Eq. (2.2) admits the latter time reversal where G is still unaffected. In addition it allows $G^* = -G$ with t as the identity transformation.

Equation (2.2) is also related to the usual linear wave equation $\frac{\partial^2 u}{\partial t^2} - \frac{\partial^2 u}{\partial x_k^2} = 0$. In contrast to the one-dimensional version, in two or higher spatial dimensions one cannot give a complete analytic solution of the wave equation. However, the square of Eq. (2.2) with $s_l = 1$ may be considered as the characteristic equation of the wave equation.

In the subsections below, all classical point symmetries and the first elements of the infinite series of generalized symmetries of Eq. (2.2) are derived. It is shown how to construct arbitrarily many additional generalized symmetries.

2.1. *Classical point symmetries*

The purpose of the present analysis is to find all those continuous groups of transformation (Lie groups) which do not change the structure of the equation under investigation if written in the new variables. In the case of Eq. (2.2) the problem simplifies to obtaining the generator

$$\mathrm{X} = \xi^t(t,\boldsymbol{x},G)\frac{\partial}{\partial t} + \xi^i(t,\boldsymbol{x},G)\frac{\partial}{\partial x_i} + \eta^G(t,\boldsymbol{x},G)\frac{\partial}{\partial G}. \tag{2.5}$$

Here X is the infinitesimal form of the desired transformation, and ξ^t, ξ^i and η^G are the corresponding infinitesimals. The exponents of the infinitesimals denote the variables they refer to, and should not be mistaken for powers.

In Oberlack *et al.* (2001) it is shown that in the case of a non-zero flow velocity field, Eq. (2.1) extended by the equation of fluid dynamics admit the usual extended Galilean group. In all of these groups G is trivially contained as an identity transformation. The only symmetry group with non-zero flow velocity which non-trivially contains the transformation of G is the group

$$\mathrm{X} = \psi(G)\frac{\partial}{\partial G}, \tag{2.6}$$

where $\psi(G)$ is largely arbitrary.

Employing Lie's first theorem (see e.g. Bluman & Kumei 1989) the symmetry Eq. (2.6) may be written as the usual transformation in global form

$$G^* = \mathcal{F}(G) \quad \text{with} \quad \frac{\mathrm{d}\mathcal{F}(G)}{\mathrm{d}G} > 0, \tag{2.7}$$

where $\mathcal{F}(G)$ is connected to $\psi(G)$ by

$$\mathcal{F}(G) = \Psi^{-1}[\epsilon + \Psi(G)] \quad \text{and} \quad \Psi(G) = \int \frac{\mathrm{d}G}{\psi(G)}. \tag{2.8}$$

Here Ψ^{-1} is the inverse of Ψ. Since Ψ has to be invertible this poses a weak constraint on ψ by means of the latter integral relation Eq. (2.8).

Application of Eq. (2.5) to Eq. (2.2) leads to a considerably-extended set of groups comprising sixteen distinct Lie groups, each of which is infinite-dimensional because each contains an arbitrary function ω_i

$$\mathrm{X}_1 = \omega_1(G)\frac{\partial}{\partial G}, \tag{2.9}$$

$$\mathrm{X}_2 = \omega_2(G)\frac{\partial}{\partial t}, \tag{2.10}$$

$$\mathrm{X}_3 = \omega_3(G)\left(t\frac{\partial}{\partial t} + x_i\frac{\partial}{\partial x_i}\right), \tag{2.11}$$

$$\mathrm{X}_{3+[j]} = \omega_{3+[j]}(G)\left(x_j\frac{\partial}{\partial x_i} - x_i\frac{\partial}{\partial x_j}\right), \quad i,j = 1,2,3 \text{ and } i<j, \tag{2.12}$$

$$\mathrm{X}_{6+[i]} = \omega_{6+[i]}(G)\frac{\partial}{\partial x_i}, \quad i = 1,2,3 \tag{2.13}$$

$$\mathrm{X}_{9+[i]} = \omega_{9+[i]}(G)\left(s_l^2 t\frac{\partial}{\partial x_i} + x_i\frac{\partial}{\partial t}\right), \quad i = 1,2,3 \tag{2.14}$$

$$\mathrm{X}_{13} = \omega_{13}(G)\left((s_l^2t^2 + x_kx_k)\frac{\partial}{\partial t} + 2s_l^2\,t\,x_i\frac{\partial}{\partial x_i}\right), \tag{2.15}$$

$$\begin{aligned}\mathrm{X}_{13+[i]} = \omega_{13+[i]}(G)\Bigg[&(s_l^2t^2 - x_kx_k + 2(x_{[i]})^2)\frac{\partial}{\partial x_{[i]}} \\ &+2x_{[i]}\left(t\frac{\partial}{\partial t} + x_k\frac{\partial}{\partial x_k} - x_{[i]}\frac{\partial}{\partial x_{[i]}}\right)\Bigg], \quad i = 1,2,3\end{aligned} \tag{2.16}$$

where the subscript $[i]$ means no summation. The enumeration in the index of several ω_i's corresponds to functions belonging to different groups. Since the task of computing Eqs.

(2.9)–(2.16) is relatively straightforward, and can in fact for the most part be aided by computer algebra systems – see Ibragimov (1996) – we omit any details of its derivation.

All ω_i are arbitrary functions of G obeying the same invertibility properties as given below Eq. (2.8). The first nine symmetries, Eqs. (2.9)–(2.13) have close relations to those admitted by Eq. (2.1) extended by the equations of fluid dynamics. In contrast, the symmetries Eqs. (2.14)–(2.16) have no counterpart in the usual G-equation (2.1) with $u \neq 0$. It is interesting to note that all of the "new" symmetries contain the laminar flame speed s_l explicitly.

All of the symmetries Eqs. (2.9)–(2.16) may be written as global transformations. Employing Lie's first theorem, which states a unique relation between the infinitesimal transformation and the global transformation, we find the global transformation groups of Eqs. (2.9)–(2.16)

$$T_1 : t^* = t, , x_i^* = x_i,$$
$$G^* = \Psi^{-1}[\epsilon + \Psi(G)] \quad \text{with} \quad \Psi(G) = \int \frac{\mathrm{d}G}{\omega_1(G)}, \tag{2.17}$$
$$T_2 : t^* = \varepsilon\omega_2(G) + t,\ x_i^* = x_i,\ G^* = G, \tag{2.18}$$
$$T_3 : t^* = \mathrm{e}^{(\varepsilon\omega_3(G))}t,\ x_i^* = \mathrm{e}^{(\varepsilon\omega_3(G))}x_i,\ G^* = G, \tag{2.19}$$
$$T_{3+[i]} : t^* = t,\ x_i^* = a_{ik}(G)x_k,\ G^* = G, \text{ with}$$
$$\mathbf{a}\cdot\mathbf{a}^T = \mathbf{a}^T\cdot\mathbf{a} = \mathbf{I},\ |\mathbf{a}| = 1, \tag{2.20}$$
$$T_{6+[i]} : t^* = t,\ x_i^* = \varepsilon\omega_{6+[i]}(G) + x_i,\ G^* = G, \tag{2.21}$$
$$T_{9+[i]} : t^* = \cosh(s_l\,\omega_p(G)\,\varepsilon)\,t\,s_l + \sinh(s_l\,\omega_p(G)\,\varepsilon)\,x_{[i]},$$
$$x_i^* = \sinh(s_l\,\omega_p(G)\,\varepsilon)\,t\,s_l + \cosh(s_l\,\omega_p(G)\,\varepsilon)\,x_{[i]},$$
$$x_j^* = x_j,\ \ i = 1,2,3\,,\ \ j = 1,2,3/i \text{ and } p = 9+i,$$
$$G^* = G, \tag{2.22}$$
$$T_{13} : t^* = \frac{(s_l^2t^2 - x_kx_k)\left[\varepsilon\omega_{13}(G)(s_l^2t^2 - x_kx_k) - t\right]}{x_kx_k - s_l^2\left[\varepsilon\omega_{13}(G)(s_l^2t^2 - x_kx_k) - t\right]^2},$$
$$x_i^* = \frac{x_i(s_l^2t^2 - x_kx_k)}{s_l^2\left[\varepsilon\omega_{13}(G)(s_l^2t^2 - x_kx_k) - t\right]^2 - x_kx_k},$$
$$G^* = G, \tag{2.23}$$
$$T_{13+[i]} : t^* = \frac{t(s_l^2t^2 - x_kx_k)}{-\left[\varepsilon\omega_p(G)(s_l^2t^2 - x_kx_k) + x_{[i]}\right]^2 + s_l^2t^2 - x_kx_k + x_{[i]}^2},$$
$$x_i^* = \frac{(s_l^2t^2 - x_kx_k)\left[\varepsilon\omega_p(G)(s_l^2t^2 - x_kx_k) + x_{[i]}\right]}{s_l^2t^2 - x_kx_k + x_{[i]}^2 - \left[\varepsilon\omega_p(G)(s_l^2t^2 - x_kx_k) + x_{[i]}\right]^2},$$
$$x_j^* = \frac{x_{[j]}(s_l^2t^2 - x_kx_k)}{-\left[\varepsilon\omega_p(G)(s_l^2t^2 - x_kx_k) + x_{[i]}\right]^2 + s_l^2t^2 - x_kx_k + x_{[i]}^2},$$
$$G^* = G,$$
$$i = 1,2,3\,,\ \ j = 1,2,3/i \text{ and } p = 13+i, \tag{2.24}$$

Unless stated otherwise, the indices i, j and k denote $1, 2, 3$. The notation for the indices i and j in Eq. (2.22) and Eq. (2.24) denote that i can be any of 1, 2 and 3, and j refers to the remaining two.

2.2. *Generalized symmetries*

In mathematical physics it is known that many fundamental equations, such as the Burgers equation or the Korteweg-de Vries equation, admit a much wider class of symmetries which go beyond the classical point symmetries called generalized symmetries (see e.g. Bluman & Kumei 1989). Some authors call them Lie-Bäcklund or Noether symmetries. Generalized symmetries are defined such that the infinitesimals ξ^t, ξ^i and η^G in Eq. (2.5) not only depend on all dependent and independent variables, but may also comprise derivatives of G up to a given order n.

The actual derivation of the generalized symmetries is almost identical to that of the classical point symmetries. However the necessary algebra becomes increasingly more tedious for large orders of derivatives in the infinitesimals. For mathematical convenience, we here adopt Boyer's formulation of the generalized symmetries. He proved that all infinitesimals of the independent variables, here ξ^t and ξ^i, may be set to zero if at least all first-order derivatives of G are included in η: see Bluman & Kumei (1989). Hence without loss of generality we search for the generalized symmetry

$$\tilde{\mathrm{X}} = \tilde{\eta}(t, x, G, \underset{1}{G}, \underset{2}{G}, \ldots)\frac{\partial}{\partial G} \tag{2.25}$$

where $\underset{n}{G}$ denotes the set of all n^{th} order spatial derivatives of G. In the present context we may exclude any time derivative of G from $\underset{n}{G}$ since it can immediately be replaced by the right-hand side of Eq. (2.2). In the following, we indicate any derivative with respect to G by index notation. The time-derivative of G is defined as $\frac{\partial G}{\partial t} \equiv G_t$ while the spatial derivatives are abbreviated by $\frac{\partial G}{\partial x_i} \equiv G_{,i}$, $\frac{\partial^2 G}{\partial x_i \partial x_j} \equiv G_{,ij}$, etc.. Any derivative with respect to $\tilde{\eta}$ is given in the usual ∂-notation.

Boyer's theorem also states that once a point symmetry such as any of Eqs. (2.9)–(2.16) is known it may readily be written in the form of Eq. (2.25) where $\tilde{\eta}$ is given – see e.g. Bluman & Kumei (1989) – by

$$\tilde{\eta} = \eta^G - G_t\,\xi^t - G_{,i}\,\xi^i = \eta^G - s_l\sqrt{G_{,m}G_{,m}}\,\xi^t - G_{,i}\,\xi^i. \tag{2.26}$$

In the latter equality, G_t has been replaced using Eq. (2.2). For example X_{10-12} in Eq. (2.14) may be written as

$$\tilde{\mathrm{X}}_{10-12} = \omega_{9+[i]}(G)\left(-s_l\sqrt{G_{,m}G_{,m}}\,x_i - G_{,i}s_l^2 t\right)\frac{\partial}{\partial G}, \quad i = 1, 2, 3. \tag{2.27}$$

From Eq. (2.26) it is apparent that any point symmetry is linear in G_t and $G_{,i}$. However, the converse may not always be true.

Keeping $\tilde{\eta}$ completely general and applying Eq. (2.25) and any necessary prolongation of $\tilde{\mathrm{X}}$ – see e.g. Bluman & Kumei (1989) – to Eq. (2.2) we obtain

$$\left[\left(\tilde{\eta}\frac{\partial}{\partial G} + \frac{\mathcal{D}\tilde{\eta}}{\mathcal{D}t}\frac{\partial}{\partial G_t} + \frac{\mathcal{D}\tilde{\eta}}{\mathcal{D}x_m}\frac{\partial}{\partial G_{,m}}\right)\left(G_t - s_l\sqrt{G_{,n}G_{,n}}\right)\right]\Big|_{\text{eqn (2.2)}} = 0, \tag{2.28}$$

where $\mathcal{D}/\mathcal{D}t$ and $\mathcal{D}/\mathcal{D}x_m$ are defined as

$$\frac{\mathcal{D}}{\mathcal{D}t} = \frac{\partial}{\partial t} + G_t\frac{\partial}{\partial G} + G_{t,i}\frac{\partial}{\partial G_{,i}} + G_{t,ij}\frac{\partial}{\partial G_{,ij}} + \ldots \tag{2.29}$$

and

$$\frac{\mathcal{D}}{\mathcal{D}x_m} = \frac{\partial}{\partial x_m} + G_{,m}\frac{\partial}{\partial G} + G_{,mi}\frac{\partial}{\partial G_{,i}} + G_{,mij}\frac{\partial}{\partial G_{,ij}} \dots \tag{2.30}$$

Expanding Eq. (2.28) we obtain

$$\begin{aligned}&\left[\frac{\partial\tilde{\eta}}{\partial t} + G_t\frac{\partial\tilde{\eta}}{\partial G} + G_{t,i}\frac{\partial\tilde{\eta}}{\partial G_{,i}} + G_{t,ij}\frac{\partial\tilde{\eta}}{\partial G_{,ij}} + \dots\right.\\ &\left. - s_l\frac{G_{,m}}{\sqrt{G_{,n}G_{,n}}}\left(\frac{\partial\tilde{\eta}}{\partial x_m} + G_{,m}\frac{\partial\tilde{\eta}}{\partial G} + G_{,mi}\frac{\partial\tilde{\eta}}{\partial G_{,i}} + G_{,mij}\frac{\partial\tilde{\eta}}{\partial G_{,ij}}\dots\right)\right]\Bigg|_{\text{eqn (2.2)}} = 0.\end{aligned} \tag{2.31}$$

As denoted by $|_{\text{eqn (2.2)}}$, when solving Eq. (2.31) the reduced G-equation, Eq. (2.2), may be introduced to replace any term of the form $G_{t,ij\dots}$ by the differential consequences of G_t. This finally leads to a single determining equation for $\tilde{\eta}$ of the form

$$\begin{aligned}&\frac{\partial\tilde{\eta}}{\partial t} - s_l\frac{G_{,m}}{\sqrt{G_{,n}G_{,n}}}\frac{\partial\tilde{\eta}}{\partial x_m} + s_l\left[\frac{G_{,im}G_{,jm}}{\sqrt{G_{,n}G_{,n}}} - \frac{G_{,im}G_{,m}G_{,jn}G_{,n}}{(G_{,k}G_{,k})^{3/2}}\right]\frac{\partial\tilde{\eta}}{\partial G_{,ij}}\\ &+\dots + s_l\Delta_{i_1i_2\dots i_n}(\underset{1}{G},\underset{2}{G},\dots\underset{n}{G})\frac{\partial\tilde{\eta}}{\partial G_{,i_1i_2\dots i_n}} = 0,\end{aligned} \tag{2.32}$$

where $\Delta_{i_1i_2\dots i_n}$ comprises all the terms emerging from the differential consequences of Eq. (2.2). Several things are important to note about Eq. (2.32). No derivative with respect to G and $G_{,i}$ appears, so any solution for $\tilde{\eta}$ can depend arbitrarily on G and $G_{,i}$.

Most importantly, Eq. (2.32) is closed. We may readily verify this by choosing $\tilde{\eta}$ to depend only on derivatives of G up to the order n indicated by $\underset{n}{G}$. Computing all differential consequences of Eq. (2.2), i.e. determining all $\Delta_{i_1i_2\dots i_n}$ up to order n, we find that they contain derivatives of G only up to $\underset{n}{G}$. Hence, Eq. (2.32) constitutes a linear hyperbolic equation in $\tilde{\eta}$ depending on the set of variables: t, $\boldsymbol{x}$, G, $G_{,i}$, $G_{,ij}$, $\dots$, $G_{,i_1i_2\dots i_n}$, where G and $G_{,i}$ appear only as parameters.

Solutions for $\tilde{\eta}$ with increasing derivative order $\underset{n}{G}$ may be successively obtained, beginning with the lowest derivative order. First, we consider $\tilde{\eta}$ solely depending on G-derivatives up to order one. Hence, we limit $\tilde{\eta}$ to be a function only of t, $\boldsymbol{x}$, G and $\underset{1}{G}$. As a consequence equation Eq. (2.32) reduces to

$$\frac{\partial\tilde{\eta}}{\partial t} - s_l\frac{G_{,m}}{\sqrt{G_{,n}G_{,n}}}\frac{\partial\tilde{\eta}}{\partial x_m} = 0. \tag{2.33}$$

The characteristic equations of Eq. (2.33) are

$$\frac{\mathrm{d}t}{\mathrm{d}\epsilon} = 1 \quad \text{and} \quad \frac{\mathrm{d}x_m}{\mathrm{d}\epsilon} = -s_l\frac{G_{,m}}{\sqrt{G_{,n}G_{,n}}}. \tag{2.34}$$

Equation (2.34) may readily be integrated to yield the complete solution of Eq. (2.33),

$$\tilde{\eta} = \mathcal{G}\left(\boldsymbol{C}, G, \underset{1}{G}\right) \quad \text{where} \quad C_i = x_i + s_l\frac{G_{,i}}{\sqrt{G_{,n}G_{,n}}}t. \tag{2.35}$$

$\mathcal{G}$ is an arbitrary function of its arguments and should be once-differentiable with respect to $\boldsymbol{C}$. Note that in determining $\boldsymbol{C}$, $G_{,i}$ appeared only as a parameter.

It is important to note that $\boldsymbol{C}$ may be considered the fundamental characteristic. It

nicely exemplifies the solution structure of Eq. (2.2) which may be interpreted, and also constructed, geometrically. Given an initial condition for the G field we may propagate it in time with the speed s_l along rays normal to each instantaneous G field, as described by the family of curves C.

The generalized symmetry Eq. (2.35) appears to be considerably simpler in form than the classical point symmetries in Subsection 2.1. However we can show that all point symmetries, Eqs. (2.9)–(2.16), are included in the solution Eq. (2.35) by virtue of Boyer's relation Eq. (2.26). E.g. the symmetries Eq. (2.14), which are rewritten in Eq. (2.27) using Boyer's formulation, can be derived from Eq. (2.35) by restricting $\tilde{\eta}$ to $\mathcal{G} = -\omega_{9+[i]} s_l \sqrt{G_{,n} G_{,n}} C_i$, $i = 1, 2, 3$. However, any solution to Eq. (2.33) which is not among Eqs. (2.9)–(2.16) using Eq. (2.26) cannot be written as a point symmetry.

Enlarging the dependence of $\tilde{\eta}$ in the next step in Eq. (2.32) by the set of variables $\underset{2}{G}$, Eq. (2.33) extends to

$$\frac{\partial \tilde{\eta}}{\partial t} - s_l \frac{G_{,m}}{\sqrt{G_{,n} G_{,n}}} \frac{\partial \tilde{\eta}}{\partial x_m} + s_l \left[\frac{G_{,im} G_{,jm}}{\sqrt{G_{,n} G_{,n}}} - \frac{G_{,im} G_{,m} G_{,jn} G_{,n}}{(G_{,k} G_{,k})^{3/2}} \right] \frac{\partial \tilde{\eta}}{\partial G_{,ij}} = 0. \tag{2.36}$$

The corresponding set of characteristic equations, Eq. (2.34) is expanded by

$$\frac{\mathrm{d}G_{,ij}}{\mathrm{d}\epsilon} = s_l \left[\frac{G_{,im} G_{,jm}}{\sqrt{G_{,n} G_{,n}}} - \frac{G_{,im} G_{,m} G_{,jn} G_{,n}}{(G_{,k} G_{,k})^{3/2}} \right]. \tag{2.37}$$

In order to solve Eq. (2.34) and Eq. (2.37) we combine the characteristic ODE's for t and $G_{,ij}$ to obtain

$$\frac{\mathrm{d}G_{,ij}}{\mathrm{d}t} = s_l \left[\frac{G_{,im} G_{,jm}}{\sqrt{G_{,n} G_{,n}}} - \frac{G_{,im} G_{,m} G_{,jn} G_{,n}}{(G_{,k} G_{,k})^{3/2}} \right] \tag{2.38}$$

Since $G_{,ij}$ is a symmetric second-order tensor, Eq. (2.38) constitutes a quadratic tensor equation in which $G_{,k}$ is a vector-valued parameter. For the purpose of solving Eq. (2.38) we derive the identity

$$\frac{\mathrm{d}G^{-1}_{,kl}}{\mathrm{d}t} = \frac{\mathrm{d}G^{-1}_{,ki} G_{,ij} G^{-1}_{,jl}}{\mathrm{d}t} = 2 \frac{\mathrm{d}G^{-1}_{,kl}}{\mathrm{d}t} + G^{-1}_{,ki} \frac{\mathrm{d}G_{,ij}}{\mathrm{d}t} G^{-1}_{,jl} \tag{2.39}$$

which may be rewritten as

$$G^{-1}_{,ki} \frac{\mathrm{d}G_{,ij}}{\mathrm{d}t} G^{-1}_{,jl} = -\frac{\mathrm{d}G^{-1}_{,kl}}{\mathrm{d}t}. \tag{2.40}$$

$G^{-1}_{,ij}$ is the matrix inverse of $G_{,ij}$ and $G_{,ik} G^{-1}_{,kj} = G^{-1}_{,ik} G_{,kj} = \delta_{ij}$. Multiplying Eq. (2.38) with $G^{-1}_{,ki}$ and $G^{-1}_{,jl}$ we find, using Eq. (2.40), that

$$-\frac{\mathrm{d}G^{-1}_{,kl}}{\mathrm{d}t} = s_l \left[\frac{\delta_{kl}}{\sqrt{G_{,n} G_{,n}}} - \frac{G_{,k} G_{,l}}{(G_{,n} G_{,n})^{3/2}} \right]. \tag{2.41}$$

Equation (2.41) may immediately be integrated with respect to t since the right-hand side does not depend on $G_{,kl}$. We introduce an additional identity from the Caley-Hamilton theorem (see Appendix A)

$$G^{-1}_{,ij} = \frac{3}{2G^3_{,kk} - 3G^2_{,kk} G_{,kk} + (G_{,kk})^3} \left[((G_{,kk})^2 - G^2_{,kk}) \delta_{ij} - 2 G_{,kk} G_{,ij} + 2 G^2_{,ij} \right] \tag{2.42}$$

where $G^n_{,ij} = \underbrace{G_{,ik_1}G_{,k_1k_2}\cdot\cdots\cdot G_{,k_{n-1}k_n}G_{,k_nj}}_{n}$. As the final solution of Eq. (2.38), we obtain the characteristic tensor

$$D_{ij} = s_l\left[\frac{\delta_{ij}}{\sqrt{G_{,m}G_{,m}}} - \frac{G_{,i}G_{,j}}{(G_{,m}G_{,m})^{3/2}}\right]t + \frac{3}{2\lambda_3 - 3\lambda_2\lambda_1 + \lambda_1^3}\left[(\lambda_1^2 - \lambda_2)\delta_{ij} - 2\lambda_1 G_{,ij} + 2G_{,ik}G_{,kj}\right]. \tag{2.43}$$

In the latter characteristic the abbreviations λ_i are defined according to $\lambda_1 = G_{,kk}$, $\lambda_2 = G_{,kl}G_{,lk}$ and $\lambda_3 = G_{,kl}G_{,lm}G_{,mk}$. Hence the complete solution to Eq. (2.32) is derived, where the derivative order $\underset{n}{G}$ has been limited to $n = 2$, as

$$\tilde{\eta} = \mathcal{H}(C, G, \underset{1}{G}, \mathbf{D}). \tag{2.44}$$

C and $\mathbf{D}$ are respectively defined by Eq. (2.35) and Eq. (2.43) and $\mathcal{H}$ is an arbitrary function of its arguments, being at least once-differentiable with respect to C and $\mathbf{D}$.

In principle the next step to obtain further generalized symmetries would be to include $\underset{3}{G}$ in $\tilde{\eta}$ in Eq. (2.32). The mathematical complexity of the characteristic equations rapidly increases when higher-order derivatives of G are introduced into $\tilde{\eta}$. However it is important to note that this can be done in principle, and leads to an infinite sequence of generalized symmetries of Eq. (2.2).

3. Summary

It is demonstrated that the G-equation for premixed combustion admits a very broad variety of symmetry properties, including those from classical mechanics. It is particularly interesting that the number of symmetries depends strongly on whether the underlying flow velocity is zero or non-zero. For zero flow, sixteen distinct symmetries have been established. For this case also, an infinite series of generalized symmetries has been established.

In Oberlack *et al.* (2001) it was shown that the symmetries of the G-equation with non-zero velocity are very useful in aiding the modeling process of the G-equation for turbulent premixed combustion. It is expected that the present findings may also be used to help improve turbulent combustion models.

The author appreciates a hint from Stavros Kassinos, who pointed out the tensor identity Eq. (2.39).

REFERENCES

ADALSTEINSSON, D. & SETHIAN, J. A. 1999 The fast construction of extension velocities in level set methods. *J. Comp. Phys.* **148**, 2-22.

BLUMAN, G. W. & KUMEI, S. 1989 *Symmetries and Differential Equations* Applied Mathematical Sciences **81**, Springer-Verlag.

FUSHCHICH, W. I., SHTELEN, W. M. & SEROV, N. I. 1993 *Symmetry Analysis and Exact Solutions of Equations of Nonlinear Mathematical Physics.* Mathematics and Its Applications, Kluwer.

FUSHCHICH, W. I. & SHTELEN, W. M. 1982 The symmetry and some exact solutions of the relativistic eikonal equation. *Lett. Nuovo Cim.* **34**, 498-502.

IBRAGIMOV, N. H. 1996 (ed.) *CRC Handbook of Lie Group Analysis of Differential Equations.* **3**: New Trends in Theoretical Developments and Computational Methods, CRC Press.

IM, H. G., LUND, T. S. & FERZIGER, J. H. 1997 Large eddy simulation of turbulent front propagation with dynamic subgrid models. *Phys. Fluids* **9**, 3826-3833.

OBERLACK, M., WENZEL, H. & PETERS, N. 2001 On symmetries and averaging of the G-equation for premixed combustion. *Combust. Theory Modelling* **5**, 363-383.

OSHER, S. & SETHIAN, J. A. 1988 Fronts propagation with curvature dependent speed: algorithm based on Hamilton-Jacobi formulations. *J. Comp. Phys.* **79**, 12-49.

PETERS, N. 1992 A spectral closure for premixed turbulent combustion in the flamelet regime. *J. Fluid Mech.* **242**, 611-629.

PETERS, N. 1999 The turbulent burning velocity for large-scale and small-scale turbulence. *J. Fluid Mech.* **384**, 107-132 .

SMILJANOWSKI, W., MOSER, V. & KLEIN, R. 1997 A capturing-tracking hybrid scheme for deflagration discontinuities. *Combust. Theory Modelling* **2**, 183-325.

SPENCER, A. J. M. 1971 Theory of Invariants. In: *Continuum Physics*, (A. C. Eringen, ed.), Vol 1, Mathematics. Academic Press, Kapitel III, 239-353.

SUSSMAN, M., SMEREKA, P. & OSHER, S. 1994 A level set approach for computing solutions to incompressible two-phase flow. *J. Comp. Phys.* **114**, 146-159.

ULITSKY, M. & COLLINS, L. R. 1997 Application of the eddy damped quasi-normal Markovian spectral transport theory in premixed turbulent flame propagation. *Phys. Fluids* **9**, 3410-3430.

WELLER, H. G., TABOR, G., GOSMAN, A. D. & FUREBY, C. 1998 Application of a flame-wrinkling LES combustion model to a turbulent mixing layer *Twenty-Seventh Symposium (Intl.) on Combustion*, The Combustion Institute, 899-907.

WILLIAMS, F. A. 1985 The Mathematics of Combustion (J. D. Buckmaster, Ed.) *SIAM*, Philadelphia, 97-131.

Appendix A. Derivation of $\mathbf{A}^{-1}$ in terms of matrix-polynomials of $\mathbf{A}$ in $\mathbb{R}^3$

In Eq. (2.41) we need to express the inverse of the symmetric tensor $G_{,ij}$, denoted in the following by $\mathbf{A}$, in terms of polynomials of $G_{,ij}$ itself. From tensor-invariant theory it is known that $\mathbf{A}^{-1}$ may be expressed in terms of $\mathbf{A}$ in the form

$$A_{ij}^{-1} = a_1\delta_{ij} + a_2 A_{ij} + a_3 A_{ij}^2, \tag{A 1}$$

where the a_i may depend on the three scalar tensor invariants of $\mathbf{A}$ denoted as

$$\lambda_1 = A_{kk}, \;\; \lambda_2 = A_{kk}^2 \;\text{ and }\; \lambda_3 = A_{kk}^3. \tag{A 2}$$

Multiplying Eq. (A 1) with $\mathbf{A}$ and expressing $\mathbf{A}^3$ in terms of lower order polynomials and scalar invariants Eq. (A 2) using the Caley-Hamilton theorem – e.g. Spencer (1971) – we obtain

$$\delta_{ij} = a_1 A_{ij} + a_2 A_{ij}^2 + a_3\left[\lambda_1 A_{ij}^2 - \frac{1}{2}A_{ij}\left(\lambda_1^2 - \lambda_2\right) + \frac{1}{3}\delta_{ij}\left(\lambda_3 - \frac{3}{2}\lambda_2\lambda_1 + \frac{1}{2}\lambda_1^3\right)\right]. \tag{A 3}$$

Ordering the scalar coefficients of δ_{ij}, A_{ij} and A_{ij}^2 we obtain a linear set of equations for the a_i, $i = 1, 2, 3$. The result for the a_i may be inserted into Eq. (A 1) to yield the final solution

$$A_{ij}^{-1} = \frac{3}{2\lambda_3 - 3\lambda_2\lambda_1 + \lambda_1^3}\left[(\lambda_1^2 - \lambda_2)\delta_{ij} - 2\lambda_1 A_{ij} + 2A_{ij}^2\right]. \tag{A 4}$$

Large-eddy simulations of combustion instability suppression by static turbulence control

By J. U. Schlüter

1. Motivation

1.1. *Combustion instabilities and coherent structures*

Current combustion research is focused on pollutant reduction and fuel efficiency. One strategy to achieve these goals is to use lean premixed flames instead of diffusion flames. However, one major drawback of lean premixed flames is their susceptibility to combustion instabilities (Putnam 1971; McManus *et al.* 1993). The control of combustion instabilities is crucial in order to progress towards highly-efficient, low-pollutant combustors.

There are several mechanisms suspected of leading to combustion instabilities, such as periodic inhomogeneities in the mixture fraction, pressure sensitivity of the flame speed and the formation of large-scale turbulent structures (Mugridge 1980; Büchner *et al.* 1993; Peters & Ludford 1983). While an attempt to suppress combustion instabilities in practical applications has to address all these sources, the current work focuses on coherent structures as the driving mechanism in creating noise.

In vortex-driven combustion instabilities (Poinsot *et al.* 1987) the roll-up of a coherent structure near the burner nozzle bundles an amount of unburned fresh gases inside and increases the flame surface dramatically (Fig. 1). As a result, the fresh gases burn rapidly at a very distinct moment. The sudden heat release creates an acoustic wave, which – given the proper time-lag – delivers an acoustic perturbation. The acoustic perturbation triggers the roll-up of the next coherent structure in the shear layer (Crow & Champagne 1971; Ho & Huang 1982; Ho & Huerre 1984) created near the edge of the burner nozzle.

The *Rayleigh criterion* can be used to determine whether this process is self-amplifying: if the sudden heat release is in phase with the acoustic wave creating the next inhomogeneity, then this cycle will be repeated with a certain frequency.

The consequences of unstable combustion are often troublesome due to the intense pressure-fluctuation levels which can occur, as well as increased heat transfer to the combustor surfaces (Lang *et al.* 1987; Büchner *et al.* 1993). These conditions can result in system performance degradation (for example: an increase in the lean blow-off limit or unsteadiness in thrust production in the case of a propulsion device), unacceptable vibration or noise levels, and, in the worst case, system failure due to structural damage (McManus *et al.* 1993). The numerical prediction of combustion instabilities is challenging and has been tried only on very simple geometries (Brookes *et al.* 1999; Veynante & Poinsot 1997; Angelberger *et al.* 2000).

1.2. *Active vs. static control*

So far, most control strategies for combustion instabilities are based on active control mechanisms (McManus *et al.* 1993). Active control is achieved by a sensor in the combustion chamber, which measures frequency and phase of a combustion oscillation. The

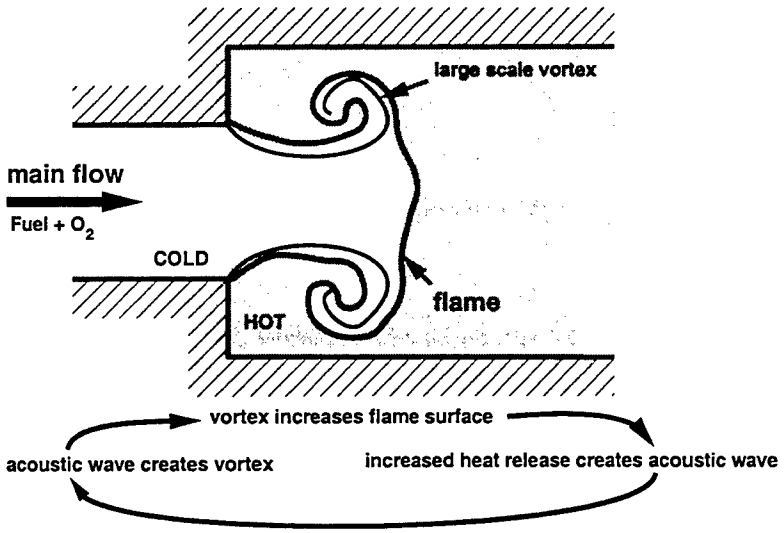

FIGURE 1. Sketch of coherent structures as the driving mechanism in combustion instabilities.

measured signal is then analyzed and a proper periodic response is determined. The response is either an acoustic perturbation or a modulation of the fuel supply (Paschereit *et al.* 1999). Active control is able to suppress combustion instabilities substantially and is already in use for numerous practical applications.

However, this apparatus for active control is rather expensive and maintenance-intensive. Furthermore, since a failure of the active control system can lead to a failure of the whole combustion system, this approach is not advisable for aircraft engines.

Static-control strategies are more robust and need a minimum of maintenance. With static control, a burner can be designed which is naturally less prone to combustion instabilities. However, to give design guidelines for static control, more information on this type of control has to be gathered.

1.3. *Static-control strategies*

Several strategies to control shear layers are known. The method that has received most attention is to use non-circular nozzle shapes like triangles (Schadow *et al.* 1988; Gutmark *et al.* 1989) and ellipses (Husain & Hussain 1983; Hussain & Husain 1987). However, the design of swirl combustors calls for axisymmetric nozzle shapes in order to generate swirl efficiently.

Other strategies involve hardware installations inside the shear layer. Honeycombs have had success in straightening the flow and destroying coherent structures efficiently (Nieberle 1986). The installation of these devices in practical burners is rather difficult, since they would have to be placed in the flame front. The excessive heat these devices would have to sustain makes the application of these installations unlikely.

One possibility of altering the nature of the shear layer fundamentally is to use a small slit near the edge at the backward-facing side of the step. Suction is a very efficient way to deflect the flow and to avoid large scale structures. However, in a premixed burner it would inevitably mean that fresh cold gases at a temperature close to the ignition point are part of the fluid sucked out of the combustion chamber. The further treatment of these gases is problematic.

The current study investigates static control in the form of a small circumferential slit

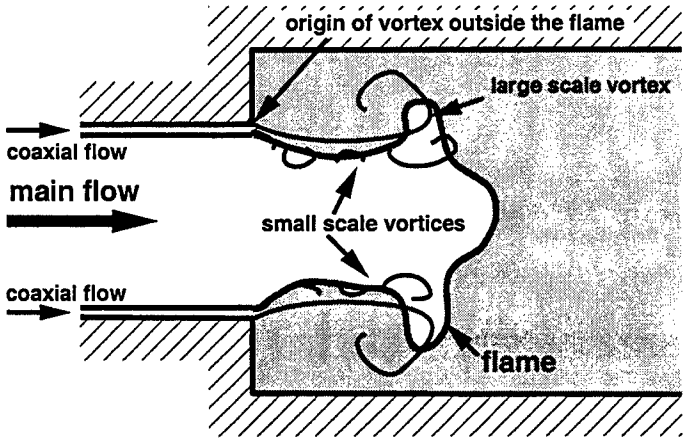

FIGURE 2. Static control by coaxial flow: The origin of large scale vortices is displaced outside the flame.

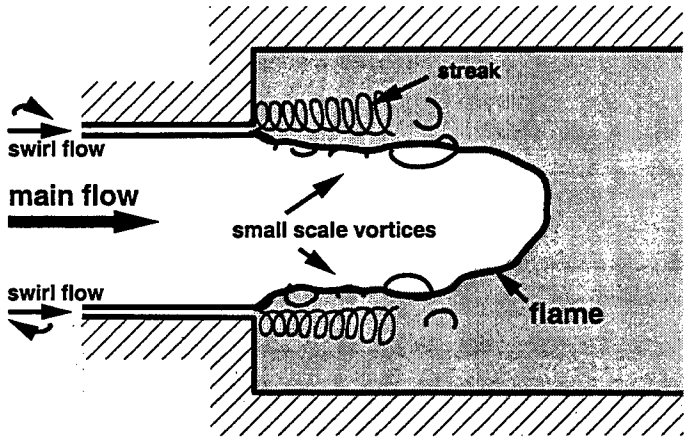

FIGURE 3. Static control by swirled coaxial flow: the generation of longitudinal streaks destroys large scale structures and enhances small scale mixing.

around the nozzle, *blowing* a coaxial flow into the combustion chamber. This coaxial flow carries less than 5% of the mass-flow rate of the main flow and can be used in two ways to control coherent structures:

(*a*) Displacement of the main shear layer (Fig. 2): the shear layer between the coaxial flow and the recirculation zone creates large-scale vortices, while the shear layer between main flow and coaxial flow creates less intense vortices, since the velocity difference is small. Although the intensity of coherent structures is unchanged, their influence decreases, since the origin of these vortices is outside of the flame front.

(*b*) Three-dimensionality of the shear layer (Fig. 3): by giving the shear layer a component in the third direction, e.g. by swirl, a second shear layer perpendicular to the main shear layer is created. As a result, a longitudinally-oriented vortex streak is created which disturbs vortex creation in the main shear layer (Fiedler 1998).

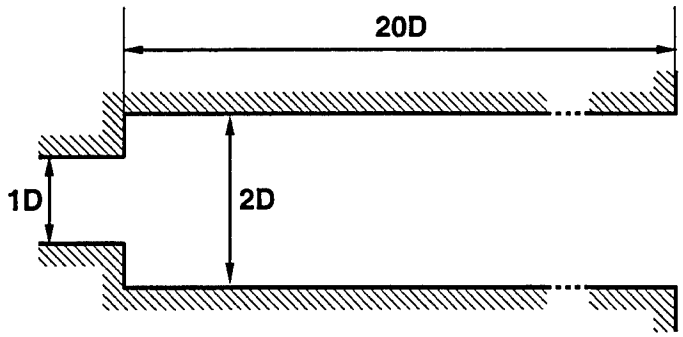

FIGURE 4. Geometry of the combustor

2. LES of static control

2.1. *Numerical tools for turbulence research*

Recent progress in numerical tools provides new elements in turbulence research. While flow solvers based on a Reynolds-averaged Navier-Stokes (RANS) formulation can predict the main flow features, Large Eddy Simulations (LES) are able to provide a detailed look at the origin, development, and decay of large scale turbulent structures. This allows a deeper insight into the dynamics which govern coherent structures, and ultimately can deliver answers on how to control the flow.

The advantage of numerical investigations over experiments is that a single parameter can be varied, leaving all other flow parameters unchanged. Experimental investigations usually encounter practical difficulties in achieving this goal.

Since the current work focuses on coherent structures as an origin of combustion instabilities, LES can be seen as the optimal tool to to find strategies to control large-scale structures in order to suppress combustion instabilities.

2.2. *Test case*

In order to obtain data about general ideas for static control, the current investigation examines a flow over an axisymmetric backward-facing step at a Reynolds-number $Re = 30,000$ (Fig. 4). This geometry corresponds to that used in an experimental investigation (Dellenback 1986; Dellenback *et al.* 1988) and extensive data for the cold flow are available.

While the experiments are carried out with both a non-swirling and a swirling flow, the LES computation focuses primarily on the non-swirled case, where vortex dynamics are better understood. The dynamics governing swirl flows are still controversial (Gupta *et al.* 1984; Keller 1995) and it is difficult to identify origin and control of a vortex structure in these flows.

2.3. *Strategy of the investigation*

It is difficult to examine naturally-excited combustion instabilities by numerical investigations. In the current investigation, therefore, the flow is forced in order to simulate periodic excitation by the combustion instability. A shear layer reacting to the periodic excitation amplifies the periodic disturbance. The quality of a static-control mechanism can be determined by the ability of the control mechanism to suppress the amplification of the excitation.

The external excitation of the flow makes it possible to determine the *potential* of a flame to create combustion instabilities. Whether a flame is finally unstable or not de-

pends on the ability of the heat release to create a periodic excitation that satisfies the Rayleigh criterion. The prediction of this feedback mechanism is tedious, since it involves computation of the acoustic wave propagation and knowledge of acoustic impedances at the boundaries of the computational domain. Here, for simplicity, acoustic effects have been explicitly excluded by using a flow solver based on a low-Mach number approximation. This makes it possible to have a detailed look at the one-way coupling between excitation and flame response. If using static control results in a reduction of the flame response to the excitation, a decrease of the ability of the flame to create an acoustic perturbation can be demonstrated, indicating a robustness against combustion instabilities.

In order to quantify the effect of a static-control device, the following procedure is employed.

First, the cold flow is examined. An LES computation of the test case is compared to the experimental data, to give an estimate of the accuracy of the applied approach.

Then, the excitation is carried out on the cold flow by a periodic modulation of the inlet profile. The shedding of coherent structures at the burner nozzle will lock into the forcing frequency, and a so-called triple decomposition can be applied to the flow variables (Hussain 1983). The instantaneous variable consists of three components; the time-independent component, the coherent (periodic) component and the incoherent turbulence:

$$f(x,t) = \bar{f}(x) + \tilde{f}(x,\phi) + f_r'(x,t) \tag{2.1}$$

where $\bar{f}(x)$ is the time-average of f, $\tilde{f}(x,\phi)$ the periodic component derived by phase-averaging, and $f_r'(x,t)$ the stochastic turbulent component.

Since $\tilde{f}(x,\phi)$ contains all periodic information about the excited flow, the kinetic energy of the periodic fluctuation:

$$\mathcal{E}(x,\phi) = \frac{1}{2}\left(\tilde{u}(x,\phi)^2 + \tilde{v}(x,\phi)^2 + \tilde{w}(x,\phi)^2\right) \tag{2.2}$$

can be computed, and its integral over all periods and the flow domain:

$$E_{per} = \int_0^{20D}\int_0^{2\pi} \mathcal{E}(x,\phi)\, d\phi\, dx \tag{2.3}$$

delivers the response of the flow system to a certain frequency. By several repetitions of the computation with different forcing frequencies, a transfer function can be determined.

In the third step, an LES computation of the cold flow with the static-control mechanism is performed. Again, several computations are made with different forcing frequencies and a transfer function is determined. The comparison of the two transfer functions delivers the effectiveness of the static-control mechanism on cold flow turbulence.

The fourth and final step involves the computation of a reacting flow field. Because of the high computational costs, only one example frequency is examined. Here the phase-averaged heat-release $\tilde{\dot{Q}}$ delivers the flame response to the excitation. The comparison between uncontrolled and controlled flames and the comparison between reacting and non-reacting flows can deliver an answer on whether flame control via turbulence control is possible.

2.4. *LES flow solver and mesh*

For the current investigation, the LES flow solver developed at the Center for Turbulence Research (Pierce & Moin 1998) has been used. The code solves the filtered momentum

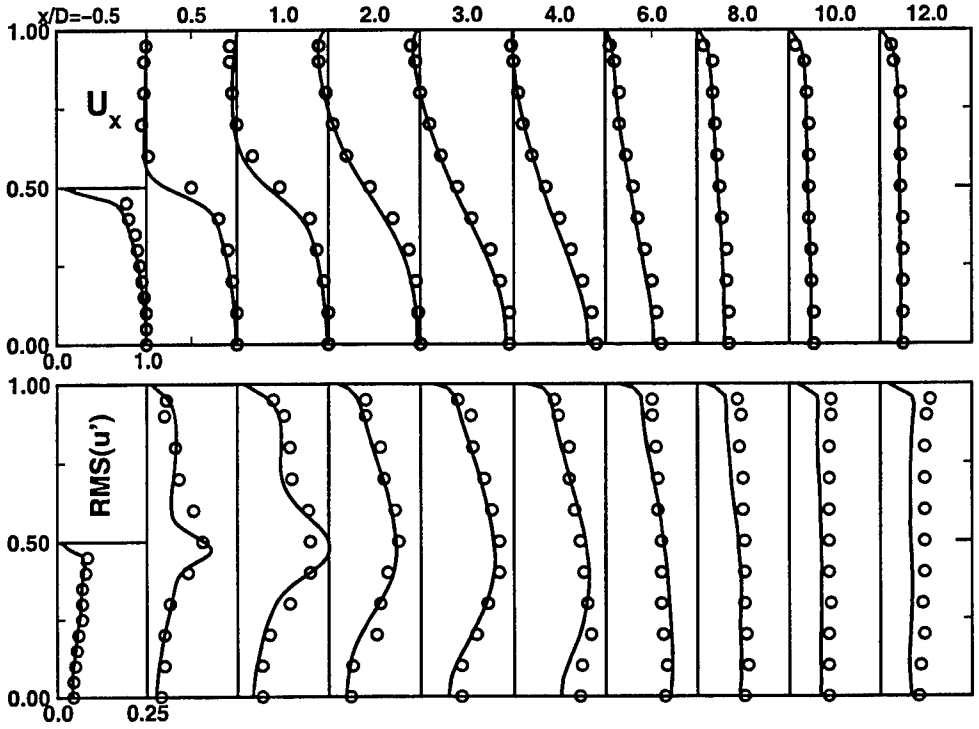

FIGURE 5. Above: mean axial velocity component $\bar{u}_x$, below: axial velocity fluctuations $\sqrt{\overline{u_x'^2}}$

equations with a low-Mach-number assumption on an axisymmetric structured mesh. As numerical method, a second-order finite-volume scheme on a staggered grid is used (Akselvoll & Moin 1996).

The subgrid stresses are approximated with an eddy-viscosity approach. The eddy viscosity is determined by a dynamic procedure (Germano *et al.* 1991; Moin *et al.* 1991).

In reacting cases, the G-equation approach is used to simulate a premixed flame. In the current case, a Bunsen burner flame has been assumed, using the same chemical characteristics as the LES computation of a similar flame (Duchamp & Pitsch 2000).

The geometry consists of an axisymmetric expansion (Fig. 4). The computational domain starts one diameter D upstream of the expansion and ends $10D$ downstream of the expansion in a convective outflow condition. The inflow velocity is generated by an independent LES computation of a periodic pipe flow which records the velocity components in the outflow plane and provides the data as inflow conditions.

The mesh consists of 384x64x64 cells, adding up to 1.6M cells. It is refined in regions of high shear, especially around the control slit. Mesh distribution of the flow with and without slit are exactly the same, with the exception of the control slit itself.

3. LES investigation on static control of the cold flow

3.1. *LES of a flow over an axisymmetric expansion*

Since experimental data are available for the cold flow of the chosen test case, the first step is to validate the LES flow solver against the experiments. Figure 5 shows a comparison of LES and experiments of the mean axial velocity and the axial-velocity fluctuations.

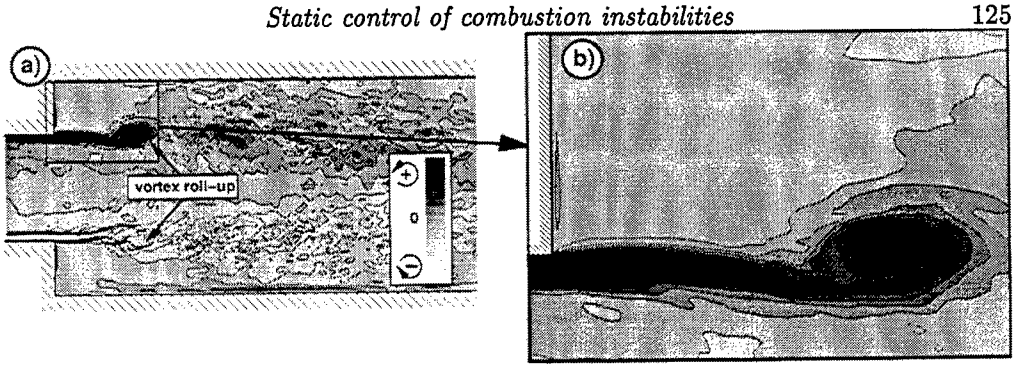

FIGURE 6. Natural, uncontrolled vortex roll-up. Non-reacting flow. Forcing frequency $St = 1.0$. Phase-averaged crosswise vorticity component $\tilde{\omega}_z$

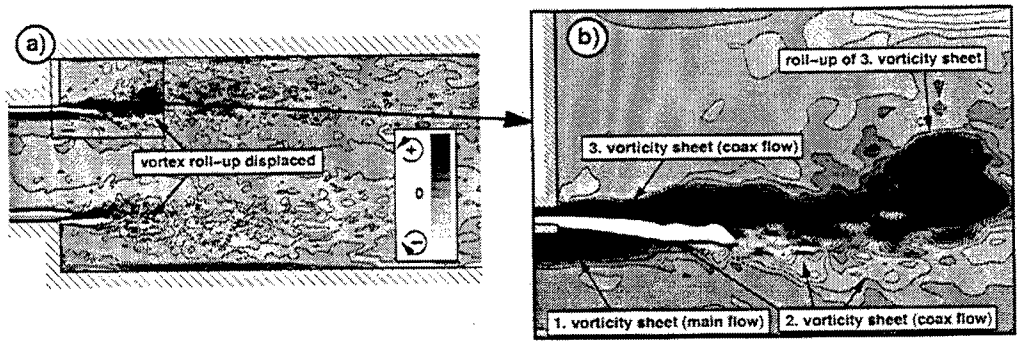

FIGURE 7. Static control by high-speed coaxial flow.($u_{coax} = 2u_{main}$). Non-reacting flow. Forcing frequency $St = 1.0$ Phase-averaged crosswise vorticity component $\tilde{\omega}_z$

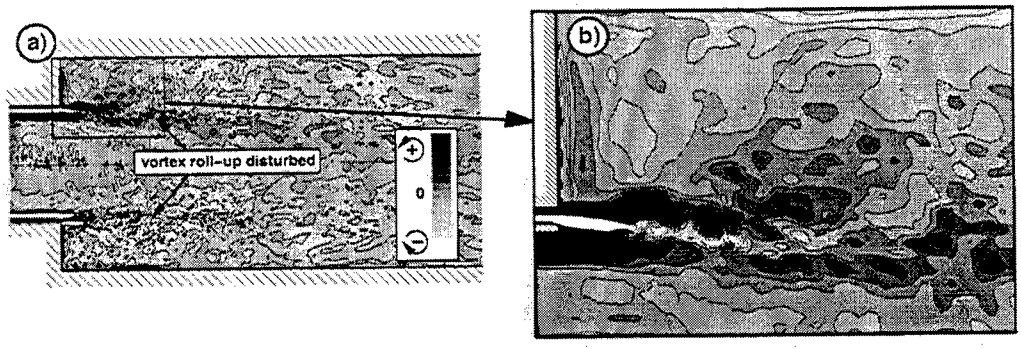

FIGURE 8. Static control by swirled coaxial flow ($u_{coax} = 1 \cdot u_{main}$, swirl number $S = 0.25$). Non-reacting flow. Forcing frequency $St = 1.0$ Phase-averaged crosswise vorticity component $\tilde{\omega}_z$

The mean axial-velocity component of the LES computation shows good agreement with the experiments, although the spreading rate of the shear layer behind the step is underestimated. The computed axial-velocity fluctuations also show good agreement with the experiment. However, the two profiles directly behind the step at $x/D = 0.5$ and $x/D = 1.0$ show some disagreements in shape. The highly-turbulent nature of the flow in this region complicates measurements and computations alike.

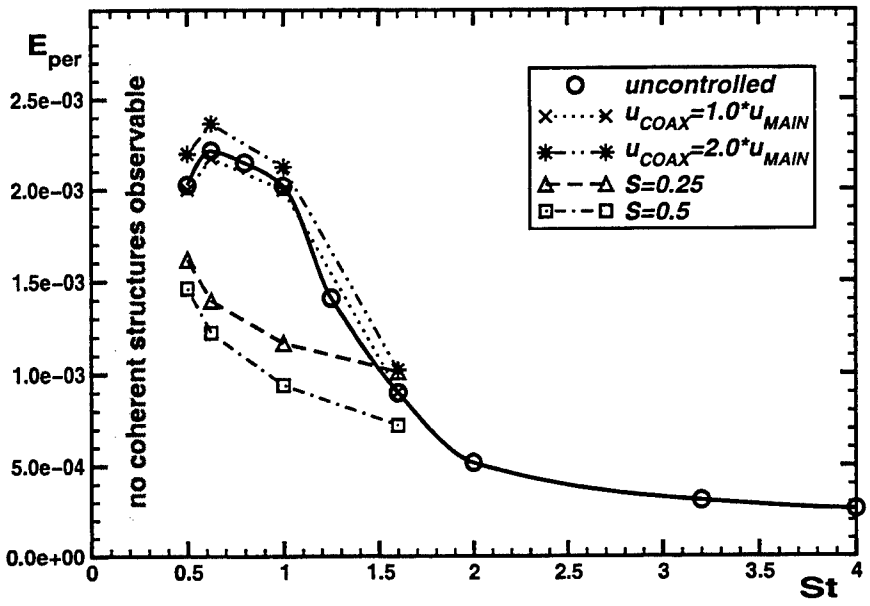

FIGURE 9. Kinetic energy E_{per} of the periodic perturbation (see eq. (2.3)) for different Strouhal-numbers $St = f \cdot D/U$

3.2. *Flow response to forcing*

Forcing the flow triggers the roll-up of coherent structures in the shear layer created by the main jet flow and the recirculation zone at the step. In order to determine the amplification of the forcing by the shear layer, the results of the LES computation are phase-averaged. The phase-averaging begins five periods after the flow forcing has been started, to allow for adjustment to the periodic excitation. The averaging is then carried out over 30 periods. A separate study showed that this number of periods is sufficient to obtain a statistically-converged phase average.

In order to visualize the vortex creation, Fig. 6a shows the the phase-averaged crosswise vorticity. The development of vortex rings with the forcing frequency can be seen. Dark spots denote counterclockwise-turning eddies and light spots clockwise-turning eddies. A close-up of the upper part of the step (Fig. 6b) shows a vorticity sheet with positive sign (dark) created by the boundary layer and the shear layer between the main flow and the recirculation zone near the step. This vorticity sheet rolls up and creates a vortex ring, which is to be manipulated in order to control a flame.

The effect of a coaxial high-speed stream on the creation of a vortex ring can be seen in Fig. 7a. The coaxial flow, here with a bulk velocity twice as high as the main flow, creates two additional vortex sheets with opposite signs. The close-up in Fig. 7b shows how the vorticity sheet with negative sign (white) shields the main flow and restrains the vorticity sheet of the main flow from rolling up into a vortex. Instead, the outermost vorticity sheet originating in the coaxial flow rolls up. Since this vortex consists mainly of fluid emanating from the coaxial flow it will have less influence on the flame front than in the uncontrolled case. However, the intensity of the vortex ring created by the coaxial flow is of approximately the same intensity as the vortex ring in the main flow in the uncontrolled case.

Figure 8a shows the employment of a swirled coaxial flow as a static-control mechanism.

Here, the axial bulk velocity of the coaxial flow is the same as the bulk velocity of the main flow, and the swirl number S:

$$S = \frac{2}{R_i + R_o} \frac{\int_{R_i}^{R_o} r^2 \bar{u}_x \bar{u}_\phi dr}{\int_{R_i}^{R_o} r \bar{u}_x^2 dr} \tag{3.1}$$

is approximately $S = 0.25$, where u_x is the axial velocity component, u_ϕ the azimuthal velocity component, R_i the inner radius of the coaxial slit, and R_o the outer radius of the coaxial slit. The effect of shielding the main flow by a vorticity sheet of opposite sign is still present (Fig. 8). Additionally, the creation of a shear layer in the azimuthal direction disturbs the vortex roll-up of the coaxial flow, and a decrease of coherence in the vortex can be determined.

In order to quantify the effect of the control mechanisms, the kinetic energy of the periodic flow perturbation was computed and integrated over the volume behind the step. Figure 9 shows the results for different Strouhal numbers ($St = fD/U$).

The natural, uncontrolled flow is denoted by circles. The maximum kinetic energy occurs near $St = 0.625$. Below that Strouhal number, the vortices created by the forcing are disturbed by the proximity of the outer wall. For sufficiently low Strouhal numbers, no coherent structures can be observed.

With increasing Strouhal number, the coherent structures shed at the step get smaller, and thus their contribution to the periodic fluctuation of the flow decreases. Above a Strouhal number of $St = 2.0$ the importance of these coherent structures is low. A comparison with the literature shows that combustion instabilities in gas turbine burners occur in the same frequency range as the amplification of periodic disturbances found here (Paschereit *et al.* 1998; Schildmacher *et al.* 2000).

The effect of the unswirled coaxial flow is not reflected in this presentation, since the vortex development is not prevented, but displaced. The kinetic energy of the coaxial flow with the same bulk velocity as the main-flow $u_{coax} = u_{main}$ is identical with the kinetic energy of the uncontrolled flow (crosses in Fig. 9). A high-speed coaxial flow ($u_{coax} = 2 \cdot u_{main}$) even amplifies the flow response (stars in Fig. 9), since the velocity difference in the outer shear layer between the coaxial flow and the recirculation zone is even higher than in the uncontrolled flow. The effectiveness of this control measure has to be shown in reacting computations.

However, using a swirled coaxial flow shows great potential even in the cold flow. Even the low swirl number $S = 0.25$ results in a considerable damping of the flow response (triangles in Fig. 9). An increase of the swirl number decreases the flow response even more (squares in Fig. 9). Here it can be seen that the swirled coaxial flow is able to damp the flow response by more than 50% over a broad frequency range.

4. LES Investigation on static control of the reacting flow

Since the computation of reacting flows is much more expensive, a full analysis like that for the cold flow cannot be given here, and so far, only the computations of one control mechanism have been carried out: the high-speed coaxial flow. In a reacting flow, the coaxial flow can carry either fresh air or hot products. The injection of fresh air near the ignition point of the flame would alter the chemical reaction of the flame in comparison to the uncontrolled flow. Since the current investigation concentrates on the attempt to control a flame mechanically and not chemically, the coaxial flow in the

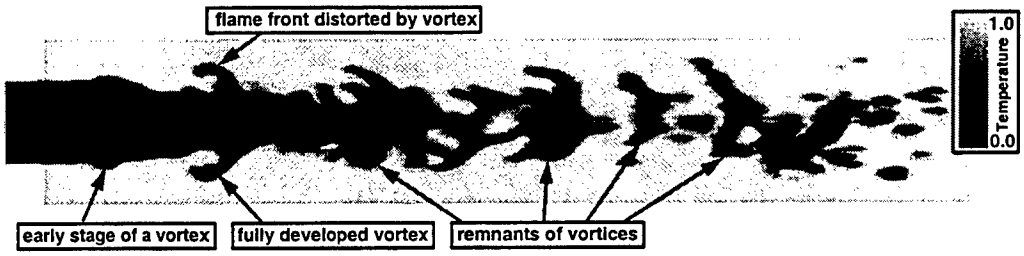

FIGURE 10. Uncontrolled flame. Instantaneous snapshot after 6 periods of forcing. Forcing frequency $St = 1.0$. Gray-scale: temperature T. Black line: G_0 (flame front).

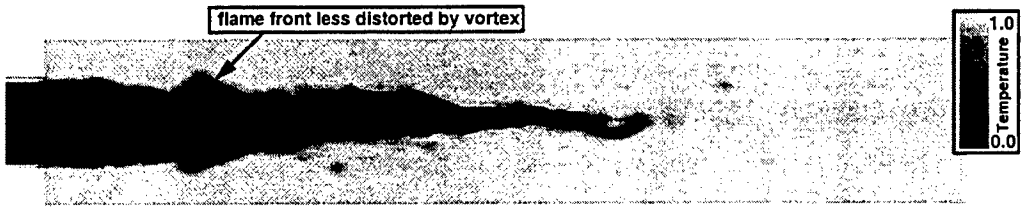

FIGURE 11. Static control by high-speed coaxial flow($u_{coax} = 2 \cdot u_{main}$). Instantaneous snapshot after 6 periods of forcing. Forcing frequency $St = 1.0$. Gray-scale: temperature T. Black line: G_0 (flame front).

computation carries hot products in order to provide the same chemical characteristics as the uncontrolled flame ignited by the recirculation zone at the dump.

The high computational costs prevent the computation of physical time-spans as long as in the cold flow. So far, the computed time-spans are shorter than the cold-flow counterparts, so a statistical analysis such as phase averaging contains more uncertainties.

Figure 10 shows an instantaneous snapshot of the temperature distribution of a periodically-excited flow. The influence of the vortices created by the forcing can be seen in different stages. In the beginning the vortices bulge the flame-front. Fully developed, the vortices create the typical mushroom-shaped distortion of the flame, and during their decay the vortices finally detach parts of the flame. These flame pockets float far downstream, where they are consumed.

Figure 11 shows the same flame with a high-speed coaxial flow. Large-scale vortices still distort the flame front, but have much less influence, since they are created outside the flame. Comparing Fig. 10 and Fig. 11, the most striking difference is that the flame with static control is more compact and seems much steadier than its uncontrolled counterpart, and no flame detachments take place. Since the small-scale mixing is enhanced by the coaxial flow, the flame length in this combustor is shorter than in the case without coaxial flow.

In order to give a quantitative measure on the efficiency of this control method the flow was averaged over nine periods. The turbulent kinetic energy of the periodic velocity fluctuations $\mathcal{E}$ was computed and integrated over all phase angles and over the volume of the combustion chamber. The employment of the coaxial flow resulted in a decrease of $\mathcal{E}$ by approximately 60% in comparison with the uncontrolled flow. This figure underlines the efficiency of the static-control method despite its simplicity.

Current investigations concentrate on the effect of control on the heat release and the influence of the swirled coaxial flow on the flame structure.

5. Conclusion

The static-control mechanism described here has proven to be an effective yet simple way to control turbulent coherent structures in a typical dump-combustor geometry. The installation of this static-control method is much easier than its active-control counterpart. The application of static control to reacting flows has shown great potential for suppressing periodic flame fluctuations.

Furthermore, LES has been a useful tool for understanding the mechanisms of vortex creation and suppression. Using a low-Mach-number code made it possible to explicitly exclude acoustic effects and pressure sensitivity of the flame, and to link the effects of the flame response directly to the forcing of the flow and the creation of large-scale vortices.

Future efforts will focus on the improvement and simplification of static control of reacting flames. Furthermore, the extension of these concepts to swirl combustors will be investigated.

REFERENCES

AKSELVOLL, K. & MOIN, P. 1996 Large-eddy simulation of turbulent confined coannular jets. *J. Fluid Mech.*, **315**, 387-411.

ANGELBERGER, C., VEYNANTE, D. & EGOLFOPOULOS, F. 2000 LES of chemical and acoustic effects on combustion instabilities. *Flow, Turbulence and Combustion* **65**, 205-222.

BROOKES, S. J., CANT R. S. & DOWLING, A. P. 1999 Modeling combustion instabilities using computational fluid dynamics. *ASME* 99-GT-112.

BÜCHNER, H., HIRSCH, C. & LEUCKEL, W. 1993 Experimental investigations on the dynamics of pulsated premixed axial flames. *Combust. Sci. and Tech.* **94**, 219-228.

CROW, S. C. & CHAMPAGNE, F. H. 1971 Orderly structure in jet turbulence. *J. Fluid Mech.* **48**, 547-591.

DELLENBACK, P. A., METZGER, D. E. & NEITZEL, G. P. 1988 Measurements in turbulent swirling flow through an abrupt axisymmetric expansion. *AIAA J.* **26**, 669-681.

DELLENBACK, P. A. 1986 Heat transfer and velocity measurements in turbulent swirling flows through an abrupt axisymmetric expansion. PhD thesis, Arizona State University.

DUCHAMP DE LAGENESTE, L. & PITSCH, H. 2000 A level-set approach to large eddy simulation of premixed turbulent combustion. *Annual Research Briefs*, Center for Turbulence Research, NASA Ames/Stanford Univ., 105–116.

FIEDLER, H. E. 1998 *Flow Control.* Control of Free Turbulent Shear Flows, (M. Gad-el-Hak, A. Pollard, & J. P. Bonnet, eds.), Springer, 335–429.

GERMANO, M., PIOMELLI, U., MOIN, P. & CABOT, W., 1991 A dynamic subgrid-scale eddy viscosity model. *Phys. Fluids A* **3**, 1760-1765.

GUPTA, A. K., LILLEY, D. G. & SYRED, N. 1984 *Swirl Flows.* Abacus Press.

GUTMARK, E., SCHADOW, K. C., PARR, T. P, HANSON-PARR, D. M. & WILSON, K. J. 1989 Non-circular jets in combustion systems. *Expts. in Fluids* **7**, 248-258.

HO, C. M. & HUANG, L. S. 1982 Subharmonics and vortex merging in mixing layers. *J. Fluid Mech.* **119**, 443-473.

HO, C. & HUERRE, P. 1984 Perturbed free shear layers. *Ann. Rev. Fluid Mech.* **16**, 365-424.

HUSAIN, H. S. & HUSSAIN, A. K. M. F. 1983 Controlled excitation of elliptic jets. *Phys. Fluids* **26**, 2763-2765.

HUSSAIN, A. K. M. F. 1983 Coherent structures – reality and myth. *Phys. Fluids* **26**, 2816-2849.

HUSSAIN, A. K. M. F. & HUSAIN, H. S. 1987 Passive and active control of jet turbulence. In *Turbulence Management and Relaminarisation*, (H. W. Liepmann and R. Narasimha, eds.), IUTAM Symposium Bangalore, India, 1987.

KELLER, J. J. 1995 On the interpretation of vortex breakdown. *Phys. Fluids* **7**, 1695-1702.

LANG, W., POINSOT, T., BOURIENNE, F., CANDEL, S. & ESPOSITO, E. 1987 Suppression of combustion instabilities by active control. *AIAA* Paper 87-1876.

MCMANUS, K. R., POINSOT, T. & CANDEL, S. M. 1993 A review of active control of combustion instabilities. *Prog. Energy Combust. Sci.*, **19**, 1-29.

MOIN, P., SQUIRES, K., CABOT, W. & LEE, S. 1991 A dynamic subgrid-scale model for compressible turbulence and scalar transport. *Phys. Fluids A* **3**, 2746-2757.

MUGRIDGE, B. D. 1980 Combustion driven oscillations. *J. Sound and Vibration* **70**, 437–452.

NIEBERLE, R., 1986 Entwicklung einer Methode der Mustererkennung zur Analyse kohärenter Strukturen und ihre Anwendung im turbulenten Freistrahl. *Fortschrittsberichte VDI*, Reihe 7: Strömungsmechanik (106), VDI Verlag.

PASCHEREIT, C. O., GUTMARK, E. & WEISENSTEIN, W. 1998 Structure and control of thermoacoustic instabilities in a gas-turbine combustor. *Combust. Sci. and Tech.* **138**, 213-232.

PASCHEREIT, C. O, GUTMARK, E. & WEISENSTEIN, W. 1999 Control of thermoacoustic instabilities in a premixed combustor by fuel modulation. *AIAA* Paper 99-0711.

PETERS,N. & LUDFORD, G. S. S. 1983 The effect of pressure variations on premixed flames. *Combust. Sci. and Tech.* **34**, 331-344.

PIERCE, C. D. & MOIN, P. 1998 Large eddy simulation of a confined coaxial jet with swirl and heat release. *AIAA* Paper 98-2892.

POINSOT, T. J., TROUVÉ, A., VEYNANTE, D., CANDEL, S. & ESPOSITO, E., 1987 Vortex-driven acoustically coupled combustion instabilities. *J. Fluid Mech.*, **177**, 265-292.

PUTNAM, A. A. 1971 *Combustion Driven Oscillations in Industry.* American Elsevier.

SCHADOW, K. C., GUTMARK, E., PARR, D. M. & WILSON, K. J. 1988 Selective control of flow coherence in triangular jets. *Expts. in Fluids* **6**, 129-135.

SCHILDMACHER K.-U., KOCH, R., KREBS, W., HOFFMANN, S. & WITTIG, S. 2000 Experimental investigations of the temporal air-fuel fluctuations and cold flow instabilities of a premixing gas turbine burner. *ASME* 2000-GT-84.

VEYNANTE, D. & POINSOT, T. 1997 Large eddy simulation of combustion instabilities in turbulent premixed burners. *Annual Research Briefs*, Center for Turbulence Research, NASA Ames/Stanford Univ., 253-274.

Combustion instability due to the nonlinear interaction between sound and flame

By Xuesong Wu†, Meng Wang AND Parviz Moin

1. Introduction

Combustion instability generally refers to the sustained pressure fluctuations of acoustic nature in a chamber where unsteady combustion takes place. It is essentially a self-excited oscillation, involving a complex interplay between unsteady heat release, the acoustic fluctuation and the vorticity field, which according to experimental observations (e.g. Poinsot *et al.* 1987, Yu, Trouve & Daily 1991, Schadow & Gutmark 1992), may be described as follows. Unsteady heat release produces sound, which then generates (Kelvin-Helmholtz) instability waves at the inlet (via a receptivity mechanism as it is referred to in laminar-turbulent transition). These waves amplify and roll up on the shear layer and finally break down into small-scale motions, thereby affecting the heat release. The whole process forms a closed loop.

An important insight into the effect of unsteady heat release on sound amplification is provided by the Rayleigh criterion, which states that an acoustic wave will amplify if its pressure and the heat release are 'in phase', i.e. the integral of the product of the pressure and the unsteady heat release over a cycle is positive. The difficulty in applying this criterion is that unsteady heat release is often part of the solution and thus not known *a priori*. A usual remedy is to extrapolate, by using available experimental data, some empirical relations between the heat release and sound fluctuation. This then leads to a thermo-acoustic problem. Such an approach has been employed by Bloxsidge, Dowling & Langhorne (1988) to describe 'reheat buzz' (Langhorne 1988). Dowling (1995) formulated this approach in a more general setting, and discussed, *inter alia*, the effects of the mean Mach number and heat distribution.

In the above semi-empirical approach, the hydrodynamic (and chemical) processes of combustion are completely by-passed. To understand the acoustic-flame coupling on a first-principles basis, one has to look into the structure of the flame as well as its associated hydrodynamic field. Fortunately, for premixed flames much knowledge about the last two aspects above has been obtained by using the powerful asymptotic approach based on the large-activation-energy assumption (Williams 1985). The reader is referred to Clavin (1985, 1994) for detailed reviews of the subject. This framework as well as relevant previous results will be used in our work. Detailed discussions will be presented in Section 2.

A thorough theoretical treatment of sound-flame coupling is unrealistic at the present for a practical combustor, where the flow is strongly vortical and turbulent. As a first step, it is necessary to restrict to the simple case where the hydrodynamic motion is primarily due to unsteady heat release and remains laminar.

A formal formulation of acoustic-flame coupling has been given by Harten, Kapila & Matkowsky (1984) for what may be called the 'high-frequency' regime, where the acoustic time scale is comparable to the transit time of the flame, $O(d/U_L)$, where d and U_L stand

† Permanent address: Department of Mathematics, Imperial College, UK

for the flame thickness and speed respectively. The resulting system is nonlinear and requires a major numerical attack. Harten *et al.* considered the flat-flame case in the limits of low frequency and small heat release, and obtained in each limit the solution which describes the effect of acoustic pressure on the flame. However, they did not consider how the flame influences the sound. This inverse process was investigated by Clavin, Pelce & He (1990), who also removed the assumption of small heat release. By closing the loop, they were able to show that the mutual interaction leads to amplification of sound, i.e. to acoustic instability. For a *flat flame*, the hydrodynamics is completely absent, with the sole coupling being through the acoustic pressure affecting the temperature.

For a *curved flame*, there exists an additional coupling mechanism. As was pointed out by Markstein (1970), the sound pressure modulates the flame and hence alters its surface area. This in turn leads to modulation of heat release, thereby affecting the sound itself. The mechanism was further analyzed by Pelce & Rochwerger (1992) in connection with the experiments of Searby (1992), who observed that sound was generated when a curved flame was propagating downwards in a tube. The curved flame is due to the well known Darrieus-Landau (D-L) instability. In developing a mathematical mode, Pelce & Rochwerger represented the curved flame by the neutrally stable D-L instability mode (which exists due to the stabilizing effect of gravity). A constant amplitude is prescribed in calculating the growth rate of sound. They showed that this coupling mechanism could be stronger by an order of magnitude than that considered in Clavin *et al.* (1990).

The present work is aimed at improving the model of Pelce & Rochwerger (1992) in two somewhat related respects. First, we note that, like any marginally-stable mode, a neutral D-L mode must modulate in a weakly-nonlinear fashion rather than stay completely neutral. According to classical weakly-nonlinear theory (Stuart 1960), if the typical magnitude of the mode is ϵ, the time scale of modulation is $O(\epsilon^{-2})$, comparable with the time scale over which the sound amplifies. Second, Searby's (1992) experiments showed that the flame was evolving, and that the sound amplified mainly as the flame was evolving from a curved pattern to a flat one. Therefore for both mathematical and physical reasons, it is necessary to take into account the evolving nature of the flame as well as the back reaction of sound on the flame. For this purpose, we give a general formulation for the sound-flame interaction in what may be regarded as the 'low-frequency' regime in the sense that the acoustic time is much longer than the transit time of the flame. By using this basic framework, the nonlinear evolution of the acoustic and flame instability modes is studied in a systematic manner.

2. Formulation

Consider the combustion of a homogeneous premixed combustible mixture in a duct of width h^*; see Fig. 1. For simplicity, a one-step irreversible exothermic chemical reaction is assumed. The gaseous mixture consists of a single deficient reactant and an abundant component, and is assumed to obey the state equation for a perfect gas.

The fresh mixture has a density $\rho_{-\infty}$ and temperature $\Theta_{-\infty}$. Due to steady heat release, the mean temperature (density) behind the flame increases (decreases) to Θ_∞ (ρ_∞). The flame propagates into the fresh mixture at a mean speed U_L, and it has an intrinsic thickness d. Let (x, y, z) and t denote the coordinates and time variables, normalized by h^* and h^*/U_L respectively. The velocity $\mathbf{u} \equiv (u, v, w)$, density ρ, temperature θ, and pressure p are non-dimensionalized by U_L, $\rho_{-\infty}$, $\Theta_{-\infty}$, and $\rho_{-\infty}U_L^2$ respectively.

We define the Mach number $M = U_L/a^*$, where the speed of sound $a^* = (\gamma p_{-\infty}/\rho_{-\infty})^{\frac{1}{2}}$, with γ being the ratio of specific heats.

A key simplifying assumption is that of large activation energy, corresponding to

$$\beta \equiv E(\Theta_\infty - \Theta_{-\infty})/\mathcal{R}\Theta_\infty^2 \gg 1 , \tag{2.1}$$

where E is the activation energy and $\mathcal{R}$ is the universal gas constant. Under this assumption the reaction occurs in a thin region of width $O(d/\beta)$ centered at the flame front. Assuming that the front is given by $x = f(y,z,t)$, it is convenient to introduce a coordinate system attached to the front,

$$\xi = x - f(y,z,t) , \quad \eta = y \quad \zeta = z ,$$

and to split the velocity $\mathbf{u}$ as $\mathbf{u} = u\mathbf{i} + \mathbf{v}$, where $\mathbf{i}$ is the unit vector along the duct. Then the governing equations can be written as (Matalon & Matkowsky 1982)

$$\frac{\partial \rho}{\partial t} + \frac{\partial \rho s}{\partial \xi} + \nabla \cdot (\rho \mathbf{v}) = 0 , \tag{2.2}$$

$$\rho\frac{\partial u}{\partial t} + \rho s\frac{\partial u}{\partial \xi} + \rho \mathbf{v}\cdot\nabla u = -\frac{\partial p}{\partial \xi} + \delta Pr\left\{\triangle u + \frac{1}{3}\frac{\partial}{\partial \xi}\left(\frac{\partial s}{\partial \xi} + \nabla\cdot\mathbf{v}\right)\right\} - \rho G , \tag{2.3}$$

$$\rho\frac{\partial \mathbf{v}}{\partial t} + \rho s\frac{\partial \mathbf{v}}{\partial \xi} + \rho \mathbf{v}\cdot\nabla \mathbf{v} = -\nabla p + \nabla f\frac{\partial p}{\partial \xi} + \delta Pr\left\{\triangle \mathbf{v} + \frac{1}{3}\left(\nabla - \nabla f\frac{\partial}{\partial \xi}\right)\left(\frac{\partial s}{\partial \xi} + \nabla\cdot\mathbf{v}\right)\right\} , \tag{2.4}$$

$$\rho\frac{\partial Y}{\partial t} + \rho s\frac{\partial Y}{\partial \xi} + \rho \mathbf{v}\cdot\nabla Y = \delta Le^{-1}\triangle Y - \delta\Omega , \tag{2.5}$$

$$\rho\frac{\partial \theta}{\partial t} + \rho s\frac{\partial \theta}{\partial \xi} + \rho \mathbf{v}\cdot\nabla\theta = \delta\triangle\theta + \delta q\Omega , \tag{2.6}$$

supplemented by the state equation $\gamma M^2 p = \rho\theta$, where $\delta = d/h^*$, $s = u - f_t - \mathbf{v}\cdot\nabla f$,

$$\triangle = \left[1 + (\nabla f)^2\right]\frac{\partial^2}{\partial \xi^2} + \nabla^2 - \nabla^2 f\frac{\partial}{\partial \xi} - 2\frac{\partial}{\partial \xi}(\nabla f\cdot\nabla) ;$$

here the operators ∇ and ∇^2 are defined with respect to η and ζ. Pr and Le denote the Prandtl and Lewis numbers respectively, and $G = gh^*/U_L^2$ is the normalized gravity force. The reaction rate Ω is taken to be described by the Arrhenius law:

$$\Omega \sim \delta^{-2}\rho Y \exp\left\{\beta\left(\frac{1}{\Theta_+} - \frac{1}{\theta}\right)\right\} , \tag{2.7}$$

where $\Theta_+ = 1 + q$ is the adiabatic flame temperature. The large-activation-energy asymptotic approach requires the Lewis number Le to be close to unity, or more precisely

$$Le = 1 + \beta^{-1}l \quad \text{with} \quad l = O(1) . \tag{2.8}$$

To make analytical progress, we assume, in addition to $\beta \gg 1$, that

$$\delta \ll 1 , \quad M \ll 1 . \tag{2.9}$$

The whole flow field then is described by four distinct asymptotic regions as illustrated in Fig. 1. In addition to the thin reaction and preheated zones, there are also hydrodynamic and acoustic regions, which scale on h^* and h^*/M respectively. In the reaction zone, the

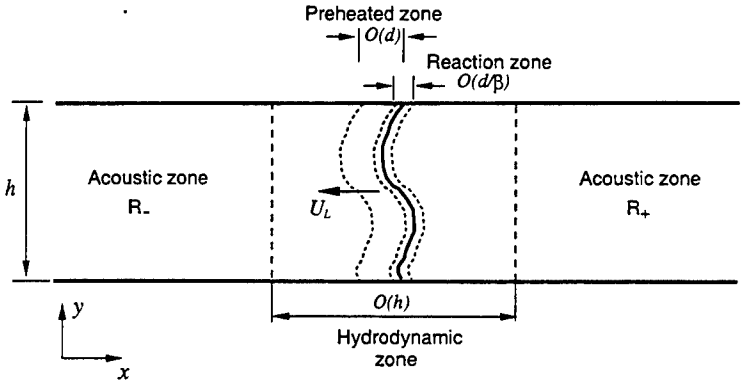

FIGURE 1. Sketch of the problem and the asymptotic structure

heat release due to the reaction balances the thermal diffusion, and the species variation balances the mass diffusion (Matkowsky & Sivashinsky 1979). In the preheated zone, the dominant balance is between the advection and diffusion. All the four regions are interactive, in that the complete solution relies on the investigation of all these regions.

The direct interaction between the sound and the flame is through the hydrodynamic region, which we now consider. In this region, the solution expands as

$$\left.\begin{array}{rcl}(\rho,\theta) &=& (R_0,\Theta)+\delta(\rho_1,\theta_1)+\dots\\ (u,\,\mathbf{v},\,f) &=& (u_0,\,\mathbf{v}_0,\,f_0)+\delta(u_1,\,\mathbf{v}_1,\,f_1)+\dots\\ p &=& (R_0G\xi)+p_0+\delta p_1+\dots\end{array}\right\}. \tag{2.10}$$

The solution for the density (Pelce & Clavin 1982, Matalon & Matkowsky 1982),

$$R_0=\begin{cases}1\equiv R_- & \xi<0\\ (1+q)^{-1}\equiv R_+ & \xi>0\,,\end{cases}$$

is accurate to all orders in δ. In the following, the subscript '0' will be omitted. Substitution of Eq. (2.10) into Eqs. (2.2)–(2.4) leads to the equations governing $(u_0,\,\mathbf{v}_0,\,p_0)$:

$$\frac{\partial s_0}{\partial\xi}+\nabla\cdot\mathbf{v}_0=0\,, \tag{2.11}$$

$$R\left\{\frac{\partial u_0}{\partial t}+s_0\frac{\partial u_0}{\partial\xi}+\mathbf{v}_0\cdot\nabla\ u_0\right\}=-\frac{\partial p_0}{\partial\xi}\,, \tag{2.12}$$

$$R\left\{\frac{\partial\mathbf{v}_0}{\partial t}+s_0\frac{\partial\mathbf{v}_0}{\partial\xi}+\mathbf{v}_0\cdot\nabla\mathbf{v}_0\right\}=-\nabla p_0+\nabla f_0\frac{\partial p_0}{\partial\xi}-RG\nabla f_0\,, \tag{2.13}$$

where $s_0=u_0-f_{0,t}-\mathbf{v}_0\cdot\nabla f_0$.

Embedded in the hydrodynamic zone are the preheated zone and the much thinner reaction zone. The jump conditions across the preheated zone were first derived by Pelce & Clavin (1982) for $\mathbf{v},\,f\ll O(1)$, and by Matalon & Matkowsky (1982) in the general case $\mathbf{v},\,f\sim O(1)$. These are

$$[u_0]=q[1+(\nabla f_0)^2]^{-\frac{1}{2}}\,,\quad [\mathbf{v}_0]=-q\nabla f_0/(1+(\nabla f_0)^2)^{1/2}\,,\quad [p_0]=-q\,. \tag{2.14}$$

The front evolution is governed by the equation

$$f_{0,t}=u_0(0^-,\eta,\zeta,t)-\mathbf{v}_0(0^-,\eta,\zeta,t)\cdot\nabla f_0-[1+(\nabla f_0)^2]^{\frac{1}{2}}\,. \tag{2.15}$$

The results Eqs. (2.14)–(2.15) were originally derived by assuming that the flow is in-

compressible. Fortunately, they are valid for low-Mach-number flows because the acoustic pressure does not directly affect the preheated zone or the reaction zone to leading order. It only contributes a small correction of a higher order (see Clavin *et al.* 1990).

The leading-order system suffices for most part of our work. However, a more general result may be derived if we include the jumps at $O(\delta)$, which were derived by Pelce & Clavin (1982) and Matalon & Matkowsky (1982). The full version is rather complex, but our subsequent analysis requires only the linearized results:

$$[u_1] = -\tfrac{1}{2}lD(q)(\nabla^2 f_0 + \nabla\cdot\mathbf{v}_0)\ , \quad [p_1] = -2\,[u_1] + q\,\nabla^2 f_0 + \ln(1+q)\frac{\partial u_0}{\partial t}\ , \tag{2.16}$$

$$[\mathbf{v}_1] = Pr\left[\frac{\partial \mathbf{v}_0}{\partial \xi}\right] + \ln(1+q)\Big\{\frac{\partial}{\partial t}(\mathbf{v}_0 + \nabla f_0) + G\,\nabla f_0\Big\} - q\,\nabla f_1\ , \tag{2.17}$$

where $D(q) = \displaystyle\int_0^\infty \ln(1+q\,\mathrm{e}^{-x})\,\mathrm{d}x$, u_0 and $\mathbf{v}_0$ as well as their derivatives are evaluated at the front $\xi = 0^-$. The function f_1 satisfies the equation

$$f_{1,t} = u_1(0,\eta,\zeta,t) + \Big\{\frac{1+q}{q}\ln(1+q) + \frac{1}{2q}lD(q)\Big\}\Big\{\nabla^2 f_0 + \nabla\cdot\mathbf{v}_0\Big\}\ . \tag{2.18}$$

3. Strongly-nonlinear sound-flame interaction: a general formulation

3.1. *Acoustic zone*

The appropriate variable describing the acoustic motion in this region is

$$\tilde{\xi} = M\xi\ . \tag{3.1}$$

Because the transverse length is much smaller than the longitudinal length, the motion is a longitudinal oscillation about the uniform mean background, and the solution, for the velocity and pressure say, can be written as

$$u = U_\pm + u_a(\tilde{\xi},t) + \dots\ , \quad p = \frac{1}{\gamma M^2} + M^{-1}p_a(\tilde{\xi},t) + \dots\ , \tag{3.2}$$

where $U_\pm$ are the mean velocities behind and in front of the flame respectively, with $U_+ - U_- = q$. The pressure p_a and velocity u_a satisfy the linearized equations

$$R\frac{\partial^2 p_a}{\partial t^2} - \frac{\partial^2 p_a}{\partial \tilde{\xi}^2} = 0\ , \quad \text{and} \quad R\frac{\partial u_a}{\partial t} = \frac{\partial p_a}{\partial \tilde{\xi}}\ . \tag{3.3}$$

As $\tilde{\xi} \to \pm 0$,

$$u_a \to u_a(0^\pm,t) + \dots\ , \quad p_a \to p_a(0,t) + p_a'(0^\pm,t)\tilde{\xi} + \dots\ .$$

As will be shown in Section 3.2, the acoustic pressure is continuous across the flame, but the flame induces a jump in u_a i.e.

$$[p_a] = 0\ , \quad [u_a] = q\Big\{\overline{(1+(\nabla F_0)^2)^{\frac{1}{2}}} - 1\Big\}\ , \tag{3.4}$$

where $\overline{\phi}$ stands for the space average of ϕ in the (η,ζ) plane, and F_0 is defined in Eq. (3.5).

3.2. *Hydrodynamic zone*

In the hydrodynamic zone, u_a and $p_{a,\tilde{\xi}}$ appear spatially uniform on either side of the flame, and can be approximated by their values at $\tilde{\xi} = 0^\pm$. To facilitate the matching

with the solution in the acoustic region, we subtract from the total field the acoustic components as well as the mean background flow, by writing

$$u_0 = U_\pm + u_a(0^\pm, t) + U_0\,, \quad p_0 = \frac{1}{\gamma M^2} + P_\pm + p'_a(0^\pm, t)\xi + P_0\,, \quad f_0 = F_a + F_0\,, \tag{3.5}$$

where $P_\pm$ is the mean pressure (with $P_+ - P_- = q$), and $F'_a = U_- - 1 + u_a(0^-, t)$. Let $\mathrm{v}_0 = \mathbf{V}_0$. Then the leading-order hydrodynamic field satisfies the following equations

$$\frac{\partial U_0}{\partial \xi} + \nabla \cdot \mathbf{V}_0 = \frac{\partial \mathbf{V}_0}{\partial \xi} \cdot \nabla F_0\,, \tag{3.6}$$

$$\frac{\partial U_0}{\partial \xi} + R\left\{\frac{\partial \tilde{U}_0}{\partial t} + S_0 \frac{\partial U_0}{\partial \xi} + \mathbf{V}_0 \cdot \nabla U_0\right\} = -\frac{\partial P_0}{\partial \xi} - R\mathcal{J}h(\xi)\frac{\partial U_0}{\partial \xi}\,, \tag{3.7}$$

$$\frac{\partial \mathbf{V}_0}{\partial \xi} + R\left\{\frac{\partial \mathbf{V}_0}{\partial t} + S_0 \frac{\partial \mathbf{V}_0}{\partial \xi} + \mathbf{V}_0 \cdot \nabla \mathbf{V}_0\right\} = -\nabla P_0 + \nabla F_0 \frac{\partial P_0}{\partial \xi} - R\mathcal{J}h(\xi)\frac{\partial \mathbf{V}_0}{\partial \xi} - RG\nabla F_0 + p'_a(0^\pm, t)\nabla F_0\,, \tag{3.8}$$

while the flame front is governed by

$$F_{0,t} = U_0 - \mathbf{V}_0 \cdot \nabla F_0 - \left\{(1 + (\nabla F_0)^2)^{\frac{1}{2}} - 1\right\}\,, \tag{3.9}$$

where $h(\xi)$ is the Heaviside step function, $\mathcal{J} = [u_a]$, and $S_0 = U_0 - F_{0,t} - \mathbf{V}_0 \cdot \nabla F_0$. Matching with the outer acoustic solution requires that

$$U_0 \to 0\,, \quad \mathbf{V}_0 \to 0\,, \quad P_{0,\xi} \to 0 \quad \text{as} \quad \xi \to \pm\infty\,. \tag{3.10}$$

The unsteady pressure and transverse velocity jumps are

$$[P_0] = 0\,, \quad [\mathbf{V}_0] = -q\nabla F_0/(1 + (\nabla F_0)^2)^{1/2}\,. \tag{3.11}$$

The hydrodynamic motion affects the ambient acoustic regions by inducing a longitudinal velocity jump. To derive this key result, we take the spatial average of Eq. (3.6) in the (η, ζ) plane, and integrate with respect to ξ to obtain $\overline{U_0} = \overline{\mathbf{V}_0 \cdot \nabla F_0}$, where the overbar denotes the mentioned spatial average. Inserting the first relation in Eq. (3.5) into Eq. (2.14), and taking the spatial average and using the second relation in Eq. (3.11), we find

$$\mathcal{J} = [u_a] = q\left\{\overline{(1 + (\nabla F_0)^2)^{\frac{1}{2}}} - 1\right\}\,. \tag{3.12}$$

On the scale of acoustic wavelength, the right-hand side is equivalent to the rate of a concentrated unsteady heat release, which is shown to be proportional to the change of the surface area of the flame.

The jump condition for U_0 becomes

$$[U_0] = q\left\{(1 + (\nabla F_0)^2)^{-\frac{1}{2}} - \overline{(1 + (\nabla F_0)^2)^{\frac{1}{2}}}\right\}\,. \tag{3.13}$$

The hydrodynamic equations, Eqs. (3.6)–(3.9), and the acoustic equations Eq. (3.3) form an overall interactive system via Eq. (3.4): the acoustic pressure modulates the flame, which in turn drives sound by producing unsteady heat release. This system uses two distinct spatial variables to describe two distinct motions so that, in terms of $\tilde{\xi}$, the acoustic motion has an $O(1)$ characteristic speed (see Eq. (3.3)), comparable with the hydrodynamic velocity. This has a significant advantage from the numerical point of view, because the acoustic speed does not impose a severe restriction on the time step.

4. A weakly nonlinear case

A flat flame may become unstable owing to differential diffusivity of mass and heat, or to the hydrodynamic effect associated with gas expansion. The latter is the D-L instability mentioned in Section 1. An interesting question is: how large-scale combustion instability is related to flame instabilities, which occur over small scales over which the unsteady flow can be treated as incompressible. A natural proposal is that combustion instability arises when acoustic modes of the chamber are excited and amplified by the flame instabilities through mutual resonance. D-L instability perhaps is the most important candidate for driving combustion instability since, for most mixtures, the Lewis number is close to unity so that the instability due to differential diffusivity is ruled out.

In general, D-L instability occurs at all wavenumbers. However it can be stabilised by gravity effect, which introduces a small-wavenumber cut-off (Pelce & Clavin 1982). The mode with this cut-off wavenumber is nearly neutral. On the other hand, an acoustic mode is neutral on a linear basis. A mutual interaction can take place between the two when their magnitudes are still small. Such a weakly-nonlinear coupling will be analysed by using the general formulation in Section 3. The present analysis is motivated by the experiments of Searby (1992), where such an effect apparently operates.

4.1. *Analysis of the hydrodynamics of the flame*

For simplicity, we assume that the flame is two dimensional. The flame is stable when the flame speed U_L is less than the critical value $U_L = (gh^*/(\pi(1+q)))^{\frac{1}{2}}$, as was shown by Pelce & Clavin (1982); see also below. Suppose that the magnitude of the nearly neutral D-L mode is of $O(\epsilon)$. Then the weakly nonlinear interaction takes place over the time scale of $O(\epsilon^{-2})$ (Stuart 1960), and thus we introduce the slow variable

$$\tau = \epsilon^2 t\,. \tag{4.1}$$

In keeping with this, U_L is allowed to deviate from its critical value by $O(\epsilon^2)$, and thus we write

$$\frac{gh^*}{U_L^2} = \pi(1+q) + \epsilon^2 g_d \equiv G_c + \epsilon^2 g_d \quad \text{with} \quad g_d = O(1)\,. \tag{4.2}$$

To take account of the effect of Markstein length, we assume that $\delta = O(\epsilon^2)$, and without losing generality we take $\epsilon^2 = \delta$.

The velocity and pressure in the hydrodynamic region expand as

$$(U_0, V_0, P_0) = \epsilon(\hat{U}_1, \hat{V}_1, \hat{P}_1) + \epsilon^2(\hat{U}_2, \hat{V}_2, \hat{P}_2) + \epsilon^3(\hat{U}_3, \hat{V}_3, \hat{P}_3) + \dots\,. \tag{4.3}$$

The expansion of F_0 is somewhat unusual and has the form

$$F_0 = \hat{F}_0(\tau) + \epsilon\hat{F}_1 + \epsilon^2\hat{F}_2 + \epsilon^3\hat{F}_3 + \dots\,, \tag{4.4}$$

where the $O(1)$ term is due to the advection of the front by the accumulated streaming effect. By substituting the expansion into Eqs. (3.6)–(3.9) and expanding to $O(\epsilon^3)$, we obtain a sequence of equations at $O(\epsilon^n)$ $(n = 1, 2, 3)$.

The leading-order solution is given by (cf. Pelce & Clavin 1982)

$$\left.\begin{aligned}(\hat{U}_1,\, \hat{P}_1,\, \hat{F}_1) &= A(\tau)\left\{(-P^{\pm}\,\mathrm{e}^{-k\xi} + C^{\pm}),\, (P^{\pm}\,\mathrm{e}^{-k\xi} - R_{\pm}G_cF_1),\, F_1\right\}(\mathrm{e}^{\mathrm{i}\,k\eta} + c.c.)\\ \hat{V}_1 &= A(\tau)P^{\pm}\,\mathrm{e}^{-k\xi}(\mathrm{i}\,\mathrm{e}^{\mathrm{i}\,k\eta} + c.c.)\end{aligned}\right\} \tag{4.5}$$

where A is the amplitude function of the D-L mode, and $C^- = 0$ to satisfy the upstream matching condition. The wavenumber $k = \pi$ so that $\hat{V}_1 = 0$ at $\eta = 0, 1$. The front

equation implies that $P^- = 0$, while the jump conditions are given by the linearized version of Eq. (3.11) and Eq. (3.13), i.e.

$$P^+ - R_+ G_c F_1 = -R_- G_c F_1, \quad -P^+ + C^+ = 0, \quad P^+ = -qkF_1 \ .$$

The requirement of a non-zero solution gives the eigen-relation: $gh^*/U_L^2 = (1+q)\pi$. The eigenfunction is normalized by setting $F_1 = 1$, and then $P^+ = C^+ = -q\pi \equiv P$.

The $O(\epsilon^2)$ terms in Eq. (4.3) and Eq. (4.4) are governed by the following equations

$$\frac{\partial \hat{U}_2}{\partial \xi} + \frac{\partial \hat{V}_2}{\partial \eta} = \frac{\partial \hat{V}_1}{\partial \xi}\frac{\partial \hat{F}_1}{\partial \eta} \ , \tag{4.6}$$

$$R\frac{\partial \hat{U}_2}{\partial t} + \frac{\partial \hat{U}_2}{\partial \xi} = -\frac{\partial \hat{P}_2}{\partial \xi} - R\Big\{\hat{U}_1\frac{\partial \hat{U}_1}{\partial \xi} + \hat{V}_1\frac{\partial \hat{U}_1}{\partial \eta}\Big\} \ , \tag{4.7}$$

$$R\frac{\partial \hat{V}_2}{\partial t} + \frac{\partial \hat{V}_2}{\partial \xi} = -\frac{\partial \hat{P}_2}{\partial \eta} - R\Big\{\hat{U}_1\frac{\partial \hat{V}_1}{\partial \xi} + \hat{V}_1\frac{\partial \hat{V}_1}{\partial \eta}\Big\} \tag{4.8}$$

$$+\frac{\partial \hat{P}_1}{\partial \xi}\frac{\partial \hat{F}_1}{\partial \eta} - RG_c\frac{\partial \hat{F}_2}{\partial \eta} + p'_{a,1}(0^{\pm},t)\frac{\partial \hat{F}_1}{\partial \eta} \ , \tag{4.9}$$

$$\hat{F}_{2,t} = \hat{U}_2(0^-,\eta,t) - \hat{V}_1(0,\eta,t)\frac{\partial \hat{F}_1}{\partial \eta} - \frac{1}{2}\Big(\frac{\partial \hat{F}_1}{\partial \eta}\Big)^2 \ , \tag{4.10}$$

subject to the jump conditions

$$\Big[\hat{U}_2\Big] = -\frac{1}{2}q\Big[(\nabla \hat{F}_1)^2 + \overline{(\nabla \hat{F}_1)^2}\Big] \ , \quad \Big[\hat{V}_2\Big] = -q\,\nabla \hat{F}_2 \ , \quad \Big[\hat{P}_2\Big] = 0 \ . \tag{4.11}$$

As the forcing terms on the right-hand side indicate, there exists a mutual interaction between the sound and flame as well as the self-interaction of the flame. The solution, for $\hat{U}_2$ and $\hat{F}_2$ say, takes the form

$$\left.\begin{array}{rcl} \hat{U}_2 &=& \hat{U}_{2,a}AB(\mathrm{e}^{\mathrm{i}k\eta} + c.c.)\,\mathrm{e}^{\mathrm{i}\omega t} + \hat{U}_{2,2}A^2(\mathrm{e}^{2\mathrm{i}k\eta} + c.c.) + \hat{U}_{2,0}A^2 \\ \hat{F}_2 &=& \hat{F}_{2,a}AB(\mathrm{i}\,\mathrm{e}^{\mathrm{i}k\eta} + c.c.)\,\mathrm{e}^{\mathrm{i}\omega t} + \hat{F}_{2,2}A^2(\mathrm{e}^{2\mathrm{i}k\eta} + c.c.) \end{array}\right\} \ . \tag{4.12}$$

At cubic order, the governing equations are found to be

$$\frac{\partial \hat{U}_3}{\partial \xi} + \frac{\partial \hat{V}_3}{\partial \eta} = \frac{\partial \hat{V}_1}{\partial \xi}\frac{\partial \hat{F}_2}{\partial \eta} + \frac{\partial \hat{V}_2}{\partial \xi}\frac{\partial \hat{F}_1}{\partial \eta} \ , \tag{4.13}$$

$$R\frac{\partial \hat{U}_3}{\partial t} + \frac{\partial \hat{U}_3}{\partial \xi} = -\frac{\partial \hat{P}_3}{\partial \xi} - RA'\hat{U}_1 - R\Big\{\hat{U}_1\frac{\partial \hat{U}_2}{\partial \xi} + \hat{U}_2\frac{\partial \hat{U}_1}{\partial \xi} + \hat{V}_1\frac{\partial \hat{U}_2}{\partial \eta} + \hat{V}_2\frac{\partial \hat{U}_1}{\partial \eta}\Big\}$$

$$+R\Big\{\hat{F}_{0,\tau} + \hat{F}'_{2,a} + \hat{V}_1\frac{\partial \hat{F}_1}{\partial \eta}\Big\}\frac{\partial \hat{U}_1}{\partial \xi} - R\mathcal{J}h(\xi)\frac{\partial \hat{U}_1}{\partial \xi} + Pr\,\nabla^2\hat{U}_1 \ , \tag{4.14}$$

$$R\frac{\partial \hat{V}_3}{\partial t} + \frac{\partial \hat{V}_3}{\partial \xi} = -\frac{\partial \hat{P}_3}{\partial \eta} - RA'\hat{V}_1 - R\Big\{\hat{U}_1\frac{\partial \hat{V}_2}{\partial \xi} + \hat{U}_2\frac{\partial \hat{V}_1}{\partial \xi} + \hat{V}_1\frac{\partial \hat{V}_2}{\partial \eta} + \hat{V}_2\frac{\partial \hat{V}_1}{\partial \eta}\Big\}$$

$$+p'_{a,1}(0,t)\frac{\partial \hat{F}_2}{\partial \eta} + \frac{\partial \hat{P}_1}{\partial \xi}\frac{\partial \hat{F}_2}{\partial \eta} + \frac{\partial \hat{P}_2}{\partial \xi}\frac{\partial \hat{F}_1}{\partial \eta} - R_{\pm}G_c\frac{\partial \hat{F}_3}{\partial \eta}$$

$$+R\Big\{\hat{F}_{0,\tau} + \hat{F}'_{2,a} + \hat{V}_1\frac{\partial \hat{F}_1}{\partial \eta}\Big\}\frac{\partial \hat{V}_1}{\partial \xi} - R\mathcal{J}h(\xi)\frac{\partial \hat{V}_1}{\partial \xi} + Pr\,\nabla^2\hat{V}_1 \ , \tag{4.15}$$

where $\mathcal{J} = qk^2$. Expansion of the front equation gives

$$\hat{F}_{1,\tau} + \hat{F}_{3,t} = \hat{U}_3(0^-,t) - \hat{V}_1\cdot\nabla\hat{F}_2 - \hat{V}_2\cdot\nabla\hat{F}_1 - \nabla\hat{F}_1\cdot\nabla\hat{F}_2 \ . \tag{4.16}$$

To this order, it is only necessary to consider the component that coincides with the fundamental of the D-L mode, and thus we write

$$(\hat{U}_3,\,\hat{P}_3,\,\hat{F}_3)=(\hat{U}_{3,1},\,\hat{P}_{3,1},\,\hat{F}_{3,1})(\mathrm{e}^{\mathrm{i}\,k\eta}+c.c.)\;,\quad \hat{V}_3=\hat{V}_{3,1}(\mathrm{i}\,\mathrm{e}^{\mathrm{i}\,k\eta}+c.c.)\;. \tag{4.17}$$

The jump conditions at this order need some attention. A direct expansion of Eq. (3.11) and Eq. (3.13) shows that at $O(\epsilon^3)$,

$$\left[\hat{U}_3\right]=-q\,\nabla\,\hat{F}_1\cdot\nabla\hat{F}_2\;,\quad \left[\hat{P}_3\right]=0\;,\quad \left[\hat{V}_3\right]=-q\,\nabla\hat{F}_3+\frac{q}{2}(\nabla\hat{F}_1)^2\,\nabla\hat{F}_1\;. \tag{4.18}$$

However, since $\delta=O(\epsilon^2)$, the $(\epsilon\delta)$ terms in Eq. (2.10) are of the same order as the $O(\epsilon^3)$ terms in Eq. (4.5). The jumps Eqs. (2.16)-(2.17) must be added to Eq. (4.18) to give

$$\left.\begin{aligned}\left[\hat{U}_{3,1}\right] &= \tfrac{1}{2}lD(k)k^2A-2qk^2\hat{F}_{2,2}A^3\\ \left[\hat{P}_{3,1}\right] &= -lD(q)k^2A-qk^2A\\ \left[\hat{V}_{3,1}\right] &= -kqF_{3,1}-Prqk^2A+\ln(1+q)(kG_cA)+\tfrac{3}{2}qk^3A^3\end{aligned}\right\}\;. \tag{4.19}$$

The equation controlling the front motion is

$$A'=\hat{U}_{3,1}(0^-)-2k^2\hat{F}_{2,2}A^3-k\hat{V}_{2,2}(0)A^3-k^2\Big\{\frac{1+q}{q}\ln(1+q)+\frac{1}{2q}lD(q)\Big\}A\;. \tag{4.20}$$

After substituting the leading- and second-order solutions into the right-hand sides of Eqs. (4.13)-(4.15), the solution for $\hat{U}_{3,1}$, $\hat{V}_{3,1}$, etc. can be written down. Inserting it into Eq. (4.19) and Eq. (4.20), we obtain the amplitude equation

$$A'=\kappa A+\gamma_sA^3-\gamma_b|B|^2A\;, \tag{4.21}$$

$$\kappa=-\frac{q}{2(1+q)}g_d-\frac{1}{2}k^2\left\{q+\frac{1+q}{q}\Big((q+2)\ln(1+q)+lD(q)\Big)\right\}\;, \tag{4.22}$$

$$\gamma_s=\Big\{-\frac{1}{2}q+\frac{3}{2}+\frac{2}{q}\Big\}k^3=(4-q)(1+q)k^3/(2q)\;, \tag{4.23}$$

$$\gamma_b=\Big\{4(R_+-R_-)^2(1+R_+/R_-)k\omega^2\sin^2(R_-^{\frac{1}{2}}\sigma\omega L)\Big\}/\Big\{(R_++R_-)^2\omega^2+4k^2\Big\}\;. \tag{4.24}$$

4.2. *Analysis of the acoustics*

The pressure and velocity of the acoustic fluctuation are expanded as

$$p_a=\epsilon B(\tau)p_{a,1}+\epsilon^3p_{a,2}+\dots\;,\quad u_a=\epsilon B(\tau)u_{a,1}+\epsilon^3u_{a,2}+\dots\;, \tag{4.25}$$

where B is the amplitude function.

To leading order, $p_{a,1}$ and $u_{a,1}$ satisfy Eq. (3.3), and they have the solution

$$\left.\begin{aligned}p_{a,1} &= \mathrm{e}^{\mathrm{i}\,\omega t}\Big[a_r^{\pm}\,\mathrm{e}^{-\mathrm{i}\,R_\pm^{\frac{1}{2}}\omega\tilde{\xi}}+a_l^{\pm}\,\mathrm{e}^{\mathrm{i}\,R_\pm^{\frac{1}{2}}\omega\tilde{\xi}}\Big]\\ u_{a,1} &= \mathrm{e}^{\mathrm{i}\,\omega t}\,R_\pm^{-\frac{1}{2}}\Big[a_r^{\pm}\,\mathrm{e}^{-\mathrm{i}\,R_\pm^{\frac{1}{2}}\omega\tilde{\xi}}-a_l^{\pm}\,\mathrm{e}^{\mathrm{i}\,R_\pm^{\frac{1}{2}}\omega\tilde{\xi}}\Big]\end{aligned}\right\} \tag{4.26}$$

where $a_r^{\pm}$ and $a_l^{\pm}$ are constants, and for convenience we take $a_l^-=\mathrm{e}^{\mathrm{i}\,R_-^{\frac{1}{2}}\sigma\omega L}$. The end conditions are: $u_{a,1}=0$ at $\tilde{\xi}=-\sigma L$, and $p_{a,1}=0$ at $\tilde{\xi}=(1-\sigma)L$, where L is related to the dimensional length of the duct l^* by $L=Ml^*/h^*$, and σ is a parameter characterizing the mean position of the flame front. Both $u_{a,1}$ and $p_{a,1}$ are continuous across the flame,

i.e. $[u_{1,a}] = 0$ and $[p_{1,a}] = 0$, as the expansion of Eq. (3.4) shows. Application of these conditions leads to the dispersion relation of the acoustic mode (cf. Clavin *et al.* 1990),

$$(R_+/R_-)^{\frac{1}{2}} \tan(R_-^{\frac{1}{2}}\sigma\omega L)\tan(R_+^{\frac{1}{2}}(1-\sigma)\omega L) = 1 \,. \tag{4.27}$$

Inserting Eq. (4.25) into Eq. (3.3), and solving the resultant equations at $O(\epsilon^3)$, we find

$$p_{a,2} = \mathrm{e}^{\mathrm{i}\,\omega t}\Big\{\Big(b_r^{\pm}\,\mathrm{e}^{-\mathrm{i}\,R_{\pm}^{\frac{1}{2}}\omega\tilde{\xi}} + b_l^{\pm}\,\mathrm{e}^{\mathrm{i}\,R_{\pm}^{\frac{1}{2}}\omega\tilde{\xi}}\Big) - R_{\pm}^{\frac{1}{2}}B'\tilde{\xi}\,\Big(a_r^{\pm}\,\mathrm{e}^{-\mathrm{i}\,R_{\pm}^{\frac{1}{2}}\omega\tilde{\xi}} - a_l^{\pm}\,\mathrm{e}^{\mathrm{i}\,R_{\pm}^{\frac{1}{2}}\omega\tilde{\xi}}\Big)\Big\} \,,$$

$$u_{a,2} = \mathrm{e}^{\mathrm{i}\,\omega t}\Big\{R_{\pm}^{-\frac{1}{2}}\Big(b_r^{\pm}\,\mathrm{e}^{-\mathrm{i}\,R_{\pm}^{\frac{1}{2}}\omega\tilde{\xi}} - b_l^{\pm}\,\mathrm{e}^{\mathrm{i}\,R_{\pm}^{\frac{1}{2}}\omega\tilde{\xi}}\Big) - B'\tilde{\xi}\Big(a_r^{\pm}\,\mathrm{e}^{-\mathrm{i}\,R_{\pm}^{\frac{1}{2}}\omega\tilde{\xi}} + a_l^{\pm}\,\mathrm{e}^{\mathrm{i}\,R_{\pm}^{\frac{1}{2}}\omega\tilde{\xi}}\Big)\Big\} \,.$$

It follows from substituting F_0 into Eq. (3.4) and expanding to $O(\epsilon^3)$ that

$$[p_{2,a}] = 0 \,, \qquad [u_{2,a}] = 2qk^2\hat{F}_{2,a}A^2B \,,$$

The above relations together with the end conditions, $u_{a,2} = 0$ at $\tilde{\xi} = -\sigma L$ and $p_{a,2} = 0$ at $\tilde{\xi} = (1-\sigma)L$, lead to the amplitude equation for the acoustic mode:

$$B' = \chi A^2 B \,, \tag{4.28}$$

$$\chi = \frac{\mathrm{i}\,2qk^3R_-^{-\frac{1}{2}}(R_+ - R_-)\Lambda}{L(\mathrm{i}(R_+ + R_-)\omega + 2k)} \,, \tag{4.29}$$

$$\Lambda = \frac{\tan(R_-^{\frac{1}{2}}\sigma\omega L)}{\sigma\sec^2(R_-^{\frac{1}{2}}\sigma\omega L) + (1-\sigma)(R_+/R_-)\sec^2(R_+^{\frac{1}{2}}(1-\sigma)\omega L)\tan^2(R_-^{\frac{1}{2}}\sigma\omega L)} \,. \tag{4.30}$$

4.3. *Amplitude equations*

The sound-flame interaction is thus described by the coupled amplitude equations

$$A'(\tau) = \kappa A + \gamma_s A^3 - \gamma_b|B|^2A \,, \quad B'(\tau) = \chi A^2 B \,. \tag{4.31}$$

Now if the flame amplitude A is taken to be a constant, then the equation for B reduces to the result of Pelce & Rochwerger (1992) with B growing exponentially. In their model, the coupling is one-way. The present work includes the back-effect of the sound on the flame, leading to a better description of the experiments of Searby (1992); see below.

The effects of the nonlinear interactions become clear if one inspects the signs of the coefficients. According to Eq. (4.29) and Eq. (4.24), $\Re(\chi) > 0$ and $\gamma_b > 0$, indicating that the flame always acts to amplify the acoustic field, while sound inhibits the flame. Note also that γ_s is positive (negative) for $q < 4$ ($q > 4$), and hence the self-nonlinearity of the flame is destabilizing for $q < 4$ and stabilizing for $q > 0$.

Assuming that the flame and sound are weak initially so that the nonlinear terms in the amplitude equations can be ignored, then the appropriate initial conditions are

$$A \sim \mathrm{e}^{\kappa\tau} \,, \quad B \sim b_0\exp\{\chi\,\mathrm{e}^{2\kappa\tau}\} \quad \text{as} \quad \tau \to -\infty \,, \tag{4.32}$$

where $b_0 \ll 1$. Figure 2 shows the evolution of A and B for $b_0 = 0.1, 0.05$, (with γ_s, γ_b and χ being arbitrarily taken to be unity). The background noise remains constant when the flame is of small amplitude, but starts to amplify when the latter has gained a certain strength. The amplification is extremely abrupt, taking place primarily when the curved flame evolves into a flat one. The flattening of the flame is caused by the back-reaction of the sound. Eventually the sound saturates at a constant level. For comparison purposes,

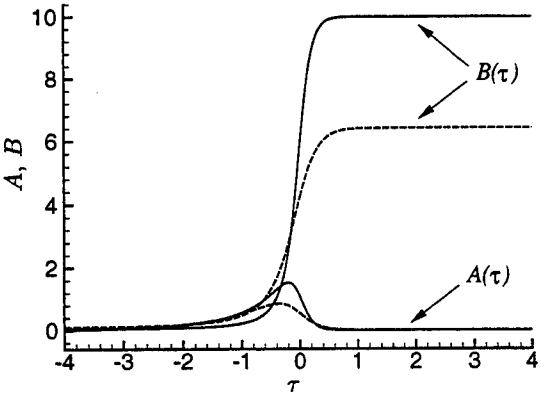

FIGURE 2. Nonlinear evolution of the acoustic amplitude B and flame amplitude A. —— $b_0 = 0.05$; ---- $b_0 = 0.1$.

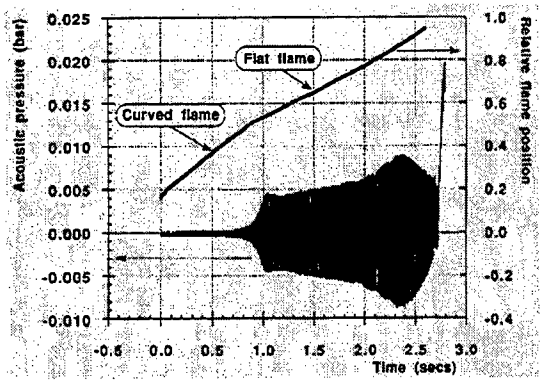

FIGURE 3. Time traces of the acoustic pressure and flame position from Searby's experiment (Fig. 3b of Searby (1992)).

Searby's experimental results are shown in Fig. 3. It is clear that the present theoretical predictions are entirely consistent with his observations in the qualitative sense.

5. Conclusions

In this paper, the acoustic-flame coupling, the key process underlying combustion instability, is studied by using matched-asymptotic-expansion techniques based on the assumptions of large activation energy and low Mach number. A general asymptotic formulation was given for the lower-frequency regime of practical relevance, for which the acoustic source is found to be directly linked to the shape of the flame. The basic framework was then used to study the weakly nonlinear interaction between an acoustic mode of the duct and a nearly-neutral D-L instability mode. A system of coupled amplitude equations was derived, and was found able to describe the experimental observations of Searby (1992) qualitatively.

We note that the present analysis can be extended to include the effect of 'weak turbulence' (i.e. convected gusts) in the oncoming fresh mixture. It would be interesting to solve the fully-nonlinear system in Section 3 numerically, with a view to addressing whether or not the coupling leads to self-sustained large-amplitude pressure oscillations.

We would like to thank Prof. Norbert Peters, Dr. Heinz Pitsch and Clifton Wall for helpful discussions.

REFERENCES

BLOXSIDGE, G. J., DOWLING, A. P. & LANGHORNE, P. J. 1988 Reheat buzz: an acoustically coupled combustion instability. Part II. Theory. *J. Fluid Mech.* **193**, 445-473.

CLAVIN, P. 1985 Dynamics behaviour of premixed flame fronts in laminar and turbulent flows. *Prog. Energy Combus. Sci.* **11**, 1-59.

CLAVIN, P. 1994 Premixed combustion and gasdynamics. *Ann. Rev. Fluid Mech.* **26**, 321-352.

CLAVIN, P, PELCE, P. & HE, L. 1990 One-dimensional vibratory instability of planar flames propagating in tubes. *J. Fluid Mech.* **216**, 299-322.

DOWLING, A. P. 1995 The calculation of thermoacoustic oscillations. *J. Sound Vib.* **180**, 557-581.

HARTEN, A. V., KAPILA, A. K. & MATKOWSKY, B. J. 1984 Acoustic coupling of flames. *SIAM J. Appl. Math.* **44**, 982-995.

LANGHORNE, P. J. 1988 Reheat buzz: an acoustically coupled combustion instability. Part I. Experiment. *J. Fluid Mech.* **193**, 417-443.

MARKSTEIN, G. H. 1970 Flames as amplifiers of fluid mechanical disturbances. *Proc. 6th Natl. Congr. Appl. Mech.*, Cambridge, Mass., pp.11-33.

MATALON, M. & MATKOWSKY, B. J. 1982 Flames as gasdynamic discontinuities. *J. Fluid Mech.* **124**, 239-259.

MATKOWSKY, B. J. & SIVASHINSKY, G. I. 1979 An asymptotic derivation of two models in flame theory associated with the constant density approximation. *SIAM J. Appl. Math.* **37**, 686-699.

PELCE, P. & CLAVIN, P. 1982 Influence of hydrodynamics and diffusion upon the stability limits of laminar premixed flames. *J. Fluid Mech.* **124**, 219-237.

PELCE, P. & ROCHWERGER, D. 1992 Vibratory instability of cellular flames propagating in tubes. *J. Fluid Mech.* **239**, 293-307.

POINSOT, T. J., TROUVE, A. C., VEYNANTE, D. P., CANDEL, S.M. & ESPOSITO, E.J. 1987 Vortex-driven acoustically coupled combustion instabilities. *J. Fluid Mech.* **177**, 265-292.

SCHADOW, K. C. & GUTMARK, E. 1992 Combustion instability related to vortex shedding in dump combustors and their passive control. *Prog. Energy Combus. Sci.* **18**, 117-132.

SEARBY, G. 1992 Acoustic instability in premixed flames. *Comb. Sci. Technol.* **81**, 221-231.

STUART, J. T. 1960 On the nonlinear mechanisms of wave disturbances in stable and unstable parallel flows. Part I: The basic behaviour in plane Poisuille flow. *J. Fluid Mech.* **9**, 353-370.

WILLIAMS, F. A. 1985 *Combustion Theory.* Benjamin Cummings, Redwood City.

YU, K. H., TROUVE, A. & DAILY, J. W. 1991 Low-frequency pressure oscillations in a model ramjet combustor. *J. Fluid Mech.* **232**, 47-72.

DNS of transition in hypersonic boundary-layer flows including high-temperature gas effects

By C. Stemmer AND N. N. Mansour

1. Motivation and Objective

Wind-tunnel experiments at hypersonic Mach numbers above 10 are extremely difficult to undertake and facilities are limited. Additionally, the stagnation conditions for free flight under atmospheric conditions can not be reproduced. This results in a limited portability of the wind-tunnel results to atmospheric conditions. Therefore, numerical investigations of hypersonic transition can be extremely valuable in developing an understanding of the transition process at hypersonic speeds.

The objective of this effort is to develop an understanding of effects of nonequilibrium chemistry on transition. Our approach is to compare hypersonic transition on a flat plate under nonequilibrium chemical and thermal conditions to hypersonic transition under equilibrium conditions.

In the 1950's and 60's, a series of hypersonic experiments was conducted in free flight. The transition location could be found but no details on the transitional structures could be recorded in these experiments (see Schneider, 1999, for a comprehensive review of supersonic and hypersonic experiments). Schneider also notes that the angles of attack of the test vehicles are uncertain. An ongoing experiment on transition at $Ma = 21$ in Novosibirsk, Russia Mironov & Maslov 2000, promises experimental verification of the numerical findings to some extent. Further detailed experiments on transition at hypersonic speeds cannot be expected in the near future.

2. Governing Equations

In order not to confuse the index notations, the index i refers to the species 1-5 and no summation is implied on this index, whereas the indices j, k and l refer to the Cartesian directions x, y and z and summation from 1-3 is implied.

The continuity equation for chemically-reacting compressible flows becomes

$$\frac{\partial \rho_i}{\partial t} + \frac{\partial}{\partial x_j}(\rho_i(u_j + u_{i,j}^D)) = W_i, \tag{2.1}$$

where W_i represents the species production terms (see Eq. 2.19) and u_D the diffusion velocities (see Eq. 2.16). Rewriting this equation with the species concentrations rather than the densities, it becomes

$$\rho \frac{Dc_i}{Dt} + \frac{\partial}{\partial x_j}(\rho_i u_{i,j}^D) = W_i, \tag{2.2}$$

where the species concentrations are given by

$$c_i = \frac{\rho_i}{\rho}. \tag{2.3}$$

Note that since

$$\sum_i c_i = 1, \tag{2.4}$$

only $(i-1)$ equations have to be solved.

The total mass is conserved

$$\frac{\partial \rho}{\partial t} + \frac{\partial}{\partial x_j}(\rho u_j) = 0. \tag{2.5}$$

The total momentum equations are

$$\rho \frac{Du_j}{Dt} = -\frac{\partial p}{\partial x_j} + \frac{\partial}{\partial x_k}\tau_{jk} \tag{2.6}$$

with

$$\tau_{jk} = \mu\left(\frac{\partial u_j}{\partial x_k} + \frac{\partial u_k}{\partial x_j}\right) + \delta_{jk}\,\lambda u_{l,l}. \tag{2.7}$$

The bulk viscosity is denoted by λ.

The energy equation for the total energy becomes

$$\rho\,\frac{D(e+u_j u_j/2)}{Dt} = -(q_j + q_j^{vib})_{,j} - (pu_j)_{,j} + \frac{\partial}{\partial x_j}(u_k\,\tau_{jk}) + \sum_i \left((\rho_i h_i u_{i,j}^D)_{,j}\right) \tag{2.8}$$

where e describes the internal energy.

The energy equation for the vibrational energy e^{vib} in the case of vibrational nonequilibrium is as follows

$$\frac{\partial e^{vib}}{\partial t} + \frac{\partial}{\partial x_j}\left(e^{vib}(u_j + u_j^D)\right) = -q_j^{vib} + Q^{T-V} + Q^{chem}. \tag{2.9}$$

For the equilibrium case, the vibrational temperature T^{vib} is equal to the translational temperature T and eq. (2.33) is used with T replacing T^{vib}.

The internal energy for the complete system is a sum of the species internal energies taking into account their concentrations,

$$e = \sum_i c_i e_i. \tag{2.10}$$

The equilibrium internal energy for one species consists of the translational, rotational and vibrational energy and the heat of formation. Note that atoms (N and O) deliver no vibrational and rotational contribution to the internal energy

$$e_i = e_i^{trans}(T) + e_i^{rot}(T) + e_i^{vib}(T^{vib}) + \Delta h_i^f. \tag{2.11}$$

The internal energy contributions from translation, rotation and vibration are assembled through the specific heats at constant volume as

$$e_i = c_{v,i}^{trans} T + c_{v,i}^{rot} T + c_{v,i}^{vib} T^{vib} + \Delta h_i^f. \tag{2.12}$$

The enthalpy is expressed as

$$h_i = c_{p,i}^{trans} T + c_{p,i}^{rot} T + c_{p,i}^{vib} + \Delta h_i^f. \tag{2.13}$$

The internal energy and enthalpy are connected through

$$h = e + \frac{p}{\rho}. \tag{2.14}$$

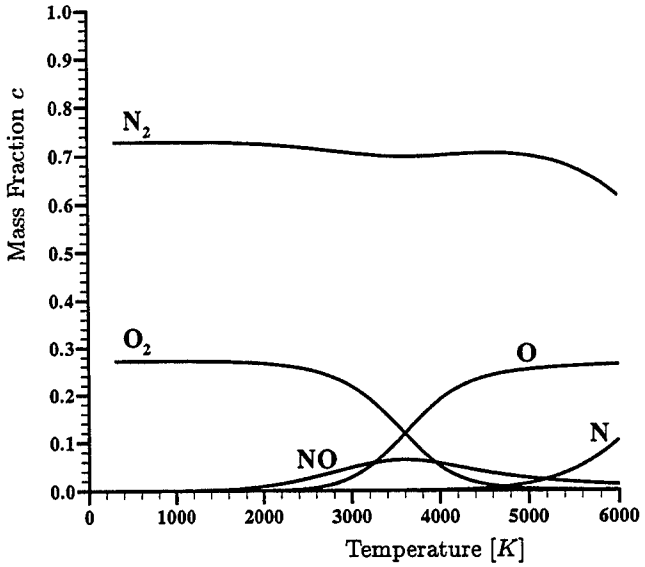

FIGURE 1. Composition of equilibrium air at 1 atm.

The fluid is treated as an ideal gas, where the following equation holds

$$p = \sum_i p_i = \sum_i \rho_i \frac{\mathcal{R}}{M_i} T. \tag{2.15}$$

For the diffusion velocities u_D, Fick's law of diffusion is employed

$$\rho_i u_j^D = -\rho D \frac{\partial c_i}{\partial x_j}, \tag{2.16}$$

where the diffusion coefficient is independent of the species.

The translational and the vibrational heat conduction is described through Fourier's law

$$q_j = -\kappa \frac{\partial T}{\partial x_j}, \qquad q_j^{vib} = -\kappa^{vib} \frac{\partial T^{vib}}{\partial x_j}. \tag{2.17}$$

2.1. *Chemical Modeling*

A five species (N_2, O_2, N, O, NO) model for air will be applied. The equilibrium composition for air at constant pressure over temperature is shown in Fig. 1. The reaction rates (k_f and k_b) are modeled in an Arrhenius manner according to (Park 1989). The model proposed by Park takes into account the translational as well as the vibrational temperature T^{vib} for each species. The vibrational temperature describes the vibrational relaxation, whereas a translational temperature includes the rotational relaxation, which is assumed to take place instantly. It only takes 9-12 molecule collisions for the rotational relaxation to complete, whereas the vibrational relaxation takes 10^5 molecule collisions to reach a steady state (the same order of magnitude as for the chemical relaxation). The seventeen chemical reactions thought to be sufficient for the modeling of air under the conditions of interest are as follows: (The reaction partner M represents any of the

five species considered; see Park, 1989.)

$$\begin{aligned} &N_2 + M \rightleftharpoons N + N + M && (reac.\ 1)\\ &O_2 + M \rightleftharpoons O + O + M && (reac.\ 2)\\ &NO + M \rightleftharpoons N + O + M && (reac.\ 3)\\ &N_2 + O \rightleftharpoons NO + N && (reac.\ 4)\\ &NO + O \rightleftharpoons N + O_2 && (reac.\ 5) \end{aligned} \tag{2.18}$$

with the production terms ($M_{N_2}, M_{O_2}, M_{NO}, M_N and M_O$ represent the species masses) :

$$\begin{aligned} W_{N_2} &= M_{N_2}(R_1 + R_4)\\ W_{O_2} &= M_{O_2}(R_2 - R_5)\\ W_{NO} &= M_{NO}(R_3 - R_4 + R_5)\\ W_N &= M_N(-2R_1 - R_3 - R_4 - R_5)\\ W_O &= M_O(-2R_2 - R_3 + R_4 + R_5) \end{aligned} \tag{2.19}$$

where

$$\begin{aligned} R_1 &= -\sum_i k_{f,1i}\left(\frac{\rho_{N_2}}{M_{N_2}}\right)\left(\frac{\rho_i}{M_i}\right) + \sum_i k_{b,1i}\left(\frac{\rho_N}{M_N}\right)^2\left(\frac{\rho_i}{M_i}\right)\\ R_2 &= -\sum_i k_{f,2i}\left(\frac{\rho_{O_2}}{M_{O_2}}\right)\left(\frac{\rho_i}{M_i}\right) + \sum_i k_{b,2i}\left(\frac{\rho_O}{M_O}\right)^2\left(\frac{\rho_i}{M_i}\right)\\ R_3 &= -\sum_i k_{f,3i}\left(\frac{\rho_{NO}}{M_{NO}}\right)\left(\frac{\rho_i}{M_i}\right) + \sum_i k_{b,3i}\left(\frac{\rho_N}{M_N}\right)\left(\frac{\rho_O}{M_O}\right)\left(\frac{\rho_i}{M_i}\right)\\ R_4 &= -k_{f,4}\left(\frac{\rho_{N_2}}{M_{N_2}}\right)\left(\frac{\rho_O}{M_O}\right) + k_{b,4}\left(\frac{\rho_{NO}}{M_{NO}}\right)\left(\frac{\rho_N}{M_N}\right)\\ R_5 &= -k_{f,5}\left(\frac{\rho_{NO}}{M_{NO}}\right)\left(\frac{\rho_O}{M_O}\right) + k_{b,5}\left(\frac{\rho_{O_2}}{M_{O_2}}\right)\left(\frac{\rho_N}{M_N}\right), \end{aligned} \tag{2.20}$$

and the forward reaction rates k_f for the five reactions considered are

$$\begin{aligned} k_{f,1} &= 2.0\times10^{15}\,(\sqrt{TT^{vib}})^{-3/2}\exp(-(59,500/\sqrt{TT^{vib}})) \quad \text{for M = molecule}\\ k_{f,1} &= 1.0\times10^{16}\,(\sqrt{TT^{vib}})^{-3/2}\exp(-(59,500/\sqrt{TT^{vib}})) \quad \text{for M = atom}\\ k_{f,2} &= 7.0\times10^{15}\,(\sqrt{TT^{vib}})^{-8/5}\exp(-(113,200/\sqrt{TT^{vib}})) \quad \text{for M = molecule}\\ k_{f,2} &= 3.0\times10^{16}\,(\sqrt{TT^{vib}})^{-8/5}\exp(-(113,200/\sqrt{TT^{vib}})) \quad \text{for M = atom}\\ k_{f,3} &= 5.0\times10^{9}\exp(-(75,500/\sqrt{TT^{vib}})) \quad \text{for M= } N_2,\ O_2\\ k_{f,3} &= 1.1\times10^{11}\exp(-(75,500/\sqrt{TT^{vib}})) \quad \text{for M= N, O, NO}\\ k_{f,4} &= 6.4\times10^{11}\,(\sqrt{TT^{vib}})^{-1}\exp(-(38,370/\sqrt{TT^{vib}}))\\ k_{f,5} &= 8.4\times10^{6}\exp(-(19,450/\sqrt{TT^{vib}})). \end{aligned} \tag{2.21}$$

The backward reaction rates k_b are calculated from the equilibrium rates through

$$k_{b,i} = k_{f,i}/K_{eq,i} \tag{2.22}$$

The equilibrium rates are defined as

$$\begin{aligned}
K_{eq,1} &= \exp(0.50989 \cdot (\sqrt{TT^{vib}}/10,000) + 2.4773 + 1.7132 \cdot \log_{10}(10,000/\sqrt{TT^{vib}}) \\
&\quad -6.5441 \cdot (10,000/\sqrt{TT^{vib}}) + 0.29591 \cdot (10^8/(TT^{vib})) \\
K_{eq,2} &= \exp(1.4766 \cdot (\sqrt{TT^{vib}}/10,000) + 1.6291 + 1.2153 \cdot \log_{10}(10,000/\sqrt{TT^{vib}}) \\
&\quad -11.457 \cdot (10,000/\sqrt{TT^{vib}}) - 0.009444 \cdot ((10^8/(TT^{vib})) \\
K_{eq,3} &= \exp(0.50765 \cdot (\sqrt{TT^{vib}}/10,000) + 0.73575 + 0.48042 \cdot \log_{10}(10,000/\sqrt{TT^{vib}}) \\
&\quad -7.4979 \cdot (10,000/\sqrt{TT^{vib}}) - 0.16247 \cdot ((10^8/(TT^{vib})) \\
K_{eq,4} &= \exp(0.96921 \cdot (\sqrt{TT^{vib}}/10,000) + 0.89329 + 0.73531 \cdot \log_{10}(10,000/\sqrt{TT^{vib}}) \\
&\quad -3.9596 \cdot (10,000/\sqrt{TT^{vib}}) + 0.006818 \cdot ((10^8/(TT^{vib})) \\
K_{eq,5} &= \exp(-0.002428 \cdot (\sqrt{TT^{vib}}/10,000) - 1.7415 - 1.2331 \cdot \log_{10}(10,000/\sqrt{TT^{vib}}) \\
&\quad -0.95365 \cdot (10,000/\sqrt{TT^{vib}}) - 0.04585 \cdot ((10^8/(TT^{vib}))
\end{aligned} \tag{2.23}$$

2.2. *Modeling of physical and transport properties*

The following relations are for a mixture of chemically-reacting gases.

2.2.1. *Specific heat at constant volume*

The specific heat at constant volume c_v for atoms is described through:

$$c_{v,i} = c_{v,i}^{trans} = \frac{3}{2} R_i. \tag{2.24}$$

The partial derivatives of the species concentrations with respect to the temperature are the contributions due to chemical reactions.

The specific heat at constant volume c_v for molecules (Vincenti & Kruger 1982) is made up as follows,

$$\begin{aligned}
c_{v,i} &= c_{v,i}^{trans} + c_{v,i}^{rot} + c_{v,i}^{vib} \\
&= \frac{3}{2} R_i + R_i + \frac{(\Theta_i^{vib}/T^{vib})^2 e^{\Theta_i^{vib}/T^{vib}}}{(e^{\Theta_i^{vib}/T^{vib}} - 1)^2} R_i,
\end{aligned} \tag{2.25}$$

where Θ_i^{vib} is the characteristic temperature of vibration of the molecular species.

2.2.2. *Specific heat at constant pressure*

The specific heat at constant pressure c_p is described by:

$$c_{p,i} = c_{v,i} + R_i T. \tag{2.26}$$

2.2.3. *Viscosity*

Blottner's formula will be employed for the modeling of the viscosity (Blottner, Johnson & Ellis 1971). This approximate formula is valid up to 10,000 K, far exceeding the temperature range of the flows investigated here. The coefficients A_{μ_i}, B_{μ_i} and C_{μ_i} are given by Blottner *et al.*

$$\mu_i = 0.1 \cdot \exp\left[C_{\mu_i} + (\ln T \cdot (B_{\mu_i} + \ln T \cdot A_{\mu_i}))\right]. \tag{2.27}$$

2.2.4. *Thermal conductivity*

The species' thermal conductivities are described employing Eucken's correction, given as (Hirschfelder, Curtiss & Bird 1964):

$$\kappa_i = \mu_i(\frac{5}{2}c_{v,i}^{trans} + c_{v,i}^{rot}), \qquad \kappa_i^{vib} = \mu_i(c_{v,i}^{vib}). \tag{2.28}$$

2.2.5. *Mixing rules for viscosity and thermal conductivity*

The mixing rule in a mixture of gases, according to (Wilke 1950), is

$$\mu_{mix} \approx \sum_{i=1}^{n} \frac{x_i \mu_i}{\sum_{j=1}^{n} x_j \Phi_{ij}} \tag{2.29}$$

with

$$\Phi_{ij} = \frac{\left[1 + (\mu_i/\mu_j)^{1/2} \, (M_j/M_i)^{1/4}\right]^2}{(8 + 8M_i/M_j)^{1/2}}$$

and

$$x_i = \frac{c_i/M_i}{\sum_{j=1}^{n}(c_j/M_j)}.$$

The same formula applies for the thermal conductivities, replacing the viscosity μ by the thermal conductivity k.

Further details of the physical modeling can be found, for example, in (Sarma 2000).

2.2.6. *Diffusion coefficient*

A constant Schmidt number $Sc = 0.5$ is assumed (Hudson 1996) which yields for the diffusion coefficient:

$$D = \frac{\mu}{\rho \, Sc} = \frac{2\,\mu}{\rho} \tag{2.30}$$

2.2.7. *Translational-vibrational energy exchange*

Vibrational energy is present only in the molecular species N_2, O_2 and NO, which are all modeled as harmonic oscillators. Therefore the following equations are valid. In case of the incorporation of anharmonic oscillatory molecules like CO_2, different relaxation and energy expressions have to be applied (Vincenti & Kruger 1982).

The translational-vibrational energy exchange is described through a Landau-Teller relaxation model (Vincenti & Kruger 1982) as,

$$Q^{T-V} = \sum_i c_i \frac{e_i^{vib,eq}(T) - e_i^{vib}(T^{vib})}{\tau_i}, \tag{2.31}$$

where the relaxation times are determined for each species as

$$\tau_i = \frac{1}{p_i} C_1 \exp((C_2/T)^{1/3}), \tag{2.32}$$

and the nonequilibrium vibrational energy depends on the vibrational temperature as

$$e_i^{vib} = \frac{\Theta_i^{vib}/T^{vib}}{e^{\Theta_i^{vib}/T^{vib}} - 1} R_i T^{vib}. \tag{2.33}$$

The equilibrium value for the vibrational energy $e_i^{vib,eq}$ follows the same expression, with T replacing T^{vib}.

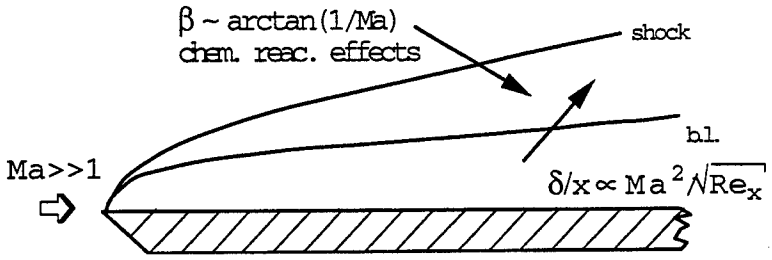

FIGURE 2. Schematic of shock location and boundary-layer edge for hypersonic boundary layers on a flat plate, showing dependence on Mach number

The chemical source term in Eq. 2.9 is expressed as the sum over the vibrational internal energy multiplied with the production terms:

$$Q^{chem} = \sum_i c_i (e_i^{vib} W_i) \tag{2.34}$$

3. Future Work

A spatial finite-difference DNS code will be applied on a Cartesian three-dimensional grid on a flat plate. The code will incorporate a shock-capturing technique, since the shock provoked by the flat-plate leading edge is the major source of nonequilibrium. For the high Mach numbers, the location of the shock and the boundary-layer edge, which is the area of linear instability for hypersonic flows, merge, and the chemical and thermal nonequilibrium in this region is expected to influence transition to a large extent (Fig. 2; see also Anderson, 1989).

For the flight conditions investigated, the data in Fig. 3 are relevant. At a speed of $V_\infty = 5.9$ Km/s, dissociation of nitrogen and oxygen can be expected. For an altitude of $h = 25$ Km, chemical and thermal equilibrium will persist at a Mach number $Ma = 20$. At an altitude of about $h = 100$ Km (Ma=20.8), full nonequilibrium conditions are present. Conditions are chosen such that ionization will not take place. This choice is consistent with the return path of the shuttle as it enters the athmosphere.

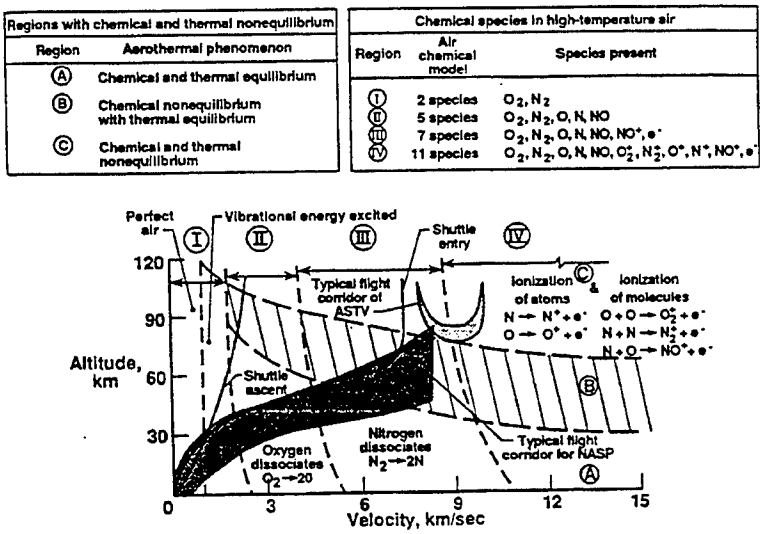

FIGURE 3. Flow regimes and thermochemical phenomena in the stagnation region of a 30.5 cm radius sphere flying in air (Gupta *et al.* 1990)

REFERENCES

ANDERSON, J. D. 1989 *Hypersonic and and High Temperature Gas Dynamics.* AIAA publication.

BLOTTNER, F. G., JOHNSON, M. & ELLIS, M. 1971 Chemically reacting viscous flow program for multi-component gas mixtures. Sandia Natl. Laboratories, SC-RR-70-754.

GUPTA, R. N., YOS, M. J., THOMPSON, R. A. & LEE, K.-P. 1990 *A review of reaction rates and thermodynamic and transport roperties for an 11-species air Model for chemical and thermal nonequilibrium calculations to 30,000K. NASA* RP-1232.

HIRSCHFELDER, J. O., CURTISS, C. F. & BIRD, R. A. 1964 *Molecular Theory of Gases and Liquids.* Wiley & Sons, New York.

HUDSON, M. J. 1996 *Linear Stability of Hypersonic Flows in Thermal and Chemical Nonequilibrium.* Ph.D. Thesis, North Carolina State University, Raleigh, NC.

MIRONOV, S. G. & MASLOV, A. A., Experimental study of secondary stability in a hypersonic shock layer on a flat plate. *J. Fluid Mech.* **412**, 259-277.

PARK, C. 1989 A review of reaction rates in high temperature air. *AIAA* Paper 89-1740.

SARMA, G. S. R. 2000 Physico-chemical modeling in hypersonic flow simulation. *Prog. Aerospace Sci.* **36**, 281-349.

SCHNEIDER, S. P. 1999 Flight data for boundary-layer transition at hypersonic and supersonic speeds. *J. Spacecraft and Rockets* **36**, 8-20.

VINCENTI, W. G. & KRUGER. C. H. 1982 *Introduction to Physical Gas Dynamics.* Krieger, Malabar, FL.

WILKE, S. P. 1950 A Viscosity Equation for Gas Mixtures. *J. Comp. Phys.* **18**, 517-519.

Temperature-fluctuation scaling in reacting boundary layers

By M. P. Martin † AND G. V. Candler ‡

1. Introduction

The boundary layers that are formed on hypersonic vehicles are hot, chemically reacting, and turbulent. Currently, the boundary layer on realistic hypersonic vehicles is simulated either assuming that the boundary layer is laminar or using simple turbulence models that have not been calibrated for hypersonic applications. Generally, the calibration of turbulence models has been done using DNS databases of incompressible flows or using perfect-gas wind-tunnel data. If we were able to perform more accurate simulations of hypersonic flows, we might find a different chemical composition of the gas, and different heating-rates, than those that are currently predicted.

In the flows of interest, the magnitude of the temperature fluctuations is very large due to the high energy content that is present. Furthermore, the chemical reaction rate is a highly non-linear function of the temperature. Therefore, temperature fluctuations may result in large variations in the reaction rates. In this paper we study the turbulence-chemistry interaction in a turbulent boundary layer and seek a scaling of the temperature fluctuations based on the resolved mean flow variables. The aim is to devise a model for the temperature fluctuations that can be used in the context of Reynolds-averaged Navier-Stokes or large-eddy simulations to predict accurate heating-rates and product formation.

Following our previous work (Martin & Candler, 2000), we use the temporally-evolving DNS database of a boundary layer at $Re_\theta = 7000$, edge-conditions of $M_e = 4.0$, $\rho_e = 0.5$ kg/m^3, $T_e = 5000$ K, and wall-temperature $T_w = 5000$ K. These conditions represent the boundary layer on a 26° wedge at a Mach number of 20 and 20 km altitude. We use a single model reaction, $\mathrm{S1} + \mathrm{M} \rightleftharpoons \mathrm{S2} + \mathrm{M}$, where species S1 and S2 have the same molecular weight and number of degrees of freedom. In this way, the gas constant is not a function of the chemical composition of the gas and changes in pressure are only caused by density and temperature variations. The reaction rates correspond to oxygen dissociation, and S1 and S2 represent molecules and atoms, respectively. Thus, production of species S1 indicates an exothermic reaction. The reaction rate and equilibrium constant expressions are taken from Gupta *et al.* (1990).

The paper is organized as follows. We first present a review of our previous work by introducing the non-dimensional parameters that govern the turbulence-chemistry interaction and the scaling functions that were found using DNS data of isotropic turbulence at conditions typical of hypersonic boundary layers. In a turbulent boundary layer, the energy transfer mechanisms are more complex than those found in isotropic turbulence. Thus, we present the temporal evolution equations for the turbulent kinetic energy and the variance of the temperature. These equations are used in the analysis of the turbulence-chemistry interaction. The results are divided in two sections. First, we

† Mechanical and Aerospace Engineering, Princeton University, Princeton, NJ 08544
‡ Aerospace Engineering and Mechanics, University of Minnesota, Minneapolis, MN 55455

present the characteristics of the mean flow and the effect of turbulent fluctuations on the mean flow motion. We then discuss the turbulent energy transfer and the scaling of the temperature fluctuations. Conclusions are given in the last section.

2. Background

The nondimensional parameters governing the turbulence/chemistry interaction are (Martin & Candler, 1998) the turbulent Mach number, the Damköhler number, the Reynolds number, and the relative heat release, namely

$$M_t = \frac{q}{a}\,, \tag{2.1}$$

$$Da = \frac{\tau_t}{\tau_c}\,, \tag{2.2}$$

$$Re_\lambda = \frac{\rho u' \lambda}{\mu}\,, \tag{2.3}$$

$$\overline{\Delta h^\circ} = -\frac{\Delta h^\circ}{c_v T + \frac{1}{2}q^2}, \tag{2.4}$$

where $q = \langle u_i' u_i' \rangle^{1/2}$ is the rms magnitude of the fluctuation velocity; a is the speed of sound; $\tau_t = k/\epsilon$ is the turbulent time scale, where k and ϵ are the turbulent kinetic energy and dissipation, respectively; $\tau_c = \rho / \left(\langle w_{S1}^2 \rangle^{1/2} \mathrm{K}_{eq} \right)$ is the chemical time scale where w is the source term, and K_{eq} is the equilibrium constant; $\lambda = q\tau_t$ is the characteristic turbulent length scale; and Δh° is the heat of the reaction.

In our previous work (Martin & Candler, 1998 and 1999), we used DNS to perform a fundamental study of isotropic turbulence interacting with finite-rate chemical reactions at conditions typical of a hypersonic boundary layer. We found that the turbulent motion is fed from the energy provided by the exothermic reactions, while the reaction rate is increased by the turbulent temperature fluctuations. This is a feedback process that takes place through the pressure-strain term in the Reynolds stress equation. The feedback is negative for endothermic reactions, resulting in a reduction in the turbulent motion. The DNS database showed that the temperature fluctuations can be expressed as a function of the governing parameters. For endothermic reactions, the temperature fluctuations scale linearly with M_t^2. Whereas for exothermic reactions, the temperature fluctuations are enhanced and can be expressed as

$$T'_{RMS}/\langle T \rangle = A(\overline{\Delta h^\circ}\ \lambda/l_E)^B \tag{2.5}$$

$$= A(\overline{\Delta h^\circ}\ M_t Da)^B \tag{2.6}$$

where A and B are constants that depend on the specific reaction and λ, also known as as the Taylor microscale, represents the distance traveled by a fluid particle moving at the speed of the turbulent intensity. The expansion length l_E is defined as $a\,\tau_c$, which is the distance traveled by acoustic radiation from the chemistry-induced temperature fluctuations. Therefore, λ/l_E represents the ratio of the characteristic distance traveled by a typical particle of fluid to the characteristic distance traveled by the acoustic radiation.

Another way to understand this ratio of length scales is to consider the variation of the strength of the chemistry-turbulence interaction. A positive temperature fluctuation increases the reaction rate, making the reaction occur more quickly, which releases more heat, further increasing the temperature. However, the feedback process can be weakened by delocalization of the interaction through turbulent motion and motion generated by

the local pressure fluctuations (also caused by the interaction). Therefore, in a simplified case where the reaction rate is held constant, the strength of the interaction varies like $(u')^2 \frac{1}{u'} \frac{1}{a} = \frac{u'}{a} = M_t$. In general, the interaction strength also varies with the reaction rate, or in non-dimensional terms, with the Damköhler number. Thus with this argument, we obtain the result shown in eq. (2).

Under the conditions chosen for our calculations of isotropic turbulence, λ/l_E was always less than one. As λ/l_E approaches one, $T'_{\rm RMS}/\langle T \rangle$ becomes large, indicating a strong turbulence-chemistry interaction. This occurs when the fluid travels a similar distance to the acoustic radiation induced by the temperature fluctuations. If λ/l_E were larger than one, the interaction would be expected to weaken because the turbulent motion would outrun the acoustic waves produced by the interaction, and the feedback process would be diminished. Also, as λ/l_E approaches zero the pressure waves outrun the fluid motion and the interaction is weak. Thus, the interaction weakens when λ/l_E departs from unity. In addition, $T'_{\rm RMS}/\langle T \rangle$ is affected by the heat released to the flow (Martin & Candler, 1998), and the length ratio must be modulated by $\overline{\Delta h^\circ}$ to give an appropriate relation for the standard deviation. When λ/l_E is greater than one, we would not expect this fit to be valid because it predicts a further strengthening of the interaction. The Reynolds number did not have a significant effect for the range of conditions that we considered. A more detailed discussion of this scaling for the temperature fluctuations can be found in Martin & Candler (1999).

3. Turbulence mechanisms

The chemical reactions act as energy sources within the turbulent boundary layer. Thus, we must address the energy exchange between the turbulence and the chemical reactions. There are four energy-exchange mechanisms that take place in turbulent boundary layers: transport, production, dissipation and diffusion of turbulence. The budget equation for the turbulent kinetic energy is

$$\frac{\partial}{\partial t}(\overline{\rho}\widetilde{k}) + \widetilde{w}\frac{\partial}{\partial z}(\overline{\rho}\widetilde{k}) = P_k + T_k + \Pi_t + \Pi_d + \phi_{dif} + \phi_{dis} \tag{3.1}$$

where

$$P_k = -\overline{\rho u_i'' w''}\,\frac{\partial u_i''}{\partial z}\,, \tag{3.2}$$

$$T_k = -\frac{1}{2}\,\frac{\partial}{\partial z}\overline{\rho u_i'' u_i'' w''}\,, \tag{3.3}$$

$$\Pi_t = -\frac{\partial}{\partial z}\overline{w'' p'}\,, \qquad \Pi_d = \overline{p'\frac{\partial u_i''}{\partial x_i}}\,, \tag{3.4}$$

$$\phi_{dif} = \frac{\partial}{\partial z}\overline{u_i'' \sigma'_{i2}}\,, \tag{3.5}$$

$$\phi_{dis} = \overline{\sigma'_{ij}\frac{\partial u_i''}{\partial x_j}}\,, \tag{3.6}$$

and P_k is the production due to the mean gradients, T_k is the redistribution of turbulent kinetic energy, Π_t is the pressure diffusion, and Π_d is the pressure dilation, ϕ_{dif} is the viscous diffusion, ϕ_{dis} is the viscous dissipation. There are other terms that appear in the equation due to the Favre averaging, however these terms are negligible. Note that

u' and u'' represent fluctuations with respect to the Reynolds and Favre averages of u, respectively.

To study the turbulent internal energy we use the evolution equation for the temperature variance, which is given by

$$\frac{D\overline{T'^2}}{Dt} = P_T + T_T + \varphi_{vdis} + \varphi_{tdif} + \varphi_{sdif} \tag{3.7}$$

where

$$\begin{aligned}
P_T &= -\frac{2}{c_v}\overline{T' \sum_s \frac{w_s h_s^\circ}{\rho_s}} \\
T_T &= -2(\gamma-1)\overline{TT'\frac{\partial u_j}{\partial x_j}} \\
\varphi_{vdis} &= \frac{2}{c_v}\overline{\frac{\tau_{ij}}{\rho}\frac{\partial u_i}{\partial x_j}T'} \\
\varphi_{tdif} &= -\frac{2}{c_v}\overline{\frac{T'}{\rho}\frac{\partial q_j}{\partial x_j}} \\
\varphi_{sdif} &= -2\gamma\overline{\frac{T'}{\rho}\frac{\partial}{\partial x_j}\sum_s \rho D\frac{\partial c_s}{\partial x_j}T}
\end{aligned} \tag{3.8}$$

and P_T is the production of temperature fluctuations due to the chemical reactions and h° is the heat of formation of species s; T_T is the transport of temperature fluctuations due to the temperature-dilatation correlation; φ_{vdis} represents the viscous dissipation of kinetic energy into internal energy; φ_{tdif} is the diffusion of temperature fluctuations due to heat conduction $q_j = -\kappa\partial T/\partial x_j$; and φ_{sdif} is the redistribution of temperature fluctuations due to the diffusion of species, where D is the species diffusivity and c_s is the mass fraction of species s. The last term, φ_{sdif} is since for our model reaction the gradients of species S1 and S2 are equal in magnitude and opposite in sign.

4. Flow characteristics

The species mass fractions are initialized to their equilibrium values at the averaged temperature. This initial state is not physical. Thus, when we turn on the reactions the flow undergoes a transient. Figure 1a shows the average temperature for the initial condition and after the transient. The gas near the wall is cooled considerably. The temporal evolution equation for the average temperature shows that the mechanisms causing this effect are the chemical source term and the thermal diffusion. Figure 1b, however, shows that the mass fraction of species S1 increases through the transient. Production of S1 indicates exothermic reactions, which would result in an increase of the average temperature. This result can be explain by looking at the budget of the terms in the evolution equation for the density of species S1, which shows that, locally, species S1 diffuses at a faster rate than the source term is destroying it. After the initial transient, the mean flow is in a quasi-equilibrium state. Although the chemical composition in typical hypersonic boundary layers is not in chemical equilibrium, these flow conditions serve to isolate the effect of turbulent fluctuations in the turbulence-chemistry interaction.

Figure 2a shows the average production of S1. There is nearly no net chemical production away from the wall. At the wall w_s is negative, indicating that destruction of S1 or endothermic reactions are dominant. As mentioned above, the mean flow is in chemical

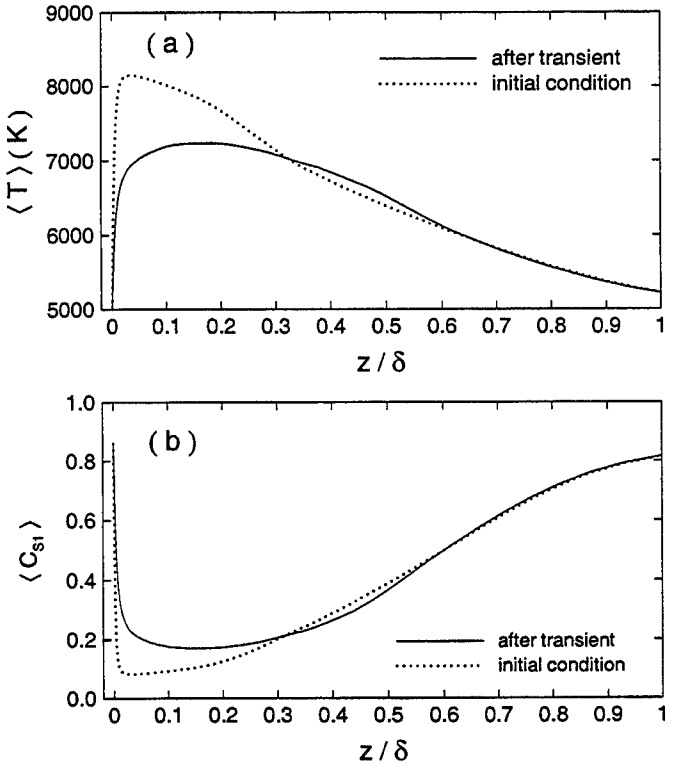

FIGURE 1. Average (a) temperature and (b) mass fraction of species S1.

equilibrium, thus the average temperature should not decrease due to the endothermic reactions. Figure 2b shows the budget for the terms in the evolution equation for $\langle T \rangle_t$. This equation is similar to the equation for $\langle T'T' \rangle_t$ but without the factors of $2T'$ in the terms on the right-hand side of eq. (4). We observe that the effect of the endothermic reactions is to decrease the temperature. Also the effect of the thermal diffusion is to cool the gas near the wall. However, these mechanisms are balanced by the large dissipation of kinetic energy into heat, which is represented by the viscous dissipation.

We now consider the effect of the turbulent fluctuations in the mean flow. Figure 3 shows the rms of the fluctuating source term normalized by its absolute magnitude. The magnitude of the fluctuations are higher than 60% of the average production at the wall and 100% elsewhere, indicating that the production of species is mainly due to fluctuations in the source term. The temperature fluctuations drive the chemical source term and since the mean flow is in equilibrium, no effect is observed in the average chemical composition of the gas, namely $\langle c_{S1} \rangle$ equals its equilibrium value based on the averaged temperature. However, we should be able to observe an effect on the magnitude of the fluctuating c_{S1}. Figure 4a shows the magnitude of the temperature fluctuations after the initial transient. The maximum is roughly 5% of the average and takes place in the viscous sublayer. A second peak of nearly the same magnitude develops in the logarithmic region. These locations are marked with symbols. For a given temperature there is a corresponding equilibrium composition of the gas. Table 1 gives the values of c_{S1} evaluated at $\langle T \rangle + T'_{RMS}$ and $\langle T \rangle - T'_{RMS}$ and normalized by $\langle c_{S1} \rangle$ (which equals c_{S1} evaluated at $\langle T \rangle$). We see that 5% fluctuation in the mean temperature can cause about

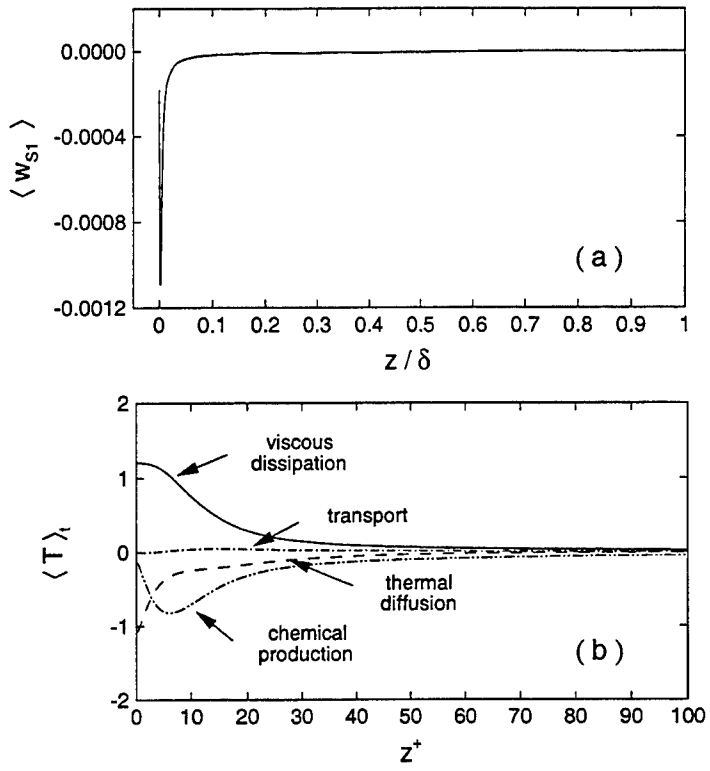

FIGURE 2. (a) Average production of species S1 normalized by $\rho_w u_\tau / z_\tau$; (b) budget for the time evolution of the average temperature normalized by $u_\tau^3 / cv\ z_\tau$.

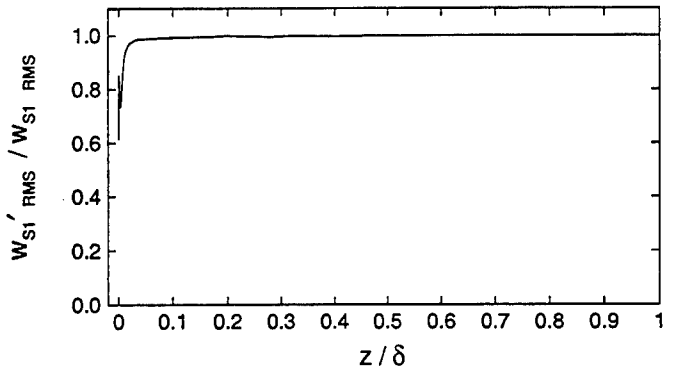

FIGURE 3. Normalized magnitude of the fluctuations in the production of species S1.

30% difference in the chemical composition. Clearly, the equilibrium composition is a very strong function of the temperature. This is reflected in the magnitude of c'_{S1} within the boundary layer, which is shown in Fig. 4b. We see that variations in the equilibrium mass fraction are nearly those produced by the temperature fluctuations.

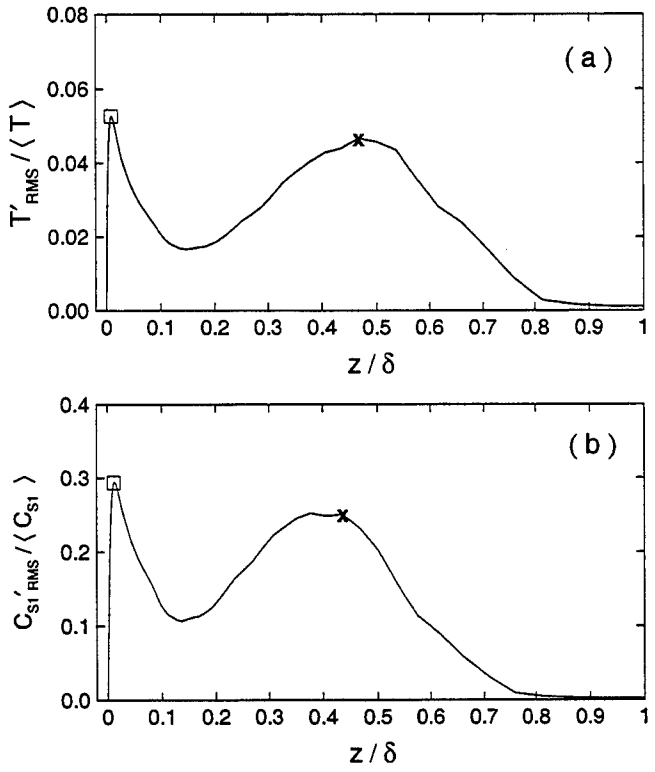

FIGURE 4. Normalized magnitude of the fluctuations in (a) temperature and (b) mass fraction of species S1.

	□	X
$c_{S1}\left(\langle T\rangle + T'_{RMS}\right)/\langle c_{S1}\rangle$	25%	24%
$c_{S1}\left(\langle T\rangle - T'_{RMS}\right)/\langle c_{S1}\rangle$	31%	31%

FIGURE 5. Equilibrium mass fraction of species S1 evaluated at the maximum and minimum local temperatures in the boundary layer and relative to its mean.

5. Turbulence-chemistry interaction

In this section we study the turbulence-chemistry interaction and the temperature fluctuation scaling by studying the budget of the terms in the evolution equations for the temperature variance and the turbulent kinetic energy. Figure 6 shows the effect of the source term on the temperature fluctuation variance. The symbols are shown for future reference. The source term has been decomposed into the forward and backward components,

$$w_{S1} = -M_{S1}\, k_f\, \frac{\rho_{S1}}{M_{S1}}\left(\frac{\rho_{S1}}{M_{S1}} + \frac{\rho_{S2}}{M_{S2}}\right) \tag{5.1}$$

$$+ M_{S1}\, k_b\, \frac{\rho_{S2}}{M_{S2}}\left(\frac{\rho_{S1}}{M_{S1}} + \frac{\rho_{S2}}{M_{S2}}\right) \tag{5.2}$$

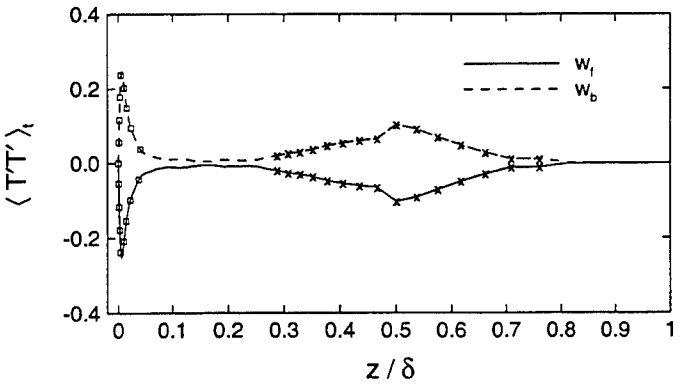

FIGURE 6. Contribution of the chemical production to $\langle T'T' \rangle_t$. The terms are normalized using $u_\tau^3/cv\ z_\tau$.

$$= w_f + w_b, \tag{5.3}$$

where ρ_s and M_s are the density and molecular weight of species s, k_f and k_b are the forward and backward reaction rates, respectively, and w_f and w_b represent the destruction and production of species S1. Thus, w_f reduces the magnitude of the temperature fluctuations as a result of endothermic reactions and w_b has the opposite effect. Figure 6 also shows that both exothermic and endothermic reactions take place within the boundary layer. Figure 7a shows the budget of $\langle T'T' \rangle$ in the near wall region. At the wall the chemical production and thermal diffusion are balanced by the viscous dissipation and transport mechanisms. The species diffusivity is negligible since the gradients of species mass fraction are equal in magnitude and opposite in sign. Figure 7b shows the same budget throughout the entire boundary layer. The chemical production and transport mechanisms enhance the temperature fluctuations, however these terms are balanced by the thermal diffusion. The species diffusion term is negligible and not shown.

Figure 8a shows the budget of the turbulent kinetic energy in the near wall region. The turbulent kinetic energy is nearly in equilibrium. Figure 8b shows the same budget across the entire boundary layer. The production term is dominant causing a net production of turbulent kinetic energy. The production and transport terms have the same oscillatory behavior in $0.1 \leq z/\delta \leq 0.3$. This behavior is similar to that of the transport term in the equation for $\langle T'T' \rangle_t$, as shown in Fig. 6b. Figure 9a is a plot of the temporal evolution of the friction velocity, u_τ. After the initial transient, the oscillations in u_τ indicate the presence of a physical mechanism that is damping and replenishing u_τ. Figure 9b shows the variation of turbulent kinetic energy across the boundary layer. Again the oscillatory behavior is observed in $0.1 \leq z/\delta \leq 0.3$, as in the transport and production mechanisms for the evolution of $\langle T'T' \rangle_t$ and $\langle \mathrm{TKE} \rangle_t$. As in isotropic turbulence (Martin & Candler, 1998), this result suggests that a feedback mechanism between the turbulent motion and the chemical reactions takes place.

The effect of endothermic reactions is to damp the temperature fluctuations. However for the conditions chosen, the turbulent kinetic energy in the boundary layer is self-sustained. Therefore, the turbulent temperature fluctuations are maintained. The exothermic reactions, however, act as heat sources increasing the temperature fluctuations. Both endothermic and reactions cause localized compressions and exothermic expansions within the boundary layer. The turbulent kinetic energy feeds from the thermal

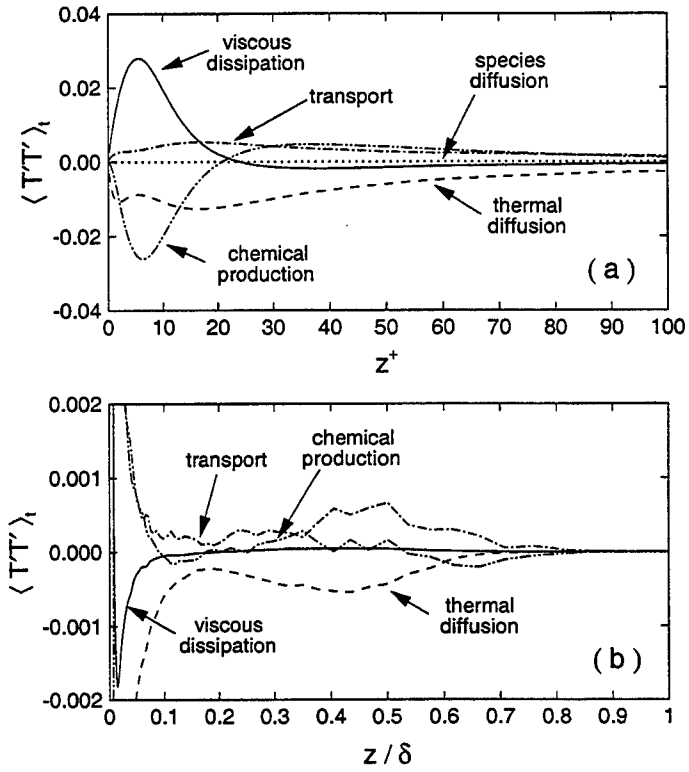

FIGURE 7. Budget of the terms in the evolution equation for $\langle T'T' \rangle_t$ (a) near the wall and (b) across the boundary layer. The terms are normalized using $u_\tau^3/cv\ z_\tau$.

energy. The results suggest that this feedback mechanism takes place through the transport term in the equation for $\langle T'T' \rangle_t$ and through the production and transport mechanisms in the equation for $\langle \mathrm{TKE} \rangle_t$. The transport term for $\langle T'T' \rangle_t$ includes the correlation between temperature fluctuations and dilatation, which explains the energy transfer between the turbulent kinetic energy and the internal energy through the chemically-induced expansions and compressions.

Figure 10 plots the magnitude of the temperature fluctuations versus the heat ratio, eq. (2), in the viscous sublayer and near $z/\delta = 0.5$. (These boundary layer locations are marked with symbols in Fig. 5.) The data includes several time steps during the simulation. The power law relation between temperature fluctuations and the heat ratio resembles that found in isotropic turbulence. The data collapse very well in the viscous sublayer, where the turbulence scales are nearly isotropic. Near the boundary layer edge however, the agreement is not so good. This could be because near the boundary layer edge the numerical resolution is not as good, since the computational grid is exponentially stretched. This can be seen in the lower population of symbols for the data near the boundary layer. It is also possible that we have not gathered sufficient statistics in time so as to get a large enough sample of data. A Reynolds number dependence is also possible, since the peak in the logarithmic region of the turbulent profiles is highly dependent on the Reynolds number. None of these reasons or others can be proven true with the small dataset that we are working with.

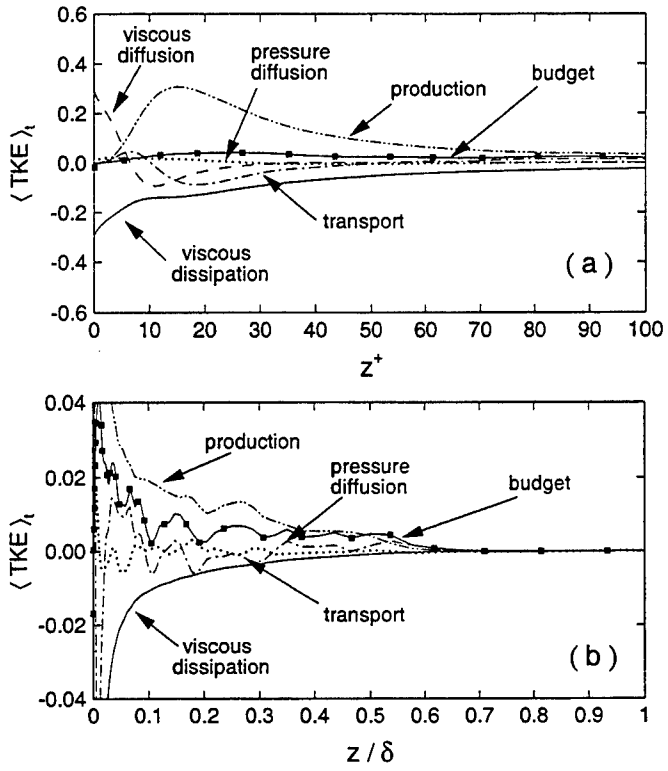

FIGURE 8. Budget of the terms in the evolution equation for $\langle\widetilde{\rho k}\rangle_t$ (a) near the wall and (b) across the boundary layer. The terms are normalized using $\rho_w u_\tau^3/z_\tau$.

6. Conclusions

In this paper, we have analyzed the direct numerical simulation database of a chemically reacting, turbulent boundary layer at Mach 4, $Re_\theta = 7000$, and isothermal wall-temperature condition. The budget of the terms in the evolution equation for the temperature show that the mean flow is in chemical equilibrium. However, the temperature fluctuations increase the reaction rates and therefore the chemistry is active throughout the boundary layer. The magnitude of the fluctuations in temperature and species mass fraction show that a 5% fluctuation in temperature can cause a 30% fluctuation in the species mass fraction. If the boundary layer is in chemical non-equilibrium, such large fluctuations in the species mass fraction may have a significant effect in the average composition of the gas and therefore in the heating rates to the wall. Additional simulations are required to verify this.

The evolution equation for the temperature fluctuations show that endothermic reactions reduce the temperature fluctuations, whereas exothermic reactions act as heat sources that increase T'_{RMS}. The budget of turbulent kinetic energy shows that the production and transport mechanisms are enhanced by the presence of reactions. The oscillations found in the evolution of the wall-friction velocity and in the profile of turbulent kinetic energy indicate the presence of a physical mechanism that is damping and replenishing the turbulent kinetic energy.

The effect of endothermic reactions is to damp the temperature fluctuations. However, the turbulent kinetic energy in the boundary layer is self-sustained. Therefore,

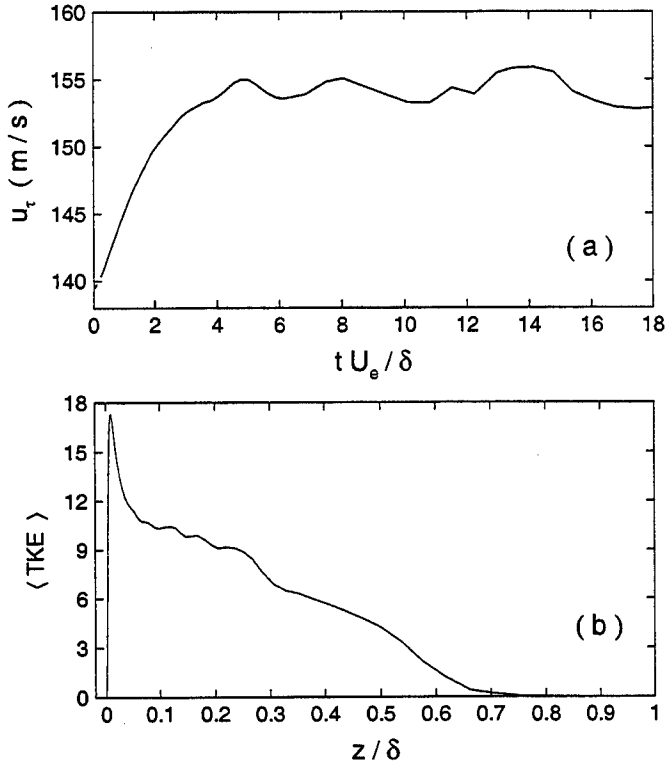

FIGURE 9. (a) Temporal evolution of the wall-friction velocity and (b) turbulent kinetic energy profile normalized using $\rho_w u_\tau^2$.

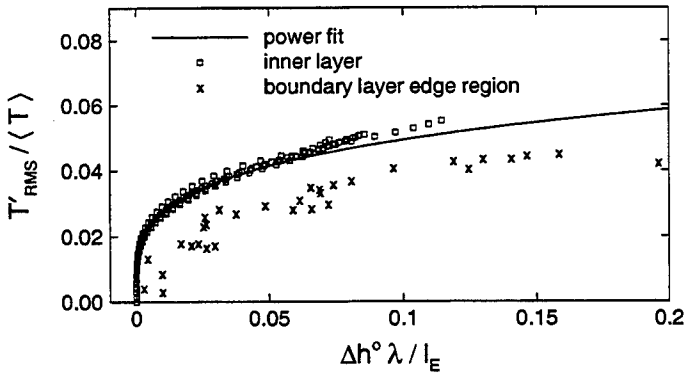

FIGURE 10. Temperature fluctuation versus heat ratio.

the turbulent temperature fluctuations are maintained. As mentioned above, exothermic reactions increase the magnitude of the temperature fluctuations and the temperature fluctuations increase the reaction rates. Both endothermic and exothermic reactions cause localized compressions and expansions within the boundary layer that feed the turbulent kinetic energy. The results suggest that this feedback mechanism takes place through the transport term in the equation for $\langle T'T' \rangle_t$ and through the production and transport mechanisms in the equation for $\langle \rho k \rangle_t$. The transport term for $\langle T'T' \rangle_t$ includes the

correlation between temperature fluctuations and dilatation, which explains the energy transfer between the turbulent kinetic energy and the internal energy through the chemically induced expansions and compressions. This result is consistent with that found using the DNS data of reacting isotropic turbulence (Martin & Candler, 1998 and 1999) and with the theoretical work of Eschenroeder (1964).

Also as in isotropic turbulence, we find that the temperature variance can be expressed as $A\left(\overline{\Delta h^\circ}\lambda/l_E\right)^B$. Where λ/l_E is obtained from the nondimensional governing parameters and represents the ratio of the characteristic distance traveled by a fluid particle to the characteristic distance of acoustic radiation. Since $\overline{\Delta h^\circ}\lambda/l_E$ is a mean flow quantity, it could potentially be used to predict the temperature fluctuations in Reynolds-averaged Navier-Stokes or large-eddy simulations. However, further testing of the scaling must be performed over a wider range of conditions.

Acknowledgments

Computer time was provided by NASA Ames Research Center and the Army High Performance Computing Research Center under the auspices of the Department of the Army, Army Research Laboratory cooperative agreement number DAAH04-95-2-0003 / contract number DAAH04-95-C-0008, the content of which does not necessarily reflect the position or the policy of the government, and no official endorsement should be inferred. This work was supported in part by the Air Force Office of Scientific Research under grant AF/F49620-01-1-0060.

REFERENCES

ESCHENROEDER, A.Q. 1964. Intensification of turbulence by chemical heat release. *Phys. Fluids* **7**, 1735-1743.

GUPTA, R.N., YOS, J.M., THOMPSON, R.A., & LEE, K. 1990. A review of reaction rates and thermodynamic and transport properties for an 11-species air model for chemical and thermal non-equilibrium calculations to 30,000 K. *NASA* Reference Publication 1232.

MARTIN, M.P., & CANDLER. G.V. 1998. Effect of chemical reactions on decaying isotropic turbulence. *Phys. Fluids* **10**, 1715-1724. Also *AIAA* Paper 96-2060 (1996).

MARTIN, M.P., & CANDLER, G.V. 1999. Subgrid-scale model for the temperature fluctuations in reacting turbulence. *Phys. Fluids* **11**, 2765-2771. Also *AIAA* Paper 97-0751 (1997).

MARTIN, M.P., & CANDLER, G.V. 2000. DNS of a Mach 4 boundary layer with chemical reactions. *AIAA* Paper 2000-0399 (2000).

Preliminary LES over a hypersonic elliptical cross-section cone

By M. P. Martin, † M. Wright, ‡ G.V. Candler, ¶ U. Piomelli, ‖ G. Weirs †† AND H. Johnson ‡‡

1. Introduction

Many aspects of transitional and turbulent flows are not fully understood. This is especially true in the hypersonic regime, where examples of unresolved issues include the effects of freestream disturbances and of three-dimensionality. In the absence of detailed experimental or computational databases to better understand these physical phenomena, we are left with excessive design conservatism and unrefined conceptual designs.

When investigating these phenomena via CFD, direct numerical simulations (DNS) are not affordable. Turbulence models provide a wide range of accuracy in predicting turbulent flows of engineering interest. Depending on the level of detail required, one may choose Reynolds-averaged Navier-Stokes (RANS) models, or use state-of-the-art subgrid scale (SGS) models in a large-eddy simulation (LES) to obtain a more refined prediction. The study of fundamental physical phenomena must be done using the best possible prediction, namely LES. However, one must keep in mind that a key feature of the prediction method should be validation by experiment.

Using the most recent laser and camera technologies, Huntley (2000) and Huntley *et al.* (2000) present the first detailed flow visualization of natural transition on a cone of elliptical cross-section at Mach 8. Mean flow features and details of the unstable modes in the boundary layer for the same configuration are given by Kimmel *et al.* (1997 and 1999) and Poggie *et al.* (2000), respectively. Because this flow is being extensively documented experimentally, and because the geometric configuration resembles that of the forebody of a hypersonic vehicle, this database is ideal to test the state of the art SGS models and LES methodology for hypersonic flows.

The present work is an ongoing effort to provide detailed flow simulations of unsteady, hypersonic, transitional or turbulent flows. In Martin *et al.* (2000a) we develop and test SGS models for compressible LES using the apriori test in compressible, isotropic turbulent flow. In Martin *et al.* (2001) we validate the LES methodology by using the results of DNS of supersonic boundary layers, and in Martin *et al.* (2000b) we extend the LES code to generalized curvilinear coordinates and validate the implementation in supersonic turbulent boundary layer flow. In this paper, we present preliminary LES results of the flow around a section of an elliptical cross-section cone away from the tip of the cone. The flow conditions, simulation procedure, preliminary flow assessments, and future work are given in the following sections.

† Princeton University, Princeton, NJ 08544
‡ Eloret Corporation, NASA Ames Research Center, Moffett Field, CA 94035
¶ Aerospace Engineering and Mechanics, University of Minnesota, Minneapolis, MN 55455
‖ Mechanical Engineering, University of Maryland, College Park, MD 20742
†† ASCI Flash Center, University of Chicago, Chicago, IL 60637
‡‡ Aerospace Engineering and Mechanics, University of Minnesota, Minneapolis, MN 55455

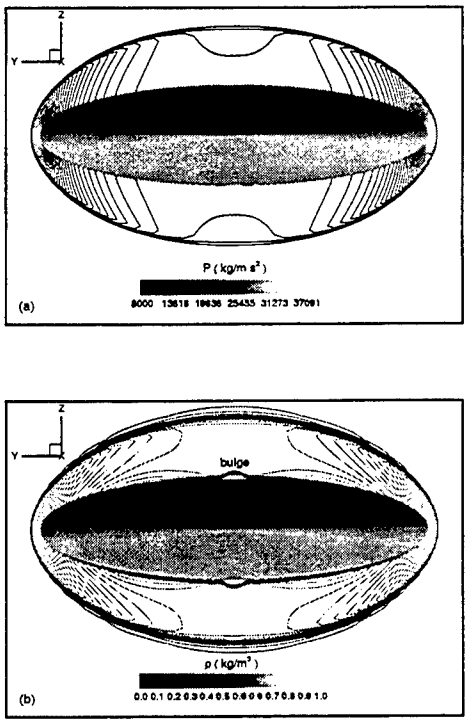

FIGURE 1. (a) Pressure and (b) density contours in the exit plane of the cone geometry for the laminar solution.

2. Geometry and flow conditions

Following the experimental configuration of Huntley *et al.* (2000), the lifting- body geometry chosen is a sharp-nosed cone of elliptical cross-section. The nominal radius of the nose of the experimental model is less than 200 μm. In our simulations, we use an ellipsoidal nose with an 80 μm diameter of nose ellipsoid measured on the major axis. The afterbody is an elliptical cross-section cone of 4:1 aspect ratio, 17.5 degrees half-angle in the major axis, and 0.242 m in length, resulting in base dimensions of 0.152 m across the major axis and 0.038 m across the minor axis.

The freestream flow conditions are $Re_\infty = 14 \times 10^6\ /m$, $M_\infty = 8$, $\rho_\infty = 0.5$, and $T_\infty = 58$ K. For these conditions, the boundary layer is fully turbulent at position x=17.5 cm from the nose (Huntley, 2000). The wall-temperature condition is prescribed to 450 K, which is nearly adiabatic. As in the experiments, air is the working fluid.

The Mach 8 flow around the cone at zero angle of attack is highly compressed behind the shock. The difference in shock strength between the major and minor axes causes a higher compression at the leading edge producing a crossflow from the leading edge to the centerline of the cone. This is illustrated in Fig. 1a. At the centerline the cross-flow velocities are zero and mass conservation induces a bulge, see Fig. 1b, where the boundary layer is twice as thick as the boundary layer in the off-center region (Huntley, 2000). Experiments show that transition occurs first on the centerline (Huntley, 2000).

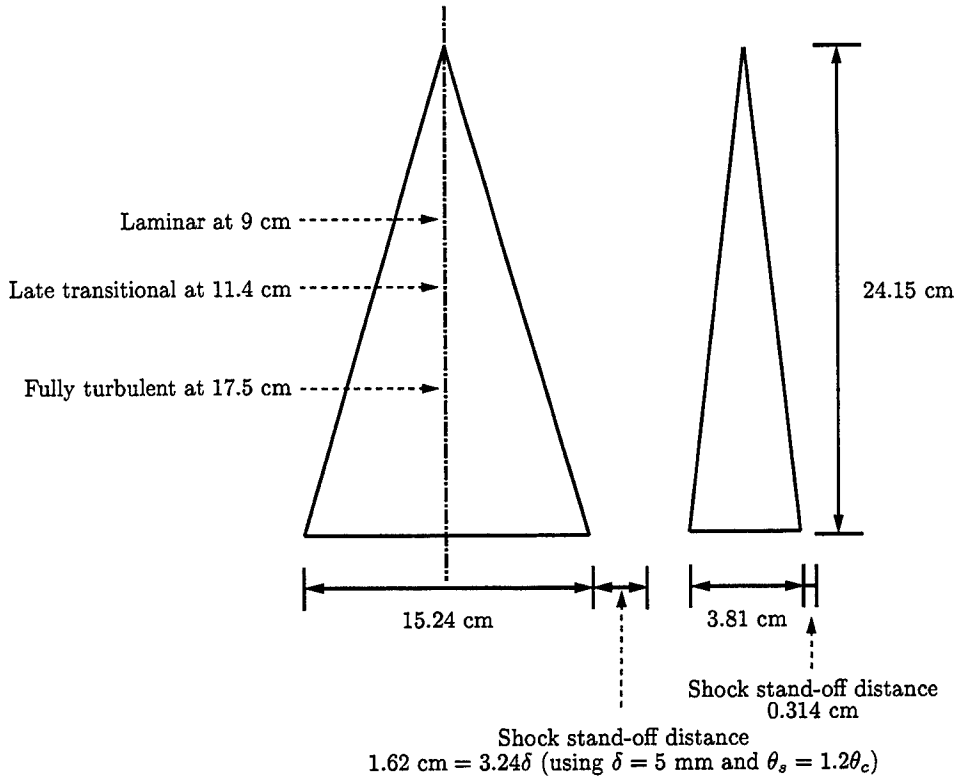

FIGURE 2. Model dimensions and key flow features required to determine the grid resolution and computational domain size.

3. Grid resolution

We estimate the resolution requirements by considering the dimensions of the turbulence structure and the data provided by the experiments. From the experimental data (Huntley, 2000), the estimated wall unit is 7.5×10^{-5} m and the boundary layer along the centerline is laminar at $x = 9$ cm, late-transitional at 11.4 cm, and fully turbulent at 17.5 cm from the nose. See Figure 2. The turbulent boundary layer at the center line is 5 to 6 mm thick. Note that the shock-standoff angle is $\theta_s = 1.2\theta_c$, where θ_s and θ_c are the shock and cone angles, respectively. The turbulence structures on a flat plate boundary layer extend about 100 wall units in the spanwise direction and a few boundary layer thicknesses in the streamwise direction.

In the spanwise direction we use a uniform grid spacing of 22 wall units. This estimate is based on the grid resolution used in previous LES of a supersonic boundary layer (Martín *et al.*, 2000). For the conditions chosen, the boundary layer at the leading edge is laminar (Huntley, 2000). Since the flow is supersonic and the cone is at zero angle of attack, the flow around the top of the cone is not affected by the flow on the bottom. Thus only the top of the cone is simulated. In the streamwise direction, the flow is laminar at $x = 9$ cm from the nose. Thus, the resolution requirements up to 9 cm from the nose are given by the grid convergence studies of the laminar flow at the nose. From $x = 9$ cm to the base of the cone we require that the maximum grid spacing on the surface is 33 wall units. In the wall-normal direction the grid is exponentially stretched, we require 0.3 and δ^+ wall units for the minimum and maximum grid spacings within the boundary

layer (Martin *et al.*, 2000), where $\delta^+ = \delta/z_\tau$ is about 70 for the turbulent case. The computational domain is large enough to include the standoff shock wave.

4. Simulation procedure

For the LES, we use a third-order accurate WENO (Weirs & Candler, 1997) to compute the convective fluxes. This scheme has low dissipation properties, and was designed to perform DNS and LES of compressible flows. The time advancement technique is based on the DPLU relaxation method of Candler *et al.* (1994) and was extended to second-order accuracy by Olejniczak & Candler (1997). The viscous fluxes are evaluated using fourth-order central differences. Finally, the transformation metrics are evaluated using fourth-order central differences so that the inaccuracy of the numerical evaluation of the metrics coefficients is less than the inaccuracy of the convected fluxes.

The initial condition will be a superposition of laminar flow and a prescribed freestream energy disturbance spectrum. To generate the laminar solution we use a finite volume code (Wright *et al.*, 1998), where we only compute 90 degrees of the cone geometry and use bilateral symmetry to reflect the resulting solution across the centerline and generate the full 180 degrees. We then interpolate the laminar solution from the finite-volume cell centers to the finite-difference grid points using tri-linear interpolation.

The required SGS terms and the model representations are given in Martin *et al.* (2000a, 2000b). To evaluate the model coefficients we use the Lagrangian-averaging operation, where the averaging is performed along a fluid particle pathline. A full description of the Lagrangian-average procedure can be found in Meneveau *et al.* (1996).

5. Preliminary flow assessments and future work

In this section we present a brief progress report on performing the LES. A portion of the cone has been initialized using the interpolated laminar solution to test the Lagrangian implementation of the SGS models. To minimize the complexity of this test, the disturbances introduced by the tri-linear interpolation are used as initial disturbances. Figures 3 through 5 show contours of the SGS terms at the exit plane of the cone on spanwise wall-normal planes. These figures include a quarter of the computational domain (centered about the centerline) in the spanwise direction, and about ten boundary layer thickness in the wall normal direction, the boundary layer thickness along the centerline is about 2 mm, three times smaller than the turbulent boundary layer thickness. Figures 3 through 5 show that the SGS terms are dominant in the bulge region. This would not be the case if the model coefficients were calculated using the ensemble average procedure.

The magnitude of the initial disturbance is very small and do not grow significantly in time. Future work includes imposing a prescribed disturbance energy spectrum and running the LES for long enough to gather sufficient statistical data to assess the effect of freestream disturbance and study the transition and turbulence phenomena.

Acknowledgments

Computer time was provided by NASA Ames Research Center and the Army High Performance Computing Research Center under the auspices of the Department of the Army, Army Research Laboratory cooperative agreement number DAAH04-95-2-0003 /

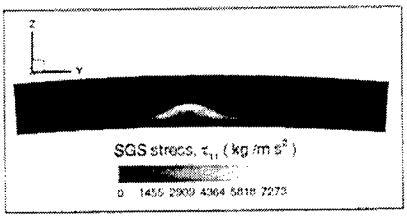

FIGURE 3. SGS stress contours on the exit plane; flow into the page.

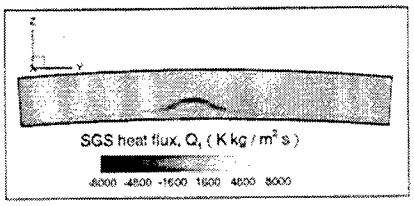

FIGURE 4. SGS heat flux contours on the exit plane; flow into the page.

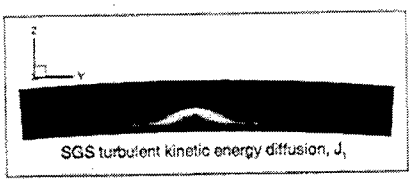

FIGURE 5. Contours of SGS turbulent kinetic energy on the exit plane; flow into the page.

contract number DAAH04-95-C-0008, the content of which does not necessarily reflect the position or the policy of the government, and no official endorsement should be inferred. This work was supported in part by the Air Force Office of Scientific Research under grant AF/F49620-01-1-0060.

REFERENCES

CANDLER, G.V., WRIGHT, W.J. & MCDONALD, J.D. 1994. Data-parallel lower-upper relaxation method for reacting flows. *AIAA J.* **12**, 2380-2386.

HUNTLEY, M. 2000 Transition on elliptic cones at Mach 8. *PhD thesis, Princeton University.*

HUNTLEY, M., WU, P., MILES, R.B., & SMITS, A.J. 2000 MHz rate imaging of boundary layer transition on elliptic cones at Mach 8. *AIAA* Paper 2000-0379.

KIMMEL, R.L., & POGGIE, J. 1999. Laminar-turbulent transition in a Mach 8 elliptic cone flow. *AIAA J.* **37**, 1080-1087.

KIMMEL, R.L., KLEIN, M.A., & SCHWOERKE, S.N. 1997. Three-dimensional hypersonic laminar boundary-layer computations for transition experiment design. *J. Spacecraft and Rockets* **34**, 409-415.

MARTIN, M.P., PIOMELLI, U., & CANDLER, G.V. 2000. Subgrid-scale models for compressible large-eddy simulations. *Theor. and Comp. Fluid Dyn.* **13**, 361-376.

MARTIN, M.P., WEIRS, G., CANDLER, G.V., PIOMELLI, U., JOHNSON, H., & NOMPELIS, I. 2000b. Toward the large-eddy simulation over a hypersonic elliptical cross-section cone. *AIAA* Paper 2000-2311.

MARTIN, M.P., PIOMELLI, U., & CANDLER, G.V. 2001. Direct and large-eddy simulations of turbulent supersonic boundary layers. *Submitted to J. Fluid Mech.*

OLEJNICZAK, D.J. , & CANDLER, G.V. 1997. A Data-parallel LU relaxation method for DNS of compressible flows. *1st International Conference in DNS and LES.*

POGGIE, J., KIMMEL, R.L., & SCHWOERKE, S.N. 2000. Traveling instability waves in a Mach 8 flow over an elliptic cone. *AIAA J.* **32**, 251-258.

WEIRS, V.G., & CANDLER, G.V. 1997. Optimization of weighted ENO schemes for DNS of compressible turbulence. *AIAA* Paper 97-1940.

WRIGHT, M.J., CANDLER, G.V., & BOSE,D. 1998. Data-parallel line relaxation method for the Navier-Stokes equations. *AIAA J.* **34**, 1371-1377.

Stochastic sub-grid modeling of drop breakup for LES of atomizing spray

By Mikhael Gorokhovski † AND Sourabh Apte

1. Motivation and objectives

Injection of a liquid jet at relatively high liquid-to-gas velocity ratios leads to very complex physical phenomena, involving the stripping of filaments from distorted liquid surfaces, turbulence-induced breakup, multiple droplet collision, etc., causing atomization. This gives rise to a broad spectrum of droplet sizes at various locations from the injector. Kolmogorov (1941) described the breakup of droplets as a discrete random process, where the probability that a parent particle breaks into a given number of droplets is independent of the parent particle size. From Lyapunov's theorem, Kolmogorov pointed out that such a general assumption leads to a log-normal distribution of particle size in the long-time limit. Predicting these probability distributions of droplet sizes due atomization is the crux of sheet-breakup modeling.

In the present work, the process of atomization is considered in the framework of a cascade of uncorrelated breakage events, independent of the initial droplet size. The cascade idea of droplet-sheet breakup due to Kolmogorov is explored by developing a stochastic sub-grid model for the production of new droplets. Finding a probability distribution function for droplet radii, during each breakup period, by solving a stochastic differential equation may give a more realistic prediction of the breakup process. A detailed theoretical analysis of Kolmogorov's model assuming the breakup frequency to depend on the radius of the parent particle, was performed by Gorokhovski & Saveliev (2001). It was shown that in the long time-limit, Kolmogorov's scaling symmetry of breakup implies fractal properties of the particle-size distribution. The photographic examination of an atomizing spray (Liu & Reitz (1993), Zhou & Yu (2000), Shavit & Chigier (1995)) also shows that atomization at high relative liquid-to-gas velocity is related to fractals implying that in a broad interval of droplet radius variation, somewhere between the initial and the maximum stable radii, there exists no distinguishable characteristic length scale. Following these observations, Kolmogorov's idea of droplet breakup seems appropriate to model the complex fragmentary process of liquid atomization.

2. Accomplishments

In this paper, Kolmogorov's discrete model has been represented in its asymptotic Fokker-Planck approximation for droplet-size distribution function. This equation was applied to simulate the droplet breakup along with Lagrangian model for spray dynamics. Computations of spray are performed for the conditions encountered in a diesel engine and the spray evolution is qualitatively compared with actual photographic examinations. This paper shows that the numerical prediction is in qualitative agreement with the experimental results. A broad spectrum of droplet sizes is simulated at each spray location with the co-existence of large and small drops.

† CNRS/University/IUT of Rouen

3. Fokker-Planck approximation for particle breakup

Let us consider an ensemble of droplets undergoing breakup at discrete time instants $t = 0, 1, 2, \ldots$. These time moments are scaled by the breakup frequency, ν, such that $(\nu t_{bu} = 1)$, where t_{bu} is the breakup time. According to Kolmogorov (1941), the number of droplets $N(r,t)$ of size $\rho \leq r$ was selected amongst all the droplets $N(t)$ at a given time t. The expectations of total number of droplets and of droplets of size $\rho \leq r$ were denoted as $\overline{N}(t)$ and $\overline{N}(r,t)$, respectively.

Consider breakups of a given particle size r within a time unit $[t, t+1]$. Let $Q(\alpha)$ be the mean number of secondary droplets produced of size $\rho \leq \alpha r (0 \leq \alpha \leq 1)$. According to Kolmogorov's hypothesis, the probability to break each parent droplet into a given number of fragments is independent of the parent droplet size. In other words, $Q(\alpha)$ does not depend on the history of breakup and is not influenced by other parent droplets. By this assumption, it follows that,

$$\overline{N}(r, t+1) = \int_0^1 \overline{N}(r/\alpha, t) dQ(\alpha) \tag{3.1}$$

Introducing the logarithm of droplet-size, $x = \log r$, Kolmogorov pointed out that the distribution function for the droplet size, $T(x,t)$, is given by

$$T(x,t) = \frac{\overline{N}(e^x, t)}{\overline{N}(t)} = \frac{N(e^x, t)}{N(t)} \tag{3.2}$$

Further, denoting $\xi = \log \alpha$ and $Q(\alpha) = Q(1) \cdot S(\xi)$, equation 3.1 can be rewritten as

$$T(x, t+1) = \int_{-\infty}^0 T(x - \xi, t) dS(\xi) \tag{3.3}$$

By Lyapunov's theorem, Kolmogorov stated that from discrete model equation 3.3, the long-time limit form of $T(x,t)$ tends to a Gaussian function. This implies that the number of droplets $N(r,t)$ is asymptotically governed by the log-normal law. On the other hand, it can be shown that the model equation 3.3 is equivalent to the Fokker-Planck approximation of droplet breakup (Gorokhovski & Saveliev (2001)),

$$\frac{\partial T(x,t)}{\partial t} + \nu(\xi) \frac{\partial T(x,t)}{\partial x} = \frac{1}{2!} \nu(\xi^2) \frac{\partial^2 T(x,t)}{\partial x^2} \tag{3.4}$$

where time and breakup frequency are introduced. The solution of equation 3.4 is a Gaussian function. This depicts the main conclusion by Kolmogorov (1941). At the same time, an influence of the initial distribution before breakup starts can also be taken into account. The solution of 3.4 is

$$T(x,t) = \int_{-\infty}^0 \frac{1}{\sqrt{2\pi \langle \xi^2 \rangle \nu t}} exp \left[\frac{-(x - x_0)^2}{2 \langle \xi^2 \rangle \nu t} \right] T_0(x_0 - \langle \xi \rangle \nu t) \, dx_0 \tag{3.5}$$

where $T_0(x_0)$ is the initial distribution of the logarithm of droplet radii and x_0 the logarithm of radius of the parent droplet. Equation 3.4 can be rewritten for the normalized distribution of radius, $f(r)$, to give:

$$\frac{\partial f(r)}{\partial t} = -\nu(\xi) \frac{\partial}{\partial r} (r f(r)) + \frac{1}{2} \nu \langle \xi^2 \rangle \frac{\partial}{\partial r} \left(r \frac{\partial}{\partial r} (r f(r)) \right) \tag{3.6}$$

The solution of equation 3.6 has the following form

$$f(r,t) = \frac{1}{r}\int_0^\infty \frac{1}{\sqrt{2\pi\langle\xi^2\rangle\nu t}} exp\left[-\frac{(\log(r_0/r) + \langle\xi\rangle\nu t)^2}{2\langle\xi^2\rangle\nu t}\right] f_0(r_0)dr_0 \qquad (3.7)$$

where $f_0(r_0)$ is the initial distribution of droplet radius before breakup starts.

4. Implementation into unstructured combustor code

The implementation of the droplet-sheet breakup module into the unstructured LES code developed by Mahesh *et al.* (2001) is straight forward, as described below. The importance of the present work compared to the commercial softwares available for Lagrangian particle tracking (e.g. KIVA) is that, we track each individual droplet within the computational domain. This requires generation of 'daughter' drops from corresponding parent droplets. Subsequently, the number of droplets within the domain increases rapidly. The droplet breakup pictures obtained, however, resemble closely the actual experimental images, as opposed to a fairly collective representation obtained from the 'parcels'-approach. Tracking each droplet, on the other hand, leads to enormous computational costs.

4.1. *General Procedure*

The modeling of the spray equation is based on a Lagrangian formulation where each computational particle represents one droplet of given size, velocity and position. These droplets are followed as they interact and exchange momentum and energy with the surrounding gas. The unstructured LES code for gas turbine combustors (Mahesh *et al.*) was modified in this work to incorporate the coupling between the Lagrangian tracking of droplets and stochastic computing of the breakup phenomenon. Two additional physical processes were included in the Monte Carlo procedure. Specifically, the product droplet velocity has been modeled and the breakup has been considered down to the local magnitude of the critical (or maximum stable) radius, r_{cr}. The liquid fuel was injected in the axial nozzle direction in the form of drops with characteristic size equal to the exit nozzle radius and the velocity known from the liquid injection rate.

Let us consider motion of a j^{th} primary drop that undergoes breakup ($r_j > r_{cr}$). Before breakup starts, the size-distribution function associated with this drop, is a Dirac-delta function. With time, which is inversely proportional to the breakup frequency (ν), new droplets are created changing the droplet-radius distribution function. We suppose that the new distribution may be described according to the solution of equation 3.7 taken at $\nu t = 1$ with $\langle\xi\rangle$ and $\langle\xi^2\rangle$ as parameters of the model. For every breakup time scale, new droplets are formed from the parent drop ($r_j > r_{cr}$) with radius sampled from equation 3.7. With subsequent breakups, the droplet is removed from the computation as its mass is depleted. After the sampling procedure, the current time, t, of the new droplets is prescribed to be zero implying that the new drops are not physically deformed. Lagrangian tracking is then continued up to the next breakup ($\nu t = 1, r_j > r_{cr}$). In the present computations, we used expressions obtained from the distribution of the logarithm of radius. The starting distribution for the logarithm of radius of the j^{th} primary drop is

$$T_{0j}(x_0) = \delta(x_0 - x_j) \qquad (4.1)$$

Using the distribution function in equation 3.5 at $\nu t_{bu} = 1$, one can express the solution by the error function,

$$T_j(x,t) = \frac{1}{2}\left[1 + erf\left(\frac{x - x_j - \langle\xi\rangle}{\sqrt{2\langle\xi^2\rangle}}\right)\right] \tag{4.2}$$

The product droplet velocity is computed by adding to the primary drop velocity a factor $\mathbf{w}_{bu}$, which is randomly distributed in a plane normal to the relative velocity of the parent drop and gas, with the magnitude determined by the radius of the parent drop and the breakup frequency, ν

$$|\mathbf{w}_{bu}| = r\nu \tag{4.3}$$

4.2. *Critical radius and breakup frequency*

The critical (or maximum stable) radius is determined when disruptive hydrodynamic forces are balanced by capillary forces

$$r_{cr} = \frac{We_{cr}\sigma}{\rho_g u_r^2} \tag{4.4}$$

where u_r is the relative velocity between liquid and gas velocity, σ the surface tension coefficient, We_{cr} the critical Weber number, which can be taken of the order of six over a wide range of Ohnesorge numbers (Gelfand *et al.* (1975), Pilch & Erdman (1987)). This expression can be further modified by estimating the mean square of relative droplet-to-gas velocity by mean viscous dissipation and Stokes time scale (Kuznezov & Sabel'nikov (1990)):

$$\langle u_r^2\rangle \approx \epsilon\tau_{st} \tag{4.5}$$

This gives a new expression for critical radius,

$$r_{cr} = \frac{36^{1/3}}{2}\left(\frac{We_{cr}\sigma\nu}{\epsilon\rho_l}\right)^{1/3} \tag{4.6}$$

This expression, however, requires a reliable knowledge of viscous dissipation rate. This critical radius, thereby, is calculated by the standard expression 4.4. Note that introducing the turbulent Weber number, $We_{tur} = \frac{\rho_g l_{tur} u_{tur}^2}{\sigma}$, and using equation 4.5, one obtains,

$$We_{cr} = \frac{1}{36}\frac{\rho_l}{\rho_g} Re_{tur} We_{tur}\left(\frac{2r_{cr}}{l_{tur}}\right)^3 \tag{4.7}$$

Assuming that at scales where breakup takes place, Re_{tur} is of the order of unity and $l_{tur} \approx \eta$, one obtains,

$$\frac{2r_{cr}}{\eta} = 3.3\left(\frac{We_\eta}{We_{cr}}\right)^{-\frac{1}{3}}\left(\frac{\rho_g}{\rho_l}\right)^{\frac{1}{3}} \tag{4.8}$$

Equation 4.8 is used to estimate the local value of $\langle\xi^2\rangle$. The choice of the breakup frequency has to be stated based on the physics of spray atomization. In this paper, the

breakup time scale is taken to be

$$t_{bu} = Core_{br}\sqrt{\frac{\rho_l}{\rho_g}}r/u_r \tag{4.9}$$

where $Core_{br} = 1.73$ is used in the present work.

4.3. *Choice of parameters* $\langle\xi\rangle$ *and* $\langle\xi^2\rangle$

Multiplying equation 3.6 by r and integrating over the entire radius range gives an expression for the first moment

$$\langle r\rangle = \langle r\rangle_{t=0} exp\left[\nu\left(\langle\xi\rangle + 0.5\langle\xi^2\rangle\right)t\right] \tag{4.10}$$

Further more, the condition

$$\langle\xi\rangle < -\frac{1}{2}\langle\xi^2\rangle \tag{4.11}$$

leads to the fact that parent droplets will disintegrate into smaller ones, $\frac{\langle r\rangle}{\langle r\rangle_{t=0}} < 0$. In this paper, the magnitude for $\langle\xi^2\rangle$ is assumed to be proportional to the maximum dispersion of radius $\langle\xi^2\rangle \propto \log 1 - \log\frac{r_{cr}}{r_j}$. Replacing in equation 4.8, η by the diameter of parent drop, one obtains

$$\langle\xi^2\rangle \approx -\log\frac{r_{cr}}{r_j} \approx const\cdot\log\left(\frac{We_{r_j}}{We_{cr}}\right)^{1/3} \tag{4.12}$$

with $const \leq 1$ and $\langle\xi\rangle$, the arbitrary parameter, obtained from equations 4.11- 4.12. In the present work, we used $const = 0.1$.

5. An illustration of Lagrangian computation of the atomizing spray

A liquid jet is injected through a single-hole nozzle into a constant pressure, room-temperature nitrogen chamber. The spray injection velocity is 102 m/s, chamber pressure 1.1 MPa, orifice diameter $300\mu m$, and the dimensions of the constant volume bomb (2.8 cm x 13.8 cm), are corresponding to the experimental conditions used by Hiroyasu & Kadota (1974). Figure 1 shows the distribution of droplets at various computational times. The near-nozzle region is mostly presented by large unbroken drops accompanied by small stripped droplets. The ligament-like liquid structures deflected outward are seen in this figure and the spray angle is close to the empirical one. The computed configuration of atomizing spray qualitatively resembles the spray observed from the experimental images. Figure 2 shows a closeup view of spray near and futher away from the injector. A broad spectrum of droplet sizes is present with local co-existence of large and small droplets, indicating the superiority of the present model over conventional droplet sheet-breakup model (Reitz & Diwakar, (1987)). The variation of spray penetration depth with time is presented in figure 3, showing reasonable comparison with the experimental measurements of Hiroyasu & Kadota (1974).

6. Summary and future plans

The stochastic modeling of the spray-sheet breakup involving Lagrangian tracking of the droplets along with LES of the gas-phase flow has been introduced. The process is considered in the framework of cascade of uncorrelated breakage events,up to the maximum

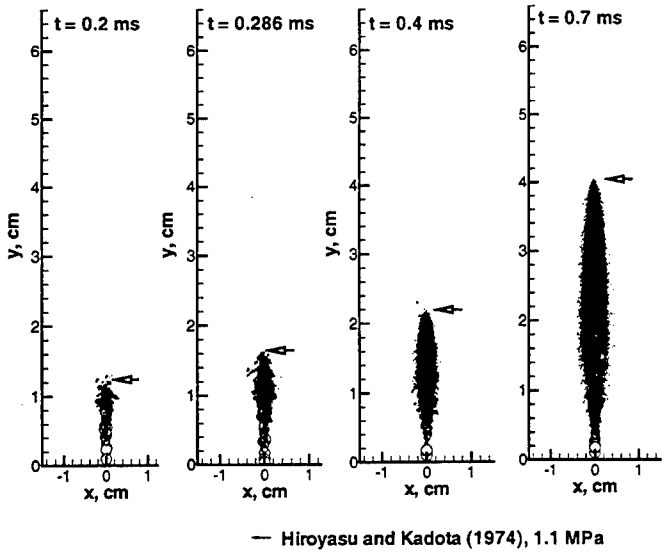

FIGURE 1. Spray penetration at different times. The size of the circles scale with individual droplet diameters.

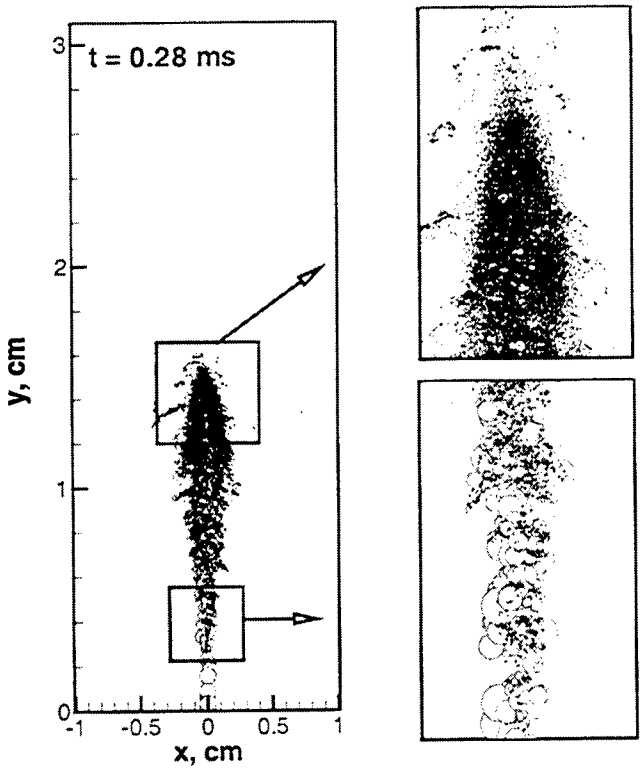

FIGURE 2. Closeup view of droplet sheet breakup showing a wide distribution of droplet radii at two locations.

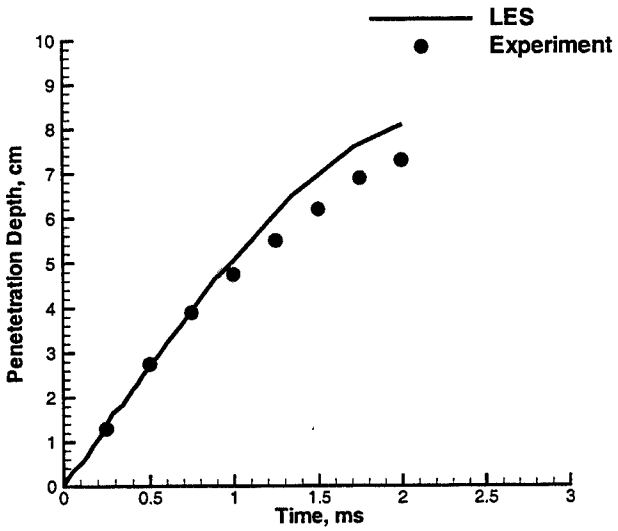

FIGURE 3. Penetration depth for 1.1 MPa.

stable (critical) droplet size, independent of its initial size . The Kolmogorov's discrete model of particle breakup can be represented by its Fokker-Planck approximation and the solution of this equation has been used for production of new droplets. Computations of spray at the diesel-like conditions were performed. The results compared with measurement showed that the computed configuration resembles qualitatively the spray photographic examination. A broad spectrum of droplet sizes is obtained at each spray location. The large number of droplets generated leads to a significant slow down of the computer code. In order to alleviate computational costs, we envisage to work on the hybrid droplets-parcels Lagrangian formulation. In this approach, if the number of droplets in a computational exceeds some pre-specified limit, they can be combined to form a parcel by conserving mass and momentum. This leads to combination of parcels and droplets within the computational domain and effectively reduces the actual number of particles being tracked.

Acknowledgments

The authors gratefully acknowledge Prof. K. Mahesh for his valuable help in setting up the gas-phase solver used in this work. We also acknowledge Dr. J. C. Oefelein for providing the Lagrangian modules developed for structured codes.

REFERENCES

KOLMOGOROV, A. N. 1941 On the log-normal distribution of particle sizes during breakup process. *Dokl. Akad. Nauk. SSSR* **31**, (2), 99-101.

GOROKHOVSKI, M. & SAVELIEV, V. 2001 Analyses of Kolmogorov's model of particle breakup and its application in the computation of air-blast-atomization in sprays. Submitted to *Phys. Fluids.*

LIU, A. B., REITZ, R. D. 1993 Mechanism of air-assisted liquid atomization. *J. Atom. Sprays* **3**, 55-75.

ZHOU, W. X., YU, Z. H. 2000 Multifractality of drop breakup in the atomization process. *Phys. Rev. E* **63**, 016302.

SHAVIT, U., CHIGIER, N. 1995 Fractal dimensions of liquid jet interface under breakup *J. Atom. Sprays* **5**, 525-543.

MAHESH, K., CONSTANTINESCU, G., APTE, S., IACCARINO, G., AND MOIN, P. 2001 large eddy simulation of gas turbine combustors. *Annual Research Briefs,* Center for Turbulence Research, NASA Ames/Stanford Univ., 3-17.

GEL'FAND, B. E., GUBIN, S. A., KOGARKO, S. M., KOMAR, S. P. 1975 Singularities of the breakup of viscous liquid droplets in shock waves. *J. Engr. Phys.*, **25**, 1140-1142.

PILCH M., ERDMAN C. A. 1987 Use of breakup time data and velocity history data to predict the maximum size of stable fragments for acceleration-induced breakup of a liquid drop, *Int. J. Multiphase Flow*, **13**, 741-757.

KUZNEZOV, V. R., SABEL'NIKOV, V. A. 1990 *Turbulence and Combustion*, Hemisphere Publishing Corporation, 362. Sabelnikov, V. A, Private communication.

REITZ, R. D., DIWAKAR, R. 1987, Structure of High-Pressure Fuel Sprays *SAE* paper 870598.

HIROYASU, M., KADOTA, T. 1974 Fuel droplet size distribution in diesel combustion chamber, *SAE* paper 740715.

FAETH, G. M., HSIANG, L. P., WU, P. K. 1995 Structure and breakup properties of sprays *Int. J. Multiphase Flow* **21**, 99-127.

Study of the turbulence modulation in particle-laden flows using LES

By Javier García †

1. Objective and motivation

One of the most interesting problems in fluid dynamics is the prediction of particle-laden turbulent flows. These flows are as diverse as pollutant dispersion in the atmosphere and contaminant transport in industrial applications. An issue of primary importance for moderately dense suspensions concerns how particles affect the turbulent flow itself, the so-called two-way coupling. It is known that the addition of particles to a turbulent flow may change the intensity significantly, even at very low volume fraction. The principal difficulty in the prediction of particle-laden turbulent flows is that traditional approaches model particle transport using the Reynolds-averaged Navier-Stokes (RANS) equations. The RANS methods do not accurately predict the Eulerian turbulence field, and it is known that accurate prediction of particle transport is strongly dependent upon providing a realistic description of the velocity field encountered along particle trajectories.

Although the most accurate approach to representing the structure of turbulence – including particle transport – is direct numerical simulation (DNS), is not practical for use as a predictive tool because it remains restricted to relatively low Reynolds numbers. An approach which is not as severely restricted in the range of Reynolds number as DNS is large eddy simulation (LES). LES predictions are less sensitive to modeling errors than RANS calculations and, since the subgrid scales are more universal than large scales, it is also possible to represent the effect of the subgrid scales using relatively simple models. A significant advantage of LES over RANS methods is that it permits a much more accurate accounting of particle-turbulence interactions. If modulation of the turbulence by particles is negligible and if the particle relaxation time is of the order of the turbulent time macro-scales, LES of gas-particle flows can be expected to be as accurate as in single-phase flow. In contrast, if two-way coupling effects are important, then the subgrid turbulence model might require modification. The principal objective of this work is application of large eddy simulation to computation of a well defined turbulent shear flow, fully developed channel flow, for which experimental results – Kulick *et al.* (1994) – exist for comparison. Also, a subgrid model which takes into account the presence of particles is proposed and evaluated.

2. Physical and numerical model

2.1. *Fluid motion*

The space-filtered continuity and time-dependent Navier-Stokes equations were used to model the continuous gas phase.

$$\frac{\partial v_{gi}}{\partial x_i} = 0 \tag{2.1}$$

† Universidad Politécnica de Madrid

$$\frac{\partial v_{gi}}{\partial t} + \frac{\partial v_{gi} v_{gj}}{\partial x_j} = -\frac{\partial}{\partial x_i}\left(\frac{p}{\rho_g}\right) + \frac{1}{Re}\frac{\partial^2 v_{gi}}{\partial x_j \partial x_j} - \frac{\partial \tau_{ij}}{\partial x_j} + \frac{f_{pi}}{\rho_g} \tag{2.2}$$

In order to take into account the particle effect on the fluid (two-way coupling) an additional term was included in the momentum equation f_p. This term is given by the sum of all forces on all particles in a fluid computational cell.

$$f_p = -\frac{1}{V_{cell}} \sum_{j=1}^{N_{cell}} f_{gj} \tag{2.3}$$

where V_{cell} is the volume of a fluid computational cell, N_{cell} is the number of particles in that cell and f_{gj} is the fluid force on the jth particle in that cell.

2.2. *Particle motion*

A Lagrangian approach is employed to predict the properties of each particle directly from the equation of motion. The particle equation of motion used in the simulations describes the motion of particles with densities substantially greater than that of the surrounding fluid, and diameters small compared to the Kolmogorov scale:

$$\frac{dv_{pi}}{dt} = -\frac{\rho_g}{\rho_p}\frac{3}{4}\frac{C_D}{d}|\mathbf{v}_p - \mathbf{v}_g|(v_{pi} - v_{gi}) \tag{2.4}$$

where v_{pi} is the velocity of the particle and v_{gi} is the velocity of the gas at the particle position. An empirical relation for C_D from Clift *et al.* (1978), valid for particle Reynolds numbers up to about 40, was employed:

$$C_D = \frac{24}{Re_p}(1 + 0.15 Re_p^{0.687}). \tag{2.5}$$

2.3. *SGS model*

The following assumptions have been made to derive the new model:

(*a*) The density of the particles is much larger than the gas density, and Basset forces and virtual mass can be neglected.

(*b*) The particles are spherical.

(*c*) The particle volume fraction is small enough that particle-particle interaction can be neglected.

(*d*) In the local movement of the particles, gravity can be neglected compared to inertia.

The equation of motion for the particles can be rewritten as follows:

$$\rho_p V_p \frac{d\mathbf{u}}{dt} = \rho_p V_p \frac{d\mathbf{v}_p}{dt} - \mathbf{F}_D \tag{2.6}$$

where $\mathbf{u}$ stands for the relative velocity between fluid and particle, and

$$\mathbf{F}_D = \frac{1}{2} C_D \rho_g S_g \mathbf{u}|\mathbf{u}|. \tag{2.7}$$

For the different turbulent length scales, λ, in the interval between the integral and Kolmogorov scales ($L > \lambda > \eta$), it is possible to scale the different terms of the equation of motion:

- For the gas phase

$$\tau_{g\lambda} \sim \frac{\lambda}{v_{g\lambda}} \sim \frac{\lambda^{2/3}}{\epsilon^{1/3}} \tag{2.8}$$

$$v_{g\lambda} \sim (\epsilon\lambda)^{1/3} \tag{2.9}$$

$$\frac{dv_g}{dt} \sim \frac{v_{g\lambda}}{\tau_{g\lambda}} \sim \frac{\lambda}{\tau_{g\lambda}^2} \sim \frac{\epsilon^{2/3}}{\lambda^{1/3}} \tag{2.10}$$

- For the particles

$$\tau_{p\lambda} \sim \frac{\lambda}{u_\lambda} \tag{2.11}$$

$$\frac{du}{dt} \sim \frac{u_\lambda}{\tau_{p\lambda}} \sim \frac{u_\lambda}{\lambda/u_\lambda} \sim \frac{u_\lambda^2}{\lambda} \tag{2.12}$$

- Drag force

$$\mathbf{F}_D \sim \frac{1}{2} C_D \rho_g S_g u_\lambda^2 \tag{2.13}$$

Substituting in the equation of motion

$$\rho_p V_p \frac{d\mathbf{u}}{dt} \sim \rho_p V_p \frac{d\mathbf{v}_g}{dt} - \mathbf{F}_D \tag{2.14}$$

we obtain for the relative velocity:

$$u_\lambda \sim (\rho_p V_p)^{1/2} \frac{\epsilon^{1/3}\lambda^{1/3}}{(\rho_p V_p + \frac{1}{2} C_D \rho_g S_p \lambda)^{1/2}}. \tag{2.15}$$

It can be seen that u_λ should have a maximum for a certain value of λ, given by:

$$\frac{\partial u_\lambda}{\partial \lambda} = 0 \rightarrow \lambda|_{u_\lambda max} = \lambda^* \sim \frac{1}{C_D} \frac{\rho_p}{\rho_g} \frac{V_p}{S_p} \rightarrow \lambda^* >> d \tag{2.16}$$

$$u^* \sim d^{1/3} \epsilon^{1/3} \left(\frac{\rho_p}{\rho_g}\right)^{1/3} \left(\frac{1}{C_D}\right)^{1/3}. \tag{2.17}$$

It is assumed that the turbulence dissipation due to the particles occurs mainly near the scale λ^*, and it will be represented by:

$$-\tau_{ij}\overline{S}_{ij}|_p \sim \rho_g C_D \left(\frac{\rho_g}{\rho_p}\right) \frac{u^{*3}}{d} \overline{\phi}_p. \tag{2.18}$$

Introducing u^* from the previous equation we obtain:

$$-\tau_{ij}\overline{S}_{ij}|_p \sim \rho_g \epsilon \overline{\phi}_p \Rightarrow -\tau_{ij}\overline{S}_{ij}|_p = C_p \rho_g \epsilon \overline{\phi}_p \tag{2.19}$$

In previous work with RANS models, by García & Crespo (2000) and Crespo *et al.* (2001)) the constant C_p has been estimated by comparison with different experiments. Then the total dissipation can be estimated as:

$$-\tau_{ij}\overline{S}_{ij} = \rho_g \epsilon (1 + C_p \overline{\phi}_p) \tag{2.20}$$

Using an eddy-viscosity model we get:

$$\nu_T = (C_s \Delta)^2 |\overline{S}| (1 + C_p \overline{\phi}_p) \tag{2.21}$$

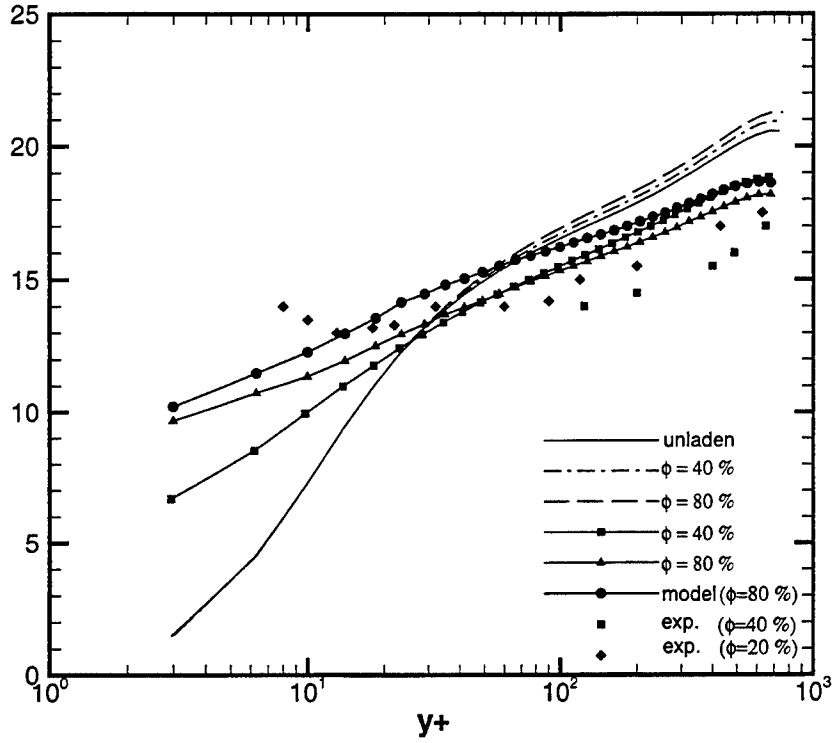

FIGURE 1. Particle streamwise mean velocity profiles, in wall units

Applying the Dynamic Procedure to obtain the model coefficient, we can obtain the Leonard term

$$\mathcal{L}_{ij} = -C \underbrace{\left(\widetilde{\overline{\Delta}}^2 |\widetilde{\overline{S}}| \widetilde{\overline{S}}_{ij} \left(1 + C_p \widetilde{\overline{\phi_p}}\right) - \overline{\Delta}^2 |\overline{S}| \overline{S}_{ij} \left(\widetilde{1 + C_p \overline{\phi_p}}\right) \right)}_{M_{ij}} \tag{2.22}$$

and, using least-squares averaging, the model parameter can be computed as:

$$C = -\frac{L_{kl} M_{kl}}{M_{kl} M_{kl}} \tag{2.23}$$

3. Simulation procedure

The calculations have been made with Pierce's code, described in Pierce & Moin (2001) implemented with Oefelein's routines for the simulation of Lagrangian particle dynamics. Large eddy simulations were performed under conditions chosen to match the experiments of Kulick *et al.* (1994). The fluid is air (kinematic viscosity $\nu = 1.5 \times 10^{-5}\,\mathrm{m^2 s^{-1}}$), and the friction velocity u_τ is $0.49\,\mathrm{ms^{-1}}$. The Reynolds number based on friction velocity and channel half-width is 644 (corresponding to a Reynolds number of 13,800 based on centerline velocity and channel half-width). The flow was resolved using $64 \times 64 \times 64$ grid

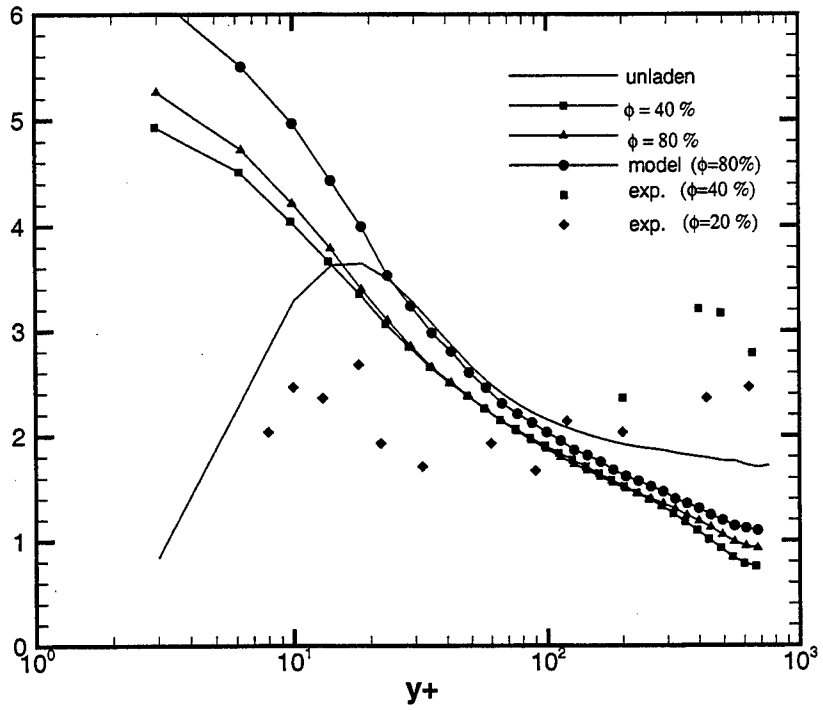

FIGURE 2. Particle streamwise fluctuations: mean-square intensity profiles, in wall units

points in the x, y, and z directions, respectively. The channel domain for the calculation was the same used by Wang and Squires (1996), $5\pi\delta/2 \times 2\delta \times \pi\delta/2$. The channel half width is $\delta = 0.02\,\mathrm{m}$. The grid spacing in wall coordinates in the x and z directions was $\Delta x^+ = 83$ and $\Delta z^+ = 17$. A stretched grid was used in the wall normal direction and the minimum grid spacing (close to the wall) was $\Delta y^+ = 1.5$.

Different values for the constant C_p have been used. At present a value of 0.9 produces the best agreement with the experimental results.

4. Results

The results obtained to date are presented in Figs. 1 to 4. In all cases, the particles used in the simulations are copper particles with density $\rho_p = 8800\,\mathrm{kgm}^{-3}$ and diameter $d = 70\,\mu\mathrm{m}$. Copper particles have been chosen for the first calculations because the effect of turbulence modulation is more intense and therefore is more sensitive to new models. The Figures show the results obtained for mass loading of 40 % and 80 %. The experimental data are taken from Kulick *et al.* (1994).

Figure 1 shows mean streamwise gas-velocity profiles. The calculated results show that mean gas-velocity profiles change slightly in the logarithmic region: this result agrees with numerical results from Yamamoto it et al. (2001). This Figure also shows the mean streamwise particle-velocity profiles. The profiles for particles are flatter than those for

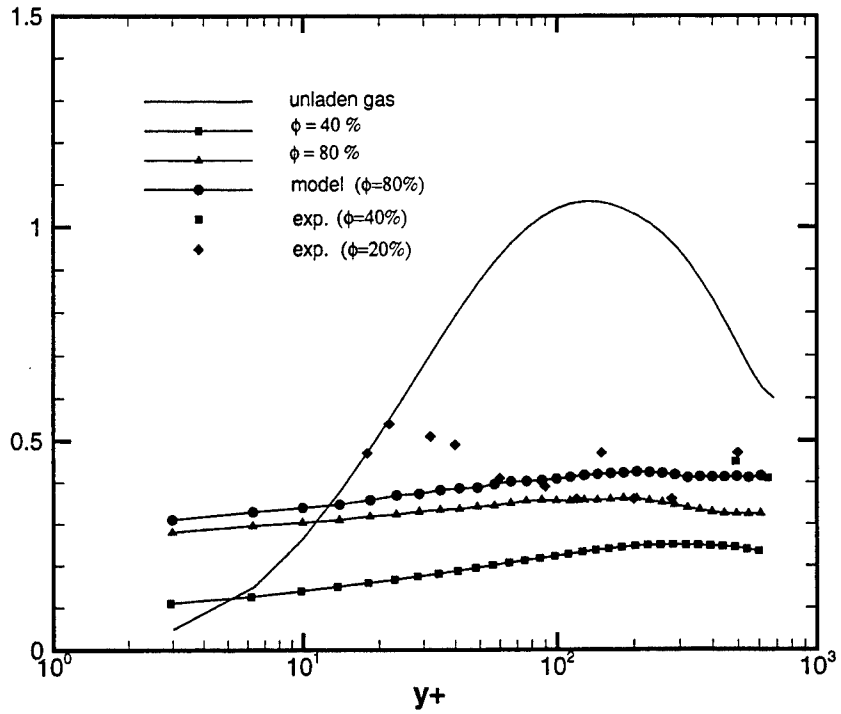

FIGURE 3. Particle wall-normal fluctuations: mean-square intensity profiles, in wall units

the gas. This trend is also observed in the experiments, where the particle velocity profiles are even flatter. The results calculated with the proposed SGS model have the same trend, but the velocities are greater than the previous results with the unmodified SGS model, and therefore greater than the experimental values.

Figure 2 shows profiles of particle streamwise fluctuation intensity profiles. The model proposed produces a profile shifted upward, mainly close to the wall. In any case, the numerical results obtained with or without the modified SGS model are similar to those obtained by Yamamoto it et al. (2001) without inter-particle collision, but the agreement between numerical calculations and experimental results is not good. The results obtained by Yamamoto it et al. (2001) with an inter-particle collision model suggest that collisions could play an important role.

Figure 3 shows fluctuation intensity profiles of the wall-normal particle velocity. In this case the numerical results agree well with the experiments. The fluctuation are larger with the proposed model, but the the opposite trend would be needed to agree with the experiments.

Figure 4 shows streamwise turbulence intensity profiles. It can be seen, in the numerical results obtained, that an increase in the mass loading produces an slight decrease in the turbulence intensity profile. But not so intense than that measured in the experiments. In this figure the proposed model does not produce a significant change compared to the SGS model without modification.

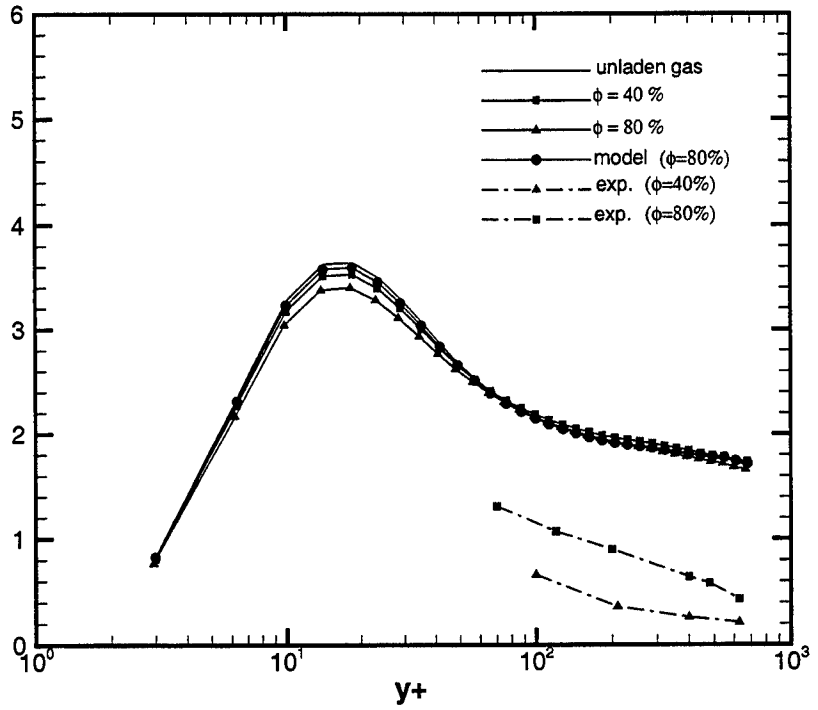

FIGURE 4. Streamwise turbulence mean-square intensity profiles, in wall units

5. Conclusions

A subgrid model that takes into account the presence of particles has been investigated. Simulations of gas-solid turbulent flow in a vertical downward channel flow at $Re_\tau = 644$ using LES were performed in order to study the proposed model. The results obtained so far indicate that it will be necessary to use a more sophisticated model to capture the complex phenomena involved in this type of flows. A recent paper suggests that inter-particle collisions could play an important role. It is also thought that an anisotropic model could improve the numerical results. These ways will be investigated in future works.

6. Acknowledgments

The author is grateful to Professor Parviz Moin for his kind invitation to the Center for Turbulence Research, and for providing the LES code used in this work and the required computing resources. The author thanks Professor J.K. Eaton for his comments. This work was supported by the Spanish Government (Estancias de investigadores españoles en centros extranjeros-PR2001-0079).

REFERENCES

BOIVIN, M., SIMONIN, O. & SQUIRES, K.D. 2000 On the prediction of gas-solid flows with two-way coupling using large eddy simulation. *Phys. Fluids* **12**, 2080-2090.

CLIFT, R., GRACE, J. R. & WEBER, M. E. 1978 *Bubbles, Drops and Particles.* Academic Press.

CRESPO, A., GRANADOS, A. L. & GARCÍA, J. 2001 Modeling of turbulence dissipation for gas-particle flows. *4th Intl. Conf. on Multiphase Flow, New Orleans.*

GARCÍA, J. CRESPO, A. 2000 A turbulent model for gas-particle jets. *J. Fluids Engg.* **122**, 505-509.

KULICK, J. D., FESSLER, J. R. & EATON, J. K. 1994 Particle response and turbulence modification in fully developed channel flow. *J. Fluid Mech.* **277**, 109-134.

PIERCE, C. D. & MOIN, P. 2001 Progress-variable approach for large eddy simulation of turbulent combustion. *Flow Physics and Computation Division, Department of Mechanical Engineering, Stanford University* Report TF-80.

WANG, Q. & SQUIRES, K. D. 1996 Large eddy simulation of particle-laden turbulent channel flow. *Phys. Fluids* **8**, 1207-1223.

YAMAMOTO, Y. *et al.* 2001 Large-eddy simulation of turbulent gas-particle flow in a vertical channel: effect of considering inter-particle collisions. *J. Fluid Mech.* **442**, 303-334.

A formulation for fast computations of rigid particulate flows

By N. A. Patankar †

1. Introduction

A formulation is presented for the direct numerical simulation of freely-moving rigid particles in fluids. This approach is an adaptation of the method described by Patankar *et al.* (2000), and does not rely on any model for fluid-particle interaction. The idea is to assume that the entire fluid-particle domain is a fluid and then to constrain the particle domain to move with a rigid motion. The fluid-particle motion is treated implicitly so that the mutual forces of interaction cancel because they are internal to the combined system. The formulation can be implemented by an immersed boundary and a fractional time-stepping technique. It is suitable for fast computations and can be employed for DNS, LES or RANS type simulations of turbulent particulate flows.

Numerical simulation techniques for solid-liquid flows, which do not use any model for fluid-particle interaction, have been developed over the past ten years. In these methods the fluid flow is governed by the continuity and momentum equations, whereas the particles are governed by the equation of motion for a rigid body. The flow field around each individual particle is resolved; the hydrodynamic force between the particle and the fluid is obtained from the solution and is not modeled by any drag law. These simulations, referred to as Direct Numerical Simulation (DNS) of solid-liquid flows, can be applied in numerous settings; e.g. sedimenting and fluidized suspensions, lubricated transport, hydraulic fracturing of reservoirs, slurries, understanding particle-turbulence interaction etc.

Hu *et al.* (1992), Hu (1996) and Hu *et al.* (2001) developed a finite-element method based on unstructured grids to simulate the motion of large numbers of rigid particles in two and three dimensions in Newtonian and viscoelastic fluids. This approach is based on an Arbitrary-Lagrangian-Eulerian (ALE) technique that uses a moving-mesh scheme to handle the time-dependent fluid domain. A new mesh is generated when the old one becomes too distorted, and the flow field is projected onto the new mesh. A combined fluid-particle weak formulation is used, where the hydrodynamic forces and torques on the particles are not calculated explicitly. Another numerical scheme based on the moving-mesh technique was developed by Johnson & Tezduyar (1996). They use a space-time finite-element formulation and a fully-explicit scheme in which the forces and torques on the particles are calculated explicitly to solve the equations of rigid motion.

Glowinski *et al.* (1999) presented a distributed Lagrange-multiplier/fictitious-domain method (DLM) for the direct numerical simulation of the motion of large numbers of rigid particles in Newtonian fluids. Their finite-element formulation permits the use of a fixed structured grid. This eliminates the need for remeshing the domain – a necessity in unstructured-grid-based methods. Structured grids also allow the use of fast and efficient solvers. In the DLM method the flow in the particle domain is constrained to be a rigid-

† Department of Mechanical Engineering, Northwestern University, Evanston

body motion using a field of Lagrange multipliers. The constraint of rigid-body motion is represented by $\mathbf{u} = \mathbf{U} + \boldsymbol{\Omega} \times \mathbf{r}$, where $\mathbf{u}$ is the velocity of the fluid at a point in the particle domain, $\mathbf{U}$ and $\boldsymbol{\Omega}$ are the translational and angular velocities of the particle, respectively, and $\mathbf{r}$ is the position vector of the point with respect to the particle centroid. The fluid-particle motion is treated implicitly using a combined weak formulation in which the mutual forces cancel.

A new DLM formulation for particulate flows was later presented by Patankar *et al.* (2000). In their approach, the rigid motion is imposed by constraining the deformation-rate tensor within the particle domain to be zero. This eliminates $\mathbf{U}$ and $\boldsymbol{\Omega}$ as variables from the coupled system of equations. This formulation recognizes that the rigidity constraint results in a stress field inside a rigid solid just as there is pressure in an incompressible fluid. The DLM formulations of Glowinski *et al.* (1999) and Patankar *et al.* (2000) were implemented by using a Marchuk-Yanenko fractional-step scheme for time discretization. A finite-element method was used.

The lattice-Boltzmann method (LBM) is an alternative scheme for simulating fluid flow problems. In LBM, simplified kinetic models, which incorporate the essential physics of the microscopic and mesoscopic equations, are constructed. The LBM has been adapted to simulate the motion of solid particles in Newtonian fluids: see Ladd (1994a), Ladd (1994b). Another approach, which uses an analytic solution near the particle and a numerical procedure away from it, was developed by Takagi *et al.* (2001).

Pan & Banerjee (1997) performed DNS of fluid-particle motion in turbulent flows. They solved the Navier-Stokes equations with an external body-source term that models the no-slip boundary condition on the surface of the particles. The source term is imposed only in the particle domain. The particle size is comparable to the computational mesh size. They use a pseudo-spectral method to solve the governing equations. All the calculations are carried out in the wave space, except for the evaluation of the non-linear advection term and the external body-source term which imposes the no-slip condition on the particle surfaces. While these results were helpful in the investigation of particle-turbulence interaction, the formulation of the problem was *ad hoc*. The expression for the source term in the particle domain was not based on rigorous theory. Iterations were required to arrive at a correct source term at each time step. Only the particle translational motion was considered, and a rigorous formulation should include the particle rotation.

Kajishima *et al.* (1999) developed an immersed-boundary approach for the DNS of turbulent rigid particulate flows. They added a source term in the fluid equation to account for the no-slip boundary condition on the fluid-particle interface. The fluid-particle momentum coupling was explicit, i.e. the fluid equations were solved with the latest known velocities of the particles and then the particle equations were solved with the latest known velocity field of the fluid. This procedure is often undesirable as it is unstable under certain circumstances: see Hu *et al.* (1992). The fully-explicit momentum coupling scheme of Kajishima *et al.* (1999) is first-order accurate in time. These issues can be particularly important in the development of robust and accurate schemes for the DNS of turbulent particulate flows.

The ALE and DLM formulations have been implemented for laminar flow conditions. Although the DLM approach has been successfully used for computations with up to 1204 spheres in three dimensions – see Pan *et al.* (2001) – the implicit coupling of fluid-particle momentum equations slows down the solution procedure. This is critical for DNS of turbulent particulate flows or for performing simulations with thousands of particles.

Methods based on explicit coupling can be unstable. In this paper we develop a technique for efficient computations of high and low Reynolds number particulate flows. The new formulation allows fast computations of particulate flows, and at the same time has implicit coupling of fluid-particle momentum equations. It can be easily implemented by using finite-element, finite-difference or finite-volume methods. It is suitable for DNS, LES or RANS type simulations of turbulent particulate flows.

In Section 2, the numerical scheme will be presented. Results will be presented in Section 3.

2. The numerical scheme

The approach in this paper is an adaptation of the formulation of Patankar *et al.* (2000). In this Section, we will first present their formulation and then introduce our new approach as a modification of their method.

2.1. *The stress-DLM formulation of Patankar et al. (2000)*

Let V be the computational space, which includes both the fluid and the particle domains. Let $P(t)$ be the particle domain. Let the fluid boundary, not shared with the particle, be denoted by ∂V. For simplicity we assume that a Dirichlet boundary condition is imposed on ∂V. The equations are presented by assuming only one particle in the computational domain. The formulation can be easily generalized beyond these assumptions. The body force is assumed to be constant so that there is no net torque acting on the particle. The governing equations for fluid motion are given by:

$$\rho_f(\frac{\partial \mathbf{u}}{\partial t} + (\mathbf{u}\cdot\nabla)\mathbf{u}) = \nabla\cdot\boldsymbol{\Sigma} + \rho_f\mathbf{g} \quad \text{in} \quad V\setminus\overline{P(t)}, \tag{2.1}$$

$$\nabla\cdot\mathbf{u} = 0 \quad \text{in} \quad V\setminus\overline{P(t)}, \tag{2.2}$$

$$\mathbf{u} = \mathbf{u}_{\partial V}(t) \quad \text{on} \quad \partial V, \tag{2.3}$$

$$\mathbf{u} = \mathbf{u}_i \quad \& \quad \boldsymbol{\Sigma}\cdot\mathbf{n} = \mathbf{t} \quad \text{on} \quad \partial P(t), \tag{2.4}$$

$$\mathbf{u}|_{t=0} = \mathbf{u}_0(\mathbf{x}) \quad \text{in} \quad V\setminus\overline{P(0)}, \tag{2.5}$$

where ρ_f is the fluid density, $\mathbf{u}$ is the fluid velocity, $\mathbf{g}$ is the acceleration due to gravity, $\mathbf{n}$ is the unit outward normal on the particle surface, $\mathbf{u}_i$ is the velocity at the fluid-particle interface $\partial P(t)$ and $\boldsymbol{\Sigma}$ is the stress tensor. The initial velocity $\mathbf{u}_0$ should satisfy Eq. (2.2). The boundary velocity in Eq. (2.3) should satisfy the compatibility condition due to Eq. (2.2). For an incompressible fluid the divergence-free constraint Eq. (2.2) gives rise to pressure in the fluid. The stress tensor is given by:

$$\boldsymbol{\Sigma} = -p\mathbf{I} + \boldsymbol{\Pi} \tag{2.6}$$

where $\mathbf{I}$ is the identity tensor, p is the pressure and $\boldsymbol{\Pi}$ is the extra stress tensor. For a Newtonian fluid $\boldsymbol{\Pi}$ represents the viscous stress, whereas for a viscoelastic fluid it represents the viscous and elastic stresses in the fluid. The extra stress depends on the deformation rate of the fluid at a given location. In a viscoelastic fluid it also depends on the history of deformation.

Patankar *et al.* (2000) treated the particle as a fluid with an additional constraint to impose the rigid motion. The governing equations for particle motion are:

$$\rho_s(\frac{\partial \mathbf{u}}{\partial t} + (\mathbf{u}\cdot\nabla)\mathbf{u}) = \nabla\cdot\boldsymbol{\Sigma} + \rho_s\mathbf{g} \quad \text{in} \quad P(t), \tag{2.7}$$

$$\nabla \cdot \mathbf{u} = 0 \quad \text{in} \quad P(t), \tag{2.8}$$

$$\nabla \cdot (\mathbf{D}[\mathbf{u}]) = \mathbf{0} \quad \text{in} \quad P(t) \quad \& \quad \mathbf{D}[\mathbf{u}] \cdot \mathbf{n} = \mathbf{0} \quad \text{on} \quad \partial P(t), \tag{2.9}$$

$$\mathbf{u} = \mathbf{u}_i \quad \& \quad \boldsymbol{\Sigma} \cdot \mathbf{n} = \mathbf{t} \quad \text{on} \quad \partial P(t), \tag{2.10}$$

$$\mathbf{u}|_{t=0} = \mathbf{u}_0(\mathbf{x}) \quad \text{in} \quad P(0), \tag{2.11}$$

where ρ_s is the particle density. Equation (2.9) represents the rigidity constraint that sets the deformation-rate tensor, $\mathbf{D}[\mathbf{u}] = (\nabla \mathbf{u} + \nabla \mathbf{u}^T)/2$, in the particle domain equal to zero. The initial velocity $\mathbf{u}_0$ should satisfy Eq. (2.9). The rigidity constraint ensures that the velocity field is divergence-free. Hence Eq. (2.8) is a redundant constraint. Nevertheless, it is retained in order to facilitate the application of the fluid equations in the entire domain. The stress inside the particle – see Patankar *et al.* (2000) – is given by

$$\boldsymbol{\Sigma} = -p\mathbf{I} + \mathbf{D}[\boldsymbol{\Lambda}] + \boldsymbol{\Pi} \tag{2.12}$$

where $\boldsymbol{\Lambda}$ is the Lagrange multiplier due to the rigidity constraint and $\boldsymbol{\Pi}$ is the extra stress tensor which depends on the deformation rate. The extra stress is zero inside the particle domain since the deformation rate is constrained to be zero. A two-dimensional case is considered for simplicity. The combined weak form of the fluid-particle equations is given by:

For $t > 0$, find $\mathbf{u} \in W_u$, $p \in L_0^2(V)$, $\boldsymbol{\Lambda} \in H^1(P(t))^2$ satisfying

$$\begin{aligned}
&\int_V \rho_f \left(\frac{\partial \mathbf{u}}{\partial t} + (\mathbf{u} \cdot \nabla)\mathbf{u} - \mathbf{g}\right) \cdot \mathbf{v}\, d\mathbf{x} - \int_V p(\nabla \cdot \mathbf{v})\, d\mathbf{x} + \int_V q(\nabla \cdot \mathbf{u})\, d\mathbf{x} \\
&+ \int_V \boldsymbol{\Pi} : \mathbf{D}[\mathbf{v}]\, d\mathbf{x} + \int_{P(t)} (\rho_s - \rho_f)\left(\frac{\partial \mathbf{u}}{\partial t} + (\mathbf{u} \cdot \nabla)\mathbf{u} - \mathbf{g}\right) \cdot \mathbf{v}\, d\mathbf{x} \\
&+ \int_{P(t)} \mathbf{D}[\boldsymbol{\Lambda}] : \mathbf{D}[\mathbf{v}]\, d\mathbf{x} + \int_{P(t)} \mathbf{D}[\boldsymbol{\Psi}] : \mathbf{D}[\mathbf{u}]\, d\mathbf{x} = 0, \\
&\forall \quad \mathbf{v} \in W_0, \quad q \in L_0^2(V) \quad \& \quad \boldsymbol{\Psi} \in H^1(P(t))^2,
\end{aligned} \tag{2.13}$$

where

$$\begin{aligned}
W_u(t) &= \{\mathbf{v} | \mathbf{v} \in H^1(V)^2, \mathbf{v} = \mathbf{u}_{\partial V}(t) \quad on \quad \partial V\}, \\
W_0(t) &= \{\mathbf{v} | \mathbf{v} \in H^1(V)^2, \mathbf{v} = \mathbf{0} \quad on \quad \partial V\}, \\
L_0^2(V) &= \{q \in L^2(V) | \int_V q\, d\mathbf{x} = 0\},
\end{aligned}$$

and $\mathbf{v}$, $\boldsymbol{\Psi}$ & q are the variations of $\mathbf{u}$, $\boldsymbol{\Lambda}$ & p, respectively. The initial conditions are given by Eq. (2.5) and Eq. (2.11). The fluid-particle interface condition is internal to the combined system. Hence there are no explicit interface-force or velocity terms in Eq. (2.13). The particle translational and angular velocities are not present in the combined form Eq. (2.13). This is especially convenient in a three-dimensional case with irregularly-shaped bodies, for which there is added complexity due to the nonlinear nature of the angular-momentum equation. Equation (2.13) is solved by a Marchuk-Yanenko fractional-step scheme. The algorithm based on this scheme, given by Patankar *et al.* (2000), is:

(1) Calculate particle velocity: given $\mathbf{u}^n$ and $P(t_n)$, find the translational velocity, $\mathbf{U}^n$, of the particle:

$$M\mathbf{U}^n = \int_{P(t^n)} \rho_s \mathbf{u}^n\, d\mathbf{x}, \tag{2.14}$$

where M is the mass of the particle. For a non-circular particle it is necessary to update

the angular position of the particle. The angular velocity, $\mathbf{\Omega}^n$, of the particle is given by

$$\mathbf{I}_p\mathbf{\Omega}^n = \int_{P(t^n)} \mathbf{r} \times \rho_s \mathbf{u}^n \, d\mathbf{x}, \tag{2.15}$$

where $\mathbf{I}_p$ is the moment of inertia of the particle.

(2) Explicit update of particle position: Compute $\mathbf{X}^{n+1}$ by the following procedure:
Set $\mathbf{X}^{n+1,0} = \mathbf{X}^n$.
do $k = 1, K$

$$\mathbf{X}^{*n+1,k} = \mathbf{X}^{n+1,k-1} + (\frac{\mathbf{U}^n + \mathbf{U}^{n-1}}{2})(\frac{\Delta t}{K}) \tag{2.16}$$

$$\mathbf{X}^{n+1,k} = \mathbf{X}^{*n+1,k} + (\frac{\mathbf{F}(\mathbf{X}^{n+1,k-1}) + \mathbf{F}(\mathbf{X}^{*n+1,k})}{2M})(\frac{\Delta t^2}{2K^2}) \tag{2.17}$$

enddo
Set $\mathbf{X}^{n+1} = \mathbf{X}^{n+1,K}$, this also gives $P(t^{n+1})$.
Set

$$\mathbf{A}_c^{n+1} = \frac{2}{\Delta t^2}(\mathbf{X}^{n+1} - \mathbf{X}^n - (\frac{\mathbf{U}^n + \mathbf{U}^{n-1}}{2})\Delta t), \tag{2.18}$$

where $\mathbf{X}$ is the position of the particle centroid and $\mathbf{F}$ denotes the collision force acting on the particles to prevent them from penetrating each other or the walls of the domain. $\mathbf{A}_c$ is the acceleration of the particle due to collision. This term provides an additional body force acting on the particle and is included in the combined momentum equation to be solved in the subsequent steps. Details of the collision-force model used in this paper can be found in Glowinski *et al.* (1999). An additional equation to update the angular position is required for non-circular particles.

(3) Fractional step 1: Find $\mathbf{u}^{n+1/3} \in W_u(t^{n+1})$ and $p^{n+1/3} \in L_0^2(V)$ satisfying

$$\int_V \rho_f(\frac{\mathbf{u}^{n+1/3} - \mathbf{u}^n}{\Delta t} - \mathbf{g}) \cdot \mathbf{v} \, d\mathbf{x} - \int_V p^{n+1/3}(\nabla \cdot \mathbf{v}) \, d\mathbf{x} + \int_V q(\nabla \cdot \mathbf{u}^{n+1/3}) \, d\mathbf{x}$$
$$+\alpha \int_V 2\eta \mathbf{D}[\mathbf{u}^{n+1/3}] : \mathbf{D}[\mathbf{v}] \, d\mathbf{x} = 0, \quad \forall \quad \mathbf{v} \in W_0 \quad \& \quad q \in L_0^2(V). \tag{2.19}$$

(4) Fractional step 2: Find $\mathbf{u}^{n+2/3} \in W_u(t^{n+1})$ satisfying

$$\int_V \rho_f(\frac{\mathbf{u}^{n+2/3} - \mathbf{u}^{n+1/3}}{\Delta t} + (\mathbf{u}^{n+2/3} \cdot \nabla)\mathbf{u}^{n+2/3}) \cdot \mathbf{v} \, d\mathbf{x}$$
$$+\beta \int_V 2\eta \mathbf{D}[\mathbf{u}^{n+2/3}] : \mathbf{D}[\mathbf{v}] \, d\mathbf{x} = 0, \quad \forall \quad \mathbf{v} \in W_0. \tag{2.20}$$

(5) Fractional step 3: Find $\mathbf{u}^{n+1} \in W_u(t^{n+1})$ and $\mathbf{\Lambda}^{n+1} \in H^1(P(t^{n+1}))^2$ satisfying

$$\int_V \rho_f(\frac{\mathbf{u}^{n+1} - \mathbf{u}^{n+2/3}}{\Delta t}) \cdot \mathbf{v} \, d\mathbf{x} + \gamma \int_V 2\eta \mathbf{D}[\mathbf{u}^{n+1}] : \mathbf{D}[\mathbf{v}] \, d\mathbf{x} - \int_{P(t^{n+1})} \rho_s \mathbf{A}_c^{n+1} \cdot \, d\mathbf{x}$$
$$+ \int_{P(t^{n+1})} \mathbf{D}[\mathbf{\Lambda}^{n+1}] : \mathbf{D}[\mathbf{v}] \, d\mathbf{x} + \int_{P(t^{n+1})} \mathbf{D}[\mathbf{\Psi}] : \mathbf{D}[\mathbf{u}^{n+1}] \, d\mathbf{x}$$
$$+ \int_{P(t^{n+1})} (\rho_s - \rho_f)(\frac{\mathbf{u}^{n+1} - \mathbf{u}^n}{\Delta t} + (\mathbf{u}^{n+2/3} \cdot \nabla)\mathbf{u}^{n+2/3} - \mathbf{g}) \cdot \mathbf{v} \, d\mathbf{x} = 0,$$
$$\forall \quad \mathbf{v} \in W_0, \quad \mathbf{\Psi} \in H^1(P(t^{n+1}))^2. \tag{2.21}$$

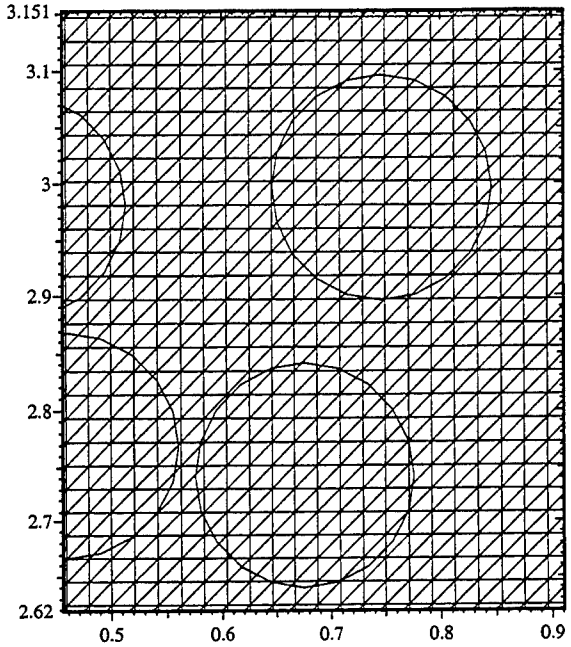

FIGURE 1. A fixed uniform triangular mesh spanning the fluid-particle domain. The circles indicate particle domains. $\mathbf{\Lambda}$ is defined on a triangular mesh (not shown in the figure) moving with the particles.

$\mathbf{\Pi}$ is replaced by the Newtonian stress with constant viscosity and is split into the three fractional steps such that $\alpha + \beta + \gamma = 1$. Patankar *et al.* (2000) and Glowinski *et al.* (1999) performed simulations with $\gamma = 0$. A fixed uniform triangular mesh was used to solve Eq. (2.19) & Eq. (2.20) over the entire domain (e.g. Fig. 1). To solve Eq. (2.21), $\mathbf{\Lambda}$ was defined on a triangular mesh moving with the particles. A linear interpolation was used to project $\mathbf{\Lambda}$ from the particle mesh to the uniform background mesh and to project $\mathbf{u}$ from the background mesh to the particle mesh. The above is a first-order time-discretization scheme. The first fractional step, Eq. (2.19), is the classical Stokes-like problem and is solved using a conjugate-gradient method. The second fractional step, Eq. (2.20), defines a nonlinear problem for velocity which is solved by using a least-squares conjugate-gradient algorithm. The third fractional step, Eq. (2.21), is solved by a Uzawa conjugate-gradient algorithm. Details are given in Patankar *et al.* (2000) and Glowinski *et al.* (1999). A Galerkin finite-element method was used.

2.2. *A new approach to impose the rigidity constraint*

The last fractional step, Eq. (2.21), adds computational cost to the solution procedure. This is the additional computational time spent to account for the presence of the particles. The last step is a projection of the velocity field on to a rigid motion in the particle domain. When $\gamma = 0$, the velocity is corrected only in the particle domains. This introduces an error in the form of small slip at the fluid-particle interface. Smaller time steps are preferable to reduce this error, especially when the particle and fluid densities are not matched. One way to minimize it is to add the buoyant-weight term in the first or second fractional step. In the numerical method the slip is smeared on the length

scale of the smallest grid size. Indeed, if $\gamma \neq 0$ then there is no slip on the interface but it increases the computational cost. A Uzawa conjugate gradient algorithm is used in the current implementations of the DLM formulation: see Glowinski *et al.* (1999) and Patankar *et al.* (2000). The correct velocity field and the corresponding Lagrange multiplier field are obtained simultaneously through an iterative procedure. Here we present a fast projection scheme that eliminates the need to solve the last fractional step by an iterative procedure when $\gamma = 0$. Even when $\gamma \neq 0$, the scheme presented can provide a significant reduction in the computational cost, at each iteration, as compared to the current implementations.

The last fractional step Eq. (2.21), with $\gamma = 0$, can be rewritten as

$$\int_{P(t^{n+1})} \rho_s \left(\frac{\mathbf{u}^{n+1} - \mathbf{u}^{n+2/3}}{\Delta t}\right) \cdot \mathbf{v}\, d\mathbf{x} = \int_{P(t^{n+1})} \mathbf{S} \cdot \mathbf{v}\, d\mathbf{x} + \int_{P(t^{n+1})} \mathbf{f} \cdot \mathbf{v}\, d\mathbf{x}, \quad (2.22)$$

where

$$\int_{P(t^{n+1})} \mathbf{S} \cdot \mathbf{v}\, d\mathbf{x} = \int_{P(t^{n+1})} \rho_s \mathbf{A}_c^{n+1} \cdot d\mathbf{x}$$

$$- \int_{P(t^{n+1})} (\rho_s - \rho_f)\left(\frac{\mathbf{u}^{n+2/3} - \mathbf{u}^n}{\Delta t} + (\mathbf{u}^{n+2/3} \cdot \nabla)\mathbf{u}^{n+2/3} - \mathbf{g}\right) \cdot \mathbf{v}\, d\mathbf{x},$$

&

$$\int_{P(t^{n+1})} \mathbf{f} \cdot \mathbf{v}\, d\mathbf{x} = - \int_{P(t^{n+1})} \mathbf{D}[\mathbf{\Lambda}^{n+1}] : \mathbf{D}[\mathbf{v}]\, d\mathbf{x}$$

$$= \int_{P(t^{n+1})} (\nabla \cdot \mathbf{D}[\mathbf{\Lambda}^{n+1}]) \cdot \mathbf{v}\, d\mathbf{x} - \int_{\partial P(t^{n+1})} (\mathbf{D}[\mathbf{\Lambda}^{n+1}] \cdot \mathbf{n}) \cdot \mathbf{v}\, d\mathbf{A}.$$

$\mathbf{S}$ is a source term that can be calculated explicitly, based on known values of the variables, and $\mathbf{f}$ is a source term, to be determined, due to the rigidity constraint. The weak form of the rigidity constraint Eq. (2.9) should be solved simultaneously with Eq. (2.22). Let us consider the strong form of Eq. (2.22), applicable in the particle domain:

$$\rho_s \left(\frac{\mathbf{u}^{n+1} - \mathbf{u}^{n+2/3}}{\Delta t}\right) = \mathbf{S} + \mathbf{f}. \quad (2.23)$$

The solution of Eq. (s2.23) can be obtained in two steps:

(a) Find $\hat{\mathbf{u}}$ by solving

$$\rho_s \left(\frac{\hat{\mathbf{u}} - \mathbf{u}^{n+2/3}}{\Delta t}\right) = \mathbf{S}. \quad (2.24)$$

(b) Find $\mathbf{u}^{n+1}$ by projecting $\hat{\mathbf{u}}$ on to a rigid body motion

$$\rho_s \left(\frac{\mathbf{u}^{n+1} - \hat{\mathbf{u}}}{\Delta t}\right) = \mathbf{f}. \quad (2.25)$$

$\hat{\mathbf{u}}$ is an intermediate velocity field in the particle domain. Solution of Eq. (2.24) is straightforward. To solve for $\mathbf{u}^{n+1}$ we need $\mathbf{f}$. An equation for $\mathbf{f}$ can be obtained by using Eq. (2.9). We get

$$\nabla \cdot (\mathbf{D}[\mathbf{u}^{n+1}]) = \nabla \cdot \left(\mathbf{D}[\hat{\mathbf{u}} + \frac{\mathbf{f}\Delta t}{\rho_s}]\right) = \mathbf{0},$$

$$\& \quad \mathbf{D}[\mathbf{u}^{n+1}] \cdot \mathbf{n} = \mathbf{D}[\hat{\mathbf{u}} + \frac{\mathbf{f}\Delta t}{\rho_s}] \cdot \mathbf{n} = \mathbf{0}. \quad (2.26)$$

The above equation implies that $\hat{\mathbf{u}} + (\mathbf{f}\Delta t)/\rho_s$ is a rigid-body motion, but it gives no

information about what this rigid motion should be. In fact, this rigid motion is the solution that we are seeking because $\hat{\mathbf{u}} + (\mathbf{f}\Delta t)/\rho_s = \mathbf{u}^{n+1}$.

We can obtain the rigid motion by imposing an additional condition that, in the projection step Eq. (2.25), the total linear and angular momenta in the individual particle domains should be conserved. The required solution is then obtained by the following procedure:

(i) Split $\hat{\mathbf{u}}$ as: $\hat{\mathbf{u}} = \hat{\mathbf{u}}_R + \hat{\mathbf{u}}'$, where $\hat{\mathbf{u}}_R$ is the velocity field of a rigid motion. It is given by:

$$\hat{\mathbf{u}}_R = \hat{\mathbf{U}} + \hat{\boldsymbol{\Omega}} \times \mathbf{r},$$
$$M\hat{\mathbf{U}} = \int_P \rho_s \hat{\mathbf{u}}\, d\mathbf{x} \quad \& \quad \mathbf{I}_p\hat{\boldsymbol{\Omega}} = \int_P \mathbf{r} \times \rho_s \hat{\mathbf{u}}\, d\mathbf{x}, \tag{2.27}$$

where $\mathbf{r}$ is the position vector of a point with respect to the centroid of the particle. This computational step is cheap since it is merely an addition (integration).

(ii) Since the linear and angular momenta should be conserved in the projection step, set $\mathbf{u}^{n+1} = \hat{\mathbf{u}}_R$ in the particle domain. This is the required solution. Note that $\mathbf{f} = -(\rho_s\hat{\mathbf{u}}')/\Delta t$.

The solution procedure above requires no iterations and is computationally cheap. We replace the last fractional step Eq. (2.21) in our previous work by this equivalent procedure. The results are presented in Section 3.

2.3. *Application to turbulent particulate flows*

The new formulation presented above is suitable for finite-volume or finite-difference immersed-boundary techniques for the simulation of freely-moving particles. The key issue that we address in this formulation is the fast implementation of the rigidity constraint, irrespective of the type of equations used to describe the fluid. Hence, it can be used in a DNS, LES or RANS type approach. As an example, we present a fractional step scheme similar to the approach of Kajishima *et al.* (1999) who performed DNS of turbulent flows with rigid particles.

For simplicity, we assume $\rho_s = \rho_f = \rho$ and a Newtonian fluid with constant viscosity. The scheme can be generalized to the unmatched-density case as in Section 2.2 above. The momentum equation is

$$\rho(\frac{\partial \mathbf{u}}{\partial t} + (\mathbf{u}\cdot\nabla)\mathbf{u}) = -\nabla p + \eta\nabla^2\mathbf{u} + \rho\mathbf{g} + \mathbf{f}, \tag{2.28}$$

where $\mathbf{f}$ is the additional source term due to the rigidity constraint Eq. (2.9) in the particle domain. In the formulation of Patankar *et al.* (2000) the source term is $\mathbf{f} = \nabla\cdot(\mathbf{D}[\boldsymbol{\Lambda}])$. The velocity field should be divergence-free in the entire domain. The above equations are to be solved on a fixed grid spanning the entire fluid/particle domain. A fractional-step scheme is summarized below:

(1) Find $\bar{\mathbf{u}}$ by solving the following equation over the entire domain

$$\rho(\frac{\bar{\mathbf{u}} - \mathbf{u}^n}{\Delta t}) = \frac{1}{2}(3\mathbf{H}^n - \mathbf{H}^{n-1}) - \nabla p^n + \frac{1}{2}\eta\nabla^2(\bar{\mathbf{u}} + \mathbf{u}^n) + \rho\mathbf{g}, \tag{2.29}$$

where

$$\mathbf{H} = -\rho(\mathbf{u}\cdot\nabla)\mathbf{u}.$$

The Adams-Bashforth method is used for the convection term and the Crank-Nicolson scheme is used for the viscous term.

(2) The projection of $\tilde{\mathbf{u}}$ on to a divergence-free velocity field $\tilde{\mathbf{u}}$ (applicable in the entire domain):

$$\nabla^2 G = \frac{\rho \nabla \cdot \tilde{\mathbf{u}}}{\Delta t}, \tag{2.30}$$

$$\rho\left(\frac{\tilde{\mathbf{u}} - \tilde{\mathbf{u}}}{\Delta t}\right) = -\nabla G. \tag{2.31}$$

(3) The projection of $\tilde{\mathbf{u}}$ on to a rigid motion in the particle domain:

$$\text{Split} \quad \tilde{\mathbf{u}} = \tilde{\mathbf{u}}_R + \tilde{\mathbf{u}}', \quad \text{where} \quad \tilde{\mathbf{u}}_R = \tilde{\mathbf{U}} + \tilde{\mathbf{\Omega}} \times \mathbf{r},$$

$$M\tilde{\mathbf{U}} = \int_P \rho_s \tilde{\mathbf{u}}\, d\mathbf{x} \quad \& \quad \mathbf{I}_p \tilde{\mathbf{\Omega}} = \int_P \mathbf{r} \times \rho_s \tilde{\mathbf{u}}\, d\mathbf{x}, \tag{2.32}$$

$$\mathbf{f} = \frac{\phi\rho(\tilde{\mathbf{u}}_R - \tilde{\mathbf{u}})}{\Delta t}, \tag{2.33}$$

$$\rho\left(\frac{\mathbf{u}^{n+1} - \tilde{\mathbf{u}}}{\Delta t}\right) = \mathbf{f}, \tag{2.34}$$

where ϕ is the particle volume fraction in a control volume associated with a given grid point: see Kajishima *et al.* (1999). Equations (2.32)-(2.34) are based on the new projection scheme presented in Section 2.2. As in the approach of Kajishima *et al.* (1999), we calculate $\mathbf{f}$ on the fixed grid nodes.

The advantage of our method is that the fluid and particle velocities are solved simultaneously, unlike the technique of Kajishima *et al.* (1999) where the fluid-particle momentum coupling was explicit. Explicit coupling is often undesirable since it can lead to instabilities: see e.g. Hu *et al.* (1992). The additional computational cost in step 3 will be negligible compared to the time required to solve the fluid equations over the entire domain.

A grid over the particle domain is not essential in the above approach. Integrations are required over the particle domains (Eq. 2.32) which do not conform with the fixed grid. The accuracy of the solution in the vicinity of the particle boundary depends on the interpolation schemes used in these integrations. The order of accuracy and the interpolation scheme can be improved, and need further investigation. Nevertheless, we believe that this is a promising approach for the simulation of large numbers of moving particles and for turbulent particulate flows, especially in light of the simulations of Kajishima *et al.* (1999).

3. Results

We validate our new formulation by presenting preliminary results of the sedimentation of two circular particles in a Newtonian fluid. We use the numerical scheme of Patankar *et al.* (2000), the only difference being that the new rigid-motion-projection scheme, in Section 2.2, is used instead of Eq. (2.21). A finite-element method is used with a triangular grid (Fig. 1).

It is known that two particles dropped close to each other in a Newtonian fluid undergo drafting, kissing and tumbling: see Fortes *et al.* (1987). This simulation has been used as a test case in our previous work.

We consider a channel 2 cm wide (x-direction) and 8 cm tall (y-direction). The fluid viscosity is 0.01 g/cm-s and the density is 1 g/cc. The particle density is 1.01 g/cc and the particle radius is 0.1 cm. Gravity acts in the negative y-direction. The simulation is

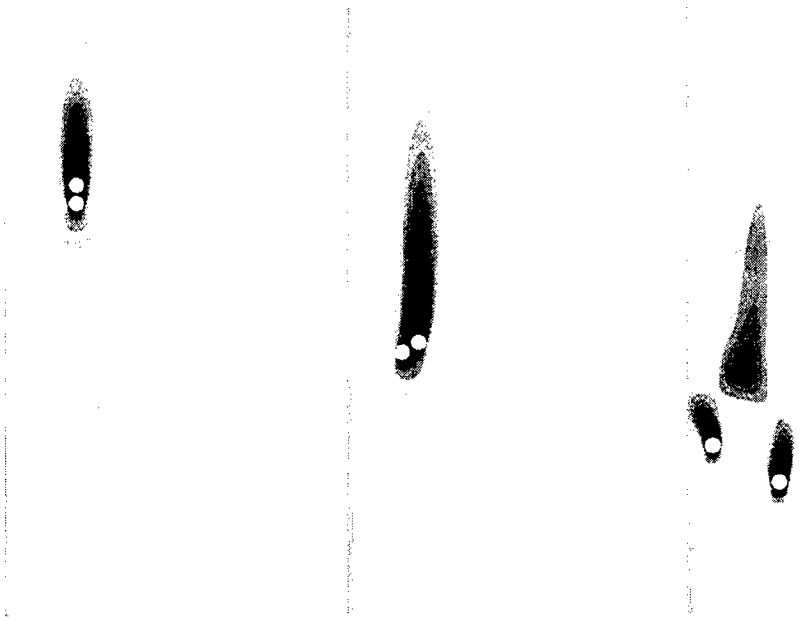

FIGURE 2. Numerical simulation of drafting, kissing and tumbling of particles in a Newtonian fluid. Contour plots of the vertical velocity in the fluid domain are shown at times $t = 1.5s$, $2s$ & $5s$, respectively. Darker shades imply higher downward velocity of the fluid. The particles are shown by white circles to make them visible; white color in the particle domains do not represent the vertical velocity.

started at $t = 0$ s by dropping two particles at the center of the channel at a height of 7.2 cm and 6.8 cm, respectively. The fixed (background) mesh size for velocity is 1/96 cm and for pressure is 1/48 cm (a coarser mesh is used for pressure to satisfy the Babuska-Brezzi condition). The particle mesh size is 1/96 cm. The time step is 0.0025 s.

Figure 2 shows the numerical simulation of drafting, kissing and tumbling of particles in a Newtonian fluid; in agreement with experimental observations. Figure 3 shows the plot of particle velocities in the vertical (y-) direction. As expected the lagging particle moves with a higher velocity and catches up with the particle in the front (drafting). The particles fall one behind the other with almost the same velocity for some time. This configuration is unstable in a Newtonian fluid. The particles eventually tumble and move apart. Convergence tests were done by changing the time step and the mesh resolution; similar results were obtained.

The numerical results are compared with those obtained using the original formulation of Patankar *et al.* (2000). The vertical-velocity plot of Patankar *et al.* (2000) differs quantitatively from Fig. 3 shown here, after the kissing and tumbling phases begin. In their case, tumbling is initiated earlier thus giving a different graph. This is inherent in these simulations, since the tumbling process is a realization of an instability and can be affected by the accuracy of the solution procedure and the modeling of the collision

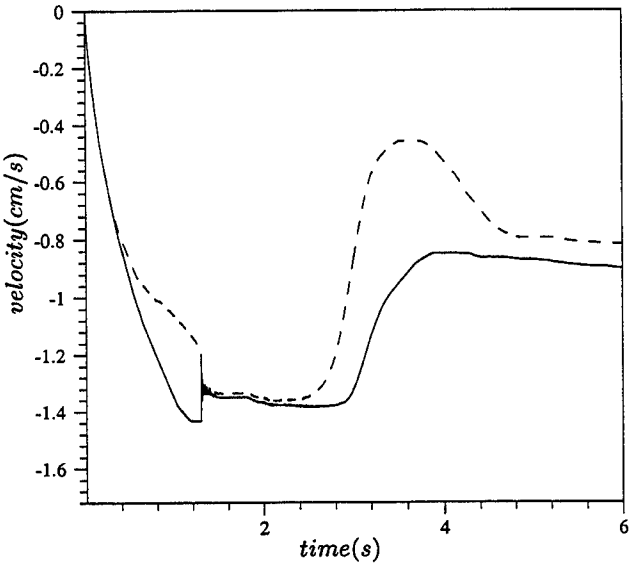

FIGURE 3. Vertical velocity of the particles. The solid line represents the velocity of the leading particle and the dashed line represents the velocity of the lagging particle.

force: see Singh, Joseph & Hesla (2001). Similar differences were also observed by T.-W. Pan (private communication).

4. Conclusions

We have developed a fast projection scheme to impose the rigidity constraint for the direct numerical simulation of rigid particulate flows. The new formulation is suitable for finite-volume or finite-difference immersed boundary techniques. The scheme is implemented by modifying the approach of Patankar *et al.* (2000). Numerical simulation of drafting, kissing and tumbling of particles has been done to validate the method.

This method can form a basis for fast computations of large numbers of moving particles. Such simulations can be used to develop models of solid-liquid flows. The new approach is also suitable for the direct numerical simulation of turbulent particulate flows since it directly improves upon the previous efforts of Kajishima *et al.* (1999). The technique is not restricted to any constitutive model for the suspending fluid. Hence, it can also be used in LES or RANS type simulations.

Acknowledgments

The author is thankful to Professor Parviz Moin for bringing some important references to his attention. The Senior Visiting Fellowship, from the Center for Turbulence Research, in August 2001 is gratefully acknowledged.

REFERENCES

FORTES, A., JOSEPH, D. D. & LUNDGREN, T. S. 1987 Nonlinear mechanics of fluidization of beds of spherical particles. *J. Fluid Mech.* **177**, 467-483.

GLOWINSKI, R., PAN, T.-W., HESLA, T. I. & JOSEPH, D. D. 1999 A distributed Lagrange multiplier/fictitious domain method for particulate flows. *Int. J. Multiphase Flow* **25**, 755-794.

HU, H. H. 1996 Direct simulation of flows of solid-liquid mixtures. *Int. J. Multiphase Flow* **22**, 335-352.

HU, H. H., JOSEPH, D. D. & CROCHET, M. J. 1992 Direct numerical simulation of fluid particle motions. *Theor. Comp. Fluid Dyn.* **3**, 285-306.

HU, H. H., PATANKAR, N. A. & ZHU, M. Y. 2001 Direct numerical simulations of fluid-solid systems using Arbitrary Lagrangian-Eulerian technique. *J. Comput. Phys.* **169**, 427-462.

JOHNSON, A. & TEZDUYAR, T. E. 1996 Simulation of multiple spheres falling in a liquid-filled tube. *Comp. Meth. Appl. Mech. Eng.* **134**, 351-373.

KAJISHIMA, T., TAKIGUCHI, S. & MIYAKE, Y. 1999 Modulation and subgrid scale modeling of gas-particle turbulent flow. *Recent Advances in DNS & LES.*, (D. Knight & L. Sakell, eds.), Kluwer Academic, 235-244.

LADD, A. J. C. 1994a Numerical simulation of particulate suspensions via a discretized Boltzmann equation. I. Theoretical foundation. *J. Fluid Mech.* **271**, 285-309.

LADD, A. J. C. 1994b Numerical simulation of particulate suspensions via a discretized Boltzmann equation. I. Numerical results. *J. Fluid Mech.* **271**, 311-339.

PAN, T.-W., JOSEPH, D. D., BAI, R., GLOWINSKI, R. & SARIN, V. 2001 Fluidization of 1204 spheres: simulation and experiment. *J. Fluid Mech.* to appear.

PAN, Y. & BANERJEE, S. 1997 Numerical investigation of the effects of large partices in wall turbulence. *Phys. Fluids* **9**, 3786-3807.

PATANKAR, N. A., SINGH, P., JOSEPH, D. D., GLOWINSKI, R. & PAN, T.-W. 2000 A new formulation of the distributed Lagrange multiplier/fictitious domain method for particulate flows. *Int. J. Multiphase Flow* **26**, 1509-1524.

SINGH, P., HESLA, T. I. & JOSEPH, D. D. 2001 Modified distributed Lagrange multiplier/fictitious domain method for particulate flows with collisions. *Int. J. Multiphase Flow*, in press.

TAKAGI, S., OĞUZ, H. N., ZHANG, Z. & PROSPERETTI, A. 2001 PHYSALIS: A new method for particle simulation. Part II: Two-dimensional Navier-Stokes flow around cylinders. *J. Comput. Phys.*, submitted.

Direct numerical simulation of polymer flow

By Y. Dubief AND S. K. Lele

1. Introduction

Although drag reduction due to the addition of small amounts of long-chain polymers has been a well-known phenomenon for about fifty years, its mechanism is still poorly understood. One of the first theories came from the time criterion (Lumley 1969), which states: for the polymer to have an effect on the flow, the characteristic relaxation time of the polymer solution must be longer than a relevant Lagrangian turbulent time scale of the flow. Following this scenario, Lumley surmises that drag reduction is caused by substantial stretching, also called the coil-stretch transition. Arguing that the coil-stretch transition does not occur in turbulent flows, Tabor & de Gennes (1986) proposed a different theory, the elastic theory, which states that the elastic energy stored in the polymer molecules is responsible for drag reduction. The polymers are thought to disrupt the turbulent cascade at the small-scale level. Furthering the elastic theory, Joseph (1990) suggested that the main effect has to be elastic since polymers attenuate small-scale turbulence. He related the phenomenon to the elastic wave speed. Recently, the onset of drag reduction and the maximum drag-reduction asymptote have been re-visited by Sreenivasan & White (2000) in the light of the elastic theory of de Gennes, leading to a provisional conclusion that the theory agrees with existing experiments. The authors also pointed out an extensive list of directions of research and many gaps in our knowledge of drag reduction by polymers.

In a different fundamental perspective, gaining deeper insight into the mechanism of drag reduction by polymer additives may reveal fine details of the regeneration cycle of near-wall turbulence. The self-sustaining nature of the turbulent flow close to the wall has been extensively discussed by Jiménez & Pinelli (1999). The authors proposed a cycle that involves the basic ingredients of the near-wall region: quasi-longitudinal vortices, streaks, mean shear and non-linear effects. Quasi-longitudinal vortices are known to produce large downwash motions that eventually generate significant wall shear stress. Choi *et al.* (1994) obtained a drag reduction of 30%, by blowing against those downwash flows. There are other experiments showing that the introduction of well-located perturbation obviously affects the cycle and reduces the drag. Since polymers are among the best drag-reducing agent available so far, they might reveal where the auto-regeneration cycle is best altered to obtain drag reduction.

In the past decade, numerical simulations have started to address polymer flow using various constitutive models. The present work follows the path opened by Sureshkumar *et al.* (1997) with the simulation of a viscoelastic channel flow based on the FENE-P model (Finitely Extensible Nonlinear Elastic–Peterlin: see below) and using a pseudo-spectral code. Even though the authors had to use unphysical parameters to match the low Reynolds number of their simulation, they were capable of showing drag reduction and velocity statistics in qualitative agreement with experiments. More recently, Min *et al.* (2001*a*) reproduced similar results using a different numerical approach based on second-order finite difference schemes. Min *et al.* (2001*b*) also investigated the role of

elastic energy through the use of an Oldroyd-B model, providing good support for the elastic wave speed theory.

In the present work, the FENE-P model is implemented in a second-order code, similar to Min *et al.* (2001*a*). The numerical issues are addressed, and some solutions are proposed. The response of coherent structures to polymer additives is investigated and some "unphysical" numerical experiments are proposed to highlight some fundamental aspects of the mechanism of drag reduction.

2. Numerical formulation

Polymer molecules have typical length scales much smaller than the smallest turbulent flow scales. Using traditional numerical schemes for flow simulation makes the explicit resolution of molecules unfeasible with current computer facilities; therefore the polymeric field has to be modelled. The evolution of polymers is predicted from bead-spring (dumbbell) models. Each dumbbell is subject to the hydrodynamic forces exerted from the flow to the beads, the spring force and Brownian forces. The balance of forces gives an evolution equation for the end-to-end dumbbell vector $\mathbf{q}$, known as the FENE model. A constitutive approach is achieved by taking into account the Brownian motion using a phase average of the product of the $\mathbf{q}$-components, which defines the conformation tensor $c_{ij} = \langle q_i q_j \rangle$. The hydrodynamic and relaxation (spring) forces are explicitely simulated; the latter force can be estimated with various models. The model used here is the FENE-P model, where P stands for the Peterlin function, f, defining the following set of equations

$$\frac{\partial c_{ij}}{\partial t} + u_k \frac{\partial c_{ij}}{\partial x_k} = c_{kj} \frac{\partial u_i}{\partial x_k} + c_{ik} \frac{\partial u_j}{\partial x_k} - \frac{1}{We}(f c_{ij} - \delta_{ij}) \ , \tag{2.1}$$

$$f = \frac{L^2}{L^2 - c_{kk}} . \tag{2.2}$$

The parameter L is the maximum polymer extension, and the Weissenberg number, We, the ratio of the polymer time scale to the flow time scales and ensures the non-dimensionality of Eq. (2.1). Finally, the contribution of polymers to the flow enters the momentum equations via the divergence of the polymeric stress tensor τ_{ij},

$$\tau_{ij} = \frac{1}{We}(f c_{ij} - \delta_{ij}) \ , \tag{2.3}$$

yielding the viscoelastic momentum equations,

$$\frac{\partial u_i}{\partial t} + u_j \frac{\partial u_i}{\partial x_j} = -\frac{\partial p}{\partial x_i} + \frac{\beta}{Re} \frac{\partial^2 u_i}{\partial x_j \partial x_j} + \frac{1-\beta}{Re} \frac{\partial \tau_{ij}}{\partial x_j} , \tag{2.4}$$

where β is the ratio of the solvent viscosity η_s to the total viscosity η.

The numerical method used to solve Eq. (2.4) is based on a semi-implicit, fractional-step method (Le & Moin 1991). Velocities are discretized in a staggered arrangement while the pressure and the polymeric tensors c_{ij} and τ_{ij} are computed from the cell-centered nodes. The Newtonian viscous stress in the wall-normal direction is advanced in time with the Crank-Nicolson scheme, while all other terms in Eqs. (2.1) and (2.4) are advanced with a third-order Runge-Kutta method. Velocity derivatives are computed using second-order finite-difference schemes. To maintain good resolution, the polymeric

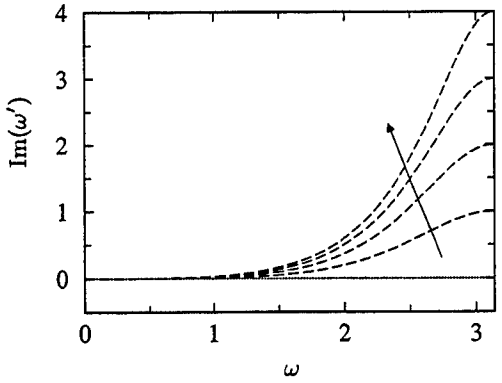

FIGURE 1. Dissipation of the compact upwind scheme (Eq. 3.3) for various ξ: ····· , $\xi = 0$ (no dissipation); ---- , ξ =0.25, 0.5, 0.75, 1. The arrow indicates the evolution of the dissipation as ξ is increased.

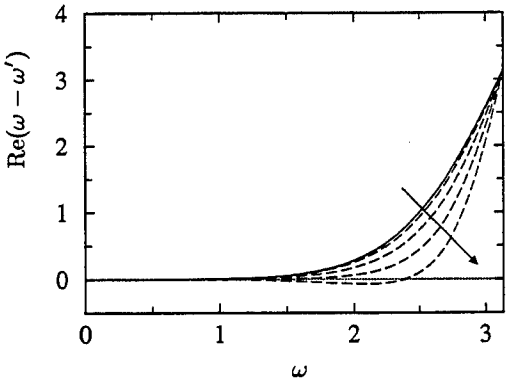

FIGURE 2. Dispersion of the compact upwind scheme (Eq. 3.3) for various ξ: ——— , exact differentiation, ····· , $\xi = 0$; ---- , ξ =0.25, 0.5, 0.75, 1.

stress derivatives are calculated with a non-dissipative fourth-order compact scheme. The advection terms of Eq. (2.1) are solved using a compact upwind scheme, following the modification by Min *et al.* (2001*a*), as explained in the following section.

3. Stabilisation of the conformation tensor advection

The resolution of the conformation tensor appears to be much more delicate than for the velocity field. Eq. (2.1) has an advection term but, unlike a passive scalar equation, does not include any diffusivity. Sharp gradients in c_{ij} develop, requiring higher-order methods suited for such specific situations.

Non-centered compact schemes have been developed to maintain high accuracy in convection-dominated problems where centered schemes, with dispersion but no dissipation, are not robust enough. The range of applications of upwind compact schemes spans from breakdown in convective flows (Christie 1985) to incompressible and compressible flows with sharp gradients (Tolstykh 1994). They have also been recently used for polymer flows by Min *et al.* (2001*a*). The latter authors solved the advection terms in the FENE-P equations with a third-order compact upwind scheme, developed by Tolstykh (1994) and adapted to the staggered grid used to solve the equations of fluid motion:

$$\begin{aligned}(2+3s^-)\phi'_{i-1} + (8+3s^- - 3s^+)\phi'_i + (2-3s^+)\phi'_{i+1} \\ = \frac{6}{\Delta}\left[(-1-s^-)\phi_{i-1} + (s^- + s^+)\phi_i + (1-s^+)\phi_{i+1}\right] ,\end{aligned} \tag{3.1}$$

The parameters s^- and s^+ denote the sign of the velocities $u_{i-1/2}$ and $u_{i+1/2}$, respectively. When $s^- = s^+ = 0$, Eq. 3.1 reduces to a fourth-order central scheme:

$$\phi'_{i-1} + 4\phi'_i + \phi'_{i+1} = \frac{3}{\Delta}[\phi_{i+1} - \phi_{i-1}] \ . \tag{3.2}$$

Min *et al.* (2001*a*) demonstrated the superiority of the compact upwind scheme relative to explicit upwind (QUICK) and central schemes (2nd-order explicit and 4th-order compact, respectively). However, as pointed out by one of the authors of Min *et al.* Choi (2001), the scheme has a low CFL (CFL$\simeq$ 0.5; see Lele 1992, for more details on the time-step

constraint using compact schemes). Choi suggested another upwind scheme, proposed by Zhong (1998), whose CFL is of the order of unity. We call this scheme CUDZ. Zhong (1998) established his upwind compact scheme so that it remains stable using high-order one-sided compact schemes at the boundaries. Yet the formulation used in Eq. (3.1) and CUDZ lose third-order accuracy for compression and dilatation points in the direction of differentiation ($s^- \neq s^+$). The error of CUDZ drops to second order at those critical points, while the rhs of Eq. (3.1) vanishes at dilatation points ($s^- = -1$, $s^+ = +1$).

To overcome this difficulty, we design a scheme which has the upwind/downwind formulation of CUDZ and reduces to Eq. (3.2) in compression or dilatation regimes. This is achieved by introducing an average of the velocity signs over the cell, $\varepsilon = \xi(s^- + s^+)/2$, where ξ is the upwinding parameter, which is allowed to vary from 0 to 1. This latter parameter is used to control the amount of dissipation and dispersion of the scheme, which is now:

$$(1+\varepsilon)\phi'_{i-1} + 4\phi'_i + (1-\varepsilon)\phi'_{i+1} = \frac{1}{\Delta}[(-3-2\varepsilon)\phi_{i-1} + 4\varepsilon\phi_i + (3-2\varepsilon)\phi_{i+1}] \ , \qquad (3.3)$$

Fig. 3 shows the dissipation and dispersion of Eq. (3.3) for five different values of ξ from 0 to 1. In these plots, ω defines the wavenumber and ω' the modified wavenumber as defined in Lele (1992). As suggested by Min *et al.* (2001*a*), this scheme is supplemented by local artificial dissipation (LAD)

$$\frac{\partial c_{ij}}{\partial x_k} = \frac{\delta_u c_{ij}}{\delta x_k} + \begin{cases} 0 & \text{if } \det(c_{ij}) > 0, \\ \kappa\Delta_k^2 \dfrac{\delta_2^2 c_{ij}}{\delta^2 x_k} & \text{if } \det(c_{ij}) \leq 0. \end{cases} \qquad (3.4)$$

The operators δ_u and δ_2 are the upwind-compact and second-order central differentiation schemes, respectively, Δ_k the grid mesh in the x_k direction and κ is a constant equal to 10^{-2}, according to Min *et al.* (2001*a*). This local dissipation is necessary to ensure that the conformation tensor remains positive-definite, hence the relation of LAD to the determinant of c_{ij}. In our own experience, the fraction of the flow affected by LAD depends on the coarseness of the grid as well as on the intrinsic dissipation of Eq. (3.3). Fig. 3 is extracted from several simulations using values of ξ for the flow and grid conditions that will be defined below. It shows the evolution in time of the spatial-average friction velocity, $\langle u_\tau \rangle_{xz}$ as a function of time, just after the polymeric field is coupled to the velocity field. The coefficient κ is the same for all simulations. The effect of ξ on the drag reduction is quite significant. Using a central compact scheme ($\xi = 0$) is associated with a high number of nodes affected by LAD, around 20%, and eventually causes the simulation to break down. The latter issue is avoided if $\xi = 0.25$; however the fraction of nodes with LAD remains large, $\simeq$ 10%. As will be shown below, the polymer drag reduction comes from the damping of vertical velocity fluctuations. When LAD affects too many points, it seems to weaken the predicted effect of polymers by smoothing out the divergence of the polymeric tensor (Eq. 2.3), resulting in a smaller drag reduction. For $\xi = 0.5$ and 0.75, the fraction of nodes that requires LAD is roughly the same, 1-2%, which is more acceptable. This fraction actually decreases when the resolution in the streamwise and spanwise directions is increased. At this stage of the study, it is still unclear which ξ produces better results. Fig. 3 shows a larger drag reduction for the transient time; however, once a statistical steady state is reached, the amount of drag reduction is roughly the same. This aspect needs further investigation and for the present study we will consider a simulation with $\xi = 0.5$ to diminish the impact of the numerical dissipation of Eq. (3.3).

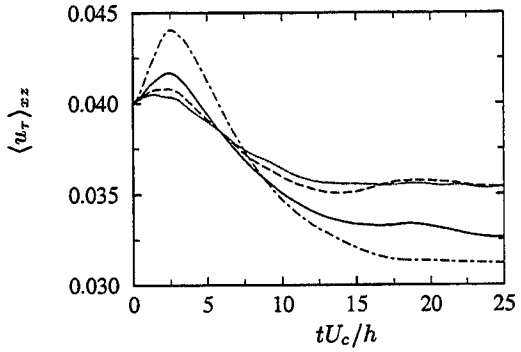

FIGURE 3. Evolution in time of the friction velocity averaged in space with various values of ξ (Eq. 3.3) for the advection term in Eq. (2.1). ····· : $\xi = 0$; ---- : $\xi = 0.25$, ——— , $\xi = 0.5$; - · - : $\xi = 0.75$.

4. Stability of the relaxation term

It would be wrong to blame the unstable numerical nature of Eq. (2.1) solely on the resolution of the advection term. A simple analysis of the behaviour of c_{ij}, as its trace approaches L^2, suggests that the positive-definiteness of the conformation tensor is also affected by the relaxation term. To illustrate our argument, we shall consider Eq. (2.1) for a one-dimensional problem, with no advection and with explicit time advancement,

$$\frac{c_{xx}^{n+1} - c_{xx}^n}{\Delta t} = 2c_{xx}^n \frac{\partial u^n}{\partial x} - \frac{1}{We}\left(\frac{L^2}{L^2 - c_{xx}^n} c_{xx}^n - 1\right) . \tag{4.1}$$

When c_{xx}^n approaches L^2, say $c_{xx} = L^2 - \varepsilon^2$, an absolute requirement for the time advancement of Eq. (4.1) is that the solution c_{xx}^{n+1} remains smaller than L^2, which implies:

$$-\varepsilon^2 + \Delta t \left[2(L^2 - \varepsilon^2)\frac{\partial u^n}{\partial x} - \frac{1}{We}\left(\frac{L^2}{\varepsilon^2}(L^2 - \varepsilon^2) - 1\right)\right] < 0 . \tag{4.2}$$

By assuming that $\varepsilon^2 \ll L^2$ and $L^4/\varepsilon^2 \gg 1$, the following condition on Δt can be derived,

$$\Delta t < \frac{\varepsilon^4}{2SL^2\left(\varepsilon^2 - \dfrac{L^2}{2SWe}\right)} , \tag{4.3}$$

where $S = \partial u^n/\partial x$. Note that Eq. (4.3) makes sense only if $\varepsilon > L^2/(2SWe)$. This relation indicates that a Euler-type scheme can easily become unstable when ε^2 is too small. If Eq. (4.2) is not satisfied, *i.e.* $c_{xx}^{n+1} > L^2$, then the Peterlin function (Eq. 2.2) becomes negative, turning the relaxation force into an extension force whose effect is to pull c^{n+2} even further beyond L^2. For this situation to occur requires only an accumulation of small numerical errors, eventually leading to a numerical breakdown. Those errors might come from the time scheme as well as the advection term as discussed in the previous section. Eq. (4.3) provides a very strict time-step restriction which can be taken as the minimum of the rhs of the relation, $\Delta t_{min} = 1/(S^2We)$. For instance, in a low-Reynolds-number channel flow, where the typical time-step is of the order $10^{-3}h/u_\tau$ for Newtonian flow, the polymeric time-step can decrease as low as $\mathcal{O}(10^{-5})h/u_\tau$ for a realistic Weissenberg number ($We = 10$). For a full simulation, the stability analysis of

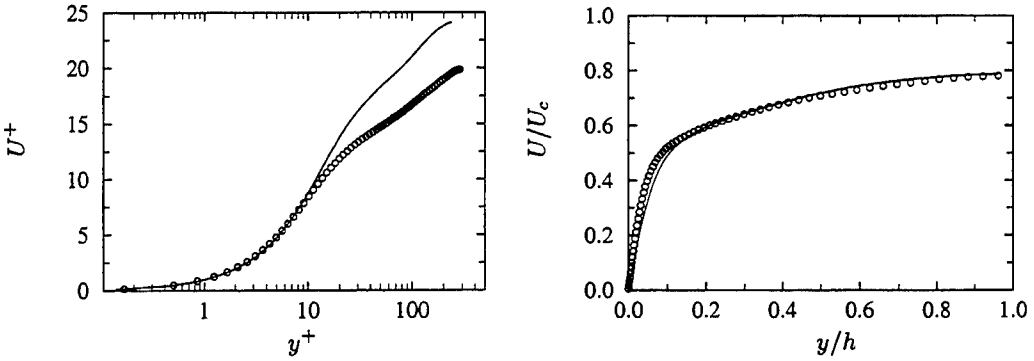

FIGURE 4. Mean velocity profiles scaled with inner (left) and outer (right) variables. o: Newtonian flow; ——— : viscoelastic flow.

Eq. (2.1) is not straightforward and has not been attempted here. The published results are somewhat conflicting on that particular issue. Sureshkumar *et al.* (1997) used a time step five times smaller than for the Newtonian case, whereas Min *et al.* (2001*a*) used CFL = 0.5, as required by their numerical scheme described earlier. An explanation of this discrepancy might be found in the numerical schemes used. Sureshkumar *et al.* (1997) stabilized the polymeric field by using the combination of an advanced semi-implicit scheme and the implementation of an extra diffusive term in Eq. (2.1), $\kappa\partial_k\partial_k c_{ij}$, where κ is a small constant of the order $10^{-2}-10^{-3}$. They used pseudo-spectral methods for spatial derivatives and it may be assumed that their procedure also helps to stabilize the advection term. Min *et al.* (2001*a*) directly addressed the positive definiteness by using LAD wherever the determinant of the configuration tensor became negative. The inherent dissipation of their compact upwind scheme at high wavenumbers may also contribute to the overall stability. Most importantly, they addressed only small We, as in the present study.

During the course of the simulations, it was found that only one or two points are at risk of diverging during the transient time of the simulation. A "cheap" solution is to re-adjust the Pertelin function (Eq. 2.2) for those points so that the trace of the conformation tensor remains bounded. The value of f is based on a critical value of ϵ derived from Eq. (4.3) with Δt given by the CFL constraint. This procedure proves to be efficient for small We and affects less than five nodes once or twice at the very beginning of the simulation. Once the transient time is over, this clipping can be safely removed. However, for higher We, an implicit scheme for the relaxation force will be necessary.

5. Results

The simulation presented here corresponds to a minimal channel flow of dimensions $\pi h \times 2h \times h$, for $Re = 7500$ based on the initial Poiseuille profile centerline velocity and the half-width h. The resolution is $64 \times 129 \times 32$ which gives $\Delta_x^+ = 15$, $\Delta_y^+ = 0.16 \rightarrow 10$ and $\Delta_z^+ = 9$. The Reynolds number based on the friction velocity for the Newtonian flow is $Re_\tau = h^+ = 295$. The Weissemberg number is equal to unity in integral scaling ($We = \lambda U/h$) which implies $We_\tau = 10$. The maximum extension L is set to 60 and $\beta = 0.9$. The maximum extension is chosen to be higher than in the work of Sureshkumar *et al.* (1997) and Min *et al.* (2001*a*) in order to approach realistic long-chain polymer molecules. The contribution of the solvent to the flow is equal to that used in previous

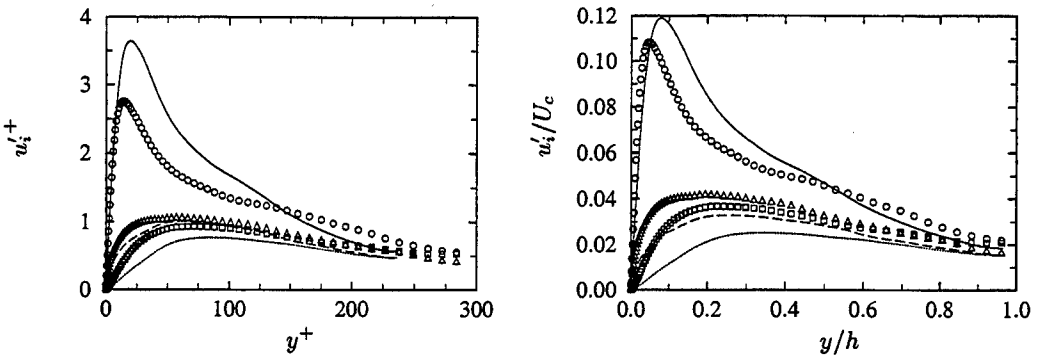

FIGURE 5. RMS of velocity fluctuations scaled with inner (left) and outer (right) variables. Symbols denote the Newtonian flow, lines the viscoelastic flow. o, ——— : u; □, ····· : v; △, - - - - : w.

studies. The initial configuration of the polymer stress tensor is the isotropic tensor ($c_{ij} = \delta_{ij}$) which implies that the flow undergoes a transient time that lasts for around 50 h/U_c. When the solution is found to be statistically steady, around 100 h/U_c, statisitics are collected over 200 h/U_c.

The measured drag reduction for our simulation is 17%. Figs. 4 and 5 show the response of the velocity statistics to the polymeric stress in wall and integral coordinates. The mean velocity profile is shifted upward in the log-region. The streamwise velocity fluctuations are increased in the near-wall region, whereas the transverse components are reduced. These results are in agreement with experimental data (Warholic *et al.* 1999) and numerical results (Sureshkumar *et al.* 1997; Min *et al.* 2001*a*). They indicate a thickening of the buffer layer and a reduction of turbulence in the transverse directions. The latter aspect can be linked to near-wall vortices. The wall-normal and spanwise velocity fluctuations are closely related to the activity of quasi-longitudinal vortices in the buffer region. Kim *et al.* (1987) explained near-wall extrema of the variance of the streamwise vorticity fluctuation by the presence of those vortices located around $y^+ = 20$. In most of the drag-reducing simulations, a decrease of the magnitude of ω_x', v' and w' is observed, suggesting a weakening of the quasi-streamwise vortices. However The evolution of ω_x', v' and w' does not explain how the near-wall vortices are modified. A simple method is to take advantage of vortex eduction schemes and conditional sampling, as shown by Dubief & Delcayre (2000). The present study relies on the Q-criterion of Hunt *et al.* (1988), which identifies regions of positive second invariant of the velocity tensor,

$$Q = \frac{1}{2}(\Omega_{ij}\Omega_{ij} - S_{ij}S_{ij}) \ , \tag{5.1}$$

as vortices. In other words, a vortex is defined as a region where the local rotation rate dominates the strain rate, Ω_{ij} and S_{ij} being the antisymmetric and symmetric parts of $\boldsymbol{\nabla}\mathbf{u}$. This criterion is also related to local minima of pressure under certain conditions as discussed by Dubief & Delcayre (2000). Yet the choice of a positive threshold is very much flow-dependent, making comparisons between flows subject to different conditions delicate. In order to reduce as much as possible the subjectiveness of coherent vortex

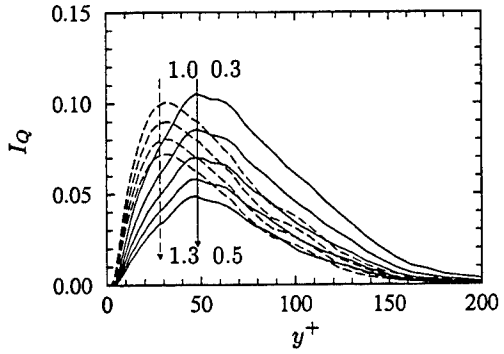

FIGURE 6. Q-vortex intermittency for viscoelatic, ——— , and Newtonian, ---- , flows.

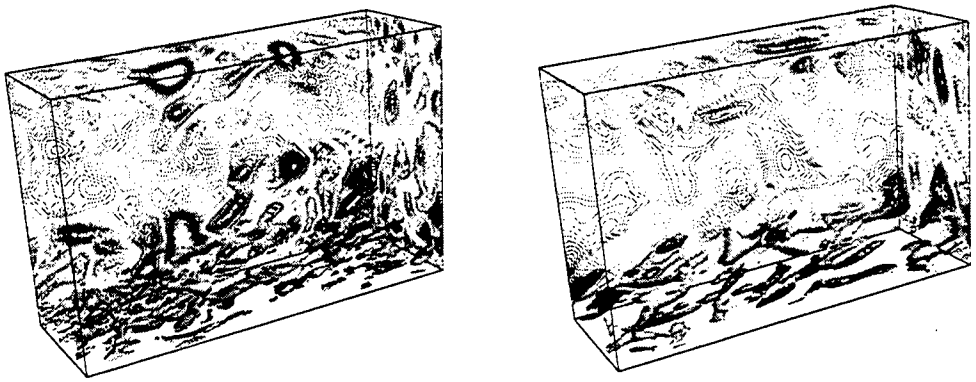

FIGURE 7. Instantaneous visualisations of the Newtonian (left) and viscoelastic (right) flow. Isosurfaces of positive Q, Newtonian case: $Q = 1U_c^2/h^2$, viscoelastic case: $Q = 0.3U_c^2/h^2$. Isocontours of wall-normal velocity, contour levels varies from $\pm 0.1U_c$. Flow from left to right.

investigation, an intermittency function can be used, defined as

$$I_Q(\mathbf{x}, t, Q_s) = \begin{cases} 0 & \text{if } Q(\mathbf{x},t) < Q_s, \\ 1 & \text{if } Q(\mathbf{x},t) \geq Q_s. \end{cases} \tag{5.2}$$

In the case of a channel flow, averaging I_Q over time and (x, z) plane gives the fraction of the flow occupied by vortices educed for $Q \geq Q_s$ at a given y. Dubief & Delcayre (2000) found that too-small thresholds cannot separate noise from vortices. As the threshold Q_s augments, the regions where I_Q is unity tend to define the skeleton of the vortices†. Fig. 6 shows a well-marked peak around $y^+ = 20$ for the Newtonian flow, defining the preferred location of the most energetic vortices in the inner region of the flow. For the viscoelastic flow, the peak is shifted to around $y^+ = 50$. This plot also indicates that the distribution of the vortices is wider under the influence of polymers.

The modifications undergone by the viscoelastic flow are apparent in Fig. 7 which plots countours of wall-normal velocity fluctuations and isosurfaces of positive Q. The thresholds are chosen from Fig. 6, so that the maximum of I_Q is around 10%. Fig.

† Note that the threshold defining the skeleton can vary in time and space for each vortex.

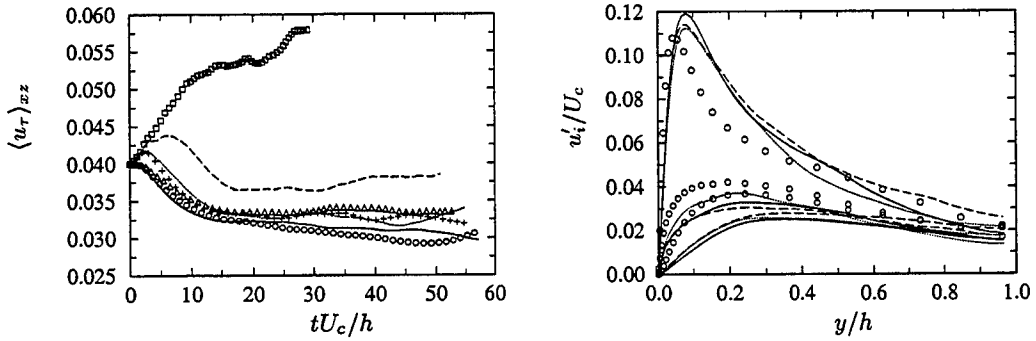

FIGURE 8. *Left*: evolution in time of the spaced averaged friction velocity. In the following nomenclature, the velocities designate in which momentum equations the viscoelastic effect is implemented for both figures. +: uvw (Eq. 2.4); □: u; ○: v; △: w; ····· : uv; ---- : uw; ——— : vw. *Right*: rms of velocity fluctuations in integral coordinates for some drag-reducing cases. ○: Newtonian flow; ——— uvw; ····· : v; ---- w. Upper curves: u'; lower curves: v'; middle curves: w'.

7 illustrates the spreading of vortices over a wider region in the vertical direction, as discussed earlier. This plot underscores the significant change in the typical length scale of v. Compared to the Newtonian case, the structures of v are much larger.

6. Numerical experiments

The previous Section has established that the transverse turbulent intensities are damped by the variation of polymeric stress, showing a direct effect on the near-wall vortices. However, the statistics proposed so far fail to show where polymers act with respect to the energetic structures of the flow. The flexibility of computer simulations permits unphysical "experiments" that provides valuable information about the dynamics of turbulence. For instance, Jiménez & Pinelli (1999) used an irrotational filter to demonstrate that the near-wall turbulence is self-sustaining, whereas the outer region is not. In our context, a straightforward experiment is to modify the divergence of polymeric stress tensor in the momentum equations, (Eq. 2.4). The simplest investigation that can be performed is to remove the viscoelastic term in one or two directions by replacing β by β_i ($\beta_i = 0.9$ or 1), where i is the velocity component index. The transient period, *i.e.* the time when the viscoelastic simulation is started, is chosen for study if there is one preferred direction in the drag-reduction process. The simulations are carried out over 2500 iterations with a CFL-controlled time-step.

For the traditional or reference simulation (see Fig. 8), the skin friction experiences a small overshoot and then undergoes a significant reduction. This feature is also found in Min *et al.* (2001*a*). The viscoelastic term in Eq. (2.4) is first switched off in all but one momentum equation. When the polymers contribute only to the streamwise momentum, the skin friction rapidly increases without any sign of reduction. As a consequence, the time-step decreases, explaining the shorter duration of the simulation. The same operation is repeated for the v- and w-momentum equations. The fastest reduction is achieved when polymers affect the wall-normal momentum. Since there is no overshoot for those two experiments, it is obvious that the initial behaviour of the skin friction is an effect of the polymeric stress on the streamwise momentum. When the viscoelastic contribution is switched off only in one direction, drag reduction is obtained in all experiments; however the reduction is noticeably smaller when the viscoelastic effects are applied on u and w

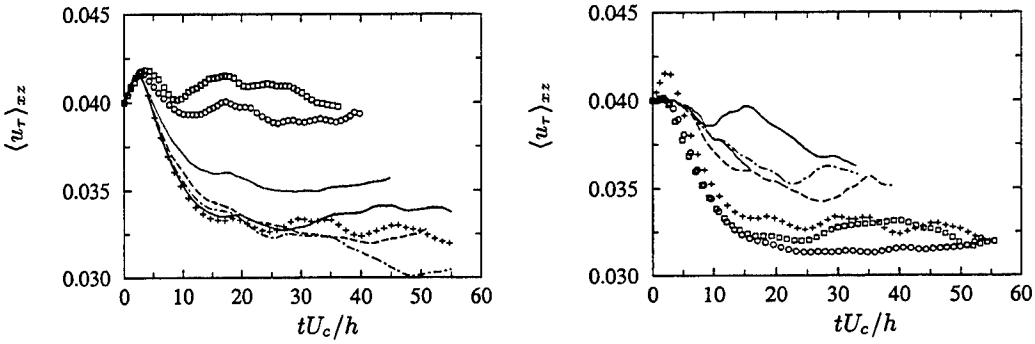

FIGURE 9. Evolution in time of the friction velocity averaged in space when the polymeric stress contribution varies according to Eq. (6.1). *Left*: β^-, viscoelastic effect from the wall up to δ; *right*: β^+, viscoelastic flow for $-h+\delta \le y \le h-\delta$. +: full viscoelastic flow (reference case); □: $\delta^+ = 6$; o: $\delta^+ = 15$; ····· : $\delta^+ = 30$; - - - - : $\delta^+ = 45$; - · - : $\delta^+ = 60$; ——— : $\delta^+ = 90$.

than for the other cases. The right-hand side of Fig. 8 compares the behaviour of the velocity fluctuations when the viscoelastic effect is implemented in the v or w-momentum. The statistics have been collected between $t = 60h/U_c$ and $120h/U_c$. The figure shows that the upward shift of u' maximum does not result from the viscoelastic effect on the u-momentum. The polymers might be responsible only for a marginal increase of this maximum. The shift is more likely dictated by the new equilibrium state reached by the thickened buffer layer.

In the second set of experiments β is a function of the vertical coordinate,

$$\beta^{\pm}(y) = \frac{1+\beta}{2} \pm \frac{1-\beta}{2} \tanh\left[\frac{\delta}{\theta}\left(\frac{\delta}{h-|y|} - \frac{h-|y|}{\delta}\right)\right] \quad , -h \le y \le +h \, , \tag{6.1}$$

where $\beta = 0.9$ and δ is the thickness of the region attached to the walls. β^- and β^+ designate the functions for which the polymeric stress is active for $h-\delta \le |y| \le h$ and $-h+\delta \le y \le h-\delta$, respectively. The parameter θ controls the transition from regions with polymer contribution to regions without and is taken equal to $\delta/25$ in order to ensure a fairly sharp cutoff. Simulations are performed for six heights $\delta = 0.02h$, $0.05h$, $0.1h$, $0.15h$, $0.2h$ and $0.3h$ or $\delta^+ = 6$, 15, 30, 45, 60 and 90 in wall coordinates using the Newtonian skin friction. The left-hand side of Fig. 9 shows that polymers need to be active across the entire buffer layer to achieve a drag reduction equivalent to the reference case. It should be noted that all curves exhibit the transient overshoot even when the polymer contribution is confined in the viscous sublayer ($\delta^+ = 6$) and no drag reduction is observed. The rhs of Fig. 9 displays the response of drag when polymers are active only in the core of the channel flow (β^+). This procedure removes the initial overshoot, showing that this sharp increase of drag results from the initial stretching of the polymers in the viscous sublayer. Again, a significant drag reduction is observed when the polymer contribution covers the buffer layer, $\delta^+ \le 15$, which is consistent with the conclusion of Jiménez & Pinelli (1999) that the cycle of near-wall turbulence is located between $y^+ = 20$ and $y^+ = 60$. For $\delta^+ = 90$, the small drag reduction can probably attributed to the modification of the outer region of the flow. In a similar way, Jiménez & Pinelli (1999) observed significant drag reduction by damping turbulence in the outer region.

These two experiments highlight important phenomena of drag reduction with polymer additives. From Fig. 8, it can be inferred that polymers extract energy from the transverse momentum. To support this argument, we have studied the sign of the viscoelastic

acceleration $\mathcal{A}_i^V = (1-\beta)/Re(\partial_i \tau_{ij})$ relative to the sign of the Newtonian acceleration, $\mathcal{A}_i^N = -u_j\partial_j u_i - \partial_i p + (\beta/Re)\partial_j\partial_j u_i$, and that of the velocity fluctuation, u_i. When $\text{sign}(\mathcal{A}_y^N) = \text{sign}(v)$, *i.e.* in regions where the flow is accelerated in the y direction, the sign of viscoelastic acceleration in the vertical direction is mainly opposite to that of the Newtonian acceleration; the fraction of such occurences is of the order of 75% over almost the entire channel. The behavior of w is similar but the fraction is a little less, of the order of 65%. Accelerations in the streamwise directions are enhanced by the viscoelastic acceleration (up to 80%) in the viscous sublayer and the lower part of the buffer layer. Although $\mathcal{A}_x^V$ works mostly against $\mathcal{A}_x^N$ when $u > 0$, in the rest of the flow, Fig. 8 clearly shows that the action of $\mathcal{A}_x^V$ away from the wall is not sufficient to prevent the drag from increasing due to the activity of the polymers near the wall (see the case where the viscoelastic effect is applied only to the u-momentum). Fig. 9 indicates that the buffer layer, corresponding to the peak in vortex concentration observed in Fig. 6, plays a key role in the drag-reduction mechanism. Therefore it may be speculated that polymers act directly inside the upwash and downwash flows triggered by quasi-streamwise vortices, which is also supported by Hur's observations†. It also follows the interpretation of Oldroyd-B simulations by Min *et al.* (2001*b*), which states that polymers store energy very near the wall and release it away from the wall. The polymers must therefore keep this energy during a time scale comparable to the duration of their advection to suitable altitude. Further investigations will be carried out to test this theory, since Fig. 9 indicates that the exchange of energy between the viscous sublayer and even the lower part of the buffer layer is not a necessity for the drag reduction mechanism.

7. Conclusion and perspectives

The present study has established the basis of a numerical method to simulate viscoelastic flows using a second-order staggered code. The implementation largely follows that of Min *et al.* (2001*a*), with some modifications for the resolution of the advective terms. Some results have been obtained, and a flow where 17% drag reduction was observed has been investigated. Using "unphysical" numerical experiments, it has been suggested that drag reduction is achieved by damping strong accelerations of the vertical velocity fluctuation as well as of the spanwise component. The phenomenon leading to drag reduction does not occur in the viscous sublayer but seem to take place over the entire buffer layer.

Future work will involve a refinement of the numerical method in order to assess the effect of numerical dissipation on the polymeric field. Also of major importance, an implicit scheme needs to be implemented for the relaxation term in the conformation tensor equations to achieve higher Weissenberg numbers. Simulations performed on larger computational domains and a wide range of Weissenberg numbers will form a database that, it is hoped, will shed light on the mechanism of drag reduction by polymer additives.

Acknowledgments

The support of DARPA is gratefully acknowledged. YD wishes to thank Drs J. Gullbrand and C. M. White for their corrections and helpful comments on the manuscript and Dr. J. S. Hur for sharing his knowledge of polymer dynamics.

† Dr. Hur performs uncoupled Brownian dynamic simulations for the same project. He observes that the molecules are significantly stretched in downwash and upwash flows.

REFERENCES

CHOI, H. 2001 Private communication.

CHOI, H., MOIN, P. & KIM, J. 1994 Active turbulence control for drag redcution in wall-bounded flows. *J. Fluid Mech.* **262**, 75–110.

CHRISTIE, I. 1985 Upwind compact finite difference schemes. *J. Comp. Phys.* **59**, 353–368.

DUBIEF, Y. & DELCAYRE, F. 2000 On coherent-vortex identification in turbulence. *J. of Turbulence* **1** (011).

HUNT, J. C. R., WRAY, A. A. & MOIN, P. 1988 Eddies, stream, and convergence zones in turbulent flows. *Proceedings of the Summer Program*, Center for Turbulence Research, NASA Ames/Stanford Univ. 193–208.

JIMÉNEZ, J. & PINELLI, A. 1999 The autonomous cycle of near-wall turbulence. *J. Fluid Mech.* **389**, 335–359.

JOSEPH, D. D. 1990 *Fluid Dynamics of Viscoelastic Liquids*. Springer-Verlag.

KIM, J., MOIN, P. & MOSER, R. 1987 Turbulent statistics in fully developed channel flow at low Reynolds number. *J. Fluid Mech.* **177**, 133–166.

LE, H. & MOIN, P. 1991 An improvement of fractional step methods for the incompressible Navier-Stokes equations. *J. Comp. Phys.* **92**, 369–379.

LELE, S. K. 1992 Compact finite difference schemes with spectral-like resolution. *J. Comp. Phys.* **103**, 16–42.

LUMLEY, J. L. 1969 Drag reduction by additives. *Ann. Rev. Fluid Mech.* **1**, 367–384.

MIN, T., YOO, J. Y. & CHOI, H. 2001*a* Effect of spatial discretization schemes on numerical solutions of viscoelastic fluid flows. *J. Non-Newtonian Fluid Mech.* **100**, 27–47.

MIN, T., YOO, J. Y., CHOI, H. & JOSEPH, D. D. 2001*b* A role of elastic energy in turbulent drag reduction by polymer additives. In *Turbulence and Shear Flow Phenomena, 2nd Int. Sympo.*, **1**, 35–40.

SREENIVASAN, K. R. & WHITE, C. M. 2000 The onset of drag reduction by dilute polymer additives, and the maximum drag reduction asymptote. *J. Fluid Mech.* **409**, 149–164.

SURESHKUMAR, R., BERIS, A. N. & HANDLER, R. A. 1997 Direct numerical simulations of turbulent channel flow of a polymer solution. *Phys. Fluids* **9**, 743–755.

TABOR, M. & DE GENNES, P. G. 1986 A cascade theory of drag reduction. *Europhys. Lett.* **2**, 519–522.

TOLSTYKH, A. I. 1994 *High accuracy non-centered compact difference schemes for fluid dynamics applications*. Series on Advances in Mathematics for Applied Science **21**. World Scientific Publishing, Singapore.

WARHOLIC, M. D., MASSAH, H. & HANRATTY, T. J. 1999 Influence of drag-reducing polymers on turbulence: effects of Reynolds number, concentration and mixing. *Expts. in Fluids* **27**, 461–472.

ZHONG, X. 1998 High-order finite-difference schemes for numerical simulations of hypersonic boundary-layer transition. *J. Comp. Phys.* **144**, 662–709.

Structure and evolution of circumstellar disks during the early phase of accretion from a parent cloud

By Olusola C. Idowu

1. Motivation and Background

The process by which a cloud of gas and dust turns into stars and planets is one of the most intriguing questions in astrophysics. One of the steps in this process is the formation of a disk surrounding a young star. The disk is important because planets may eventually form within it and because it feeds mass to the star. The circumstellar disk has two phases in its evolution. The first is characterized by accretion from the parent cloud directly to the protostar and on to a radially growing disk whose size is comparable to the stellar radius. In the second phase, accretion from the cloud to the disk has ceased. The flow at this later phase of evolution is nearly Keplerian and there is observational data at both mm and infrared wavelengths to provide guidance for theoretical work on the structure of the disk. In contrast, very little is known about the dynamics of the disk in the first phase of evolution because the forming disk is heavily obscured by the parent cloud.

Shu (1977) described the mechanism for the spherically symmetric collapse of an initially isothermal cloud. He suggested that the collapse occurs through the outward propagation of a spherical rarefaction wave. The expanding wave front reduces the support of pressure gradient (against gravity) behind it. This allows gas particles to fall radially inward increasing the mass of the central protostar. For the formation of a disk to take place it is necessary for there to be rotation in the parent cloud. To describe this process Cassen & Moosman (1981), and Terebey, Shu & Cassen (1984) assumed that the cloud collapses in an axisymmetric manner and each gas particles falls with a specific angular momentum $j = rU_\phi$ where r is the radius in cylindrical polar coordinates (Fig. 1) and U_ϕ is the azimuthal velocity. The axis z in Fig. 1 represents the axis of a cylindrical coordinate system. Surfaces of constant angular momentum are represented by nested cylinders. As the rarefaction front propagates, a significant fraction of the infalling gas will possess enough angular momentum so that it can miss the central protostar and become incorporated to the growing disk around the central star. In the present work we consider the evolution of the disk from the time $t_0 = \xi t_*$ where ξ is any positive number and t_* represents the time when the cloud begins to miss the central star defined as

$$t_* = \left(\frac{16 r_*}{\Omega_0^2 a m_0^3}\right)^{1/3}, \tag{1.1}$$

r_* is the initial stellar radius, a is the speed at which the rarefaction front propagates, Ω_0 is the rotation rate of the parent cloud and m_0 is a dimensionless number equal to 0.975 (Terebey, Shu & Cassen (1984)).

If we assume that the total energy in the infalling cloud is small compared to gravitational potential energy (negative), and kinetic energy (positive) at the point of impact-

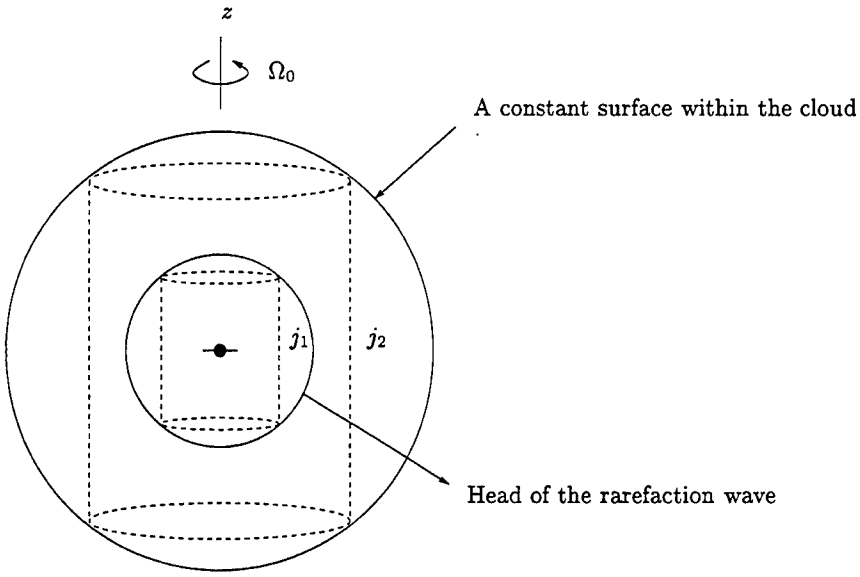

FIGURE 1. Inside-out collapse of a rotating cloud showing the surfaces of constant angular momentum

ing the disk, then the fluid element arrives at a state of essentially free fall. Therefore the streamlines approaching the disk are well approximated by zero-energy orbits, i.e., parabolic trajectories. Cassen & Moosman (1981), Ulrich (1976), and Terebey, Shu & Cassen (1984) have used this basic fact to derive the velocity and density of infalling cloud onto the disk surrounding the central protostar. The velocity for the infalling particle in spherical polar co-ordinates (σ, θ, ϕ) is given by

$$U_\sigma = -\left(\frac{GM}{\sigma}\right)^{1/2}\left(1+\frac{\cos\theta}{\cos\theta_0}\right)^{1/2} \tag{1.2}$$

$$U_\theta = \left(\frac{GM}{\sigma}\right)^{1/2}\left(\frac{\cos\theta_0-\cos\theta}{\sin\theta}\right)\left(1+\frac{\cos\theta}{\cos\theta_0}\right)^{1/2} \tag{1.3}$$

$$U_\phi = \left(\frac{GM}{\sigma}\right)^{1/2}\frac{\sin\theta_0}{\sin\theta}\left(1-\frac{\cos\theta}{\cos\theta_0}\right)^{1/2} \tag{1.4}$$

where θ is the co-latitude and ϕ is the azimuthal angle. The density distribution is given by

$$\rho = -\left(\frac{\dot{M}}{4\pi\sigma^2 U_\sigma}\right)\left[1-\left(1-\frac{\cos\theta}{\cos\theta_0}\right)(1-2\cot^2\theta)\right]^{-1} \tag{1.5}$$

where the angle θ_0 is the inclination of each orbital plane relative to the rotation axis; it is related to the disk radius R_d by

$$\cos^3\theta_0 - \left(1-\frac{\sigma}{R_d}\right)\cos\theta_0 - \frac{\sigma}{R_d}\cos\theta = 0 \tag{1.6}$$

The disk radius R_d is obtained from Eq. (1.1) at a given t_0 and Ω_0. G is the gravitational constant, M is the mass of the central star, and $\dot{M}$ is the mass accretion rate onto the

star given by

$$\dot{M} = \frac{m_0 a^3}{G} \tag{1.7}$$

(Terebey, Shu & Cassen (1984)). In cylindrical polar coordinates (r, ϕ, z), radial and axial velocities become

$$U_r = -\left(\frac{GM}{r}\right)^{1/2}\left(1+\frac{\cos\theta}{\cos\theta_0}\right)^{1/2}\left(\frac{1-\cos\theta\cos\theta_0}{\sin\theta}\right) \tag{1.8}$$

$$U_z = -\left(\frac{GM}{r}\right)^{1/2}\left(1+\frac{\cos\theta}{\cos\theta_0}\right)^{1/2}\cos\theta_0 \tag{1.9}$$

while U_ϕ remains the same.

Using Eqs. (1.4), (1.5) and (1.8), Stahler *et al* (1994) considered the motion of gas within a vertically mixed thin disk. The thin disk approximation consists of neglecting any variation in the vertical direction.

The goal of the present work is to study via numerical simulation, the processes that occur within the disk as it accretes material. The motion resulting from the infalling streams is assumed to be governed by the Euler equations for compressible gas flow. The main finding so far is that the gas initially within the disk races towards the protostar at supersonic speed to form an equatorial concentration of mass close to the interior boundary of the disk. The mass concentration reduces the radial velocity which in turn diminishes the rate of accretion of gas from the disk to the central protostar from the inner boundary. The flow parameter scaling and the equations of motion used for the simulation are described in the next two sections. Some preliminary results from the flow simulation is discussed in the last section.

2. Non-dimensionalization

Let us begin by denoting all dimensional quantities by tildes. The basic parameters of the problem are the rotation rate of the parent cloud $(\widetilde{\Omega}_0)$, the initial cloud temperature $(\widetilde{T}_0)$, the time since the beginning of the collapse $(\widetilde{t}_0)$, the specific heat capacity of the gas at constant pressure $(\widetilde{c}_p)$, the ratio of specific heats (γ) and the gravitational constant $(\widetilde{G})$. From these basic parameters we can derive other parameter. These are the gas constant $(\widetilde{R} = \widetilde{c}_p(\gamma-1)/\gamma)$, the initial speed of sound $(\widetilde{a}_0 = \sqrt{\gamma\widetilde{R}\widetilde{T}_0})$, the mass accretion rate $(\widetilde{\dot{M}})$ from Eq. (1.7), and the mass of the central star $(\widetilde{M} = \widetilde{\dot{M}}\widetilde{t}_0)$. The four parameters used to scale the flow are $\widetilde{G}\widetilde{M}$, $\widetilde{c}_p$, $\widetilde{\dot{M}}$ and the initial radius of the disk $\widetilde{R}_d$ obtained from $\widetilde{\Omega}_0$ via Eq. (1.1). The initial conditions of the flow is expressed in these four parameter. Quantities are non-dimensionalized as follows

$$\rho = \frac{\widetilde{\rho}(\widetilde{G}\widetilde{M})^{1/2}\widetilde{R}_d^{3/2}}{\widetilde{\dot{M}}}, \qquad (u_r, u_\theta, u_z) = \frac{(\widetilde{u}_r, \widetilde{u}_\theta, \widetilde{u}_z)}{\widetilde{V}_k} \tag{2.1}$$

$$P = \frac{\widetilde{P}}{\widetilde{\rho}\widetilde{V}_k^2}, \qquad T = \frac{\widetilde{T}\widetilde{c}_p}{\widetilde{V}_k^2}, \qquad \Phi = \frac{\widetilde{\Phi}}{\widetilde{V}_k^2} \tag{2.2}$$

$$r = \frac{\widetilde{r}}{\widetilde{R}_d}, \qquad z = \frac{\widetilde{z}}{\widetilde{R}_d}, \qquad t = \frac{(\widetilde{t}-\widetilde{t}_0)\widetilde{V}_k}{\widetilde{R}_d}, \tag{2.3}$$

where

$$\widetilde{V}_k = \sqrt{\frac{\widetilde{G}\widetilde{M}}{\widetilde{R}_d}}, \tag{2.4}$$

The initial Mach number of the parent cloud is given as

$$Ma = \sqrt{\frac{\widetilde{G}\widetilde{M}}{(\gamma\widetilde{R})\widetilde{R}_d\widetilde{T}_0}} \tag{2.5}$$

Values used for the simulation discussed in this report are $\widetilde{G} = 6.67 \times 10^{-11}\,\mathrm{N.m^2/kg^2}$, $\xi = 3$, $\widetilde{M} = 2 \times 10^{29}\,\mathrm{kg}$ $(0.1M_\odot)$, $\widetilde{R}_d = 2.06 \times 10^{10}\,\mathrm{m}$ (0.14Au), $\widetilde{T}_0 = 20\,K$ (initial cloud temperature), and $\gamma\widetilde{R} = 1.4 \times 10^4\,\mathrm{m^2/(s^2K)}$ (gas constant for molecular Hydrogen). This gives the a cloud rotation rate $\widetilde{\Omega}_0 = 2.6 \times 10^{-14}\,s^{-1}$, mass accretion rate $\widetilde{\dot{M}} = 3.5 \times 10^{-5}\,M_\odot/\mathrm{yr}$ and Mach number $Ma = 48$.

3. Equations of motion and numerical methods of solution

The flow of the gas within the disk is governed by the compressible Euler equations with a gravitational force due to a central point mass:
Continuity equation

$$\frac{\partial\rho}{\partial t} + \frac{1}{r}\frac{\partial}{\partial r}(r\rho u_r) + \frac{1}{r}\frac{\partial}{\partial\theta}(\rho u_\theta) + \frac{\partial}{\partial z}(\rho u_z) = 0 \tag{3.1}$$

Momentum equations

$$\frac{\partial}{\partial t}(\rho u_r) + \frac{1}{r}\frac{\partial}{\partial r}(r\rho u_r^2) + \frac{1}{r}\frac{\partial}{\partial\theta}(\rho u_\theta u_r) + \frac{\partial}{\partial z}(\rho u_r u_z) - \frac{\rho u_\theta^2}{r} = -\frac{\partial P}{\partial r} - \rho\frac{\partial\Phi}{\partial r} \tag{3.2}$$

$$\frac{\partial}{\partial t}(\rho u_\theta) + \frac{1}{r}\frac{\partial}{\partial r}(r\rho u_r u_\theta) + \frac{1}{r}\frac{\partial}{\partial\theta}(\rho u_\theta^2) + \frac{\partial}{\partial z}(\rho u_\theta u_z) + \frac{\rho u_r u_\theta}{r} = -\frac{1}{r}\frac{\partial P}{\partial\theta} \tag{3.3}$$

$$\frac{\partial}{\partial t}(\rho u_z) + \frac{1}{r}\frac{\partial}{\partial r}(r\rho u_r u_z) + \frac{1}{r}\frac{\partial}{\partial\theta}(\rho u_\theta u_z) + \frac{\partial}{\partial z}(\rho u_z^2) = -\frac{\partial P}{\partial z} - \rho\frac{\partial\Phi}{\partial z} \tag{3.4}$$

Energy equation

$$\frac{\partial}{\partial t}(e) + \frac{1}{r}\frac{\partial}{\partial r}(ru_r(e+P)) + \frac{1}{r}\frac{\partial}{\partial\theta}(u_\theta(e+P)) + \frac{\partial}{\partial z}(u_z(e+P)) = 0 \tag{3.5}$$

where

$$e = \frac{\rho T}{\gamma} + \frac{\rho}{2}(u_r^2 + u_\theta^2 + u_z^2) + \rho\Phi \tag{3.6}$$

is the total energy. The gravitational potential term is given as

$$\Phi = -\frac{GM}{(r^2+z^2)^{1/2}} \tag{3.7}$$

As a prelude to proper modeling of radiative cooling, we assumed the flow is isothermal i.e replacing the energy equation with $T = T_0$.

3.1. *Numerical methods, boundary and initial conditions*

The numerical methods used for solving the above equations are similar to those used in studies of compressible jet flow by Freund (1997) and his code was used as a starting

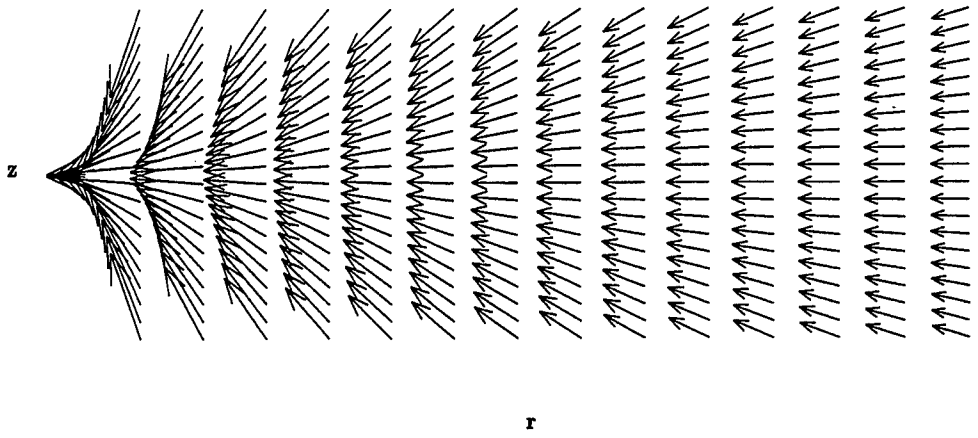

FIGURE 2. Initial velocity in a meridional (zr) plane. The protostar is on the left of the diagram. $(r_{min}, z_{min}) = (0.1, -3.5)$, $(r_{max}, z_{max}) = (2.0, 3.5)$

point. Spatial discretization in all directions was done using the sixth-order Padé-like scheme developed by Lele (1992). The details of the discretization schemes are discussed by Freund (1997). The fourth-order Runge-Kutta method was used for time advancement. To ensure stability we compute a time step based on the Courant-Friedrichs-Lewy (CFL) criterion.

These numerical schemes were tested for different steady-state compressible gas flows: solid body rotation, radially converging flow (nozzle flow), and adiabatic flow of gas in vertical hydrostatic balance between thermal pressure and the z-component of gravity.

At the top, bottom, and outer radial boundaries of the computational domain, the flow may be locally supersonic or subsonic depending on the choice of initial conditions. To determine the local flow at these boundaries, we apply the non-reflecting boundary condition of Giles (1990) using the Cassen and Moosman flow (described earlier) as the reference flow. To start the simulation we need an initial condition which we expect will form a steady or statistically stationary state. For the results shown here we assume that the initial condition is the same as the Cassen and Moosman flow except that to eliminate collisions of gas particles at the midplane of the disk, we diminished the axial velocity Eq. (1.9) to zero at the midplane using the function $f(z) = \tanh(z/\epsilon z_{max})$ where $\epsilon = 0.3$. We did not specify any boundary condition at the inner boundary because the initial Cassen and Moosman flow at this boundary is radially supersonic. We assumed that the gas is initially isothermal. The initial velocity field and density are shown in Figs. 2 and 3 respectively.

4. Results

We observed that the gas initially inside the disk races towards the star to form an equatorial concentration of mass close to the inner boundary of the disk (Fig. 4). The mass concentration significantly reduces the radial velocity within the same region (Figs. 5, 6 and 7). As the simulation progresses, the flow at the inner boundary eventually becomes subsonic, making our assumption of a supersonic outflow at the inner boundary invalid: at this point we stopped the simulation. It is possible that the equatorial concentration

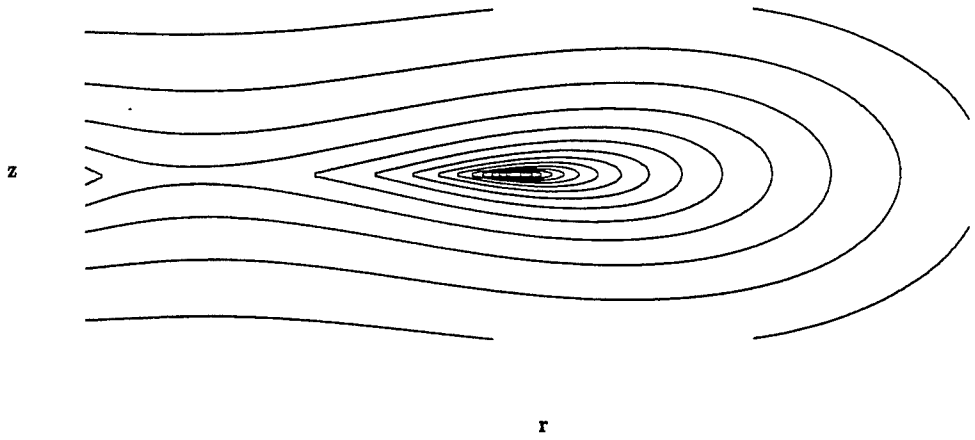

FIGURE 3. Initial log of density contours. The maximum value is 3.024 and the minimum is -0.852. $(r_{min}, z_{min}) = (0.1, -3.5)$, $(r_{max}, z_{max}) = (2.0, 3.5)$

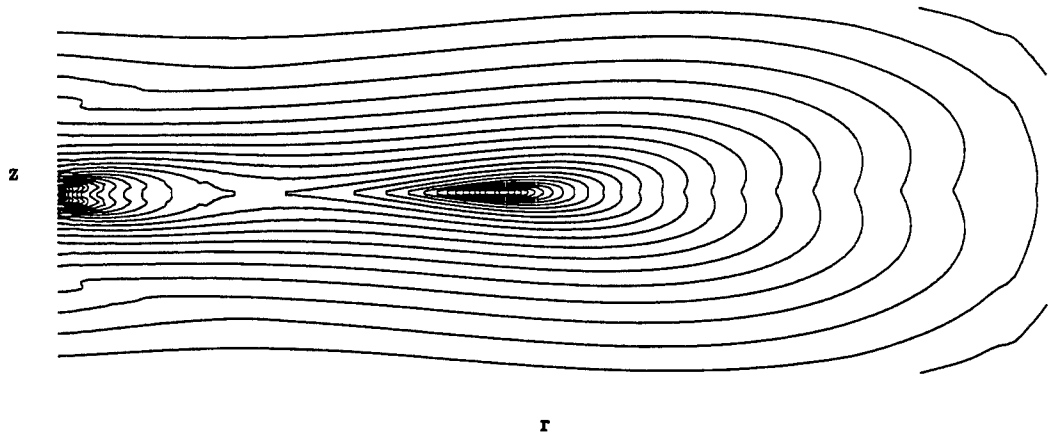

FIGURE 4. Log of density contours in meridional plane showing the equatorial concentration of density at the inner boundary. $(r_{min}, z_{min}) = (0.1, -3.5)$, $(r_{max}, z_{max}) = (2.0, 3.5)$

of mass is a transient behavior and it will eventually be pushed into the protostar when there is sufficient build up of mass within the disk. To answer this question properly we need to adopt a more suitable boundary condition for the inner boundary of the disk. This boundary condition should allow waves propagating from inside the disk to leave the computational domain and disallow any incoming waves. The Giles boundary condition used for the other boundary cannot be used for this because a reference flow at the inner boundary is unknown. The mass flux at the inner boundary of the computational domain ($\dot{M}_{out}$) was reduced significantly (Fig. 8) because of the decreasing radial velocity at the inner boundary. The quantity plotted in Fig. 8 should be unity at steady state. Clearly, the calculation is very far from such a state. Our future research efforts will first concentrate on the processes involved in the approach of a circumstellar disk to steady state and then study instabilities and turbulence evolving from this state.

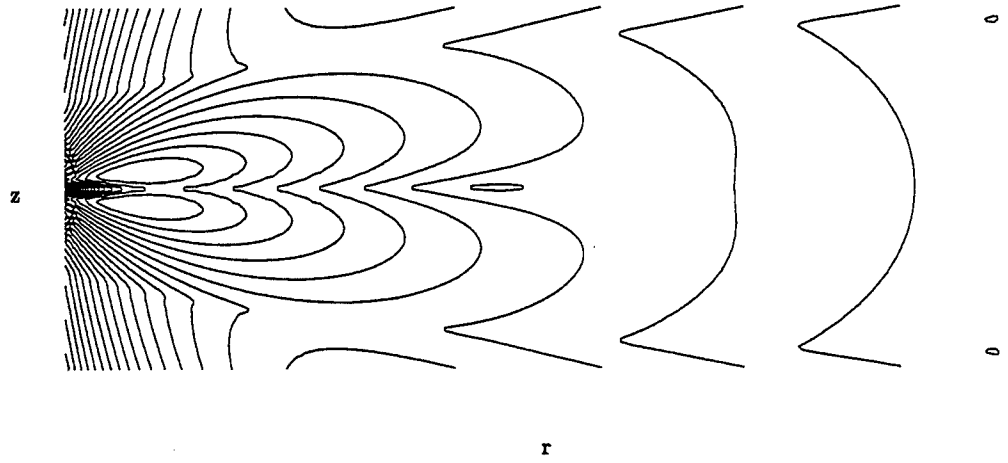

FIGURE 5. Contour plot of the radial velocity at time $t = 0.002$. Co-ordinates of the corners of the computational box are $(r_{min}, z_{min}) = (0.1, -3.5)$, $(r_{max}, z_{max}) = (2.0, 3.5)$

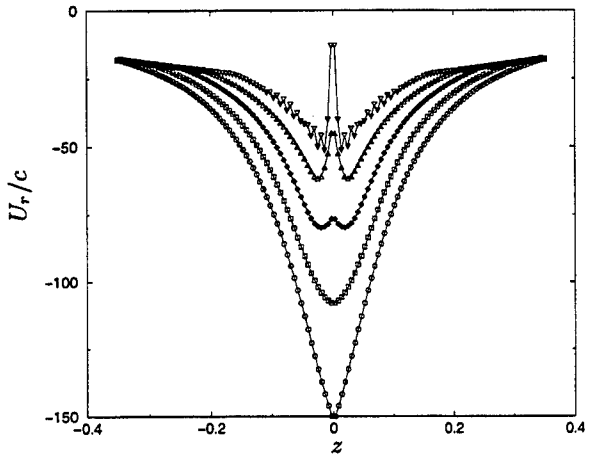

FIGURE 6. Evolution of radial velocity at the inner boundary normalized by the local speed of sound. $\circ : t = 0.0000$; $\square : t = 0.0004$; $\diamond : t = 0.0009$; $\triangle : t = 0.0014$; $\triangledown : t = 0.0019$

Acknowledgments

The author gratefully acknowledges Dr. Karim Shariff and Dr. Steven Stahler for valuable discussions and contributions during the course of this work.

REFERENCES

CASSEN P. & MOOSMAN A. 1981 On the formation of protostellar disks, *ICARUS* **48**, 353–376.

STAHLER S.W., KORYCANSKY D.G., BROTHERS M.J., & TOUMA J 1994 The early evolution of protostellar disks, *Astrophys. J.* **431**, 341–358.

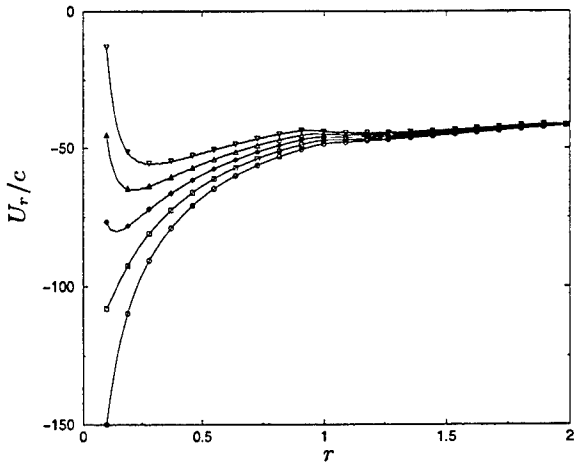

FIGURE 7. Normalized radial velocity at the midplane at different times. ○ : $t = 0.0000$; □ : $t = 0.0004$; ◇ : $t = 0.0009$; △ : $t = 0.0014$; ▽ : $t = 0.0019$

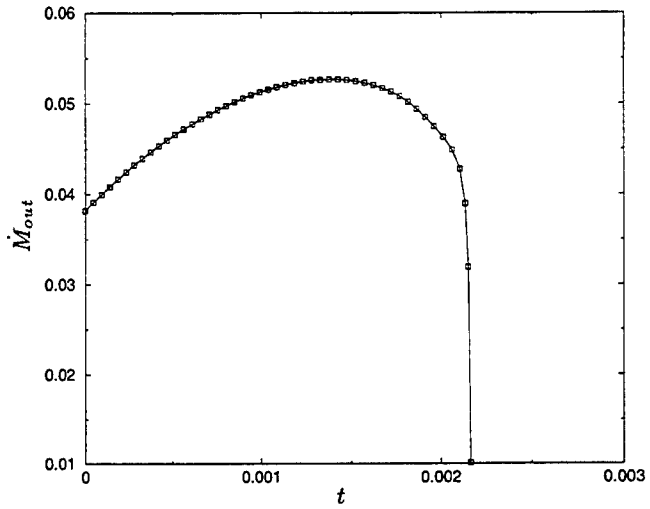

FIGURE 8. Mass flux at the inner radial boundary normalized by the total mass influx into the computational domain.

TEREBEY S., SHU F.H., & CASSEN P. 1984 The collapse of the cores of slowly rotating isothermal clouds, *Astrophys. J.* **286**, 529–551.

SHU F.H. 1977 Self-similar collapse of isothermal spheres and star formation, *Astrophys. J.* **214**, 488–497.

ULRICH, R.K. 1976 An infall model for the T Tauri phenomenon, *Astrophys. J.* **210**, 377–391.

FREUND, J.B., MOIN, P. & LELE, S.K. 1997 Compressibility effects in a turbulent annular mixing layer, *Dept. of Mech. Engr., Stanford University* **Report No. TF–72**

LELE, S.K. 1992 Compact finite difference schemes with spectral-like resolution, *J. Comp. Phys.* **103**, 16–42.

GILES, M.B. 1990 Nonreflecting boundary conditions for Euler equation calculations, *AIAA J.* **18**, 2050–2058.

Modeling blood flow in a porcine aorta bypass graft: realization of physiological conditions

By V. Favier AND C. A. Taylor†

1. Motivation and objectives

Atherosclerosis, a vascular disease in which plaque deposits form in blood vessels, does not occur uniformly throughout the body. Rather, it is more likely to occur in regions of complex flow associated with vessel branching (Zarins & Taylor 1998). It is generally believed that low wall shear stress and high particle residence time in the regions of complex flow increase the susceptibility of blood vessels to disease by altering the permeability of the endothelium (mono-layer of cells at blood-vessel interface) and reducing the efflux of cholesterol from the wall. Surgical interventions, including bypass grafting are also affected by blood flow conditions. Further, it is thought that flow recirculation and stasis are important factors in intimal hyperplasia (cell proliferation in the inner layer of blood vessels that can lead to obstruction of grafts (Dilley, Mc Geachie & Prendergast 1988). The chemical process of clotting may result at the site of a surgical wound and also on the surface of any artificial device that has been inserted. Lately, in areas of flow recirculation and stasis, the probability for clot formation has been shown to considerably increase (Gewertz *et al.* 1992).

Quantification of blood flow is important for research in such disease, and the development of devices and clinical procedures to treat it. The techniques of experimental fluid mechanics have been effectively used in the context of artificial models to characterize flow patterns. Recently, diagnostic imaging techniques, which include ultrasound and magnetic resonance imaging, have allowed non-invasive, *in vivo* flow quantification. However, full velocity fields and derived quantities such as shear stress are difficult to obtain using *in vitro* or *in vivo* methods. Perhaps even more significant is the fact that for these methods new physical models have to be constructed to examine the effect of geometric variations. This is time-consuming and costly for *in vitro* models and impractical for *in vivo* methods. Clearly, the need exists for computational methods capable of simulating blood flow using virtual models.

Early computational studies used simple idealized models of the vascular system. Perktold and colleagues examined blood flow in rigid and deformable models of carotid arteries (Perktold, Resch & Peter 1991; Perktold & Rappitsch 1995). Taylor *et al.* quantified blood flow in an idealized model of the human abdominal aorta under resting and exercise conditions (Taylor, Hughes & Zarins 1998a; Taylor, Hughes & Zarins 1999). Milner *et al.* (1998) and Taylor, Hughes & Zarins (1998b) examined blood flow in models of the end-to-side anastomosis (downstream connection of the end of a bypass graft to side of a host artery).

To increase accuracy of the simulations and reproduce the anatomy where the arterial walls are curved and irregular, geometric models can be constructed from volumetric image data including magnetic resonance imaging (MRI) and computed tomography

† Stanford University, Mechanical Engineering & Surgery

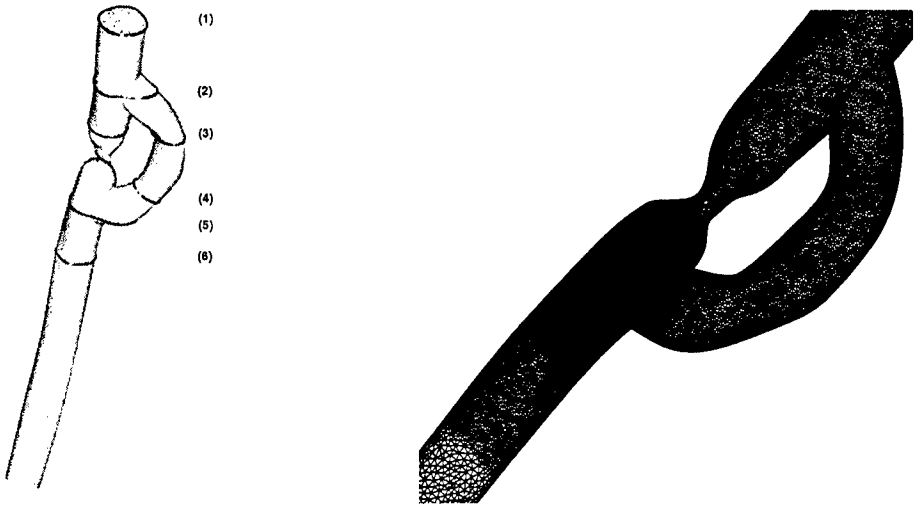

FIGURE 1. Model of the pig aorta (straight vessel) and bypass graft (curved vessel). Location of the measured cross-sections (1)-(6) (left). Mesh refinement at the stenosis (right).

(CT) data (Taylor, Hughes & Zarins 1996; Milner *et al.* 1998; Cebral & Lohner 2001). These patient-specific anatomic models can be modified to reflect alternate treatment plans and have the potential to be used to predict outcomes of interventions and design-improved procedures for individual patients (Taylor, Hughes & Zarins 1999).

However, anatomical accuracy is not enough to simulate blood flow in human arteries or treatment plans. Blood flow is significantly altered under different physiological states (at rest and exercise for example), and varies from person to person. Few computational investigations have combined anatomic models reconstructed from image data with actual physiologic boundary conditions. Ku *et al.* (2001) used a Dacron band to create a restriction (stenosis) in the descending thoracic aorta of pigs and then bypassed this stenosis with a Dacron graft. This aorto-aorto bypass graft was imaged using magnetic resonance angiography (MRA) and blood-flow velocity was measured in the aorta above the proximal connection of the graft to the aorta, using phase-contrast magnetic resonance imaging (PC-MRI). This flow velocity data was used to calculate the volumetric flow rate which in turn was used to prescribe fully-developed pulsatile flow boundary conditions (based on Womersley theory) at the inlet of the computational model. Computed flow rates in the bypass graft and native aorta compared favorably to the flow rates obtained from PC-MRI measurements in these locations. A limitation of this prior investigation is that a Womersley boundary condition was employed, and the effect of this idealized boundary condition on blood flow rate and velocity patterns was not examined.

In this paper, we describe the effect of inflow boundary conditions on flow rate and velocity in the porcine aorto-aorto bypass model. We compare results of computational solutions performed using a Womersley inflow boundary condition and inflow velocity mapped directly from PC-MRI data.

2. Methods

The anatomic model is constructed from MRA data as follows. A vessel path is identified and two-dimensional slice planes are positioned along this path in the volumetric

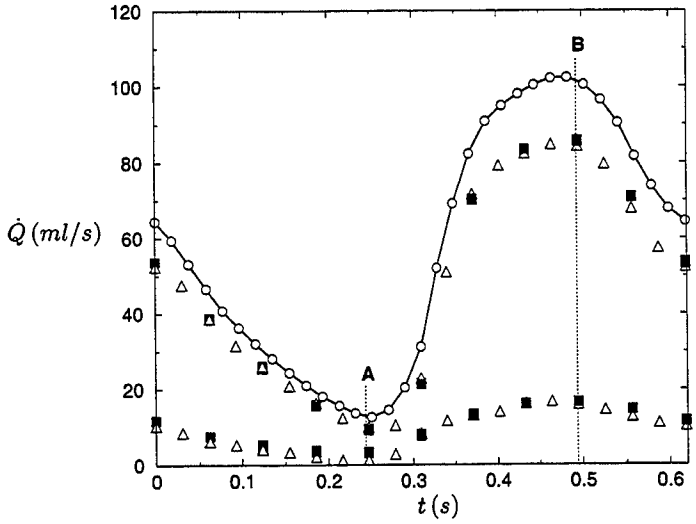

FIGURE 2. Flow rate, $\dot{Q}$, versus time, t. Time A: end diastole, time B: peak systole. o–o: experimental data, ■: flow rate in the graft (top) and in the aorta (bottom) for the Womersley profile, Δ: flow rate in the graft (top) and in the aorta (bottom) for the three-component profile.

image data. A level-set method is used to extract closed curves representing the vessel boundary in each two-dimensional plane (Wang, Dutton & Taylor 1999). A surface is lofted through these curves and a solid model constructed (see Fig. 1).

An automatic finite-element mesh generator is used to discretize the solid model (SCOREC, Rensselaer Polytechnic Institute, Troy, NY). For the calculations described in the present study, a 1.2 million tetrahedral element mesh was used. It is refined in the vicinity of the stenosis and coarsened in the most distal region (Fig. 1, right).

As a first approximation we assume that the vessel walls are rigid and that blood behaves as a Newtonian fluid (Taylor, Hughes & Zarins 1998a). With these simplifications, the incompressible Navier-Stokes equations which describe the problem are given by:

$$\begin{aligned} u_{i,i} &= 0 \\ \dot{u}_i + u_j u_{i,j} &= -(p_{,i}/\rho) + \tau_{ij,j} + f_i \end{aligned} \tag{2.1}$$

The density ρ is constant, u_i is the i^{th} component of the velocity, p the pressure, f_i the prescribed body force, τ_{ij} the viscous stress tensor given by $\tau_{ij} = \nu(u_{i,j} + u_{j,i})$, and ν is the kinematic viscosity, where $\nu = \mu/\rho$.

Velocity and pressure are solved using a stabilized finite element method (Taylor, Hughes & Zarins 1998b; Jansen, Whiting & Hulbert 2000). A traction-free boundary condition is used at the outlet.

Two different pulsatile velocity profiles are imposed at the inlet of the calculation domain: the actual velocities measured using PC-MRI (including in-plane components) or an idealized Womersley velocity profile derived from the measured flow rate.

Womersley theory is based on the analytical solution of the Navier-Stokes equations in the case of a fully-developed pulsatile flow in a straight circular cylinder (of radius R). Keeping these assumptions in mind, it can be applied to blood flow such that when the flow rate, $\dot{Q}(t)$, is known, the axial velocity profile can be derived. Given the period of the cardiac cycle ($T = 2\pi/\omega$), a Fast Fourier Transform is used to extract the frequency content of the flow waveform. The Fourier coefficients B_n and the Womersley velocity

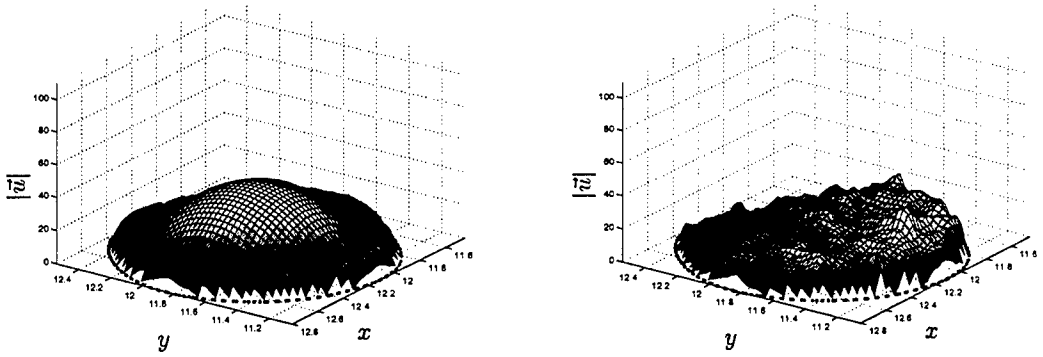

FIGURE 3. Surface plot of the velocity magnitude at cross-section (1), at end diastole for the Womersley profile (left) and the three-component profile (right).

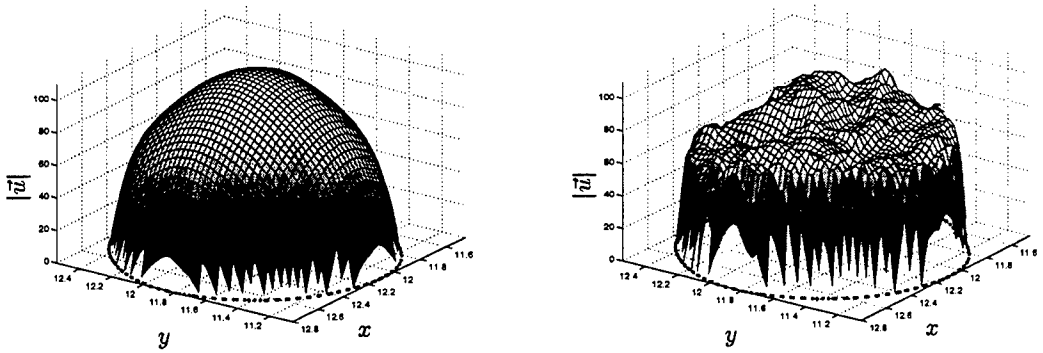

FIGURE 4. Surface plot of the velocity magnitude at cross-section (1), at peak systole for the Womersley profile (left) and the three-component profile (right).

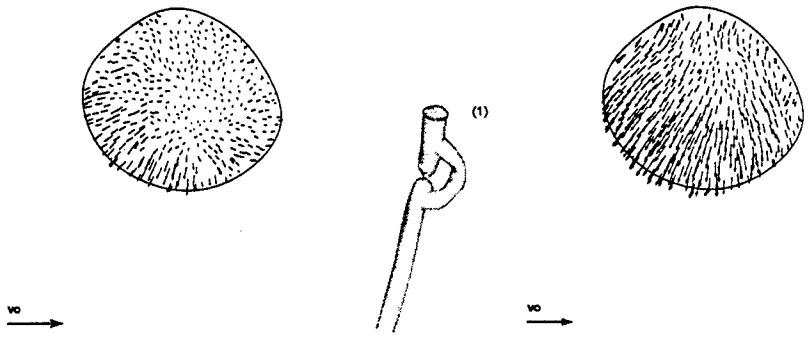

FIGURE 5. In-plane velocity vectors for the three-component profile at cross-section (1), at end diastole (left) and peak systole (right). Reference vector: $|\vec{v}_o| = 40\, cm.s^{-1}$

profile in terms of the radius r and the time t are given by:

$$\dot{Q}(t) = \sum_{n=0}^{N} B_n e^{in\omega t} \text{ and } u(r,t) = \frac{2B_o}{\pi R^2}\left[1-\left(\frac{r}{R}\right)^2\right] + \sum_{n=1}^{N} \frac{B_n}{\pi R^2}\left[\frac{1-\frac{J_o\left(\alpha_n \frac{r}{R} i^{3/2}\right)}{J_o\left(\alpha_n i^{3/2}\right)}}{1-\frac{2J_1\left(\alpha_n i^{3/2}\right)}{\alpha_n i^{3/2} J_o\left(\alpha_n i^{3/2}\right)}}\right] e^{in\omega t}$$

where J_o and J_1 are Bessel functions, and $\alpha_n = R\sqrt{(n\omega)/\nu}$.

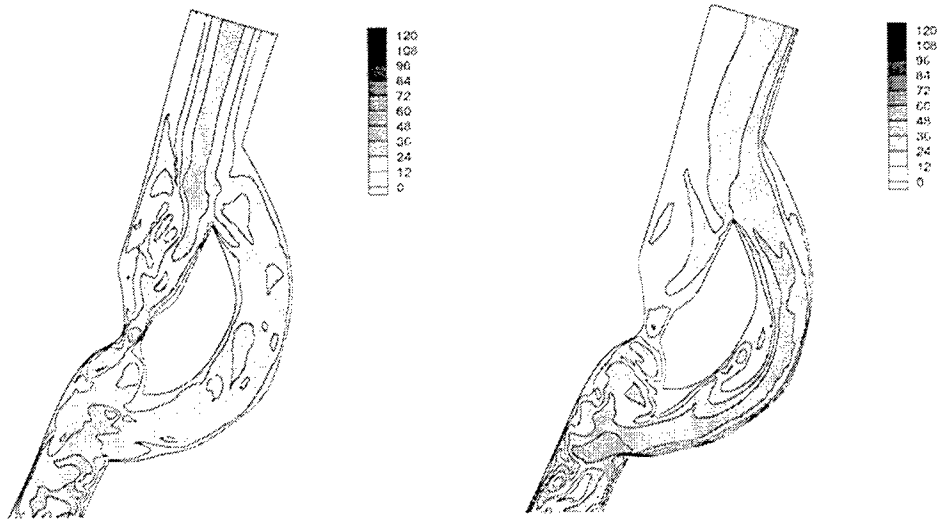

FIGURE 6. Contours of the velocity magnitude along a transverse cross-section at end diastole, for the Womersley profile (left) and the three-component profile (right).

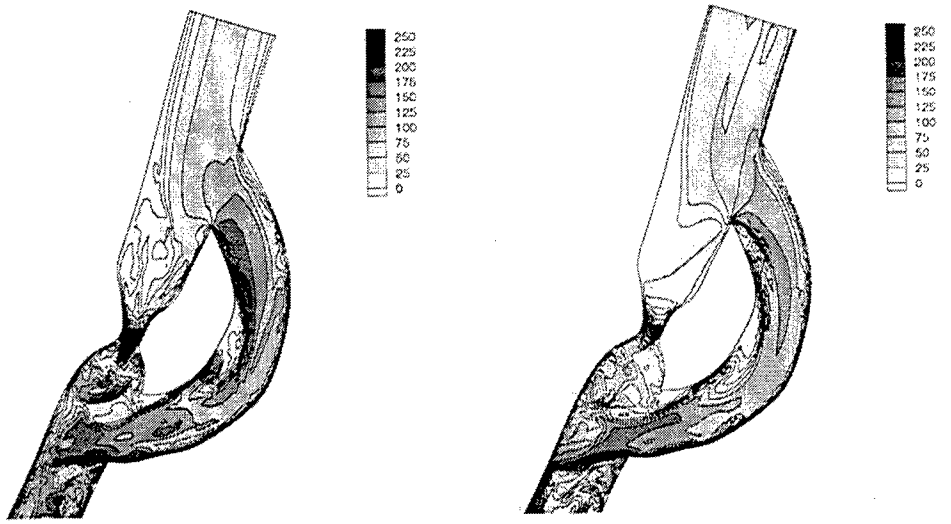

FIGURE 7. Contours of the velocity magnitude along a transverse cross-section, at peak systole, for the Womersley profile (left) and the three-component profile (right).

In our simulations, the Womersley number is $\alpha_1 = 5.5$ and the period is $T = 0.62$ s. The Reynolds number measured at the inlet varies from 320 at end diastole (time A, Fig. 2) to 2550 at peak systole (time B, Fig. 2).

The flow rate is calculated from the measured data (Fig. 2, open circles). As we do not have a circular inlet, we first calculate the Womersley velocities for a constant radius, R, corresponding to the maximum radius of the lumen, and then the resulting velocity profile is mapped on the real geometry. The shape of the velocity profile is kept similar (with zero values at the boundaries and a maxima at the centroid of the vessel), and the flow rate is conserved, leading to a "quasi-Womersley" profile. The measured three-component and idealized velocity profiles are shown in Fig. 3 at end diastole and in Fig. 4 at peak

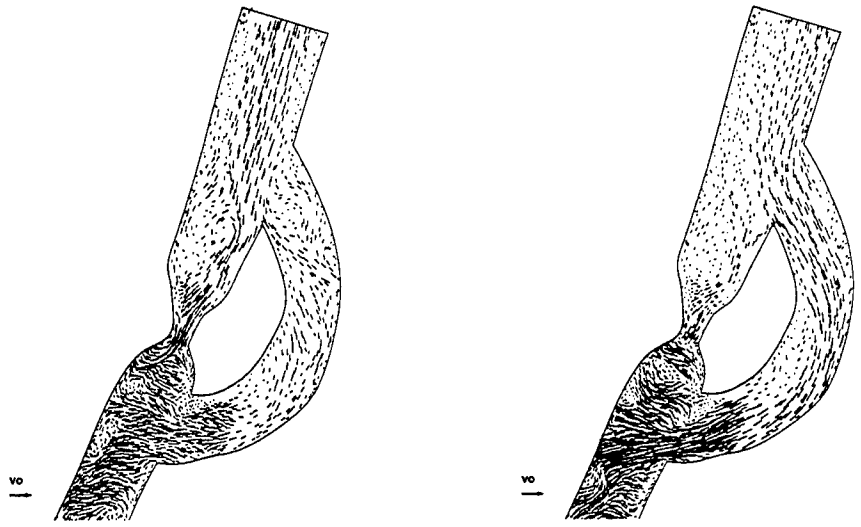

FIGURE 8. In-plane velocity vectors along a transverse cross-section, at end diastole, for the Womersley profile (left) and the three-component profile (right). Reference vector: $|\vec{v}_o| = 80\, cm.s^{-1}$

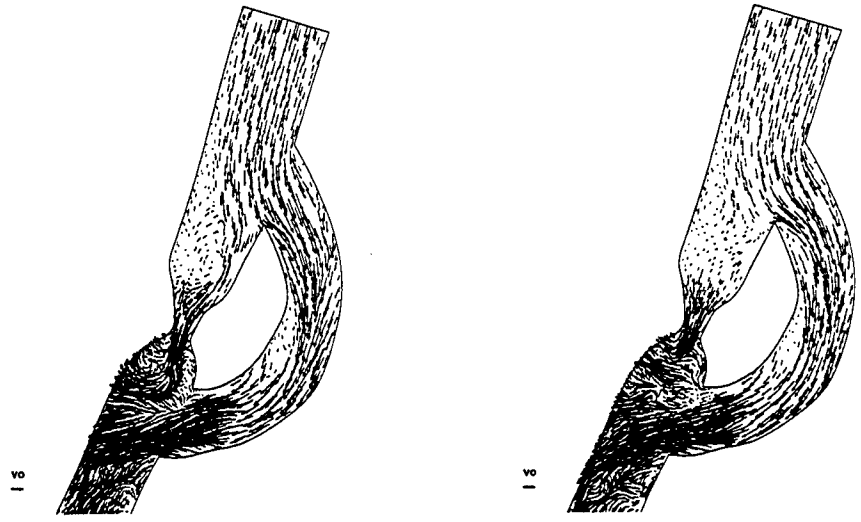

FIGURE 9. In-plane velocity vectors along a transverse cross-section, at peak systole, for the Womersley profile (left) and the three-component profile (right). Reference vector: $|\vec{v}_o| = 80\, cm.s^{-1}$

systole. In contrast to the three-component velocity profile which is irregular (Fig. 3 and 4, right), the Womersley solution is characterized by a smooth profile (Figs 3 and 4, left). The in-plane velocity for the three-component velocity profile is shown on Fig. 5 at end diastole (left) and peak systole (right). The descending aorta is curved in such a way that the in-plane component of the velocity vector is not negligible at the inlet of the bypass graft. The flow is directed towards the bypass graft. The in-plane velocity for the idealized Womersley boundary condition is prescribed to be zero.

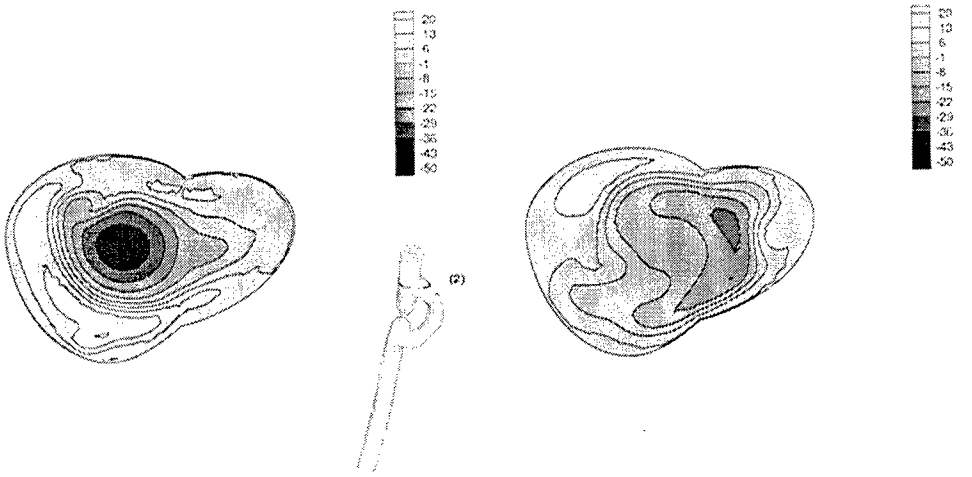

FIGURE 10. Contours of the through-plane velocity at cross-section (2), and end diastole, for the Womersley profile (left) and the three-component profile (right).

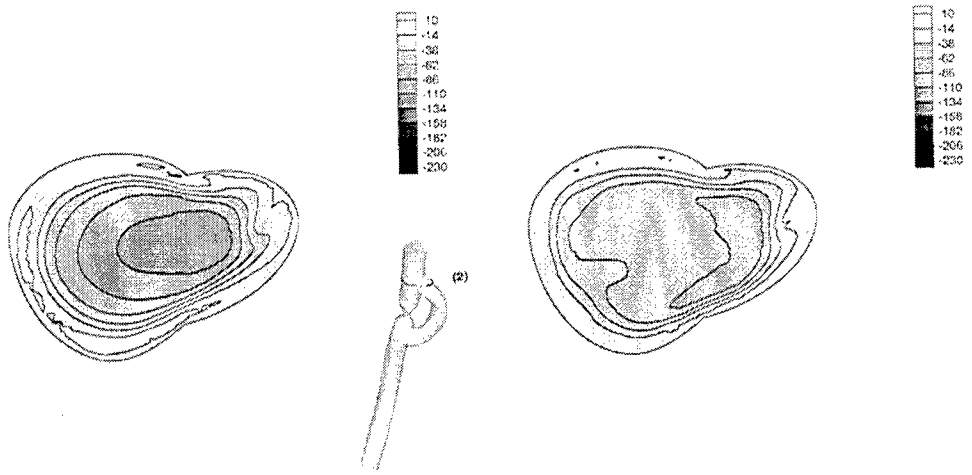

FIGURE 11. Contours of the through-plane velocity at cross-section (2), at peak systole, for the Womersley profile (left) and the three-component profile (right).

3. Results

With a prescribed velocity at the inlet we compute the three-dimensional velocity fields. We compare the volumetric flow rates in the native aorta and bypass graft (cross-section (3), Fig. 1) and the velocity fields for the idealized Womersley inlet boundary condition and measured three-component inlet velocity profile.

The measured velocity profile at the inlet (cross-section (1), Fig. 1) was used to compute the inlet flow rate (Fig. 2, open circles). From the simulation of the two inflow velocity profiles, we observe that the graft and aorta flow rates measured at cross-section (3) (Fig. 1) are very similar. The three-component inlet velocity profile simulation (Fig. 2, black squares) and the Womersley inlet velocity profile simulation (Fig. 2, open triangles)

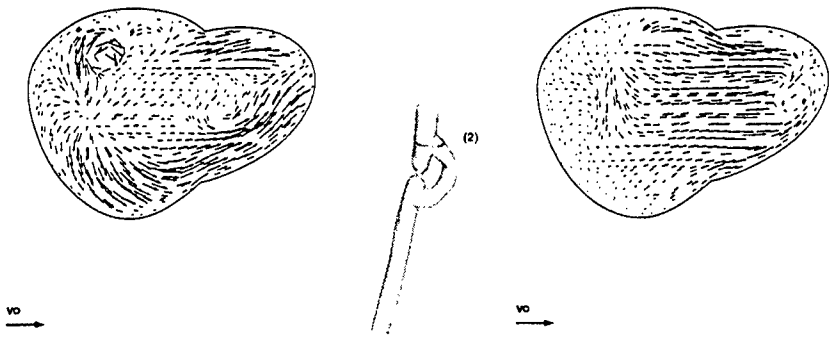

FIGURE 12. In-plane velocity vectors at cross-section (2), at end diastole, for the Womersley profile (left) and the three-component profile (right). Reference vector: $|\vec{v}_o| = 40\, cm.s^{-1}$

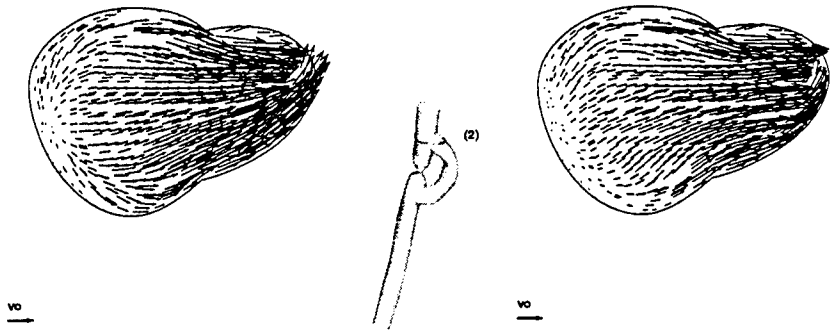

FIGURE 13. In-plane velocity vectors at cross-section (2), at peak systole, for the Womersley profile (left) and the three-component profile (right). Reference vector: $|\vec{v}_o| = 40\, cm.s^{-1}$

show the same variations in time. The average values of the flow rate in the aorta, $\dot{Q}_a$, and in the bypass, $\dot{Q}_b$, are approximately 16% and 84% respectively. This corresponds to the experimental data, where $\dot{Q}_a \approx 22\%$ of the inlet flow rate and $\dot{Q}_b \approx 86.6\%$ of the inlet flow rate. Note that, due an estimated error of 10% in the measurements, the sum of the aorta and bypass flow rates exceeds that measured at the inlet.

In Figs. 6, 7, 8 and 9, a transverse cross-section through the domain enables us to observe the influence of the inlet boundary condition on the velocity field. At peak systole one can observe the existence of a recirculation zone in the inside wall of the bypass due to the curvature of the bypass graft. In the three-components case, a separation zone which is not seen with the Womersley boundary condition appears along the inside wall at the entrance to the bypass. This is particularly noticeable in Figs. 7 and 9. Downstream of the stenosis, the main orientation of the in-plane velocity vectors is similar using both inflow velocity conditions, and the influence of the inlet conditions decreases.

Cross-sections (2) and (3) are located in the vicinity of the inlet of the domain. Solutions at these locations demonstrate the influence of the two different inflow velocity profiles. With the Womersley profile, for cross-section (2) at end diastole, the through-plane velocity component is centered in the aorta (Fig. 10, left). When the flow increases,

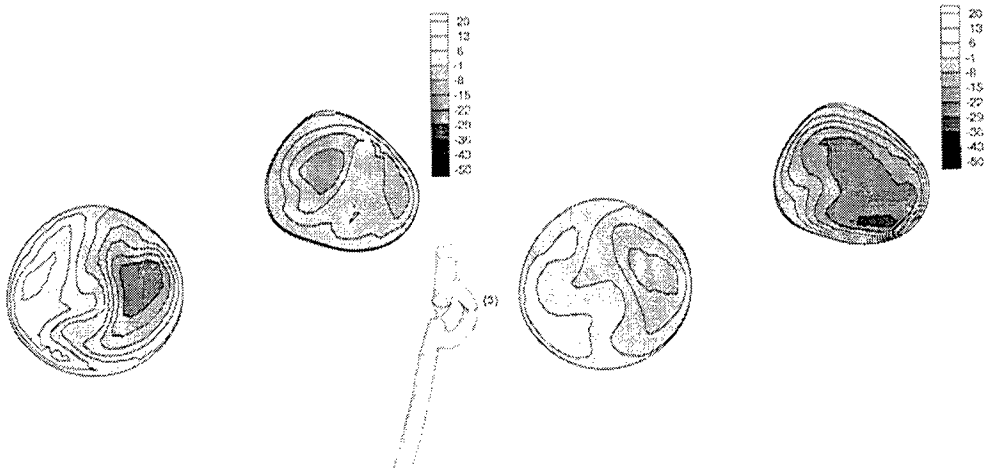

FIGURE 14. Contours of the through-plane velocity at cross-section (3), at end diastole, for the Womersley profile (left) and the three-component profile (right).

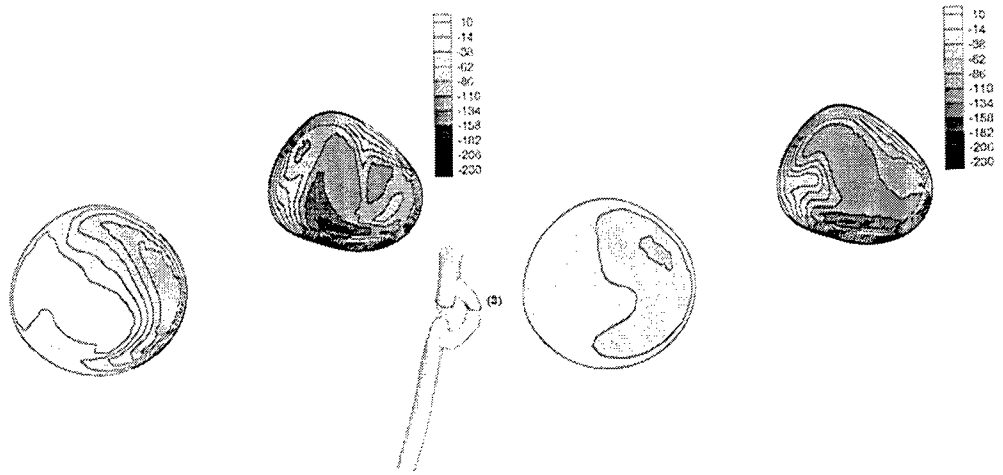

FIGURE 15. Contours of the through-plane velocity at cross-section (3), at peak systole, for the Womersley profile (left) and the three-component profile (right).

at peak systole, the maximum of the through-plane velocity shifts towards the bypass, where the flow rate, $\dot{Q}_b$, is higher (Fig. 11, left). The in-plane velocity vectors indicate that the fluid follows the path imposed by the geometry of the bypass (Fig. 13, left). With the three-component profile, the maximum of the through-plane velocity is off center at end diastole and peak systole (Fig. 10 and 11, right).

Downstream, at cross-section (3), in both cases at peak systole, the maximum of the through-plane velocity is located in the front side of the bypass (Fig. 14). The bypass is now indeed curved towards the front of the Figure. With the Womersley profile, this redirection of the fluid gives rise to some flow disturbances at peak systole, as revealed by the in-plane velocity vectors (Fig. 17 left vs. right). With the three-component profile, the flow follows a more natural path since it is guided from the inlet towards the bypass.

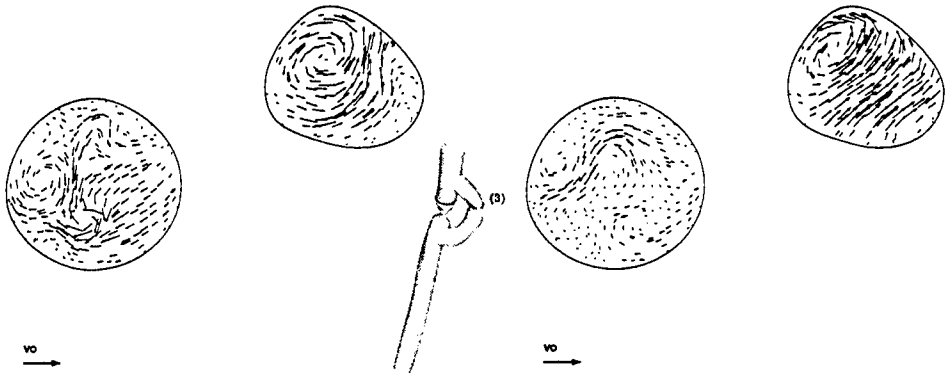

FIGURE 16. In-plane velocity vectors at cross-section (3), at end diastole, for the Womersley profile (left) and the three-component profile (right). Reference vector: $|\vec{v}_o| = 40\,cm.s^{-1}$

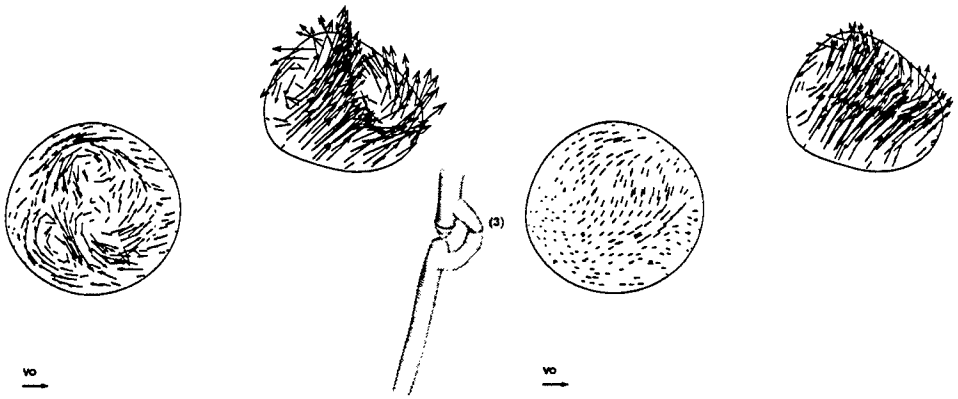

FIGURE 17. In-plane velocity vectors at cross-section (3), at peak systole, for the Womersley profile (left) and the three-component profile (right). Reference vector: $|\vec{v}_o| = 40\,cm.s^{-1}$

The contours of the through-plane velocity show the location of the recirculation zone previously discussed. Due to the influence of the bypass graft, the maximum of the through-plane velocity in the aorta is skewed towards the bypass side of the aortic wall (Fig. 14 and 15). The through-plane velocity is however more uniform with the three-component profile than with the Womersley profile.

For the cross-sections further downstream (not shown here), there is less difference between the two inlet velocity boundary condition profiles. Further downstream, the geometry and flow distribution (same in both cases) dominate the flow characteristics.

4. Conclusion and future plans

We have examined the effect of inlet velocity profile on flow rate and velocity features in a porcine aorto-aorto bypass model. Either the three components of the measured velocity were prescribed as an inlet boundary condition, or the measured flow rate was used to calculate a Womersley profile for the through-plane velocity (the in-plane velocity is zero). We do not observe any effect on flow rates using either approach. Hence, if only the flow distribution is of interest, the Womersley inlet profile can be used in simulations.

In this case, only through-plane velocity measurements are needed to acquire the flow rate during the cardiac cycle. While flow distribution is unaffected by the inlet velocity profile, the velocity patterns are altered. The Womersley profile and the three-component profile show local differences in the recirculation zone and in the maximum velocity locations. Although not shown here, these differences decrease downstream of the bypass model. Since complex recirculating flow and regions of wall shear stress correlate with atherosclerosis, intimal hyperplasia and clot formation, three-dimensional simulations of blood flow using actual velocity profiles are of interest.

The effect of the boundary conditions on flow rate and velocity profile should be examined experimentally in other subjects (different pigs had distinct stenosis degree and bypass geometry) before further conclusions are made. In addition, comparisons of the computed velocity with experimental data will be conducted.

REFERENCES

CEBRAL, J. R. & LOHNER, R. 2001 From medical images to anatomically accurate finite element grids. *Int. J. Num. Methods Engng.* **21**, 985-1008.

DILLEY, R. J., MC GEACHIE, J. K. & PRENDERGAST, F. J. 1988 A review of the histologic-changes in vein-to-artery grafts with particular reference to intimal hyperplasia. *Arch. Surg.* **123**, 691-696.

GEWERTZ, B. L., GRAHAM, A., LAWRENCE, P. F., PROVAN, J. & ZARINS, C. K. 1992 Diseases of the vascular system. *Essentials of general surgery*, Williams & Wilkins, 328-347.

JANSEN, K. E., WHITING, C. H. & HULBERT, G. M. 2000 A generalized-alpha method for integrating the filtered Navier-Stokes equations with a stabilized finite element method. *Comput. Meth. Appl. Mech. Engng.* **190**, 305-319.

KU, J. P., DRANEY, M. T., ARKO, F. R., LEE. W. A., CHAN, F., PELC, N. J., ZARINS, C. K. & TAYLOR, C. A. 2001 *In Vivo* validation of numerical predictions of blood flow in arterial bypass grafts. Submitted for publication to *Ann. of Biomed. Engng.*

MILNER, J. S., MOORE, J. A., RUTT, B. K., & STEINMAN, D. A. 1998 Hemodynamics of human carotid artery bifurcations: Computational studies with models reconstructed from magnetic resonance imaging of normal subjects. *J. Vasc. Surg.* **28**, 143-156.

PERKTOLD, K. & RAPPITSCH, G. 1995 Computer-simulation of local blood-flow and vessel mechanics in a compliant carotid-artery bifurcation model. *J. Biomech.* **28**, 845-856.

PERKTOLD, K., RESCH, M. & PETER, R. 1991 Three-dimensional numerical analysis of pulsatile flow and wall shear stress in the carotid artery bifurcation. *J. Biomech.* **24(6)**, 409-420.

STEINMAN, D. A. & ETHIER, C. R. 1994 The effect of wall distensibility on flow in a two-dimensional end-to-side anastomosis. *J. Biomech. Engng.* **116**, 294-301.

TAYLOR, C. A., DRANEY, M. T, KU, J. P., PARKER, D., STEELE, B. N., WANG, K. & ZARINS, C. K. 1999 Predictive medicine: Computational techniques in therapeutic decision-making *Computer Aided Surgery* **4(5)**, 231-247.

TAYLOR, C. A., HUGHES, T. J. R. & ZARINS, C. K. 1996 Computational investigations in vascular disease. *Computers in Physics* **10**, 224-232.

TAYLOR, C. A., HUGHES, T. J. R. & ZARINS, C. K. 1998a Finite element modeling of 3-dimensional pulsatile flow in the abdominal aorta: relevance to atherosclerosis. *Ann. Biomed. Engng.* **26(6)**, 1-13.

TAYLOR, C. A., HUGHES, T. J. R. & ZARINS, C. K. 1998b Finite element modeling of flow in arteries. *Comput. Methods Appl. Mech. Engng.* **158**, 155-196.

TAYLOR, C. A., HUGHES, T. J. R. & ZARINS, C. K. 1999 Effect of exercise on hemodynamic conditions in the abdominal aorta. *J. Vasc. Surg.* **29**, 1077-89.

ZARINS, C. K. & TAYLOR, C. A. 1998 Hemodynamic factors in atherosclerosis. *Vascular surgery: a comprehensive review.* Moore, W. S. (Ed.), Saunders Company, 97-110.

WANG, K. C, DUTTON, R. W. & TAYLOR, C. A. 1999 Level Sets for vascular model construction in computational hemodynamics. *IEEE Engineering in Medicine and Biology* **18**, 33-39.

An evolutionary algorithm for multi-objective optimization of combustion processes

By Dirk Büche †, Peter Stoll‡ AND Petros Koumoutsakos ¶

1. Motivation and objectives

We study the optimization of the spatial distribution of fuel injection rates in a gas turbine burner. An automated procedure is implemented for the optimization. The procedure entails an evolutionary optimization algorithm and an automated interface for the modification of the parameters in the experimental setup for the fuel injection and for the post-processing.

The evolutionary algorithm is capable of handling multiple objectives in a Pareto setup and of efficiently accounting for noise in the objective function. The parameterization considers eight analogue valves for controlling the fuel distribution, and the evaluation tool is an experimental test-rig for a gas turbine burner. A measurement chamber and a microphone are used to analyze the emissions and the pulsation of the burner, respectively. These two values are taken as objectives for the evolutionary algorithm. The algorithm is shown to converge to a Pareto front and the analysis of the resulting parameters elucidates further relevant physical processes.

2. Accomplishments

2.1. *Evolutionary algorithms*

Evolutionary Algorithms (EAs) such as Genetic Algorithms and Evolution Strategies are biologically-inspired optimization algorithms, imitating the process of natural evolution, and are becoming important optimization tools for several real-world applications. They use a set of solutions (population) to converge to the optimal design(s). The population-based search allows easy parallelization, and information can be accumulated so as to generate accelerated algorithms. EAs are robust optimization methods. They do not require gradients of the objective function, they can handle noisy objective functions, and they may avoid premature convergence to local minima.

2.1.1. *Multi-objective evolutionary algorithms for noisy objectives*

Real-world applications, like product-design optimization, often imply multiple objectives. For example, the cost and the quality of products are two conflicting objectives, usually tackled by interdisciplinary design teams. Hence no single best solution exists, but a set of compromise solutions. The complete set of compromise solutions is referred to as the nondominated or Pareto set of solutions. They represent the best solutions to

† Institute of Computational Science, Swiss Federal Institute of Technology (ETH), Zürich, Switzerland
‡ Alstom Power Technology, Segelhof, 5405 Dättwil, Switzerland
¶ Institute of Computational Science, Swiss Federal Institute of Technology (ETH), Zürich, Switzerland

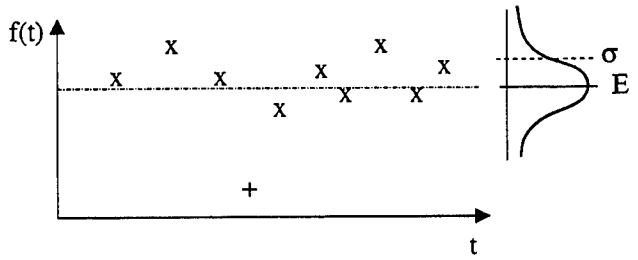

FIGURE 1. Illustration of noise and outliers in an experiment. For repeated measurements of the same operating point, the objective value f (marked by an $\times$) changes, governed by a normal distribution with mean E and standard deviation σ. An outlier solution is added to the figure and marked with a $+$.

the problem and are characterized by the definition that no other solution exists that is superior in all objectives.

The Strength Pareto Evolutionary Algorithm (SPEA) of Zitzler & Thiele (1999) is a well-established Pareto-optimization algorithm, which uses the dominance criterion for the fitness assignment and selection of solutions. Noise may change the dominance relation between different solutions. Dominated solutions may become nondominated and the selection may be missleaded. Noise is addressed in two recent publications of Teich (2001) and Hughes (2001), which adapt the Pareto ranking scheme of Goldberg (1989) by defining probabilities of dominance between noisy solutions. Both methods assume either a uniform or a normal distribution of the noise and can benefit from a priori knowledge of its magnitude.

In addition, a measurement may fail completely, producing outliers, i.e. arbitrary non-physical results. This is illustrated in Fig. 1. SPEA is an elitistic algorithm, i.e. it keeps the best solutions found so far until superior successors are found. Elitism is critical for optimizing experimental setups. The optimization algorithm might get stuck in an outlier solution which dominates all present solutions. Thus we propose three modifications for an extended multi-objective algorithm to overcome the problem of noise and outliers:

(*a*) *domination dependent lifetime:* In contrast to elitism, which may preserve elitist (nondominated) solutions for an infinite time, a maximal lifetime κ is assigned to each individual. For evolution strategies, algorithms with implemented lifetime κ are referred to as (μ, κ, λ) algorithms (Bäck, Hoffmeister & Schwefel 1991). The novel approach is that the lifetime is variable and related to the dominance of a solution. The lifetime is shortened if the solution dominates a major part of the present nondominated solutions. This limits the impact of a solution.

(*b*) *re-evaluation of solutions:* In EAs, solutions with expired lifetime are usually deleted. In contrast, we re-evaluate all nondominated solutions whose lifetime has expired, and add them to the population. This enables good solutions to stay in the evolutionary process, but their objective values will change due to the noise in the re-evaluation.

(*c*) *extended update of the secondary population:* The SPEA algorithm updates the elitist solutions always with the current population. We propose to extend the update to *all* solutions with non-expired lifetime. This reduces loss of information.

2.1.2. *Performance comparison*

The performance of the *extended SPEA* is analyzed on a set of test functions. The extended algorithm is compared with the *standard SPEA* of Zitzler & Thiele (1999) and with a *non-elitistic SPEA*. The non-elitistic SPEA is obtained from the standard SPEA

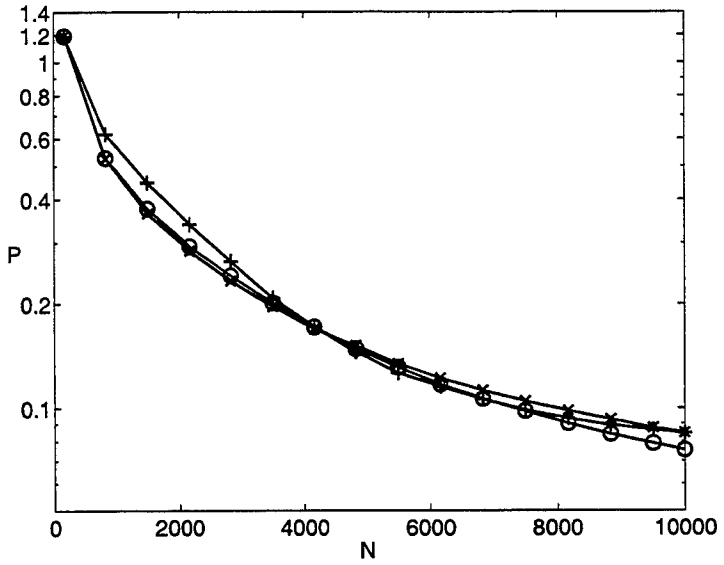

FIGURE 2. Convergence of the extended SPEA [circular symbol] on the noise-free test function 1, compared with the standard SPEA [cross symbol] and a non-elitistic SPEA [plus symbol]. The mean distance P of the present nondominated solutions to the analytical Pareto front is plotted over the number of function evaluations N.

by setting the lifetime of all individuals to one. Three test functions are considered. From Deb (1999), a two-objective minimization problem for an arbitrary number of real design variables $x_{i,\ i=1...n}$ is chosen as the first test function:

$$f_1 = x_1$$
$$f_2 = \frac{1}{x_1}\left(1 + \sum_{i=2}^{n} x_i^2\right), \tag{2.1}$$

The number of design variables n is set to 7, and the design variables are bounded with $x_1 \in [0.5, 2]$ and $x_{i,\ i\neq 1} \in [-1, 1]$. The second test function is obtained by adding, to the first test function, normally distributed noise with zero mean and a standard deviation of 0.8. The third test function is identical to the first function except for generating outliers that replace the original solutions. With a probability of 1% per objective function, the objective value is divided by a factor of 10, hence producing an outlier with an improved value. The convergence of the extended, non-elitistic and standard SPEA algorithm is given for the three test functions in Figs. 2, 3 and 4. As a convergence measure, the mean distance P to of the present nondominated solutions to the analytical Pareto front is plotted over the number of function evaluations N. The comparison shows that the performance of the extended algorithm is equal to the standard algorithm if no noise occurs, but superior to the standard and non-elitistic algorithm if noise or outliers are involved.

2.2. *Atmospheric combustor test-rig*

Air entering a gas turbine flows through a compressor, then reacts with fuel in a combustion chamber, and is finally expanded in a turbine. The difference in power between the turbine output and the compressor input is the net power that can be used, say, to

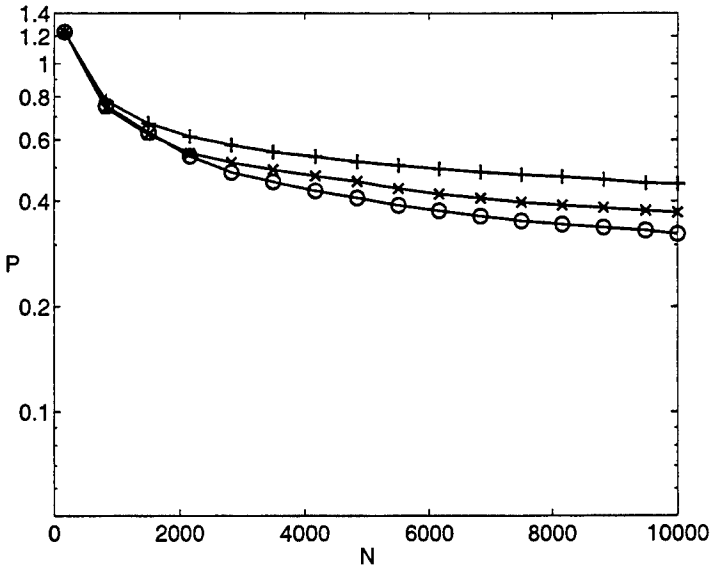

FIGURE 3. Convergence of the extended SPEA [circular symbol] on test function 2 with normal distributed noise, compared with the standard SPEA [cross symbol] and a non-elitist SPEA [plus symbol]. The mean distance P of the present nondominated solutions to the analytical Pareto front is plotted over the number of function evaluations N.

generate electricity. The combustion chambers of Alstom's larger gas turbines, e.g. GT24 and GT26, are annular around the turbine axis, with a set of burners aligned in the annulus. We consider the optimization of a single burner in an atmospheric test-rig as illustrated in Fig. 5. Preheated air enters through the plenum chamber and is mixed with fuel in the low-emission burner by swirl. The burner stabilizes the combustion flame in a predefined combustion area by a controlled vortex breakdown. The burned air leaves the test-rig through an exhaust. The burner exit temperature is about 1600 to $1700K$. The fuel is natural gas or oil and enters though injection holes, which are uniformly distributed along the burner. The fuel mass flows through the injection holes are the design variables of the setup. The mass-flow distribution is controlled by 8 continuous valves. Each valve controls the mass flow through a set of adjacent injection holes along the burner axis. In order to keep the operating conditions constant, the total fuel mass flow is fixed, reducing the number of free design variables for the optimization from 8 to 7. The NO_x emissions and the pulsation of the burner are the two objectives to be minimized.

2.3. *Optimization results*

An optimization run is performed using the extended SPEA algorithm and evaluating a total of 326 different burner settings. All solutions are plotted in Fig. 6. The initial solution is marked in the figure, and represents a setting with equal mass flow through all valves. The solutions found by the optimization process dominate the initial solution, i.e. are superior in both objectives. The occurrence of a wide Pareto front underlines the conflict in minimizing both objectives and just (Pareto) compromise solutions can be found.

In the figure, boxes mark five different areas along the Pareto front. For the solutions within the boxes, the valve settings are printed in Fig. 7. For better illustration, the

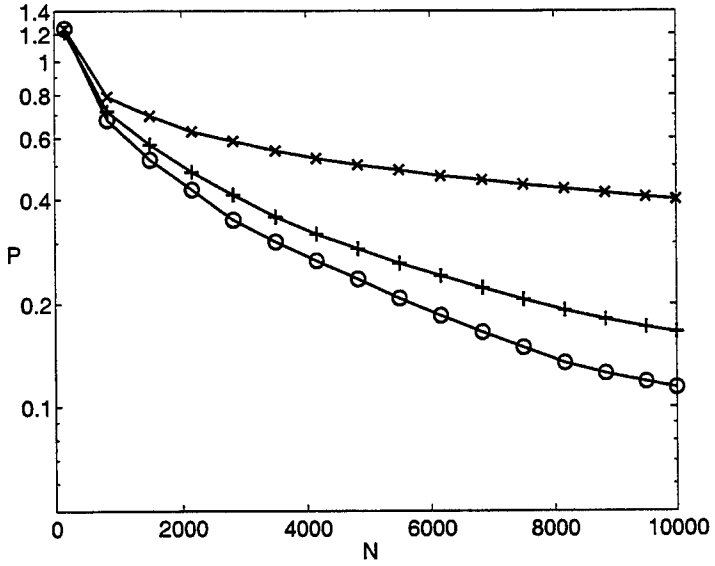

FIGURE 4. Convergence of the extended SPEA [circular symbol] on test function 3 with outliers, compared with the standard SPEA [cross symbol] and a non-elitistic SPEA [plus symbol]. The mean distance P of the present nondominated solutions to the analytical Pareto front is plotted over the number of function evaluations N.

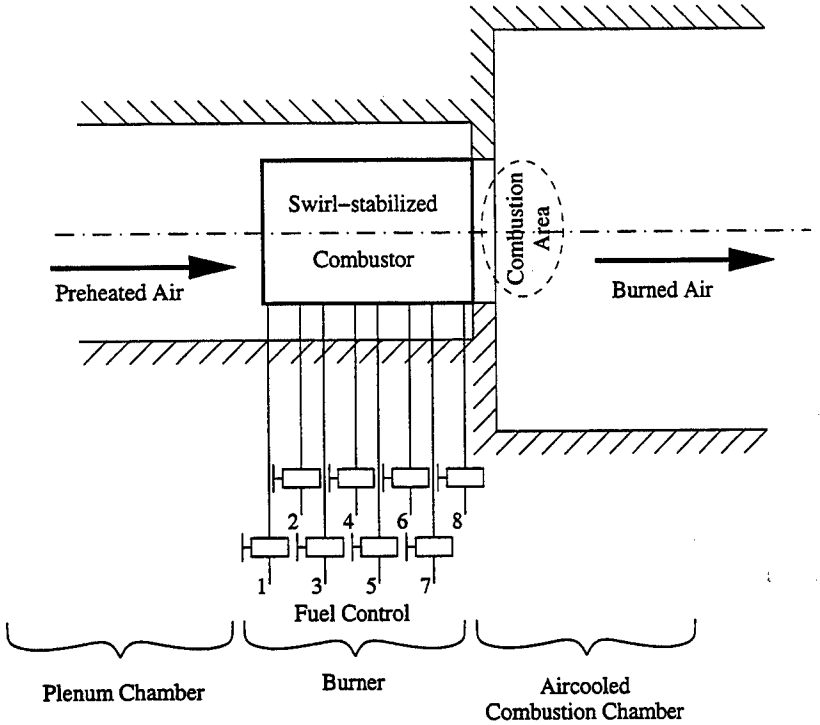

FIGURE 5. Sketch of the atmospheric combustion test rig with a low-emission swirl stabilized burner. The rates of fuel mass flow through the injection holes are the design variables of the setup. The NO_x emissions and the pulsation of the burner are the two objectives to be minimized.

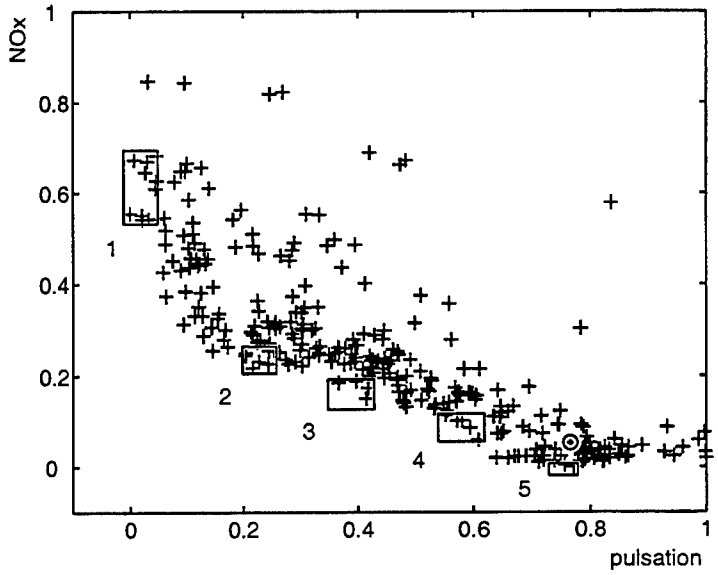

FIGURE 6. All measured solutions of the burner optimization run [plus symbol] and initial solution [circular symbol]. 5 boxes mark different areas along the Pareto front

settings are connected with a line.
Box 1 and 5 are at the extreme ends of the Pareto front. Box 1 represents Pareto solutions with high NO_x emissions, but low pulsation. The corresponding valve settings show an increased fuel mass flow at valves 1, 2 and 4, while the flow at valves 5 and 6 is reduced. (Refer to Fig. 5 for a sketch of the valve placement.) The basic physics behind these settings is that the increased mass flow through valves 1 and 2 leads to rich combustion in the center of the burner.

The rich combustion zone stabilizes the flame, but increases the NO_x emissions. The lean zones are in the middle of the burner, at valves 5 and 6.
Box 5 contains solutions with minimal NO_x emissions, but high pulsation. The mass flow through each valve is about the same, generating no rich combustion zones. Compared to the initial solution, the small mass flow increase at valves 5 and 8 leads to lower NO_x emissions, while the pulsation is unchanged.
This burner optimization follows a series of successful application of optimization tools in the field of turbomachinery design (Dornberger, Büche & Stoll 2000; Dornberger *et al.* 2000; Müller, Walther & Koumoutsakos 2001).

2.3.1. *Statistical analysis*

One of the interesting features of the resulting Pareto front is the almost linear change in valve settings along the front. At Box 1 five valves have either strongly increased or decreased mass flow and the amplitude is constantly decreasing from Box 1 to 5 until it reaches an almost equal mass flow for all valves in Box 5. This indicates simple dependencies of the valves on the objective functions. Fig. 8 contains a scatterplot for the valve settings and objective functions of all measured solutions. A scatterplot contains all possible 2D subspace plots for all design variables and objectives. The plot in column 9 and row 10 contains the objective space with the Pareto front. Most interesting are

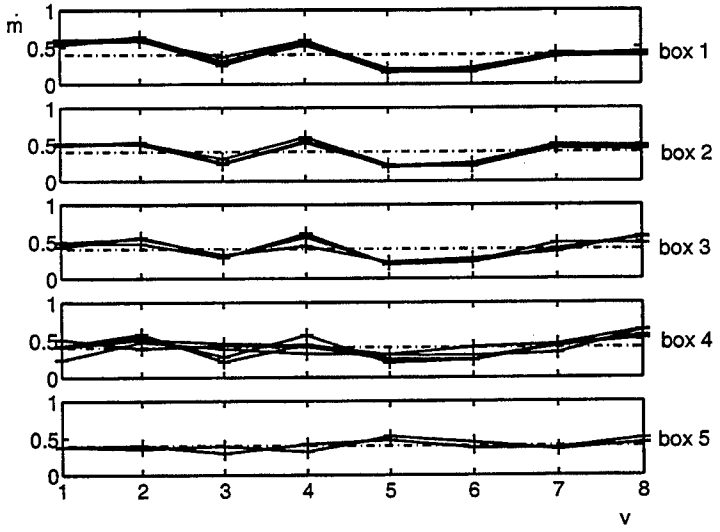

FIGURE 7. Mass flow $\dot{m}$ through the valves $V_{i,i=1...8}$ for solutions along the Pareto front, marked by 5 boxes of Fig. 6.

the last two rows, containing the correlation of the valves with the objective functions. For example, the horizontal and vertical axis of the plot in row 9, column 1 represent valve 1 and the NO_x emission, respectively. Strong correlation is expressed by narrow stripes at $\pm 45°$ to the axis. No correlation is implied by an axially symmetrical area of solutions. Strong correlation can be observed between valves 1, 2, 5, 6 and the two objective functions.
The correlation coefficients for the design variables and objectives are given in Fig. 9. They complement the results from the scatterplot. For all valves, the correlation coefficients have opposite signs for the two objectives. Therefore, changing the fuel injection in any of the valves always improves one objective while the other is worsened. Large coefficients indicate a strong correlation and occur between valves 1, 2, 5, 6 and the two objective functions. On increasing the mass flow through valve 1 and 2, the emissions increase while the pulsation decreases, and conversely for valves 5 and 6.
It has to be remembered that these observations hold for solutions obtained through an optimization process. The distribution of the solution in the scatterplot in Fig. 8 illustrates that they do not cover the whole design space. Hence, these solutions are not uniformly distributed in the design space and may not be representative.

2.3.2. *Noise analysis*

The extended SPEA algorithm that is used for burner optimization contains the special feature of re-evaluating solutions after their lifetime expires (Sec. 2.1.1). Among the 326 evaluated solutions, 40 were re-evaluated at least once by the optimizer. Comparing the difference in NO_x between a solution and the re-evaluated one, the maximal difference is about 8% of the objective range and the mean difference is 2%. For the pulsation, the maximal and mean differences are 13% and 4%, respectively. Thus the noise in the pulsation is more critical to the optimization. The large ratio of the maximal to the mean difference indicate the rare occurrence of outliers and the presence of noise in the objective measurement of all solutions.

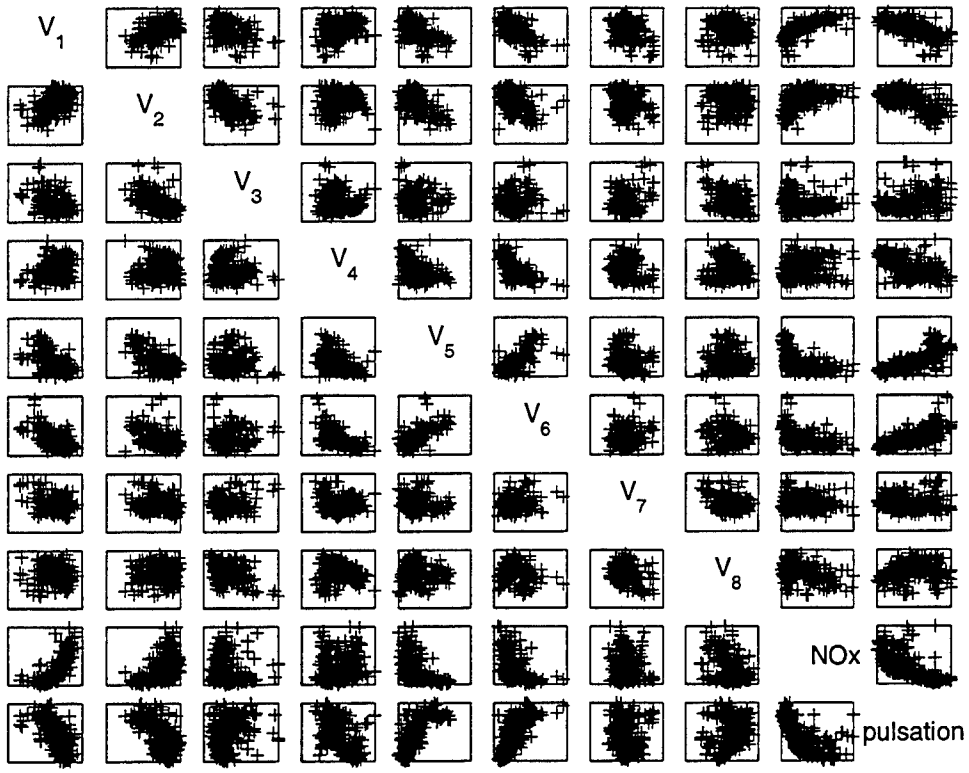

FIGURE 8. Scatterplot representing all possible combinations of 2D plots for the valves $V_{i,i=1...8}$ and the two objectives NO_x and pulsation.

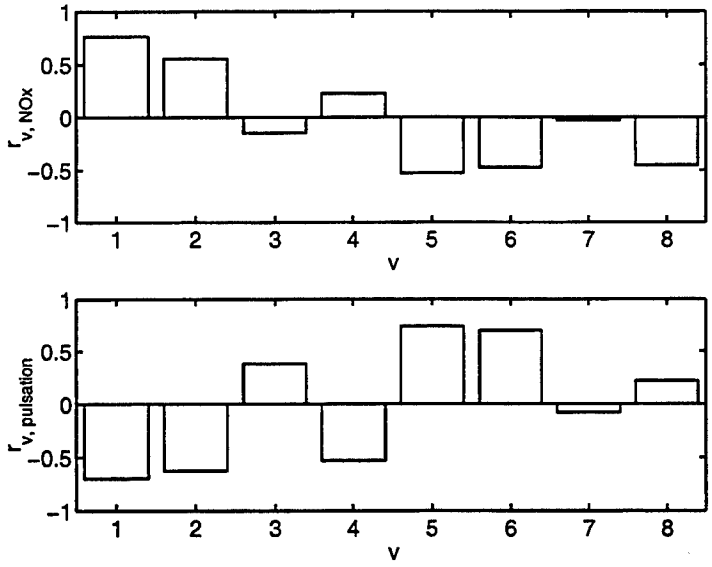

FIGURE 9. Correlation coefficient r between the mass flow through the 8 valves V and the two objectives NO_x and pulsation.

3. Conclusions

The present work demonstrates the capabilities of an automated optimization applied to the design process of gas turbine burners. The process, which includes an evolutionary algorithm, produces in an automated fashion an experimental Pareto front for minimizing pulsation and emissions of the burner. Automated optimization can be considered a supporting tool in a design process, complementing physical understanding as well as trial-and-error design. As a next step, the number of valves will be increased. This allows more flexibility in the fuel distribution and also allows non-axisymmetric distribution.

4. Acknowledgments

The results were obtained at the atmospheric test-rig of Alstom Power in Baden-Dättwil, Switzerland. For the realization of the experiments the authors wish to thank Bruno Schuermans. Special thanks to Rolf Dornberger and Christian Oliver Paschereit, whose initiatives led to this work.

REFERENCES

BÄCK, T., HOFFMEISTER, F. & SCHWEFEL, H.-P. 1991 A survey of evolution strategies. *Proc. 4th Int. Conf. on Genetic Algorithms and their Applications* (R. K. Belew, ed.), Morgan Kaufmann Publishers.

DEB, K. 1999 Multi-objective genetic algorithms: Problem difficulties and construction of test problems. *IEEE J. Evolutionary Comp.* **7**, 205-230.

DORNBERGER R., BÜCHE, D. & STOLL, P. 2000 Multidisciplinary optimization in turbomachinery design. *ECCOMAS 2000*, CMNM 102. Barcelona, Spain.

DORNBERGER R., STOLL P., BÜCHE D. & NEU, A. 2000 Multidisciplinary turbomachinery blade design optimization. *AIAA* paper 2000-0838.

GOLDBERG, D. E. 1989 *Genetic Algorithms in Search, Optimization, and Machine Learning*, Addison-Wesley.

HUGHES, E. J. 2001 Evolutionary multi-objective ranking with uncertainty and noise. *Proc. 1st Conf. on Evolutionary Multi-Criterion Optimization*, (E. Zitzler *et al.*, eds.), Zürich, Switzerland.

MÜLLER, S., WALTHER, J. & KOUMOUTSAKOS, P. 2001 Evolution strategies for film cooling optimization. *AIAA J.* **39**, 537-539.

TEICH, J. 2001 Pareto-front exploration with uncertain objectives. *Proc. 1st Conf. on Evolutionary Multi-Criterion Optimization*, (E. Zitzler *et al.*, eds.), Zürich, Switzerland.

ZITZLER, E. & THIELE, L. 1999 Multiobjective evolutionary algorithms: A comparative case study and the Strength Pareto Approach. *IEEE Trans. on Evolutionary Computation* **3**, 257-271.

Shape optimization for aerodynamic noise control

By Alison L. Marsden, Meng Wang AND Bijan Mohammadi †

1. Introduction

Noise generated by turbulent boundary layers near the trailing edge of lifting surfaces continues to pose a challenge for many applications. Much of the previous work on this topic has focused on development of accurate computational methods for the prediction of trailing edge noise. For instance, aeroacoustic calculations of the flow over an airfoil using large-eddy simulation (LES) and aeroacoustic theory have been presented in Wang & Moin (2000). These results compare favorably with the experiments of Blake (1975) and Blake and Gershfeld (1988). To make the simulations more cost-effective, Wang & Moin (2001) successfully employed wall models in the trailing-edge flow LES; this resulted in a drastic reduction in computational cost with minimal degradation of the flow solutions. In this study, we extend the earlier work to noise control, using shape optimization and control theory in conjunction with the simulation tools developed previously.

For trailing-edge noise control, a shape design method based on control theory for partial differential equations and a gradient-based minimization algorithm is employed to optimize the trailing-edge shape. The main difficulty in gradient-based optimization methods is the calculation of the gradient of the cost function with respect to the control parameters. The most widely-used method is to solve an adjoint equation in addition to the flow equations. While the adjoint method has been successful in many aerodynamic calculations, (e.g. Jameson *et al.* 1998; Pironneau 1984), it is expensive and not well suited to unsteady flow problems. In addition, the adjoint equation is dependent on the flow solver and thus is not portable. Because of these issues, we have employed the method of incomplete sensitivities for the gradient evaluation. This method, developed by Mohammadi & Pironneau (2001), offers the advantage that effects of geometric changes on the flow field can be neglected when computing the gradient of the cost function. This makes it far more cost effective than solving the full adjoint problem. In LES-based aeroacoustic shape design, the efficiency of the optimization routine is crucial. The use of incomplete gradients allows us to perform the optimization with only a small additional cost to the flow computation.

In order to validate and gain experience with the method of incomplete sensitivities, we have applied it to a model problem consisting of the two-dimensional unsteady laminar flow over an airfoil. This problem allows us to define the cost function based on aeroacoustic theory. In this article, we present results for the model problem which show a significant reduction in the cost function. We also discuss the addition of aerodynamic constraints. Section 2 outlines the problem formulation and the definition of the cost function. Sections 3 and 4 discuss the gradient evaluation and the optimization procedure. Results are presented in Section 5.

† University of Montpellier, France

2. Formulation and cost function definition

We begin by formulating the general optimization problem. Given a partial differential equation $A(\mathbf{U}, \mathbf{q}, \mathbf{a}) = 0$ defined in the domain Ω with control parameters $\mathbf{a}$, state variables $\mathbf{U}$ and geometric entities $\mathbf{q}$, we wish to minimize a given cost function $J(\mathbf{U}, \mathbf{q}, \mathbf{a})$. The control problem can be stated as

$$\min_{\mathbf{a}} \{J(\mathbf{U}, \mathbf{q}, \mathbf{a}) : A(\mathbf{U}, \mathbf{q}, \mathbf{a}) = 0 \ \forall x_i \in \Omega, \ \ b(\mathbf{U}, \mathbf{q}, \mathbf{a}) = 0 \ \forall x_i \in \partial\Omega\} \tag{2.1}$$

where $b(\mathbf{U}, \mathbf{q}, \mathbf{a})$ is the boundary condition of the PDE. The cost function can be reduced by finding its gradient with respect to the control parameters, and then moving the parameters in the direction of negative gradient. In our problem, the state equations are the Navier-Stokes equations and the cost function is related to the acoustic source.

We now outline the derivation of the cost function. For unsteady laminar flow past an airfoil at low Mach number, the acoustic wavelength associated with the vortex shedding is typically long relative to the airfoil chord. Noise generation from an acoustically-compact surface can be expressed as follows, using Curle's extension to the Lighthill theory (Curle 1955),

$$\rho \approx \frac{M^3}{4\pi} \frac{x_i}{|\mathbf{x}|^2} \dot{D}_i(t - M|\mathbf{x}|), \qquad \dot{D}_i = \frac{\partial}{\partial t} \int_S n_j p_{ij}(\mathbf{y}, t) d^2\mathbf{y} \tag{2.2}$$

where ρ is the dimensionless acoustic density at far field position $\mathbf{x}$, $p_{ij} = p\delta_{ij} - \tau_{ij}$ is the compressive stress tensor, n_j is the direction cosine of the outward normal to the airfoil surface S, M is the free stream Mach number, and $\mathbf{y}$ is the source field position vector. All the variables have been made dimensionless, with airfoil chord C as the length scale, free stream velocity U_∞ as velocity scale, and C/U_∞ as the time scale. The density and pressure are normalized by their ambient values. Note that Eq. (2.2) implies the three-dimensional form of Lighthill's theory, which is used here to compute the noise radiated from unit span of a two-dimensional airfoil. The radiation is of dipole type, caused by the the fluctuating lift and drag forces.

The mean acoustic intensity can be obtained from Eq. (2.2),

$$I = \frac{M^6}{16\pi^2|\mathbf{x}|^2} \overline{\left(\dot{D}_1 \cos\theta + \dot{D}_2 \sin\theta\right)^2} \tag{2.3}$$

where the overbar denotes time averaging, and $\theta = \tan^{-1}(x_2/x_1)$. To minimize the total radiated power, we need to minimize the integrated quantity

$$\int_0^{2\pi} I(r, \theta) r d\theta = \frac{M^6}{16\pi|\mathbf{x}|} \left(\overline{\dot{D}_1^{\,2}} + \overline{\dot{D}_2^{\,2}}\right). \tag{2.4}$$

Hence, the cost function is defined as

$$\overline{J} = \overline{\left(\frac{\partial}{\partial t} \int_S n_j p_{1j}(\mathbf{y}, t) d^2\mathbf{y}\right)^2} + \overline{\left(\frac{\partial}{\partial t} \int_S n_j p_{2j}(\mathbf{y}, t) d^2\mathbf{y}\right)^2} \tag{2.5}$$

which corresponds exactly to the acoustic source function.

3. Gradient evaluation

Given shape variables $\mathbf{q}$, flow field $\mathbf{U}$, and control parameters for the surface deformation $\mathbf{a}$, the cost function is $J(\mathbf{U}, \mathbf{q}, \mathbf{a})$. The complete expression for the gradient of the

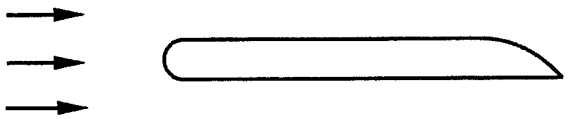

FIGURE 1. Model airfoil used in shape optimization. The upper right section is allowed to deform.

cost function is

$$\frac{dJ}{da_i} = \frac{\partial J}{\partial a_i} + \frac{\partial J}{\partial q_j}\frac{\partial q_j}{\partial a_i} + \frac{\partial J}{\partial U_k}\frac{\partial U_k}{\partial q_j}\frac{\partial q_j}{\partial a_i}. \tag{3.1}$$

Using the incomplete-sensitivities assumption of Mohammadi & Pironneau (2001), we neglect the effects of geometry changes on the flow field when computing the gradient of the cost function. This assumption is valid for the general class of problems in which the cost function can be defined in terms of a surface integral. We therefore neglect the third term in Eq. (3.1) and compute the gradient as follows

$$\frac{dJ}{da_i} \approx \frac{\partial J}{\partial a_i} + \frac{\partial J}{\partial q_j}\frac{\partial q_j}{\partial a_i}. \tag{3.2}$$

This technique has been successfully applied in a variety of applications (see for example Mohammadi *et al.* 2000, Mohammadi 1999). For the present problem, the cost function is based on the surface pressure (plus small viscous stresses). Since a_i causes surface perturbations in the normal direction, and since $dp/dn \approx 0$, the incomplete-sensitivity assumption is particularly justifiable.

4. Optimization procedure

In this Section, we outline the steps in the algorithm used to optimize the airfoil shape using the method of incomplete sensitivities. With the cost function J defined in Section 2, the steps in the algorithm are as follows. We first parameterize the surface deformation using a polynomial

$$\delta y = \sum_i a_i x^i, \tag{4.1}$$

where δy is the surface displacement in the normal direction at the tangential coordinate x, and a_i are the polynomial coefficients.

The gradient of the cost function with respect to the coefficients, dJ/da_i, is computed numerically. At each simulation time step, each coefficient is perturbed by a small amount ϵ and the resulting surface displacement δy is found. Based on incomplete sensitivities, the state is kept unchanged as we compute $J(a_i + \epsilon)$. We can then find the derivative using a finite difference

$$\frac{dJ}{da_i} = \frac{J(a_i + \epsilon) - J(a_i)}{\epsilon}. \tag{4.2}$$

The gradient is averaged in time to obtain $\overline{dJ/da_i}$ until it converges. The surface points on the airfoil are then displaced according to

$$\delta a_i = -\lambda\overline{\frac{dJ}{da_i}}, \quad \delta y = \sum_i (a_i + \delta a_i)x^i \tag{4.3}$$

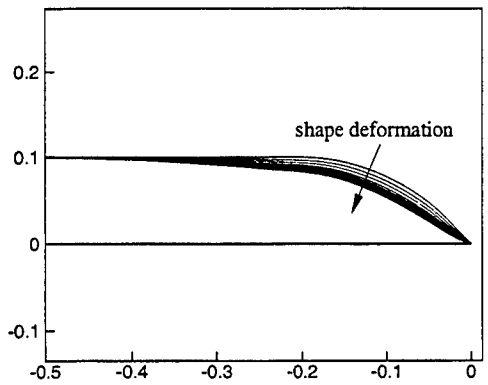

FIGURE 2. Convergence of shape for $Re = 2,000$.

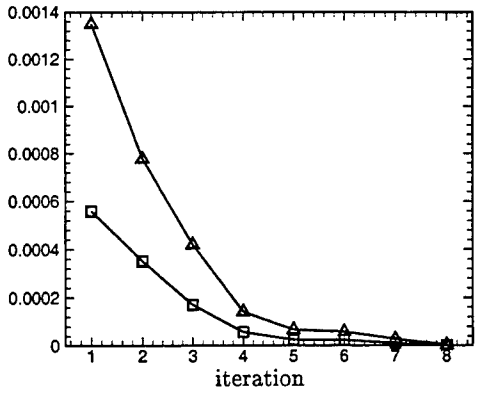

FIGURE 3. Convergence of cost function for $Re = 2,000$, □ mean value of J , △ maximum value of J.

where λ is a scaling parameter.

The new shape is found by deforming the surface according to $y = y_0 + \delta y$. At the completion of each iteration, a new mesh is generated and the flow simulation is performed again until the solution is statistically converged. Iteration continues until the airfoil converges to a final shape. The method of incomplete sensitivities offers large savings over other methods because the flow field is frozen in the gradient evaluation, so the cost of the method is only slightly higher than the cost of the flow solver.

5. Results and discussion

To validate the optimization methodology, a model problem of the two-dimensional unsteady laminar flow over a shortened Blake airfoil (Blake 1975), shown in Fig. 1, is considered. The initial trailing-edge tip angle is 45 degrees, and the right half of the upper surface is allowed to deform. Both end points are kept fixed and the slope of the upper surface must be continuous. The flow simulation is performed using the incompressible Navier-Stokes solver described in Wang & Moin (2000). For noise generation by large-scale vortex shedding at low Mach numbers, the airfoil is acoustically compact, and dipole radiation described by Eq. (2.2) prevails.

The efficacy of the optimization technique is demonstrated in the following two test cases, with chord Reynolds numbers of 2,000 and 10,000. Results from the lower Reynolds number case are shown in Figs. 2 through 5. The shape was changed in successive iterations as shown in Fig. 2, and the corresponding evolution of the mean and maximum values of the time-dependent cost function is depicted in Fig. 3. After eight iterations, the cost function is reduced to nearly zero. Fig. 4 shows the instantaneous streamwise velocity contours from the flow fields with the initial (upper figure) and final (lower figure) shapes. The final state exhibits a much more stable wake, where the flow in the vicinity of the trailing-edge is nearly parallel and steady. The lift and drag history for the low Re case are shown in Fig. 5. These plots show that the lift has increased and the drag has decreased. More importantly we see that the amplitude of oscillations in lift and drag have decreased, verifying that the unsteady dipole sources have been reduced.

For the higher Reynolds number case, the results are less dramatic, but still verify

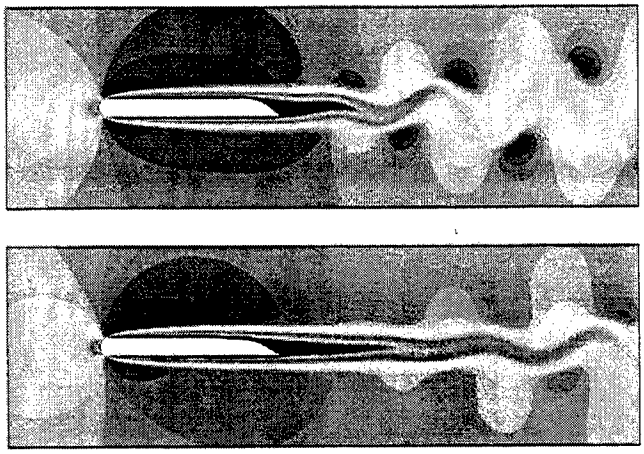

FIGURE 4. Instantaneous streamwise velocity contours for $Re = 2,000$. Upper: initial shape (contour levels from -0.06 to 1.22); Lower: final shape (contour levels from -0.05 to 1.23).

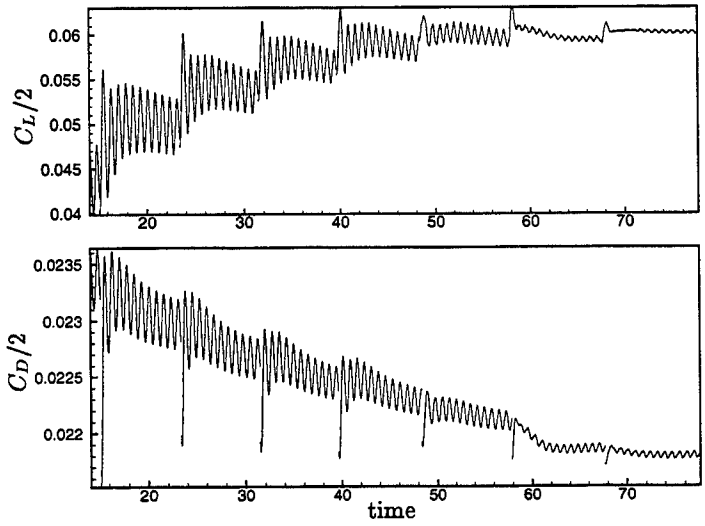

FIGURE 5. Time history of lift (upper figure) and drag (lower figure) coefficients for $Re = 2,000$.

that the method works to reduce the cost function. Figs. 6 and 7 show the convergence histories of the shape and the cost function, respectively. The maximum value of the cost function is decreased by approximately 32% at the final (8th) iteration. An examination of the instantaneous flow fields shows less significant change in vortex shedding patterns between the initial and final shapes, indicating that the flow is less sensitive to the trailing-edge shape at this higher Reynolds number. It is likely that by allowing a larger section of the surface to deform, a greater reduction in the cost function can be achieved.

In practical applications, it is often necessary to impose aerodynamic and geometric constraints, often in the form of additive penalty functions. For instance, we may wish to ensure that the lift does not decrease, and the drag does not increase, from their

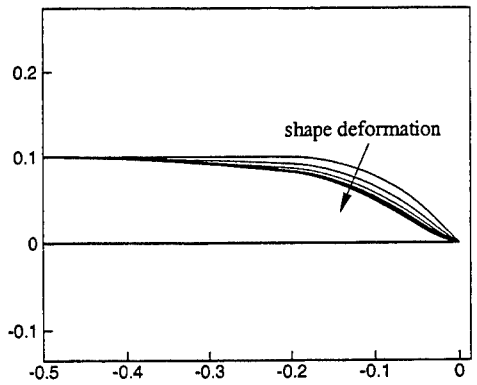

FIGURE 6. Convergence of shape for Re = 10,000.

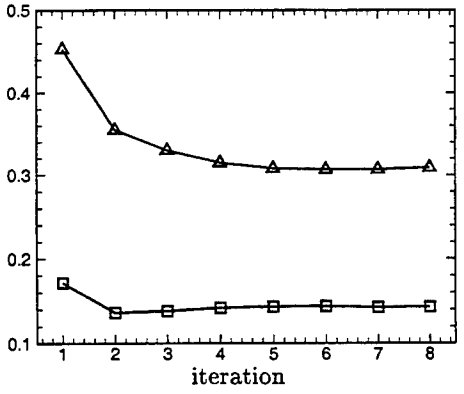

FIGURE 7. Convergence of cost function for Re = 10,000, □ mean value of J , △ maximum value of J.

initial values. For the two cases discussed above, as the cost function decreases, the wake becomes narrower, the lift increases and the drag decreases (Fig. 5), which is consistent with the desirable aerodynamic properties. However, for more complex cases, constraints may be essential to meeting engineering requirements.

In general, imposing a penalty function means redefining the cost function as follows

$$J = J_{\text{orig}} + \alpha C_1 + \beta C_2, \tag{5.1}$$

where α and β are weighting coefficients and C_1 and C_2 are constraints. For example, the lift and drag constraints could be

$$C_1 = \max\left(\frac{C_{L_o} - C_L}{C_{L_o}}, 0\right), \tag{5.2}$$

$$C_2 = \max\left(\frac{C_D - C_{D_o}}{C_{D_o}}, 0\right), \tag{5.3}$$

where C_{L_o} and C_{D_o} are the target lift and drag coefficients. Other constraints may be added for thickness, volume, etc.

6. Conclusions and future work

In summary, we have formulated and implemented a shape-optimization technique for reducing the aerodynamic noise from a lifting surface. The method is based on control theory, and uses the incomplete gradient of the cost function. The latter is directly related to the acoustic source functions. Results for the unsteady laminar model problem at two Reynolds numbers are very encouraging, and the method offers great cost savings over previous methods. We have demonstrated a rapid convergence of the shape and significant reduction in the noise generated by vortex shedding and wake instability.

In order to test the robustness of the method, we plan to allow more flexibility in surface deformation, and at the same time add constraints. By allowing both the upper and lower surfaces to deform, we hope to achieve a greater reduction in the cost function at higher Reynolds numbers. For this test case, it will be essential to add aerodynamic constraints such as those discussed in Section 5.

Once the method is fully validated, we plan to extend this technique to fully-turbulent trailing-edge flows past an acoustically noncompact airfoil. One major issue involved will be defining a surface-based cost function in order to use incomplete gradients. One possibility is the analysis of Howe (1999) who defines an equivalent surface source in terms of an "upwash velocity" on the surface. In contrast, the classical trailing-edge noise theory of Ffowcs Williams & Hall (1970) is based on a volume integral. Alternatively, a more crude surface approximation of the cost function can be used so long as it is well correlated with the true acoustic source function. The choice of cost function will be influenced to some degree by whether the objective is to reduce noise in a band of frequencies of primary interest, or to reduce the total radiated power.

REFERENCES

BLAKE, W. K. 1975 A statistical description of pressure and velocity fields at the trailing edge of a flat strut. *David Taylor Naval Ship Research and Development Center* Report 4241, Bethesda, Maryland.

BLAKE, W. K. & GERSHFELD, J. L. 1988 The aeroacoustics of trailing edges. *Frontiers in Experimental Fluid Mechanics*, (M. Gad-el-Hak, ed.), Springer-Verlag, 457-532.

CURLE, N. 1955 The influence of solid boundary upon aerodynamic sound. *Proc. Roy. Soc. Lond. A* **231**, 505-514.

FFOWCS WILLIAMS, J. E. & HALL, L. H. 1970 Aerodynamic sound generation by turbulent flow in the vicinity of a scattering half plane. *J. Fluid Mech.* **40**, 657-670.

HOWE, M. S. 1999 Trailing edge noise at low Mach numbers. *J. Sound Vib.* **255**, 211-238.

JAMESON, A., MARTINELLI, L. & PIERCE, N. A. 1998 Optimum aerodynamic design using the Navier-Stokes equations. *Theoret. Comp. Fluid Dynamics* **10**, 213-237.

MOHAMMADI, B. 1999 Dynamical approaches and incomplete gradients for shape optimization. *AIAA* Paper 99-3374.

MOHAMMADI, B., MOLHO, J. I. & SANTIAGO, J. G. 2000 Design of minimal dispersion fluidic channels in a CAD-free framework. *Proc. 2000 Summer Program*, Center for Turbulence Research, NASA Ames/Stanford Univ., 49-62.

MOHAMMADI, B. & PIRONNEAU, O. 2001 *Applied Shape Optimization for Fluids*, Oxford University Press.

PIRONNEAU, O. 1984 *Optimal Shape Design for Elliptic Systems*. Springer-Verlag, New York.

WANG, M. & MOIN, P. 2000 Computation of trailing-edge flow and noise using large-eddy simulation. *AIAA J.* **38**, 2201-2209.

WANG, M. & MOIN, P. 2001 Wall modeling in LES of trailing-edge flow. *Proc. 2nd Int. Sympo. on Turbulence and Shear Flow Phenomena*, Stockholm, Sweden, **II**, 165-170.

Incomplete sensitivities in design and control of fluidic channels

By B. Mohammadi, R. Bharadwaj, J. I. Molho AND J. G. Santiago

1. Motivation and objectives

Control of distributed systems has various industrial applications, as it is often desired to keep complex multi-disciplinary systems in some given state. Definition or parameterization of control space is the first main issue we face when formulating a control problem. Usually, one wishes to keep the parameterization space dimension as small as possible to limit the complexity of the problem. In addition, for any control approach to be effective, it should be realizable during the time the system is still controllable. Computational cost is therefore another critical issue. Our aim in this paper is to discuss alternative remedies for these two problems. We discuss the behavior of an electrokinetic microchannel system where the control variables include both the geometry of the microchannels and the temporal control of potentials. In a real system, the geometric control is achieved by the realization of etched microchannel structures using microlithography techniques. Flow control is accomplished by applying electric potentials along microchannels. We discuss the behavior of our design and control platform for two complementary classes of problems: the situation where the number of controls is small (a potential field) and where the number of controls is large (the geometry of a microchannel turn).

We use our sub-optimal control technique, using accurate gradient evaluation, for the first class of problems. For second class, we show that the sub-optimal control is also efficient using incomplete evaluation of the gradient, but only for a limited class of cost functions. Our motivation here comes from the fact that, for a control algorithm based on gradient methods to be efficient, the design should have the same complexity as the direct problem. We therefore need a cheap and easy gradient evaluation somehow avoiding the adjoint equation solution.

Since the problem involves electrostactics, electromigration, and fluid motion, we couple several differential state equations in the simulation. In that context, the gradient-based minimization algorithm is reformulated as a dynamic system, which is considered as an extra state equation for the parameterization. This formulation makes it easier to understand the coupling between different components of the simulation. We look for the solutions to our optimization problem as stationary solutions of a second order dynamic system. In addition, for the system to have global search features, we use the natural instability of second order hyperbolic systems (Attouch & Cominetti 1996).

2. Dynamic shape optimization and state control

Consider the following optimization or control problem:

$$\min_{x(t)} J(x(t), q(x), U(q), \nabla U(q)), \tag{2.1}$$

$$E(x(t), q(x), U(q), \nabla U(q)) = 0,$$

$$g_1(x(t)) \leq 0, g_2(q) \leq 0, g_3(q, U(q)) \leq 0,$$

where J is the cost function, $x \in R^n$ describes the parameterization, q describes geometrical entities (normals, surfaces, volumes,...), $U \in R^N$ denotes the state variables, $E \in R^N$ is the time dependent state equations, g_1 defines the constraints on the parameterization, g_2 those on geometrical quantities and g_3 defines the state constraints. Details of the definition of the control and design configurations are given by Mohammadi & Santiago (2001).

2.1. *State equations*

The problem of interest here concerns separation of charged species in an aqueous electrolyte solution by application of an electric field. The driving force for separation is the differences in electrophoretic mobilities (Probstein 1995).

The electric field $E = -\nabla\phi$ (V/m) is the solution of the following Poisson-Boltzmann equation for the potential ϕ:

$$\nabla.E = -\Delta\phi = \frac{1}{\epsilon_r\epsilon_0}\rho_e, \quad \text{in } \Omega \tag{2.2}$$

$$\phi(\Gamma_{in}) = v_1, \quad \phi(\Gamma_{out}) = v_2,$$

$$\phi = \phi_3 \quad \text{or} \quad \frac{\partial\phi}{\partial n} = 0 \quad \text{on other boundaries.}$$

where $\rho_e = \sum_{i=1}^{n} F z_i C_i$ is the net charge density (Coulomb/m^3), $z_i \in \mathbf{Z}$ is the valence number for the species i of molar concentration C_i (mol/m^3). F is the Faraday constant ($F = 96500$) and ϵ_r and ϵ_o are the permittivity constants (respectively the relative and free space permittivities). The dielectric constant $\epsilon_r\epsilon_0 \sim 10^{-9}$. It is important to notice that for most applications, the net charge density is nearly zero in the bulk.

The flow velocity is described by the Navier-Stokes equation with Lorentz forces:

$$\rho\frac{\partial U}{\partial t} - \mu\Delta U + \nabla p = \rho_e\nabla\phi, \quad \text{in the channel} \tag{2.3}$$

$$U = 0 \quad \text{on channel walls,}$$

$$-\mu\frac{\partial U}{\partial n} + p.n = 0 \quad \text{in and outflow boundaries.}$$

One difficulty in simulating electroosmotic flows is the computation of the velocity field in the electrical double layer(EDL). EDL refers to the interfacial region between the wall and the bulk solution, where ions having charge opposite to that of the channel wall, accumulate when the wall is brought into contact with the solution. The thickness of the EDL, at typical salt concentrations, is a few nanometers. Thus a very fine mesh near the channel surface is needed to describe the flow in the EDL. To avoid this computationally expensive step, the classical no-slip condition at the wall can be replaced by defining a shear plane near the wall. The velocity at the shear plane is given by the Smoluchowski equation:

$$U = \frac{-\epsilon_0\epsilon_r E\zeta}{\mu}, \tag{2.4}$$

where μ is the dynamical viscosity (Kg/(m s)), ρ the flow density (Kg/m^3), p the pressure (Pascal) and U the flow velocity (m/s).

$\zeta(C_i)$, called the zeta potential, is the potential at the slip plane. Zeta potential is a function of the surface charge density and the local species concentration.

The species are advected using the following advection-diffusion-reaction equations:

$$\frac{\partial C_i}{\partial t} = -\nabla . j_i, \tag{2.5}$$

where

$$j_i = -\nu_i z_i F C_i \nabla \phi - D_i \nabla C_i + C_i U + R_i(C), \tag{2.6}$$

where ν_i is the electrophoretic mobility, D_i is the diffusivity and R_i is the rate of reaction for species i.

An equation for the generation of charge density can be derived by summation over the species conservation equations:

$$\frac{\partial \rho_e}{\partial t} = -\nabla . i = 0, \tag{2.7}$$

where i is the current charge density:

$$i = F \sum_{i=1}^{n} z_i j_i,$$

where j_i is given by Eq. (2.6). In addition, we have $\sum_i R_i = 0$.

Away from the EDL, aqueous electrolyte solutions have negligible net charge density (i.e. $\rho_e = 0$). For such a case, the above equations yield a new equation for the potential ϕ instead of the Poisson-Boltzmann equation:

$$-F \nabla . ((\sum_{i=1}^{n} \nu_i z_i C_i) \nabla \phi) = \nabla . (\sum_{i=1}^{n} D_i z_i \nabla C_i). \tag{2.8}$$

This ensemble of governing equations is quite complex and it would be preferable not to use the above set of equations for sensitivity evaluation. This is the motivation behind using incomplete sensitivities presented below (Mohammadi & Pironneau 2001).

2.2. *Closure equation for $x(t)$*

In our approach, minimization algorithms are seen as closure equations for the parameterization. In other words, we introduce a new time-dependent problem for $x(t)$. This can also be seen as an equation for the structure. We can show that most linear or quadratic gradient-based minimization algorithms can be expressed in the following form:

$$-\dot{x} + \epsilon \ \ddot{x} = F(\Pi, M^{-1}, (\nabla_{xx} J)^{-1}, \nabla_x J), \tag{2.9}$$

where F is a function of the exact or incomplete gradient and of the inverse of the Hessian of the cost function. It also takes into account the projection over the admissible space Π and the smoothing operator we use when using the CAD-free parameterization (Mohammadi & Pironneau 2001). Usually, Π does not depend on p except when using mesh adaptation.

Let us consider the particular case of $\epsilon > 0$, where we recover the so called heavy ball method (Attouch & Cominetti 1996; Cabot 2001 and Mohammadi 1999b). The aim of this approach is to access different minima of the problem, and not only the nearest local minimum, by facilitating escape from the local minima by introduction of second-order perturbation terms. The difference with the original heavy-ball method is that here the method is seen as a perturbation of the first-order derivative while in the original method the steepest descent is seen as a perturbation of the hyperbolic second-order system.

This reformulation is suitable for numerical experiments as it enables us to tune the perturbation to be as small as possible. This is especially true for complex applications (e.g., with coupled physics), as the optimization process otherwise becomes difficult.

Another interesting feature of the dynamic minimization algorithm is a possible coupling between several balls (points in the admissible control space) to improve the global search ability by communicating information between balls on their respective state. The idea is therefore to solve the pseudo-unsteady system (Mohammadi 1999b) from different ball positions and to couple the paths using exchange of information about global gradients (Cabot 2001). Consider, q balls $x_j, j = 1, .., q$, following the motion prescribed by q pseudo-unsteady systems:

$$-\dot{x_j} + \epsilon \ \ddot{x_j} = -(F_j + G_j), \tag{2.10}$$

where F_j is as in Eq. (2.9) and G_j a global gradient representing the interaction between balls (recall that each ball is a design configuration). To reach the global minima, the number of balls has to be large enough. A good estimate for this number is given by the dimension of the design space (n). Even with this number the complexity is negligible compared to that of evolutionary algorithms. Our experience shows that the following choice of G_j is satisfactory(see example below):

$$(G_j)_i = \sum_{k=1, k\neq j}^{q} \frac{J_j - J_k}{||x_j - x_k||^2}(x_{j_i} - x_{k_i}), \quad \text{for} \quad j = 1, .., q, \quad i = 1, .., n. \tag{2.11}$$

However, in CAD-free parameterization, n can be quite large and, due to the required computational effort for one simulation, we cannot afford more than a few (say 3 or 4) shape evolutions at the same time. This approach can therefore be seen as an improvement over the search capacity of the original algorithm. In addition, the process is suitable for a distributed treatment as in evolutionary-type minimizations.

We show below the behavior of the pseudo-unsteady systems with two balls and constant λ and ϵ for the minimization of a function having several local minima (the global minimum is reached at (0,0)). For $(x, y) \in]-10, 10[\times]-10, 10[$ consider J defined by:

$$J(x, y) = 1 - \cos(x)\cos(\frac{y}{\sqrt{2}}) + \frac{1}{50}((x - y/2)^2 + 1.75y^2). \tag{2.12}$$

The aim is to show that the heavy-ball method improves a global-minimum search by facilitating escape from the local minima. However, finding the global minima requires several trials, but coupling several heavy balls can help in finding the global minima, even though individual balls may not converge to the global minima.

3. Sensitivities and incomplete sensitivities

Consider the following general simulation loop:

$$J(x) : x \rightarrow q(x) \rightarrow U(q(x)) \rightarrow J(x, q(x), U(q(x))).$$

The gradient of J with respect to x is:

$$\frac{dJ}{dx} = \frac{\partial J}{\partial x} + \frac{\partial J}{\partial q}\frac{\partial q}{\partial x} + \frac{\partial J}{\partial U}\frac{\partial U}{\partial q}\frac{\partial q}{\partial x}. \tag{3.1}$$

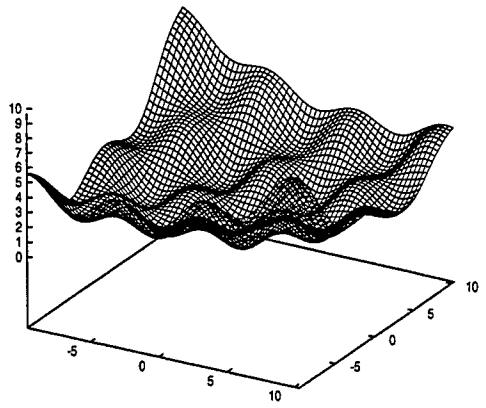

FIGURE 1. Graph of $J(x, y)$ given by 2.12.

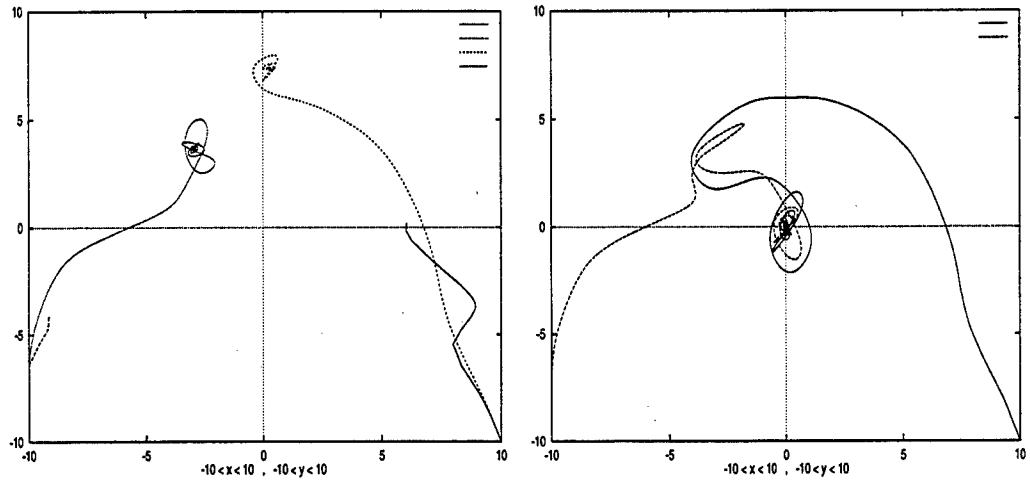

FIGURE 2. Left: Paths for the steepest-descent and heavy-ball methods starting from two different points. Right: By coupling the two balls in the heavy-ball method using the global gradient, the global minimum is reached.

If the following requirements hold, we can introduce incomplete evaluation of this gradient, reducing the computational cost:

- If both the cost function and control space are defined on the shape (or on some part of it),
- if J is of the form

$$J(x) = \int_{\text{shape}} f(x)g(u)d\gamma,$$

- and if the local curvature of the shape is not too large.

The incomplete-sensitivity approach means that we can drop the last term in Eq. (3.1). This does not mean, as seen below, that a precise evaluation of the state is unnecessary,

but that for a small change in the shape the state will remain almost unchanged, while geometrical quantities have variations of the same order as for the shape.

3.1. *Illustration of a few simple examples*

The argument behind incomplete sensitivities has already been successfully used in the so called classical equivalent-injection boundary conditions. These conditions are designed to study the effect of small deformations to the shape without actually analyzing deformations. Recall the implicit relation for the slip velocity on a fixed shape (subscript f) reproducing its displacement (subscript m). If we suppose that $u_m \sim u_f$, which means that the sensitivity with respect to the shape dominates, we have (Mohammadi 1999a):

$$u_f.n_f = -u_f(n_m - n_f) + V.n_m, \tag{3.2}$$

where V is the speed of the moving shape in the fixed frame attached to the fixed shape. In the same way, sensitivity analysis for the product $u.n$ with respect to the shape x gives:

$$\frac{d}{dx}(u.n) = \frac{\partial u}{\partial x}.n + u\frac{\partial n}{\partial x} \sim u\frac{\partial n}{\partial x}, \tag{3.3}$$

where as for the transpiration condition above we supposed that $\frac{\partial u}{\partial x} << \frac{\partial n}{\partial x}$. We see that the state has to be accurate, and that it is more important to have an exact state evaluation and an approximate gradient rather than a precise (in term of operators accounted in the linearization) gradient evaluation based on a wrong state. This point is critical as designers are penalized by the cost of sensitivity evaluations which frequently drives them to use coarser meshes in the optimization than the meshes they normally use for simulations without optimization.

Consider as cost function $J = au_x(a)$ and as state equation the following steady advection-diffusion equation:

$$\begin{aligned} &u_x - Pe^{-1}\ u_{xx} = 0, \\ &\text{on }]a,1[,\ \ u(a) = 0,\ \ u(1) = 1. \end{aligned} \tag{3.4}$$

The solution of this equation is:

$$u(x) = \frac{\exp(Pe^{-1}\ a) - \exp(Pe^{-1}\ x)}{\exp(Pe^{-1}\ a) - \exp(Pe^{-1})}. \tag{3.5}$$

We are looking for $J_a(a) = u_x(a) + a(u_x)_a(a)$. We are in the domain of applicability of the incomplete sensitivities, where the cost function involves products of state and geometrical quantities and is defined at the boundary:

$$J_a(a) = u_x\ (a)(1 + a\frac{Pe^{-1}\ \exp(Pe^{-1}\ a)}{\exp(Pe^{-1}\ a) - \exp(Pe^{-1})}). \tag{3.6}$$

The second term in the parenthesis is the state-linearization contribution which is negligible for large Peclet number. In all cases, the sign of the sensitivity is always correct.

The analysis also holds for nonlinear PDEs such as the Burgers equation. Indeed, consider as cost function $J(a) = au_x(a)$ and as state the steady solution of the Burgers equation

seen before, a being the left boundary location:

$$u_t + 0.5(u^2)_x = 0.3xu, \quad \text{on }]a,1[, \quad u(a) = 1, \quad u(1) = -0.8. \tag{3.7}$$

We have $J_a(a) = u_x(a) + a(u_x)_a(a)$. We are in the domain of applicability of incomplete sensitivities. In view of the Burgers equation, we have $u_x(a) = 0.3\,a$ and the exact gradient ($J_a(a) = 0.3a + 0.3a$) can be compared to the incomplete one ($0.3a$). We can see again that the sign of the gradient is correct (as is always the case) and there is only a factor of 2 between the exact and incomplete gradients.

Another example concerns the sensitivity analysis for the flow rate of a Poiseuille flow in a channel driven by a constant pressure gradient (p_x) with respect to the channel width. The walls are at $y = +/-a$. The flow velocity satisfies:

$$u_{yy} = \frac{p_x}{\nu}, \quad u(-a) = u(a) = 0. \tag{3.8}$$

The analytical solution satisfying the boundary conditions is: $u(a,y) = \frac{p_x}{2\nu}(y^2 - a^2)$.

The flow rate is given by $J(a) = \int_{-a}^{a} u(a,y)dy \quad (= \frac{-2p_x a^3}{3\nu})$. The gradient is given by (using the boundary conditions in Eq. (3.8)):

$$\frac{dJ}{da} = \int_{-a}^{a} \partial_a U(a,y)dy = \frac{-2a^2 p_x}{\nu}, \tag{3.9}$$

while the incomplete sensitivity vanishes. Indeed, in this example we are not in the (Mohammadi & Pironneau 2001) domain of applicability of sensitivity analysis because the cost fnction is not a product of the state and geometrical entities.

Now consider the following cost function obtained by multiplying the flow rate by a: $\tilde{J}(a,u) = \int_{-a}^{a} au(a,y)dy$, which has sensitivity given by:

$$\frac{d\tilde{J}}{da} = J + a\frac{dJ}{da} = \frac{-p_x a^3}{\nu}(\frac{2}{3} + 2), \tag{3.10}$$

and here the incomplete sensitivity is $\frac{-2p_x a^3}{3\nu}$. This quantity always has the right sign and is a good example of how to reduce the cost of sensitivity evaluation by an appropriate redefinition of cost function.

4. Reduced complexity models and incomplete sensitivities

As described earlier, we drop the sensitivity with respect to the state in incomplete sensitivities. One way to improve this approximation cheaply is to use reduced models to provide these sensitivities. In other words, consider the following reduced model for the definition of $\tilde{U} \sim U$:

$$x \to q(x) \to \tilde{U}(q(x))(\frac{U}{\tilde{U}}),$$

where $\tilde{U}$ is the solution of a reduced low-complexity model (wall functions, for instance). The last term is an identification term for the reduced model, to produce the same results as the full state equation.

The incomplete gradient of J with respect to x can be improved by adding the last

part from the exact gradient, but computed based on this model:

$$\frac{dJ}{dx} \sim \frac{\partial J(U)}{\partial x} + \frac{\partial J(U)}{\partial q}\frac{\partial q}{\partial x} + \frac{\partial J(U)}{\partial U}\frac{\partial \tilde{U}}{\partial q}\frac{\partial q}{\partial x}\frac{U}{\tilde{U}}. \tag{4.1}$$

We can see that $\tilde{U}$ is never used, only $\partial\tilde{U}/\partial q$. It is also important to notice that the reduced models need to be valid only over the support of the control parameters. We see below an example of such simplification.

5. Cost function and its redefinition

The original cost function we consider is designed to minimize the skew and band dispersion for the advected species and uses the fact that the iso-contours of an advected specie C need to remain normal to the flow velocity:

$$J(x) = \int_{\omega} (\nabla C \times U(\alpha))^2 dx. \tag{5.1}$$

We see that we are not in the admissibility domain of incomplete sensitivities becasue the cost function is defined over the whole channel.

To be suitable for incomplete sensitivities, we introduce the following approximate cost function, based on migration time along the walls of the channel to minimize the skew:

$$\begin{aligned} J(x) = (\int_{\Gamma_i} \frac{ds}{U.\vec{\tau}} - \int_{\Gamma_o} \frac{ds}{U.\vec{\tau}})^2 \; &+ (\textstyle\int_{\Gamma_i} \|\frac{\partial \vec{n}}{\partial s}\| - \int_{\Gamma_i^0} \|\frac{\partial \vec{n}}{\partial s}\|)^2 \\ &+ (\textstyle\int_{\Gamma_o} \|\frac{\partial \vec{n}}{\partial s}\| - \int_{\Gamma_o^0} \|\frac{\partial \vec{n}}{\partial s}\|)^2, \end{aligned} \tag{5.2}$$

where s is the curvilinear coordinate and $(\vec{\tau}, \vec{n})$ a local orthonormal basis. The last two terms have been introduced to control wall regularity. Indeed, we noticed that losing regularity increases band dispersion. We can see that the new cost function is much more complicated, but it is suitable for incomplete sensitivity reducing the cost of gradient calculation.

Finally, to reduce the dependency on the state, we express the velocity along the wall using Eq. (2.4). Hence, we rewrite the first term as:

$$(\int_{\Gamma_i} \frac{-\mu ds}{\epsilon_0 \epsilon_r \zeta(\vec{\tau}.\vec{E})} - \int_{\Gamma_o} \frac{-\mu ds}{\epsilon_0 \epsilon_r \zeta(\vec{\tau}.\vec{E})})^2, \tag{5.3}$$

where ζ dependence on the concentration field of species is neglected for sensitivity evaluation.

6. Application to microfluidic devices

The control and design problem we consider concerns a microfluidic electrophoretic separation device. In these devices a very narrow sample plug is electroosmotically extracted from the sample reservoir into the separation channel. Then an axial electric field is applied in the separation channel and the various ionic species in the sample plug separate according to their electrophoretic mobilities. The resolution, defined as the ratio of distance between two nearby sample peaks to the characteristic standard deviation, can be enhanced by increasing the separation channel length. However the total channel length is limited by the device area. Therefore, to maximize the channel length per unit

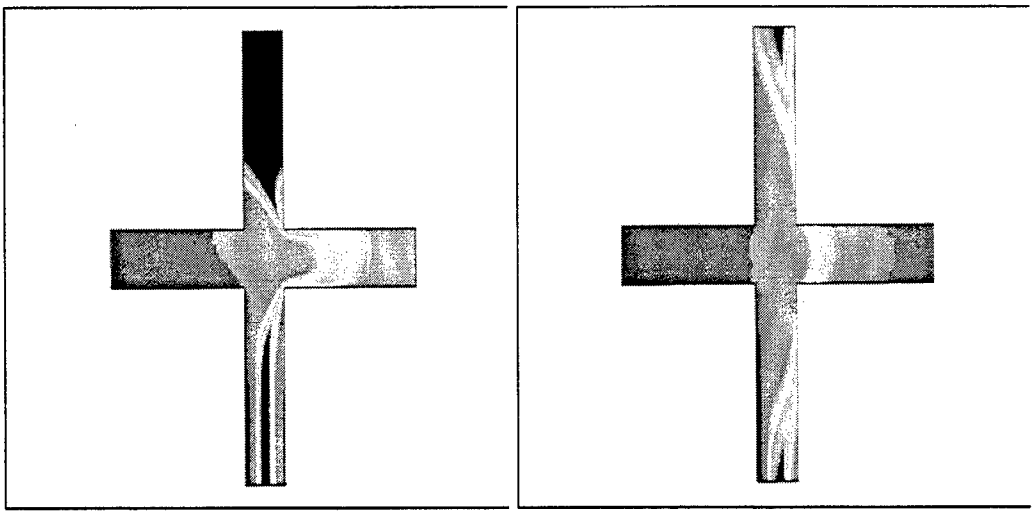

FIGURE 3. Extraction algorithm. Left: extracted band without control through the external field. Right: with control, the band dispersion has been reduced.

device area, 180 degree channel turns are incorporated. These turns permit more compact designs. However, these turns also cause sample plug dispersion, for two reasons. First, species near the inner curve travel a shorter distance and secondly, there is an electric field gradient normal to the channel, highest near the inner radius. Thus species near the inner radius travel faster than those near the outer radius. The total sample plug variance is governed by both the injected sample plug and dispersion induced by the turns. For high resolution separations it is essential to reduce and control the sample plug skew and dispersion (Probstein 1995; Culbertson *et al.* 1998 and Molho *et al.* 2001).

The problem of minimization of the dispersion of the initial extracted sample plug is solved by tuning the external electric field in a cross geometry. Once the plug is injected it is convected, and the aim is to design the optimum 180 turns to minimize the skew and dispersion. Indeed, the skew and dispersion are due only to changes in the curvature of the channel. The control parameterization is therefore based, for shape optimization, on a geometrical CAD-free model (Mohammadi 1997) and for the initial control problem on the externally applied electric field. Hence in the first case the size n of the control space is large, while it is small in the second case.

7. Concluding Remarks

The main ingredients of our minimal-complexity control and optimization platform are incomplete sensitivity evaluation and dynamic minimization algorithms. The minimal complexity has to be understood in the sense that design or control have the same cost as the solution of the direct problem. We have successfully applied these ideas to design and control microfluidic devices to reduce sample plug dispersion and skew. Current efforts concern the extension of the present approach to optimize sample stacking. Sample stacking is an extensively used technique in biochemical analysis for enhancing the concentration to detect trace-level sample constituents.

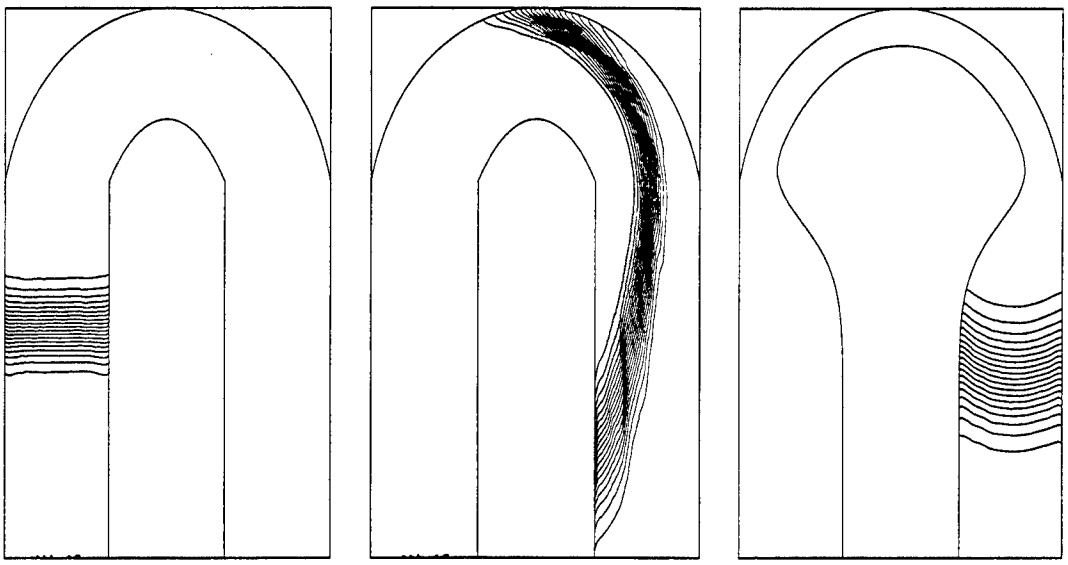

FIGURE 4. Design of 180 degree turns minimizing the band skew. Left: the original turn. Right: optimized. The initial band geometry is almost conserved enabling high resolution electrophoretic separations.

REFERENCES

ATTOUCH, H. & COMINETTI, R. 1996 A dynamical approach to convex minimization coupling approximation with the steepest descent method. *J. Diff. Equations* **128**, 519-540, 1996.

CABOT, A. 2001 Etude mathématiques de systèmes dynamiques pour minimisation globale. PhD Thesis, University of Montpellier.

CULBESTON, C. T., JACOBSON, S. C. & RAMSEY, J. 1998 Dispersion sources for compact geometries on microchips. *Analytical Chem.* **70**, 3781-3789.

MOHAMMADI, B. 1997 Practical applications to fluid flows of automatic differentiation for design problems. *Von Karman Institute* Lecture Series 1997-05.

MOHAMMADI, B. 1999a Flow control and shape optimization in aeroelastic configurations. *AIAA* paper 99-0182.

MOHAMMADI, B. 1999b Dynamical approaches and incomplete gradients for shape optimization and flow control. *AIAA* paper 99-3374.

MOHAMMADI, B. & PIRONNEAU, O. 2001 *Applied Shape Design for Fluids*, Oxford Univ. Press.

MOHAMMADI, B. & J. SANTIAGO, J. 2001 Simulation and design of extraction and separation fluidic devices. *M2AN* **35**, 513-523

MOLHO, J., HERR, A., SANTIAGO, J., KENNY, T. BRENNEN, R., GORDON, G., & MOHAMMADI, B. 2001 Optimization of turn geometries for on-chip electrophoresis. *Analytical Chem.* **73**, 1350-1360.

PROBSTEIN R.F. 1995 *Physicochemical Hydrodynamics*, Wiley.

Efficient Fast Multipole Method for low frequency scattering

By Eric Darve

1. Introduction

1.1. *Motivation*

The Fast Multipole Method (FMM) is a numerical method which has found wide acceptance in the scientific community. It is a fast summation method for potentials in $1/r$ and has applications in many areas such as Laplace and Poisson equations, particle simulations, molecular dynamics, etc. Another application of the FMM to Maxwell and Helmholtz equations (kernel in $\exp(\imath\kappa r)/r$) was initiated by Rokhlin (1990). However the derivation of the FMM for Maxwell/Helmholtz has two major drawbacks. First, the method fails when the size of the clusters becomes very small compared to the wavelength. This problem is known as sub-wavelength breakdown. The second limitation is the fact that numerically the approximation error of the method cannot be reduced beyond $\sim 10^{-4}$ relative error even when the number of poles is increased. This is due to numerical instabilities which, when coupled to roundoff errors, lead to a divergence of the method as the number of poles is increased beyond a certain threshold. In particular these two limitations mean that the FMM cannot be used for computations where the distribution of points is highly inhomogeneous (discretization of small details on the surface of the object for example) or when high accuracy is required (because of cavity resonances for example). We have developed a new variant of the FMM with complexity $n \log n$ which is based on plane wave expansions. This new formulation leads to a method which is stable at all frequencies (no sub-wavelength breakdown) and is arbitrarily accurate. This method is more efficient and mathematically simpler than previous methods, such as the ones described in Greengard (1998) or Hu, Chew and Michielssen (1999). It is also more efficient than the traditional FMM for Maxwell/Helmholtz at high frequencies, discussed by Darve (1999) and Engheta (1992). In this article we propose a review of the traditional multipole techniques for potentials in $\exp(\imath\kappa r)/r$ and describe our new technique based on plane wave expansions.

1.2. *Overview of the article*

We start with a general overview of the article where we present the main results and achievements.

We are interested in the application of the Fast Multipole Method (FMM) to Maxwell or Helmholtz equations. When these equations are solved using integral equations, the free-space Green's kernel is defined as:

$$K(\boldsymbol{x},\boldsymbol{y}) = \frac{\exp(\imath\kappa|\boldsymbol{x}-\boldsymbol{y}|)}{|\boldsymbol{x}-\boldsymbol{y}|}$$

This kernel can be approximated using the following expansion:

$$\frac{e^{\imath\kappa|x+y|}}{|x+y|} = \lim_{l\to+\infty} \int_{S^2} e^{\imath\kappa\langle\sigma,y\rangle}\, T_{l,\sigma}(x)\, d\sigma \tag{1.1}$$

where S^2 is the unit sphere. We denote by $|\bullet|$ the modulus and by $\langle\bullet,\bullet\rangle$ the scalar product. The function $T_{l,\sigma}(x)$ is defined by:

$$T_{l,\sigma}(x) = \imath\kappa \sum_{m=0}^{l} \frac{(2m+1)\imath^m}{4\pi} h_m^{(1)}(\kappa|x|) P_m(\cos(\sigma,x)) \tag{1.2}$$

where $h_m^{(1)}$ is a spherical Bessel function and P_m is a Legendre polynomial. This expansion has been widely used, in particular by Song *et al.* (1997), Epton & Dembart (1995) and Darve (1999), etc.

This expansion has a major disadvantage, which is the divergence of $h_m^{(1)}(\kappa|x|)$ for $m \to +\infty$ and for $|x| \to 0$: see Eq. (2.1). This leads to two kinds of numerical instabilities. First, when the size of the clusters becomes too small the transfer function $T_{l,\sigma}(x)$ starts diverging. This corresponds to a situation where we have a large number of points concentrated in a region of diameter D where $D \ll \lambda$, the wavelength. This is often called the sub-wavelength breakdown. Secondly, to reduce the error ϵ of the method we need to increase l. However when l becomes large compared to $\kappa|x|$, $T_{l,\sigma}(x)$ starts diverging. This means that because of strong numerical instabilities we are not able to reduce the error arbitrarily. For practical cases, the error ϵ is bounded below by approximately 10^{-4}.

Our new formulation of the FMM, the Plane Wave Fast Multipole Method (PW-FMM), is based on the following expansion:

$$\frac{e^{\imath\kappa|r|}}{|r|} = \frac{\imath\kappa}{2\pi} \int_{S^{z+}} e^{\imath\kappa\langle\sigma,r\rangle}\, d\sigma + \frac{1}{\pi} \int_{\chi=0}^{+\infty} \int_{\phi=0}^{2\pi} e^{-\chi^2 z}\, e^{\imath\sqrt{\chi^4+\kappa^2}(x\cos\phi+y\sin\phi)}\, \chi\, d\chi\, d\phi \tag{1.3}$$

with $r = (x,y,z)$ and S^{z+} is the upper hemisphere (subset of the unit sphere of all points with positive z-coordinate). See Eq. (3.1). These two terms have very simple values in the case $x = y = 0$, $z > 0$:

$$\frac{\imath\kappa}{2\pi} \int_{S^{z+}} e^{\imath\kappa\langle\sigma,r\rangle}\, d\sigma = \imath\kappa \int_0^1 e^{\imath\kappa z\zeta}\, d\zeta = \frac{1}{z}(e^{\imath\kappa z} - 1)$$

$$\frac{1}{\pi} \int_{\chi=0}^{+\infty} \int_{\phi=0}^{2\pi} e^{-\chi^2 z}\, e^{\imath\sqrt{\chi^4+\kappa^2}(x\cos\phi+y\sin\phi)}\, \chi\, d\chi\, d\phi = \int_0^{+\infty} e^{-\nu z}\, d\nu = \frac{1}{z}$$

Their sum is equal to $\frac{e^{\imath\kappa z}}{z}$, as expected. The integrand for the first integral is a smooth and oscillating function while the second integral contains the singularity for $|x| \to 0$.

The new formula is formally similar to Eq. (1.1). However it has the considerable advantage of involving only functions which are well-behaved. Instead of one transfer function as before (see Eq. (1.2)), we have two transfer functions defined as:

$$T_\sigma(r) = \frac{\imath\kappa}{2\pi}\, e^{\imath\kappa\langle\sigma,r\rangle}\, \mathbf{1}_{S^{z+}}(\sigma)$$

$$T^e_{\chi,\phi}(r) = \frac{1}{\pi}\, \chi\, e^{-\chi^2 z}\, e^{\imath\sqrt{\chi^4+\kappa^2}(x\cos\phi+y\sin\phi)}\, \mathbf{1}_{[0;+\infty]}(\chi)$$

where $\mathbf{1}_{S^{z+}}$ is the characteristic function of the set S^{z+}, i.e.

$$\mathbf{1}_{S^{z+}}(\sigma) = \begin{cases} 1 & \text{if } \sigma \in S^{z+} \\ 0 & \text{if } \sigma \notin S^{z+} \end{cases}$$

and $\mathbf{1}_{[0:+\infty]}(\chi)$ is the characteristic function of the set $[0:+\infty]$ for χ.

This plane-wave expansion has been used previously by L. Greengard *et al.* (1998). However their method is different from ours. In particular, it requires transformation operators to go from a traditional multipole expansion to a plane-wave expansion and vice-versa. In the opinion of the author, our new derivation is more consistent and conceptually simpler as we use only one kind of expansion, the plane-wave expansion. The FMM described in Greengard *et al.* involves steps with complexity p^3 where p^2 is the number of terms in the multipole expansion for a given cluster. In contrast, all operations for PW-FMM have complexity p^2.

The PW-FMM can also be used for $1/|r|$ by setting $\kappa = 0$ in Eq. (1.3). This leads to the following expansion:

$$\frac{1}{|r|} = \frac{1}{\pi} \int_{\chi=0}^{+\infty} \int_{\phi=0}^{2\pi} e^{-\chi^2 z}\, e^{i\chi^2(x\cos\phi + y\sin\phi)}\, \chi\, d\chi\, d\phi \tag{1.4}$$

The techniques presented in this article can thus be readily applied to $1/|r|$ (Laplace equation, particle simulations, etc.).

We start this article by pointing out the limitations of the FMM for Maxwell and Helmholtz equations, in particular the fact that it is unstable at low frequency (Section 2). Then we describe our new technique, PW-FMM (Section 3), starting with the first term in the expansion (1.3) (Section 3.1) and ending with a description of the second term (Section 3.2).

2. Fast Multipole Method for electrodynamics scattering problems

To justify the need for a new method we start by describing the limitations of the traditional FMM for Maxwell/Helmholtz or high frequency FMM (HF-FMM) as we will call it from now on. The reasons for this name will become apparent in the next section.

2.1. *Numerical instabilities*

The HF-FMM has been successfully used in many large scale applications, for example by Song *et al.* (1997), Chew *et al.* (1997), Song *et al.* 1998, Darve (1999) and Darve (2000). Figures 1 and 2 illustrate some of the computations done by Darve using the FMM for radar scattering problems.

However there are two cases for which large numerical instabilities limit the usefulness of the FMM. Let us consider the transfer function defined by Eq. (1.2). The asymptotic behavior of $h_m^{(1)}(x)$ is

$$|h_m^{(1)}(x)| \sim \begin{cases} \sqrt{\dfrac{2}{e}} \left(\dfrac{2m+1}{e}\right)^m \dfrac{1}{|x|^{m+1}} & \text{for } m \to +\infty \\ \dfrac{1\cdot 3\cdot 5 \ldots (2m-1)}{|x|^{m+1}} & \text{for } x \to 0 \end{cases} \tag{2.1}$$

The numerical instabilities are caused by the divergence of $h_m^{(1)}(x)$ when $m \to +\infty$ or $x \to 0$.

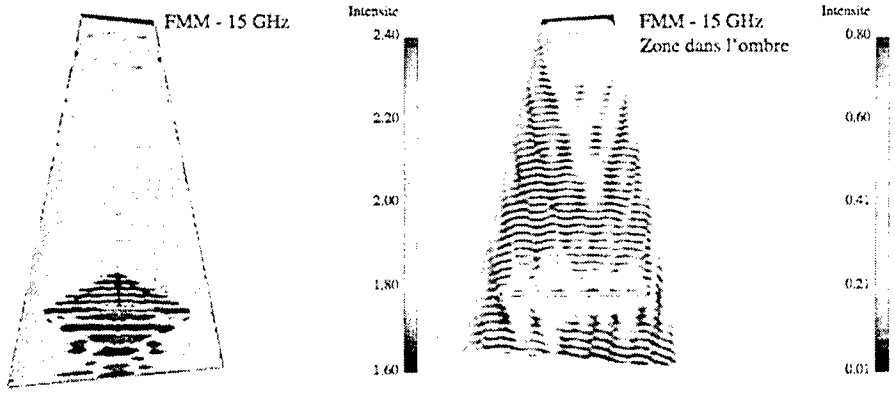

FIGURE 1. Example of an electromagnetics computation using the FMM. The code CEM3D was developed by E. Darve while at Paris 6 University. The geometry of the object was provided by Aerospatiale.

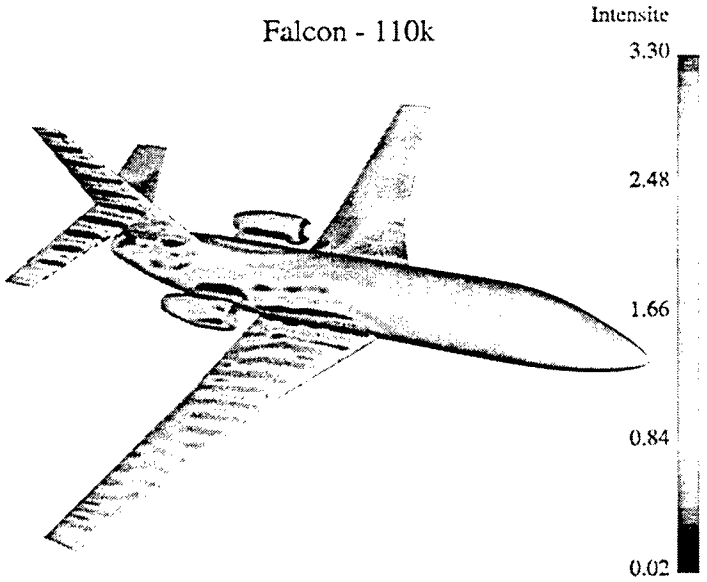

FIGURE 2. Example of an electromagnetics computation using the FMM. The code CEM3D was developed by E. Darve while at Paris 6 University. The geometry of the airplane was provided by Dassault-Aviation.

In the FMM for electromagnetic scattering, the size of the smallest clusters is chosen so that the number of floating-point operations is of order $n \log n$. This is done by optimizing with respect to the computational expense of the far away interactions (approximated using the HF-FMM) and of the close interactions (exact evaluation). In particular, if the density of the points on the surface of the scattering object is increased, optimal complexity is achieved by reducing the size of the smallest clusters. If z_1 and z_2 are the centers of two clusters, $|z_1 - z_2|$ is proportional to the size of the clusters. Numerical instabilities appear when $\kappa|z_1 - z_2|$ becomes too small. Once $\kappa|z_1 - z_2| \ll m$, the function $h_m^{(1)}(\kappa|z_1 - z_2|)$ diverges (see Eq. (2.1)). This means that the transfer function $T_{l,z}(\sigma)$

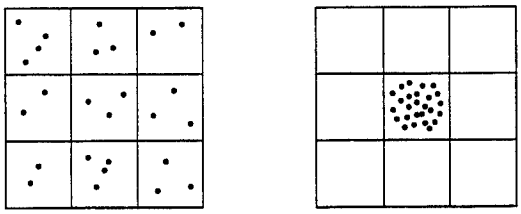

FIGURE 3. In the case of low-frequency scattering, the asymptotic complexity of the FMM is no longer of order $n \log n$. Suppose that ρ is the largest size of a cluster below which the computation is unstable. When the diameter of the object is smaller than ρ, the FMM consists of a single cluster containing all the points. All interactions have to be computed in a direct manner, without the use of the FMM. Then the complexity is on the order of n^2 rather than $n \log n$.

diverges once $\kappa|z_1 - z_2| \ll l$. When implemented on a computer, this divergence causes large numerical instabilities because of roundoff errors.

The maximum density of points is large for very inhomogeneous distributions of points, or for low-frequency scattering when the diameter of the scattering object is very small compared to the wavelength (see Fig. 3). In these two cases, the numerical instabilities are so large that the FMM can no longer be used. Note that this behavior is very different from the behavior of the FMM for $1/r$ for which there is no such limitation.

The purpose of our new method is to remove this limitation on the size of the clusters. This guarantees a complexity in $n \log n$ for any distribution of points even if this distribution is very inhomogeneous.

Numerical instabilities can also appear when the error ϵ is smaller than some threshold. We know that ϵ for HF-FMM is, among other things, a function of l. More precisely a smaller ϵ requires a larger l. Considering Eq. (2.1), we see that $h_m^{(1)}(\kappa|z_1 - z_2|)$ starts to diverge if m becomes larger than $\kappa|z_1 - z_2|$. Thus if we decrease the tolerance criterion ϵ in HF-FMM below a certain threshold, the function $T_{l,z}(\sigma)$ diverges and again roundoff errors lead to numerical instabilities.

As a conclusion, even though the algorithm is well-behaved analytically, strong numerical instabilities prevent the use of HF-FMM for low frequency applications and high accuracy computations.

2.2. *Comparison with other variants of the FMM*

Numerous authors, such as Greengard *et al.* (1998), Hu *et al.* (1999) and Hu & Chew (1999), have devised algorithms to tackle this problem. However these algorithms are not entirely satisfactory. The low-frequency Fast Multipole Method (LF-FMM) of Greengard and Rokhlin (1987) is a very complex scheme and requires complex transformations from multipole expansions to plane wave expansions and vice-versa. The Fast Inhomogeneous Plane Wave Expansion method of Hu *et al.* (1999) has the disadvantage of lacking a clear mathematical foundation, and several theoretical issues have not been satisfactorily settled. In particular, error and rates of convergence have not been well estimated so far.

We propose a new method, called Plane Wave Fast Multipole Method (PW-FMM) which is based on plane wave expansions. It is related to Rokhlin-Greengard's and Hu-Chew's techniques. However, it has the advantage of being simpler and more efficient and precise error estimations can be derived.

Unlike HF-FMM, PW-FMM is stable at all frequencies and any accuracy can be achieved with this method. Moreover we will show that for high-frequency applications the number of floating-point operations is less in PW-FMM.

3. Plane Wave Fast Multipole Method

Vectors are denoted using bold face, e.g. $\boldsymbol{v}$. Integers are denoted using Latin letters, e.g. n, while real numbers are denoted using Greek letters, e.g. λ.

The PW-FMM is based on the following expansion:

$$\frac{e^{\imath\kappa|\boldsymbol{r}|}}{|\boldsymbol{r}|} = \frac{\imath\kappa}{2\pi}\int_{S^{z+}} e^{\imath\kappa\langle\boldsymbol{\sigma},\boldsymbol{r}\rangle}\,d\boldsymbol{\sigma} + \frac{1}{\pi}\int_{\chi=0}^{+\infty}\int_{\phi=0}^{2\pi} e^{-\chi^2 z}\, e^{\imath\sqrt{\chi^4+\kappa^2}(x\cos\phi+y\sin\phi)}\,\chi\,d\chi\,d\phi \quad (3.1)$$

where $\boldsymbol{r} = (x, y, z)$. The set S^{z+} is the subset of S^2 of all the points with positive z-coordinate:

$$S^{z+} = \{\boldsymbol{\sigma} = (x, y, z),\ |\boldsymbol{\sigma}| = 1, z > 0\}$$

The variable χ has dimension of the square root of a frequency. It can be readily seen that Eq. (3.1) is a good candidate for a fast multipole method. Indeed if discretization points $\boldsymbol{\sigma}_q$ and $\boldsymbol{\sigma}_q^e$ and weights ω_q and ω_q^e are chosen, Eq. (3.1) can be written in the following manner:

$$\begin{aligned}\frac{e^{\imath\kappa|\boldsymbol{x}_i-\boldsymbol{x}_j|}}{|\boldsymbol{x}_i-\boldsymbol{x}_j|} \sim &\sum_q \omega_q\, T_{\sigma_q}(\boldsymbol{z}_1-\boldsymbol{z}_2)\, f_{\sigma_q}(\boldsymbol{x}_i-\boldsymbol{z}_1) f_{\sigma_q}(\boldsymbol{z}_2-\boldsymbol{x}_j)\\ &+\sum_q \omega_q^e\, T^e_{\sigma_q^e}(\boldsymbol{z}_1-\boldsymbol{z}_2)\, f^e_{\sigma_q^e}(\boldsymbol{x}_i-\boldsymbol{z}_1) f^e_{\sigma_q^e}(\boldsymbol{z}_2-\boldsymbol{x}_j)\end{aligned}$$

with

$$\begin{aligned}\boldsymbol{\sigma}_q &= (\sin\theta_q\cos\phi_q, \sin\theta_q\sin\phi_q, \cos\theta_q)\\ T_\sigma(\boldsymbol{z}) &= \exp(\imath\kappa\langle\boldsymbol{\sigma},\boldsymbol{z}\rangle)\\ f_\sigma(\boldsymbol{x}) &= T_\sigma(\boldsymbol{x})\end{aligned}$$

and

$$\begin{aligned}\boldsymbol{\sigma}_q^e &= (\chi_q, \phi_q)\\ T^e_\sigma(\boldsymbol{z}) &= \chi\ \exp(-\chi^2 \boldsymbol{z}_z)\ \exp(\imath\sqrt{\chi^4+\kappa^2}(\boldsymbol{z}_x\cos\phi + \boldsymbol{z}_y\sin\phi))\\ f^e_\sigma(\boldsymbol{x}) &= \exp(-\chi^2\boldsymbol{x}_z)\ \exp(\imath\sqrt{\chi^4+\kappa^2}(\boldsymbol{x}_x\cos\phi + \boldsymbol{x}_y\sin\phi))\end{aligned}$$

Bold face is used for 3D points while an index in normal face x, y, or z designate the x, y, or z coordinate of a point. The new basis functions for PW-FMM can be used in exactly the same manner as for HF-FMM. We now describe in more detail the behavior of the basis functions in Fourier space, and more specifically the fact that they are band-limited in Fourier space.

We define:

- Propagating term : $\int_{S^{z+}} e^{\imath\kappa\langle\boldsymbol{\sigma},\boldsymbol{x}\rangle}\,d\boldsymbol{\sigma}$.
- Evanescent term : $1/\pi\int_{\chi=0}^{+\infty}\int_{\phi=0}^{2\pi} e^{-\chi^2\boldsymbol{x}_z}\, e^{\imath\sqrt{\chi^4+\kappa^2}(\boldsymbol{x}_x\cos\phi+\boldsymbol{x}_y\sin\phi)}\,\chi\,d\chi\,d\phi$.

3.1. *Propagating term*

The propagating term is the simplest of the two terms. It is almost identical to the basis function for HF-FMM. However there is a significant fact which must be recognized.

In the Multipole to Multipole step of the FMM we proceed as usual. The functions

f_{C_k} are computed as:

$$f_{C_k}(\sigma_q) = \sum_{x_i \in C_k} u_i \, e^{\imath\kappa\langle \sigma_q, x_i - z_k\rangle} \tag{3.2}$$

Then, in the Multipole to Local step, the functions g_{C_k} are computed as:

$$g_{C_k}(\sigma_q) = \sum_r e^{\imath\kappa\langle \sigma_q, z_k - z_r\rangle} \, f_{C_r}(\sigma_q)$$

However at this point some care must be taken. One may think that the usual interpolation can be performed for Local to Local transformations. However, the final integration is over S^{z+} only, so that the integration is actually:

$$\int_{S^{z+}} e^{\imath\kappa\langle \sigma, z_r - x_j\rangle} g_{C_k}(\sigma)\, d\sigma = \int_{S^2} \left\{ e^{\imath\kappa\langle \sigma, z_r - x_j\rangle} \mathbf{1}_{S^{z+}}(\sigma) \right\} g_{C_k}(\sigma)\, d\sigma$$

An efficient implementation of the FMM requires that we can efficiently Fourier-transform band-limited functions, and these transforms are defined on S^2 rather than S^{z+}. The function $e^{\imath\kappa\langle \sigma, z_r - x_j\rangle}\mathbf{1}_{S^{z+}}(\sigma)$ has a very slowly decaying Fourier spectrum because of the discontinuity. As a consequence, the number of sample points on S^2 will be very large. This approach does not lead to an $n \log n$ method and therefore is not good.

The solution consists in moving the characteristic function to the transfer function. We define the transfer function as

$$T_\sigma(z_k - z_r) = \mathbf{1}_{S^{z+}}(\sigma) \, e^{\imath\kappa\langle \sigma, z_k - z_r\rangle}$$

Now the functions g_{C_k} are defined as:

$$g_{C_k}(\sigma) = \sum_r \mathbf{1}_{S^{z+}}(\sigma) \, e^{\imath\kappa\langle \sigma, z_k - z_r\rangle} \, f_{C_r}(\sigma)$$

and the final integration is:

$$\int_{S^2} e^{\imath\kappa\langle \sigma, z_r - x_j\rangle} \, g_{C_k}(\sigma)\, d\sigma$$

In Darve (1999), it is shown that $e^{\imath\kappa\langle \sigma, z_r - x_j\rangle}$ has a bandwidth on the order of $\kappa|z_r - x_j|$. The functions $f_{C_r}(\sigma_q)$ have a bandwidth of the same order, more precisely $\kappa \max|x_i - z_k|$ (see Eq. (3.2)). Thus we can retain only the first $\kappa(|z_r - x_j| + \max|x_i - z_k|)$ frequencies in $T_\sigma(z_k - z_r)$. If we denote by ρ the length of the side of the cubic clusters, then

$$\kappa|z_r - x_j| \le \kappa\rho \qquad \kappa \max|x_i - z_k| \le \kappa\rho$$

Thus we need on the order of $2\kappa\rho$ frequencies for $T_\sigma(z_k - z_r)$. To obtain the most efficient form of the FMM it is crucial always to retain the minimal number of frequencies, as this will affect the number of sample points required on the unit sphere.

Numerical tests of accuracy must be made to find the precise relation between the tolerance criterion ϵ and the exact number of frequencies that need to be retained. T is constructed in the following manner:

PROCEDURE 1 (CONSTRUCTION OF T). *We describe the construction of T for the propagating term when a transfer is to be performed in the direction $+z$. First we need to find the minimum number of frequencies l needed for $T_\sigma(z_k - z_r)$ for a given accuracy ϵ. This number is on the order of $2\kappa\rho$ where ρ is the size of a cluster. Then we Fourier-*

transform

$$\mathbf{1}_{S^{z+}}(\sigma)\, e^{i\kappa\langle\sigma, z_k - z_r\rangle},$$

retain only the first l frequencies and inverse-Fourier-transform our function to obtain $T_\sigma(z_k - z_r)$. *We now have a transfer function with the minimal number of frequencies and thus the minimal number of sample points for a given error* ϵ.

For all other directions $z-$, $x\pm$ *and* $y\pm$, *the same construction applies. This defines the transfer functions for all possible directions.*

We did some numerical tests to illustrate this construction. Consider the following function:

$$f_C(\theta, \phi) = \sum_{i=1}^{10} u_i\, e^{i\langle(\theta,\phi), x_i\rangle}$$

where x_i are random points inside a sphere of radius 16, and u_i are random coefficients. We compute:

$$\int_{\theta=-\pi/2}^{\pi/2} f_C(\theta, 0)\, e^{i\langle(\theta,0), z\rangle}\, d\theta \tag{3.3}$$

where z is equal to $(32, 32, 64)$. We now denote

$$T_\infty(\theta) = e^{i\langle(\theta,0),z\rangle}\mathbf{1}_{[-\pi/2:\pi/2]}(\theta)$$

We wish to show that using Procedure 1 for $T_\infty(\theta)$ allows accurately computing integral (3.3) with a relatively small number of sample points for $f_C(\theta, 0)$. Procedure 1 is applied in the following way. We Fourier transform $T_\infty(\theta)$, retain the lowest p frequencies, and set the higher frequencies to zero. Then we take the inverse Fourier transform. Let us denote the resulting function by T_p. We then approximate integral (3.3) using:

$$\frac{2\pi}{2p+1} \sum_{q=1}^{2p+1} f_C(\frac{2\pi q}{2p+1}, 0)\, T_p(\frac{2\pi q}{2p+1})$$

We proved that the bandwidth of $f_C(\theta, 0)$ in θ is on the order of the radius of the sphere, 16. Thus we expect a very fast convergence once p is larger than 32. Figure 4 shows that this is indeed the case. Consider the case with 64 sample points: at this resolution the error is down to 1.7×10^{-9}, so the computation is very accurate. This corresponds to a case where the transfer function $T_\infty(\theta)$ is under-resolved. The number of sample points 64 is too small to resolve the high frequencies of the function. Figure 5 represents the exact transfer function $T_\infty(\theta)$ and the low-frequency approximate T_p that is used for $p = 64$. However since $f_C(\theta, 0)$ is band limited and its bandwidth is on the order of 16, the computation is accurate if we use T_p rather than T_∞. It may seem paradoxical that increased accuracy is achieved by modifying the function $T_\infty(\theta)$. The argument is that since $f_C(\theta, 0)$ is band limited, the contribution of any frequency in $T_\infty(\theta)$ that is higher than 16 in this case is negligible. However since we only use 64 sample points for the discrete approximation of the integral, these high frequencies contribute. By smoothing $T_\infty(\theta)$ we exactly remove any contribution from the high frequencies and thus improve the accuracy.

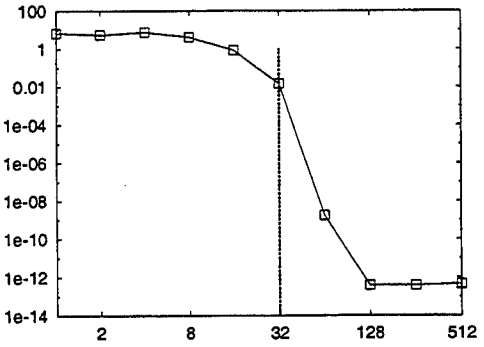

FIGURE 4. The figure represents the decrease of the error with the number of sample points for the computation of $\int_{\theta=-\pi/2}^{\pi/2} f_C(\theta,0)\, e^{\imath\langle(\theta,0),x\rangle}\, d\theta$. The vertical thick line | is located at 32. Once the number of sample points is larger than the diameter of the sphere (32 in this case) the convergence is very fast.

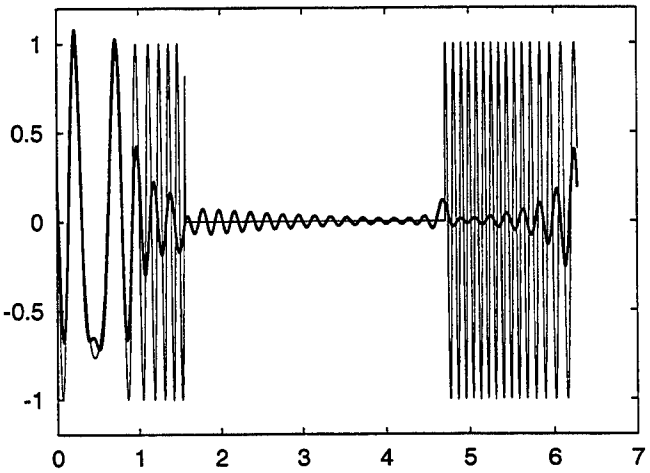

FIGURE 5. This figure compares the function $T_\infty(\theta)$ (thin line —) with the smooth function T_p (thick line —) used in the integration.

3.2. *Evanescent term*

Consider two points x_i in cluster C_1 with center z_1, and x_j in cluster C_2 with center z_2. We have the following expansion:

$$\frac{e^{\imath\kappa|x_i-x_j|}}{|x_i-x_j|} = \frac{\imath\kappa}{2\pi}\int_{S^{z+}} e^{\imath\kappa\langle\sigma,x_i-x_j\rangle}\, d\sigma$$

$$+\frac{1}{\pi}\int_{\chi=0}^{+\infty}\int_{\phi=0}^{2\pi} e^{-\chi^2(x_i-x_j)_z}\, e^{\imath\sqrt{\chi^4+\kappa^2}((x_i-x_j)_x\cos\phi+(x_i-x_j)_y\sin\phi)}\,\chi\, d\chi\, d\phi$$

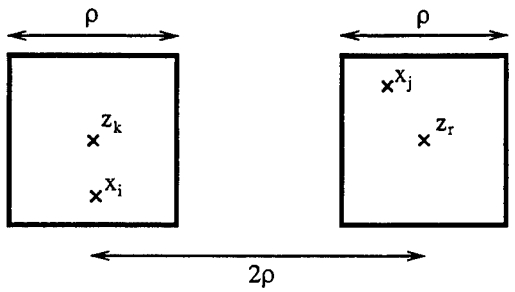

FIGURE 6. Size and distance between clusters. ρ is the length of the side of the clusters and 2ρ is the minimal distance between two clusters which are not neighbors.

The integrand for the evanescent term can be split into three functions:

$$F_{x_i-z_1}(\chi,\phi) = e^{-\chi^2(x_i-z_1)_z}\ e^{i\sqrt{\chi^4+\kappa^2}((x_i-z_1)_x\cos\phi+(x_i-z_1)_y\sin\phi)}$$

$$T_{z_1-z_2}(\chi,\phi) = \mathbf{1}_{[0;+\infty]}(\chi)\ \chi\ e^{-\chi^2(z_1-z_2)_z}\ e^{i\sqrt{\chi^4+\kappa^2}((z_1-z_2)_x\cos\phi+(z_1-z_2)_y\sin\phi)}$$

$$G_{z_2-x_j}(\chi,\phi) = e^{-\chi^2(z_2-x_j)_z}\ e^{i\sqrt{\chi^4+\kappa^2}((z_2-x_j)_x\cos\phi+(z_2-x_j)_y\sin\phi)}$$

The evanescent term is now equal to:

$$\mathcal{I}(x_i-x_j) = \frac{1}{\pi}\int_{\chi=-\infty}^{+\infty}\int_{\phi=0}^{2\pi} F_{x_i-z_1}(\chi,\phi)\,T_{z_1-z_2}(\chi,\phi)\,G_{z_2-x_j}(\chi,\phi)\,\chi\,d\chi\,d\phi. \tag{3.4}$$

In order to reduce the number of sample points χ and ϕ, the functions $F_{x_i-z_1}$ and $G_{z_2-x_j}$ need to be band limited in Fourier space for the variables χ and ϕ. For the variable χ, this condition is not true, as $(x_i-z_1)_z$ and $(z_2-x_j)_z$ can have either sign and thus $e^{-\chi^2(x_i-z_1)_z}$ and $e^{-\chi^2(z_2-x_j)_z}$ may be diverging exponentials. However $(x_i-z_1)_z$ and $(z_2-x_j)_z$ satisfy the following equations, where ρ is the size of clusters C_1 and C_2 (see Fig. 6):

$$(x_i-z_1)_z \geq \frac{-\rho}{2}, \tag{3.5}$$

$$(z_2-x_j)_z \geq \frac{-\rho}{2}, \tag{3.6}$$

$$(z_1-z_2)_z \geq 2\rho. \tag{3.7}$$

Suppose we multiply $F_{x_i-z_1}(\chi,\phi)$, $G_{z_2-x_j}(\chi,\phi)$ and $T_{z_1-z_2}(\chi,\phi)$ by the following factors:

$$\tilde{F}_{x_i-z_1}(\chi,\phi) \stackrel{\text{def}}{=} \exp(-\chi^2\frac{3\rho}{4})\ F_{x_i-z_1}(\chi,\phi) \tag{3.8}$$

$$\tilde{T}_{z_1-z_2}(\chi,\phi) \stackrel{\text{def}}{=} \exp(\chi^2\frac{3\rho}{2})\ T_{z_1-z_2}(\chi,\phi) \tag{3.9}$$

$$\tilde{G}_{z_2-x_j}(\chi,\phi) \stackrel{\text{def}}{=} \exp(-\chi^2\frac{3\rho}{4})\ G_{z_2-x_j}(\chi,\phi) \tag{3.10}$$

then the functions $\tilde{F}_{x_i-z_1}(\chi,\phi)$ and $\tilde{G}_{z_2-x_j}(\chi,\phi)$ are band limited for χ. The factors were chosen so that the decay, when χ goes to infinity, of

$$\tilde{F}_{x_i-z_1}(\chi,\phi)\,\tilde{G}_{z_2-x_j}(\chi,\phi)$$

is similar to the decay of $\tilde{T}_{z_1-z_2}(\chi,\phi)$. More precisely, we have the following bounds:

$$|\tilde{T}_{z_1-z_2}(\chi,\phi)| \leq |\chi| \ \exp(-\chi^2\frac{\rho}{2})$$

$$|\tilde{F}_{x_i-z_1}(\chi,\phi)\,\tilde{G}_{z_2-x_j}(\chi,\phi)| \leq \exp(-\chi^2\frac{\rho}{2})$$

A procedure similar to Procedure 1 can be used to construct $T^e_{z_1-z_2}$ from $\tilde{T}_{z_1-z_2}$.

We do not detail the implementation and sampling procedure for variables ϕ and χ. It is similar to the construction of Section 3.1 and is based on studying the decay of the Fourier spectrum of f_{C_k} for ϕ and χ.

4. Conclusion

The new scheme presented in this article is based on plane-wave expansion. Unlike previous formulations, it is stable at all frequencies and is more accurate. This Plane Wave FMM (PW-FMM) involves a decomposition of $\exp(\imath kr)/r$ using two kinds of plane waves: evanescent and propagating. The basic tools required for PW-FMM are similar to the traditional FMM formulation (HF-FMM), but PW-FMM is stable at all frequencies and more accurate than HF-FMM.

Stability at all frequencies allows PW-FMM to be used as an adaptive method, i.e. it is possible to consider adaptive trees, where the number of levels varies depending on the concentration of points. For scattering applications, this means that the method remains efficient even if tiny details of the surface need to be meshed using a large number of points concentrated in a small volume. This is not possible with HF-FMM because of the sub-wavelength "breakdown".

A future publication will present the implementation of PW-FMM, a precise description of the various optimization steps which can be performed, and some numerical results. In particular, it will contain an analysis of the performance of the method and its accuracy.

REFERENCES

CHENG, H., GREENGARD, L. & ROKHLIN, V. 1999 A fast adaptive multipole algorithm in three dimensions. *J. Comp. Phys.* **155**, 468-498.

CHEW, W. C., JIN, J. M., LU, C. C., MICHIELSSEN, E. & SONG, J. M. 1997 Fast solution methods in electromagnetics. *IEEE Trans. on Anten. and Propa.* **45**, 533-543.

DARVE, E. 1997 Fast-multipole: a mathematical study (abridged version). *C. R. Acad. Sci. Paris*, **Série I**, 1037-1042.

DARVE, E. 1999 *Méthodes multipôles rapides: résolution des équations de Maxwell par formulations intégrales.* Ph.D. in Applied Math., Université Pierre et Marie Curie, Paris.

DARVE, E. 1999 The fast multipole method (i): error analysis and asymptotic complexity. *SIAM J. Num. Anal.* **38**, 98-128.

DARVE, E. 2000 The fast multipole method: numerical implementation. *J. Comp. Phys.* **160**, 195-240.

ENGHETA, N., MURPHY, W. D., ROKHLIN, V. & VASSILIOU, M. S. 1992 The fast multipole method (FMM) for electromagnetic scattering problems. *IEEE Trans. on Anten. and Propa.* **40**, 634-641.

EPTON, M. A. & DEMBART, B. 1995 Multipole translation theory for three-dimensional laplace and helmholtz equations. *SIAM J. Sci. Comput.* **16**, 865-897.

GREENGARD, L. & ROKHLIN, V. A fast algorithm for particle simulations. *J. Comp. Phys.* **73**, 325-348.

GREENGARD, L., HUANG, J., ROKHLIN, V. & WANDZURA, S. 1998 Accelerating fast multipole methods for low frequency scattering. *IEEE Comp. Sci. & Engineering Mag.* **5**, 32-38.

HU, B. & CHEW, W. C. 1999 Fast inhomogeneous plane wave algorithm for electromagnetic solutions in layered medium structures. In *36th Ann. Tech. Mtg., Soc. of Engg. Sci.*, Austin, Texas.

HU, B., CHEW, W. C., MICHIELSSEN, E. & ZHAO, J. 1999 Fast inhomogeneous plane wave algorithm (FIPWA) for the fast analysis of two-dimensional scattering problems. University of Illinois, Urbana, *Research Report* CCEM-5-99.

ROKHLIN, V. 1990 Rapid solution of integral equations of scattering theory in two dimensions. *J. Comp. Phys.* **86**, 414-439.

SONG, J. M., LU, C. C. & CHEW, W. C. 1997 Multilevel fast multipole algorithm for electromagnetic scattering by large complex objects. *IEEE Trans. on Anten. and Propag.* **45**, 1488-1493.

SONG, J. M., LU, C. C., CHEW, W. C. & LEE, S. W. 1998 Fast illinois solver code (FISC). *IEEE Anten. and Propag. Mag.* **40**, 27-33.

WHITE, C. A. & HEADGORDON, M. 1996 Rotating around the quartic angular-momentum barrier in fast multipole method calculations. *J. Chem. Phys.* **105**, 5061-5067.

Calculating free energies using average force

By **Eric Darve** AND **Andrew Pohorille** † ‡

1. Introduction

Many molecular-dynamics computer simulations of chemically and biologically interesting systems are devoted to calculating free-energy changes along selected degrees of freedom. In some instances, the full free-energy profile is of interest. For example, nonmonotonic changes in the free energy of two small, hydrophobic species in water as a function of their separation, observed in computer simulations, Ludemann (1996), reflect the changing patterns of hydrophobic hydration and provide important tests of analytical theories of hydrophobic interactions; Pratt (1977). Free-energy maps of small peptide units in vacuum and in water shed light on conformational preferences of the protein backbone; Brooks (1998). The free-energy profiles associated with the transfer of solutes through water-membrane systems yield solute distributions and permeation rates across membranes: see Wilson (1996), Pohorille (1999). In other instances, calculations of free-energy profiles provide a means of estimating the free-energy difference between the end-points which, in turn, yields the relative stabilities of the corresponding states of the system. Determinations of conformational equilibria in flexible molecules and association constants between molecular species are among important applications of such calculations: see Giraldo (1998), Schaefer (1998).

The free-energy changes along the chosen generalized coordinates can be calculated from molecular simulations by a variety of techniques: see Frenkel (1996), Berne (1997). Most of them require that a sufficient, thermally-representative sample of states of the system is generated at different values of these coordinates. This leads to the interpretation of the free-energy changes along the chosen coordinates as the potential of mean force exerted by other coordinates. Only a few methods for calculating this potential can be conveniently, efficiently and generally combined with computer simulations. One such class of methods relies on obtaining the probability density function, $P(\xi_1, \ldots, \xi_p)$, of finding the system at values $\xi_1, \ldots, \xi_p$ of the p selected generalized coordinates. Once this probability density function is estimated with satisfactory accuracy, the potential of mean force, $A(\xi_1, \ldots, \xi_p)$, can be readily calculated as

$$A(\xi_1, \ldots, \xi_p) = -k_B T \log P(\xi_1, \ldots, \xi_p) \tag{1.1}$$

where T is temperature and k_B is the Boltzmann constant.

Another, general, method for calculating the potential of mean force requires calculating the derivatives $\frac{\partial A}{\partial \xi}$ in a series of calculations, in which ξ_i is constrained to fixed values distributed along $[\xi_i^{min}, \xi_i^{max}]$ in the range of interest. Then, the potential of mean force is recovered by numerical integration. The derivative of the free energy is related to the constraint force needed to keep the system at the fixed value of ξ_i. The exact nature of this relationship was a subject of some debate; see Van Gunsteren (1989), Straatsma (1992), Mülders (1996), den Otter (1998), den Otter & Briels (2000). Several initial

† Exobiology Branch, NASA Ames Research Center
‡ Dept. Pharmaceutical Chemistry, University of California, San Francisco

suggestions were found to be valid only under special circumstances; see Van Gunsteren (1989), Straatsma (1992), Mülders (1996). Only recently, the generally valid and practical to use formula was derived for one-dimensional (den Otter (1998), Sprik (1998), Ruiz-Montero (1997)) and multi-dimensional cases (den Otter & Briels 2000). In this paper, this formula is derived in the general context of multi-dimensional reaction coordinates for constrained and unconstrained simulations. All previous derivations were done in the case of constrained simulations only. This formula requires that the constraint force is corrected by geometric factors that depend on $\xi_1, \ldots, \xi_p$ but not on other (usually difficult to define) generalized coordinates. Since the constraint force can be readily calculated in computer simulations, e.g. using the algorithms SHAKE, see Ryckaert (1977), or RATTLE, see Andersen (1983), practical applications of this method are quite feasible.

Compared to the probability-density method, the constraint-force method has several advantages. In particular, it does not require a good guess of the biasing potential to achieve efficient sampling of $\xi_1, \ldots, \xi_p$. Providing such a guess could be a difficult task, especially for qualitatively new problems. Further, data analysis is markedly simpler; no procedure for matching results obtained for overlapping windows is required. However, the constraint-force method also suffers from several disadvantages. It may be inaccurate or inefficient if the potential of mean force is a rapidly-changing function of $\xi_1, \ldots, \xi_p$. In complex cases, involving, for example, the insertion of a peptide into a membrane or the induced fit of an inhibitor into an enzyme, preparation of the system at consecutive, fixed values of the selected degrees of freedom may be difficult, and subsequent equilibration of the system may be slow. In some instances, application of the constraint-force method may lead to quasi-non-ergodic behavior. Finally, information about the dynamic behavior of the system, which may also be of interest in a simulation, is not available in this approach.

In this paper, we propose an alternative and equally general approach to calculating the potential of mean force, which combines several desired features of both methods. As in the constraint-force method, the potential of mean force is obtained by integrating its derivative. This derivative, however, is calculated from unconstrained rather than constrained simulations. The centerpiece of our method is a new, general formula that connects $\partial A/\partial \xi_i$ with the instantaneous force acting on ξ_i. This force acts along the gradient of ξ_i such that if subtracted from the equations of motion the acceleration of ξ_i is zero. This instantaneous force can be also related to the forces of constraint in a constrained simulation. Then, the forces of constraint are applied to maintain ξ_i at a constant value, and the force acting on ξ_i is exactly equal and opposite to these forces of constraint.

The formula that relates $\partial A/\partial \xi_i$ to the instantaneous force acting on ξ_i is different in unconstrained simulations and constrained simulations. However, as will be shown below, it converges to the den Otter-Briels formula at the appropriate limits. The value of the new formula is not only in providing another route to calculating the potential of mean force but also in clarifying the relationship between the thermodynamic force and the force of constraint. By doing so it forms the theoretical basis for highly-efficient methods to calculate the potential of mean force and to investigate rare events (Darve (2001)).

In the next section we derive the formula for $\partial A/\partial \xi_i$. This is done in two steps. First, the expression for $\partial A/\partial \xi_i$ in unconstrained simulations of a Hamiltonian system is obtained. Then, this expression is generalized so that it applies when the system is only approximately Hamiltonian, as is the case in adiabatic approximation. Then we consider two numerical examples – rotation around the C-C bond of 1,2-dichloroethane immersed

in water, and transfer of fluoromethane across the water-hexane interface. These examples involve only a single reaction coordinate. Applications to multidimensional cases will be considered separately. We close the paper with a comparison of the new method with its alternatives.

2. Theory

2.1. *Generalized coordinates*

We assume that we have a set of M particles and we denote by N the total number of degrees of freedom of our system ($N = 3M$). We further assume that exists a Hamiltonian, H, for this system:

$$H(x_1, \dots, x_N, p_1, \dots, p_N) = \frac{1}{2} \sum_i \frac{p_i^2}{m_i} + \Phi(x_1, \dots, x_N)$$

$$\frac{dx_i}{dt} = \frac{\partial H}{\partial p_i}$$

$$\frac{dp_i}{dt} = -\frac{\partial H}{\partial x_i}$$

where $(x_1, \dots, x_n)$ are Cartesian coordinates, $(p_1, \dots, p_n)$ are the conjugated momenta, Φ is the potential and t is time.

We suppose that a set of $N - p$ functions $(q_1, \dots, q_{N-p})$ can be defined such that $(\xi_1, \dots, \xi_p, q_1, \dots, q_{N-p})$ forms a complete set of generalized coordinates. We will often denote by x the vector $(x_1, \dots, x_N)$, and similarly for ξ, q, p_ξ and p_q.

The derivative with respect to ξ_i is defined as the derivative computed with ξ_j, $j \neq i$ and q_k, $k = 1, \dots, N - p$ constant. Using the definition of A, Eq.(1.1), we can write:

$$\frac{\partial A}{\partial \xi_i} = -k_B T \frac{\frac{\partial P}{\partial \xi_i}}{P} \tag{2.1}$$

The probability density P for a canonical ensemble can be written as a function of the Hamiltonian H of the system:

$$P(\xi_1^*, \dots, \xi_p^*) = \frac{1}{\mathcal{N}} \int dx_1 \dots dx_N dp_1 \dots dp_N \; \delta(\xi_1 - \xi_1^*) \dots \delta(\xi_p - \xi_p^*) \exp(-\frac{H}{k_B T}) \tag{2.2}$$

where $\mathcal{N}$ is a normalization factor.

We introduce additional notation to express the Hamiltonian H as a function of the generalized coordinates.

The Jacobian, J, of the transformation from Cartesian to generalized coordinates is denoted by

$$J \stackrel{def}{=} \begin{pmatrix} J_\xi \\ J_q \end{pmatrix} \tag{2.3}$$

where J_ξ are the first p lines and J_q are the remaining lines. We define matrix Z as:

$$Z \stackrel{def}{=} J M^{-1} J^t$$

where J^t is the transpose of matrix J and M is the mass matrix:

$$M = \begin{pmatrix} m_1 & 0 & \dots & 0 \\ 0 & m_2 & \dots & 0 \\ \dots & \dots & \dots & \dots \\ \dots & \dots & \dots & m_N \end{pmatrix}$$

Matrix Z can be written as:

$$Z = \begin{pmatrix} Z_\xi & Z_{\xi q} \\ Z_{q\xi} & Z_q \end{pmatrix}$$

where Z_ξ is a $p \times p$ matrix, $Z_{\xi q}$ a $p \times (N-p)$ matrix, and Z_q a $(N-p) \times (N-p)$ matrix.

The inverse of Z is denoted by A:

$$A = \begin{pmatrix} A_\xi & A_{\xi q} \\ A_{q\xi} & A_q \end{pmatrix}$$

Using generalized coordinates, the Hamiltonian of the system takes the form:

$$H(\xi, q, p_\xi, p_q) = \frac{1}{2} p_\xi^t Z_\xi p_\xi + \frac{1}{2} p_q^t Z_q p_q + p_\xi^t Z_{\xi q} p_q + \Phi(\xi, q) \tag{2.4}$$

where p_ξ^t and p_q^t are the transposes of vectors p_ξ and p_q.

Inserting the expression for P from Eq. (2.2) into (2.1), we obtain:

$$\frac{\partial A}{\partial \xi_i} = \frac{\int dq dp_q dp_\xi \, \frac{\partial H}{\partial \xi_i} \exp(-\frac{H}{k_B T})}{\int dq dp_q dp_\xi \, \exp(-\frac{H}{k_B T})} \tag{2.5}$$

with a change of variables from Cartesian coordinates to generalized coordinates. For all functions F, we define the statistical average of F at fixed $\xi^* = (\xi_1^*, \dots, \xi_p^*)$ as:

$$\begin{aligned} \langle F \rangle_{\xi^*} &= \frac{\int dx_1 ... dx_N dp_1 ... dp_N \, \delta(\xi_1 - \xi_1^*) ... \delta(\xi_p - \xi_p^*) \, \exp(-\frac{H}{k_B T}) \, F(x_1, \dots, x_N)}{\int dx_1 ... dx_N dp_1 ... dp_N \, \delta(\xi_1 - \xi_1^*) ... \delta(\xi_p - \xi_p^*) \, \exp(-\frac{H}{k_B T})} \\ &= \frac{\int dq dp_q dp_\xi \, F(x_1, \dots, x_N)}{\int dq dp_q dp_\xi \, \exp(-\frac{H}{k_B T})} \end{aligned}$$

where in the last equation $\xi = \xi^*$. With this notation, we can rewrite Eq. (2.5) as:

$$\frac{\partial A}{\partial \xi_i} = \left\langle \frac{\partial H}{\partial \xi_i} \right\rangle_\xi \tag{2.6}$$

After differentiating both sides of Eq. (2.4) and integrating over p_ξ and p_q, we obtain a new expression for Eq. (2.6)

$$\nabla_\xi A = \left\langle \nabla_\xi \Phi + k_B T \, \nabla_\xi \log |J| \right\rangle_\xi \tag{2.7}$$

The derivative of the free energy can be seen as resulting from two contributions: the mechanical forces acting along ξ and the variations of the volume element associated with the generalized coordinates. This formula has been previously derived in many papers, e.g. Ruiz-Montero (1997) and den Otter & Briels (2000), and is also given by Frenkel and Smit (1996).

2.2. *Thermodynamic force*

In this and the following Sections, we use the fact that, for a given ξ^*, it is possible to choose a basis q such that:

$$Z_{q\xi}(\xi^*, q) = 0, \quad \forall q. \tag{2.8}$$

This choice of q leads to a simplified derivation of our analytical results.

Eq. (2.6) explicitly depends on the choice of all generalized coordinates, including q. As this is not practical from a computational point of view, we now modify this equation to obtain an expression independent of the choice of q. This is done by analytically integrating as many terms as possible in Eq. (2.6).

We start by simplifying the notation:

$$x'_i \stackrel{def}{=} \sqrt{m_i}\, x_i \qquad \nabla'_i \stackrel{def}{=} \frac{1}{\sqrt{m_i}} \frac{\partial}{\partial x_i} \tag{2.9}$$

$$p'_{x_i} \stackrel{def}{=} \frac{p_{x_i}}{\sqrt{m_i}} \tag{2.10}$$

The symbol $\cdot$ denotes a dot product or a matrix-vector product.

We start from the equation for the time evolution of p_{ξ_i}:

$$\frac{dp_{\xi_i}}{dt} = -\frac{\partial H}{\partial \xi_i} \tag{2.11}$$

The momentum vector p_ξ is defined as the derivative of the Lagrangian with respect to $\dot{\xi}$:

$$p_{\xi_i} \stackrel{def}{=} \sum_j [A_\xi]_{ij} \frac{d\xi_j}{dt} + \sum_k [A_{\xi q}]_{ik} \frac{dq_k}{dt} \tag{2.12}$$

We can differentiate both sides of Eq. (2.12) with respect to t and use Eq. (2.11) to obtain an expression for $\frac{\partial H}{\partial \xi_i}$. As the right-hand side of Eq. (2.12) is the sum of two products, its derivative contains four terms:

$$\begin{aligned} \frac{\partial H}{\partial \xi_i} = -\frac{dp_{\xi_i}}{dt} = &- \sum_j \frac{d[A_\xi]_{ij}}{dt} \frac{d\xi_j}{dt} - \sum_j [A_\xi]_{ij} \frac{d^2\xi_j}{dt^2} \\ &- \sum_k \frac{d[A_{\xi q}]_{ik}}{dt} \frac{dq_k}{dt} - \sum_k [A_{\xi q}]_{ik} \frac{d^2 q_k}{dt^2} \end{aligned} \tag{2.13}$$

Because q satisfies Eq. (2.8), the last term in Eq. (2.13) is equal to zero. Eq. (2.13) can be further transformed using the chain rule of derivation to obtain:

$$\frac{\partial H}{\partial \xi_i} = -\sum_j [Z_\xi^{-1}]_{ij} \frac{d^2\xi_j}{dt^2} + \sum_{jk} [Z_\xi^{-1}]_{ij} \left[\frac{\partial Z_\xi}{\partial x'} \cdot p'_x\right]_{jk} p_{\xi_k} - \sum_k \frac{d[A_{\xi q}]_{ik}}{dt} \frac{dq_k}{dt} \tag{2.14}$$

By expressing p'_x in terms of p_ξ and p_q, one can prove that the second term of Eq. (2.14) is equal to

$$\begin{aligned} \sum_{jk} [Z_\xi^{-1}]_{ij} \left[\frac{\partial Z_\xi}{\partial x'} \cdot p'_x\right]_{jk} p_{\xi_k} = &\sum_{jklr} [Z_\xi^{-1}]_{ij} \frac{\partial [Z_\xi]_{jk}}{\partial x'_l} [J'_\xi]_{rl}\, p_{\xi_r} p_{\xi_k} \\ &+ \sum_{jklr} [Z_\xi^{-1}]_{ij} \frac{\partial [Z_\xi]_{jk}}{\partial x'_l} [J'_\xi]_{r+p,l}\, p_{q_r} p_{\xi_k} \end{aligned} \tag{2.15}$$

where J' is defined as J but with x replaced by x'.

In the last equation, we have split the right-hand side into odd and even functions of p_ξ and p_q . We want to compute

$$\int dp_q dp_\xi \exp(-\frac{H}{k_B T}) \frac{\partial H}{\partial \xi_i}$$

Because we chose a basis q such that Eq. (2.8) is true, the function $\exp(-\frac{H}{k_B T})$ is even in p_ξ and p_q. Therefore in Eq. (2.15), all odd terms in p_ξ and p_q cancel whereas even terms contribute. An analytical integration over p_{ξ_k} leads to:

$$\Big\langle \sum_{jk} [Z_\xi^{-1}]_{ij} \, [\frac{\partial Z_\xi}{\partial x'} \cdot p'_x]_{jk} \, p_{\xi_k} \Big\rangle_\xi = k_B T \Big\langle \sum_{jkrl} [Z_\xi^{-1}]_{ij} \frac{\partial [Z_\xi]_{jk}}{\partial x'_l} [Z_\xi^{-1}]_{kr} \frac{\partial \xi_r}{\partial x'_l} \Big\rangle_\xi \qquad (2.16)$$

Using the fact that vectors $\frac{1}{m_s} \frac{\partial q_r}{\partial x_s}$ satisfy Eq. (2.8) and are therefore orthogonal to $\nabla\xi_1$,..., $\nabla\xi_p$, one can prove that the third term on the right-hand side of Eq. (2.14) does not contribute to $\langle \nabla_\xi H \rangle_\xi$. In matrix notation, inserting Eq. (2.16) in Eq. (2.14) gives:

$$\langle \nabla_\xi H \rangle_\xi = k_B T \, \langle \sum_l \frac{1}{m_l} Z_\xi^{-1} \cdot \partial_l Z_\xi \cdot Z_\xi^{-1} \cdot \nabla \xi \rangle_\xi \; - \; \langle Z_\xi^{-1} \frac{d^2 \xi}{dt^2} \rangle_\xi \qquad (2.17)$$

where we denote $\partial_l Z_\xi = \frac{\partial Z_\xi}{\partial x_l}$.

If we denote by λ the vector of RATTLE Lagrange multipliers – Andersen (1983) – they are by definition such that:

$$Z_\xi \lambda \stackrel{def}{=} -\frac{d^2 \xi}{dt^2}. \qquad (2.18)$$

We now summarize what we have obtained so far. We started our derivation from Eq. (2.6), which relates the derivative of A with respect to ξ_i to the average of $\frac{\partial H}{\partial \xi_i}$. We observed that this expression is not very useful, because it depends on a particular choice of generalized coordinates. We transformed this expression by analytically integrating some terms and obtained Eq. (2.17). This new expression is much more useful than the initial one, Eq. (2.6), as it can be computed numerically without any explicit reference to a particular choice of generalized coordinates. Finally, by inserting Eq. (2.18) in the last term of Eq. (2.17), we obtain:

$$\nabla_\xi A = \Big\langle \lambda + k_B T \sum_l \frac{1}{m_l} Z_\xi^{-1} \cdot \partial_l Z_\xi \cdot Z_\xi^{-1} \cdot \partial_l \xi \Big\rangle_\xi \stackrel{def}{=} \Big\langle F_\xi^{(1)} \Big\rangle_\xi \qquad (2.19)$$

Eq. (2.19) has a similar interpretation to Eq. (2.7) although the terms are different. The first term λ is related to the force acting along ξ, which is the opposite of the constraint force. The second term $\sum_l \frac{1}{m_l} \partial_l Z_\xi^{-1} \cdot \partial_l \xi$ is a correction term which accounts for the variation of an infinitesimal volume element in generalized coordinates.

2.3. *Decoupled degrees of freedom*

It is often desirable to consider a situation where ξ is decoupled from the other degrees of freedom. By decoupling we mean that $\frac{d^2 \xi}{dt^2}$ is not a function of the coordinates q, but instead is governed by some other equation of motion. In the previous paper, Darve (2001), we derived the formula for $\frac{\partial A}{\partial \xi}$ that applies to a single reaction coordinate. In this paper, this formula is generalized to a multi-dimensional case.

One example of decoupling is a constrained simulation in which ξ is constant. In this

case $\dot{\xi} = 0$ and $\frac{d^2\xi}{dt^2} = 0$. We will see that using Eq. (2.19) we recover the result of den Otter and Briels (2000). Our derivation can thus be seen as a generalization of their result. Another choice, which was previously discussed in Darve (2001), is a diffusion equation such that the motion of ξ is random and approximately adiabatic. The choice of a Langevin equation is a convenient one because adiabatic approximation can be achieved simply by varying the diffusion constant.

Deriving the relation for $\nabla_\xi A$ in the decoupled case requires modifying the probability density of p_ξ. Previously this density was given by:

$$f_\xi = \exp(-\frac{\frac{1}{2}p_\xi^t Z_\xi p_\xi}{k_B T}) \tag{2.20}$$

For a constraint simulation, f_ξ becomes a Dirac delta function at the location of the constraint whereas for the other decoupled case, f_ξ is a constant function. Since the equation for the decoupled case can be used for an arbitrary f_ξ, it can be seen as a generalization of Eq. (2.19). Thus, one can implement the equation for the decoupled case (Eq. (2.21)) and use it in all situations.

After calculating analytically the integral over p_ξ in Eq. (2.19) with f_ξ given by Eq. (2.20), we obtain the correction for the decoupled case:

$$\frac{\partial A}{\partial \xi_i} = \frac{\left\langle \frac{1}{|Z_\xi|^{1/2}} \left(\lambda + \sum_j [Z_\xi^{-1}]_{ij} \left((\frac{d\xi}{dt})^t \cdot \tilde{\mathcal{H}}_j \cdot (\frac{d\xi}{dt}) + \frac{k_B T}{2} \nabla' \xi_j \cdot \nabla' \log |Z_\xi| \right) \right) \right\rangle_\xi}{\left\langle \frac{1}{|Z_\xi|^{1/2}} \right\rangle_\xi} \tag{2.21}$$

In this equation, we have used the notation $\tilde{\mathcal{H}}_j$ for:

$$\tilde{\mathcal{H}}_j = Z_\xi^{-1} \, J'_\xi \, \mathcal{H}_j \, (J'_\xi)^t \, Z_\xi^{-1} \tag{2.22}$$

Note that $\tilde{\mathcal{H}}_j$ is a function only of the first and second derivatives of ξ with respect to Cartesian coordinates, and thus can be easily computed numerically.

2.4. *Constrained simulation*

In the particular case of a constraint simulation, $\dot{\xi} = 0$, which leads to:

$$\frac{\partial A}{\partial \xi_i} = \frac{\left\langle \frac{1}{|Z_\xi|^{1/2}} \left(\lambda + \frac{k_B T}{2} \sum_j [Z_\xi^{-1}]_{ij} (\nabla' \xi_j \cdot \nabla' \log |Z_\xi|) \right) \right\rangle_\xi}{\left\langle \frac{1}{|Z_\xi|^{1/2}} \right\rangle_\xi} \tag{2.23}$$

This is the formula obtained by den Otter and Briels. Note that this formula is applicable to the case of several degrees of freedom. Several authors derived a similar equation for a single reaction coordinate (see den Otter (1998), Sprik (1998)). Note that in Eq. (2.23), Z_ξ is a matrix, $|Z_\xi|$ denotes its determinant and λ is a vector. This contrasts with the case of a single reaction coordinate in den Otter (1998), Sprik (1998).

3. Numerical Results

To examine the performance of the method based on Eq. (2.21), we studied two test cases. One example involved calculating the potential of mean force for the rotation of the C-C bond in 1,2-dichloroethane (DCE) dissolved in water. In the second example, the potential of mean force for the transfer of fluoromethane (FMet) across the water-hexane interface was obtained.

The first system consisted of a DCE molecule surrounded by 343 water molecules, all placed in a cubic box whose edge length was 21.73 Å. This yielded a water density approximately equal to 1 g/cm^3. The second system contained one FMet molecule and a lamella of 486 water molecules in contact with a lamella of 83 hexane molecules. This system was enclosed in a box, whose x, y-dimensions were 24 × 24 Å^2 and the z-dimension, perpendicular to the water-hexane interface, was equal to 150 Å. Thus, the system contained one liquid-liquid interface and two liquid-vapor interfaces. The same geometry was used in a series of previous studies on the transfer of different solutes across the water-hexane interface; see Darve (2001). In both cases, periodic boundary conditions were applied in the three spatial directions.

For DCE in water, the potential of mean force was calculated along ξ, defined as the Cl-C-C-Cl torsional angle. For the transfer of FMet across the water-hexane interface, ξ was defined as the z component of the distance between the centers of mass of the solute and the hexane lamella (since both cases involved only one-dimensional potentials of mean force, we drop the subscript i following ξ). For each system, three sets of calculations were performed. They yielded $A(\xi)$, using the probability-density method and the methods of the constraint force from unconstrained and constrained simulations.

To obtain $A(\xi)$ from the probability density method, a series of simulations was performed. For DCE, we used a single window and a biasing potential obtained previously (Darve (2001)). The trajectory was 2 ns long. For FMet, ξ was constrained by a harmonic potential in five overlapping windows. No biasing potential was applied. For each window, a molecular-dynamics trajectory 2.4 ns long was obtained. From this trajectory the probability density, $P(\xi)$, was calculated. The probability density in the full range of ξ was constructed by matching $P(\xi)$ in the overlapping regions of consecutive windows. $A(\xi)$ was calculated from the complete $P(\xi)$ using Eq. (1.1).

Calculations of $\frac{\partial A}{\partial \xi}$ from unconstrained simulations were very similar. For DCE, we used a biasing potential and one window. For FMet we did not use a biasing potential and divided the full range of ξ into five windows. In these simulations, however, there was no need for windows to overlap. The molecular-dynamics trajectory in each window was 1.5 ns long. In each molecular dynamics step, the force of constraint was calculated using RATTLE. Since no biasing force was applied the average force in each bin along ξ was simply the arithmetic average of the instantaneous forces.

$\frac{\partial A}{\partial \xi}$ was obtained from constrained simulations by generating a series of trajectories, in which ξ was fixed at several values uniformly spanning the full range of interest. For DCE, simulations were carried out at 37 values of ξ in the range between 0 and 180 deg. This corresponds to 5 deg separation between two values of ξ. For FMet, ξ was fixed at 102 values between -10.1 Å and 10.1 Å (0.2 Å separation between two values). The constraints on ξ were enforced using RATTLE. The average thermodynamic force was obtained by correcting the calculated constraint force according to Eq. (2.23). Once calculations of $\frac{\partial A}{\partial \xi}$ were completed for all discrete values of ξ, $A(\xi)$ was obtained by numerical integration.

The potentials of mean force for rotation of DCE in water and transfer of FMet across the water-hexane interface, obtained from all three methods, are shown in Figs. 1 and 2, respectively. For DCE, gauche and trans conformations were found to have nearly the same free energy, and were separated by a barrier 4.2 kcal/mol high. The gauche conformation corresponds to a torsion angle of about +/− 60 deg (i.e. Cl is not in the plane defined by C-C-Cl) and the trans conformation corresponds to a torsion angle of 180 deg (i.e. this is the conformation where the two Cl are on the opposite sides of the C-

C bond). These results are in close agreement with the results obtained previously using the same potential functions (Benjamin (1993), Pohorille (1993)). For FMet, the free energy between dissolving this molecule in water and in hexane was found to be 0.6 kcal mol^{-1}. An appreciable minimum in the potential of mean force, approximately 1.4 kcal mol^{-1} deep, was observed near the interface. A very similar profile of $A(\xi)$ was obtained using the particle-insertion method of Pohorille, Chipot, New and Wilson (1996).

4. Discussion

In both numerical examples presented in the previous section, the method based on calculating the probability density along ξ and both methods relying on calculating $\frac{\partial A}{\partial \xi}$ yield the potentials of mean force that are identical to within statistical error. This confirms applicability of Eq. (2.19) to the calculation of the potential of mean force in unconstrained simulations.

The method based on Eq. (2.19) has an important advantage over the probability density method. No post-processing of the data obtained from different windows, such as WHAM (Kumar (1995)), is needed. The average force in a given bin along ξ is simply the arithmetic average of instantaneous forces recorded in this bin in all windows (if different biasing forces were used in different windows they have to be subtracted before the average is calculated). In fact, no overlapping between consecutive windows is needed if a sufficiently good estimate of the average force is obtained from one window.

The new approach does not suffer from the disadvantages of the method based on calculating the force in constrained simulations. These disadvantages were discussed in the Introduction. In addition, calculating the forces of constraints becomes less demanding. In constrained simulations, analytical formulas for calculating forces of constraints cannot be used. Instead, iterative procedures with very low tolerance, sometimes requiring double-precision arithmetic, have to be applied. This is needed to prevent drift of the constraint from the preset value due to the accumulation of numerical errors. This problem, however, does not exist in unconstrained simulations. Accuracy in calculating the forces of constraints does not influence motion of the system. This calculation is just a measurement performed on the system and should be done sufficiently accurately that numerical errors associated with this measurement have only negligible contribution to the statistical error of the average force. This is not a very stringent requirement.

This work was supported by the NASA Exobiology Program. The authors thank Dr. M. A. Wilson for helpful comments.

REFERENCES

ANDERSEN, H. C. 1983 RATTLE: a 'velocity' version of the SHAKE algorithm for molecular dynamics calculations. *J. Comput. Phys.* **52**, 24-34.

BENJAMIN, I. & POHORILLE, A. 1993 Isomerization reaction dynamics and equilibrium at the liquid-vapor interface of water — a molecular dynamics study. *J. Chem. Phys.* **98**, 236-242.

BERNE, B. J. & STRAUB, J. E. 1997 Novel methods of sampling phase space in the simulation of biological systems. *Curr. Opin. Struct. Biol.* **7**, 181-189.

BROOKS, C. L., III 1998 Simulations of protein folding and unfolding. *Curr. Opin. Struct. Biol.* **8**, 222-226.

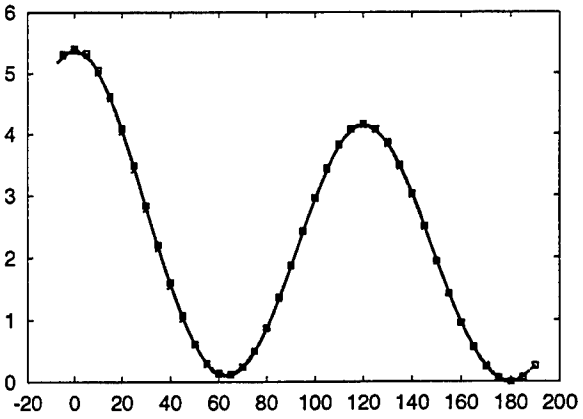

FIGURE 1. The free energy of rotating DCE around the C-C bond computed using the probability density method (———) and the methods of the constraint force from unconstrained (—□ —) and constrained simulations (—× —). On the x-axis is the value of the Cl-C-C-Cl torsional angle (in deg). On the y-axis is the free energy (in kcal mol^{-1}).

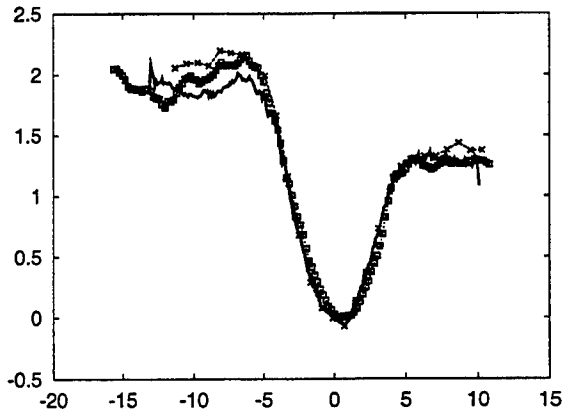

FIGURE 2. The free energy of transferring FMet across the water-hexane interface computed using the probability density method (———) and the methods of the constraint force from unconstrained (—□ —) and constrained simulations (—× —). On the x-axis is the value of of the reaction coordinate ξ (in Å). On the y-axis is the free energy (in kcal mol^{-1}).

CHERN, S. S., CHEN, W. H. & LAM, K. S. 1999 *Lectures on differential geometry.* World Scientific.

DARVE, E., WILSON, M. A. & POHORILLE, A. 2001 Calculating free energies using scaled-force molecular dynamics algorithm. *Mol. Sim.*, in press.

DEN OTTER, W. K. 2000 Thermodynamic integration of the free energy along a reaction coordinate in Cartesian coordinates. *J. Chem. Phys.* **112**, 7283-7292.

DEN OTTER, W. K. & BRIELS, W. J. 2000 Free energy from molecular dynamics with multiple constraints. *Mol. Phys.* **98**, 773-781.

DEN OTTER, W. K. & BRIELS, W. J. 1998 The calculation of free-energy differences by constrained molecular-dynamics simulation. *J. Chem. Phys.* **109**, 4139-4146.

FRENKEL, D. & SMIT, B. 1996 *Understanding molecular simulation.* Academic Press.

GIRALDO, J., WODAK, S. J. & VAN BELLE, D. 1998 Conformational analysis of GPA and GPAP in aqueous solution by molecular dynamics and statistical methods. *J. Mol. Biol.* **283**, 863-882.

JORGENSEN, W. L., CHANDRASEKHAR, J., MADURA, J. D., IMPEY, R. W. & KLEIN, M. L. 1983 Comparison of simple potential functions for simulating liquid water. *J. Chem. Phys.* **79**, 926-935.

JORGENSEN, W. L., MADURA, J. D. & SWENSON, C. J. 1984 Optimized potential energy functions for liquid hydrocarbons. *J. Am. Chem. Soc.* **106**, 6638-6646.

KUMAR, S., ROSENBERG, J. M., BOUZIDA, D., SWENDSEN, R. H. & KOLLMAN, P. A. 1995 Multidimensional free-energy calculations using the weighted histogram analysis method. *J. Comput. Chem.* **16**, 1339-1350.

LUDEMANN, S., SCHREIBER, H., ABSEHER, R. & STEINHAUSER, O. 1996 The influence of temperature on pairwise hydrophobic interactions of methane-like particles: a molecular-dynamics study of free-energy. *J. Chem. Phys.* **104**, 286-295.

MARTYNA, G. J., KLEIN, M. L. & TUCKERMAN, M. 1992 Nose-Hoover chains — the canonical ensemble via continuous dynamics. *J. Chem. Phys.* **97**, 2635-2643.

MÜLDERS, A., KRÜGER, P., SWEGAT, W. & SCHLITTER, J. 1996 Free energy as the potential of mean constraint force. *J. Chem. Phys.* **104**, 4869-4870.

POHORILLE, A. & WILSON, M. A. 1993 Isomerization reactions at aqueous interfaces. *Reaction Dynamics in Clusters and Condensed Phases — The Jerusalem Symposia on Quantum Chemistry and Biochemistry* (Jortner, J., Levine, R. D. & Pullman, B., eds.), Kluwer, Dordrecht, **26**, 207.

POHORILLE, A., CHIPOT, C., NEW, M. H. & WILSON, M. A. 1996 Molecular modeling of protocellular functions.
Pacific Symposium on Biocomputing '96 (Hunter, L. & Klein, T. E., eds.), World Scientific, Singapore, 550-569.

POHORILLE, A. & WILSON, M. A. 1996 Excess chemical potential of small solutes across water-membrane and water-hexane interfaces. *J. Chem. Phys.* **104**, 3760-3773.

POHORILLE, A., WILSON, M. A., CHIPOT, C., NEW, M. H. & SCHWEIGHOFER, K. S. 1999 Interactions of small molecules and peptides with membranes. Lesczynski, J. (Ed.), *Computational Molecular Biology*, Theoretical and Computational Chemistry, Elsevier, Amsterdam, 485-526.

PRATT, L. R. & CHANDLER, D. 1977 Theory of hydrophobic effect. *J. Chem. Phys.* **67**, 3683-3704.

RUIZ-MONTERO, M. J., FRENKEL, D. & BREY, J. J. 1997 Efficient schemes to compute diffusive barrier crossing rates. *Mol. Phys.* **90**, 925-941.

RYCKAERT, J., CICCOTTI, G. & BERENDSEN, H. J. C. 1977 Numerical integration of the Cartesian equations of motion for a system with constraints: molecular dynamics of n-alkanes. *J. Comp. Phys.* **23**, 327-341.

SCHAEFER, M., BARTELS, C. & KARPLUS, M. 1998 Solution conformations and thermodynamics of structured peptides: molecular dynamics simulation with an implicit solvation model. *J. Mol. Biol.* **284**, 835-848.

SPRIK, M. & CICCOTTI, G. 1998 Free energy from constrained molecular dynamics. *J. Chem. Phys.* **109**, 7737-7744.

STRAATSMA, T. P., ZACHARIAS, M. & MCCAMMON, J. A. 1992 Holonomic constraint contributions to free-energy differences from thermodynamic integration molecular-dynamics simulations *Chem. Phys. Lett.* **196**, 297-302.

VAN GUNSTEREN, W. F. 1989 Methods for calculation of free energies and binding constants: Successes and problems, In *Computer Simulation of Biomolecular Systems: Theoretical and Experimental Applications*, Van Gunsteren, W. F. & Weiner, P. K. (Eds.), ESCOM, 27-59.

WILSON, M. A. & POHORILLE, A. 1996 Mechanism of unassisted ion transport across membrane. *J. Am. Chem. Soc.* **118**, 6580-6587.

Buckyballs in water: structural characteristics and energetics

By
E. M. Kotsalis, R. L. Jaffe, J. H. Walther, T. Werder AND P. Koumoutsakos

1. Motivation and Objectives

The 1985 discovery by Curl, Kroto, and Smalley of the molecule C60 (dubbed "buckminsterfullerene" and nicknamed the "buckyball") marked the first time that elementary carbon was found to form stable molecules in which the atoms are arranged in closed shells. Ever since then, chemists have found numerous ways to produce variations on that theme, generically dubbed "fullerenes". One such class of molecules is that of the carbon nanotubes, which are novel structures with unique mechanical and electrical properties (Odom *et al.* 2000). Applications of buckyballs have been proposed in fluidic sensor technology (Wang *et al.* 1996; Amao *et al.* 1999). The interaction of the buckyball with the surrounding fluid is therefore of great importance. In this study we consider the structural characteristics and energetics of buckyballs in water using molecular-dynamics simulations. Specifically, we report on the breathing frequency of a buckyball in water, and characterize the carbon-water interface through water density profiles and the orientation of the water molecules. Finally we consider the energetics involved in introducing a buckyball into water to study the hydrophobic-hydrophilic behaviour of the buckyball water interface.

2. Accomplishments

2.1. *Method of calculation*

The buckyball-water system is studied using molecular-dynamics simulations. The water molecules are modeled by the flexible SPC potential which features harmonic stretch and bend terms between the oxygen and hydrogen atoms. The non-bonded interactions involve a Coulomb term between the partial charges of the water, computed using a smooth truncation, and a Lennard-Jones term between the oxygens of the water (Walther *et al.* 2001). The buckyball is modeled by terms describing Morse bond stretch, harmonic cosine bending and a 2-fold torsion potentials. We also consider Lennard-Jones interactions between carbon-carbon (excluding 1-2 and 1-3 pairs) and oxygen-carbon atoms. The water molecules are initially placed on a regular cubic or rectangular lattice for the simulation of one or two buckyballs in water, respectively. The system is equilibrated to obtain the desired temperature of 300 K using velocity scaling. The timestep is 0.2 fs which has been proved sufficient for stability of the trajectory and conservation of energy. The initial placement of the water molecules does not allow a predetermined bulk water density in the vicinity of the buckyball. Therefore, during the equilibration we adjust the size of the computational box by re-positioning the periodic boundaries to match the target bulk density of water ρ_0 of $997\,\mathrm{kg\,m^{-3}}$.

TABLE 1. Summary of cases considered. n_{WM} denotes the number of water molecules and n_B the number of buckyballs in the simulation. Case 12 corresponds to a simulation of the buckyball in vacuum and the cases with $n_B = 0$ correspond to a pure water simulation. r_C is the long-range cutoff we used and S is the initial wall-to-wall distance of the two buckyballs.

Case	n_{WM}	n_B	r_C(Å)	S (Å)
1	702	1	9.50	
2	702	1	12.66	
3	1304	1	15.83	
4	961	2	12.66	4.676
5	1018	2	12.66	6.676
6	1019	2	12.66	7.676
7	1123	2	12.66	8.676
8	1120	2	12.66	10.676
9	1120	2	12.66	12.676
10	729	0	9.50	
11	729	0	12.66	
12	0	1	12.66	

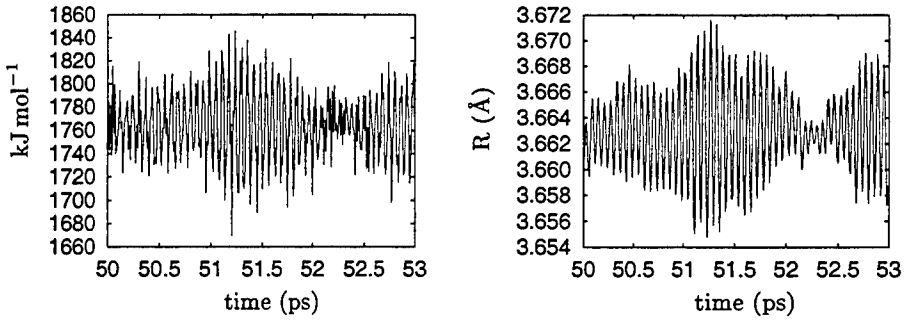

FIGURE 1. Left: The carbon-carbon Lennard-Jones interaction energy. Right: The oscillation of the radius of the buckyball.

2.2. *Buckyball in vacuum*

Previous studies of carbon nanotubes (CNT's) in vacuum and in water (Walther *et al.* 2001) indicated that the present CNT potentials provide an accurate description of the breathing mode of the CNT. The present studies extend the validation of the potentials by considering buckyballs in vacuum and in water. The simulation for the buckyball in vacuum was conducted for 6 ps with an initial 2 ps equilibration. The predicted breathing mode extracted from the time history of the radius of the buckyball is 542 cm^{-1}. This result is in good agreement with the experimental Raman spectroscopy value of 491 cm^{-1} (Venkateswaran *et al.* 1999). A useful observation is that the energy due to carbon-carbon Lennard-Jones interaction also oscillates with a frequency of 542 cm^{-1}. Introducing the buckyball in water increased the frequency of the breathing mode to 546 cm^{-1} and the Lennard-Jones potential oscillated with a frequency of 547 cm^{-1} (see also Fig. 1). A similar, small increase was also observed in the CNT case (Walther *et al.* 2001). The characteristics of all the MD trajectories are shown in Table 1.

2.3. *Buckyball in water*

Molecular-dynamics trajectories were computed for a buckyball in water. Three cases were considered: Case 1 with the buckyball surrounded by 702 water molecules and a cutoff of $3\sigma_{oo}$ (9.5Å); Case 2 with the buckyball surrounded by the same number of water molecules but with a cutoff of $4\sigma_{oo}$ (12.66Å); and Case 3 with a long-range cutoff of $5\sigma_{oo}$ and the buckyball surrounded this time by 1304 water molecules (Table 1). The size of the computational box in Cases 1 and 2 was $28 \times 28 \times 28$ Å and in Case 3 it was $34 \times 34 \times 34$ Å. We performed these three different simulations in order to get cutoff independent results. The choice of a cutoff length of $4\sigma_{oo}$ is sufficient because Cases 2 and 3 revealed no significant difference in the orientation of the water molecules and in the number of the hydrogen bonds that are built, and there was no noticeable distinction between their radial density profiles (see Fig. 2). We will present here the results from Case 2. The statistics are collected after the equilibration every 20 fs until 50 ps of the system with a total of 1500 samples.

2.3.1. *Radial density profiles*

The radial density profiles of the water for Case 2 shown in Fig. 2 are sampled in 60 spherical bins of constant spacing extending from the surface of the buckyball. The coincidence of the peaks in the oxygen and hydrogen profiles at a distance r^* of 3.2 Å measured from the surface of the buckyball indicates that the water molecules tend to be tangential to the buckyball surface. It is important to note that the closest oxygen-to-buckyball surface is detected at a distance of 2.3 Å and the closest hydrogen at distance of 1.3 Å. The difference in these distances corresponds to the OH bond length. From the plots (see also Fig. 2) we may conclude that the water molecules stand off approximately 3.2 Å from the surface of the buckyball.

2.3.2. *Angle profiles*

Let r_{BO} denote the line from the buckyball center to the oxygen atom of a water molecule. The spatial orientation of the water molecules is probed by considering the following three angles: (i) the angle ϕ formed by r_{BO} and the dipole moment, (ii) the angle ψ between r_{BO} and each of the OH-bonds and (iii) the angle α formed by r_{BO} and the normal to the plane of the water molecule (see Fig. 3). Because of the planar symmetry of water we compute the absolute value of α. The orientation of the water is computed at a distance of 2.8, 3.2, 3.9, 4.7, 5.9 and 7.4 Å from the buckyball surface to the oxygen of a water molecule, respectively. At a distance of 2.8 Å and 3.2 Å the plane of the water (α-angle) clearly shows the preference for an angle of about 180° (see Fig. 4) indicating that the HOH-plane is tangential to the surface of the buckyball. The peaks in the distributions become less pronounced, and the most probable angle shifts to 160° and 140° at distances of 3.9 and 4.7 Å, respectively. At a distance of 5.9 Å there is a slightly elevated probability for an angle of 90°. This distance corresponds to the second peak in the water density profile. Concerning the orientation of the dipole moment (ϕ-angle), at distances of 2.8 and 3.2 Å, the angles are distributed around 90° with an average of 88° (see Fig. 5). It can be seen that the distributions become broader as the distance increases. The profile for the orientation of the OH-bonds (ψ-angle: see Fig. 6) at 2.8 Å shows that the strongest preference is for an angle of about 95° which confirms, like the previous angle profiles, that the HOH-plane is tangential. As the distance is increased, the profile has its peaks at 100°, 110°, 123°, and finally 180° at a distance of 5.9 Å: this corresponds to a rotation of the plane around its normal. Finally, at a distance of 7.4 Å,

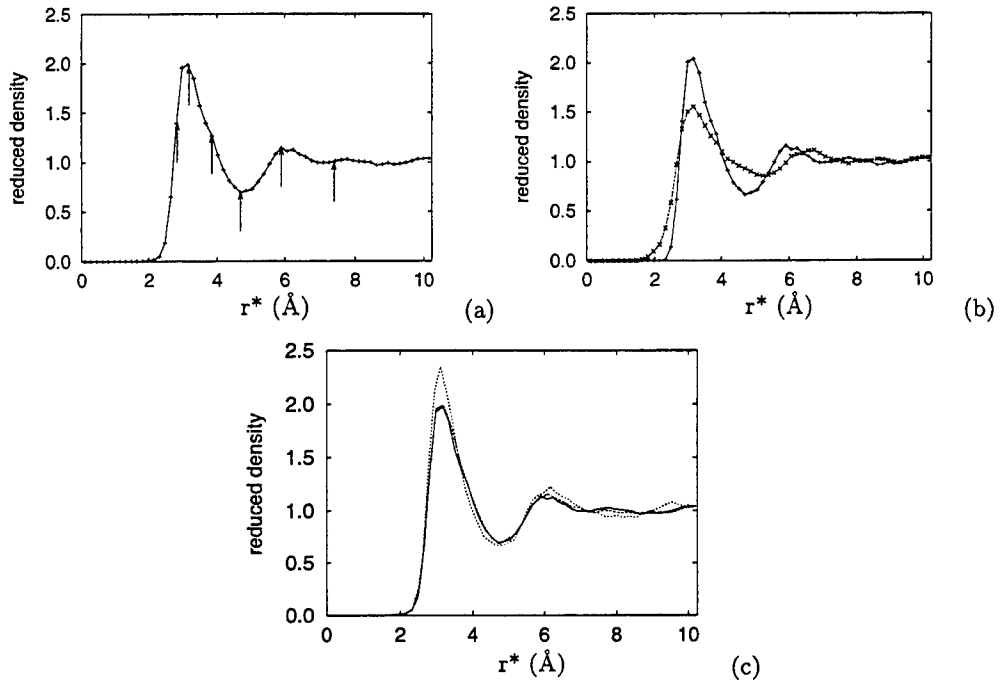

FIGURE 2. (a): The radial density profile of water for Case 2. The arrows indicate the center of the bins used for the profiles of the orientation of the water. (b): Oxygen density profile. —+—: (ρ_O/ρ_O^0) and hydrogen density profile - -×- -: (ρ_H/ρ_H^0) for Case 2 where ρ_O^0 and ρ_H^0 are the bulk densities of oxygen and hydrogen, respectively. r* is the distance from the surface of the buckyball. c): The radial density profiles for Cases 1, 2 and 3. There is no noticeable distinction between the ones of the Cases 2 and 3. In Case 1 the value of the reduced density at the first peak is 17.5 % higher.

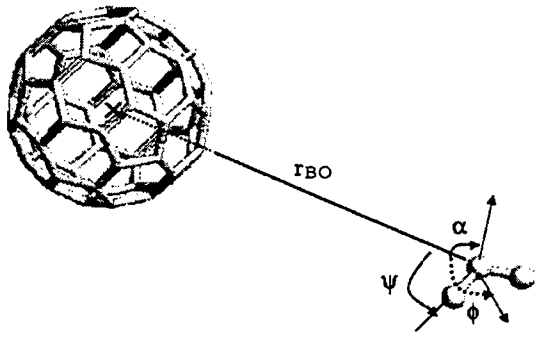

FIGURE 3. Definition of the dipole (ϕ), OH (ψ) and plane (α) angles.

bulk properties have been reached and all the angles are equally probable, as expected in bulk water.

2.3.3. *Hydrogen-bond profile*

It is well known that liquid water has a network of hydrogen bonds. The introduction of the buckyball into water results in a disruption of these hydrogen bonds. The number

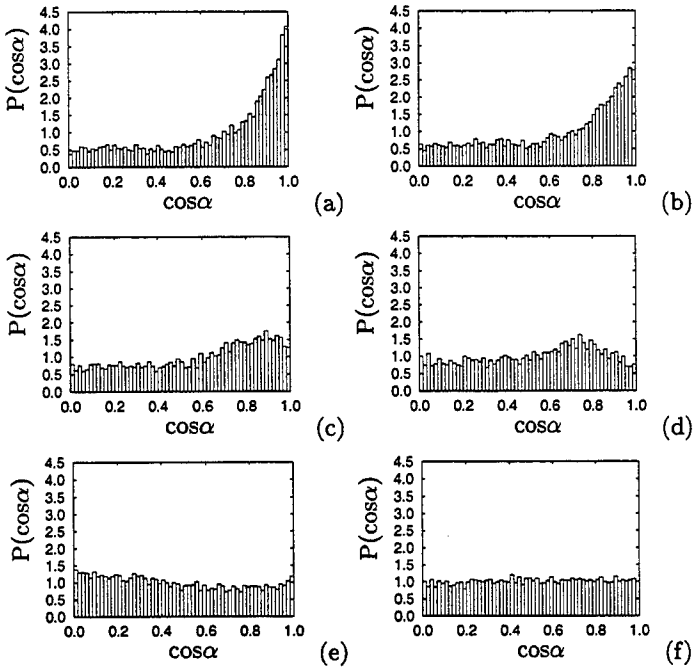

FIGURE 4. (a)-(f): The probability distributions show the orientation of the plane (α) for the distances of 2.8, 3.2, 3.9, 4.7, 5.9 and 7.4 Å from the surface of the buckyball, respectively. We compute the absolute value of the cosine because of the planar symmetry of water. (Case 2)

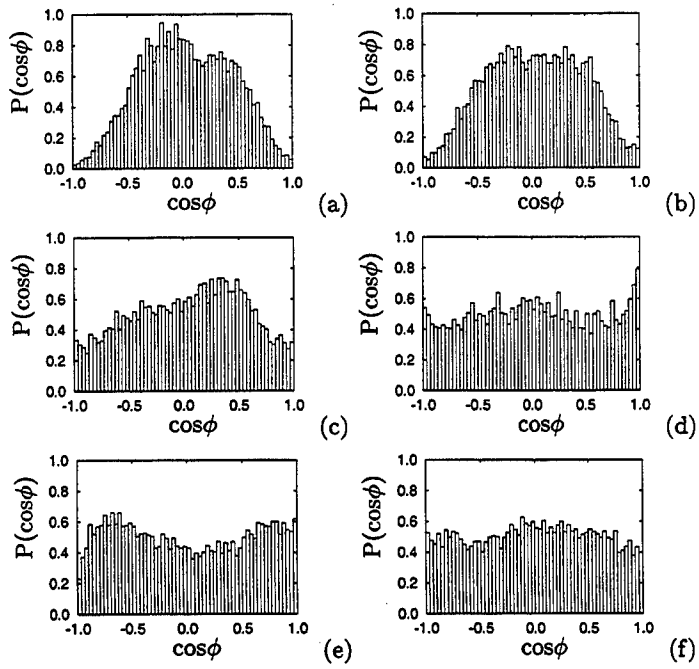

FIGURE 5. (a)-(f): The probability distributions show the orientation of the dipole moment (ϕ) for the distances of 2.8, 3.2, 3.9, 4.7, 5.9 and 7.4 Å from the surface of the buckyball, respectively. (Case 2)

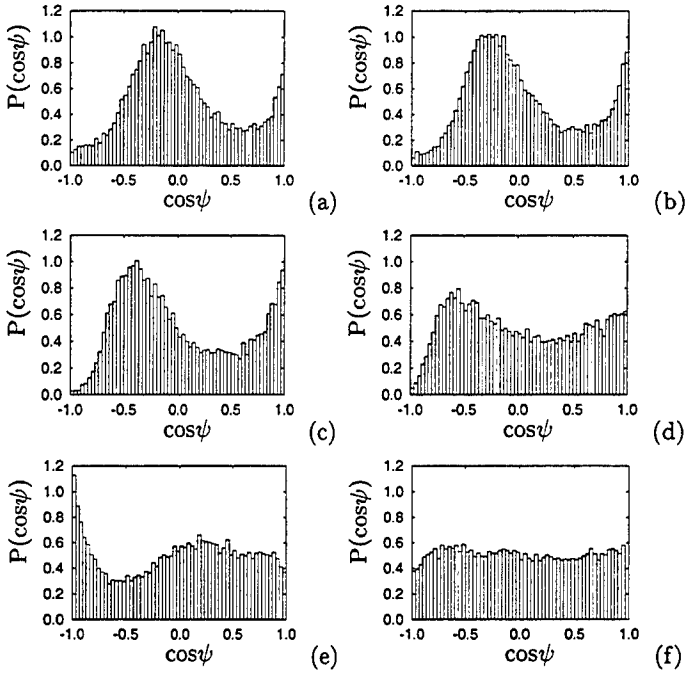

FIGURE 6. (a)-(f): The probability distributions show the orientation of the OH bonds (ψ) for the distances of 2.8, 3.2, 3.9, 4.7, 5.9 and 7.4 Å from the surface of the buckyball, respectively. (Case 2)

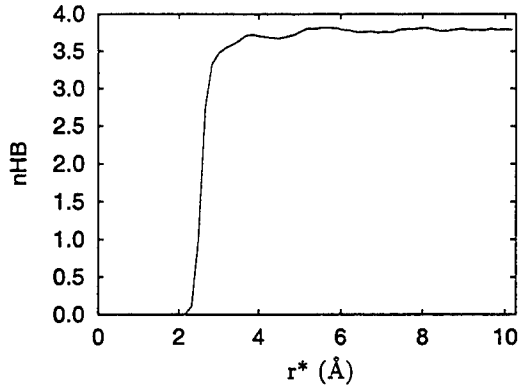

FIGURE 7. This figure shows the number of hydrogen bonds per water molecule in the vicinity of the buckyball. (Case 2)

of hydrogen bonds per water molecule (as shown in Fig. 7) decreases from 3.79 in the bulk to 2.75 at the buckyball water interface. A reduction to 3.67 is also observed at the lowest peak of the radial density profile at a distance of 4.7Å. The results are consistent with previous findings for the CNT case (Walther *et al.* 2001) and there are no noticeable curvature effects.

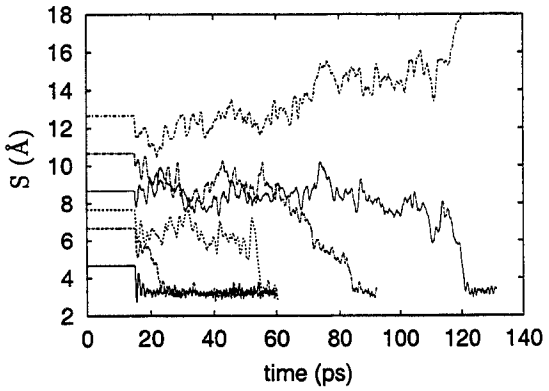

FIGURE 8. Time history of the minimum carbon-carbon (S) spacing between two buckyballs in water. The initial centre-of-mass (COM) spacing is: —: 12 Å; – –: 14 Å; - - -: 15 Å; ···: 16 Å; -·-: 18 Å; - - - -: 20 Å.

2.4. *Two buckyballs in water*

To study the hydrophobic interaction between buckyballs in water, we conduct simulations of two buckyballs initially placed at a center of mass distance of 12, 14, 15, 16, 18, and 20 Å, corresponding to a wall-to-wall distance of 4.676, 6.676, 7.676, 8.676, 10.676 and 12.676 Å, respectively (see Fig. 8). The center of mass of the buckyballs is fixed during the first 15 ps of the equilibration to allow the water to stabilize between the buckyballs. After the release of the buckyballs each system is equilibrated for another 10 ps and the simulations are continued to a maximum of 130 ps depending on the observed drying behaviour. A cutoff of $4\sigma_{oo}$ was used throughout (see Table 1 for the list of the simulations). The number of hydrogen bonds that the buckyballs will disrupt depends on the exposed surface between them and the water. That surface area is minimised when the buckyballs move close together (drying) so that there is no water between them. In this state their centers of mass will come to a distance of 10.5 Å as observed in the simulations and they will not allow the existence of water between them. For distances up to 15 Å drying takes place in less than 60 ps (Fig. 8). In Case 7 (16 Å) drying is completed at about 120 ps. The fact that in Case 8 (18 Å) the buckyballs came together in a time period smaller than in Case 7 is due to random motion of the system. When we placed the buckyballs at a distance of 20 Å, drying had not yet taken place at 120 ps. Snapshots of the atomic structure from the simulations are shown in Figs. 9, 10 and 11 for Cases 5 and 7.

2.5. *Energetics*

The introduction of (hydrophobic) fullerenes in water requires energy in order to create the accommodating cavity in the water. In a related study, the energy involved in solvating a (16,0) carbon nanotube was found to require approximately 29 kJ mol^{-1} (Walther *et al.* 2001). The corresponding surface tension of the curved CNT-water interface was found to be 127 dynes cm^{-1}, and similar to the value found for the planar liquid-vapour interface of 124 dynes cm^{-1}, indicating a negligible curvature effect.

The surface tension of the two-buckyball system considered in § 2.4 is computed for the dry, equilibrium state shown in Fig. 11. The surface area of the water is estimated as 1060.72 Å^2. This corresponds to the surface of two intersecting spheres, with the radius of the buckyball plus the distance to the first peak of the radial density profile (3.2Å). The surface energy is calculated from the difference between the average potential energy

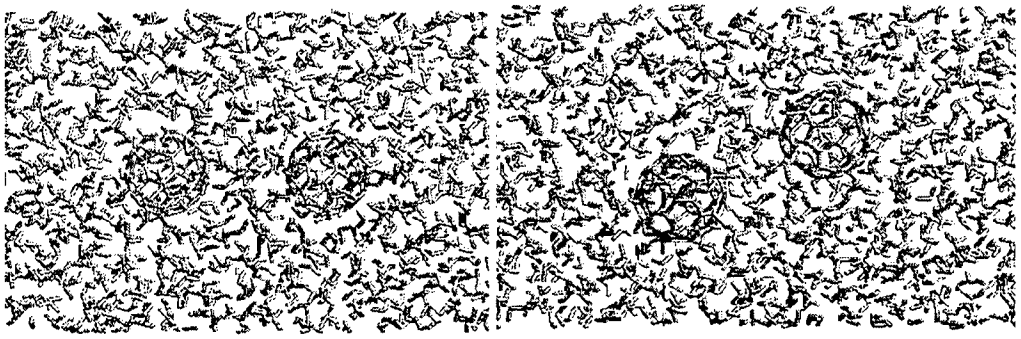

FIGURE 9. Left: The two buckyballs of Case 5 just before they are released at 15 ps. The water molecules are stable. Right: The two buckyballs of Case 7 at a center-of-mass spacing of 10.5 Å after 125 ps.

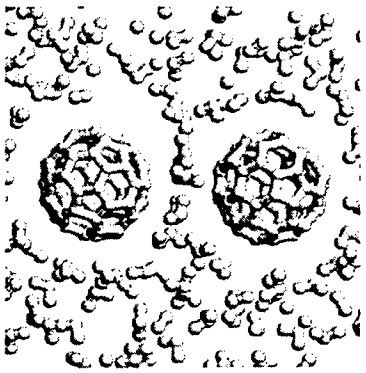

FIGURE 10. The two buckyballs of Case 5 at a center-of-mass spacing of 12.6 Å after 20 ps. The thickness of the water slab in the direction normal to the paper is 6 Å.

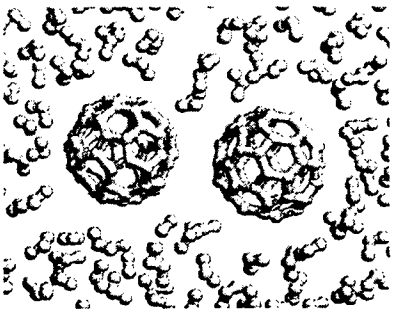

FIGURE 11. The two buckyballs of Case 5 at a center-of-mass of 10.5 Å after 60 ps. The thickness of the water slab in the direction normal to the paper is 6 Å.

(per water molecule) of bulk water, $-43.44 \pm 0.15\,\mathrm{kJ\,mol^{-1}}$ (Case 11) and the elevated potential energy of the buckyball-water system, $-42.33 \pm 0.13\,\mathrm{kJ\,mol^{-1}}$ (Case 5: 1018 water molecules). Thus the computed surface energy is 177 dynes $\mathrm{cm^{-1}}$, which consists of a 40 % increase compared to the CNT-water interface, indicating a significant curvature effect. However, further studies are being conducted to confirm this result. The systems consisting of a single buckyball in water did not allow an accurate extraction of the surface energy, due to the smallness of the surface area.

3. Conclusions and Future Work

We found that the water molecules stand approximately 3.2 Å from the buckyball, and their plane is oriented tangential to the buckyball surface at the buckyball-water interface. At the interface the number of hydrogen bonds per water molecule was found to be 2.75. We also found that the surrounding water did not affect the breathing mode of the buckyball. We showed that if we place two buckyballs in water the drying will take place within a time period of 60 ps for a distance between their centers of mass up to 15 Å. In the cases of 16 and 18 Å distance, the drying was complete within a period of 125 ps. For the case of 20 Å distance, drying did not occur at all. Also, we analysed in detail the energetics of the process of introducing two buckyballs into water. The surface energy in the case of introducing two buckyballs in water at an initial distance of 14 Å is large than in the case of carbon nanotubes (Walther *et al.* 2001), due to curvature effects. Future work will include further validation of the interacting potentials and the behaviour of functionalised buckyballs.

REFERENCES

ALLEN, M. P. & TILDESLEY, D. J. 1987 *Computer Simulation of Liquids*. Clarendon Press, Oxford.

AMAO, Y., ASAI, K. & OKURA, I. 1999 High sensitive oxygen sensor based on quenching of triplet-triplet absorption of fullerene c-60-polystyrene film. *Chemistry Letters* (1), 95–96.

GAO, G., ÇAĞIN, T. & GODDARD III, W. A. 1998 Energetics, structure, mechanical and vibrational properties of single-walled carbon nanotubes. *Nanotech.* **9**, 184–191.

VAN GUNSTEREN, W. & BERENDSEN, H. 1990 Computer simulation of molecular dynamics: Methodology, applications, and perspectives in chemistry. *Angew. Chem.* **29**, 992–1023.

HAILE, J. M. 1992 *Molecular Dynamics Simulations. Elementary Methods*. John Wiley & Sons, New York.

LEVITT, M., HIRSHBERG, M., LAIDIG, K. E. & DAGGETT, V. 1997 Calibration and testing of a water model for simulation of the molecular dynamics of proteins and nucleic acids in solution. *J. Phys. Chem. B* **101**, 5051–5061.

ODOM, T. W., HUANG, J.-L., KIM, P. & LIEBER, C. M. 2000 Structure and electronic properties of carbon nanotubes. *J. Phys. Chem. B* **104**, 2794–2809.

SAITO, R., DRESSELHAUS, G. & DRESSELHAUS, M. S. 1998 *Physical Properties of Carbon Nanotubes*. Imperial College Press, London.

TELEMAN, O., JÖNSSON, B. & ENGSTRÖM, S. 1987 A molecular dynamics simulation of a water model with intramolecular degrees of freedom. *Mol. Phys.* **60**, 193–203.

VENKATESWARAN, U. D., RAO, A. M., RICHTER, E., MENON, M., RINZLER, A., SMALLEY, R. E. & EKLUND, P. C. 1999 Probing the single-wall carbon nanotube bundle: Raman scattering under high pressure. *Phys. Rev. B* **59**, 10928–10934.

WALTHER, J. H., HALICIOGLU, T., JAFFE, R. & KOUMOUTSAKOS, P. 2001 Carbon nanotubes in water: Structural characteristics and energetics. *J. Phys. Chem. B* **105**, 9980–9987.

WANG, L., WANG, X., OTTOVA, A. & TIEN, H. 1996 Iodide sensitive sensor-based on a supported bilayer-lipid membrane containing a cluster form of carbon (fullerene C60). *Electroanalysis* **8**, 1020–1022.

Instability of Blasius boundary layer in the presence of steady streaks

By Xuesong Wu† AND Jisheng Luo‡

1. Motivation and objectives

It is well known that the instability of boundary layers is sensitive to the mean velocity profile, so that a small distortion to the basic flow may have a detrimental effect on its stability. The main interest of the present paper is in investigating the mechanisms by which a relatively weak distortion can significantly affect the instability of an otherwise-uniform Blasius flow. Specifically, we shall address two issues: (a) how the Tollmien-Schlichting instability, which operates in the absence of any distortion, is modified by a weak distortion, and (b) whether or not a weak distortion is able to cause inviscid instability.

Many factors can cause three-dimensional steady or unsteady distortions in the form of streamwise or longitudinal vortices. These include small steady or unsteady perturbations superimposed on the oncoming flow, imperfections at the leading edge, crossflow instability, and Görtler vortices induced by surface curvature, as well as certain excitation devices. Distortion of this kind also arises due to the nonlinear interaction between pairs of Tollmien-Schlichting waves. The resulting perturbed flows are spanwise-dependent but essentially unidirectional, i.e. the transverse velocity components are much smaller than the streamwise component. The instability of such transversely sheared flows has attracted a great deal of interest because it appears to be related to various aspects of the transition process, such as secondary instabilities and by-pass transition.

A distortion of particular interest occurs when the boundary layer is subject to relatively high free-stream turbulence level. As was first observed by Dryden (1936) and Taylor (1939), small low-frequency three-dimensional perturbations in the free stream produce significant distortion within the boundary layer, leading to alternating thickening and thinning of the layer in the spanwise direction. Steady disturbances also cause a similar type of variation (Bradshaw 1965). Recent experimental studies show that the distortions are in the form of elongated streaks (see e.g. Kendall 1985, Westin *et al.* 1994, Alfredsson & Matsubara 2001, and references therein), now commonly referred to as the Klebanoff mode, as a tribute to the contribution of Klebanoff (1971). These experiments have provided fairly complete quantitative data about the characteristics of Klebanoff modes themselves. However, the instability of the streaks and its role in the transition process remain poorly understood. The main obstacle of course is the random nature (in both time and space) of free-stream disturbances and the associated Klebanoff motion, which make a quantitative study extremely hard. Numerous researchers instead investigated steady distortions, induced in a controlled manner.

Hamilton & Abernathy (1994) used surface roughness elements to create single or multiple streamwise vortices. These vortices cause the distorted flow profile to have an

† Permanent address: Department of Mathematics, Imperial College, UK
‡ Department of Mechanics, Tianjin University, China

inflection point. An inflection point, however, does not always lead to the inviscid instability. Only when the distortion exceeds a certain critical magnitude do localized inviscid-instability waves start to appear. These waves may decay, or occasionally develop into turbulent spots if the distortion strength is just above the critical value. As the distortion is increased further, the local instability leads to persistent self-sustaining turbulent spots.

Asai, Fukuoka & Nishioka (2000) and Asai (2001) investigated in detail the instability of an isolated streak, which was produced by a small screen set normal to the wall. The low-speed streak was shown to support both symmetric (varicose) and antisymmetric (sinuous) modes. These investigators mapped out the amplitude development as well as the spatial structure of each mode.

Bakchinov *et al.* (1995) generated periodically-distributed longitudinal vortices by arranging roughness-element arrays in a regular spacing along the spanwise direction. For strong modulation, inviscid-instability modes were found to develop out of the background disturbances, and their frequencies were well above those of unstable TS waves in the Blasius flow. At moderate modulation, instability waves with typical frequencies of T-S waves can be observed, but they amplify more rapidly than in the Blasius flow.

Obviously, the instability of boundary layers subject to finite-amplitude steady distortions is an interesting and important problem in its own right, and an attack on it requires a major numerical study. The main concern of this paper is with the sensitivity of the boundary-layer instability to a steady distortion. For this purpose, it is appropriate to consider the case where the distortion is relatively weak that it represents a sort of 'imperfection'. A weak distortion has the advantage of being more amenable to analytical treatment, yet as we shall argue, the resulting simple model may well offer relevant insights to the case of stronger distortion.

There have been numerous theoretical studies of the instability of shear flows (boundary layers or channel flows) perturbed by distortions in the form of streaks. The interested reader is referred to Anderson *et al.* (2001) for relevant references. Often the streaks were modeled in a rather *ad hoc* fashion. In the present work, we insist that the distortions must be realizable, at least in principle, i.e. they may be generated by either by a specific excitation device or by external disturbances. At any rate, they must be appropriate (approximate) solutions to the Navier-Stokes equations. To fix the idea, we consider the instability of the steady distortion that has been considered by Goldstein & Wundrow (1995), The basic observation is that the Blasius profile has small curvature near the wall, so that even a small distortion may lead to an inflection point and possibly to essentially-inviscid instabilities.

The essential physical and analytical insights can be gained by an asymptotic approach based on a high-Reynolds-number assumption, which stands as the only means for providing a self-consistent mathematical description of the key process involved.

2. Theoretical considerations

2.1. *Formulation*

We consider the two-dimensional incompressible boundary layer due to a uniform flow U_∞ past a semi-infinite flat plate. As in Goldstein & Wundrow (1995), a small-amplitude spanwise-dependent motion is assumed to be imposed at a distance L downstream from the leading edge. The Reynolds number is defined as

$$R = U_\infty L/\nu \,, \tag{2.1}$$

where ν is the kinematic viscosity. We shall assume that $R \gg 1$.

The flow is to be described in the Cartesian coordinate system (x, y, z), with its origin at the location where the crossflow is introduced, where x, y and z denote distances in the streamwise, normal and spanwise directions respectively, and they are all non-dimensionalized by $\delta = LR^{-1/2}$, the boundary-layer thickness at $x = 0$. The time variable t is normalized by δ/U_∞. The velocity (u, v, w) is non-dimensionalized by U_∞, while the non-dimensional pressure p is introduced by writing the dimensional pressure as $(p_\infty + \rho U_\infty^2 p)$, where p_∞ is a constant and ρ is the fluid density.

The profile of the Blasius boundary layer, $U_B(y)$, has the behaviour that as $y \to 0$,

$$U_B(y) \to \lambda y - \frac{\lambda^2}{48} y^4 + \dots$$

where the skin friction

$$\lambda = \lambda_0 (1 + x R^{-\frac{1}{2}})^{-1/2} \quad \text{with} \quad \lambda_0 \approx 0.332 \,. \tag{2.2}$$

Let Λ denote the characteristic length scale over which the spanwise variation of the imposed flow occurs. We assume that Λ is much larger than the local boundary-layer thickness δ, i.e.

$$\sigma \equiv \frac{\delta}{\Lambda} \ll 1 \,,$$

so that the variation of the distortion can be described by the slow variable

$$Z = \sigma z \,. \tag{2.3}$$

A crossflow $\epsilon_M W_0(y, Z)$ is imposed at $x = 0$ by some excitation device. In the laboratory this may be achieved by inserting a thin wire with non-uniform cross-section into the main part of the boundary layer. A small screen set normal to the wall, as in the experiments of Asai *et al.* (2000), probably produces a similar effect.

The mean-flow distortion so generated is analyzed in detail by Goldstein & Wundrow (1995), who show that the flow in the region $x = O(\sigma^{-1})$ is fully interactive, but the distortion is too weak to affect the instability. The important location is at $x = O(\sigma^3 R^{\frac{1}{2}})$, where the perturbed streamwise velocity profile develops an inflection point in the wall layer $y = O(\sigma)$, if the imposed crossflow has a magnitude $\epsilon_M \sim R^{-\frac{1}{2}} (\ln \sigma)^{-1}$. For *periodic distortion*, a pair of oblique modes is in resonance with the distortion if the spanwise wavelength of the former is twice that of the latter. The characteristic streamwise wavelength of the instability modes is found to be comparable with that of the mean-flow distortion. The growth rate induced by the resonance has the same order of magnitude as that due to viscosity if $\sigma = O(R^{-\frac{1}{20}})$ but is larger if $\sigma \gg R^{-\frac{1}{20}}$. In the latter case, the instability is inviscid.

The main interest of the present paper will be *localized distortion* since distortions of this form were produced and studied in number of experiments. It will be shown that an inviscid instability may occur in a region farther downstream than that considered by Goldstein & Wundrow (1995).

The region in which this instability operates, as well as its characteristic time and length scales, can be determined by a scaling argument based on three considerations. First, suppose that at a typical streamwise location $x \sim l \gg O(\sigma^3 R^{\frac{1}{2}})$, the wall layer has a width $y \sim \hat{\sigma}$. Then the balance between the advection term $U_B \frac{\partial}{\partial x}$ and the diffusion term $R^{-\frac{1}{2}} \frac{\partial^2}{\partial y^2}$ in the streamwise momentum equation requires that

$$\frac{\hat{\sigma}}{l} \sim \frac{R^{-\frac{1}{2}}}{\hat{\sigma}^2} \,. \tag{2.4}$$

Secondly, for the distortion to be able to induce an essentially-inviscid instability, its curvature must be comparable to the $O(\hat{\sigma}^2)$ curvature of the Blasius flow in the wall layer, that is

$$\frac{\epsilon_D}{\hat{\sigma}^2} \sim \hat{\sigma}^2 \ , \tag{2.5}$$

where ϵ_D stands for the magnitude of the streamwise velocity of the distortion. Thirdly, if we seek instability modes with $O(\hat{\sigma})$ streamwise wavenumbers, then their growth rate would be of $O(\hat{\sigma}^4)$. It turns out that such modes exist if

$$\hat{\sigma}^5 \sim \sigma^2 \ . \tag{2.6}$$

This relation ensures that the spanwise modulation appears at the same order as the streamwise evolution in the final amplitude equation; this point will become clear later.

It follows from Eqs. (2.4) and (2.6) that the instability will operate in the region where $x \sim l = O(R^{\frac{1}{2}}\sigma^{\frac{6}{5}})$, and so we introduce the variable

$$\hat{x} = x/(\sigma^{\frac{6}{5}}R^{\frac{1}{2}}) \ . \tag{2.7}$$

For $\hat{x} = O(1)$, the instability modes that the perturbed mean flow can support have streamwise wavelength of $O(\sigma^{-\frac{2}{5}})$, much shorter than the $O(\sigma^{-1})$ spanwise length scale of the distortion. The phase speed is $O(\hat{\sigma})$ so that the frequency is $O(\sigma^{\frac{4}{5}})$. Without losing generality, in the rest of the paper we put

$$\hat{\sigma} = \sigma^{\frac{2}{5}} \ .$$

2.2. *Solution for the mean-flow distortion*

The solution for the distortion was considered in detail by Goldstein & Wundrow (1995). The required solution corresponds to the downstream limit of theirs, and also it is only necessary to present the solution in the viscous wall region, which has a width of $O(\sigma^{\frac{2}{5}})$. The appropriate transverse variable is

$$Y = \frac{y}{\sigma^{\frac{2}{5}}} \ . \tag{2.8}$$

The mean flow expands as

$$U = \hat{\sigma}\lambda_0 Y + \hat{\sigma}^4(\tilde{U} - \frac{\lambda_0^2}{48}Y^4 - \frac{1}{2}\lambda_0\hat{x}Y) + \dots \ , \tag{2.9}$$

$$W = R^{-\frac{1}{2}}\sigma^{-\frac{3}{5}}(\tilde{W} + \dots) \ . \tag{2.10}$$

The solution is simply the first terms of (3.43) in Goldstein & Wundrow (1995), namely

$$\tilde{U} = \bar{\sigma}\hat{x}B'(Z)F(\eta) \ , \quad \tilde{W} = \bar{\sigma}B(Z)G(\eta) \ , \tag{2.11}$$

where the similarity variable is defined as

$$\eta = (\lambda_0/\hat{x})^{\frac{1}{3}}Y \ . \tag{2.12}$$

The functions F and G satisfy the equations

$$F''' + \frac{1}{3}\eta^2 F'' - \frac{2}{3}\eta F' = -G, \quad G'' + \frac{1}{3}\eta^2 G' = 0 \ . \tag{2.13}$$

They are subject to the boundary conditions

$$F = F'' = G = 0 \quad \text{at} \quad \eta = 0 \ , \tag{2.14}$$

$$F \to \ln\eta\ , \quad G \to 1 \quad \text{as} \quad \eta \to \infty. \tag{2.15}$$

The boundary-value problem Eqs. (2.13)–(2.15) was solved numerically.

It should be pointed out that the curvature alteration in the wall layer is much larger than that in the main region despite the fact the streamwise velocities in both layers have the the same order of magnitude. This feature turns out to be important for the instability of the perturbed flow.

3. Results

3.1. *Linear instability*

When $\hat{x} = O(1)$, the distortion to the mean flow is still small in the whole flow field. An important point to note is that in the viscous wall region the curvature of the mean-flow distortion is comparable with that of the original Blasius flow, that is, the curvature of the total mean flow is altered by $O(1)$ in relative terms, and moreover becomes spanwise-dependent. This leads to a fundamental change of the instability property.

As was indicated by the scaling argument in Section 2, the admissible modes have streamwise wavenumbers of $O(\hat{\sigma})$, frequencies of $O(\hat{\sigma}^2)$ and growth rates of $O(\hat{\sigma}^4)$; so we introduce

$$\zeta = \hat{\sigma}\alpha x - \hat{\sigma}^2\omega t\ , \quad X = \hat{\sigma}^4 x\ , \tag{3.1}$$

to describe the rapid oscillation and the relatively slow amplification of the modes respectively, where α and ω are the scaled wavenumber and frequency. We expand α and the phase speed $c \equiv \omega/\alpha$ as

$$\alpha = \alpha_0 + \hat{\sigma}\alpha_1 + \dots\ , \quad c = \frac{\omega}{\alpha} = c_0 + \hat{\sigma}c_1 + \dots\ .$$

The most unstable modes that the perturbed flow can support must have a spanwise length scale comparable with that of the distortion. Modes with a shorter spanwise length scale may be treated in a quasi-planar manner, but they have smaller growth rates, and moreover their phase speeds would be a function of Z, contradicting the experimental observation of Asai (2001) and Bakchinov *et al.* (1995) that the phase speed is constant along the spanwise direction. Such modes will be discarded. Therefore the spanwise variation of relevant instability waves is described by the variable Z. In the main part of boundary layer, the modes take the form, to leading order,

$$u = \epsilon A(X, Z)\bar{u}_1(y)\,\mathrm{e}^{\mathrm{i}\zeta} + \text{c.c.} + \dots, \tag{3.2}$$

where ϵ represents the magnitude of the modes, and A is the amplitude function.

Since the wavelength of the instability modes is long compared with the boundary layer thickness, the linear instability problem is governed by a five-zoned asymptotic structure that is akin to that for the upper-branch instability of the unperturbed Blasius boundary layer (cf. Bodonyi & Smith 1981, Goldstein & Durbin 1986). It consists of the upper layer, the main layer, the Tollmien layer, the viscous Stokes layer as well as the critical layer centered at the position where the basic flow velocity equals the phase velocity c.

The solution in each of these regions can be obtained by following what is now a fairly routine procedure (see e.g. Wu, Stewart & Cowley 1996). Matching these solutions gives the leading-order dispersion relation

$$c_0 = \frac{\alpha_0}{\lambda_0}\ , \tag{3.3}$$

and the relation for the growth rate

$$A_X - \frac{\mathrm{i}}{4\alpha_0} A_{ZZ} = (c^+ - c^-) + \Big[\frac{\lambda_0^2}{2R^{\frac{1}{4}}\hat{\sigma}^5(2\alpha_0 c_0)^{\frac{1}{2}}} + \mathrm{i}\chi_0\Big]A \,, \tag{3.4}$$

where $(c^+ - c^-)$ is the jump across the critical layer. In the linear regime ($\epsilon \ll 1$),

$$c^+ - c^- = \pi c_0 Y_c \Big\{-\frac{c_0^2}{4} + \tilde{U}_{YY}(Y_c, Z)\Big\}A \,, \tag{3.5}$$

where $Y_c = c_0/\lambda_0$ is the scaled critical level. Inserting Eq. (3.5) into Eq. (3.4) gives

$$A_X - \frac{\mathrm{i}}{4\alpha_0} A_{ZZ} = \Big(\gamma_0 + \gamma(Z)\Big)A \,, \tag{3.6}$$

where

$$\gamma_0 = -\frac{\pi c_0^4}{4\lambda_0} + \frac{\lambda_0^2}{2R^{\frac{1}{4}}\hat{\sigma}^5(2\alpha_0 c_0)^{\frac{1}{2}}} \,, \tag{3.7}$$

$$\gamma(Z;\hat{x}) = \pi c_0^2 (\frac{\hat{x}}{\lambda_0})^{\frac{1}{3}} F''(\eta_c)\bar{\sigma}B'(Z) \equiv \tilde{\gamma}(\hat{x})\bar{\sigma}B'(Z) \,, \tag{3.8}$$

with $\eta_c = \frac{c_0}{\lambda_0}(\frac{\lambda_0}{\hat{x}})^{\frac{1}{3}}$. Here use has been made of Eqs. (2.11) and (2.12), and the logarithmic factor $\bar{\sigma}$ has been absorbed into the definition of B. Obviously γ_0 is the growth rate in the absence of the distortion, with the second term in γ_0 representing the contribution from the viscous Stokes layer, which is the sole instability mechanism when the distortion is absent.

The derivation of Eq. (3.6) is based on the fact that the major curvature alteration occurs in a wall layer. As is indicated by Eq. (3.6), in this case the curvature alteration in the wall region is the sole quality that characterizes the instability of the perturbed flow; the distortion in the main part of the boundary layer turns out to be largely irrelevant.

Equation (3.6) can be viewed as a Schrödinger equation with a purely imaginary potential $\mathrm{i}\gamma(Z)$. It admits solution of the form

$$A = \Phi(Z)\,\mathrm{e}^{(a+\gamma_0)X} \,, \tag{3.9}$$

where a is a complex constant, and $\Phi(Z)$ satisfy

$$\Phi_{ZZ} = 4\mathrm{i}\alpha_0\Big(\gamma(Z) - a\Big)\Phi \,. \tag{3.10}$$

For localized $\gamma(Z)$, the boundary conditions are

$$\Phi(Z) \to \mathrm{e}^{\mp(-4\mathrm{i}\alpha_0 a)^{\frac{1}{2}}Z} \quad \text{as} \quad Z \to \pm\infty \,, \tag{3.11}$$

where the square root is taken to be the one with a positive real part so that Φ decays to zero $\pm\infty$. We can derive a general result similar to the familiar 'semicircle theorem':

$$\min\gamma(Z) < \Re(a) < \max\gamma(Z) \,. \tag{3.12}$$

Equation (3.10) with Eq. (3.11) forms an eigenvalue problem to determine a. The real part of a represents the *excess growth rate* induced by the mean-flow distortion or streak. Depending on the size of $\hat{\sigma}$, the instability may be of quite different nature. Equations (3.7) and (3.8) indicate that the growth rate due to the viscosity is negligible if $\hat{\sigma} \gg R^{-\frac{1}{20}}$ or equivalently if the magnitude of the streamwise velocity of the distortion satisfies

$$\epsilon_D \gg R^{-\frac{1}{5}} \,.$$

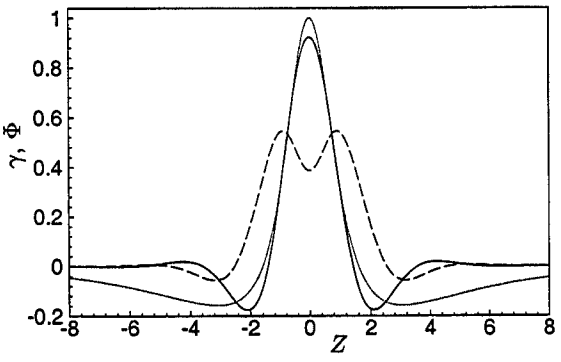

FIGURE 1. Distribution of distortion and eigenfunction, ····· distortion, ——— Φ_r ---- Φ_i.

This implies that, when the distortion exceeds some threshold, the instability becomes essentially inviscid, with the growth rate

$$\kappa \equiv a_r - \frac{\pi c_0^4}{4\lambda_0} , \tag{3.13}$$

although it may be argued that inclusion of the viscous growth in this case would give a more general result. When $\epsilon_D \sim R^{-\frac{1}{5}}$, the distortion provides a modification to the viscous growth rate, and the modes may be viewed as a kind of *modified T-S waves*, even though they do not necessarily reduce to the usual T-S waves at the zero-distortion limit.

The eigenvalue problem Eqs. (3.10)–(3.11) is solved numerically for a spanwise distribution of the form

$$B'(Z) = B_0 \,\mathrm{sech}(\frac{Z}{d}) \tanh Z , \tag{3.14}$$

where d is a measure of the spanwise length scale of the distortion. Figure 1 depicts a typical shape, which is quite similar to that in the experiments of Asai *et al.* (2000) and Asai (2001). Also shown in the Figure is a typical distribution of the eigenfunction Φ. Clearly, the instability mode is confined to the region of the mean-flow distortion, and decays rapidly away from it. The mode is symmetric, i.e. varicose, in nature. No anti-symmetric (or sinuous) mode has been found. Asai *et al.* (2000) attributed the varicose modes to the inflection point in the normal direction $U_{YY} = 0$, and the sinuous modes to the inflection in the spanwise profile, $U_{ZZ} = 0$. The former is present in our theory, but the latter is absent. That sinuous modes are absent from our results is consistent with the conclusion of Asai *et al.*

In order to understand the general properties of the problem, calculations were first performed for the artificial case where $\tilde{\gamma} = 1$. The variation of a_r with B_0 is plotted in Fig. 2a for two fixed values of d. It shows that $a_r > 0$ when the distortion exceeds a *threshold magnitude* B_c. Below B_c, the localized mode does not exist. Instead there exists a continuous spectrum for which a is purely imaginary so that Φ is only bounded at $Z = \pm\infty$. The continuous spectrum can be viewed as the usual T-S waves, whose shape is deformed by $\gamma(z)$ but whose growth rates are not affected. The existence of a threshold means that the localized modes do not reduce to the usual T-S waves as the distortion is reduced; instead they merge with the continuous spectrum.

Figure 2b shows the variation of a_r with d. For each fixed B_0, there exists a threshold

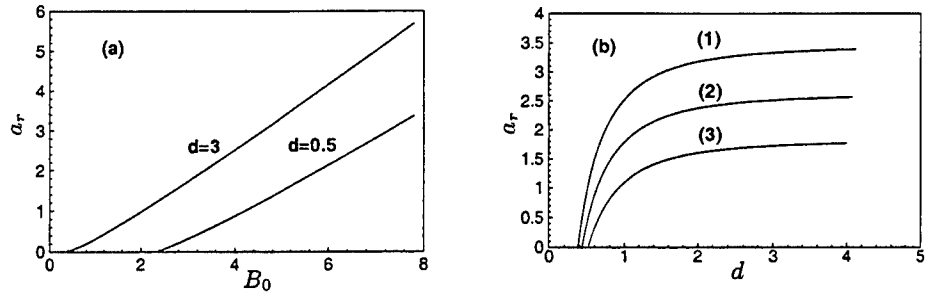

FIGURE 2. Variation of a_r with B_0 and d. Curves (1)-(3) correspond to $B_0 = 5$, 4 and 3.

d_c above which a localized mode comes into existence. The growth rate increases with the spanwise length scale d, and quickly saturates at the 'two-dimensional limit' when d is large enough. This conclusion is in agreement with the experimental finding of Asai (2001), although in his experiments the distortion has a rather large magnitude. It seems reasonable to suggest that the present simple theory captures some generic feature of the instability.

Next we present the instability results for the particular distortion considered in Section 2, for which $\tilde{\gamma}$ depends on $\hat{x}$ and is evaluated by solving Eqs. (2.13)–(2.15) numerically. It is found that $F > 0$ but $F'' < 0$, and as a result $\tilde{\gamma} < 0$ (see Eq. (3.8)). Therefore according to the result shown in Fig. 2, inviscid instability is possible only for $B_0 < 0$, i.e. when the distortion is characteristic of a low-speed streak.

For a given B_0, the inviscid growth rate $\kappa(\omega, \hat{x})$ as defined by Eq. (3.8) will be a function of $\hat{x}$ and $\omega = \alpha_0 c_0$, the frequency of the instability mode. As shown in Fig. 3a, in the streamwise region in which the distortion is significant, the perturbed flow supports a band of instability modes. The instability will manifest itself as an oscillation of the streak. In Fig. 3b, we plot the variation of the growth rate κ with $\hat{x}$ for three typical values of ω. As is illustrated, a mode with a suitable frequency experiences amplification in a finite streamwise region, beyond which it decays. The spatial extent and the frequency range of the unstable modes can best be demonstrated by plotting the contours of the growth rate $\kappa(\omega, \hat{x})$ in the $\hat{x} - \omega$ plane; see figure 4. For $B_0 = -7$, the perturbed flow is unstable in the streamwise window between $\hat{x} \approx 1.2$ and $\hat{x} \approx 19$. The unstable frequency band varies with $\hat{x}$, but roughly speaking the overall range is between $\omega = 0.2$ and 1.2. The frequency of the most unstable modes in the upstream end is fairly small, but increases with the downstream distance, implying that the oscillation of the streak will become progressively more rapid.

3.2. *Nonlinear instability*

As an instability mode amplifies, nonlinear effects may become important. For an instability wave with an asymptotically small growth rate, it is now well recognized that the dominant nonlinear interactions will first take place within the critical layer to produce a velocity jump across this layer. For reviews, see e.g. Goldstein (1994) and Cowley & Wu (1994). For the present problem, the nonlinear jump becomes comparable with the linear jump when

$$\epsilon = \hat{\sigma}^{\frac{17}{2}} . \tag{3.15}$$

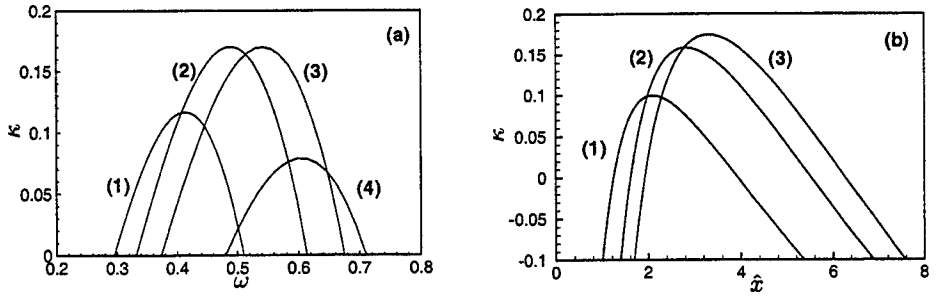

FIGURE 3. Inviscid growth rates κ of localized modes for $B_0 = -6$. (a) κ v.s. ω at $\hat{x} = 2$, 3,4 and 6, represented by curves (1)-(4) respectively. (b) κ v.s $\hat{x}$ for $\omega = 0.37$, 0.45 and 0.50 represented by curves (1)-(3) respectively.

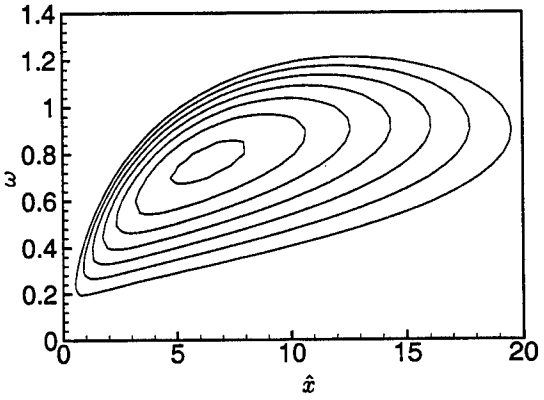

FIGURE 4. Contours of growth rates ($B_0 = -7$). The outermost contour corresponds to the neutral curve $\kappa(\omega, \hat{x}) = 0$.

We also assume that the Reynolds number scales with $\hat{\sigma}$ as follows

$$R^{-\frac{1}{2}} = r\hat{\sigma}^{13} \tag{3.16}$$

so that the viscous diffusion appears as a leading-order effect in the critical layer, where r is a parameter of order one, reflecting the effect of viscosity. In passing we note that the experiments of Bakchinov *et al.* (1995), in which the instability of a Blasius boundary layer subject to a spanwise-dependent distortion was investigated, point to the existence of a well defined critical layer, in which the mode attains its largest magnitude.

The nonlinear jump is the same as that calculated by Wu (1993) and Wu *et al.* (1996). Inserting that jump into Eq. (3.4), we obtain the amplitude equation that describes the nonlinear instability of the perturbed flow

$$A_X - \frac{\mathrm{i}}{4\alpha_0} A_{ZZ} = \Big(\gamma_0 + \gamma(Z)\Big)A + \mathrm{i}\,N(X, Z)\ , \tag{3.17}$$

where the nonlinear term

$$N = \int_0^\infty \int_0^\infty K(\xi, \eta|s)\Big\{\xi^3 A(X-\xi)A(X-\xi-\eta)A^*_{ZZ}(X-2\xi-\eta)$$

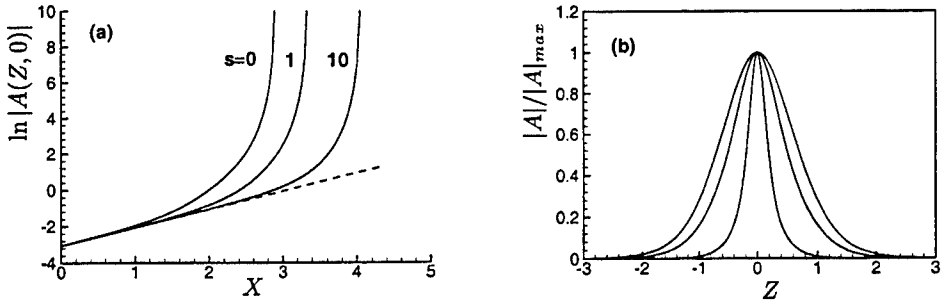

FIGURE 5. Nonlinear evolution of a localized mode ($\omega = 0.8$, $\hat{x} = 6.5$). (a) The amplitude on the symmetry plane $\ln|A(X,0)|$ *v.s.* X for $s = 0$ (purely inviscid case), 1 and 10. ····· the linear limit. (b) Spanwise distribution of $|A|$ at $X = 3.02$, 3.54 for $s = 1$, showing self-focusing as X increases. The least 'compact' of the three curves corresponds to the linear limit.

$$+\xi^2\eta A(X-\xi)\Big[A(X-\xi-\eta)A_Z^*(X-2\xi-\eta)\Big]_Z$$
$$+\xi^3\Big[A(X-\xi)A(X-\xi-\eta)A_Z^*(X-2\xi-\eta)\Big]_Z\Big\}\,\mathrm{d}\xi\,\mathrm{d}\eta\,, \quad (3.18)$$

with

$$K(\xi,\eta|s) = \mathrm{e}^{-s(2\xi^3+3\xi^2\eta)}\,, \quad s = \frac{1}{3}\alpha_0^2\lambda_0^2 r\,.$$

In Eq. (3.17), the amplitude function has been suitably renormalized so that the coefficient multiplying $\mathrm{i}N$ is unity. The amplitude A should match with the linear solution upstream, and so we have

$$A \to \Phi(Z)\,\mathrm{e}^{(a+\gamma_0)X} \quad \text{as} \quad X \to -\infty\,. \quad (3.19)$$

The nonlinear amplitude equation Eq. (3.17) was solved for the localized distortion. The mode was chosen to be the most unstable one in Fig. 4, which exists at $\hat{x} \approx 6.5$ and has frequency $\omega = 0.8$. The nonlinear evolution of $|A(X,0)|$, the amplitude on the symmetry plane, is shown in Fig. 5a for three viscous parameter values. Nonlinearity enhances the amplification, and apparently leads to a singularity at a finite distance downstream. Viscosity delays the formation of the singularity but cannot eliminate it. Figure 5b shows that the nonlinear effect deforms the shape of the mode, and a singularity of self-focusing type appears to be forming at $Z = 0$. A plausible structure for this singularity was proposed in Wu (1993). In the vicinity of the singularity, the present theory breaks down and strong three-dimensionality may act to 'regularize' the solution.

4. Conclusions and discussions

In this paper, we have shown that the instability of Blasius boundary layer can be significantly modified, and even fundamentally altered, by certain small-amplitude distortions which feature low-speed streaks. This occurs when the curvature of the distortion becomes comparable to that of the Blasius profile in a suitable vicinity of the wall. A self-consistent asymptotic theory is presented for distortions whose spanwise length scale is larger than the boundary-layer thickness. The instability of the perturbed flow is shown

to be governed by a remarkably simple system, a Schrödinger equation with a purely imaginary potential.

A moderate distortion induces an excess growth rate comparable to that due to viscosity, and the instability modes can be viewed as a kind of modified T-S wave. This modification however is non-trivial because the spanwise shape is dictated by the distortion. The modes do not reduce to the usual T-S waves in the zero-distortion limit.

When the strength of the distortion exceeds a certain threshold, essentially-inviscid localized instability arises. The characteristic streamwise wavelength of the instability modes is much shorter than the spanwise length scale of the distortion, and their characteristic frequencies are higher than those of typical T-S waves on Blasius flow. Also the instability occurs in a limited streamwise window, and hence on the purely linear basis, the instability modes will die out. However they can enter a nonlinear regime if a significant magnitude is attained. The continued nonlinear development of these modes is governed by a modified form of the evolution equation derived by Wu (1993), and the nonlinear effect is found to be strongly destabilizing, causing the amplitude to break down rapidly in the form of a finite-distance singularity. The instability may lead to patches of streak oscillation, which may well breakdown into turbulent spots.

While the theory is built upon a set of rather restricted asymptotic relations, it does appear to be capable of reproducing the major laboratory observations qualitatively. For instance, the existence of a threshold magnitude and the occurrence of oscillation patches are in agreement with the conclusions of Hamilton & Abernathy (1994). As mentioned above, the theoretical prediction that the growth rate increases with the spanwise length scale of the distortion is consistent with the measurements of Asai (2001). The predicted frequency range of the inviscid unstable modes, as well as the excess growth exhibited by the T-S waves confirm the findings of Bakchinov *et al.* (1995).

It should be noted that the distortions in the experiments are actually comparable with the basic Blasius flow so that they must be governed by nonlinear equations as opposed to the linear equations employed in our theory. Based on the above broad agreement, it seems reasonable to argue that the nonlinear structure of the distortion should not affect the qualitative feature of the instability, and that the simple model captures the key physics of the instability. From the qualitative point of view, the failure to describe the sinuous instability mode seems to be the only obvious shortcoming of the model.

The work of XW was carried out during his sabbatical in 2001 at ICASE NASA Langley and Center for Turbulence Research, Stanford University (USA). The hospitality and financial support of these institutions are gratefully acknowledged. It is a great pleasure to thank Prof. H. Zhou, Prof. Parviz Moin, Prof. Paul Durbin, Prof. W. C. Reynolds and Prof. P. Bradshaw for helpful discussions and comments. Thanks also go to Dr. M. Asai for making available a preprint of his experimental results.

REFERENCES

ANDERSSON, P., BRANDT, L., BOTTARO, A. & HENNINGSON, D. S. 2001 On breakdown of boundary layer streaks. *J. Fluid Mech.* **428**, 29-60.

ASAI, M., FUKUOKA, A. & NISHIOKA, M. 2000 Experimental investigation of the instability of low-speed streak in a boundary layer. In *Proc. of the ICTAM 2000, Chicago.*

ASAI, M. 2001 Development of instability modes of a low-speed streak. (Preprint).

BAKCHINOV, A. A., GREK, G. R., KLINGMANN, B. G. B. & KOZLOV, V. V. 1995 Transition experiments in a boundary layer with embedded streamwise vortices. *Phys. Fluids* **7**, 820-832.

BODONYI, R. J. & SMITH, F. T. 1981 The upper-branch stability of the Blasius boundary layer, including non-parallel flow effects. *Proc. R. Soc. Lond.* A**373**, 65-92.

BRADSHAW, P. 1965 The effect of wind-tunnel screens on nominally two-dimensional boundary layers. *J. Fluid Mech.* **22**, 679-687.

COWLEY, S. J. & WU, X. 1994 Asymptotic methods and solutions in transition modeling. In *Progress in Transition Modeling*, AGARD Report 793.

DRYDEN, H. L. 1936 Air flow in the boundary layer near a plate. *NACA* Report 562.

GOLDSTEIN, M. E. 1994 Nonlinear interactions between oblique instability waves on nearly parallel shear flows. *Phys. Fluids* A**6**, 724-735.

GOLDSTEIN, M. E. & DURBIN, P. A. 1986 Nonlinear critical layers eliminate the upper branch of spatially growing Tollmien-Schlichting waves. *Phys. Fluids* **29**, 2334-2345.

GOLDSTEIN, M. E. & WUNDROW, D. W. 1995 Interaction of oblique instability waves with weak streamwise vortices. *J. Fluid. Mech.* **284**, 377-407.

HAMILTON, J. & ABERNATHY, F. 1994 Streamwise vortices and transition to turbulence. *J. Fluid Mech.* **264**, 185-212.

KENDALL, J. M. 1985 Experimental study of disturbances produced in pre-transitional laminar boundary layer by weak free stream turbulence. *AIAA* Paper 85-1695.

KLEBANOFF, P. S. 1971 Effect of free-stream turbulence on a laminar boundary layer. *Bulletin. Am. Phys. Soc.* **16**.

MATSUBARA, M. & ALFREDSSON, P. H. 2001 Disturbance growth in boundary layers subjected to free-stream turbulence. *J. Fluid Mech.* **430**, 149-168.

TAYLOR, G. I. 1939 Some recent developments in the study of turbulence. In *Proc. of the Fifth International Congress for Applied Mechanics* (J. P. Den Hartog & H. Peters, eds.) Wiley, 294-310.

WESTIN, K. J., BOIKO, A.V., KLINGMANN, B. G. B, KOZLOV, V. V. & ALFREDSSON, P. H. 1994 Experiments in a boundary layer subjected to free stream turbulence. Part I. Boundary layer structure and receptivity. *J. Fluid Mech.* **281**, 193-218.

WU, X. 1993 Nonlinear temporal-spatial modulation of near-planar Rayleigh waves in shear flows: formation of streamwise vortices. *J. Fluid Mech.* **256**, 685-719.

WU, X., STEWART, P. A. & COWLEY, S. J. 1996 On the weakly nonlinear development of Tollmien-Schlichting wave-trains in boundary layers. *J. Fluid Mech.* **316**, 133-171.

Effects of long-wavelength Klebanoff modes on boundary-layer instability

By Xuesong Wu† AND Meelan Choudhari‡

1. Introduction

It is known that low-frequency components of three-dimensional vortical disturbances in the free stream can be entrained into the boundary layer due to the nonparallel flow effect, producing significant distortion in the form of alternate thickening and thinning of the layer in the spanwise direction. This observation goes back to Dryden (1936) and Taylor (1939) who, in fact, suggested that the entrained vortex motion, rather than the Tollmien-Schlichting (T-S) instability, was the cause of transition to turbulence. The dispute continued until the experiments of Schubauer and Skramstad (1948), which were conducted by minimizing the free-stream perturbations, fully validated the instability theory of Tollmien (1929) and Schlichting (1933). Since then, most research efforts have focused on transition at low levels of free-stream turbulence.

There has also been a significant amount of research on transition at moderate to high free-stream turbulence levels, primarily because of its relevance to turbomachinery flows. This has led to renewed interest in the findings of Dryden (1936) and Taylor (1939). Recent experimental studies (see e.g. Kendall 1985, Westin *et al.* 1994, Matsubara & Alfredsson 2001, and the references therein) show that the boundary layer filters out the high-frequency components of free-stream turbulence, while amplifying the low-frequency parts of the signature. The distortion within the boundary layer is dominated by streamwise velocity fluctuations, which are manifested in the form of longitudinal vortices or streaks. These streaks are now referred to as Klebanoff modes, in recognition of the contribution of Klebanoff (1971). In this paper, we shall refer to them as Klebanoff distortions or fluctuations, so as to avoid possible confusion when genuine instability modes are being discussed.

The boundary-layer response to small-amplitude unsteady vortical disturbances was calculated by Gulyaev *et al.* (1989) and Choudhari (1996) using linearized unsteady boundary-layer equations. Leib *et al.* (1999) pointed out that this approach is restricted to the region relatively close to the leading edge where the spanwise length scale of the perturbation is much larger than the local boundary-layer thickness. The continued growth of the perturbation amplitude and boundary-layer thickness implies that nonlinearity and cross-flow ellipticity will become significant sufficiently farther downstream, at which point the flow must be governed by boundary-*region* equations. For further work in the context of boundary-region equations, the reader is referred to the papers by Wundrow & Goldstein (2001), Goldstein & Wundrow (1998) and other references therein.

Direct laboratory investigations of the transition process in the presence of Klebanoff fluctuations have been made by a number of investigators. At moderate levels of free-stream turbulence, Arnal & Juillen (1978) and Kendall (1990) have observed intermittent appearance of wave packets inside the boundary layer. While their exact origin remains unclear, a series of experiments conducted by Kendall (1991, 1998) has helped reveal

† Permanent address: Department of Mathematics, Imperial College, UK
‡ NASA Langley Research Center, Hampton, VA

some unusual attributes of these wavepackets. First, they appear only when the free-stream turbulence exceeds a threshold amplitude of about 0.1%. Second, their growth rates are considerably larger than those of the T-S waves, being also dependent on the turbulence level. Third, the frequencies of these waves are significantly higher than those of T-S instability. Finally, these packets are more confined laterally, spreading rather slowly in the spanwise direction as they propagate downstream. Thus far, there has been no physical explanation for the above features. However, the present findings will shed some new lights on these observations.

Rather than studying naturally-occurring wavepackets, Watmuff (1997) used a harmonic point source to generate spanwise-localized wavetrains in a controlled fashion. He found that even a weak Klebanoff perturbation can induce severe distortions of the higher-frequency wavetrain, such that any comparison with calculations that do not account for the presence of Klebanoff modes becomes almost meaningless.

In addition to investigating the role of conventional T-S waves during transition in the presence of moderate free-stream turbulence, it is also important to examine alternative instability mechanisms. Streak instability, in particular, has attracted much attention in recent years. Matsubara, Bakchinov & Alfredsson (2000) reported that streaks or Klebanoff modes are unstable, and this can lead to a meandering and oscillation of the streaks and an eventual breakdown into turbulent spots.

In an effort to understand streak breakdown, Andersson *et al.* (2001) modeled the streak structure by a steady, spanwise-periodic distortion to a Blasius boundary layer. An inviscid stability analysis based on Floquet theory suggested that the streaks become unstable only when the amplitude of the associated streamwise velocity perturbation exceeds approximately 26% of the free-stream velocity. This estimate is perhaps too high to be representative of typical Klebanoff distortion in natural disturbance environments. The present theory, however, suggests that the unsteadiness of the Klebanoff distortion (even if at rather low frequencies) may exert a significant effect on the resulting high-frequency secondary instabilities (see §2.2).

Direct numerical simulations of transition due to high free-stream turbulence were performed first by Rai & Moin (1993), and more recently by Jacobs & Durbin (2001). The latter found that the boundary-layer response to free-stream turbulence was indeed dominated by low-frequency streaks. However, these streaks appeared to be fairly stable and it was only after they had lifted up to the outer part of the boundary layer to form a 'backward jet' that the breakdown to turbulent spots occurred.

In this paper, we investigate the instability of a Blasius boundary layer perturbed by Klebanoff distortions. Our main interest will be in relatively small-amplitude distortions, which are not atypical of many experimental situations. As in Wu & Luo (2001, referred to as I hereafter), we shall address two issues: (a) how the T-S instability, which operates in the absence of any distortion, is modified by a weak Klebanoff distortion, and (b) whether or not a weak distortion can induce a predominantly-inviscid instability. An asymptotic approach based on the high-Reynolds-number assumption is used, aimed at a systematic and consistent treatment of both the Klebanoff fluctuation and the secondary instability of the resultant perturbed flow. To make analytical progress, we also assume that the spanwise length scale of the Klebanoff distortion is larger than the thickness of the boundary layer. While the assumptions made will, no doubt, restrict the validity of the conclusions obtained, we believe that the analytical simplicity of this approach provides extra insights that might not have been easily apparent using a less restrictive, but primarily numerical, approach.

2. Formulation

Consider the two-dimensional incompressible boundary layer due to a uniform flow with velocity U_∞ past a semi-infinite flat plate. Superimposed on the incoming stream is a small-amplitude, three-dimensional vortical disturbance (i.e., a *gust*) that is advected at the free-stream speed. For simplicity, we assume that the gust is harmonic in time, with a frequency of $k_1 U_\infty/\Lambda$, where k_1 denotes the non-dimensional frequency parameter and Λ represents the dimensional length scale of the gust in the spanwise direction.

The flow is to be described in the Cartesian coordinate system (x, y, Z), with its origin at the plate leading edge. Here, x, y and Z denote the streamwise, normal, and spanwise coordinates nondimensionalized with respect to Λ. The time variable t is normalized by Λ/U_∞ and the velocity components (u, v, w) and pressure p are normalized by U_∞ and ρU_∞^2, respectively, where ρ denotes the fluid density. The Reynolds number $R_\Lambda \equiv U_\infty \Lambda/\nu$ is assumed to be a large parameter throughout this analysis (i.e., $R_\Lambda \gg 1$).

The streamwise and normal velocity components of the Blasius flow are given by

$$(U_B, V_B) = \left\{ F'(\eta),\ (2xR_\Lambda)^{-\frac{1}{2}}(\eta F' - F) \right\},$$

where $\eta = R_\Lambda^{1/2} y/\sqrt{2x}$ and $F(\eta)$ satisfies the Blasius boundary-value problem

$$F''' + FF'' = 0\,, \quad \text{with} \quad F(0) = F'(0) = 0; \quad F'(\infty) = 1\,. \tag{2.1}$$

2.1. *Flow distortion associated with Klebanoff modes*

The boundary-layer response to a three-dimensional convected gust was analyzed by Gulyaev *et al.* (1989), Choudhari (1996) and Leib *et al.* (1999). Similar to their work, the velocity field of the disturbance superimposed on the oncoming flow has the form

$$\mathbf{u}_\infty = \epsilon_D \left(\hat{u}_\infty B'(Z), \hat{v}_\infty B'(Z), \hat{w}_\infty B(Z) \right) \mathrm{e}^{\mathrm{i}\, k_1 (x-t) + \mathrm{i}\, k_2 y}\,, \tag{2.2}$$

where ϵ_D represents the gust amplitude, and k_1 and k_2 denote the streamwise and transverse wavenumbers, respectively. We assume that $k_1,\ k_2 \ll 1$ so that $\hat{w}_\infty \ll \hat{u}_\infty,\ \hat{v}_\infty$ $(= O(1))$. Note that we now allow for a general spanwise dependence of the gust via the arbitrary function $B(Z)$.

The inviscid solution can be written as (Leib *et al.* 1999)

$$\mathbf{u}_D = \epsilon_D [\mathbf{u}_\infty + \nabla \phi] \tag{2.3}$$

where ϕ denotes the potential. To the required order, ϕ is governed by the boundary value problem

$$\nabla^2 \phi = 0\,, \tag{2.4}$$

$$\left.\begin{aligned} &\nabla\phi \to 0 \quad \text{as} \quad y \to \infty\,; \\ &\phi(x,0) = 0 \quad (x<0), \quad \phi_y(x,0) = -\hat{v}_\infty B'(Z)\, \mathrm{e}^{\mathrm{i}\, k_1 (x-t)} \qquad (x>0). \end{aligned}\right\} \tag{2.5}$$

The full solution to Eqs. (2.4)-(2.5) can be found by the standard Wiener-Hopf technique. However, for the purpose of stability analysis, we confine ourselves to the region $x \gg 1$ and $k_1 \ll 1$, such that $k_1 x = O(1)$. The inviscid solution under these conditions can be obtained by neglecting the x-derivative term in Eq. (2.4) and solving the resultant two-dimensional Laplace equation in the half-space $y > 0$. This yields the slip-velocity components in the streamwise and spanwise directions

$$u_s \approx \hat{u}_\infty, \quad w_s \approx \hat{v}_\infty \frac{\partial}{\partial Z} \int_{-\infty}^{\infty} \frac{B(\zeta)}{\zeta - Z}\, \mathrm{d}\zeta\,. \tag{2.6}$$

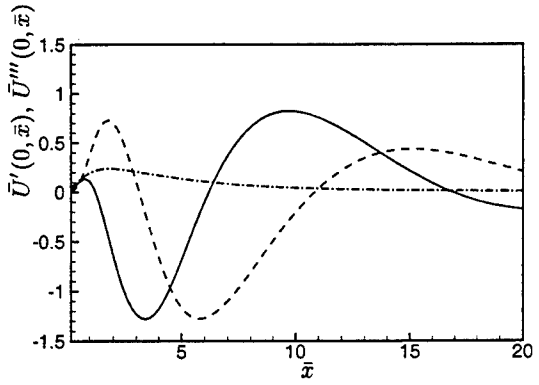

FIGURE 1. Variation of $U'''(0,\bar{x})$ (—— real part, ---- imaginary part) and $|U'(0,\bar{x})|$ (– · – · –) with $\bar{x}$.

The distortion within the boundary layer is a small perturbation to the Blasius flow, and its leading-order solution takes the form

$$(\tilde{U},\tilde{V},\tilde{W}) = \Big[-\frac{w_s'(Z)}{k_1}\bar{U}, -\frac{w_s'(Z)}{k_1}\bar{V}, w_s(Z)\bar{W}\Big]\,\mathrm{e}^{-\mathrm{i}\,\bar{t}} + c.c. + \dots \,. \tag{2.7}$$

where we put $\bar{x} = k_1 x$ and $\bar{t} = k_1 t$. The functions $(\bar{U},\bar{V},\bar{W})$ are governed by the linearized unsteady boundary-layer equations (Leib *et al.* 1999)

$$\frac{\partial\bar{U}}{\partial\bar{x}} - \frac{\eta}{2\bar{x}}\frac{\partial\bar{U}}{\partial\eta} + \frac{\partial\bar{V}}{\partial\eta} + \bar{W} = 0\,, \tag{2.8}$$

$$-\mathrm{i}\bar{U} + F'\frac{\partial\bar{U}}{\partial\bar{x}} - \frac{F}{2\bar{x}}\frac{\partial\bar{U}}{\partial\eta} - \frac{\eta F''}{2\bar{x}}\bar{U} + F''\bar{V} = \frac{1}{2\bar{x}}\frac{\partial^2\bar{U}}{\partial\eta^2}\,, \tag{2.9}$$

$$-\mathrm{i}\bar{W} + F'\frac{\partial\bar{W}}{\partial\bar{x}} - \frac{F}{2\bar{x}}\frac{\partial\bar{W}}{\partial\eta} = \frac{1}{2\bar{x}}\frac{\partial^2\bar{W}}{\partial\eta^2}\,. \tag{2.10}$$

The appropriate boundary conditions are

$$\bar{U} = \bar{V} = \bar{W} = 0 \quad \text{at} \quad \eta = 0\,; \quad \bar{U} \to 0, \quad \bar{W} \to \mathrm{e}^{\mathrm{i}\,\bar{x}} \quad \text{as} \quad \eta \to \infty. \tag{2.11}$$

In the upstream limit ($\bar{x} \to 0$), the flow becomes quasi-steady and its solution matches that of Crow (1966),

$$\bar{U} \to \tfrac{1}{2}\bar{x}\eta F''\,, \quad \bar{V} \to \tfrac{1}{4}(\eta^2 F'' - 3\eta F' - F)\,, \quad \bar{W} \to F'\,. \tag{2.12}$$

It turns out the instability of the perturbed flow at a given streamwise location is controlled by two local quantities, viz., $\bar{U}'(0,\bar{x})$ and $\bar{U}'''(0,\bar{x})$. Their variation with $\bar{x}$ is shown in Fig. 1.

2.2. *Scaling arguments*

The Klebanoff distortion in the boundary layer is concentrated in the streamwise region where $\bar{x} = O(1)$, i.e., at a distance of $l^* = O(k_1^{-1}\Lambda)$ downstream from the leading edge. Accordingly, we now introduce the Reynolds number based on l^*:

$$R = \frac{U_\infty l^*}{\nu} = R_\Lambda(\frac{l^*}{\Lambda})\,. \tag{2.13}$$

Analysis shows that the effect of Klebanoff distortion is most significant for those instability modes whose growth characteristics are controlled by the curvature of the

perturbed flow in the vicinity of the wall. A crucial observation is that, for the low-frequency (but unsteady) distortion,

$$\bar{U}'' \sim \eta \quad \text{as} \quad \eta \to 0 \,. \tag{2.14}$$

In a wall region, therefore, the Klebanoff fluctuation with suitable k_1 and ϵ_D may alter the curvature of the Blasius profile by $O(1)$, while the perturbation to the streamwise velocity itself remains small. This, in turn, can lead to fundamental changes in the nature of instability in the flow. This scenario is rather different from the case of a completely steady distortion, for which $\bar{U}'' \sim \eta^2$ as $\eta \to 0$ and, therefore, no new instability can emerge until the distortion amplitude becomes $O(1)$. Thus, there exists a crucial difference between steady and unsteady distortions, no matter how low the frequency of the unsteady distortion.

The characteristic length and time scales of the linear instability of the perturbed base flow, as well as the required strength of the distortion, is determined through a scaling argument as described below.

Consider a wall layer of thickness $\hat{\sigma}$ relative to the mean boundary-layer thickness of $R^{-\frac{1}{2}}l^*$ ($\hat{\sigma} \ll 1$). The curvature of the distortion becomes comparable with that of the Blasius profile itself when

$$\epsilon_D \hat{\sigma} (\frac{l^*}{\Lambda}) \sim \hat{\sigma}^2 \,. \tag{2.15}$$

We now seek instability waves whose streamwise wavenumbers (non-dimensionalized by $R^{\frac{1}{2}}/l^*$) are also of $O(\hat{\sigma})$.

While the growth rates of the instability modes are controlled by the distortion in the wall region, the distortion in the bulk of the flow also affects the instability wave by producing an $O(\hat{\sigma})$ correction to the phase speed and wavenumber. We will show that this correction is crucial to determining the spanwise distribution of the instability mode. The appropriate treatment can be given only when

$$\hat{\sigma}^{\frac{3}{2}} \sim \frac{R^{-\frac{1}{2}}l^*}{\Lambda} \,. \tag{2.16}$$

The exact reason for choosing the above scaling will be given in the next section.

From Eq. (2.13), Eq. (2.15) and Eq. (2.16), it follows that the streamwise wavenumber of the resultant instability waves is related to the other flow parameters via:

$$\hat{\sigma} \sim R_\Lambda^{-\frac{1}{3}} (\frac{l^*}{\Lambda})^{\frac{1}{3}} \,, \tag{2.17}$$

and that the required magnitude of the distortion is

$$\epsilon_D \sim R_\Lambda^{-\frac{1}{3}} (\frac{l^*}{\Lambda})^{-\frac{2}{3}} \,. \tag{2.18}$$

It can be shown that, for the Klebanoff distortion to induce an $O(1)$ (or larger) change in the viscous growth rate of the instability modes of interest in an unperturbed Blasius flow, we need to have $\hat{\sigma} \gg R^{-\frac{1}{20}}$. On the other hand, the foregoing analysis was based on the assumption that $\hat{\sigma} \ll 1$. These considerations impose the following restriction on the range of streamwise locations where the present analysis is formally valid:

$$R_\Lambda^{\frac{17}{23}} \ll \frac{l^*}{\Lambda} \ll R_\Lambda \,. \tag{2.19}$$

While the Klebanoff distortion modulates on the slow variables $\bar{x}$ and $\bar{t}$, instability

waves oscillate on the much faster variables $\hat{\sigma}R^{\frac{1}{2}}\bar{x}$ and $\hat{\sigma}^2R^{\frac{1}{2}}\bar{t}$. We thus introduce

$$\zeta = \hat{\sigma}R^{\frac{1}{2}}(\alpha\bar{x} - \hat{\sigma}\omega\bar{t}) \ , \tag{2.20}$$

to describe the oscillation of the carrier wave, where the scaled wavenumber α and scaled frequency ω are given via

$$\alpha = \alpha_0 + \hat{\sigma}\alpha_1 + \hat{\sigma}^2\alpha_2 \ , \quad c \equiv \omega/\alpha = c_0 + \hat{\sigma}c_1 + \hat{\sigma}c_2 + \dots \ .$$

The amplitude of the instability wave amplifies on the variable $X = \hat{\sigma}^4R^{\frac{1}{2}}\bar{x}$, which exceeds the viscous growth rate of the lower branch T-S modes when $\hat{\sigma} >> R^{-1/32}$. Since X is also much faster than $\bar{x}$ according to Eq. (2.17) and Eq. (2.19), the space and time modulation of the distortion can be treated as parametric when the stability of the perturbed flow is studied.

3. Results: intermittent instability

For the scalings identified in the previous section, the linear instability of the perturbed flow is governed by a five-zoned asymptotic structure similar to the case of a steady distortion that was analyzed in I. Unlike that distortion, however, the Klebanoff distortion in the main deck ($\hat{y} = \frac{\Lambda R^{\frac{1}{2}}}{l^*}y = (2\bar{x})^{\frac{1}{2}}\eta = O(1)$) interacts with the instability wave. This interaction has to be analyzed in order to determine the mode shape in the spanwise direction. In the main deck, the total streamwise velocity of the base flow is given by

$$U_B + \hat{\sigma}U_D(\hat{y}, Z; \bar{x}, \bar{t}) \quad \text{with} \quad U_D = -w_s'(Z)\Big(\bar{U}\,\mathrm{e}^{-\mathrm{i}\,\bar{t}} + c.c.\Big) \ , \tag{3.1}$$

whereas the associated fluctuation induced by the instability wave takes the form

$$u = \Big\{A(X)\Phi(Z)\hat{U}_0(\hat{y}) + \hat{\sigma}A(X)\Phi_1(Z)\hat{U}_1 + \hat{\sigma}^2\Phi_2(Z,X)\hat{U}_2 + \hat{\sigma}^3\hat{U}_3 + \dots\Big\}\,\mathrm{e}^{\mathrm{i}\,\zeta} + c.c., \tag{3.2}$$

where $A(X)$ is the amplitude of the wave. The solution in the other four decks can be sought via similar expansions. Imposing asymptotic matching requirements up to $O(\hat{\sigma}^2)$ leads to an eigenvalue problem involving the (standard) Schrödinger equation

$$-\Phi_{ZZ} = \Big(\psi(Z; \bar{x}, \bar{t}) - \alpha_s\Big)\Phi \ , \tag{3.3}$$

for the spanwise distribution of the instability mode. Here, the "potential" ψ is given by

$$\psi(Z; \bar{x}, \bar{t}) = \frac{2\lambda_D(Z)\alpha_0^2}{\lambda} = -\frac{2\alpha_0^2}{(2\bar{x})^{\frac{1}{2}}\lambda}(\bar{U}'\,\mathrm{e}^{-\mathrm{i}\,\bar{t}} + c.c.)w_s'(Z) \equiv -\tilde{\psi}(\bar{x}, \bar{t})w_s'(Z), \tag{3.4}$$

and α_s represents the eigenvalue parameter.

It now becomes clear that the reason for choosing Eq. (2.16) was to ensure a balance between the spanwise variation Φ_{ZZ} and the wavenumber correction $\alpha_s\Phi$ in Eq. (3.3). Without retaining Φ_{ZZ}, α_s would be parametrically dependent on the spanwise variable Z. Then the first- and second-order derivatives with respect to Z would produce secular terms proportional to $\bar{x}$ and $\bar{x}^2$, thereby invalidating the entire perturbation expansion scheme.

There is extensive literature on the Schrödinger operator. For our purpose, it suffices to mention that for a localized potential that is not negative-definite, the spectrum of the Schrödinger operator includes discrete eigenvalues with real-valued eigenfunctions that decay exponentially as $Z \to \pm\infty$. For later analysis, it is convenient to normalize the eigenfunction such that $\int_{-\infty}^{\infty}\Phi^2\,\mathrm{d}\,Z = 1$. The Schrödinger operator also has a continuous

spectrum, for which Φ remains finite and oscillatory as $Z \to \pm\infty$; however, only the discrete spectrum is considered in this paper.

The analysis can be carried to higher orders in a routine manner (cf. Wu, Stewart & Cowley 1996). The crucial equation, which determines the leading order growth rate, is obtained by considering the next, i.e., fourth term in the expansion for each deck. The final result is given by

$$-\frac{\mathrm{i}}{4\alpha_0}\Phi_{2,ZZ} = \mathrm{i}\Big\{\frac{\lambda_D(Z)\alpha_0}{2\lambda} - \alpha_s\Big\}\Phi_2 - A_X\Phi + \Big(\gamma_0 + \gamma(Z)\Big)A\Phi + \mathrm{i}\,\chi(Z,X)\ , \qquad (3.5)$$

$$\gamma_0 = -\frac{\pi c_0^4}{4\lambda} + \frac{\lambda^2}{2R^{\frac{1}{4}}\hat{\sigma}^5(2\alpha_0 c_0)^{\frac{1}{2}}}\ ,$$

$$\gamma(Z;\bar{x},\bar{t}) = -\frac{\pi c_0^3}{\lambda^2}(2\bar{x})^{-\frac{3}{2}}\Big\{\bar{U}'''(0,Z;\bar{x})\,\mathrm{e}^{-\mathrm{i}\,\bar{t}} + c.c.\Big\}w_s'(Z) \equiv -\tilde{\gamma}(\bar{x},\bar{t})w_s'(Z)\ , \qquad (3.6)$$

where χ is a real-valued function that does not affect the growth rate of the disturbance.

Equation (3.5) is an inhomogeneous Schrödinger equation. The standard procedure of imposing the solubility condition yields $A_X = (\gamma_0 + \kappa_d)A$, where

$$\kappa_d = \int_{-\infty}^{\infty} \gamma(Z)\Phi^2\,\mathrm{d}\,Z\ . \qquad (3.7)$$

The growth rate therefore corresponds to $(\gamma_0 + \kappa_d)$, κ_d being the *excess growth rate* induced by the distortion. When $\hat{\sigma} >> R^{-\frac{1}{20}}$, the excess growth rate becomes much larger than the second term in γ_0, which corresponds to the viscous contribution to the growth rate (Goldstein & Durbin 1986). In other words, the instability modes of interest are now predominantly inviscid, with a growth rate that is given by

$$\kappa = -\frac{\pi c_0^4}{4\lambda} + \int_{-\infty}^{\infty} \gamma(Z)\Phi^2\,\mathrm{d}\,Z\ . \qquad (3.8)$$

As the distortion amplitude is further increased, the inviscid growth rate continues to increase and, when $\hat{\sigma} \gg R^{-1/32}$, it exceeds the growth rate of the longer wavelength lower-branch modes which are described by the triple-deck structure and correspond to the most-unstable modes of the unperturbed flow. Clearly, the nature of the instability has been fundamentally altered at this stage.

In summary, we have seen that the asymptotic regime studied above describes a continuous transition as the distortion amplitude is varied, from a modified form of the short-wavelength, viscous modes in an unperturbed Blasius flow to primarily-inviscid modes that eventually dominate the overall instability of the perturbed flow. Because the structure of these modes can be localized in the spanwise direction and, in general, is completely dictated by the shape of the Klebanoff distortion, we will refer to these modes as *localized T-S modes*.

In order to aid our subsequent discussion, we first present solutions for the spanwise distribution $B(Z) = \frac{d^3 Z}{Z^2+d^2}$. A localized distribution of this type is believed to be appropriate to Klebanoff distortions with a finite correlation distance in Z (i.e., relative to Λ) although, of course, periodic distributions (corresponding to large coherence in Z) can also be analyzed rather easily. It follows from Eq. (2.6) that

$$-w_s'(Z) = \frac{B_0(1 - 3Z^2/d^2)}{(Z^2/d^2 + 1)^3} \equiv B_0 S(Z)\ , \quad \text{with} \quad B_0 = 2\pi\hat{v}_\infty\ . \qquad (3.9)$$

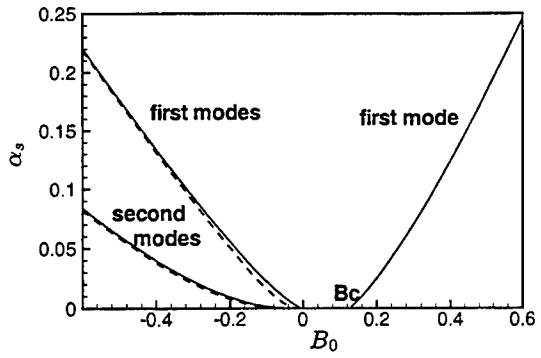

FIGURE 2. Eigenvalues α_s *v.s.* B_0: ——— varicose modes, ---- sinuous modes.

All of the calculations presented in this paper pertain to the (arbitrary) choice of $d = 4$.

Just to illustrate the behavior of the spectrum, we first set $\tilde{\psi} = 1$ in Eq. (3.4) and plot the eigenvalues α_s for a range of B_0 (Fig. 2). Symmetric (varicose) modes can be found for both positive and negative B_0, except for the gap $0 < B_0 < 0.16 = B_c$ where they do not exist. Unlike the Schrödinger operator with a purely imaginary potential (i.e., the case analyzed in I), the standard Schrödinger equation also admits anti-symmetric (sinuous) modes in addition to the varicose ones. These modes appear only for negative B_0. For $B_0 < 0$, there also exist higher modes, symmetric or anti-symmetric, and they are distinguished by the number of zeros in the corresponding eigenfunctions. These higher modes are generally less unstable than the first ones and, accordingly, will not be discussed here any further.

Equations (3.3), (3.4) and (3.6) are used in conjunction with Eq. (3.8) to compute the inviscid growth rate due to the Klebanoff distortion. The growth rates of both the sinuous and varicose modes at three separate instants of time are shown in Fig. 3 for the case of $\bar{x} = 2.0$ and $B_0 = 1.4$. Observe that the sinuous modes have considerably larger growth rates than the varicose modes. For this reason, we shall focus on the anti-symmetric modes henceforth. Indeed, in the experiments of Matsubara & Alfredsson (2001), the sinuous modes were observed to occur more frequently.

As described earlier in the context of Fig. 2, the sinuous modes exist only when $\tilde{\psi}(\bar{x}, \bar{t})$ is negative, i.e., at those instants during the Klebanoff-mode cycle when the perturbed flow is characterized by a significant low-speed streak. This finding is consistent with most experimental observations. Furthermore, the instability occurs only in that part of cycle when $\tilde{\gamma}(\bar{x}, \bar{t})$ is also negative. On the other hand, γ and ψ tend to 0 as both $\bar{x} \to 0$ and $\bar{x} \to \infty$ (see also Fig. 1). Thus, γ and ψ have appreciable sizes over only a restricted window in the streamwise direction. The instability modes under consideration are, therefore, expected to be localized in space as well as in time.

This local and intermittent nature of the instability can be demonstrated by plotting the growth-rate contours in the $\omega - \bar{x}$ plane at various instants, as shown in Figs. 4a-d for the case of $B_0 = 1.4$. At $\bar{t} = -1.8$, a small 'bubble' of instability is observed within the $\omega - \bar{x}$ plane, indicating that the instability starts at a slightly earlier time. As time increases, the 'bubble' grows in both spatial and spectral extent, reaching its maximum at $\bar{t} \approx -0.82$, after which the 'bubble' shrinks and finally disappears, before re-emerging during the next cycle of the Klebanoff mode. Of course, given the disparity between the temporal scales of the Klebanoff mode and the instability waves, the latter

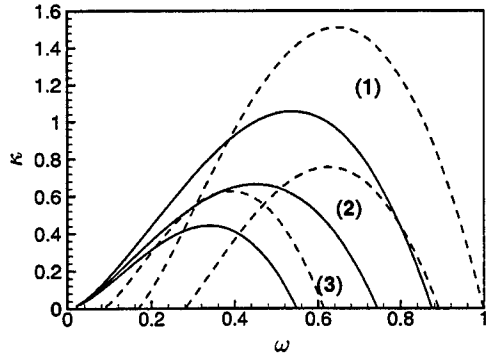

FIGURE 3. Instability caused by a Klebanoff distortion. The streamwise location is fixed at $\bar{x} = 2.0$ and $B_0 = 1.4$. The Figure shows the growth rates of varicose (———) and sinuous modes (- - - -) at three instants: (1) $\bar{t} = \phi(\bar{x}) - \frac{3}{4}\pi$; (2) $\bar{t} = \phi(\bar{x}) - \frac{7}{8}\pi$; (3) $\bar{t} = \phi(\bar{x}) - \frac{29}{32}\pi$.

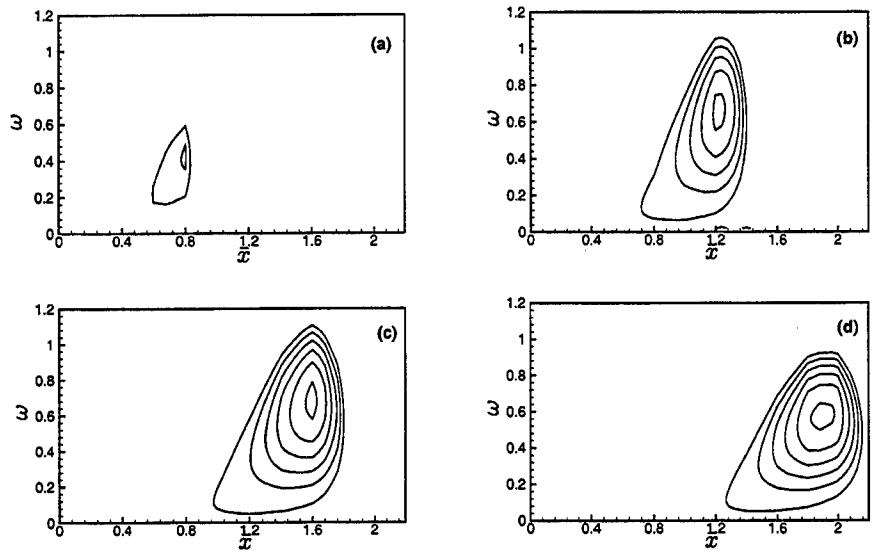

FIGURE 4. Contours of growth rates of the local instability induced by a Klebanoff mode ($B_0 = 1.4$). Figures (a)-(d) correspond to the instants $\bar{t} = -1.8, -1.25, -0.82, -0.44$.

could amplify substantially within a single period of modulation and, therefore, reach sufficiently high amplitudes to induce a local breakdown. In reality, the modulation is stochastic so that this local instability takes place randomly as, indeed, has been observed in the experiments of Kendall (1985).

From Figs. 4a-d, one may deduce useful information about the spatio-temporal behaviour of the instability. The localized structure of the instability wave in both x and Z suggests that the unstable modes would be manifested as patches of oscillations. Strictly speaking, the center of these patches can only be determined after considering the complex history of the disturbance motion. However, it may still be useful to model the center of a patch as being close to the $\bar{x}$ location that corresponds to the growth rate maximum in Figs. 4a-d. From $\bar{t} = -1.80$ to $\bar{t} = -0.82$, the center of the patch migrates from $\bar{x} = 0.8$ to 1.6, yielding an apparent patch *convection velocity* of $V_c \approx 0.82$. Though

this prediction is based on a number of simplifying assumptions, migration of patches at such a speed appears to have been observed in experiments as well.

4. Discussions and conclusions

In this paper, we have investigated the effect of long-wavelength Klebanoff fluctuations on the instability of the Blasius boundary layer. By using an asymptotic approach based on the high-Reynolds-number assumption, we have derived a self-consistent, albeit simplified, mathematical model, which appears to capture certain key elements of this problem. Specifically, our analysis indicates that relatively weak Klebanoff fluctuations, which do not alter the velocity profile by $O(1)$, may change the near-wall curvature of the underlying Blasius flow by $O(1)$. This, in turn, has the effect of modifying and even fundamentally altering the instability of the boundary-layer flow. Specifically, a localized distortion may induce both sinuous and varicose modes of instability. However, the sinuous modes are found to be more unstable, in general.

When the distortion is just strong enough to produce an excess growth comparable to viscous growth, these modes may be viewed as modified T-S waves. However as the strength of the distortion exceeds a threshold range (in an asymptotic sense), the instability becomes essentially inviscid, and the characteristic frequencies and growth rates are now much higher than those of the T-S waves in an unmodified Blasius flow. Because the Klebanoff distortion modulates the base flow in both t and x, its effect on the instability is intermittent in time and localized in space, i.e., it is manifested only during a certain phase of the modulation and in a limited window along the streamwise direction. In particular, the dominant sinuous modes appear during the phase in which the flow is characterised by low-speed streaks.

An interesting feature of the instability modes analyzed in this paper is that, despite the low-frequency nature of the Klebanoff distortion, the unsteadiness of the latter plays a crucial role in this model. Specifically, the above instability modes would not have been predicted for a small-amplitude Klebanoff distortion if it had been treated as being steady. Moreover, the intermittent nature and the convection of unstable patches or spots are both attributable to the unsteadiness of the distortion.

The qualitative predictions of our theory are consistent with laboratory observations. Our results indicate that the streaks can become unstable even without appreciable changes in the Blasius profile. This is precisely what Matsubara *et al.* (2000) concluded on the basis of their experimental studies. The predicted patches of oscillations have been observed in numerous experiments. The elevated growth of instability wave packets in the presence of Klebanoff distortion has also been observed in the experiments by Kendall (1991), as mentioned in the Introduction.

The seemingly puzzling and conflicting experimental observations can be reconciled to some degree when reinterpreted in the light of our theoretical results. As mentioned in §1, the wavepackets develop out of the background disturbance and amplify downstream. Kendall (1990) associated these with T-S waves. We believe that they are likely to be packets of the local T-S waves identified in this paper, rather than the usual T-S waves in an unmodified Blasius flow. These local T-S waves exhibit virtually all of the unusual characteristics observed by Kendall: the onset threshold, the excess growth, and the range of higher frequencies. Since their growth rates depend on the magnitude of the Klebanoff fluctuation, it is to be expected that their amplitude at a particular observation point should have a nonlinear relation with the magnitude of the Klebanoff motion. Since the

spanwise extent of these local T-S modes is determined by the Klebanoff distortion, it is not surprising that they undergo little lateral spreading.

The extreme sensitivity of the boundary-layer response to harmonic point excitation (Watmuff 1997, 1998) can also be explained. In the presence of Klebanoff fluctuations, a point excitation definitely generates local T-S modes as well. Therefore, the general response cannot be represented as a summation of the conventional T-S waves, as was done in the calculation. This may be the reason why a meaningful comparison is not possible unless the Klebanoff fluctuation is substantially reduced.

Jacobs & Durbin (2001) concluded from their direct numerical simulations of bypass transition that the streaks close to the wall are stable. Our results seem to be in conflict with this finding. There could be a number of reasons for the disagreement. It might be that the present instability is so weak that it is masked by other more vigorous processes. Alternatively, it is plausible that the instability modes identified herein were not excited in their simulations. Finally, the energy of the free-stream disturbances in their simulation is contained in a band of rather high frequencies (an order-of-magnitude higher than typical frequencies of T-S waves) and, therefore, the streaks are not a linear response to the low-frequency components. Rather, they are generated nonlinearly by the interaction of higher-frequency components. The question as to whether or not this is the cause of the discrepancy remains open at this point.

The present work is, of course, far from being a complete or quantitatively accurate description of the problem. The primary shortcoming is its neglect of the spanwise ellipticity of the Klebanoff fluctuation. The more general problem for Klebanoff distortions with an $O(1)$ wavelength, including the effects of nonlinearity and stochasticity, is currently under investigation. Nonetheless, the simplicity of the current model, together with the physical insights derived from it, appear to justify the assumptions made herein. The theory, we believe, sheds useful light on a very complex process which has so far eluded a first-principles explanation.

The work of XW was carried out during his sabbatical in 2001 at ICASE NASA Langley and the Center for Turbulence Research. He would like to thank Professors Parviz Moin, Paul Durbin, W. C. Reynolds and Peter Bradshaw for helpful discussions and comments.

REFERENCES

ANDERSSON, P., BRANDT, L., BOTTARO, A. & HENNINGSON, D. S. 2001 On breakdown of boundary layer streaks. *J. Fluid Mech.* **428**, 29-60.

ARNAL, D. & JUILLEN, J .C. 1978 Contribution expérimental a l'étude de la réceptivité d'une couche limite laminaire, à la turbulence de l'écoulement général. *ONERA Tech.* No. 1/5018 AYD.

CHOUDHARI, M. 1996 Boundary-layer receptivity to three-dimensional unsteady vortical disturbances in free stream. *AIAA* Paper 96-0181.

CROW, S. C. 1966 The spanwise perturbation of two-dimensional boundary layers. *J. Fluid Mech.* **24**, 153-164.

DRYDEN, H. L. 1936 Air flow in the boundary layer near a plate. *NACA* Report 562.

GOLDSTEIN, M. E. & DURBIN, P. A. 1986 Nonlinear critical layers eliminate the upper branch of spatially growing Tollmien-Schlichting waves. *Phys. Fluids* **29**, 2334-2345.

GOLDSTEIN, M. E. & WUNDROW, D. W. 1998 On the environmental realizability of algebraically growing disturbances and their relation to Klebanoff modes. *Theo. Comp. Fluid Dyn.* **10**, 171-186.

GULYAEV, A. N., KOZLOV, V., KUZNETSOV, V. R., MINEEV, B. I. & SEKUNDOV, A. N. 1989 Interaction of laminar boundary layer with external turbulence. *Izv. Akad. Nauk SSSR Mekh. Zhid. Gaza* **6**, 700-710.

KENDALL, J. M. 1985 Experimental study of disturbances produced in pre-transitional laminar boundary layer by weak free stream turbulence. *AIAA* Paper 85-1695.

KENDALL, J. M. 1990 Boundary-layer receptivity to free-stream turbulence. *AIAA* Paper 80-1504.

KENDALL, J. M. 1991 Studies on laminar boundary layer receptivity to freestream turbulence near a leading-edge. In *Boundary Layer Stability and Transition to Turbulence* (D. C. Reda, R. H. Reed & R. Kobayashi, eds.). ASME FED, **114**, 23-30.

KENDALL, J. M. 1998 Experiments on boundary-layer receptivity to freestream turbulence. *AIAA* Paper 98-0530.

KLEBANOFF, P. S. 1971 Effect of free-stream turbulence on a laminar boundary layer. *Bulletin. Am. Phys. Soc.* **16**.

JACOBS, R. G. & DURBIN, P. A. 2001 Simulations of bypass transition. *J. Fluid Mech.* **428**, 185-212.

LEIB, S. J., WUNDROW, D. W. & GOLDSTEIN, M. E. 1999 Effect of free-stream turbulence and other vortical disturbances on a laminar boundary layer. *J. Fluid Mech.* **380**, 169-203.

MATSUBARA M., BAKCHINOV A. & ALFREDSSON, P. H. 2000 In *Proc. IUTAM Symposium on Laminar-Turbulent Transition* (H. Fasel & W. Saric, eds.). Springer.

MATSUBARA, M. & ALFREDSSON, P. H. 2001 Disturbance growth in boundary layers subjected to free-stream turbulence. *J. Fluid Mech.* **430**, 149-168.

RAI, M. M. & MOIN, P. 1993 Direct numerical simulation of transition and turbulence in a spatially evolving boundary layer. *J. Comput. Phys.* **109**, 169-192.

SCHLICHTING, H. 1933 Zur Entstehung der Turbulenz bei der Plattenstromung. *Nachr. Ges. Wiss. Göttingen Math.-Phys. Kl. 1933*, 181-208.

TAYLOR, G. I. 1939 Some recent developments in the study of turbulence. In *Proc. 5th Intl. Congr. Appl. Mech.* (J. P. Den Hartog & H. Peters, eds.). Wiley, 294-310.

TOLLMIEN, W. 1929 Über die Entstehung der Turbulenz. *Nachr. Ges. Wiss. Göttingen Math.-Phys. Kl. 1929*, 21-44.

WATMUFF, J. H. 1997 Interactions between Klebanoff modes and TS waves in a Blasius boundary layer. *AIAA* Paper 97-0558.

WATMUFF, J. H. 1998 Detrimental effects of almost immeasurably small freestream nonuniformities generated by wind-tunnel screens. *AIAA J.* **36**, 379-386.

WESTIN, K. J., BOIKO, A. V., KLINGMANN, B. G. B., KOZLOV, V. V. & ALFREDSSON, P. H. 1994 Experiments in a boundary layer subjected to free stream turbulence. Part I. Boundary layer structure and receptivity. *J. Fluid Mech.* **281**, 193-218.

WU, X., STEWART, P. A. & COWLEY, S. J. 1996 On the weakly nonlinear development of Tollmien-Schlichting wave-trains in boundary layers. *J. Fluid Mech.* **316**, 133-171.

WU, X. & LUO, J. 2001 Instability of Blasius boundary layer in the presence of steady streaks. *Annual Research Briefs*, Center for Turbulence Research, NASA Ames/Stanford Univ., 293–304.

WUNDROW, D. W. & GOLDSTEIN, M. E. 2001 Effect on a laminar boundary layer of small-amplitude streamwise vorticity in the upstream flow. *J. Fluid Mech.* **426**, 229-262.

The large-scale organization of autonomous turbulent wall regions

By Javier Jiménez†, Oscar Flores‡ AND Manuel García-Villalba‡

1. Introduction

It has become clear in the last few years that wall-bounded turbulence below $y^+ \approx 80$ is a relatively autonomous system which not only functions in almost the normal way when the outer flow is artificially removed (Jiménez & Pinelli, 1999), but which is otherwise responsible for the generation of part of the turbulent energy dissipated in the outer flow regions (Jiménez, 1999). The structures in this near-wall layer scale approximately in wall units. None of this can of course be taken as proof that there is no interaction in natural wall turbulence between the inner and the outer layers, or that the inner layer is not modified by the presence of the core flow. It nevertheless suggests that any interaction is probably weak and affects only secondary aspects of the flow dynamics.

It has also been known for some time that there are structures in the outer flow which are very large, with lengths that scale at least in part with the boundary layer thickness (Perry, Henbest & Chong, 1986; Jiménez, 1998; Kim & Adrian, 1999). These structures contain most of the turbulent kinetic energy in the overlap region, and it is to be expected that their effect should be felt in some way by the near-wall structures (Hunt & Morrison 2000). Since the ratio between the boundary layer thickness, h, and the viscous wall length scale is the friction Reynolds number $Re_\tau = u_\tau h/\nu$, the outer structures become much larger than the near-wall ones as Re_τ increases. It can then be expected that any outer-inner interaction should include in that limit the large-scale organization of the near-wall layer.

The purpose of this paper is to explore that organization, and to attempt to clarify its origin. To that effect we will present numerical experiments in which the outer flow is effectively removed, and in which the scaling in wall variables should be strict. The nature of the interaction between the different layers will then be studied by comparing the large scales of these autonomous walls with those of full turbulent flows at various Reynolds numbers.

The organization of the paper is as follows. The numerical technique used to isolate the wall region is described in Section 2. The results, with special emphasis on the large-scale spectral characteristics of the isolated walls, are then discussed in Section 3 and compared with those of experimental and numerical full turbulent flows. Finally some conclusions are offered and opportunities for future work are explored.

2. The numerical experiments

The numerical scheme used for the autonomous simulations is similar to that described by Jiménez & Pinelli (1999) and by Jiménez & Simens (2001), but the method has been slightly modified, and the version described here should be preferred to those in the

† Also at U. Politécnica de Madrid
‡ U. Politécnica de Madrid

previous references. The Navier–Stokes equations are integrated in the form of evolution equations for the wall-normal vorticity ω_y and for $\phi = \nabla^2 v$, using a pseudospectral code with Fourier expansions in the two wall-parallel directions and Chebychev polynomials in y, as in Kim, Moin & Moser (1987). At each time step the right-hand sides of the two evolution equations are multiplied by a damping mask $1 - \Delta t\, F(y)$, where

$$F(y) = 0 \quad \text{if} \quad y \leq \delta_1, \qquad F(y) = 1/T \quad \text{if} \quad y \geq \delta_2, \tag{2.1}$$

with the two limits connected smoothly by a cubic spline. Each time step can be written schematically as

$$\omega(t + \Delta t) = [\omega(t) + \Delta t N(t)][1 - \Delta t F(y)] \approx \omega(t) + \Delta t[N(t) - F(y)\omega(t)], \tag{2.2}$$

where ω stands for any of the two evolution variables, and N represents the full right-hand side of the Navier-Stokes equations. To the lowest order Eq. (2.2) is the discretization of

$$\partial_t \omega - N = -F(y)\omega. \tag{2.3}$$

In this interpretation the mask, where active, acts as a zeroth-order damping term for the evolution variables, both of which are related to the vorticity, and T is a damping time which is independent of the length scale of the fluctuations. In practice the time stepping is a third-order Runge-Kutta in which the masking filter is applied at each substep, and T has to be multiplied in Eq. (2.2) by $3/2$ to be consistent with Eq. (2.3). The Navier–Stokes equations are not modified at all below the mask lower limit δ_1.

When T is compared with the time λ^2/ν needed by molecular viscosity to damp a fluctuation of size λ, it defines a cut-off length scale $\lambda = (\nu T)^{1/2}$. Fluctuations shorter than this length are predominantly damped by viscosity, while longer ones are damped by the numerical mask. This scale is expressed in wall units as

$$\lambda^+ = T^{+1/2}. \tag{2.4}$$

In the experiments in this paper $T^+ \approx 1$, and all the fluctuations in the masked layer are essentially suppressed by the mask. While this is true for vorticity fluctuations, irrotational ones are not affected, and the outer edge of the Navier-Stokes layer is bounded by a potential core which prevents the formation of viscous boundary layers at the mask boundary.

While the flows in Jiménez & Pinelli (1999) and Jiménez & Simens (2001) were integrated at constant mass flux in a channel, the present experiments are carried at constant driving stress in a 'semi-infinite' domain. No-slip impermeable boundary conditions are imposed at $y = 0$, and the velocities are matched to the outer potential fluctuations at the edge of the computational domain, $y = 1$, using the method introduced by Corral & Jiménez (1995). The Chebychev polynomials of the wall-normal expansions are defined in a domain which is twice as high as the actual computational one, and only even or odd polynomials are used, depending on the variable to be represented. The mask height is adjusted so that the vorticities are essentially zero at the edge of this computational domain, so that their wall-normal spectral expansions remain accurate. The expansions of the variables which extend into the potential region, such as the velocities, are supplemented by exponentials. The coefficient of the $\exp[\mathrm{i}(\alpha x + \beta z)]$ Fourier component of the wall-normal velocity is, for example, expanded in terms of odd Chebychev polynomials plus the extra basis functions,

$$\exp[\pm(\alpha^2 + \beta^2)^{1/2} y], \tag{2.5}$$

which are homogeneous solutions of the Helmholtz equation satisfied by that particular Fourier mode as a consequence of incompressibility. Corral & Jiménez (1995) adjusted the coefficients of those extra functions to ensure the impermeability condition at $y = 0$ and the vanishing of the potential fluctuations as $y \to \infty$. The present code incorporates the extra freedom of substituting the condition at infinity by an impermeable slip boundary at $y = H > 1$, where the streamwise, wall-normal and spanwise velocity components, u, v and w, satisfy

$$v = 0, \qquad \partial_y u = \partial_y w = 0. \tag{2.6}$$

The limit $1/H \to 0$ recovers the semi-infinite domain discussed above.

The evolution equations for the (0, 0) Fourier modes of u and w cannot be expressed in terms of ω_y and ϕ, and are not modified by the numerical mask. Their expansions are also special. The exponentials are replaced by linear functions,

$$a_0 + b_0 y, \tag{2.7}$$

whose coefficients have to adjusted. Because there are no Reynolds stresses in the region where the mask is active, and because no mean pressure gradient is applied, the mean velocity profiles in the potential core are linear in y, with a slope b_0 that can be chosen arbitrarily (see Fig. 1*a*). The additive constant a_0 is then determined by the boundary condition at the wall. In our experiments the asymptotic slope of the profile of w is taken as zero, but that of u provides the driving force for the flow and determines the wall friction. All experiments in this paper are scaled so that the height of the computational domain is $y^+ = 120$. Note however that this height is irrelevant, because no turbulent flow extends above the mask height, which is always lower. The relevant turbulent Reynolds number is the height of the damping function $\delta_1^+ = u_\tau \delta_1 / \nu$, which determines the largest possible wall-normal size of the turbulent structures.

Since the goal of this paper is to study the large-scale organization of the wall, the simulations are carried out in computational boxes whose streamwise and spanwise periodicities are long, $L_x^+ \approx 10^4$, and wide, $L_z^+ \approx 10^3$. The resolution is in all cases $\Delta x^+ = 9$ and $\Delta z^+ = 5$ before dealiasing by the 2/3 rule, resulting in 1536×192 collocation points for the largest of the computational boxes discussed below. In the wall-normal direction, along which the expansion is not dealiased, 49 even or odd Chebychev modes are used. The first collocation point is at $y^+ = 0.06$.

3. Results

As already reported by Jiménez & Pinelli (1999), the turbulence statistics in these large autonomous boxes agree well with those of regular simulations in the unmasked layer, at least as long as $\delta_1^+ \gtrsim 50$. To avoid complications with marginal mask heights, all the experiments in this paper are run with $\delta_1^+ = 72$. Some of the resulting statistics are compared in Fig. 1 with the results for a complete channel at $Re_\tau = 550$ (del Álamo & Jiménez, 2001). The mean velocity shows a short 'logarithmic' layer before joining the linear profile of the irrotational region, while the velocity and vorticity fluctuations agree well with the results of the full channel up to about half the mask height. The peaks of the vorticity profiles located just above δ_1 are artifacts of the damping mask. They have already been described by Jiménez & Simens (2001), and are due to the reconnection of the vortex lines after they are truncated by the damping. The results for the other fluctuating quantities are similar to those included in the figure.

Our present concern is the spectral distribution of the turbulent energy among the

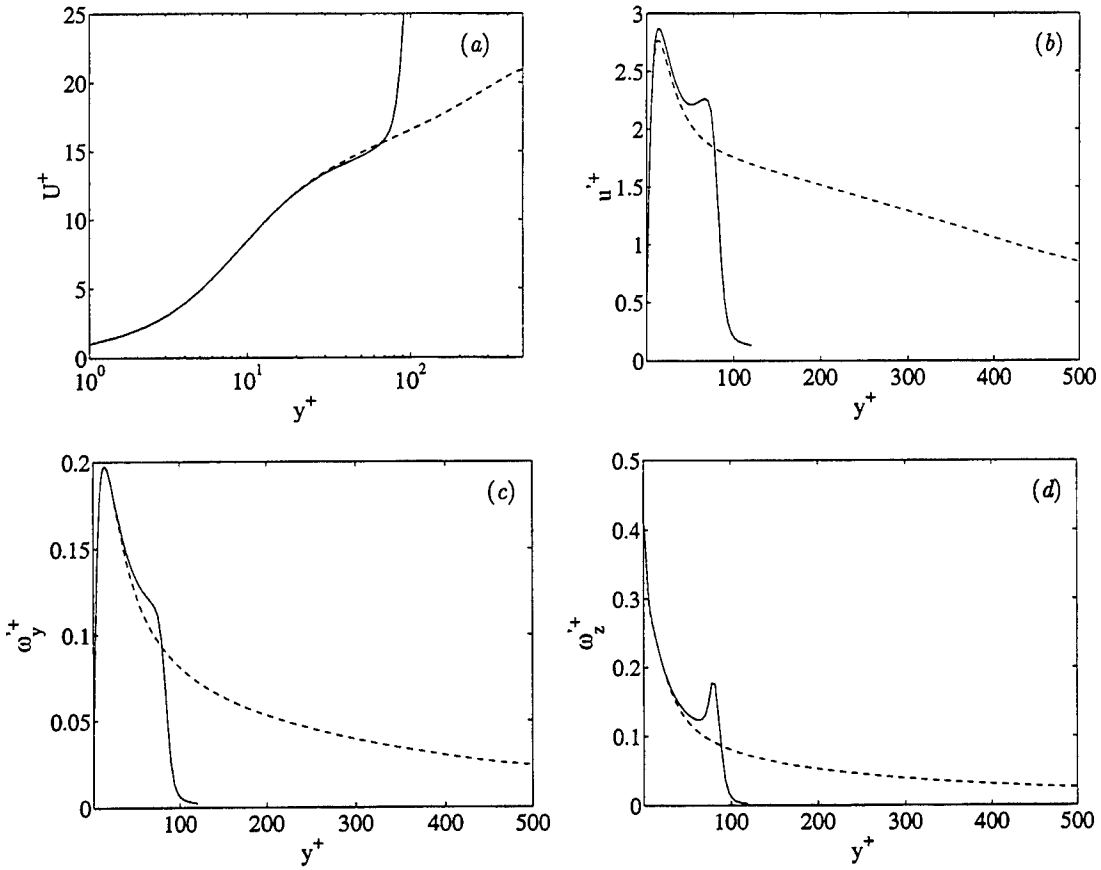

FIGURE 1. Mean profiles for: ——— , an autonomous wall $\delta_1^+ = 72$, $\delta_2^+ = 108$, $L_x^+ = 1.2 \times 10^4$, $L_z^+ = 10^3$, $1/H = 0$; ---- , a complete channel, $Re_\tau = 550$, $L_x^+ = 1.4 \times 10^4$, $L_z^+ = 7 \times 10^3$. (*a*) Mean velocity. (*b*) Streamwise velocity fluctuations. (*c*) Wall-normal vorticity fluctuations. (*c*) Spanwise vorticity fluctuations.

different size ranges. It was shown by Jiménez & Pinelli (1999) that these autonomous flows contain structures which are visually indistinguishable from the velocity streaks and quasi-streamwise vortices found in the near-wall region of regular wall turbulence (Robinson 1991), and that they share with them their characteristic streamwise and spanwise length scales, $\lambda_x^+ \times \lambda_z^+ \approx 500 \times 100$, and their advection velocity $U_c^+ \approx 14$. Individual structures of similar sizes have been isolated by different methods in simplified Poiseuille flows (Jiménez & Moin 1991; Jiménez & Simens 2001; Waleffe 2001) and Couette flows (Nagata 1990; Waleffe 1998), and the intuitive reason for their scaling properties is that the presence of the wall constrains the wall-normal velocity fluctuations to sizes of the order of the wall distance.

On the other hand Townsend (1976) noted that no such constraint exists for the wall-parallel fluctuations, which can be larger. He named those hypothetical large structures 'inactive' because they could not, by themselves, create Reynolds stresses. We noted in the introduction that very large structures have indeed been identified and studied in the logarithmic layer. Hites (1997) measured the longitudinal velocity spectrum in boundary layers over a wide range of Reynolds numbers. He found that above $y^+ \approx 40$ the streamwise velocity spectrum is bimodal, with a shorter peak that scales in wall units

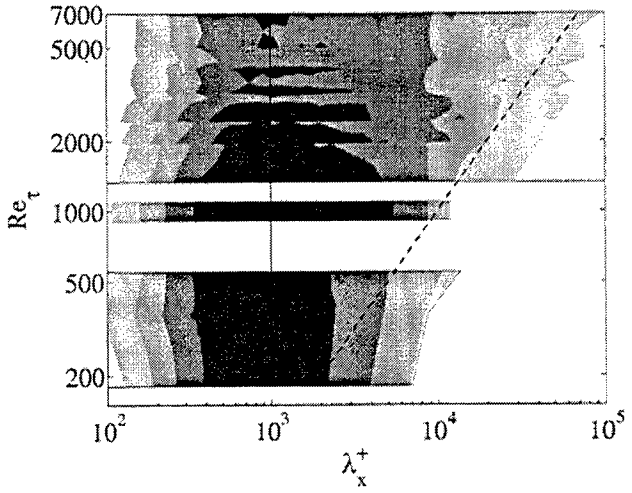

FIGURE 2. Longitudinal energy spectra for various near-wall flows. $y^+ = 20$. Gray levels correspond to the magnitude of $k_x E_{uu}$, as a function of the wavelength $\lambda_x = 2\pi/k_x$. Each line corresponds to a different Reynolds number. The upper block is interpolated from fifteen spectra of boundary layers (Hites, 1997). The lower one is interpolated from three numerical channels at $Re_\tau = 180$, 360 and 550 (del Álamo & Jiménez, 2001). The middle line is the autonomous wall computation in Fig. 1, whose Reynolds number has been assigned in a completely arbitrary manner. The dashed line is $\lambda_x = 10h$, where h is either the channel half-height or the boundary layer thickness, and the solid one is $\lambda_x^+ = 1000$.

and a longer one that scales in outer units, but he noted that the longer peak disappears below that height. His conclusions are strengthened by the comparison by Österlund *et al.* (2000) of the same data with spectra obtained on a different installation by a different group, as well as by the results obtained by Kim & Adrian (1999) in pipe flows above $y^+ = 100$. Older data to the same effect are summarized in Jiménez (1998). Most of those studies are restricted to the upper buffer layer and to the logarithmic layer, and do not emphasize the near-wall region.

More recently Metzger & Klewicki (2001) compared spectra at $y^+ = 15$ in two boundary layers with $Re_\theta = 2000$ and 5×10^6, and found a large excess of low-frequency energy in the latter with respect to the former. DeGraaff & Eaton (2000) made a comparative study of several boundary layers in a range of Reynolds numbers similar to those of Hites (1997). Although they did not measure spectra, they found that the intensity of the near-wall peak of the longitudinal velocity fluctuations, which is well inside the near-wall region, increases slowly with Reynolds number, again pointing to an effect of the outer flow on the wall layer.

In fact, a careful replotting of the available data very close to the wall confirms that the structures in this region are also subject to large-scale effects. This can be seen in Fig. 2 which shows longitudinal spectra of the streamwise velocity at $y^+ = 20$. The contour plot corresponds to individual premultiplied spectra which have been stacked together as a function of their Reynolds numbers, and which are treated as if they were a single function of Re_τ and of the streamwise wavelength $\lambda_x = 2\pi/k_x$. The upper block in the figure corresponds to the boundary layers in Hites (1997), while the lower one corresponds to three numerical channels by del Álamo & Jiménez (2001). The single spectrum between the two blocks will be discussed below.

It is clear that the long-wavelength end of the spectrum moves to the right as the Reynolds number increases, and that in the boundary layers it is approximately located at ten times the boundary layer thickness. The long-wavelength end of the channel spectra also lengthens with Reynolds number, but it does not seem to follow the same law. This disagreement is probably only apparent, and the spectra of the two highest-Reynolds number channels collapse fairly well with those of the boundary layers when the boundary layer thickness is defined as 2.5 times the channel half height. This is not unreasonable, since the outer part of the boundary layer, characterized by intermittent incursions of irrotational fluid, is missing from the channels, each of whose walls can roughly be described as the inner, fully-turbulent, part of a boundary layer. The main short-wavelength peak of the spectra remains relatively constant at $x^+ \approx 1000$ within this Reynolds numbers range.

Note that the large structures in the long-wavelength end of the spectra, with lengths of the order of $10^4 - 10^5$ wall units, are unlikely to be individual streaks. It is tempting to conclude that their origin is the distortion of the near-wall layer by the outer flow, which imposes on the wall its own large scales, but it is also possible that the wall organizes itself. Such self-organization is observed in many nonlinear systems, and it is of some interest to determine whether the near-wall large scales are autonomous or exogenous. Their expected behavior would be different in each case. If they were forced from outside it might, for example, be possible to control them by acting on the outer flow, while if the organization is self-induced such controls would probably be ineffective.

The question can be tested using the autonomous numerical simulations described in Section 2, since in them there are no outer structures with which the wall can interact. Figure 3 displays two-dimensional spectra from a numerical channel at $Re_\tau = 550$ (del Álamo & Jiménez, 2001), and from an autonomous wall with $\delta_1^+ = 72$. Both are computed in periodic boxes which are chosen to be as large as possible to minimize the interference of the computational domain with the large structures.

The first surprise is the almost perfect correspondence between the autonomous case and the fully-turbulent case, which strongly suggests that the large-scale organization of the wall regionis not due to the outer flow. There are no turbulent fluctuations above $y^+ \approx 80$ in the autonomous case. The agreement is specially good for the wall-normal component, for which the structures are relatively short and narrow. Their size more or less agrees with the individual vortex–streak structures isolated by Jiménez & Moin (1991). The second surprise is that the large structures of the streamwise velocity, and to a certain extent those of w, are actually *longer* in the autonomous wall than in the full channel. This also runs counter to the idea that the outer flow is the origin of the large near-wall scales.

The one-dimensional spectrum of u in the autonomous wall has been included in the compilation in Fig. 2 as the narrow line in the gap between the high-Reynolds number boundary layers and the channels. The Reynolds number assigned to it in the figure, $Re_\tau = 1000$, is completely arbitrary since, if any Reynolds number could be assigned to that flow, it would be the height $\delta_1^+ = 72$ of the numerical mask. The fact that this spectrum does not look out of place in its arbitrary location emphasizes that it is much longer than what could be expected from its thickness. The same conclusion can be drawn from the comparison of the one-dimensional spectra in Fig. 3(b).

The apparently contradictory observations that, on the one hand the large-scale structures are present in autonomous walls lacking an outer flow, while on the other hand they are limited in real boundary layers to lengths shorter than a fixed multiple of the

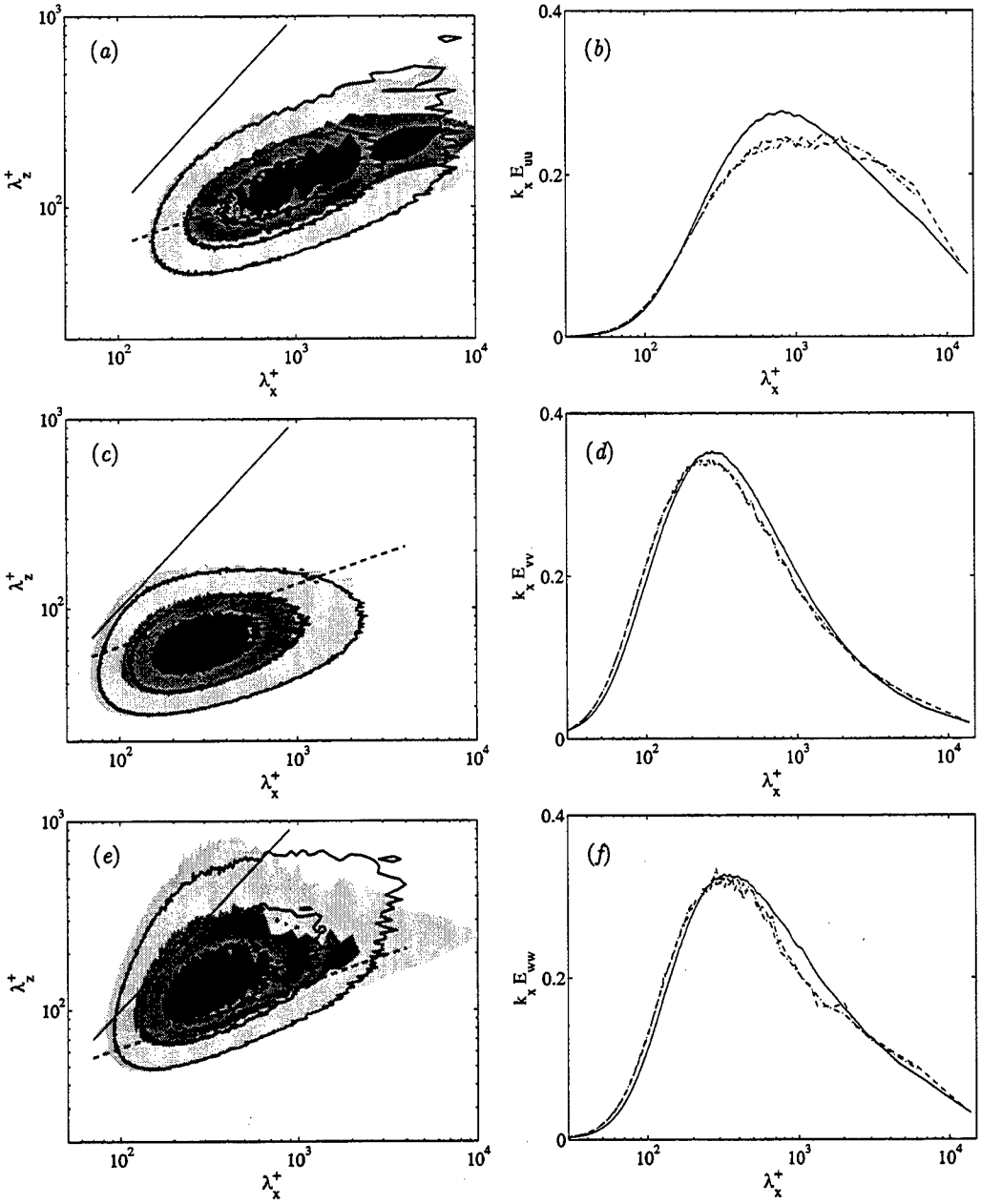

FIGURE 3. (*a*), (*c*), (*e*) Premultiplied two-dimensional velocity spectra, $k_x K_z E^{2D}(\lambda_x, \lambda_z)$, as functions of the streamwise and spanwise wavelengths. $y^+ = 16$. Shaded contours are the autonomous wall in Fig. 1. Lines are a full turbulent channel with $Re_\tau = 550$ (del Álamo & Jiménez, 2001). The solid lines are $\lambda_x = \lambda_z$, and correspond to horizontally isotropic structures. The dashed lines have logarithmic slopes 1/3, and pass through $\lambda_x^+ = \lambda_z^+ = 50$. The contours are (0.25, 0.5, 0.75) times the maximum value of each spectrum. (*b*), (*d*), (*f*) One-dimensional streamwise spectra, $k_x E(\lambda_x)$, for the same data. ——— , full channel; - - - - , the autonomous wall in Fig. 1. —·— , an autonomous wall with the same parameters except $L_x^+ = 6 \times 10^3$. (*a*), (*b*) Streamwise velocity. (*c*), (*d*) Wall-normal velocity. (*e*), (*f*) Spanwise velocity.

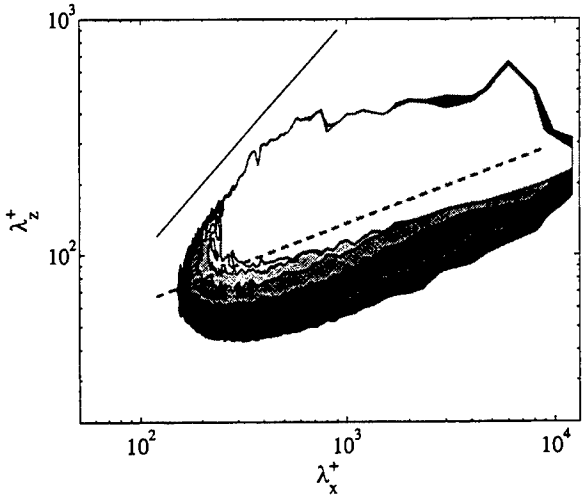

FIGURE 4. Each shaded contour is a premultiplied two-dimensional spectrum of the streamwise velocity at a different distance from the wall. From darker to lighter $y^+ = 10(10)60$. The flow is the autonomous wall in Fig. 1, and the contour values are the same as the outermost contour in Fig. 3. The length of the two axes correspond to the size of the computational box. The two trend lines are as in Fig. 3.

flow thickness, are best reconciled by assuming that the autonomous wall layer would by itself form infinitely long structures, and that the effect of the outer flow is to break those very long structures into pieces which are *shorter* than a given length. This is not as unlikely as it may seem, since the aspect ratio of the longest structures in Fig. 3(a) is already $L_x/y = 200$, and it is difficult to see how such a number might differ from infinity in terms of dynamics.

This raises the question of why the autonomous spectrum decreases sharply at its long-wave end in Fig. 3(b). In other words, why it is not really infinitely long. Part of the answer might be the interference of the finite size of the box, since the decrease appears only in the second longest numerical harmonic, which is probably strongly influenced by the finite domain. This possibility is reinforced by the behavior of the autonomous spectra farther from the wall. The good correspondence with the spectra of the full flows is maintained up to $y^+ \approx 40$, but higher up the autonomous box is both too short and in particular too narrow to contain its own structures. This is seen in Fig. 4 which shows spectra as a function of wall distance. The highest level in that figure is already close to the numerical mask, at it is clear that it is constrained at it widest point by the width of the box. It is plausible to suppose that one result of that constriction might be to limit the extent of the spectra everywhere. On the other hand, an attempt to reproduce that effect using shorter numerical boxes did not produce clear results. The right-hand side of Fig. 3 contains spectra from two autonomous simulations, in addition to those from the full channel. The results discussed up to now have been those from the longest autonomous box, but the figure also shows another set of spectra from a box of the same width, but only half as long. They are difficult to distinguish from those in the longer box and, in particular, the E_{uu} spectrum in the shorter box does not show a sharp drop in its longest harmonic comparable to that in the longer box. More work is needed before the effect of box size is clarified, and more extensive simulations are in progress.

It is clear from Fig. 3 that the longer scales are also wider, and that this part of the

flow is far from being isotropic. This is specially true of the longitudinal velocity, and it is interesting that the 'ridge' in that spectrum follows fairly closely the power law

$$\lambda_x \sim \lambda_z^3. \tag{3.1}$$

It is dangerous to extrapolate similarity laws from limited experimental data without a plausible theoretical model, but del Álamo & Jiménez (2001) found the same power law in complete channels near the wall, giving some support to the idea that the relation might be real. The spectra of the other two velocity components are closer to being isotropic.

Del Álamo & Jiménez (2001) show that, in the logarithmic layer of complete wall-bounded flows, the two-dimensional spectra satisfy a different power law

$$\lambda_x \sim \lambda_z^2, \tag{3.2}$$

and they speculate that it may be related to the downstream spreading of perturbations induced on the mean velocity profile by localized transverse velocities. In essence they propose that Eq. (3.2) is a reflection of the form of the similarity solutions of the diffusion-advection equation,

$$\partial_x u = (\partial_{yy} + \partial_{zz})u, \tag{3.3}$$

which take the form

$$u = x^{-1}\widehat{u}(y/x^{1/2},\, z/x^{1/2}). \tag{3.4}$$

The relation Eq. (3.2) would derive from the form of the spanwise similarity variable in Eq. (3.4).

A similar argument can be used to support Eq. (3.1). Near the wall the mean flow velocity is closer to a pure shear than to the approximately- constant velocity of the logarithmic layer. The diffusion equation then takes the form

$$y\partial_x u = (\partial_{yy} + \partial_{zz})u, \tag{3.5}$$

whose similarity solutions are

$$u = x^{-1}\widehat{u}(y/x^{1/3},\, z/x^{1/3}), \tag{3.6}$$

leading to Eq. (3.1). Note that these arguments can only be treated as indicative, since the diffusion at the scale of these large structures is probably due to smaller-scale turbulence, while both Eq. (3.3) and Eq. (3.5) assume a constant eddy viscosity.

4. Conclusions

We have shown that the self-sustaining small-scale structures of the near-wall region are able to organize themselves into much larger scales, especially visible in the spectra of the streamwise velocity component. In the absence of any outer flow the length of these large structures appears to be infinite, at least within the limits of the present numerical simulations, but in actual turbulent flows they scale as multiples of the flow thickness. We have suggested that this interaction takes the form of a shortening of the near-wall structures by the random perturbations originating in the outer flow.

The precise mechanism of this interaction is not clear from the present experiment. The numerical parameter H at which the slip boundary condition (2.6) is applied was introduced for this purpose, on the assumption that the postulated infinite length of the structures in the autonomous simulations was a reflection of the infinite distance

at which the irrotational boundary condition was applied. An autonomous box was run using $H = 2$, which corresponds to a slip wall at $y^+ = 240$ but, while the spectra shortened a little, the effect was too weak to be considered as a model for the interaction in real flows. Presumably the rotational fluctuations of the turbulent core flows are more effective in disturbing the wall that the irrotational fluctuations in our model.

We have shown that the width of the near-wall large structures scales like the cube root of their length, and we have proposed a simple scaling explanation for that power law. The assumption is that the large u-structures are the dissipating wakes of the perturbations introduced in the mean profile by occasional small-scale sweeps or ejections. The essence of this argument is that the large scales, being very anisotropic and therefore subject to very different time scales in their transverse and longitudinal directions, can be modelled as linear objects which only see the small-scale turbulence as either an eddy viscosity or as a random forcing. If this is true, it should possible to derive quantitative predictions on their spectra from the properties of some modified Orr-Sommerfeld or Squires equation.

This work was supported in part by the Spanish CICYT contract BFM2000-1468 and by ONR grant N0014-00-1-0146. O.F. and M.G-V. were supported in part by undergraduate fellowships from the Universidad Politécnica of Madrid. We are grateful to J.C. del Álamo and P. Bradshaw for reading an early version of the manuscript and providing useful suggestions.

REFERENCES

CORRAL, R. & JIMÉNEZ, J. 1995 Fourier/Chebyshev methods for the incompressible Navier Stokes equations in infinite domains, *J. Comput. Phys.* **121**, 261–270.

DEGRAAFF, D.B. & EATON, J.K. 2000 Reynolds number scaling of the flat-plate turbulent boundary layer, *J. Fluid Mech.* **422**, 319–346.

DEL ÁLAMO, J.C. & JIMÉNEZ, J. 2001 Direct numerical simulation of the very-large anisotropic scales in a turbulent channel. *Annual Research Briefs*, Center for Turbulence Research, NASA Ames/Stanford Univ., 329–341.

HITES, M.M. 1997 Scaling of high-Reynolds number turbulent boundary layers in the National Diagnostic Facility. *Ph. D. Thesis* Illinois Inst. of Technology.

HUNT, J.C.R. & MORRISON, J.F. 2000 Eddy structures in turbulent boundary layers. *Eur. J. Mech. B - Fluids* **19**, 673–694.

JIMÉNEZ, J. 1999 The physics of wall turbulence, *Physica* A **263**, 252–262.

JIMÉNEZ, J. 1998 The largest scales of turbulent wall flows. In *CTR Ann. Res. Briefs*, Stanford Univ. 137–154.

JIMÉNEZ, J. & MOIN, P. 1991 The minimal flow unit in near wall turbulence. *J. Fluid Mech.* **225**, 221–240.

JIMÉNEZ, J. & PINELLI A. 1999 The autonomous cycle of near wall turbulence, *J. Fluid Mech.* **389**, 335–359.

JIMÉNEZ, J. & SIMENS, M.P. 2001 Low-dimensional dynamics in a turbulent wall, *J. Fluid Mech.*, **435**, 81–91.

KIM, K.C. & ADRIAN, R.J. 1999 Very large-scale motion in the outer layer. *Phys. Fluids* **11**, 417–422.

KIM, H.T., KLINE, S.J. & REYNOLDS, W.C. 1971 The production of turbulence near a smooth wall in a turbulent boundary layers. *J. Fluid Mech.* **50**, 133-160.

KIM, J., MOIN, P. & MOSER, R. 1987 Turbulence statistics in fully developed channel flow at low Reynolds number. *J. Fluid Mech.* **177**, 133–166.

METZGER, M.M. & KLEWICKI, J.C. 2001 A comparative study of near-wall turbulence in high and low Reynolds numbers boundary layer, *Phys. Fluids* **13**, 692–701.

MOSER, R., KIM, J. & MANSOUR, N.N. 1999 Direct numerical simulation of a turbulent channel flow up to $Re_\tau = 590$. *Phys. Fluids* **11**, 943–945.

NAGATA, M. 1990 Three-dimensional finite-amplitude solutions in plane Couette flow: bifurcation from infinity. *J. Fluid Mech.* **217**, 519–527.

ÖSTERLUND, J.M., JOHANSSON, A.V., NAGIB, H.M. & HITES, M.H. 2000 Spectral characteristics of the overlap region in turbulent boundary layers. Extended abstract for *Int. Congr.Theor. Appl. Math. 2000*, Chicago.

PERRY, A. E., HENBEST, S. & CHONG, M. S. 1986 A theoretical and experimental study of wall turbulence. *J. Fluid Mech* **165**, 163–199.

ROBINSON, S.K. 1991 Coherent motions in the turbulent boundary layer. *Ann. Rev. Fluid Mech.* **23**, 601–639.

TOWNSEND, A.A. 1976 *The Structure of Turbulent Shear Flow.* Cambridge Univ. Press, 2nd. ed., p. 135.

WALEFFE, F. 1998 Three-dimensional coherent states in plane shear flows. *Phys. Rev. Letters* **81**, 4140–4143.

WALEFFE, F. 2001 Exact coherent structures in channel flow. *J. Fluid Mech.* **435**, 93–102.

Direct numerical simulation of the very large anisotropic scales in a turbulent channel

By Juan C. del Álamo† AND Javier Jiménez‡

1. Introduction

Over the last decades the knowledge on the small scales of turbulent wall flows has experienced a significant advance, especially in the near-wall region where the highest production of turbulent energy and the maximum turbulence intensity occur. The development of computers has played an important role in this progress, making direct numerical simulations affordable (Kim, Moin & Moser, 1987), and offering wider observational possibilities than most laboratory experiments.

The large scales have received less attention, and it has not been until recently that their significance and their real size have been widely recognized, thanks in part to the experiments by Hites (1997) and Kim & Adrian (1999), and to the compilation of experimental and numerical data by Jiménez (1998). Two are the main reasons for this. In the first place, when Townsend (1976) originally proposed the existence of very large anisotropic scales (VLAS) in the overlap layer under the 'attached eddy' hypothesis, he described them as 'inactive', not containing Reynolds stresses. Perry, Henbest & Chong (1986) repeated that assertion in their elaboration of Townsend's model, and this has probably contributed to their relative neglect by later investigators. Jiménez (1998) showed however that this characterization is only partly correct, and that the VLAS carry a substantial fraction of the Reynolds stresses. We will provide in this report further evidence that they carry a substantial part of the turbulent energy in the flow and that they are 'active' in Townsend's sense.

The large size of these scales also makes them difficult to study, both experimentally and numerically. Many of the high-Reynolds number laboratory experiments lack spectral information, have too few wall distances, or have data records which are too short to capture the largest scales. Moreover, most of of them contain only streamwise information, and data on the spanwise scales are scarce. The requirements of both a very large box and a high Reynolds number has made direct numerical simulation of the VLAS unapproachable until today. Previously available numerical databases were restricted to low Reynolds numbers, with little or no separation between the small and large scales (Kim, Moin & Moser, 1987), or to small computational boxes which interfere with the VLAS (Moser, Kim & Mansour, 1999; Abe, Kawamura & Matsuo, 2001).

The purpose of this report is to serve as a preliminary description of a newly compiled numerical database of the characteristics of the large scales in turbulent channel flow at moderate Reynolds numbers.

† School of Aeronautics UPM, 28040 Madrid, Spain
‡ Also at School of Aeronautics UPM, 28040 Madrid, Spain

	Re_τ	Δx^+	Δz^+	Δy^+_{max}	L_x/h	L_z/h	N_x	N_z	N_y	Numerics
Moser *et al.* (1999)	590	7.2	3.6	7.2	2π	π	512	512	257	Spectral
Abe *et al.* (2001)	640	8.0	5.0	8.2	6.4	2	512	256	256	Second order FD
Present case 1	550	8.9	4.5	6.7	8π	4π	1536	1536	257	Spectral
Present case 2	180	8.9	4.5	6.1	12π	4π	768	512	97	Spectral

TABLE 1. Summary of cases. The resolution is measured in collocation points

2. The numerical experiment

Our investigation has been carried on a direct numerical simulation of the turbulent incompressible flow in plane channels at Reynolds numbers $Re_\tau = 180$ and $Re_\tau = 550$, based on the wall friction velocity, u_τ, and on the channel half-width h. The emphasis in this report will be on the latter of those two simulations. The numerical code is fully spectral, using dealiased Fourier expansions in the streamwise and spanwise directions, and Chebychev polynomials in the wall-normall one, as in Kim, Moin & Moser (1987). Although there are computations in the literature at somewhat higher, although comparable, Reynolds numbers (Moser, Kim & Mansour, 1999; Abe, Kawamura & Matsuo, 2001; see table 1), we believe that this is the first simulation in which the numerical box is large enough not to interfere with the largest structures in the flow.

The experimental results for high-Reynolds number turbulent wall flows (see the references given in the previous section) reveal that the premultiplied one-dimensional streamwise velocity spectrum $k_x E^{1D}_{uu}(k_x, y)$ has two peaks. The first one is in the wall region and scales in wall units. Its position does not vary with the distance y to the wall and corresponds to the size of the buffer layer streaks. At the top of the buffer layer, the first peak coexists with a second one which scales in outer units and is characteristic of the outer region. The second peak becomes stronger as the Reynolds number increases and its position corresponds to the VLAS. Its length increases with y and reaches a maximum of $4 - 15\,\delta$ (where δ is the characteristic flow thickness) at a wall distance which scales in outer units and which depends on the type of flow. Beyond that level, the peak moves to shorter wavelengths, until the streamwise turbulent energy becomes associated to scales of length $\lambda_x \approx \delta$ at $y = \delta$. With this information in mind, and with the aid of tests cases performed at $Re_\tau = 180$ and $Re_\tau = 550$ in boxes of different sizes, we have used a box of size $L_x \times L_y \times L_z = 8\pi h \times 2h \times 4\pi h$ in the streamwise, wall-normal and spanwise directions for our $Re_\tau = 550$ simulation.

The longest scales in the numerical channels occur in the streamwise velocity u at $y \approx 0.5h$. Fig. 1*(a)* displays the premultiplied one-dimensional spectra $k_x E^{1D}_{uu}(k_x)$ at that level. It is clear that the most energetic structures have lengths of $2 - 5h$, which are represented by the Fourier modes $5 - 12$ in our simulation at $Re_\tau = 550$, and $7 - 18$ in the one at $Re_\tau = 180$. The dynamics of the first few Fourier modes are affected by the periodicity of the box, essentially because their resolution in wavelength space is too coarse to provide a healthy interaction amongst the different length scales. The even-odd structure of the long-wave end of the $1 - D$ spectrum at $Re_\tau = 550$ in Fig. 1*(a)* is probably due to this effect. It also appears at other wall distances, and has been observed in numerical channels performed with completely different numerics (Guglielmo Scovazzi, private communication).

The widest scales appear at the center of the channel in the spanwise velocity w, whose

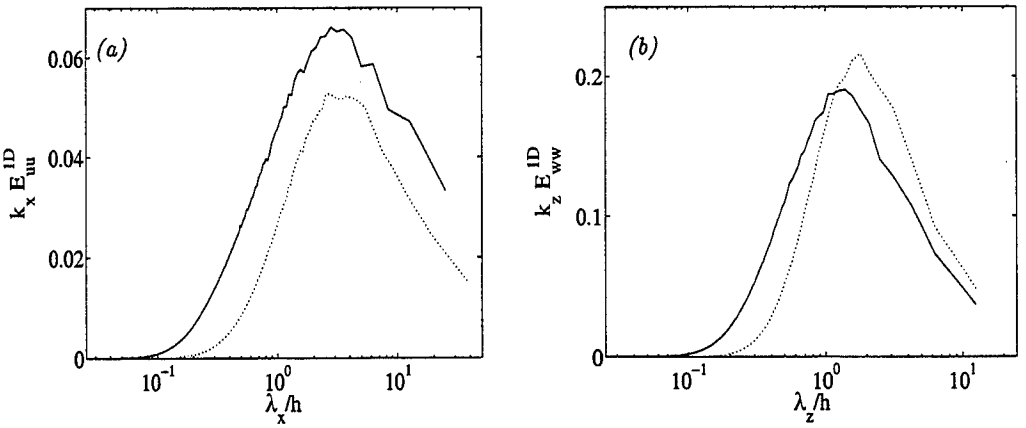

FIGURE 1. Premultiplied one-dimensional spectra at $y = 0.5h$. ——, present $Re_\tau = 550$; ·····, present $Re_\tau = 180$. *(a)* $k_x E^{1D}_{uu}(k_x)$. *(b)* $k_z E^{1D}_{ww}(k_z)$;

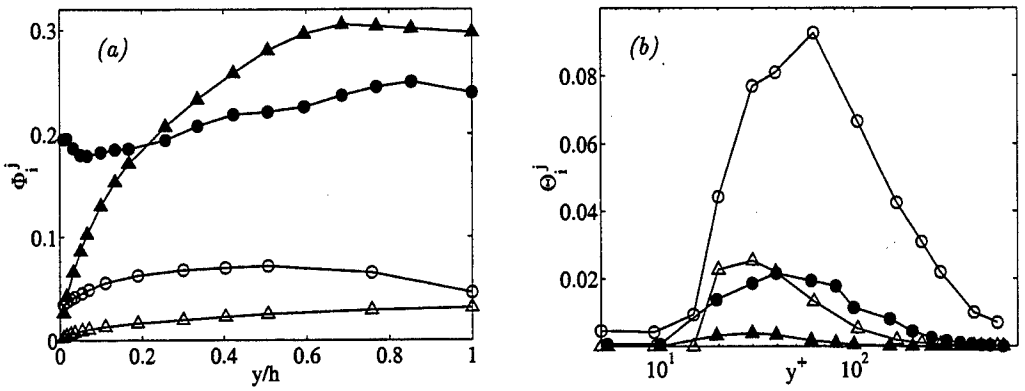

FIGURE 2. *(a)* Ratio Φ^j_i between the unresolved and total energies for the (i) velocity component along the direction (j), as a function of y. ○, Φ^x_u; △, Φ^z_w. *(b)* Fraction Θ^j_i of the energy of the derivative of the (i) velocity component with respect to the direction (j), which is aliased along that same direction, plotted as a function of y. ○, Θ^x_v; △, Θ^z_u. In all cases, the open symbols refer to the present $Re_\tau = 550$ simulation, and the closed ones to the one by Moser, Kim & Mansour (1999) at $Re_\tau = 590$.

transverse one-dimensional spectra $k_z E^{1D}_{ww}(k_z)$ have been represented in Fig. 1*(b)*. In this case the peaks of the spectra are sharper than those in Fig. 1(a). Thus, although the most energetic structures are again associated to low Fourier modes ($6-13$ at $Re_\tau = 550$ and $5-9$ at $Re_\tau = 180$), there is relatively less energy in the poorly-represented modes than in the streamwise direction.

A more quantitative check of the adequacy of the numerical box is to calculate the fractions Φ^x_u and Φ^z_w respectively of the streamwise energy $\langle u'^2 \rangle$ contained in the Fourier modes $k_x = 0$, $k_z \neq 0$, and of the spanwise energy $\langle w'^2 \rangle$ contained in the Fourier modes $k_x \neq 0$, $k_z = 0$. These ratios give an idea of how much turbulent energy is contained in fluctuations which are longer or wider than the numerical box, and which are treated numerically as if they were *uniform* in x or z. In Fig. 2(a) we represent Φ^x_u and Φ^z_w from our DNS at $Re_\tau = 550$ and from Moser, Kim & Mansour (1999). Note that in the latter,

with $L_x \times L_z = 2\pi h \times \pi h$, roughly 20% of the energy of u is contained in structures which are longer than the numerical box, and that the behavior of w in z is even worse in the outer region, where 30% of its energy is unresolved. From these data we conclude that the box of that simulation is too small to represent the largest flow structures, and that even the present one is in some ways marginal. It should however be noted that numerical experiments at $Re_\tau = 180$ in a shorter box with $L_x = 8\pi$, instead of 12π, showed very little degradation in the resolved part of the longitudinal spectra. On the other hand, low resolution experiments in a box of length $L_x = 6\pi$ at the higher Reynolds number showed signs of contamination of the spectral peak by the numerical effects mentioned above for the long spectral modes.

The grid resolution, given in table 1, is intermediate between those used by Moser, Kim & Mansour (1999) for their cases $Re_\tau = 180$ and $Re_\tau = 590$, and is slightly marginal for the smallest scales, specially in the x direction. The result is a spurious accumulation of enstrophy in the short-wavelength tails of the spectra of the velocity derivatives, where they are improperly represented. The most underresolved derivatives are $\partial_x v$ in x and $\partial_z u$ in z. Fig. 2*(b)* displays the fractions Θ_v^x and Θ_u^z of the enstrophy contained in these underresolved tails in a way similar to Fig. 2*(a)*. The underresolved enstrophy is in this case defined as the integral of the 'hook' in the premultiplied spectrum of the derivative in question, from the highest wavenumber to the location of its first minimum. There is more or less five times more underresolved enstrophy in our numerical channel that in the one from Moser, Kim & Mansour (1999). The comparison of Figs. 2*(a)* and 2*(b)* shows that the improperly resolved enstrophy at the short-wave ends of the spectra is of the same order as that of the improperly resolved energy in their long-wave ends.

To achieve stationary statistics for structures of wavelength λ the simulation has to be run for several turnover times λ/u_τ, which becomes fairly expensive in these long boxes. Our experience with test cases at $Re_\tau = 180$ indicates that to have some confidence in the statistics of the largest scales the simulation should be run for roughly 10 wash-out times L_x/U_b, where U_b is the bulk mean velocity of the flow. The statistics presented here for the $Re_\tau = 550$ case have been collected during 10 wash-out times, after discarding initial transients.

3. Results

3.1. *Two-dimensional velocity spectra in the near-wall region*

Figs. 3 and 4 display linearly spaced isocontours of the premultiplied two-dimensional energy spectra $\phi_{ij} = k_x k_z E_{ij}(\lambda_x, \lambda_z, y)$ as functions of the wavelength vector $(\lambda_x, \lambda_z) = (2\pi/k_x, 2\pi/k_z)$. Note that

$$\langle u_i' u_j' \rangle = \int_0^\infty \int_0^\infty \phi_{ij}(\lambda_x, \lambda_z, y)\, \mathrm{d}(\log \lambda_x)\, \mathrm{d}(\log \lambda_z), \tag{3.1}$$

so that these figures express how much energy is contained in structures of length λ_x and width λ_z. The shaded contours come from the simulation at $Re_\tau = 550$, while the line contours are from the one at $Re_\tau = 180$. The four wall distances in Fig. 3 are $y^+ = 15$, $y^+ = 90$, $y = 0.2h$, $y = 0.5h$, corresponding respectively to the bottom and the top of the buffer layer, and the bottom and the core of the outer region. In Fig. 4 the three wall distances are $y^+ = 15$, $y^+ = 90$ and $y = 0.5h$.

In the wall region the spectrum of the streamwise velocity (Fig. 3*a*) peaks around $\lambda_x^+ \approx 700$, $\lambda_z^+ \approx 100$, which is the size of the buffer layer streaks. The spectra of the two

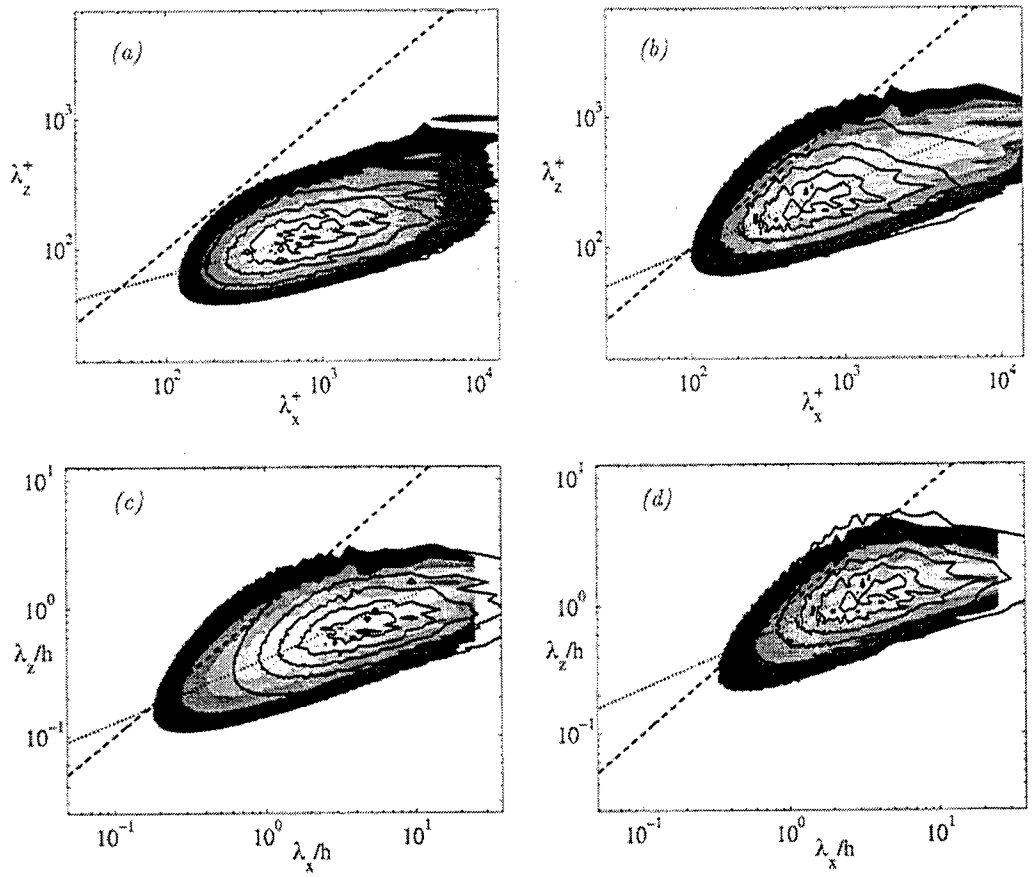

FIGURE 3. Premultiplied two-dimensional spectra ϕ_{uu} of the streamwise velocity, as functions of the streamwise and spanwise wavelengths at three representative wall distances. *(a)* Wall units, $y+ = 15$; *(b)* Wall units, $y+ = 90$ ($y = 0.5h$ at $Re_\tau = 180$); *(c)* Outer units, $y = 0.2h$ ($y^+ = 90$ at $Re_\tau = 550$); *(d)* Outer units, $y = 0.5h$. Shaded contours, $Re_\tau = 550$; line contours, $Re_\tau = 180$. In all the cases there are five linearly increasing contours. ···· , locus of two-dimensional isotropic structures $\lambda_z = \lambda_x$; the dotted line in *(a)* is $\lambda_x^+ \sim (\lambda_z^+)^3$, passing through $\lambda_x^+ = \lambda_z^+ = 50$; those in *(b)*, *(c)* and *(d)* are $\lambda_x y = \lambda_z^2$, and the point where this line crosses the dashed one corresponds to three-dimensionally isotropic structures.

other velocity components peak around $\lambda_x^+ \approx 250$, $\lambda_z^+ \approx 50 - 100$ (see Figs. 4*a* and 4*b*), corresponding approximately to the dimensions of an individual system of counterrotating quasi-streamwise vortices (Kim, Moin & Moser, 1987).

There is still not general agreement about the scaling in the near-wall region. Contrary to the classical idea that inner scaling should work close enough to the wall, several experimentalists have found evidence suggesting that this is not so, and in particular that the streamwise normal stress $\langle u'^2 \rangle$ increases with the Reynolds number throughout the wall layer, when expressed in wall units at a fixed y^+. Some of these researchers (DeGraaf & Eaton, 2000; Perry & Li, 1990) have argued that the Reynolds number dependence is due to the contribution of Townsend's (1976) 'inactive' motions. They note that this contribution scales in outer units, and are motivated by this observation to introduce 'mixed' scaling in which $\langle u'^2 \rangle$ is proportional to the geometric mean of the

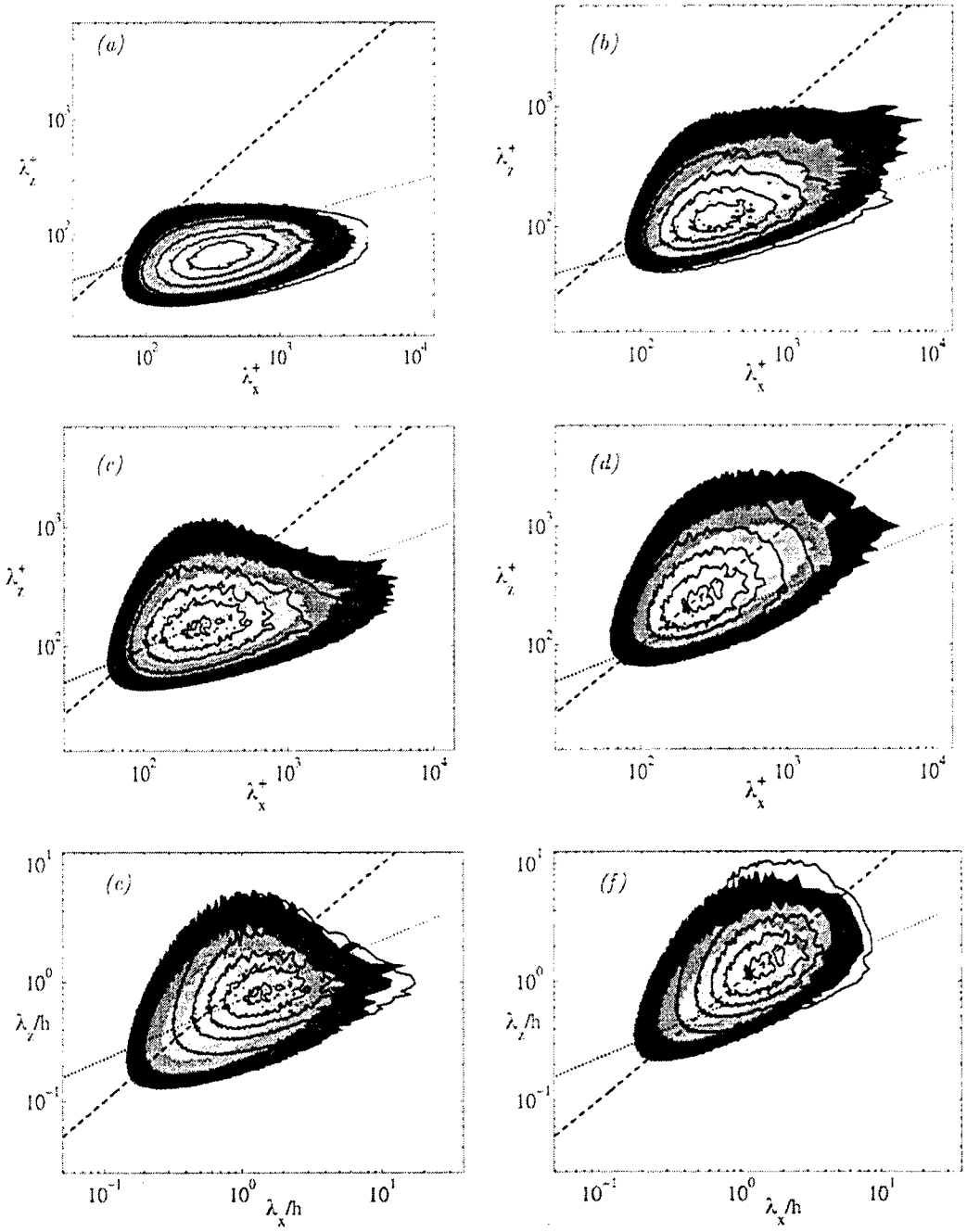

FIGURE 4. Premultiplied two-dimensional spectra as functions of the streamwise and spanwise wavelengths at three representative wall distances. *(a), (c) (e),* ϕ_{vv}; *(b), (d) (f),* ϕ_{ww}. *(a), (b)* Wall units, $y+ = 15$; *(c), (d)* Wall units, $y^+ = 90$ ($y = 0.5h$ at $Re_\tau = 180$); *(e), (f)* Outer units, $y = 0.5h$. Shaded contours, $Re_\tau = 550$; line contours, $Re_\tau = 180$. In all the cases there are five linearly increasing contours. ····· , locus of two-dimensional isotropic structures $\lambda_z = \lambda_x$; the dotted lines in *(a)* and *(b)*, are $\lambda_x^+ \sim (\lambda_z^+)^3$ passing through $\lambda_x^+ = \lambda_z^+ = 50$; those in *(c), (d), (e)* and *(f)* are $\lambda_x y = \lambda_z^2$ and the point where both lines cross in those figures corresponds to three-dimensionally isotropic structures.

friction and outer velocities. Hites (1997) presents a similar argument, but favors an interpretation in which the inner and outer contributions are scaled independently, with no simple overall law. Jiménez, Flores & García-Villalba (2001), using data from Hites (1997) and from the present numerical simulations show that the short-wavelength end of the one-dimensional streamwise u spectrum at $y^+ = 20$ scales well in inner units, while its long-wavelength end scales in outer units. It was already noted by Townsend (1976) that the no-slip impermeability condition at the wall does not limit the size of the u and w velocity structures, while the effect of the no-slip condition is limited in height to a few wall units. We can therefore expect the large scales, even if they originate far from the wall, to penetrate deep into the near-wall layer, causing $\langle u'^2 \rangle$ to have both local and global contributions.

In fact, the only region of the two-dimensional u-spectra in Fig. 3(*a*) that does not collapse well in wall units is the upper-right corner, which corresponds to the large structures which dominate the outer-layer spectra in Figs. 3*(c)* and 3*(d)*. As we move deeper into the buffer layer the energy contained in the large scales increases (Fig. 3*b*), in agreement with the common observation that the collapse of $\langle u'^2 \rangle$ in inner scaling worsens as the wall distance increases. Recent experimental spectra by Metzger & Klewicki (2001) at $y^+ = 15$ in the atmospheric boundary layer show that a substantial fraction of the streamwise turbulent energy is contained in very large structures at those extremely high Reynolds numbers ($Re_\theta \sim 10^6$). Jiménez, Flores & García-Villalba (2001) have argued that the effect is actually repressing, with the outer large scales preventing the wall streaks from becoming 'infinitely' long.

It is worth pointing out that the u spectrum in this region lies approximately along the power law

$$\lambda_x^+ \sim \left(\lambda_z^+\right)^3, \tag{3.2}$$

implying that, while the structures of the streamwise velocity become wider as the become longer, they also become more elongated, since they progressively separate from the spectral locus of two-dimensional isotropy. The spectrum of w does not share this property and is more isotropic in the (x, z) plane. The spectrum of v is very anisotropic in the near-wall region, but as we move away from the wall it develops a second isotropic component (Fig. 4*c,e*) whose relative strength increases with the wall distance, and which becomes dominant close to the center of the channel.

3.2. *The very large anisotropic scales in the outer layer*

Above $y^+ \approx 60$, the spectrum of the streamwise velocity becomes quite different from the spectra of the wall-normal and spanwise velocities, as we can see in Figs. 3 and 4. The spectrum of u is anisotropic and has two components. The first one is associated to small scales, and collapses fairly well for our two Reynolds numbers when plotted as a function of $(\lambda_x^+,\ \lambda_z^+)$ at a constant y^+ (Figs. 3*a* and 3*b*). The second one is related to large anisotropic structures and collapses well when plotted at a constant y/h as a function of $(\lambda_x/h,\ \lambda_z/h)$ (Figs. 3*c* and 3*d*). Below $y^+ \approx 60$ the small-scale component is the most important one, and the peak of the spectrum collapses in wall units as in Fig. 3*(a)*. Far from the wall ($y \gtrsim 0.3h$), it is the large-scale component which dominates, and the peak of the spectrum collapses in outer units as in Fig. 3*(d)*. This description suggests that, at least in turbulent channels at moderate Reynolds numbers, there exists a family of u structures in the inner region which scales in wall units and another one in the outer region which scales in outer units.

The present results resemble those of the high-Reynolds number experiments of Hites

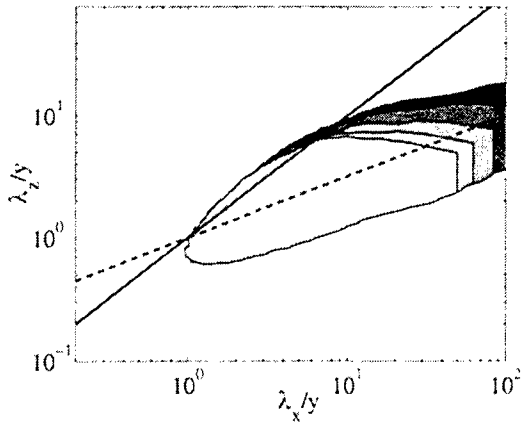

FIGURE 5. Superimposed contours of 0.2 times the maximum of ϕ_{uu} at five wall distances in the outer layer (from dark to light $y = 0.1h(0.1h)0.5h$). They are represented as functions of the streamwise and spanwise wavelengths nondimensionalized with the wall distance. ——— , locus of two-dimensional isotropic structures $\lambda_z/y = \lambda_x/y$; ···· , $(\lambda_z/y)^2 = \lambda_x/y$. The point where both lines cross corresponds to three-dimensionally isotropic structures.

(1997) and Kim & Adrian (1999), although there is a significant difference. In the numerical channels the two spectral peaks corresponding to the VLAS and the wall streaks never coexist. Instead, we observe an intermediate region of wall distances ($y^+ \gtrsim 60$, $y \lesssim 0.3h$) where the peaks of the u spectra do not collapse in inner or in outer units (Figs. 3*c* and 3*d*). One reason for this discrepancy may be that the viscous and the large-scale components of the u spectra have comparable intensities in our moderate-Reynolds number simulations. Hunt & Morrison (2000) have noted that the energy contained in the outer structures increases with the Reynolds number and will eventually become much larger than that in the inner ones, so that the large scales would eventually become dominant even very near the wall. The failure to observe an overlap in our simulations could be related to that effect; although we clearly observe the two spectral components in the two-dimensional spectra, the outer one is never strong enough in the inner region to appear as a peak in the one-dimensional spectra. On the other hand, new measurements at extremely high Reynolds numbers by Morrison *et al.* (2001) in pipes do not show any region in the flow with double spectral peaks for the one-dimensional u-spectra, and the question should therefore be consider as still open.

The spectra of v and w are also in this region more isotropic than those of u. The spectrum for w is closer to two-dimensional isotropy than that of v, but it is flatter, in the sense that it is both wider and longer than v for a given height. It is difficult from the present results to obtain clear spectral scaling laws for the transverse velocity components. In the lower part of the outer layer the small scales of the spectra collapse well in inner units (Figs. 4*c* and 4*d*), similarly to what happens with the streamwise velocity, but in this case the large scales do not collapse in outer units. Further away from the wall we have been unable to find any scaling that collapses the spectra at $Re_\tau = 180$ with those at $Re_\tau = 550$. In Figs. 4*(e)* and 4*(f)* the spectra are represented in outer units and only collapse, and even then imperfectly, for the largest scales.

The two-dimensional spectrum of the streamwise velocity exhibits a different behavior in the outer layer than in the wall region (see Eq. 3.2). Fig. 5 displays superimposed contours of ϕ_{uu} at five different wall distances in the outer layer ranging from $y = 0.1h$ (light) to $y = 0.5h$ (dark). The spectra are nondimensionalized with y and collapses well

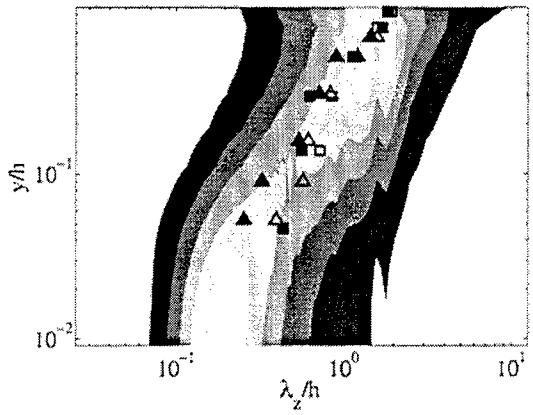

FIGURE 6. Premultiplied 1–D spectrum of streamwise velocity, in outer units. The shaded contours are the present $Re_\tau = 550$ simulation; the symbols are experiments by Nakagawa & Nezu (1981). ▲ and △ , $Re_\tau = 696$; ■ and □ , $Re_\tau = 318$. Open symbols, $\langle\lambda\rangle_s$; closed symbols, $\langle\lambda\rangle_e$.

along the dashed line, which corresponds to the power law

$$\lambda_x y = {\lambda_z}^2. \tag{3.3}$$

A possible explanation for this power law is that the structures in the streamwise velocity are the decaying wakes of approximately isotropic v and w structures. Those of diameter λ_z decay in times of order λ_z^2/ν_T under the action of an eddy viscosity ν_T, leaving 'wakes' in the streamwise velocity whose length is

$$\lambda_x \sim U_b \lambda_z^2/\nu_T, \tag{3.4}$$

assuming that they are convected at a velocity of the order of the bulk velocity. The choice of a constant advection velocity implies that necessarily the large structures feel the wall, since velocity itself is not a Galilean invariant.

The relation (3.3) not only expresses how ϕ_{uu} is organized in the plane (λ_x, λ_z) at a given wall distance. Since Eq. (3.4) links the coefficient of the power law in Eq. (3.3) to the magnitude of the eddy viscosity, the fact that all the spectra in Fig. 5 are aligned along a single line implies that ν_T is proportional to y, in agreement, and in strong support, to the similarity arguments about the scaling of the Reynolds stresses used in the standard derivations of the logarithmic velocity profile. It also helps understand why the outer structures become more isotropic with wall distance (which can be noticed from the displacement of the contours in figure 5), since the decaying time of the wakes decreases as the eddy viscosity increases. It should however be noted that the eddy viscosity in this flow, as measured from the mean velocity profile, only increases approximately linearly up to $y \approx 0.2$, and is constant thereafter, so that most of the spectra in Fig. 5 are outside the region of linear dependence. The present model can therefore only be taken as indicative until detailed calculations are carried out using the real eddy viscosity distribution. How it can be reconciled with the different power law (3.2) observed near the wall is briefly discussed in Jiménez, Flores & García-Villalba (2001).

The spectra of the three velocity components suggest that the u structures in the outer flow region resemble the buffer layer streaks, although they differ from them in that they are themselves turbulent, and in that it is unclear whether they are flanked by quasi-streamwise vortices. They seem however to be associated with roughly isotropic turbulent structures of the transverse velocities whose width increases with y (Fig. 4), but whose

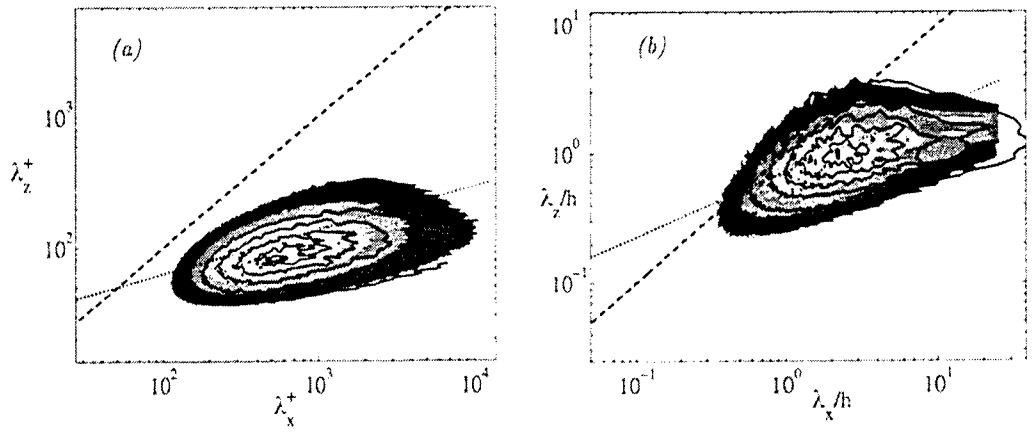

FIGURE 7. Premultiplied two-dimensional cospectra as functions of the streamwise and spanwise wavelengths at two representative wall distances. *(a)* Wall units, $y^+ = 15$; *(b)* Outer units, $y = 0.5h$. Shaded contours, $Re_\tau = 550$; line contours, $Re_\tau = 180$. In all the cases there are five linearly increasing contours. ···· , locus of two-dimensional isotropic structures $\lambda_z = \lambda_x$; the dotted line in *(a)* is $\lambda_x^+ \sim (\lambda_z^+)^3$, passing through $\lambda_x^+ = \lambda_z^+ = 50$; that in *(b)* is $\lambda_z y = \lambda_z^2$.

kinematics are unknown. The u-VLAS also widen with wall distance, specially above the buffer layer. This is shown in Fig. 6, which displays the transverse one-dimensional spectrum $k_z E_{uu}^{1D}$ at $Re_\tau = 550$. The spectrum has been plotted as a function of λ_z and y, and it has been non-dimensionalized with the local streamwise energy $\langle u'^2 \rangle(y)$. The figure therefore shows how much energy is associated to u structures of a certain width λ_z at a given distance to the wall. The figure also includes the widths of the u structures obtained by Nakagawa & Nezu (1981). They measured the spanwise organization in a turbulent open channel with a free surface using the autocorrelation of the streamwise velocity conditionally averaged with the presence of ejections, $\langle \lambda \rangle_e$, and sweeps, $\langle \lambda \rangle_s$. Their data agree reasonably well with ours even in the outer region, where the different geometrical configurations could be expected to affect the nature of the flow. The transverse one-dimensional spectra of the transverse velocity components, not shown here, behave with y very much like those of u.

3.3. *The cospectrum*

The cospectrum is particularly important because its integral is the Reynolds stress $\langle u'v' \rangle$, and determines the mean velocity profile U and the production of turbulent kinetic energy.

Fig. 7 shows the premultiplied two-dimensional cospectra in the near-wall and in the outer regions of the flow in the same fashion as the two-dimensional premultiplied velocity spectra. They resemble much more the premultiplied spectra of u in Figs. 3(a) and 3(d) than those of v in Figs. 4(a) and 4(e). This is true at all wall distances. The cospectra collapse in inner scaling in the near-wall region and in outer scaling in the outer region, in the same way as the u-spectra. But unlike the latter the cospectra fully collapse in wall units in the near-wall region, suggesting that the outer large structures do not affect the Reynolds stresses very close to the wall. This result agrees with the experiments by DeGraaff & Eaton (2000), who found that $\langle u'v' \rangle$ scales in inner units close to the wall and give support to the law of the wall $U^+ = U^+(y^+)$. Jiménez (1998) also noted that

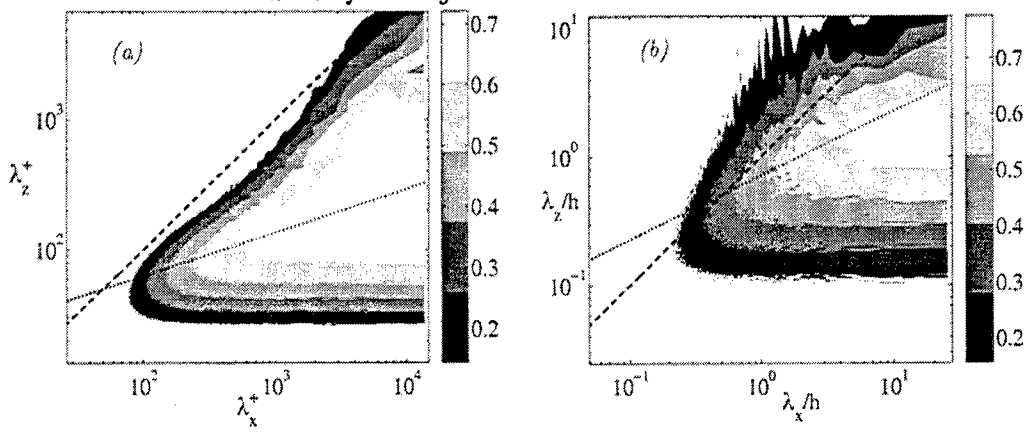

FIGURE 8. Structure parameter σ_{uv} as a function of the streamwise and spanwise wavelengths at two representative wall distances. Present $Re_\tau = 550$. *(a)* wall units, $y^+ = 15$; *(b)* outer units, $y = 0.5h$. In both cases there are five linearly increasing contours. ····· , locus of two-dimensional isotropic structures $\lambda_z = \lambda_x$; the dotted line in *(a)* is $(\lambda_z^+)^3 \sim \lambda_x^+$ passing through $y^+ = 50$; that in *(b)* is $\lambda_z^2 = y\lambda_x$.

the one-dimensional experimental cospectra in the logarithmic layer scaled with y much better than any of the other available velocity components.

It is of special interest that in the outer region, the VLAS carry a substantial fraction of the Reynolds stresses even if they are not present in the spectra of the wall-normal velocity in Fig. 4*(e)*. Jiménez (1998) observed that the vanishing of the *premultiplied* spectrum of v for long or for wide waves is not sufficient to imply that the *premultiplied* cospectrum also vanishes in that limit, as it had been previously assumed (Perry, Henbest & Chong, 1986). Let

$$E_{uv} = \sigma_{uv}(E_{uu}E_{vv})^{1/2}, \tag{3.5}$$

where σ_{uv} is the structure parameter, which measures the correlation between u and v and the efficiency of those fluctuations in transporting momentum. In the present simulations, E_{vv} is independent of λ_x for the long scales and consequently, the premultiplied v spectrum

$$\frac{(2\pi)^2 E_{vv}}{\lambda_x \lambda_z},$$

goes to zero as $1/\lambda_x$ when $\lambda_x \gg 1$, while ϕ_{uu} decays more slowly. It then follows from the square root in in Eq. (3.5) that in the limit of very long wavelengths the behavior of the premultiplied cospectrum depends on the prefactor σ_{uv}.

Fig. 8 displays the spectral distribution of the structure parameter in the near-wall region and in the outer layer. Its magnitude is low around $\lambda_x = \lambda_z$, where it is approximately a function of the distance to that line, in agreement with the intuitive idea that isotropic turbulence cannot transport momentum. On the other hand, σ_{uv} approaches unity for the VLAS, which are thus shown to be very efficient in transporting momentum. The result is that they actually carry an important fraction of the Reynolds stresses in the outer flow, as shown in Fig. 7.

4. Discussion and conclusions

We have performed the first direct numerical simulation of turbulent channel flow using both a computational domain big enough to capture the largest structures in the outer flow and a Reynolds number high enough to observe some separation between those structures and the ones in the near-wall region.

The results show that there are very large elongated structures in the outer region of turbulent channel flow whose size scales with h. We have suggested that they can be understood as the wakes left by compact isotropic structures decaying under the action of an eddy viscosity as they are convected by the mean flow. Both the spectra and flow visualization suggest that the VLAS are also very high, and that they can hit the walls, which would help understand the Reynolds number dependence in the scaling of $\langle u'^2 \rangle$ in the near-wall region (Perry & Li, 1990; DeGraaf & Eaton, 2000). We have seen that the large structures in the outer layer widen with the wall distance faster than the buffer layer streaks, reaching widths of order of the channel height. The observed widening may be linked to the downstream evolution of the wakes that we have suggested as the origin of the VLAS. The large anisotropic structures in the outer flow not only carry a substantial fraction of the kinetic energy of the flow, but also a substantial fraction of the Reynolds stresses, and are therefore 'active' in the sense of Townsend (1976).

We have noted that our Reynolds number is still too low to draw strong scaling conclusions for some of the variables involved, because the separation between the outer and inner scales of the flow is still moderate. Computer limitations do not allow direct numerical simulations in the range of Reynolds numbers in Hites (1997), Kim & Adrian (1999), Metzger & Klewicki (2001) and Morrison *et al.* (2001) in a near future, although some of the open questions can probably be addressed at much lower Reynolds numbers. Large eddy simulations could be very valuable in this respect if they could be shown to represent the VLAS sufficiently well. The wake model that we have proposed suggests that they should, but it is still not sufficiently clear what is the origin of the forcing of those wakes, and whether they are independent of the detailed dynamics of the wall, which is imperfectly resolved by the LES.

This work was supported in part by the Spanish CICYT contract BFM2000-1468 and by ONR grant N0014-00-1-01416. We are specially indebted to the CEPBA/IBM center at Barcelona, and to IBM and the U. Politècnica de Catalunya, which have gracciously donated the computer time needed for most of the simulations. Thanks are also due to R.D. Moser who reviewed a preliminary version of this manuscript.

REFERENCES

ABE, H., KAWAMURA, H. & MATSUO, Y. 2001 Direct numerical simulation of fully developed turbulent channel flow with respect to the Reynolds number dependence. *J. Fluids Eng.* **123**, 382-393.

DEGRAAFF, D. B. & EATON, J. K. 2000 Reynolds-number scaling of the flat-plate turbulent boundary layer. *J. Fluid Mech.* **422**, 319-346.

HITES, M. H. 1997 Scaling of high-Reynolds number turbulent boundary layers in the National Diagnostic Facility. *Ph. D. Thesis,* Illinois Inst. of Technology.

HUNT, J.C.R. & MORRISON, J.F. 2000 Eddy structures in turbulent boundary layers. *Eur. J. Mech. B - Fluids* **19**, 673–694.

JIMÉNEZ, J. 1998 The largest structures in turbulent wall flows. *Annual Research Briefs*, Center for Turbulence Research, NASA Ames/Stanford Univ., 943-945.

JIMÉNEZ, J., FLORES, O. & GARCÍA-VILLALBA, M. 2001 The large scale organization of autonomous turbulent walls. *Annual Research Briefs*, Center for Turbulence Research, NASA Ames/Stanford Univ., 317–327.

KIM, K. C. & ADRIAN, R. J. 1999 Very large-scale motion in the outer layer. *Phys. Fluids A* **11**, 417-422.

KIM, J., MOIN, P. & MOSER, R. D. 1987 Turbulence statistics in fully developed channel flow at low Reynolds number. *J. Fluid Mech.* **177**, 133-166.

METZGER, M. M. & KLEWICKI, J. C. 2001 A comparative study of near-wall turbulence in high and low Reynolds number boundary layers. *Phys. Fluids A* **13**, 692-701.

MORRISON, J.F., JIANG, W., MCKEON, B.J. & SMITS, A.J. 2001 Reynolds-number dependence of streamwise velocity spectra in turbulent pipe flow. *Submitted Phys. Rev. Lett.*

MOSER, R. D., KIM, J. & MANSOUR, N. N. 1999 Direct numerical simulation of turbulent channel flow up to $Re_\tau = 590$. *Phys. Fluids A* **11**, 943-945.

NAKAGAWA, H. & NEZU, I. 1981 Structure of space-time correlations of bursting phenomena in an open channel flow. *J. Fluid Mech.* **104**, 1-43.

PERRY, A. E., HENBEST, S. & CHONG, M. S. 1986 A theoretical and experimental study of wall turbulence. *J. Fluid Mech.* **165**, 163-199.

PERRY, A. E. & LI, J. D. 1990 Experimental support for the attached eddy hypothesis in zero pressure gradient boundary layers *J. Fluid Mech.* **218**, 405-438.

SMITH, R. W. 1988 Effect of Reynolds number on the structure of turbulent boundary layers *Ph. D. Thesis,* Dept. of Mech. and Aerospace Engg., Princeton Univ.

TOWNSEND, A. A. 1976 *The Structure of Turbulent Shear Flows*, 2nd. ed., Cambridge U. Press.

CFD analysis of flow in an open-jet aeroacoustic experiment

By Stephane Moreau †, Gianluca Iaccarino, Michel Roger ‡ AND Meng Wang

1. Motivation and background

When considering the sound emitted by a rotating machine such as an engine cooling fan, an airplane turbofan, or an air-conditioning unit, one major contributor to the overall noise is the blade trailing edge noise. It comes from the conversion of local flow perturbations at this geometric discontinuity into acoustic waves propagating in space. Depending on the flow Reynolds number (based on the local chord length) and the trailing edge geometry, this acoustic scattering is associated with most of the broadband component and some narrower band structures of the far-field acoustic spectrum (Brooks & Hodgson 1981; Blake & Gershfeld 1988). This mechanism also provides the minimum noise configuration of such machines when all interactions with their environment (inlet turbulence ingestion and flow distortion, rotor-stator interaction with the downstream stationary components) are removed (Wright 1976; Caro & Moreau 2000).

The study of trailing-edge noise or airfoil self-noise has received much attention mainly in the late seventies and early eighties. It involved measurements of wall pressure fluctuation spectra and far-field acoustic spectra on various two-dimensional aerodynamic profiles in anechoic wind tunnels (*e.g.* Blake 1975; Blake & Gershfeld 1988; Fink 1975; Brooks & Hodgson 1981). The experimental database has been used in the late nineties to validate numerical prediction methods for trailing edge aeroacoustics (*e.g.* Wang and Moin 2000). For typical engine cooling fan applications, which involve transitional and turbulent flows at Reynolds numbers of $O(10^5)$, numerical simulations require the resolution of the noise-generating eddies over a range of length scales. The traditional unsteady Reynolds-averaged Navier-Stokes (RANS) approach needs to be substituted by the more expensive large-eddy simulations (LES) to yield the necessary unsteady surface pressure fluctuations and the near-field fluctuating Reynolds stress that provide the acoustic source functions. The radiated noise can then be computed using aeroacoustic theory such as an integral solution to the Lighthill equation (Wang 1998; Manoha *et al.* 2000; Wang & Moin 2000).

In all previous LES simulations (Manoha *et al.* 2000; Wang & Moin 2000), the airfoils were assumed to be in free air. In contrast, most trailing-edge aeroacoustics experiments (with the exception of Blake (1975) where no acoustic measurement was made) have been conducted in open-jet wind tunnel facilities, where the airfoil is immersed in a jet downstream of the nozzle exit. The proximity of the airfoil to the jet nozzle exit and the limited jet width relative to the airfoil thickness can cause the airfoil pressure loading and flow characteristics to deviate significantly from those measured in free air, and hence alter the radiated noise field. The present work is aimed at quantifying these installation effects and providing insights into the flow physics in this type of open-jet experiment. A systematic CFD study, based on RANS models, of flow conditions in a recent experiment

† VALEO Motors and Actuators, France
‡ Ecole Centrale de Lyon (ECL), France

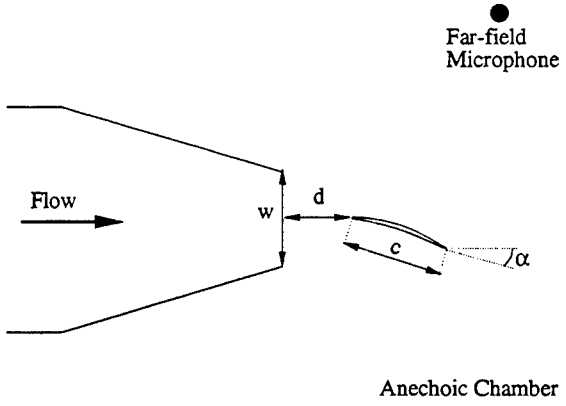

FIGURE 1. Sketch of an open-jet aeroacoustic experiment.

at Ecole Centrale de Lyon (ECL) (Roger 2001) is carried out and compared with flows over an isolated airfoil in a uniform stream. The results shed some light on the fidelity of the flow conditions in the previous numerical simulations of trailing-edge experiments, and provide guidance for the appropriate boundary conditions needed in future LES of such experiments.

2. Experimental setup

In order to measure only the airfoil self-noise the aerodynamic profile must be isolated as much as possible from the inlet duct providing the necessary air flow in a large quiet environment. Moreover, the inlet duct should have a low background noise and have a low residual turbulence ($\leq 1\%$), which explains the maximum outlet sections of about 0.5 m in the majority of test facilities. Finally, to avoid contamination of the acoustic signals by the flow field, the air stream should be confined, away from the far-field microphones. All the above criteria tend to show that an open-jet anechoic wind tunnel provides the best experimental compromise. The smaller anechoic wind tunnel at ECL is shown in Fig. 1.

Recently, Roger (2001) performed measurements using a NACA0012 airfoil and a blade profile provided by Valeo Motor and Actuators. The former is used to provide validation against the earlier experiment of Brooks & Hodgson (1981). The latter is a much thinner airfoil (about 4% thickness to chord ratio compared to 12% for the NACA0012), with both blunt leading and trailing edges. It has been designed to achieve low drag by controlling the chordwise diffusion (hence called "CD profile"). Moreover, the NACA0012 is symmetric whereas the Valeo airfoil is cambered, with a camber angle of about 12 degrees. The flow conditions for the CD profile are a free stream velocity of 16 m/s and a Reynolds number Re_c of about 1.2×10^5. The actual experimental setup is comparable to that used by Brooks & Hodgson (1981). The geometric angle of attack of the airfoil can be continuously adjusted.

Flush mounted Remote Microphone Probes (RMPs: see Perennes 1999) on the airfoil allow the measurements of both the mean wall static pressure and the fluctuating pressure spectra. A movable microphone is placed in the far field to collect the acoustic spectra

simultaneously. Finally, tuft visualizations are used to estimate the flow separation zones and a hot wire rake is employed to measure the wake velocity profiles close to the trailing edge. Good repeatability has been achieved on this data set. At zero degree angle of attack ($\alpha = 0°$) the flow is fully attached whereas at $\alpha = 2°$ a separation region appears near the trailing edge. Further increase in the angle of attack shows the presence of a laminar separation bubble at the leading edge. At much larger incidence ($\alpha \approx 15°$), the airfoil seems to be completely stalled, which is confirmed by a tuft survey along the chord.

Airfoil Tested	c	s	d	w
NACA0012 (Brooks & Hodgson 1981)	61.0	46.0	15.0	30.0
NACA0012 (Roger 2001)	10.0	30.0	10.0	13.0
Valeo CD (Roger 2001)	13.0	30.0	10.0	13.0

Table 1. Comparison of some aeroacoustic experimental dimensions (in cm)
c = chord, s = span, d = distance from nozzle exit to airfoil nose, w = jet width.

The various length scales involved in the above experiment are compared in table 1 with data corresponding to the experiment of Brooks & Hodgson (1981). By examining the chord to span ratio, we can estimate the possible 3D effects induced by the side plates. Brooks & Hodgson's (1981) experiment exhibits some 3D influence as indicated by the non-uniform surface pressure spectra in Fig. 8 of their paper. In contrast, Roger's experiments are expected to be free of these effects at midspan where the RMP sensors are mounted. By comparing the airfoil thickness and the jet width (or nozzle exit width), we obtain an estimate of the blockage induced by the airfoil in the jet; it is significant in Brooks & Hodgson's experiment. Moreover, data from jet boundary corrections for airfoil tests in open-jet wind tunnels (Knight & Harris 1985) suggest that all the experiments in Table 1 suffered from significant variations of the effective angles of attack. The jet width also provides the extent of its potential core and therefore gives an estimate of the interaction of the shear layers created at the nozzle lips with the airfoil. If a typical core length of four to five jet widths is assumed, by comparison with the airfoil chord length and thickness, it becomes clear that such interaction is present in Brooks & Hodgson's setup. Finally, the distance from the nozzle exit to the airfoil leading edge gives a hint of the potential interaction between the nozzle and airfoil flows and the consequent local modification of the flow angle of attack. The above-mentioned effects do not appear important in Blake's (1975) experiment because the airfoil is fully inside the jet nozzle, and the nozzle width is 48 times the airfoil thickness.

3. Numerical study

Two-dimensional RANS simulations have been carried out to investigate the effect of the experimental setup on the airfoil aerodynamic loading and on the flow field development. Configurations ranging from the complete setup reported in Fig. 1 to an isolated (free air) airfoil are considered.

The RANS calculations are performed using unstructured grids (Fig. 2) generated by a quadrilateral advancing-front algorithm (Blacker *et al.* 1991). The mesh around

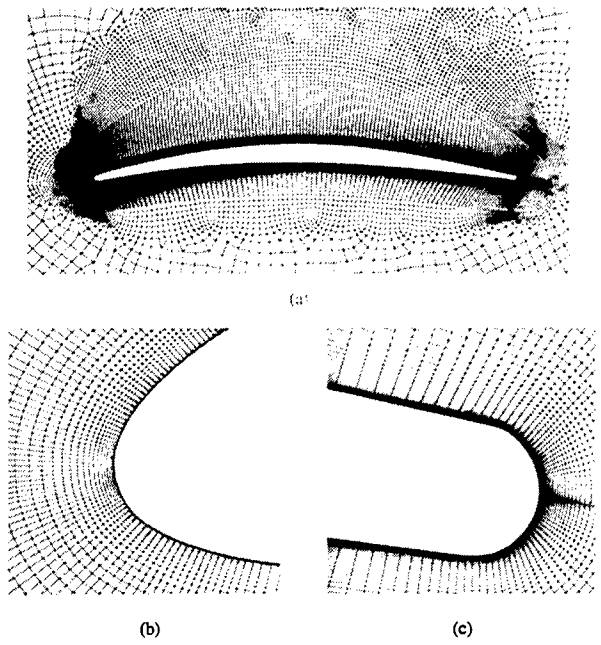

FIGURE 2. Unstructured grids for the Valeo CD airfoil (a); close-ups of the leading edge (b) and trailing edge (c). A particularly refined and smooth grid is required in the leading edge area where a laminar separation is expected at large angles of attack.

the airfoil has been refined so that accurate representation of the leading-edge laminar bubble and trailing-edge turbulent separation can be achieved. The outer grid is then generated according to the domain considered (Fig. 3).

Simulations presented here at $Re_c = 120,000$ were performed using the $v^2 - f$ turbulence model (Durbin 1995; Iaccarino 2001). Additional calculations using different turbulence models have been carried out by Henner *et al.* (2001) at Valeo, and show comparable results when the k-ω and SST models are employed. This observation is consistent with the findings of Kalitzin (1999).

3.1. *Grid sensitivity study*

Grid-sensitivity studies are conducted in the simplest case of an isolated airfoil. The simulations are performed using the computational domain shown in Fig. 3a; a rectangular box with about four chord lengths above and below the airfoil and six chord lengths upstream and downstream of the airfoil. The incoming flow is assumed uniform, corresponding to the mean velocity at the nozzle exit; inlet boundary conditions are applied on the left and bottom boundaries. On the upper and right boundaries a constant pressure condition is used. Two unstructured grids have been used; the coarse one has only about 30,000 cells whilst the finer mesh has 55,000 cells. In addition, calculations performed on a multiblock grid generated by Valeo (Henner *et al.* 2001) with 66,000 elements are presented. The simulations were carried out at an angle of attack $\alpha = 8^o$. The pressure and skin-friction distributions are shown in Fig. 4. At this angle of attack a laminar separation bubble near the leading edge and a trailing-edge recirculation are present (cf. Fig. 4b). The calculations on different grids show remarkably good agreement.

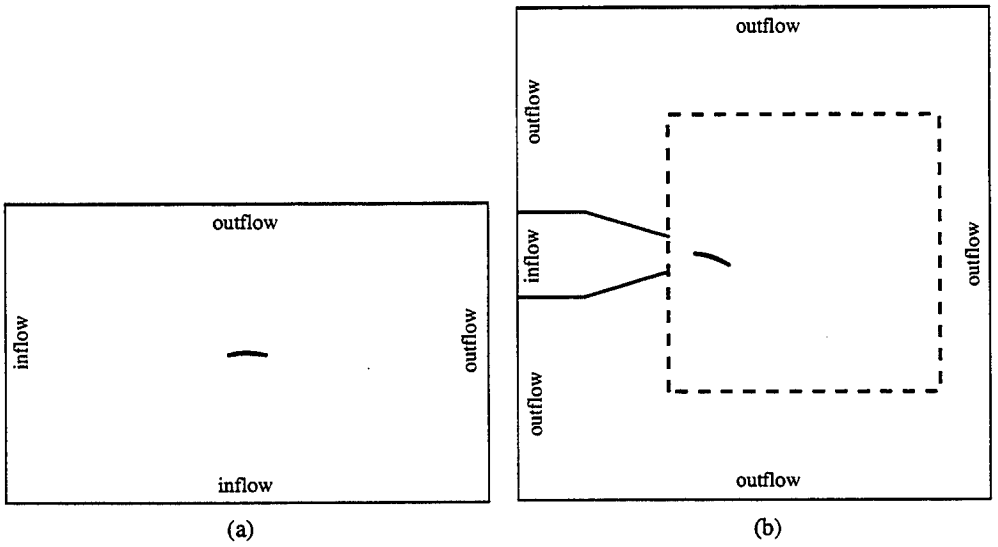

FIGURE 3. Computational domains used for (a) the isolated airfoil and (b) the full wind-tunnel setup (the dashed line represents a simplified wind tunnel setup).

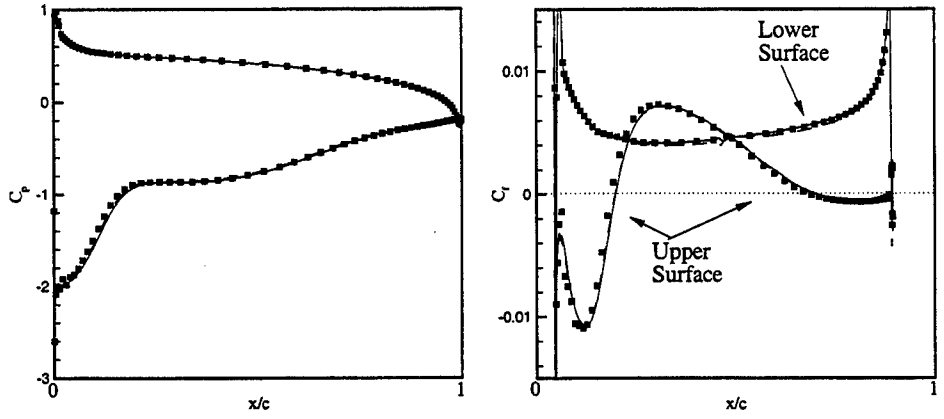

FIGURE 4. Grid sensitivity study; (a) pressure and (b) skin friction distribution on the airfoil surface. ——— : unstructured fine grid, – – – line: unstructured coarse grid; ▪ : Valeo multiblock grid.

3.2. *Wind tunnel simulations*

The simulation of the complete wind tunnel setup has been carried out in the domain shown in Fig. 3b. The width of the jet nozzle exit is 13 cm. Pressure distributions are shown in Fig. 5, together with the measurements and the isolated-airfoil calculations for angle of attack $\alpha = 12°$.

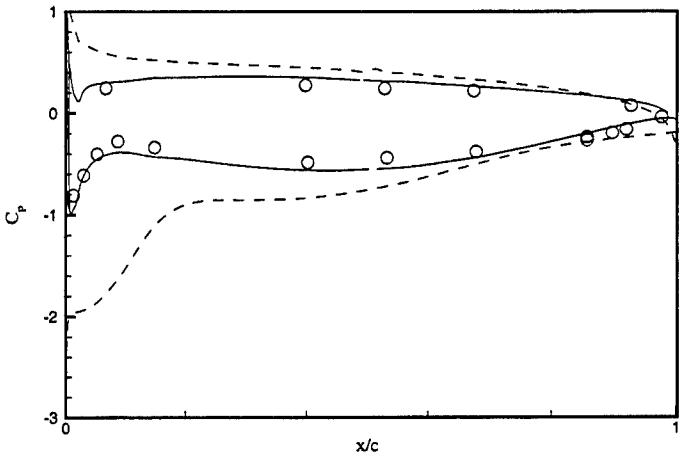

FIGURE 5. Pressure loading on the airfoil surface at $\alpha = 12°$. ——— : full wind tunnel simulation; – – – : isolated airfoil; o : experiments.

The agreement between the full wind-tunnel simulation and the experiment is satisfactory, whereas a very different loading is obtained in the case of an isolated airfoil. This is also shown in Fig. 6, where the velocity contours are plotted for both simulations. The isolated-airfoil computation shows a large laminar separation bubble near the leading edge and a separation near the trailing edge. In contrast, in the computation for the wind-tunnel domain, the shear layers emanating from the lips of the nozzle exit have a strong influence on the flow around the airfoil, and the boundary layers remain attached to the airfoil. Additional simulations performed at Valeo (Henner *et al.* 2001) show that a similar pressure distribution (and flow field) is obtained when the same airfoil is placed in a cascade setup. It was argued that the shear layers coming from the nozzle lips confine the flow in a manner similar to that of a blade row in a cascade.

It is evident that a simple correction for angle of attack, which is commonly employed to account for the effect of the open jet (*e.g.* Brooks *et al.* 1986), cannot be successful in this situation. Interestingly, most of the aeroacoustic experiments cited above have similar geometrical configurations, and are therefore affected by the finite jet width and interference from the nozzle exit.

3.3. *Effect of jet width*

Having established and explained the large differences between the isolated airfoil case and the same airfoil in an open-jet acoustic tunnel, we then studied the influence of the jet width on the velocity and pressure distributions. The motivation for this study is to provide guidance for the design of future experiments with minimal interference effects, and for setting up the appropriate LES boundary conditions if such interference is present.

A somewhat simplified computational domain has been considered. It starts at the jet exit and encloses the airfoil at the correct relative location, as denoted by the dashed-line box in Fig. 3b. Computations have been done for Several jets, with exit width ranging from 13 cm to 50 cm. The airfoil angle of attack is $\alpha = 8°$ in all cases. The velocity distribution near the nose shows no laminar separation for jet sizes of up to 40 cm

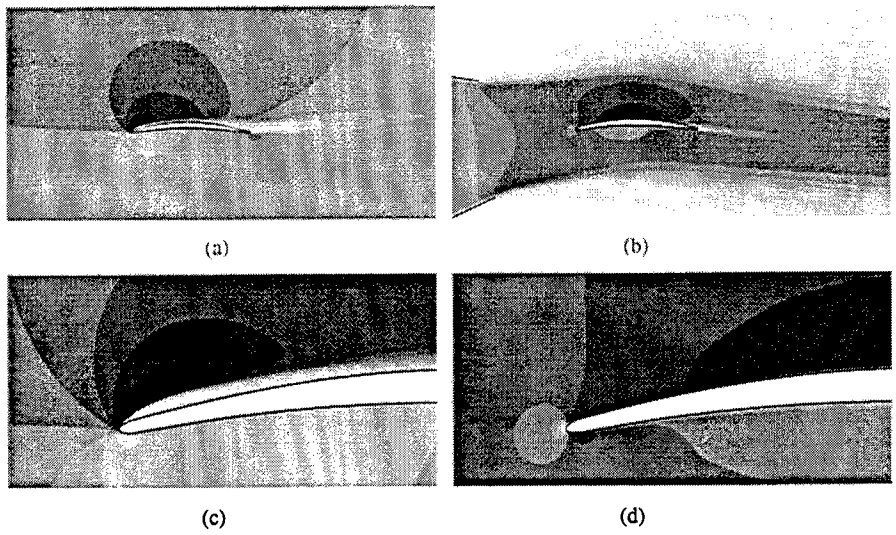

FIGURE 6. Contours of velocity magnitude. (a)(c) isolated airfoil, (b)(d) full wind tunnel simulation. Dark areas correspond to high velocity.

(*e.g.* Figs. 7a and 7b). Although separation is present when the jet width is increased to 50 cm (cf. Fig. 7c), it is very weak compared to the isolated airfoil case shown in Fig. 7d. The jet-width effect is also confirmed by the corresponding pressure distribution curves shown in Fig. 8.

Except in the immediate vicinity of the trailing-edge, the pressure loading on the rear part of the airfoil approaches that of an isolated airfoil as the jet width is increased. On the other hand, the leading-edge pressure distribution remains substantially different, indicating that the proximity of the airfoil to the jet exit must be accounted for.

4. Conclusions

A detailed RANS simulation of a full open-jet wind tunnel experiment has shown strong effects of the jet nozzle and the finite jet width on the aerodynamic loading and flow characteristics. When the jet width is not sufficiently large compared to the frontal "wetted" area of the airfoil, the airfoil behaves in a manner closer to a cascade than to an isolated profile. The significant modification of the lift distribution and flow field can in turn affect the nature of the sound radiation. These effects have implications for the appropriate boundary conditions needed to conduct LES of open-jet aeroacoustic experiments, and could be responsible for the discrepancies among some earlier experimental and computational studies (*e.g.* the different boundary layer thicknesses observed by Manoha *et al.* (2001)). To reproduce the experimental flow conditions accurately, free-stream boundary conditions are not adequate (unless the jet is very wide). More realistic conditions based on experimental velocity profiles or RANS calculations should be imposed.

A simpler computational model of the open-jet acoustic tunnel with an inlet velocity profile of variable width has also been devised. This configuration captures most of the experimental setup effects in open-jet facilities, particularly in the aft section of the

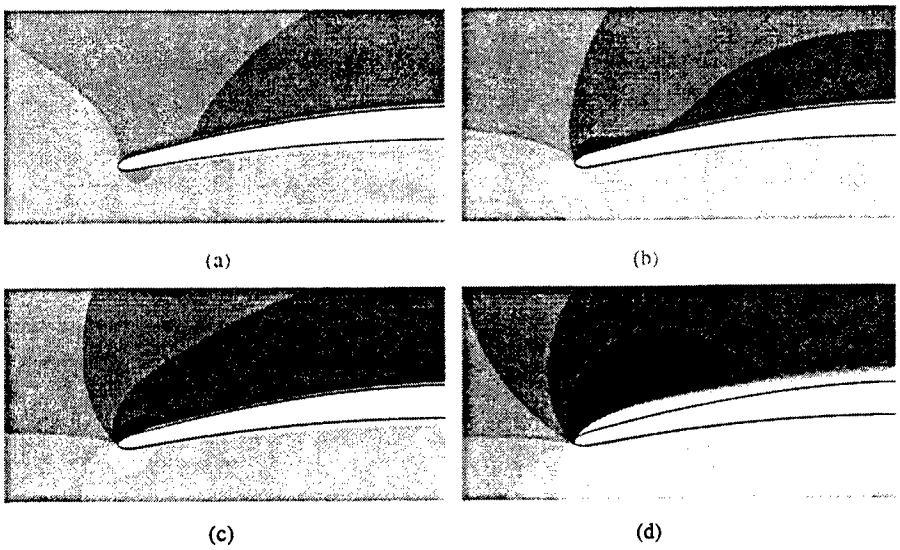

FIGURE 7. Contours of velocity magnitude. Jet width: (a) 13cm, (b) 30cm, (c) 50cm, (d) ∞ (isolated airfoil). Dark areas correspond to high velocity.

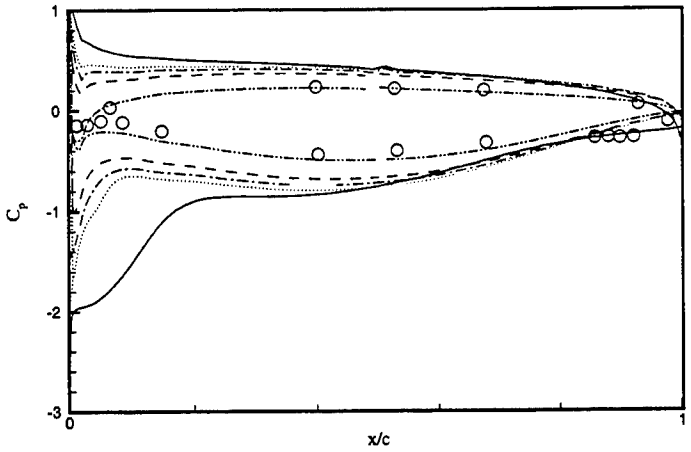

FIGURE 8. Pressure loading on the airfoil surface at $\alpha = 8°$. ——— : isolated airfoil; —··— : w = 13cm; – – – : w = 30cm; —·— : w = 40cm; ····· : w = 50cm; o : experiments.

airfoil which is critical to trailing-edge noise. The simplified configuration allows for quick parametric studies of the dependence of flow conditions on the airfoil profiles and the angle of attack, which is particularly useful for the design of experiments as well as for RANS and LES simulations.

REFERENCES

BLACKER T.D., STEPHENSON M.B. & CANANN S. 1991 Analysis automation with paving: a new quadrilateral meshing technique. *Advances in Engineering Software*, **56**, 332-337.

BLAKE, W.K. 1975 A statistical description of pressure and velocity fields at the trailing edge of a flat strut. *David Taylor Naval Ship Research and Development Center* Report 4241.

BLAKE, W.K. & GERSHFELD, J.L. 1988 The aeroacoustics of trailing edges. In *Frontiers in Experimental Fluid Mechanics* (M. Gad-el-Hak, ed.), Springer-Verlag, ch. 10.

BROOKS, T.F. & HODGSON, T.H. 1981 Trailing edge noise prediction from measured surface pressures. *J. Sound and Vibration* **78**, 69-117.

BROOKS T.F., MARCOLLINI, M.A. & POPE, D.S. 1986 Airfoil trailing edge flow measurements. *AIAA J.* **24**, 1245-1251.

CARO, S. & MOREAU, S. 2000 Aeroacoustic modeling of low pressure axial flow fans. *AIAA* Paper 2000-2094.

DURBIN, P.A. 1995 Separated flow computations with the k-ϵ-v^2 model. *AIAA J.* **33**, 659-664.

FINK, M.R. 1975 Experimental evaluation of trailing edge and incidence fluctuation noise theories. *AIAA* Paper 75-206.

HENNER, M., STANCIU, M., MOREAU S., AUBERT, S. & FERRAND, P. 2000 Unsteady rotor-stator interactions in automotive engine cooling fan systems. *Proceedings of the ISUAAAT 2000 Conference*, Ecully, September 2000.

KALITZIN, G. 1999 Application of the $v^2 - f$ model to aerospace configurations. *Annual Research Briefs*, Center for Turbulence Research, NASA Ames/Stanford Univ., 289-300.

IACCARINO, G. 2001 Predictions of a turbulent separated flow using commercial CFD codes. *J. Fluids Engg.* **123**, 1-10.

KNIGHT, M. & HARRIS, T.A. 1985 Experimental determination of jet boundary corrections for airfoil tests in four open wind tunnel jets of different shapes. *NACA* Report 361.

MANOHA, E., DELAHAY, C., SAGAUT, P., MARY, I., BEN KHELIL, S. & GUILLEN, P. 2001 Numerical prediction of the unsteady flow and radiated noise from a 3D lifting airfoil. *AIAA* Paper 2001-2133.

MANOHA, E., TROFF, B. & SAGAUT, P. 2000 Trailing edge noise prediction using large-eddy simulation and acoustic analogy. *AIAA J.* **38**, 575-583.

PERENNES S. 1999 Caractérisation des sources de bruit aérodynamique à basses fréquences de dispositifs hypersustentateurs. Doctorate Thesis, Laboratoire de Mecanique des Fluides et d'Acoustique, Ecole Centrale de Lyon, France.

ROGER M. 2001 Private communication.

WANG, M. 1998 Computation of trailing-edge noise at low Mach number using large-eddy simulation. *Annual Research Briefs*, Center for Turbulence Research, NASA Ames/Stanford Univ., 91-106.

WANG, M. & MOIN, P. 2000 Computation of trailing-edge flow and noise using large-eddy simulation. *AIAA J.* **38**, 2201-2209.

WRIGHT, S.E. 1976 The acoustic spectrum of axial flow machines. *J. Sound Vib.* **45**, 165-223.

RANS solvers with adaptive structured boundary non-conforming grids

By Sekhar Majumdar, Gianluca Iaccarino, AND Paul Durbin

1. Motivation and objectives

The objective of the present work is to develop robust RANS solvers for accurate computation of flow and heat transfer in complex geometries, such as arise in engineering design. In CFD analysis, the most time-consuming process is often the generation of an acceptable grid — whether it is a boundary-conforming, curvilinear mesh, or even a completely unstructured mesh. The present work focuses mainly on RANS solution of viscous and turbulent flows, where the relevant governing equations always impose strict requirements on the grid and on the solution algorithm. The special problems that arise in RANS solvers, coupled to turbulence models, have not been addressed in the literature on locally refined, Cartesian meshes, or in papers on the use of boundary non-conforming grids.

The ideal would be to develop a RANS code, with advanced turbulence models, that can perform flow and heat transfer analysis directly on the CAD representation of a surface, avoiding the cumbersome process of surface meshing. Such a development would have the potential for an enormous impact on applied computational analysis. The present research aims to exploring promising avenues in this direction.

1.1. *Issues with Cartesian meshes*

Flow solvers using Cartesian meshes have two major issues: (1) how to define a complex shaped surface accurately and (2) how to satisfy the relevant boundary conditions for the governing equations of pressure, velocity and turbulence scalars at any point lying on a curved boundary surface. These issues are addressed in available literature under two different approaches. An approach using forcing functions was originally proposed by Peskin (1972) and pursued further by Mohd–Yusof (1997), Verzicco *et al* (2000) and Fadlun *et al* (2000). The forcing technique is most natural when applied to the Navier-Stokes equations for momentum; but formulation of forcing terms for turbulence model equations could be very cumbersome. The basic idea is that a forcing term is added to the equations in cells intersected by a boundary; the magnitude and direction of the force is adjusted so that the boundary conditions are satisfied.

The other approach is designated as cell cutting: here, Cartesian faces of cells that are intersected by the curved surface are replaced by the surface face. Such splitting generates non-rectangular cells, which may be handled efficiently only by an unstructured flow solver.

In the present work a new approach, designated as an extended Ghost Cell Method, is being explored for RANS applications. It promises to provide the flexibility needed for imposing the various boundary conditions of interest in turbulence modeling. Indeed, the approach is simply to impose the specified boundary condition by interpolation onto a surface that does not coincide with a computational mesh surface – or, more correctly,

to use the condition on that non-computational surface to extrapolate the variable value to a ghost node, inside the body.

1.2. *Special issues in RANS computation*

The RANS equations for incompressible flow are

$$\begin{aligned} D_t U &= \frac{1}{\rho}\nabla P + \nabla \cdot \left[(\nu + \nu_T)(\nabla U + \nabla^t U)\right] \\ \nabla \cdot U &= 0 \end{aligned} \tag{1.1}$$

The point to note here is that ν_T is an eddy viscosity which is determined by further transport equations. A variety of models are discussed in Durbin & Pettersson Reif (2000). Generic issues in solving turbulence models can be illustrated by reference to the widely used $k - \varepsilon$ model.

The transport equations for k and ε are

$$\begin{aligned} D_t k &= 2\nu_T |S|^2 - \varepsilon + \nabla \cdot [(\nu + \nu_T)k] \\ D_t \varepsilon &= \frac{C_{\epsilon 1} 2\nu_T |S|^2 - C_{\epsilon 2}\varepsilon}{T} + \nabla \cdot [(\nu + \nu_T/\sigma_\epsilon)\nabla \varepsilon] \end{aligned} \tag{1.2}$$

A distinction from conservation equations is obvious: the right-hand sides contain source and sink terms. In the major part of a turbulent shear layer there is a rough balance between sinks and sources. The source and sink terms strongly couple the k equation to the ε equation and this argues for a coupled solution. (This is believed to be one reason why explicit solution algorithms are not effective on turbulence models. The usual rationale is that explicit methods are not efficient for bringing the source terms into balance. Implicit schemes are better and are the basis of most robust routines for solving turbulence models.)

Another source of stiffness occurs near the boundaries. The no-slip conditions on Eq. (1.2) are

$$k(0) = 0, \qquad \varepsilon(0) = \lim_{y \to 0} 2\nu k / y^2.$$

This is imposed numerically by evaluating the right-hand side at the first computational point above the surface. The factor of $1/y^2$ can cause numerical stiffness if the k and ε equations are not solved as a coupled, implicit system.

Adequate near-wall resolution is required to properly compute heat transfer, skin friction and flow separation. In general the grid should be strongly anisotropic, with small spacing in the wall-normal direction. This grid requirement is tied to the geometry, and mandated by the boundary layers. Separated shear layers can exist within the flow; they also demand local grid refinement, although now tied to the flow field, not the geometry. To capture such features the anisotropic refinement needs to be adapted to the solution.

The established approach to handle the above-mentioned issues is to construct body fitted meshes – structured or unstructured – with high resolution next to solid surfaces. Sometimes the mesh is adapted in the course of the solution – usually on unstructured grids. The present approach differs in both respects: the near-wall refinement is intended to be done with a Cartesian grid, without body fitting. Boundary conditions are imposed by an interpolation method designated as a generalized 'Ghost Cell' approach. Similarly, flow as well as the boundary adaptation are carried out by locally refining a quasi-

structured grid inside the flow and the refinement is non-isotropic which can be easily achieved in a Cartesian grid environment.*

During the last six months, attempts have been made to develop the two different aspects of this research project in parallel. The first part concentrates on the method of local refinement in structured Cartesian grids: the second part explores the appropriate interpolation or reconstruction schemes to handle the boundary conditions, while solving the RANS equations using a finite-difference solver and a Cartesian grid not conforming to the body surfaces. Accomplishments so far are described below in two different subsections.

2. Accomplishments

2.1. *Local refinement using Cartesian grids*

2.1.1. *Methodology*

Most research on solution-adaptive gridding has been reported for unstructured solution methods (Mavripilis, 1995). Local adaptation involves inserting nodes within a pre-existing mesh. Local mesh refinement is considered to be suited only to unstructured solution algorithms because the element connectivity is explicit and local. However, in the present work we propose a somewhat analogous method that can be developed for structured grid algorithms.

The locally adaptive method proposed herein is motivated by the idea of *iblanking* (Benek *et al*, 1985); the terminology, *iblank*, comes from a variable name used in computer codes. Originally *iblanking* was a device to insert geometry into a structured grid by extending the grid inside the body, then blanking out the interior portion. The region inside the body is decoupled from the fluid via boundary conditions. In the original approach the interior region is solved, although the equations there are arbitrary It is straightforward to revise such algorithms so that the blanked region is skipped, requiring neither storage of variables nor solution of equations. For present purposes, the notionally blanked portion of the grid could be larger than the active portion. Our solution algorithm skips the blanked portion.

Conceptually, our method consists of adding grid lines where needed, and blanking out all but the portion of those lines that lies in the area where higher resolution is required. Since the blanked portion is skipped, the actual method adds line segments (refer to Fig. 4). The line segments lie on an underlying, notional, structured grid. The notional grid would be constructed from active and blanked nodes, as illustrated by Fig. 1. The black circles denote an initial, coarse grid. The gray circles indicate points added through local refinement. They amount to inserting an extra grid line in the k-direction, a portion of which is active, the rest blanked — as indicated by the open circles. A discrete solution scheme must be adapted for this class of grids.

The node labeled H (usually called a 'hanging node') in Fig. 1a is connected to three active nodes. To complete the finite difference stencil a solution value is interpolated to the point labeled I. Note that I is *only* used to complete the stencil at H; otherwise it is treated as blanked. The interpolation stencil determines the effective finite difference scheme, and its local accuracy.

For instance, if the value at I is linearly interpolated between its vertical neighbors, then the 6-point stencil in Fig. 1b is implied by the 5-point stencil in figure 1a. A centrally-differenced j derivative is second-order accurate for a symmetric stencil:

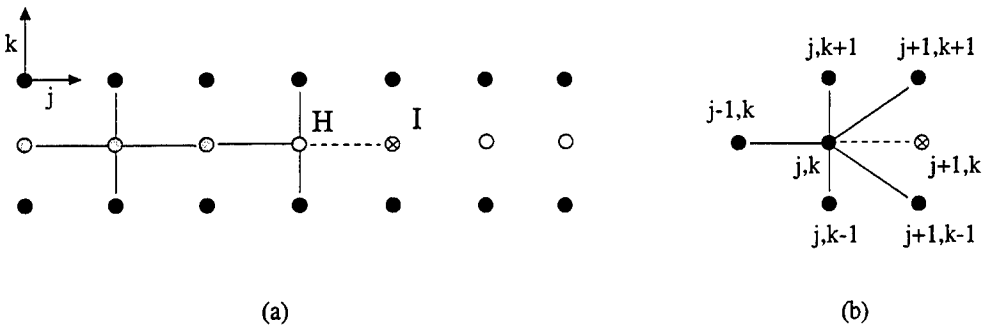

FIGURE 1. Finite difference stencils for hanging nodes. (a) Active (●, ⊛) and blanked (○) grid points. Points indicated by ● show the initial grid; those indicated by ⊛ are added through refinement; ⊗ is an interpolated point (*H* Hanging Node; *I* Interpolation Node). (b) Effective stencil at an interpolation node.

$\delta_j u = \frac{1}{2}(u_{j+1} - u_{j-1})$. However, with an interpolated value as in figure 1b, the accuracy becomes first order because of the asymmetry:

$$\delta_j u_{j,k} = \frac{1}{2}\left(\frac{1}{2}(u_{j+1,k+1} + u_{j+1,k-1}) - u_{j-1,k}\right) \tag{2.1}$$

irrespective of the fact that the value $u_{j+1,k} = \frac{1}{2}(u_{j+1,k+1} + u_{j+1,k-1})$ is a second-order interpolation in the k-direction.

In a 2-D grid of N^2 nodes, the number of hanging nodes will be $O(N)$. Hence the global error of a second-order method on complete stencils would not be reduced by first-order accuracy adjacent to interpolation points. However, the local dissipative error due to first-order convection might be undesirable. Local accuracy can be increased by modifying the interpolation stencil. The formula

$$u_{j+1,k} = \frac{1}{2}(u_{j+1,k+1} + u_{j+1,k-1}) - \frac{1}{2}(u_{j,k+1} + u_{j,k-1} - 2u_{j,k}) \tag{2.2}$$

provides a second-order difference.

2.1.2. *Application examples*

Fig. 2 shows the block refinement of the grid for flow over a backstep. The coarse grid is refined uniformly in two blocks. The upper right corners of each block contain unacceptable interpolation points; in order to apply the interpolation formula Eq. (2.2) no other inactive points should appear in the stencil. The encircled regions contain locations where deletions are needed to form acceptable interpolation stencils.

A flow computation has been performed on the grid of Fig. 2. The full domain extends over $-4 < x < 35$, $0 < y < 6$ with a symmetry condition at $y = 6$. Streamlines, velocity vectors and convergence history are displayed in Fig. 3. This particular grid is simply block-refined; it is not adapted locally to the solution. It serves primarily to illustrate the effectiveness of the solution algorithm and to show that the solution continues smoothly across the interpolation points. Also, no numerical instabilities are encountered.

Second order formulae for the interpolation Eq. (2.2) are used in this computation. The convergence history of Fig. 3 is for a pseudo a time-step of $\Delta t = 2.5$ based on free-stream speed and step height of unity; this corresponds to a fine grid CFL number of 6.5. With

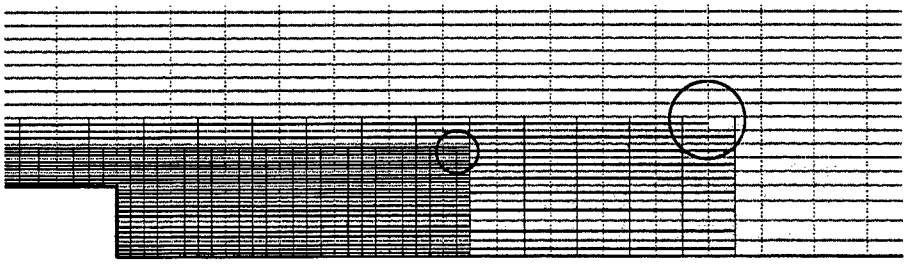

FIGURE 2. Block refinement for flow over backstep. Two levels of refinement are shown. The y-axis has been magnified by a factor of 2. Faint lines are the coarse grid. Circles indicate where the interpolation points were revised.

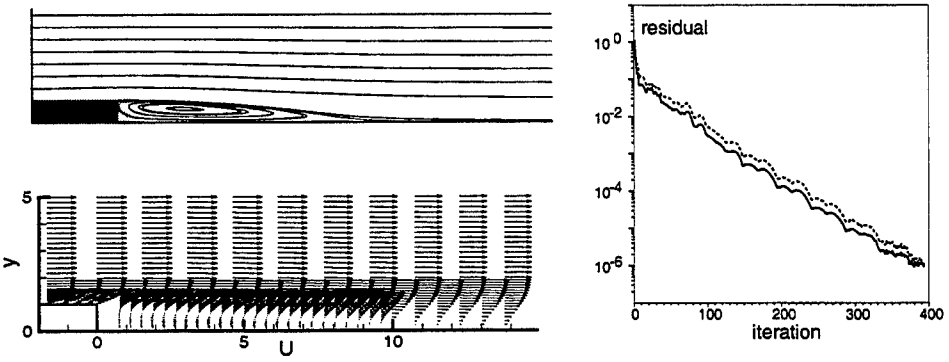

FIGURE 3. Streamlines and velocity vectors for backstep at step height Reynolds number=200 on grid of figure 2. The full domain is $-4 < x < 35$, $0 < y < 5$. Residual plot shows the maximum absolute residual (solid) and maximum divergence (dashed).

$\Delta t = 10.5$ the same level of convergence (*i.e.*, to single precision) was obtained in only 300 iterations.

As a further example of application of the present technique, an adaptive grid refinement for the driven cavity flow proposed by Ghia *et al* (1985) is shown in Fig. 4. The adaptation function is based on a linear combination of velocity and pressure gradients. The initial (uniform) grid consists of 20×20 cells; three successive refinement steps are employed. The final mesh is shown at the left of Fig. 4. Active nodes are clustered in the eddies and near to the walls. The refinement is distinctly non-isotropic.

The streamlines at the right of Fig. 4 show the presence of secondary recirculation regions at the lower corners, in good qualitative agreement with benchmark results of Ghia *et al* (1985). A more quantitative comparison is reported in Fig. 5: velocity profiles on vertical and horizontal centerlines are reported there for the adapted grid, and are compared to the solution on a uniform 100×100 grid. The agreement between these two solutions is quite good. Note that the locally-refined solution cuts through the highly-irregular grid at the center of the cavity. The grid in Fig. 4 contains 4,683 active points; the finest level corresponds to a 80×80 full grid.

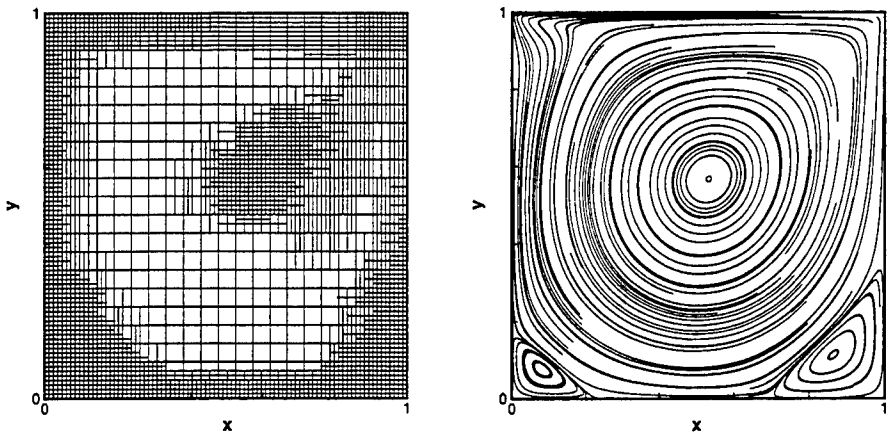

FIGURE 4. Computational grid and streamlines for the flow in a square cavity at Re = 1,000 using adaptive locally refined grids. Hanging nodes are interpolated using Eq. (2.2).

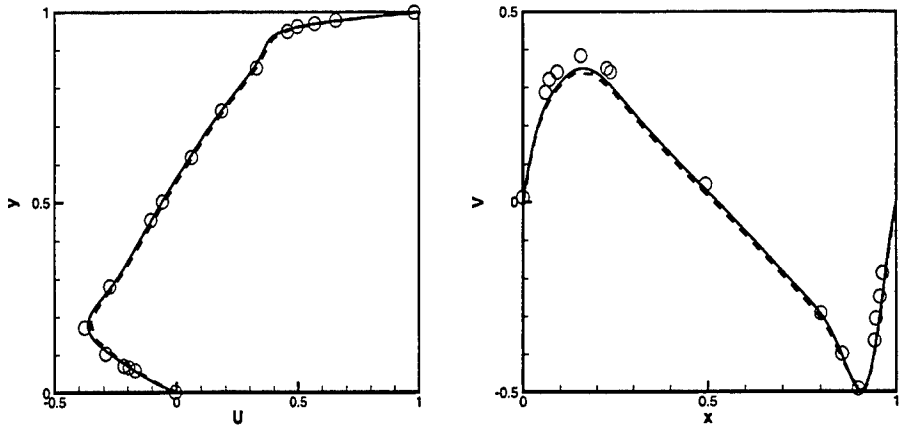

FIGURE 5. Velocity components in vertical and horizontal centerline; flow in a square cavity at Re = 1,000. ——— Uniform mesh; ---- Locally refined grid, o : Ghia *et al.*, (1982)

2.2. *Ghost-cell method for RANS solvers*

2.2.1. *Basic concept*

The first step in this method is to tag all grid nodes according to whether they are inside, outside or bound the body. Points that bound the body are inside, but have at least one neighbor outside as shown in Fig. 6a. The body around which the flow is to be computed is usually represented as a closed polygon. The tagging can be done using an efficient search method. The computational node in question is connected by a linear segment to a point chosen far outside the body polygon to be scanned. One then determines whether this line segment is intersected by the body polygon. If the number

of intersections is even or zero, the node is outside the body: if the number of intersection is odd the node is inside.

Once the inside nodes are identified, the boundary nodes lying inside the body and connected to at least one computation node in the flow domain are marked as the Ghost nodes or Ghost points in the flow computation. The flow solver senses the presence of the boundary through the values of flow variables at the ghost nodes, which are computed using a local Reconstruction Scheme involving the ghost node and some of its neighboring flow nodes. The interpolation function and the relevant boundary and domain where the interpolation function can be evaluated matters of choice. Polynomial functions are usually efficient since these are compatible with the finite-difference stencils which link the ghost node to the flow computation nodes. The solution accuracy depends to a great extent on the degree of the interpolating polynomials used. But polynomials of higher degree, although expected to be more accurate, may often lead to serious boundedness problems and hence to numerical instability. Three different interpolation procedures have been attempted so far for a few validation test cases. The variable values at the ghost cell can be updated either in an implicit or an explicit manner, depending on the coupled flow solver. Implicit updating is in general observed to have enhanced numerical stability whereas explicit updating of the ghost node values often requires very low underrelaxation factors for numerical convergence.

2.2.2. *Interpolation procedures*

1. Linear interpolation in triangular domain

The simplest approach to linking the ghost node to the surrounding fluid nodes is to construct a triangle where the ghost node forms one of the vertices and the other two nodes lie in the flow domain. These triangles can be chosen by the user depending on the configuration: see Fig. 6a, where G is the ghost node, $F1$ and $F2$ are the fluid nodes and B, the midpoint of the intercept, is assumed to be the wall node where the boundary conditions are satisfied through the interpolation procedure.

A simple linear interpolation formula in a 2D space is taken as

$$\phi = a_1 x + a_2 y + a_3 \tag{2.3}$$

The flow solver usually needs the variable values at the ghost node as weighted combination of the values at the neighboring nodes, in the following form

$$\phi_G = w_1 \phi_1 + w_2 \phi_2 + w_B \phi_B \tag{2.4}$$

It is therefore most convenient to evaluate the relevant weighting coefficients and the neighboring node indices in a pre-processor and use them later in the flow solver. The weighting coefficients can always be expressed in terms of the interpolating polynomial in the following form:

$$[w_1, w_2, w_3]^t = T^{-1}[x_G, y_G, 1]^t \tag{2.5}$$

where in the case of a linear interpolation T is a 3×3 matrix, whose elements can be computed from the coordinates of the three boundary points of the interpolation space. Either the values or the normal derivatives are specified on that boundary. x_G, y_G are the coordinates of the ghost point.

In the preliminary calculations this simple linear relationship is used to extrapolate the ghost-point value at G — which obviously lies outside the interpolation space. The major drawback experienced with such extrapolation is that large, negative weighting

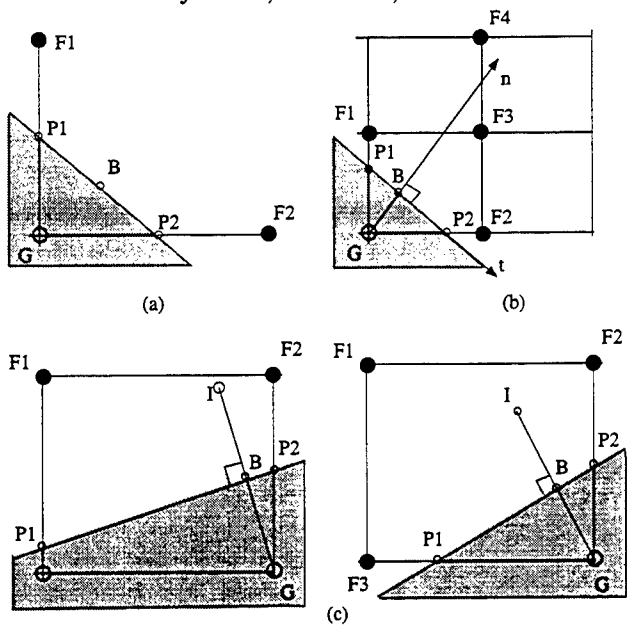

FIGURE 6. Schematic representation of the interpolation procedure; (a) Linear interpolation, (b) Quadratic interpolation, (c) Bilinear interpolation (G Ghost point, I Image point)

coefficients are often encountered. Although these are algebraically correct, they can lead to to severe numerical instability of the coupled flow-solution algorithm.

Using the concept of an image point inside the flow domain for each ghost node is a better procedure to ensure suitable weighting coefficients of the neighboring nodes. In this approach, an image point I is identified in the fluid, along the normal to the boundary through the ghost node G. It lies at a distance equal to that of the ghost node from the same boundary (Fig. 6c). The value of the flow variable is first evaluated at this image point using the chosen interpolation scheme. The principle of maxima can be used to show that if a linear (or bilinear) interpolation scheme is employed, the weighting coefficients are guaranteed to be positive and less than unity. However this argument is not valid when normal derivative conditions on a solution variable are applied at any boundary point of the interpolation space. The value at the ghost node can be expressed, assuming a linear variation along the line connecting G and I, as

$$\phi_G = 2\phi_B - \phi_I. \tag{2.6}$$

The wall boundary conditions are satisfied at B, the foot of the perpendicular from the ghost point G on the wall segment. For velocities and some of the turbulence scalars, the value of ϕ may be set to zero at B on a non-moving wall;. but for pressure or turbulence dissipation (ϵ), the wall value also needs to be evaluated from the neighboring node information in order to obtain the ghost-point value.

2. Bilinear interpolation in rectangular domain

If the interpolating polynomial is assumed to be bilinear in a 2D space, it involves four constants and hence needs four conditions to be specified on the boundary of the interpolation space. For a given body polygon, it is quite straightforward to compute the intersection-point coordinates on the different cell boundaries of the grid network.Thus any ghost node forming one corner of a grid rectangle may have two different types of

intersection as shown in Fig. 6c. In both cases, however, the two fluid nodes and the two wall-intersection nodes may be used for evaluation of the relevant weighting coefficients for the image point. The polynomial in this case may be written as

$$\phi = a_1 x + a_2 y + a_3 xy + a_4. \tag{2.7}$$

The wall intersection points $P1$ and $P2$ on the computational grid lines are used in evaluation of the interpolating polynomial, and the wall boundary conditions are satisfied at the point B. The required weighting coefficients are computed using the same principle described for linear interpolation in triangular space – only the matrix T connecting the interpolation point coordinates will now be different.

3. Linear-quadratic interpolation along wall-normal direction

Most second-order-accurate, finite-difference flow solvers use quadratic variation of flow variables in the direction normal to the wall. The higher order interpolation during reconstruction is therefore expected to retain the formal second order accuracy of the scheme. If the flow variables are assumed to vary in a quadratic manner along the wall normal direction and linearly along the wall, the interpolating polynomial is:

$$\phi = a_1 n^2 + a_2 n + a_3 t + a_4 nt + a_5 \tag{2.8}$$

where the wall coordinates n and t as shown in Fig. 6b. The normal to the wall intersects the adjacent grid lines at two points and the variable values at these two points in turn depend on the neighboring flow node values. Hence the five constants of the assumed polynomial are evaluated from the four neighboring flow nodes, marked with filled-in circles, and the wall point (Fig. 6b). The ghost-node value is either extrapolated or evaluated using the concept of an image point. The use of the image point in case of a quadratic interpolation may produce better weighting coefficients, but their values are no longer guaranteed to be positive and less than unity as they are in the linear interpolation scheme.

2.2.3. *Test cases*

The numerical method of the RANS flow solver to which the present ghost cell approach is coupled is based on a Cartesian, two-dimensional Navier Stokes code. The discretization technique is cell-vertex, finite differences over structured meshes. The convection term is third-order upwind biased; diffusion terms are second-order centered. The pseudo-time integration is implicit and the equations are solved in a coupled manner. The implicit matrices are inverted by Gauss-Seidel line relaxation. The ghost-cell procedure has so far been tested for two laminar flows, using linear or bilinear interpolation, and for a simple turbulent flow using quadratic interpolation.

1. Laminar flow around a semi-circular cylinder at Reynolds number of 150

A semi-circular shape was chosen to avoid flow unsteadiness and vortex shedding observed for circular cylinders at this Reynolds number. This calculation uses the linear interpolation scheme in triangular domains around the ghost points. Three grids of different grid fineness are used, covering the cylinder zone by 20×20, 40×40 and 80×80 uniformly-spaced grids. These provide 43, 87 and 177 ghost points respectively to represent the curved boundary. The finest Cartesian grid used, superimposed on a boundary-fitted (radial polar) grid of approximately the same grid spacing, is shown in Fig. 7. Results obtained from the boundary-fitted grid calculation are compared in Fig. 8 to those of the present ghost-cell procedure.

The present results with the finest grid are observed to be the closest to the solution

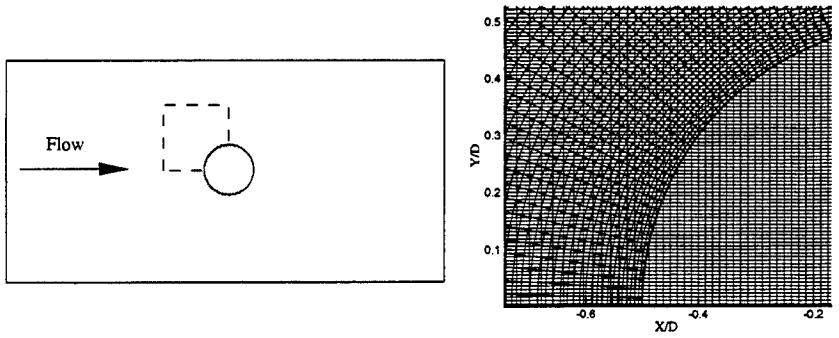

FIGURE 7. Test problem for semi-circular cylinder and close view of the Cartesian grid overlapped with the boundary-conforming radial polar grid

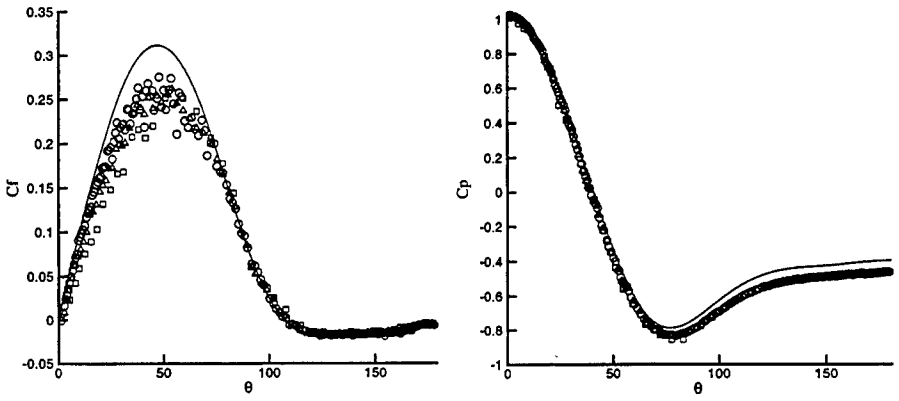

(a) (b)

FIGURE 8. Circumferential variation of (a) skin-friction and (b) pressure coefficient for flow around a cylinder ($Re = 150$). ——— : Radial polar grid, (o , △ , □) Cartesian grid with o 177 ghost points , △ 87 ghost points and □ 43 ghost points.

obtained from the boundary-fitted grid. The discrepancies observed in the maximum value of the skin friction and for the surface pressure in the post-separation region may be attributed to the inaccuracy introduced by the linear interpolation procedure used for local reconstruction. The mild kinks or wiggles are always observed in Cartesian grid calculations with ghost cells. This may perhaps be attributed to the circumferential variation of the distance between the wall point where the boundary conditions are satisfied, and the corresponding ghost point. In a boundary-fitted grid, the normal distance of the near-wall point can be systematically controlled and maintained to vary continuously along the body surface. On the other hand in the boundary non-conforming situation, the distance between the wall and the ghost point, primarily decided by the geometry of the body and the Cartesian grid intersection, may often have an erratic variation along the body surface.

2. Laminar flow past a two-dimensional bump

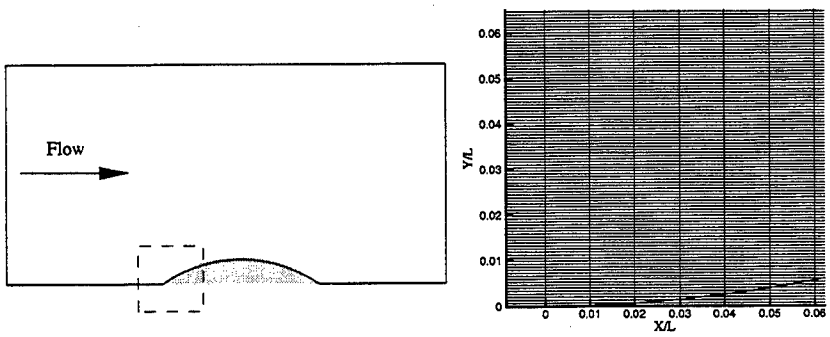

FIGURE 9. Test problem for flow past a two-dimensional bump and close view of the Cartesian grid.

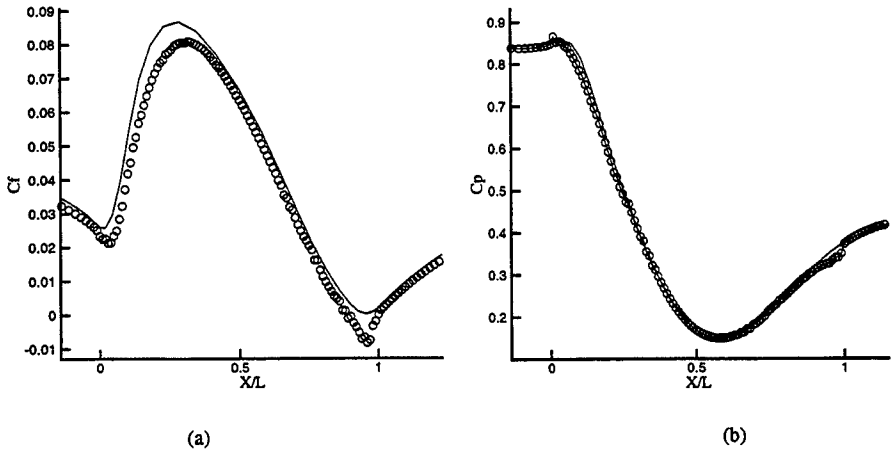

(a) (b)

FIGURE 10. Longitudinal variation of (a) skin-friction and (b) pressure coefficient for flow past a bump ($Re = 1000$). ——— : boundary-conforming grid, o non-conforming grid.

This test case has been chosen to validate the present ghost-cell procedure for two-dimensional turbulent flow in a geometry for which detailed measurement data of Webster *et al* (1996) are available. Because handling the boundary conditions for turbulence scalars is not so straightforward, attempts have first been made to analyse laminar flow over the same geometry and to compare the results with other calculations using boundary-conforming grids. The surface bump on the lower wall of a channel is defined by three tangential circular arcs and is shown schematically in Fig. 9. The boundary layer experiences the effects of significant surface curvature and streamwise pressure gradient. The present calculation uses uniform plug flow at the channel inlet at a flow Reynolds number of 1000, based on the bump chord length.

A close-up view of the rectangular grid used near the concave root of the bump is also shown in Fig. 9 . As stated earlier, the difficulty in using the boundary-non-conforming grid is the lack of control on the resolution near the boundary. The only way to obtain

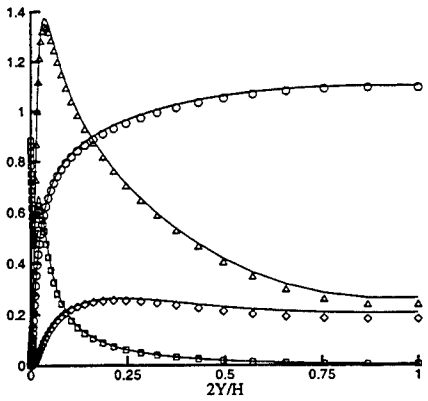

FIGURE 11. Transverse variation of mean velocity and turbulence quantities for fully developed channel flow (Re based on half channel height = 10,000). ——— boundary conforming grid, o △ □ ◇ non-conforming grid (o U, △ 100k, □ 50 ϵ and ◇ 100 v^2).

adequate resolution is to use a very fine uniformly-spaced grid in the region covered by the intersecting curved boundary. The present calculation uses a 201×201 Cartesian grid, out of which 101×101 points cover the bump region. Since the bump height is only about 6.5% of the chord length, the grid aspect ratio is always of the order of 15 near the bump surface region. This computation uses bilinear interpolation in rectangular interpolation space coupled to the image-point concept discussed in the previous section.

Fig. 10 shows the longitudinal variation of the surface pressure and the skin-friction coefficient for the flow, computed in the present procedure directly from the spatial interpolation scheme used in the local reconstruction. Comparison to results obtained from boundary-conforming grid for the same configuration at the same Reynolds number shows excellent agreement for the surface pressure distribution; but the skin friction is observed to be under-predicted by about 5%, especially near the top of the bump. Usually skin friction is very sensitive to the resolution of the boundary layer. In a boundary-non-conforming grid environment, this resolution would always vary along the body surface and inadequate resolution at some of the longitudinal sections may lead to inaccurate near-wall velocities and hence a wrong value of C_f.

Some mild kinks are observed in the results based on the ghost-cell procedure, especially near the beginning and end of the bump, where the weighting coefficients of the interpolation procedure suddenly change from the uniform value over the flat part of the channel to new values as the bump starts or ends. It is further observed that as the flow Reynolds number is increased, the amplitude of these wiggles grows, and may eventually lead to numerical instabilities.

3. Fully developed turbulent flow in a plane 2D channel

This simple example is chosen to test the capability of the present ghost-cell procedure when coupled to a RANS solver with a standard turbulence model. The boundary non-conformity is maintained by placing the channel wall between two horizontal grid lines. Quadratic interpolation along the boundary-normal direction is used in this case.

The $v^2 - f$ turbulence model (Durbin, 1995) is used for this RANS computation of channel flow. In the reconstruction procedure, the boundary conditions satisfied at the wall point are $U = V = k = v^2 = f = \partial p/\partial y = 0$. Evaluation of the non-zero value of the

turbulence dissipation ϵ at the wall point is however not so obvious. The value of ϵ at wall points is set to $2\nu k/y^2$ where k is the turbulence kinetic energy at the near-wall node at a normal distance y from the wall surface. As mentioned in Section 1, such a boundary condition can cause undesirable numerical stiffness and was therefore implemented in a coupled. implicit manner.

Fig. 11 shows the transverse profiles of the mean longitudinal velocity and different turbulence quantities computed using the conventional body-conforming as well as the present body-non-conforming grids. Reasonable agreement between the two results demonstrates the accuracy of the ghost cell procedure with quadratic interpolation, at least when the body boundaries are parallel to either of the Cartesian grid directions.

3. Conclusions and future tasks

The ghost-cell procedure to handle complex-shaped curved boundaries using a Cartesian grid has been validated for a few two-dimensional flow situations. Work is in progress to study the numerical stability of the procedure — especially how to ensure numerically amenable values of the interpolation weights, and to eliminate the large-amplitude oscillations of the solution which are often observed at high flow Reynolds number.

The validation examples have shown that adequate near-wall resolution can be obtained in the present method only by using a very fine grid. This usually implies many wasteful, inactive nodes in a fixed Cartesian grid. Therefore the local refinement procedure, already developed for structured Cartesian grids, now needs to be coupled to the ghost-cell procedure to develop an efficient and accurate RANS solver. We then propose to extend the methodology to three-dimensional flow and validated against measurement and/or other computation data for some turbulent flow examples of industrial interest.

4. Acknowledgements

The first author gratefully acknowledges the financial support provided by the Center for Turbulence Research and by the National Aerospace Laboratories, Bangalore, India.

REFERENCES

BENEK, J. A., BUNING, P. G., STEGER, J. L., 1985 A 3-D Chimera grid embedding technique, *AIAA* Paper 85-1523.

DURBIN, P. A. & PETTERSSON REIF, B. A. 2000 *Statistical Theory and Modeling for Turbulent Flow.* Wiley, New York.

DURBIN, P. A. 1995 Separated flow computations with the $k-\epsilon-v^2$ model. *AIAA J.* **33**, 659–664.

FADLUN, E.A., VERZICCO, R., ORLANDI, P. & MOHD-YUSOF, J. 2000 Combined immersed-boundary/finite-difference methods for three-dimensional complex flow simulations. *J. Comp. Phys.* **161**, 35.

GHIA, U., GHIA, K. N., SHIN, C. T. 1985 High-Re solutions for incompressible flow using the Navier-Stokes equations and a multigrid method. *J. Comp. Phys.* **48**, 387–411.

MAVRIPILIS, D. J. 1995 Unstructured mesh generation and adaptivity. *Von Karman Inst. for Fluid Dynamics*, Lecture Series 1995-02.

MOHD–YUSOF, J. 1997 Combined immersed–boundary/B–spline methods for simulations of flows in complex geometries, *A*nnual Research Briefs, Center for Turbulence Research, NASA Ames/Stanford Univ. 317–327.

PESKIN, C. S 1972 Flow patterns around heart valves: a numerical method. *J. Comp. Phys.*, **10**, 252–271.

VERZICCO, R., MOHD–YUSOF, J., ORLANDI, P. AND HAWORTH, D. 2000 Large–eddy–simulation in complex geometric onfigurations using boundary body forces. *AIAA J.* **38**, 427.

WEBSTER, D. R., DEGRAAFF, D. B. AND EATON, J. K. 1996 Turbulence characteristics of a boundary layer overa two-dimensional bump. *J. Fluid Mech.* **320**, 53-69.

Modeling the "rapid" part of the velocity/pressure-gradient correlation in inhomogeneous turbulence

By S. V. Poroseva

1. Motivation and objectives

The Reynolds-stress transport equation (RSTE) includes the velocity/pressure-gradient correlation $< p_{,j}u_i >$. Following Rotta (1951), it is common practice to split this correlation into two parts: the pressure-strain correlation $< pu_{i,j} >$ and the pressure-diffusion part $< pu_i >_{,j}$. This approach has advantages if one simulates homogeneous turbulence with a two-equation turbulence model. In homogeneous turbulence, both the pressure diffusion term $< pu_i >_{,i}$ and the pressure-strain term $< pu_{i,i} >$ do not contribute to the transport of the turbulent kinetic energy (k).

In inhomogeneous turbulent flows, however, the modeling of the pressure-diffusion term in the k-equation is challenging. Direct numerical simulation (DNS) data from free shear flows (Rogers & Moser 1994; Moser *et al.* 1998) show that the contribution of the pressure diffusion in the turbulent kinetic energy balance is not negligible, especially in the central core of the flow. The current practice of using a single model for both the pressure diffusion and the turbulent diffusion is not likely to be successful because the two have qualitatively different profiles. It was shown by Lumley (1978), that in homogeneous turbulence the "slow" part of the pressure diffusion term can be modeled as

$$-\frac{1}{\rho} < pu_i >_{,i}^{(s)} = \frac{1}{5} < u_m u_m u_i >_{,i} . \tag{1.1}$$

Thus, a model for the turbulent diffusion can absorb only this "slow" term. The contribution of the "rapid" part and the surface integral in the exact integral expression for the pressure diffusion term (Chou 1945) should also appear in the modeled turbulent kinetic energy transport equation.

Judging by DNS data, the term $< pu_i >_{,j}$ cannot be ignored in the transport equations for Reynolds stresses and should be modeled as well as the pressure-strain term $< pu_{i,j} >$. Thus, two models for the pressure-containing correlations are necessary, and splitting the correlation $< p_{,j}u_i >$ into two parts becomes a disadvantage. The direct modeling of the correlation $< p_{,j}u_i >$ is a natural choice. Here, models for the "rapid" part of the velocity/pressure-gradient correlation in the Reynolds-stress transport equation (RSTE) and of the pressure-diffusion term in the turbulent kinetic energy transport equation (Poroseva 2000) are considered and tested against post-processed DNS data from a wake and a mixing layer (Rogers & Moser 1994; Moser *et al.* 1998).

2. Model expressions

To derive the model for the "rapid" part of $< p_{,j}u_i >$ in inhomogeneous turbulence, it was suggested by Poroseva (2000) to go back to the original idea of Chou (1945)

and consider the exact integral expression for the velocity/pressure-gradient correlation $< p_{,j}u_i >$. This expression holds rigorously in an incompressible flow. For a compressible flow, it works as an approximation. The "rapid" part of that expression can be written as following:

$$-\frac{1}{\rho} < p_{,j}u_i >^{(r)} = -\frac{1}{2\pi} \int\int\int \left[U'_{m,n} < u'_n u_i >'_{,m}\right]'_{,j} \frac{1}{r} dV'. \tag{2.1}$$

The prime "$'$" indicates that the quantities should be evaluated at a point P', with coordinates x'_i, which ranges over the volume V', and r is the distance from point P' to point P with coordinates x_i. The correlation on the left-hand side of Eq. (2.1) is evaluated at point P, whereas all derivatives on the right side are taken at P'. The integrand in Eq. (2.1) is non-zero only over the volume where the two-point correlation $< u'_n u_i >$ (or more precisely $< u'_{n,m} u_i >$) does not vanish. In other words, for a fixed point P, only those points P' which lie within the length scale of the two-point correlation measured from P, contribute to the integral in Eq. (2.1). If one assumes that the function $U'_{m,n}$ varies more slowly than the two-point correlation within the volume determined by the length scale of the two-point correlation, then, to the first approximation, we can rewrite Eq. (2.1) as

$$-\frac{1}{\rho} < p_{,j}u_i >^{(r)} = -\frac{1}{2\pi} U_{m,n} \int\int\int < u'_n u_i >'_{,mj} \frac{1}{r} dV' \tag{2.2}$$

(Chou 1945). Notice that this is not an assumption of turbulence homogeneity: all functions are regarded as functions of space coordinates.

Chou (1945) suggested modeling the sum of the two pressure-containing correlations as

$$\Pi_{ij}^{(r)} = -\frac{1}{\rho}(< p_{,j}u_i > + < p_{,j}u_j >)^{(r)} = a_{nmji} U_{m,n},$$

though no specific form for the tensor function a_{nmji} was derived in his work. The idea to model not the sum, but each correlation separately, was applied for the first time to the pressure-strain correlation $< pu_{i,j} >$ by Rotta (1951). This idea has been found more fruitful for the correlation $< p_{,j}u_i >$ also (Poroseva 2000) and it yields

$$-\frac{1}{\rho} < p_{,j}u_i >^{(r)} = a_{nmji} U_{m,n}$$

and

$$\Pi_{ij}^{(r)} = (a_{nmji} + a_{nmij}) U_{m,n},$$

where

$$a_{nmji} = \frac{1}{2\pi} \int_{V'} < u'_n u_i >'_{,mj} \frac{1}{r} dV'.$$

In this way, more specific conditions can be imposed on a_{nmji}:

(i) symmetry in permutation of indices m and j;

(ii) from continuity: $a_{mmji} = 0$;

(iii) from Green's theorem: $a_{njji} = 2 < u_n u_i >$,

and a number of model coefficients can be eliminated. The final model expression for a_{nmji} includes two coefficients:

$$a_{nmji} = -\frac{1}{5}(< u_iu_j > \delta_{mn} + < u_iu_m > \delta_{jn}) + \frac{4}{5} < u_iu_n > \delta_{jm} + \tag{2.3}$$
$$C_1[\frac{1}{2}(< u_iu_j > \delta_{mn} + < u_iu_m > \delta_{jn}) + < u_iu_n > \delta_{jm} +$$
$$k(\delta_{ij}\delta_{mn} + \delta_{im}\delta_{jn}) - < u_ju_m > \delta_{in} -$$
$$2(< u_ju_n > \delta_{im} + < u_mu_n > \delta_{ij})] +$$
$$C_2[\frac{1}{2}(< u_iu_j > \delta_{mn} + < u_iu_m > \delta_{jn} - < u_ju_n > \delta_{im} -$$
$$< u_mu_n > \delta_{ij}) + k\delta_{in}\delta_{jm} - \frac{3}{2} < u_ju_m > \delta_{in}].$$

Then the model for the "rapid" part of the pressure-containing term in the RSTEs is

$$\Pi_{ij}^{(r)} = -\frac{1}{\rho}(< p_{,i}u_j > + < p_{,j}u_i >) = \tag{2.4}$$
$$-\left(\frac{1}{5} + \frac{1}{2}C_1 + C_2\right)(< u_iu_m > U_{m,j} + < u_ju_m > U_{m,i})$$
$$+\left(\frac{4}{5} - C_1 - \frac{1}{2}C_2\right)(< u_iu_m > U_{j,m} + < u_ju_m > U_{i,m})$$
$$+k(C_1 + C_2)(U_{i,j} + U_{j,i}) - (4C_1 + C_2) < u_mu_n > U_{m,n}\delta_{ij}.$$

Note that expression Eq. (2.4) is obtained with the assumption of flow incompressibility. Thus terms in Eq. (2.3) that involve δ_{mn} make no contribution in Eq. (2.4).

Coefficients C_1 and C_2 are, in the general case, unknown functions of several parameters (see discussions in Lumley 1978; Reynolds 1987; Ristorcelli 1995; Girimaji 2000). However, the behavior of these functions can be specified for some known limit states of turbulence.

Setting $< u_iu_j >= 2/3k\delta_{ij}$ it is easy to show that expression Eq. (2.3) satisfies, for any values of the coefficients C_1 and C_2, the exact solution for isotropic turbulence subjected to sudden distortion (Rotta 1951; Crow, 1968; Reynolds 1976)

$$a_{nmji} = k\left(\frac{8}{15}\delta_{ni}\delta_{mj} - \frac{2}{15}(\delta_{nm}\delta_{ji} + \delta_{nj}\delta_{mi})\right).$$

In the case of homogeneous turbulence, an additional condition based on permutation of the indices n and i can be imposed on Eq. (2.3). It results in the following relation between model coefficients:

$$\frac{1}{5} - \frac{5}{2}C_1 - C_2 = 0. \tag{2.5}$$

Under the condition given by Eq. (2.5), model Eq. (2.4) for $\Pi_{ij}^{(r)}$ transforms to the known model of Launder *et al.* (1975). Note that this connection between coefficients exists only in a homogeneous flow, and does not hold in the general case.

Model Eq. (2.4) for $\Pi_{ij}^{(r)}$ is realizable. If $< u_\alpha u_\alpha >$ ($\alpha = 1, 2, 3$) are the eigenvalues of the Reynolds-stress tensor, then we obtain the following realizability constraint

$$\Pi_{11}^{(r)} = 0, \text{ if } < u_1u_1 >= 0$$

corresponding to the limit state of two-component turbulence (Schumann 1977; Pope 1985; Shih *et al.* 1994). Index 1 is chosen arbitrarily. Writing Eq. (2.4) for $\Pi_{11}^{(r)}$, one gets

$$\Pi_{11}^{(r)} = 2k(C_1 + C_2)U_{1,1} + (-4C_1 - C_2) < u_m u_n > U_{m,n} = 0$$

or

$$C_1 = -C_2 \frac{2kU_{1,1} - < u_m u_n > U_{m,n}}{2kU_{1,1} - 4 < u_m u_n > U_{m,n}}. \tag{2.6}$$

Taking into account that among all eigenvalues only $< u_2 u_2 >$ and $< u_3 u_3 >$ are not equal to zero and $< u_2 u_2 > + < u_3 u_3 >= 2k$ as well as $U_{m,m} = 0$, then Eq. (2.6) can be rewritten as

$$C_1 = -C_2 \frac{U_{1,1}(4k - < u_\beta u_\beta >) + 2U_{\beta,\beta}(k - < u_\beta u_\beta >)}{U_{1,1}(10k - 4 < u_\beta u_\beta >) + 8U_{\beta,\beta}(k - < u_\beta u_\beta >)}. \tag{2.7}$$

where $\beta = 2$ or 3 (no summation on β). This condition is satisfied with $C_1 = C_2 = 0$, for instance, but it allows other solutions for specific turbulence states. Again, this connection between coefficients is valid only in the two-component limit. Consideration of two-component homogeneous turbulence is interesting itself and will be addressed in the future. Here, we simply notice that Eq. (2.5) and Eq. (2.7) do not contradict each other, but for specific turbulence states they fully define the set (C_1, C_2).

In the transport equation for the turbulent kinetic energy, model expression Eq. (2.4) for $\Pi_{ij}^{(r)}$ contracts to a model for the "rapid" part of the pressure diffusion term with the only model coefficient:

$$-\frac{1}{\rho} < pu_i >_{,i}^{(r)} = \left(-\frac{3}{5} + C_k\right) P \tag{2.8}$$

where

$$C_k = \frac{15}{2} C_1 + 3C_2. \tag{2.9}$$

Here, $P = - < u_i u_j > \frac{\partial U_i}{\partial x_j}$. The coefficient C_k is a function of the same parameters as coefficients C_1 and C_2. In homogeneous turbulence, substitution of Eq. (2.5) in Eq. (2.9) gives $C_k = 0.6$.

An important question in modeling the pressure diffusion term $< pu_i >_{,i}$ is whether a model expression for this term should be of the diffusive type also. However, this question addresses the complete model for $< pu_i >_{,i}$, which includes "rapid", 'low", and "surface" parts in inhomogeneous turbulence, and does not apply to each part separately. Only the "rapid" part is the concern of the present study. Moreover, the properties of a model for $< pu_i >_{,i}$ should not be considered separately from a model for the trace of the dissipative tensor ε_{ij}. On the contrary, the physical assumptions and mathematical approximations used in deriving the two models should be the same if the models are to be consistent. This is the only way one can hope for inaccuracy in a model for one term to be compensated for by a model for another term. In other words, the equality sign stands not between each exact term and a model expression for it, but between the sum of exact terms and the sum of models for them:

$$< pu_i >_{,i} - \nu < u_{i,j} u_{i,j} >= \frac{1}{2}(\Pi_{ii}^{(M)} - \varepsilon_{ii}^{(M)}).$$

With such an approach, the properties of the sum should be conserved in modeling rather than the properties of each term separately. The commonly-used model $\varepsilon_{ij} = 2/3\delta_{ij}\varepsilon$ is not consistent with any known model for Π_{ij} to the author's knowledge. More work should be done in this direction.

3. Results

Post-processed DNS data for the wake (Moser *et al.* 1998) were used to evaluate terms in the model expression Eq. (2.4). Eq. (2.8) was tested against DNS data in two flows: the plane mixing layer (Rogers & Moser 1994) and the plane wake (Moser *et al.* 1998). DNS data for the pressure diffusion in the turbulent kinetic energy balance (solid lines) are compared with model profiles (dashed lines) in Fig. 1. Because at present DNS data are not available separately for the "slow" and "rapid" parts of the pressure diffusion, only evaluation of the joint performance of Eq. (1.1) and Eq. (2.8) is possible. Therefore, inaccuracies of model Eq. (1.1), derived under the assumption of turbulence homogeneity (Lumley 1978), are absorbed in the value of C_k. To calculate model profiles, DNS data for the production and turbulent diffusion terms are used. The optimal value of the coefficient C_k in Eq. (2.8) is determined by adjusting the maximum of a calculated profile to match the maximum of the DNS profile. Its value was found to be equal to 0.52 in the mixing layer (Fig. 1a) and 0.5 in the wake (Fig. 1b).

DNS profiles of $\Pi_{12}^{(r)}$, $\Pi_{11}^{(r)}$, and $\Pi_{33}^{(r)}$ in the wake (solid lines) are compared to model ones (dashed lines) in Fig. 2. Model profiles are obtained by substituting the DNS data for the mean velocity and Reynolds stresses in the model expression Eq. (2.4) for $\Pi_{ij}^{(r)}$. The coefficient $C_1 = 0.4$ was chosen by matching the calculated profiles to the DNS ones. The value of C_2, $C_2 = -5/6$, is calculated from Eq. (2.9) using known C_k and C_1. The agreement between the DNS data and the calculated profiles is very good, except that the levels of $\Pi_{11}^{(r)}$ and $\Pi_{33}^{(r)}$ are slightly overpredicted. One of the possible reasons for this disagreement is the dependence of C_2 on the coefficient C_k, which is not exact, but absorbs the inaccuracies of the model for the "slow" part of the pressure diffusion.

It is important to clarify the question of the functional form of the coefficients C_k, C_1, and C_2. Conditions Eq. (2.5) and Eq. (2.7) provide relationships between the coefficients in particular limit states of turbulence, but do not indicate on what parameters the coefficients depend. This information can be partly drawn from DNS, experimental data, and results from RANS calculations of classical self-similar free shear flows, equilibrium boundary layers with and without pressure gradients, and separated flows. Such flows were calculated by Poroseva (2000) and Poroseva & Iaccarino (2001), using the k-ε turbulence model with the "rapid" part of the pressure diffusion term taken into account. Good predictions for mean velocity, shear stress, friction coefficient, and turbulent kinetic energy profiles were obtained in all test flows.

The value of C_k in Poroseva (2000) and Poroseva & Iaccarino (2001) is calibrated by matching the non-dimensional turbulent kinetic energy level in the flow. Consequently, its value depends on the conditions which determine that level. The turbulent kinetic energy level is not unique even in the same flow. Indeed, it does appear from both experiments and DNS (see discussion in Rogers & Moser 1994 and Moser *et al.* 1998) that, even in geometrically-equivalent flow situations at the same Reynolds number, multiple asymptotic states are observed. This difference between alternative states manifests itself in both the statistics and the flow structure. Under appropriate scaling, the mean-velocity and shear-stress profiles are universal or near universal, but normal stresses and turbulent

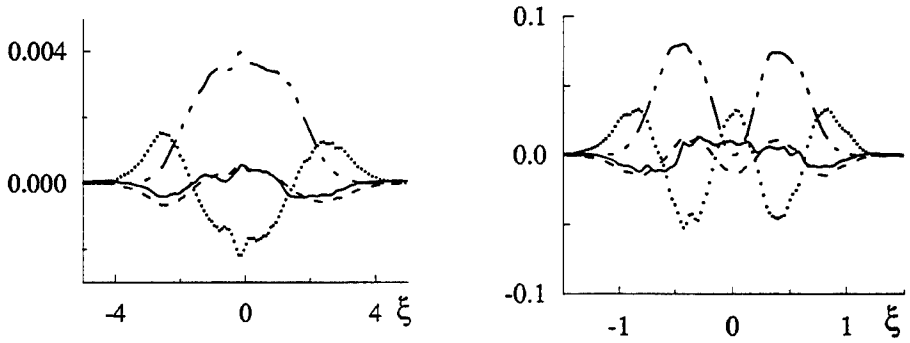

FIGURE 1. Partial turbulent kinetic energy balance: a) mixing layer, b) wake. (----) calculated pressure diffusion profiles; (—··—) DNS production, (———) DNS pressure diffusion, (·····) DNS turbulent diffusion.

kinetic energy profiles are non-unique. DNS confirms that statistical differences reflect the differences in the large-scale structure of turbulence, which depends strongly "on uncontrolled and possibly unknown properties of the initial or inlet conditions" (Moser *et al.* 1998). Also, large-scale structure is influenced by flow geometry, boundary conditions, external forces etc. (Tsinober 1998). Among other factors connected with large-scale structure are Reynolds number and flow geometry. The coefficient C_k seems to be influenced by both factors. However, the database used by Poroseva (2000) and Poroseva & Iaccarino (2001) does not facilitate distinguishing their influence on the coefficient value, as data for different test flows were obtained at different Reynolds numbers.

On the other hand, the coefficient C_k is an explicit function Eq. (2.9) of the two coefficients C_1 and C_2, which are linked to each other by Eq. (2.7) in the two-component turbulence limit. Because mean velocity gradients are involved in that expression, a functional dependence of C_k on velocity gradients could be expected. However, each test flow was successfully reproduced with the same value of C_k. Moreover, mean velocity gradients, like mean velocity components, appear not to be sensitive to initial or inlet conditions, whereas large-scale structure and, as a result, the value of C_k strongly depend on them. This suggests that although there may be some dependence of the coefficient on mean velocity gradients, it seems to be of secondary importance in inhomogeneous flow.

4. Conclusions

In the present research, model expressions for the "rapid" parts of the velocity/pressure-gradient correlation in the RSTE and the pressure diffusion in the turbulent kinetic energy transport equation (Poroseva 2000) were evaluated using DNS data. For the velocity/pressure-gradient correlation such data are available in a wake (Moser *et al.* 1998). For the pressure diffusion, there exist DNS data in two flows: a wake and a mixing layer (Rogers & Moser 1994; Moser *et al.* 1998). DNS data and calculated model profiles agree very well.

The contribution of the "rapid" part of the pressure diffusion appears in the standard k-ε equation through an additional model coefficient C_k. THere is probably some dependence of the coefficient on mean velocity gradients, but it is apparently of secondary importance. Each test flow was successfully reproduced with a constant value of C_k in Poroseva (2000) and Poroseva & Iaccarino (2001). The value $C_k = 0.6$ can be rigorously

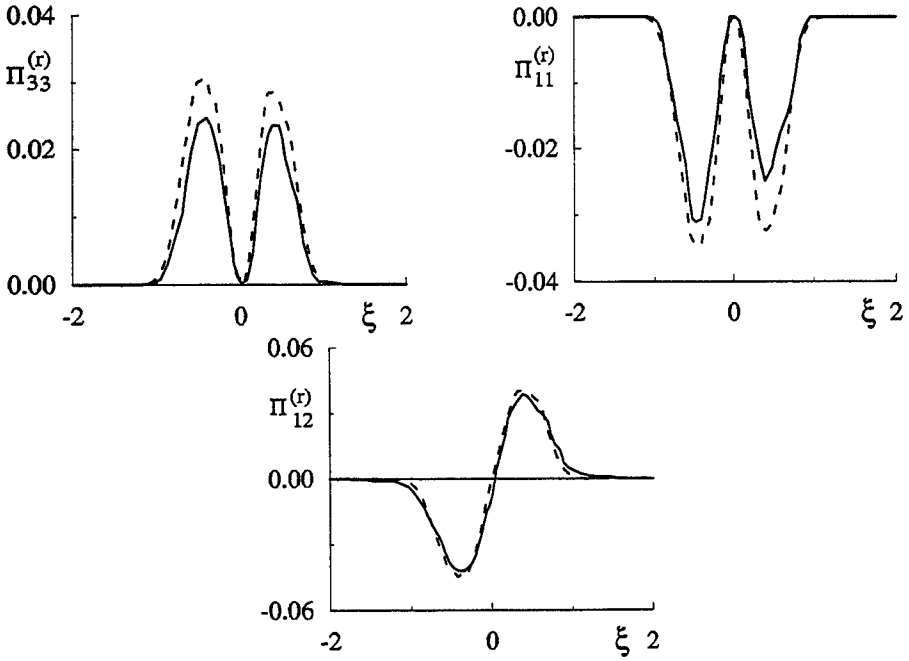

FIGURE 2. "Rapid" part of velocity/pressure-gradient correlations in the Reynolds-stress budget in the wake. (———) DNS profiles, (----) calculated profiles

derived for homogeneous turbulence. However, the optimum value of the coefficient in inhomogeneous flows changes from flow to flow, depending on different factors controlling the large-scale turbulence structure. Among these factors are initial or inlet conditions, Reynolds number, flow geometry, and boundary conditions. These conditions make large-scale structure non-universal, even in geometrically equivalent flow situations at the same Reynolds number, as DNS and experimental data demonstrate. Moreover, it is not obvious that all conditions controlling the large scales have been defined and, even if they were known, the link between them and the large-scale structure they produce may not necessarily be evident and predictable.

Acknowledgments

The author would like to thank Dr. M. M. Rogers (NASA-Ames) for providing the DNS database and Mr. C. A. Langer (Mechanical Engineering Dept., Stanford University) for pointing out some references and for fruitful discussions.

REFERENCES

CHOU, P. Y. 1945 (Also Zhou) On velocity correlations and the solutions of the equations of turbulent fluctuation. *Quart. Appl. Math.* **3**, 38-54.

CROW, S. C. 1968 Viscoelastic properties of fine-grained incompressible turbulence. *J. Fluid Mech.* **33**, 1-20.

GIRIMAJI, S. S. 2000 Pressure-strain correlation modelling of complex turbulent flows. *J. Fluid Mech.* **422**, 91-123.

LAUNDER, B. E., REECE, G. J. & RODI, W. 1975 Progress in development of a Reynolds-stress turbulent closure. *J. Fluid Mech.*, **68**, 537-566.

LUMLEY, J. L. 1978 Computational modeling of turbulent flows. *Adv. Appl. Mech.* **18**, 123-177.

MOSER, R. D., ROGERS, M. M. & EWING, D. W. 1998 Self-similarity of time-evolving plane wakes. *J. Fluid Mech.* **367**, 255-288.

POPE, S. B. 1985 PDF methods for turbulent reactive flows. *Prog. Energy Combust. Sci.* **11**, 119-192.

POROSEVA, S. V. 2000 New approach to modeling the pressure-containing correlations. *Proc. 3rd Int. Symp. on Turbulence, Heat and Mass Transfer,* (Nagoya, Japan), 487-493.

POROSEVA, S. V. & BÉZARD, H. 2001 On ability of standard k-ε model to simulate aerodynamic turbulent flows. *CFD J.* **9**, 464-470.

POROSEVA, S. V. & IACCARINO, G. 2001 Simulating separated flows using the k-ε model. *Annual Research Briefs*, Center for Turbulence Research., NASA Ames/Stanford Univ., 375–383.

REYNOLDS, W. C. 1976 Computation of turbulent flows. *Ann. Rev. Fluid Mech.* **8**, 183-208.

REYNOLDS, W. C. 1987 Fundamentals of turbulence for turbulence modeling and simulation. *Lecture Notes for Von Karman Institute, AGARD* CP-93.

RISTORCELLI, J. R., LUMLEY, J. L. & ABID, R. 1995 A rapid-pressure covariance representation consistent with the Taylor-Proudman theorem materially-frame-indifferent in the 2D limit. *J. Fluid Mech.* **292**, 111-152.

ROGERS, M. M. & MOSER R. D. 1994 Direct simulation of a self-similar turbulent mixing layer. *Phys. Fluids* **6**, 903-923.

ROTTA, J. C. 1951 Statistische Theorie nichthomogener Turbulenz. 1. *Z. Phys.* **129**, 547-572.

SHIH, T.-H., SHABBIR, A. & LUMLEY, J. L. 1994 Realizability in second moment turbulence closures revisited. *NASA* TM 106469.

TSINOBER, A. 1998 Is concentrated vorticity that important? *Euro. J. Mech. - B/Fluids.* **17**(4), 421-449.

Simulating separated flows using the k-ε model

By **Svetlana Poroseva AND Gianluca Iaccarino**

1. Background and motivation

Two-equation turbulence models (Jones & Launder 1972; Launder & Sharma 1974) are widely used in industrial CFD applications although their shortcomings are well known. Model limitations have different origins: the performance of the Boussinesq assumption and the choice of the second turbulence scale to build the eddy viscosity have been investigated thoroughly (Cousteix & Aupoix 1997; Apsley & Leschziner 2000). The present paper focuses on the turbulent kinetic energy transport equation and on the modeling parameters in the standard k-ε model based on the linear Boussinesq assumption.

The model coefficients in turbulence modeling are usually kept constant in turbulent flows with different geometry and at different Reynolds numbers. Various criteria have been used to define *universal* values for the constants: the decay of isotropic turbulence is usually considered to fix the value of $C_{\varepsilon 2}$; the slope of the mean-velocity profile in boundary layers (the Karman constant) determines a relationship between the constants σ_ε, C_μ, $C_{\varepsilon 1}$ and $C_{\varepsilon 2}$. The use of these asymptotic constraints on the model constants provides a formally-consistent model.

The k-ε model constants have assumed different values depending on the applications. Several investigators (Durbin 1991, 1995; Yakhot and Orszag 1986; Shih *et al.* 1995) have introduced a variable $C_{\varepsilon 1}$ depending on various geometrical and flow parameters (i.e. the strain rate, wall distance, vorticity magnitude, etc.) to introduce the effect of the near-wall anisotropy. Similarly, it was demonstrated by Lumley (1978), Reynolds (1987), Ristorcelli (1995) and Girimaji (2000) that, in turbulence models based on Reynolds-stress transport equations, the coefficients should be functions of flow parameters.

In a previous study (Poroseva & Bézard 2001) it was shown that, after tuning the coefficients, the standard k-ε model was successful in reproducing the measured mean-velocity and shear-stress profiles for several flows (self-similar free shear flows and equilibrium boundary layers in different pressure gradients). According to that study, the coefficients C_μ and $C_{\varepsilon 2}$ have the standard values, 0.09 and 1.92 respectively; the relation between coefficients σ_k and σ_ε is more important for the model accuracy than their absolute values. This is especially important in unbounded flows where turbulent diffusion plays a significant role. A constant ratio $\sigma_\varepsilon/\sigma_k = 1/0.67 = 1.5$ was recommended for practical purposes instead of the standard values, $\sigma_\varepsilon = 1.3$ and $\sigma_k = 1$. The value of the coefficient $C_{\varepsilon 1}$, has a strong effect on the calculated results; its value depends on the type of flow considered and on the Reynolds number.

The rationale behind the choice of the value of the coefficient $C_{\varepsilon 1}$ goes back to the formulation of the transport equation for turbulent kinetic energy originally derived assuming homogeneous turbulence. It was shown by Poroseva (2001) that the "rapid" part of the pressure diffusion term can be modeled as an extra production term in the k-equation. The same contribution appears in the ε equation through the coefficient $C_{\varepsilon 1}$. Following the work by Poroseva & Bézard (2001) a modified $k-\varepsilon$ model with tuned coefficients is applied to simulate separated flows in a planar diffuser, over a backstep, in a channel with wavy walls, and in an axisymmetric combustion chamber (Fig. 1).

2. Turbulence modeling

The exact equation for the turbulent kinetic energy in incompressible flows can be derived from the Navier-Stokes equations:

$$U_i \frac{\partial k}{\partial x_i} = - < u_i u_j > \frac{\partial U_i}{\partial x_j}$$

$$- < \nu \frac{\partial u_i}{\partial x_k} \frac{\partial u_i}{\partial x_k} > + \nu \frac{\partial^2 k}{\partial x_j^2} - \frac{1}{2} \frac{\partial}{\partial x_j} < u_i u_i u_j > + < \frac{\partial p}{\partial x_i} u_i > \qquad (2.1)$$

where U_i and u_i represent the mean and fluctuating velocity components respectively, p is the instantaneous pressure and $< - >$ represents the time average. The terms on the right hand side are the turbulent kinetic energy production (P_k), the dissipation (ε), the molecular diffusion, the turbulent diffusion and the pressure diffusion. The latter is usually split into "slow" and "rapid" parts; Lumley (1978) showed that the slow part can be modeled as a diffusion process and, therefore, incorporated into the turbulent diffusion term.

Poroseva (2001) suggested a model for the "rapid" part of the velocity-pressure gradient correlation $< p_{,j} u_i >$. In the turbulent kinetic energy transport equation, the model contracts (at $j = i$ and summation over indexes) to a model for the "rapid" part of the pressure diffusion. The *new* proposed form for the k equation is:

$$U_i \frac{\partial k}{\partial x_i} = P_k - \varepsilon + \frac{\partial}{\partial x_j} \left[\left(\nu + \frac{\nu_t}{\sigma_k} \right) \frac{\partial k}{\partial x_j} \right] + \left(-\frac{3}{5} + C_k \right) P_k, \qquad (2.2)$$

where the last term on the right hand side shows the contribution of the "rapid" part of the pressure diffusion. It must be pointed out that this formulation for the "rapid" part of the pressure diffusion is similar to the model derived *ad hoc* by Demuren *et al.* (1996) by analyzing DNS data; according to this work the C_k coefficient should vary between 0.6 and 0.9. Equation (2.2) is an extension of the standard k equation but it still does *not* represents the velocity/pressure-gradient correlation explicitly; the slow contribution is still lumped in with the turbulent diffusion term.

The equation for the turbulence dissipation ε closely resembles Eq. (2.2):

$$u_i \frac{\partial \varepsilon}{\partial x_i} = (C_{\varepsilon_1} P - C_{\varepsilon_2} \varepsilon) \frac{\varepsilon}{k} + \frac{\partial}{\partial x_j} \left[\left(\nu + \frac{\nu_t}{\sigma_\varepsilon} \right) \frac{\partial \varepsilon}{\partial x_j} \right] \qquad (2.3)$$

Finally the eddy viscosity is defined as :

$$\nu_t = C_\mu \frac{k^2}{\varepsilon} \qquad (2.4)$$

The standard values of the model coefficients are:

$$C_\mu = 0.09;\ C_{\varepsilon 1} = 1.44;\ C_{\varepsilon 2} = 1.92;\ C_k = 0.6;\ \sigma_k = 1;\ \sigma_\varepsilon = 1.3.$$

The value $C_k = 0.6$ corresponds to homogeneous turbulence (Poroseva, 2001). This model will be referred to as model LS1.

A second set of constants has been used (LS2)

$$C_\mu = 0.09;\ C_{\varepsilon 2} = 1.92;\ \sigma_k = 1;\ \sigma_\varepsilon = 0.67$$

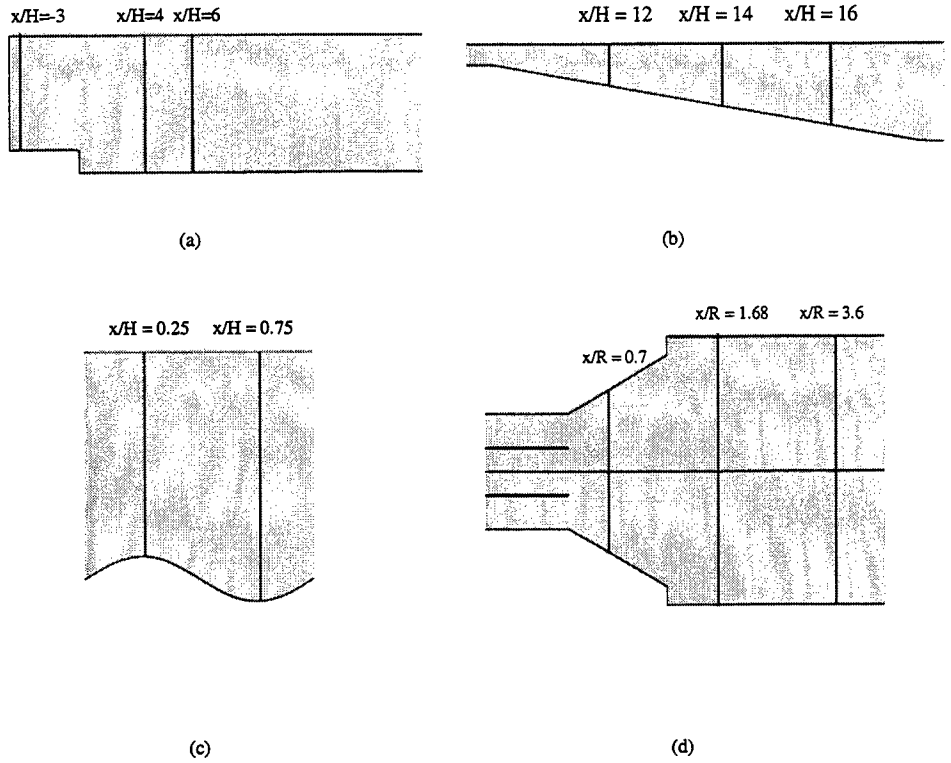

FIGURE 1. Test problems considered: (a) Backstep; (b) Diffuser; (c) Wavy Channel; (d) Combustion Chamber

The values of $C_{\varepsilon 1}$ and C_k have been chosen to *fit* the experimental data for each test case and will be reported later.

Equations (2.2-2.4) represent the high-Reynolds-number form of the k-ε model; the damping function approach proposed by Launder & Sharma (1974) has been used to *correct* the behavior of turbulent quantities in the viscous dominated near-wall regions.

Results obtained using the four-equation $v^2 - f$ model (Durbin 1995) are also included for comparison.

3. Results and discussion

The steady two-dimensional Reynolds-averaged Navier-Stokes equations for an incompressible fluid are solved using a commercial CFD code (Fluent v5.3).

The first problem selected is the backstep flow (Jovic & Driver 1995), reported in Fig. 1a. The Reynolds number based on the inlet velocity and the step height is 5,100. The flow at the inlet is a fully developed boundary layer. Separation is fixed at the step and the expansion generates a large recirculating region with strong negative velocity and

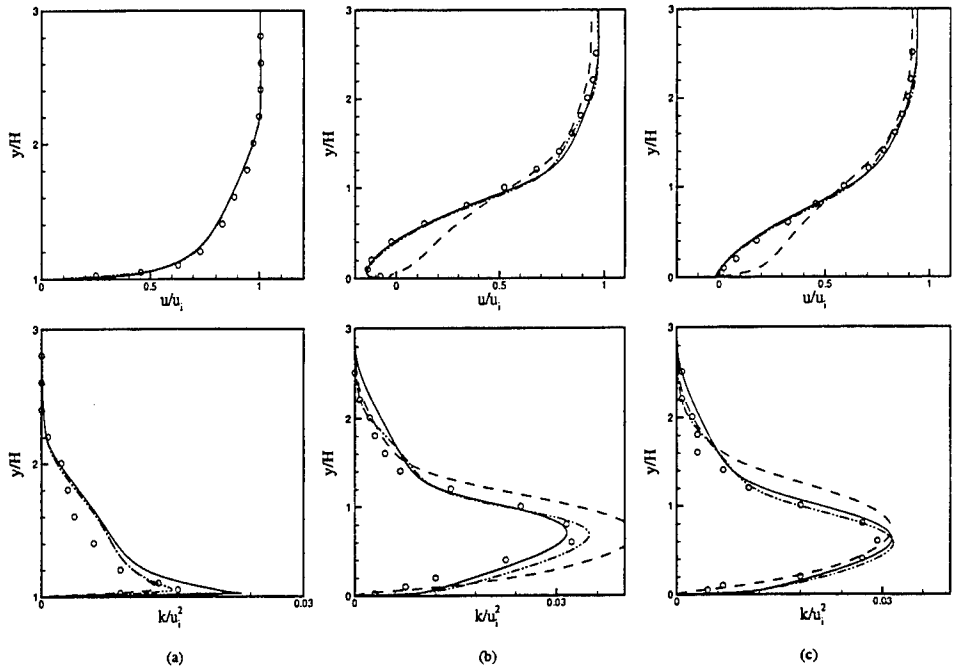

FIGURE 2. Results for the flow over a backstep: velocity (top) and turbulent kinetic energy profiles (bottom). (a) x/H = -3; (b) $x/H = 4$; (c) $x/H = 6$. o : experiments; ---- : model LS1; ——— : model LS2; —··— : $v^2 - f$ results.

high turbulent kinetic energy (measurements are available at several stations downstream the step). The coefficients for the model LS2 are defined as $C_{\varepsilon 1} = 1.85$ and $C_k = 0.8$. Figure 2 shows results for streamwise velocity and turbulent kinetic energy (scaled by the inlet velocity). All three models predict similar profiles upstream of the step (Fig. 2a). Downstream, the LS1 does not correctly reproduce the separation zone, whereas the LS2 and $v^2 - f$ models are in good agreement with the experimental data (Figs. 2b-2c). In addition, the LS1 fails to predict the correct friction coefficient c_f in the recirculating bubble and underestimates c_f in the recovery region, whilst the other models produce very similar friction levels (Fig. 3).

The second test case is the flow in an asymmetric diffuser (Fig. 1b). The flow is fully developed at the inlet. The Reynolds number based on the bulk velocity and the inlet height is 20,000. The presence of a mild adverse pressure gradient induces separation on a smooth surface, which is very challenging for turbulence models. Mean velocity and turbulent kinetic energy profiles are available as well as skin friction (Buice & Eaton 1997) to identify the extent of the separated region. As in the previous case, the LS1 predictions are in poor agreement with the measurements; on the other hand, the model LS2 (with coefficients $C_{\varepsilon 1} = 1.5$ and $C_k = 0.6$) is accurate in predicting both the mean velocity and the turbulent kinetic energy (Fig. 4). The LS2 model captures the extent of the separation region very well (Fig. 5).

The third case is the flow in a periodic wavy channel (Fig. 1c). The Reynolds number based on the bulk velocity and the average channel height is 11,000. The flow separates on the downhill slope and reattaches uphill; only mean velocity measurements are available

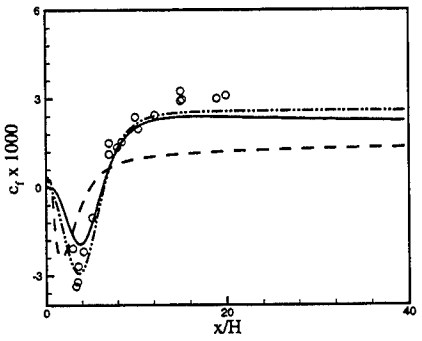

FIGURE 3. Results for the flow over a backstep: skin friction coefficient. o : experiments; ---- : model LS1; ——— : model LS2; —·—· : $v^2 - f$ results.

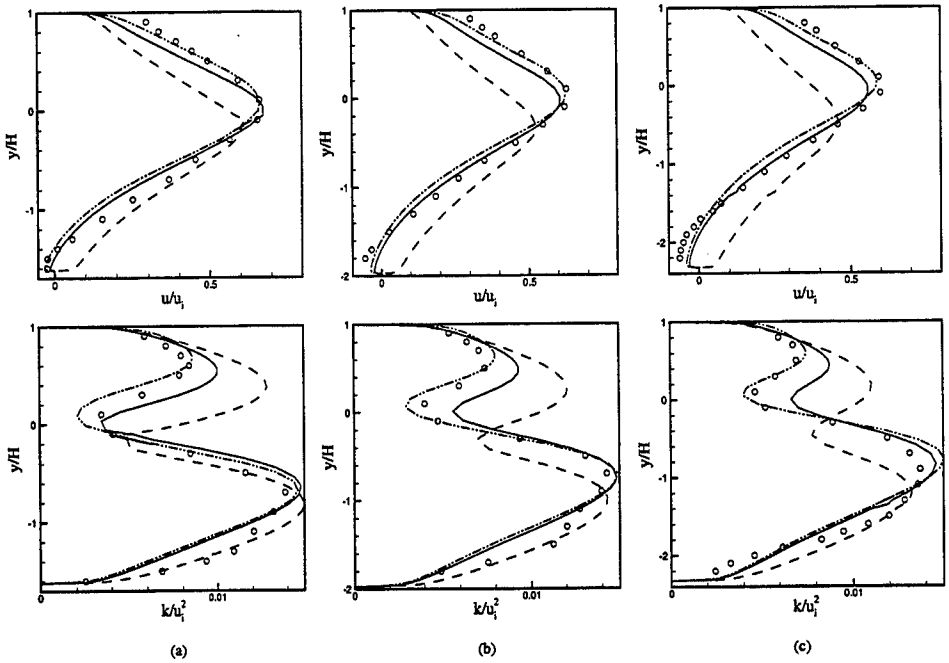

FIGURE 4. Results for the flow in a diffuser: velocity (top) and turbulent kinetic energy profiles (bottom). (a) $x/H = 24$; (b) $x/H = 28$; (c) $x/H = 32$. o : experiments; ---- : model LS1; ——— : model LS2; —·—· : $v^2 - f$ results.

in this case (Kuzan 1986). All the models are reasonably accurate in predicting the velocity profiles. The coefficients used for the LS2 model are $C_{\varepsilon 1} = 1.5$ and $C_k = 0.6$.

The fourth case is an axisymmetric combustion chamber (Fig. 1d). A central pipe stream and an annular swirling stream enter a large cylindrical chamber, and in response to a strong adverse pressure gradient a small recirculating region is created. The Reynolds number based on the pipe bulk velocity and diameter is 75,000. Streamwise and swirl

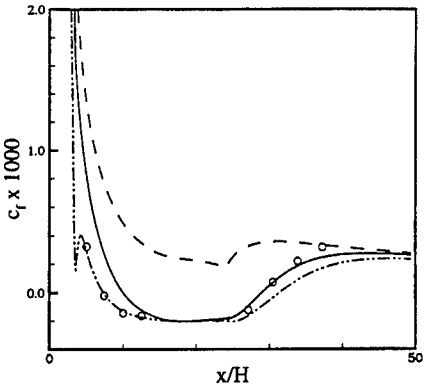

FIGURE 5. Results for the flow in a diffuser: skin friction coefficient. o : experiments; ---- : model LS1; ——— : model LS2; —··— : $v^2 - f$ results.

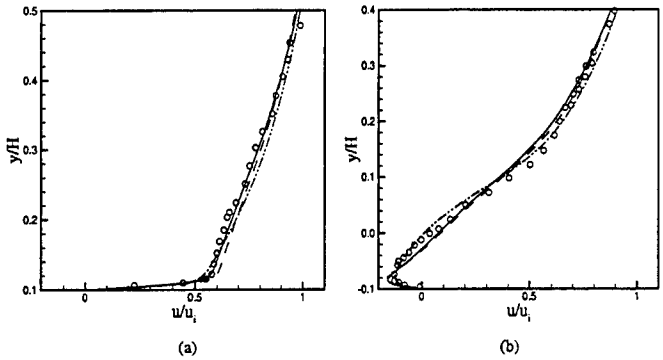

FIGURE 6. Results for the flow in a wavy channel: axial velocity profiles. (a) $x/H = 0.25$; (b) $x/H = 0.75$. o : experiments; ---- : model LS1; ——— : model LS2; —··— : $v^2 - f$ results.

velocities are measured at various stations in the chamber (Hagiwara *et al.* 1986). The coefficients used in this case are $C_{\varepsilon 1} = 1.7$ and $C_k = 0.6$.

Model LS1 considerably overestimates the extent of the recirculating bubble and the velocity on the chamber axis; models LS2 and $v^2 - f$, on the other hand, predict the velocity quite accurately (Fig. 7). The swirl velocity is reproduced fairly well by all models.

4. Conclusions and future plans

A modified form of the turbulent kinetic energy equation that explicitly accounts for the "rapid" part of the pressure diffusion term (Poroseva, 2001) has been tested for separated flows. The production term in the equation is controlled by an additional coefficient (C_k) related to the $C_{\varepsilon 1}$ coefficient in the ε equation. The choice of the coefficients in the $k - \varepsilon$ models is known to be critical for the accuracy of the numerical predictions. The results presented in this work complement the results for free shear flows and equilibrium

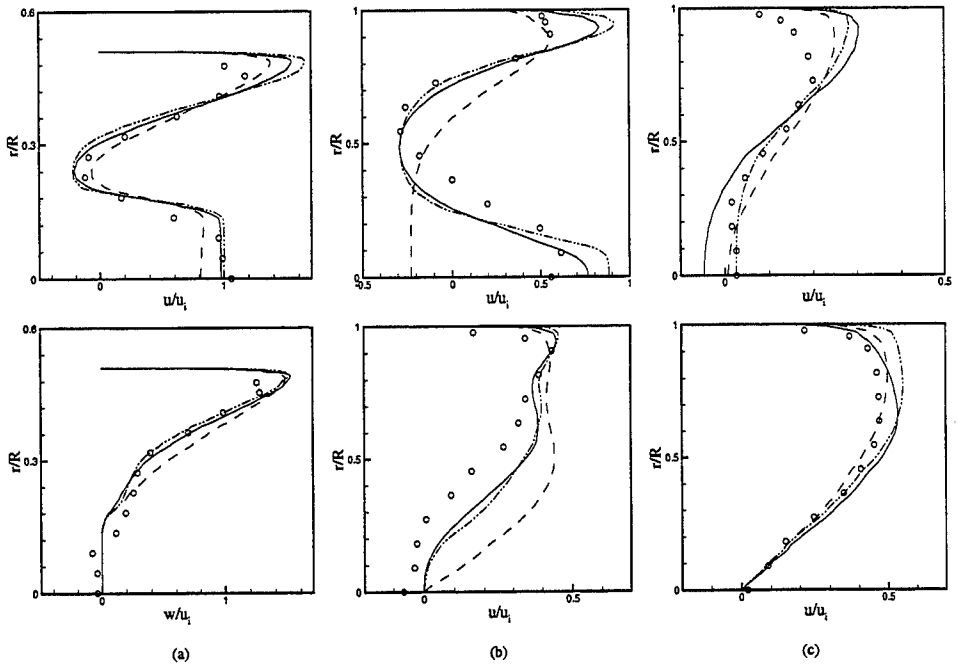

FIGURE 7. Results for the flow in a combustion chamber: axial (top) and swirl velocity component profiles (bottom). (a) $x/R = 0.7$; (b) $x/R = 1.68$; (c) $x/R = 3.6$. o : experiments; ---- : model LS1; ——— : model LS2; —··— : $v^2 - f$ results.

boundary layers reported by Poroseva & Bezard (2001), and indicate the optimal values for these coefficients for massively-separated flows.

It is worth noting that the C_k values found in this study are within the range suggested by Demuren *et al.* (1996) from the analysis of DNS data of wakes and mixing layers.

The proposed form of the turbulent kinetic energy equation is not complete. It reflects only the additional contribution of the rapid part of the pressure diffusion term. In order to derive the complete form of the equation in inhomogeneous turbulence, two more issues must be considered: (i) modeling the "slow" part of the pressure diffusion term in inhomogeneous turbulence, (ii) consistency of the models for the velocity-pressure gradient correlation Π_{ij} and the dissipation tensor ε_{ij}. These issues will be addressed in the future.

Several formulations are available in the literature to define the value of $C_{\varepsilon 1}$ as function of various flow and geometrical parameters. As an example, in the $v^2 - f$ model (Durbin, 1995) the following function is used:

$$C_{\varepsilon 1} = 1.3 + 0.25/\left[1 + (0.15d/D)^2\right]^4$$

Here d is the distance from the walls and D is a turbulence length scale proportional to $k^{3/2}/\varepsilon$. This corresponds to a linear interpolation between a near wall value of 1.55 and a free stream value of 1.3. Other formulations (Shih 1998) use the ratio between production and dissipation of turbulent kinetic energy to achieve the same goal of interpolating between two values of $C_{\varepsilon 1}$. Future work will address the influence of different formulas on the computed results.

REFERENCES

APSLEY D. D. & LESCHZINER, M. A. 2000 Advanced turbulence modeling of separated flow in a diffuser. *Flow, Turbulence and Combustion* **63**, 81-112.

BUICE, C. U. & EATON, J. K. 1997 Experimental investigation of flow through an asymmetric plane diffuser. *Thermosciences Divn., Dept. of Mech. Engg., Stanford Univ.* Report No. TSD-107.

COUSTEIX, J. & AUPOIX, B. 1997 Modèles de turbulence: principes et applications. *In: Proc. 16eme Congres Canadien de Mécanique Appliqué*

DEMUREN, A. O., ROGERS, M. M., DURBIN, P. & LELE, S. K. 1996 On modeling pressure diffusion in non-homogeneous shear flows *Proc. 1996 Summer Program*, Center for Turbulence Research, NASA Ames/Stanford Univ., 63-74.

DURBIN, P.A. 1991 Near-wall turbulence closure modelling without damping functions. *Theor. Comput. Fluid Dynamics* **3**, 1-11.

DURBIN, P. A. 1995 Separated flow computations with the k-ε-v^2 model. *AIAA J.* **33**, 659-664.

GIRIMAJI, S. S. 2000 Pressure-strain correlation modelling of complex turbulent flows. *J. Fluid Mech.* **422**, 91-123.

HAGIWARA, A., BORTZ, S., & WEBER, R. 1986 Theoretical and experimental studies on isothermal, expanding swirling flows with application to swirl burner design. Results of the NFA 2-1 Investigation. *Intl. Flame Res. Foundn.* Doc. No F259/a/3/

JONES, W. P. & LAUNDER, B. E. 1972 The prediction of laminarization with a two-equation model of turbulence. *Int. J. Heat Mass Transfer* **15**, 1-32.

JOVIC, S. & DRIVER, D. 1995 Reynolds number effect on the skin friction in separated flows behind a backward-facing step. *Expts. in Fluids* **18**, 464-472.

KUZAN, J. D. 1986 Velocity measurements for turbulent separated and near-separated flows over solid waves. *Ph.D. Thesis*, Department of Chemical Engineering, University of Illinois at Urbana.

LAUNDER, B. E. & SHARMA, B. I. 1974 Application of the energy-dissipation model of turbulence to the calculation of flow near a spinning disc. *Letters in Heat and Mass Transfer* **1**, 131-138.

LUMLEY, J. L. 1978 Computational modeling of turbulent flows, *Adv. Appl. Mech.* **18**, 123-177.

POROSEVA, S. V. 2001 Modeling the "rapid" part of the velocity-pressure gradient correlation in inhomogeneous turbulence. *Annual Research Briefs*, Center for Turbulence Research, NASA Ames/Stanford Univ., 367–374

POROSEVA, S. V. & BEZARD, H. 2001 On ability of standard k-ε model to simulate aerodynamic turbulent flows. *CFD Journal* **9**, 464-470.

REYNOLDS, W. C. 1987 Fundamentals of turbulence for turbulence modeling and simulation. *Lecture Notes for Von Karman Institute,* AGARD CP-93.

RISTORCELLI, J. R., LUMLEY, J. L. & ABID, R. 1995 A rapid-pressure covariance representation consistent with the Taylor-Proudman theorem materially-frame-indifferent in the 2D limit. *J. Fluid Mech.* **292**, 111-152.

SHIH, T. H., LIOU, W. W., SHABBIR, A., YANG, Z. & ZHU, J. 1995 A new k-ε eddy viscosity model for high Reynolds number turbulent flows. *Computers & Fluids* **24**, 227-238.

YAKHOT, V. & ORZAG, S. 1986 Renormalization group analysis of turbulence. *J. of Sci. Comput.* **1**, 1-51.

Wall corrections in modeling rotating pipe flow

By S. V. Poroseva

1. Motivation and objectives

The presence of a wall significantly influences the turbulence structure of a flow. Wall effects are naturally described by the exact transport equations for turbulence characteristics with appropriate boundary conditions imposed. In practice, however, turbulent flow features are simulated with the averaged Navier-Stokes equations in which some terms must be modeled. This implies that the model expressions used for those terms should respond correctly to the presence of the wall.

The terms to be modeled in the averaged Navier-Stokes equations are dissipative tensors, pressure-containing correlations, and turbulent diffusion terms. Modern turbulence models are mostly based on the second-order weighted averages of the Navier-Stokes equations, the Reynolds-stress transport equations (RSTE), from which simpler, industry-oriented turbulence models are then derived. To date, model expressions for the dissipative tensor ε_{ij}, the pressure-containing correlations Π_{ij} and the turbulent diffusion term have been derived based on assumptions which are not consistent for the different terms. Moreover, some of those assumptions are too simplified to reflect the real physics of a flow: they hold only for some limiting states of turbulence that are rarely (if at all) met in real flows. As a result, turbulence models do not naturally reproduce wall effects, and usually need additional wall corrections. It is important to clarify which model expressions contribute most to model failure and are therefore in most need of such corrections. The present study is not an attempt to solve this problem in general, but only in a particular case of turbulent flow: flow in an axially-rotating cylindrical pipe. This flow is of interest because it relates to phenomena encountered in various engineering systems involving boundary layers on rotating surfaces, *e.g.*, heat exchangers and rotor cooling systems.

It was shown by Kurbatskii & Poroseva (1999) that the commonly-used model of Daly & Harlow (1970) for the turbulent diffusion does not adequately describe the behavior of the third-order velocity moments in a pipe flow. At present, the tensor-invariant model of Hanjalić & Launder (1972) is the best choice for modeling turbulent diffusion in the RSTE. Though it is less accurate in predicting the third-order moments than models based on the transport equations for these moments, the HL model provides results which are quantitatively comparable with those obtained using more accurate models. Also, it is cheaper and more robust in different combinations of Reynolds and rotation numbers. The difference between results obtained with the DH and HL models is large, especially near a wall, and increases with swirl. The tensor-invariant model for the turbulent diffusion significantly improves the description of turbulence structure near a wall, especially with large wall rotation. Nevertheless, in a stationary pipe, changing the DH model to a more adequate turbulent diffusion model does not solve the problem of inaccurate prediction of the turbulent intensities near a wall. The model expressions for the dissipative tensor and the pressure-containing correlations (Launder *et al.* 1975) used in Kurbatskii & Poroseva (1999) still need additional wall corrections (So & Yoo 1986; Gibson & Launder 1978).

Of the other two terms in the RSTE that need to be modeled, the present study focuses on the pressure-containing correlations. One of the reasons for this is the fact that little progress has been made in modeling the dissipative tensor. With the state of art in this field, it is possible to say that including or excluding wall corrections in commonly-used models for ε_{ij} does not make those models more or less physical. To date, their main function is more to compensate for inaccuracies in modeling other terms, rather than to reproduce the dissipative process itself accurately. In contrast, progress in modeling the pressure-containing correlations is more noticeable. New approaches based on more refined physical assumptions (*e.g.* Speziale *et al.* 1991; Kassinos *et al.* 2000, 2001) have been developed in the last decade. It could be expected that their performance should depend less on wall corrections. One of the objectives of this work was to clarify this question.

Rotation can have a crucial role in the development of wall corrections to model expressions for the pressure-containing correlation. It was noticed by Gibson & Launder (1978) that, in a stably-stratified boundary layer, wall effects diminish as stability is increased. Though the physical mechanism of influence of rotation on a pipe flow structure differs from that of stable stratification, the analogy between those two flows is very well known. Thus, it can be expected that wall effects in a rotating pipe flow will diminish with increasing rotation number N, defined as the ratio of the pipe wall velocity W_o to the mean-flow velocity at the pipe center U_o. Indeed, it was found by Poroseva *et al.* 2000, 2001) that including the wall effects (Gibson & Launder 1978; Durbin 1991) in turbulence models, such as the structure-based Q model (Kassinos *et al.* 2000, 2001) and the non-linear SSG model (Speziale *et al.* 1991), does not decisively improve the ability of the models to describe a flow under rotation, though it does improve the description of turbulence structure in a stationary pipe flow. The maximum value of the rotation number N at which a model still appropriately reproduces the turbulence structure is the same in both cases; whether wall effects are included in the model or not. Moreover, the stronger the rotation, the smaller the influence of wall effects on flow characteristics. This conclusion relates in larger degree to the mean-velocity components and shear stresses. Turbulent kinetic energy is more sensitive to the description of wall effects. This question is the second focus of the present work.

2. Models

There are two ways to evaluate the performance of different model expressions for the pressure-strain correlations. The most physical way would be to use direct numerical simulation (DNS). This gives complete information in the case of low-Reynolds-number flows. However, with increasing Reynolds number, the contribution of the different physical mechanisms to turbulence processes changes. Therefore, some conclusions valid at low Reynolds numbers will not necessarily hold for high Reynolds numbers. Such a situation could be expected for wall effects, which are the focus of the present study. The flow in the current work was calculated at two Reynolds numbers, 2×10^4 and 4×10^4, which are too high to apply DNS. For such Reynolds numbers, another way to evaluate model expressions for Π_{ij} can be used. Namely, to calculate the flow with a turbulence model, in which model expressions for the turbulent diffusion and the dissipative tensor are kept the same, but the model for the pressure-containing correlations is adjusted.

The transport equation governing the evolution of the Reynolds stresses has the fol-

lowing form

$$\frac{\bar{D} < u_i u_j >}{Dt} = P_{ij} + D_{ij} + \Pi_{ij} - \varepsilon_{ij}.$$

Here,

$$\frac{\bar{D}}{Dt} = U_j \frac{\partial}{\partial x_j} + \frac{\partial}{\partial t},$$

U_i are the mean velocity components, and u_i are the fluctuating velocity components. Cartesian tensor notation is used throughout the text for the sake of simplicity. The production term $P_{ij} = - < u_i u_k > U_{k,j} - < u_j u_k > U_{k,i}$ does not need modeling. The diffusion term D_{ij} includes the molecular diffusion $\nu(< u_i u_j >_{,kk})$ (ν is the kinematic viscosity), which also does not need modeling, and the turbulent diffusion $- < u_i u_j u_m >_{,m}$. The DH model (Daly & Harlow 1970):

$$< u_i u_j u_k >= -C_{s1}\tau(< u^m u_k >< u_i u_j >_{,m})$$

has been chosen to model the turbulent diffusion in the present study. Here, $C_{s1} = 0.18$ and the time scale τ is modeled as $\tau = k/\varepsilon$, where ε is the dissipation rate of the turbulent kinetic energy k. Though the HL model (Hanjalić & Launder, 1972) proved to give better results in a pipe flow (Kurbatskii & Poroseva, 1999), the main focus of the present study is evaluation of the performance of the pressure-containing correlation models, not suggestions for a complete RSTE model, and the simplest turbulent-diffusion model serves for this aim.

The pressure-containing correlation term $\Pi_{ij} = -(< u_i p_{,j} > + < u_j p_{,i} >)/\rho$ (p is the pressure fluctuation, ρ is the flow density) is usually split into the pressure-strain correlations $< (u_{i,j} + u_{j,i})p > /\rho$ and the pressure-velocity correlations $-(< u_i p >_{,j} + < u_j p >_{,i})/\rho$. Then the correlations $-(< u_i p >_{,j} + < u_j p >_{,i})/\rho$ are either combined with the turbulent diffusion term or neglected. Neither practice has solid justification, but at the moment this issue will be skipped and the same approach will be used throughout this work. Thus, progress in modeling the pressure-containing correlations mostly relates to modeling the pressure-strain correlations. Based on previous work on modeling a pipe flow (for a review see, *e.g.*, Poroseva *et al.* 2000), the following model expressions for the pressure-strain correlations were chosen for evaluation: the IP model and the full LRR (Launder *et al.* 1975), the linearized SSG (Gatski & Speziale 1993) and the non-linear SSG (Speziale *et al.* 1991). All models can be represented by the same expression:

$$\Pi_{ij} = -(C_1'\varepsilon + 2C_1'^* P)b_{ij} + C_2'\varepsilon\left(b_{ik}b_{kj} - \frac{1}{3}b_{kl}b_{kl}\delta_{ij}\right) + \left(C_3' - C_3'^*\sqrt{b_{kl}b_{kl}}\right)kS_{ij}$$
$$+C_4'k\left(b_{ik}S_{jk} + b_{jk}S_{ik} - \frac{2}{3}b_{kl}S_{kl}\delta_{ij}\right) + C_5'k(b_{ik}\Omega_{jk} + b_{jk}\Omega_{ik})$$

with different coefficients:

$$\text{IP}: (C_1',\ C_1'^*,\ C_2',\ C_3',\ C_3'^*,\ C_4',\ C_5') = (3.6,\ 0,\ 0,\ 0.8,\ 0,\ 1.2,\ 1.2)$$
$$\text{LRR}: (C_1',\ C_1'^*,\ C_2',\ C_3',\ C_3'^*,\ C_4',\ C_5') = (3.6,\ 0,\ 0,\ 0.8,\ 0,\ 1.75,\ 1.31)$$
$$\text{LSSG}: (C_1',\ C_1'^*,\ C_2',\ C_3',\ C_3'^*,\ C_4',\ C_5') = (3.4,\ 1.8,\ 0,\ 0.36,\ 0,\ 1.25,\ 0.4)$$
$$\text{SSG}: (C_1',\ C_1'^*,\ C_2',\ C_3',\ C_3'^*,\ C_4',\ C_5') = (3.4,\ 1.8,\ 4.2,\ 0.8,\ 1.3,\ 1.25,\ 0.4)$$

Here, $b_{ij} = 1/2(< u_i u_j > /k - 2\delta_{ij}/3)$, $S_{ij} = (U_{i,j} + U_{j,i})/2$ and $\Omega_{ij} = (U_{i,j} - U_{j,i})/2$. Note that in the present study the value of the coefficient C_1' in the LRR model is 3.6 instead of the usual 3.0.

A new approach, which offers an alternative to the standard method based on the modeling of the RSTE, is the structure-based Q model (Kassinos *et al.* 2000, 2001). A preliminary formulation of this approach has been evaluated here also. The pressure effects are treated in the Q model in a more profound way: non-local effects are taken into account by incorporating additional structure tensors into the model. Details of the transport equation for the third-rank **Q**–tensor can be found in Kassinos *et al.* (2000) and Poroseva *et al.* (2000, 2001).

The dissipation tensor ε_{ij} is modeled by the isotropic expression, with a correction for low Reynolds numbers near a solid wall, as

$$\varepsilon_{ij} = \frac{2}{3}\delta_{ij}\varepsilon + 2\nu\frac{< u_i u_j >}{x_n^2} \tag{2.1}$$

(So & Yoo 1986), where x_n is the normal distance to a pipe wall and δ_{ij} is the Kronecker delta tensor. The equation for the dissipation rate of the turbulent kinetic energy is used in the following form

$$\frac{\bar{D}\varepsilon}{Dt} = \left[(\nu\delta_{jk} + C_\varepsilon\tau < u_j u_k >)\,\varepsilon_{,j}\right]_{,k} + \frac{1}{\tau}\left(C_{\varepsilon 1}P - C^*_{\varepsilon 2}\varepsilon\right) - \frac{2\nu\varepsilon}{x_n^2}f_1. \tag{2.2}$$

Here, $P = P_{ii}/2$. The model coefficients are: $C_\varepsilon = 0.18$ (0.22 for the Q model), $C_{\varepsilon 1} = 1.54$ (1.5 for the Q model), $C^*_{\varepsilon 2} = C_{\varepsilon 2}f_2$ in a stationary pipe flow and $C_{\varepsilon 2} = 11/6$. The functions f_1 and f_2 are damping functions (So & Yoo 1986): $f_1 = \exp\,(-0.5x_n u_{*0}/\nu)$, where u_{*0} is the friction velocity, and $f_2 = 1 - 2/9\ exp\left[-\left(k^2/(6\nu\varepsilon)\right)^2\right]$. In rotating flows the model coefficient $C^*_{\varepsilon 2}$ is a function of the "Richardson number"

$$C^*_{\varepsilon 2} = \max(1.4, C_{\varepsilon 2}f_2(1 - C_R Ri)), \quad C_R = 2, \tag{2.3}$$

$$Ri = \frac{\frac{\partial W}{\partial r}\frac{W}{r}}{\left(\frac{\partial W}{\partial r}\right)^2 + \left(\frac{\partial U}{\partial r}\right)^2}.$$

The restrictive condition on the value of $C^*_{\varepsilon 2}$ is imposed to avoid excessive values of the dissipation rate close to a wall, which would be predicted in rotating flows.
Modification of the $C^*_{\varepsilon 2}$ coefficient by the Richardson number is necessary to reproduce correctly the effects of strong turbulence suppression observed in an initial pipe section. It was found by Kurbatskii & Poroseva (1999) and Poroseva *et al.* (2000, 2001) that the choice of a model for the pressure-strain correlation, and the presence of additional wall corrections to that model, do not solve the problem, and an Ri modification is still necessary. In this study, more models are examined to clarify the question.

When the fully-developed part of the flow is simulated with the same $C_R = 2$, turbulence is suppressed very soon, at $N = 0.5$. This contradicts the experimental observations (Kikuyama *et al.*, 1983; Nishibori *et al.* 1987; Imao *et al.*, 1996) which show decreasing turbulence level with increasing rotation, but not full suppression. On the contrary, they show the existence of some limit state, which is rather insensitive to further increase of rotation and to Reynolds number. The level of turbulence is lower than in a stationary pipe, but not by much. Therefore, the present RANS calculations of a fully-developed rotating pipe flow are made with $C_R = 0$. In (2.3), U and W are the axial and the circumferential mean velocity components respectively, r is the radial coordinate.

The presence of damping functions in Eqs. (2.2)-(2.3) is also not influenced by the pressure-strain correlation model. It relates to formulation of a model for the dissipative

tensor. Though it is evident that a more physical alternative to Eqs. (2.1)-(2.3) should be sought in the future, in a pipe flow this formulation provides good, stable results with different combinations of Reynolds and rotation numbers. Moreover, with such a formulation, the step size in the axial direction is significantly larger than, for instance, that in the formulation used by Kassinos *et al.* (2000) and Poroseva *et al.* (2000, 2001). The issue of computing time becomes very important when complex model expressions for Π_{ij} are incorporated into the model.

3. Results

All approaches to modeling the pressure-strain correlation have been evaluated at two Reynolds numbers, 2×10^4 and 4×10^4. Note again that all parts of the turbulence model except the pressure-strain model were kept the same for all computations. The same flow conditions were applied as in the experiments (Kikuyama *et al.*, 1983; Zaets *et al.* 1985): a rotating flow was obtained by conveying a fully-developed turbulent flow from a stationary cylindrical pipe into a rotating cylindrical section of the same diameter. As experiments demonstrate (Kikuyama *et al.*, 1983; Zaets *et al.* 1985; Nishibori *et al.* 1987; Imao *et al.* 1996), it is possible to distinguish two regions in a rotating pipe flow, with different turbulence structure. In the initial pipe section, with a length of about $30D$ ($D = 2R$ is the pipe diameter), strong suppression of turbulence characteristics is observed (Zaets *et al.* 1985). After suppression, however, statistical quantities increase in value and eventually stabilize at some level which is lower than in a stationary flow, but not by much (Nishibori *et al.* 1987). This is the region of fully-developed turbulence, which is observed beyond about $170D$ for any Reynolds number (Kikuyama *et al.*, 1983; Imao *et al.* 1996).

In the calculations, the grid was non-uniform in r, the total number of nodes being 128 (64 for the Q-model) at $Re = 4 \times 10^4$ and 68 at $Re = 2 \times 10^4$.

The RSTE model with the IP model expression for the pressure-strain correlation does crucially need additional wall corrections. The turbulent diffusion model has practically no influence on mean-velocity components (Kurbatskii & Poroseva, 1999). Results for different turbulence characteristics at $Re = 2 \times 10^4$ are in strong disagreement with experimental data (Imao *et al.* 1996). The disagreement increases significantly with increasing rotation number. Profiles of the axial mean velocity are shown on Fig.1a. With increasing Reynolds number ($Re = 4 \times 10^4$), the dependence of the model results on additional wall modifications decreases for the mean velocity components (Fig. 1b) and the shear stress (Fig. 2a). However, the turbulent kinetic energy does need additional wall corrections. The higher the value of the rotation number, the less critical the wall corrections become. This is especially true at higher Reynolds number.

The mean velocity profiles calculated with the LRR, LSSG, SSG, and Q models are given in Figs. 3-4.

Nearly all models predict the axial mean velocity well, in a stationary pipe and with increasing rotation number (up to $N = 1$). Only the non-linear SSG model already fails at $N = 1, Re = 2 \times 10^4$, predicting complete turbulence suppression. This contradicts the experimental data (Kikuyama *et al.*, 1983; Nishibori *et al.* 1987; Imao *et al.* 1996). The other models do not fail at $N = 1$, but they show the same incorrect tendency to turbulence suppression and fail at larger N. One must conclude that modern turbulence models provide trustworthy results in a rotating pipe flow only at moderate rotation

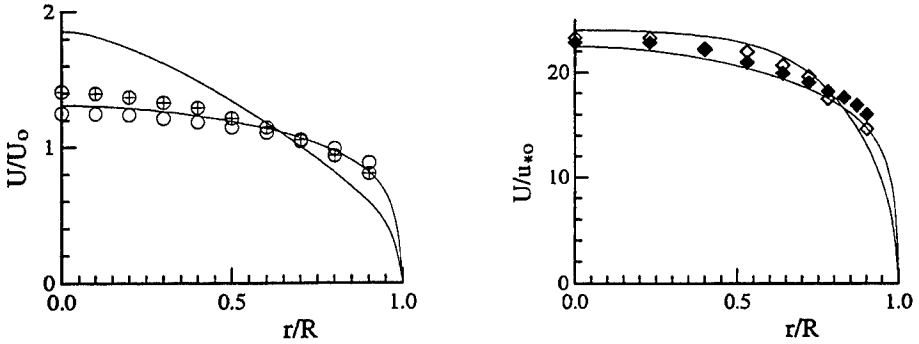

FIGURE 1. Axial mean velocity at a) $Re = 2 \times 10^4$, b) $Re = 4 \times 10^4$. Calculations: (——) IP model. Experiments: a) (○) $N = 0.$, (⊕) $N = 0.5$ (Imao *et al.* 1996); b) (♦) $N = 0.$, (◇) $N = 0.6$ (Zaets *et al.* 1985)

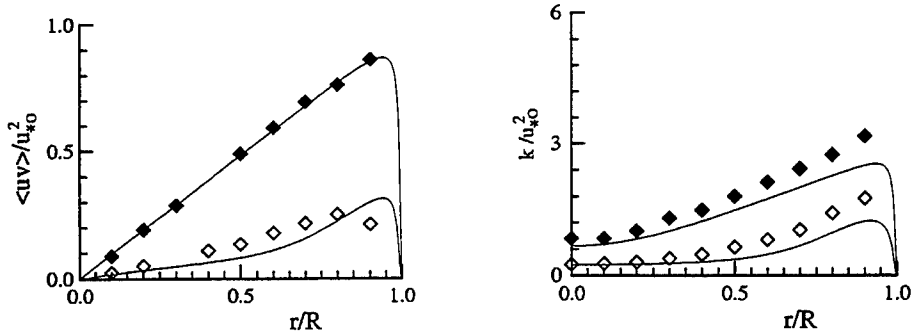

FIGURE 2. Calculations by the IP model at $Re = 4 \times 10^4$: a) shear stress, b) turbulent kinetic energy (see notation in Fig. 1b).

numbers ($N \leq 1$). The additional wall corrections developed to date do not improve this situation (Poroseva *et al.* 2000, 2001).

At higher Reynolds number, $Re = 4 \times 10^4$, solutions obtained with the different models become very close to each other.

At $Re = 4 \times 10^4$ results for the circumferential mean velocity are more sensitive to model choice than results for the axial mean velocity (Fig. 4a). However, with increasing Re, profiles calculated with different models again become close to each other (Fig. 4b). The LSSG gives slightly better profiles at $Re = 2 \times 10^4$ than the other models. The LRR and SSG models generally give very similar results, but the LRR does not fail at $N = 1$.

The second-order statistics are shown in Figs. 5-9. All models overpredict the normalized shear-stress profile $< uv >$ at $Re = 2 \times 10^4$ (Fig. 5a: U_m is the area-mean axial flow velocity). At $Re = 4 \times 10^4$ the results are in very good agreement with the data (Fig. 5b). In a stationary pipe flow no additional wall correction is necessary. With increasing rotation, some difference between calculated and experimental profiles is observed in the near-wall region. However, this difference can easily be corrected by changing the turbulent diffusion model from the DH model to the tensor-invariant HL, as was shown by Kurbatskii & Poroseva (1999) (see Figs. 7 and 8 in that work).

The choice of a turbulent diffusion model is also important for correct prediction of the turbulent kinetic energy in a fully-developed rotating pipe flow. If the IP model expression is combined with the DH turbulent diffusion model in the RSTE turbulence

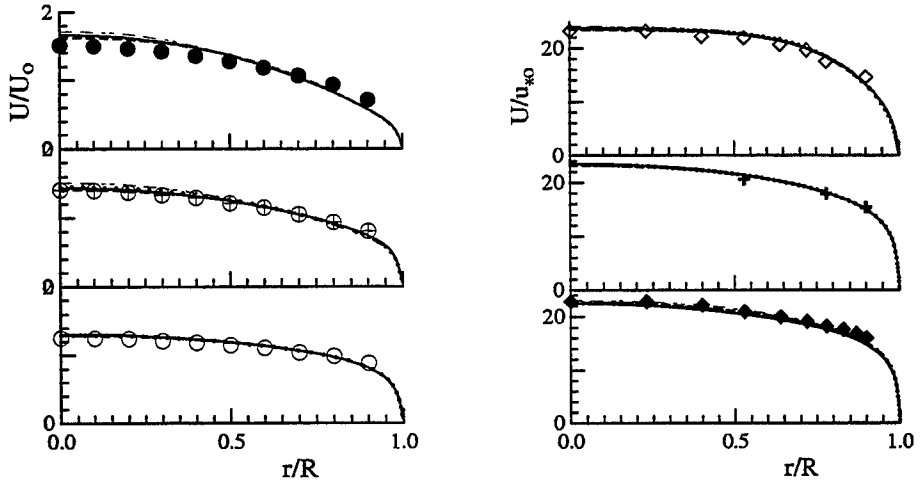

FIGURE 3. Axial mean velocity at a) $Re = 2 \times 10^4$, b) $Re = 4 \times 10^4$. Calculations: (———) LRR, (----) LSSG; (·····) SSG; (—··—) Q. Experiments: a) (○) $N = 0.$, (⊕) $N = 0.5$, (●) $N = 1.$; b) (♦) $N = 0.$, (+) $N = 0.15$, (x) $N = 0.3$, (◊) $N = 0.6$

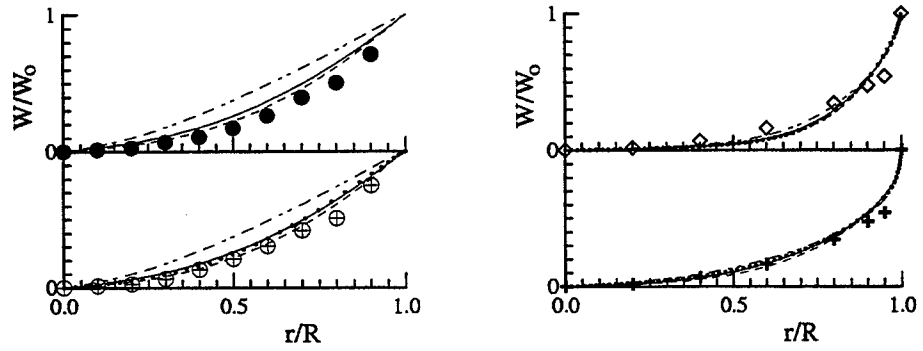

FIGURE 4. Circumferential mean velocity at a) $Re = 2 \times 10^4$, b) $Re = 4 \times 10^4$ (see notation in Fig. 3).

model, the turbulent kinetic energy is significantly overpredicted (Fig. 9 in Kurbatskii & Poroseva, 1999): the calculated level is even higher than in a stationary pipe flow, in strong contradiction of the experimental data. As has been found in the present study, the use of more refined model expressions for the pressure-strain correlation does not solve this problem. All models predict the turbulent kinetic energy in a fully-developed rotating pipe flow to be greater than in a stationary pipe flow. In Fig. 6a only the profile for the LRR model is shown at $N = 0.5$. The other models give qualitatively similar results, which are omitted from the plot to reduce the number of curves. The rest of the curves on Fig. 6a correspond to $N = 0$. Wall modifications do not improve these results either (Kurbatskii & Poroseva, 1999; Poroseva *et al.* 2000, 2001). However, using the HL turbulent-diffusion model instead of the DH model did help to correct results in Kurbatskii & Poroseva (1999). Possibly, this will also solve the problem when other model expressions for the pressure-strain correlation are incorporated into the RSTE model. Additional calculations at $Re = 2 \times 10^4$ and lower should be made to clarify the role of the turbulent diffusion model in RSTE model performance.

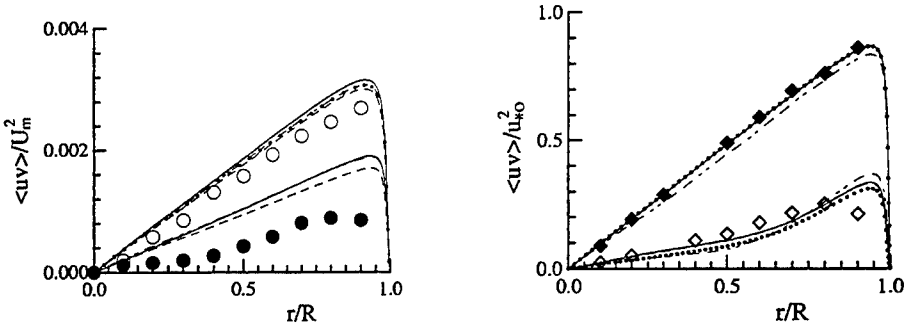

FIGURE 5. Shear stress at a) $Re = 2 \times 10^4$, b) $Re = 4 \times 10^4$ (see notation in Figure 3).

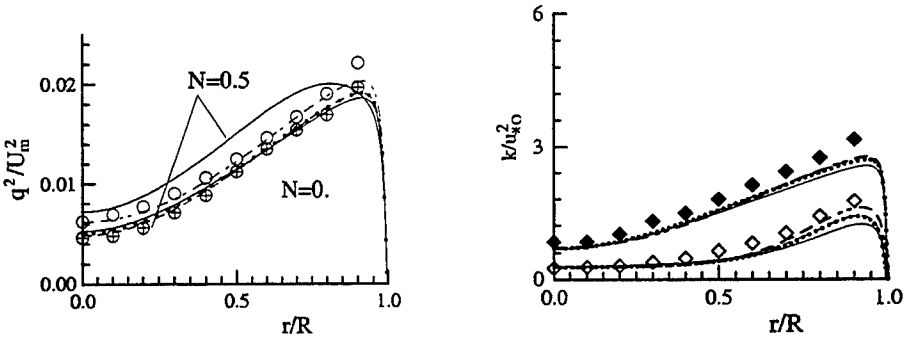

FIGURE 6. Turbulent kinetic energy at a) $Re = 2 \times 10^4$, b) $Re = 4 \times 10^4$ (see notation in Figure3).

In a stationary pipe flow at $Re = 2 \times 10^4$, the Q model predicts the turbulent kinetic energy better (Fig. 6a). Wall corrections are necessary only in the region $(0.8 \leq r/R \leq 1)$. Figure 6b shows profiles for the turbulent kinetic energy at $Re = 4 \times 10^4$. They are in better agreement with the experimental data than for $Re = 2 \times 10^4$. Also, the results obtained by different models are close to each other, though the Q-model becomes better, relative to the other models, with increasing rotation. It is seen that in a stationary pipe flow all models need additional wall corrections. With increasing rotation, the necessity for such corrections significantly decreases.

The partition of turbulent kinetic energy between different components in a stationary pipe flow is shown in Figs. 7 and 8. For more detailed information in the near-wall area, the data of Laufer (1954) are also given in Fig. 7. Those data were obtained at $Re = 5 \times 10^4$ and therefore can be used only for qualitative comparison.

At $Re = 4 \times 10^4$(Fig. 7), all models reproduce each component of the turbulent kinetic energy in the core of the flow very well. The LRR model yields a $< u^2 >$ profile which lies rather far from the experimental data in the remainder of the flow. The LSSG provides slightly better results than the other models for all components. The SSG needs corrections for $< w^2 >$ more than other models. All models need corrections near the wall, in regions which are roughly $(0.8 \leq r/R \leq 1)$ for normalized $< u^2 >$ and even smaller, $(0.9 \leq r/R \leq 1)$, for $< v^2 >$ and $< w^2 >$. It is seen in the plots that it is the axial component of the turbulent kinetic energy that mostly needs additional treatment. Radial $< v^2 >$, and to a lesser degree circumferential $< w^2 >$ components, though they

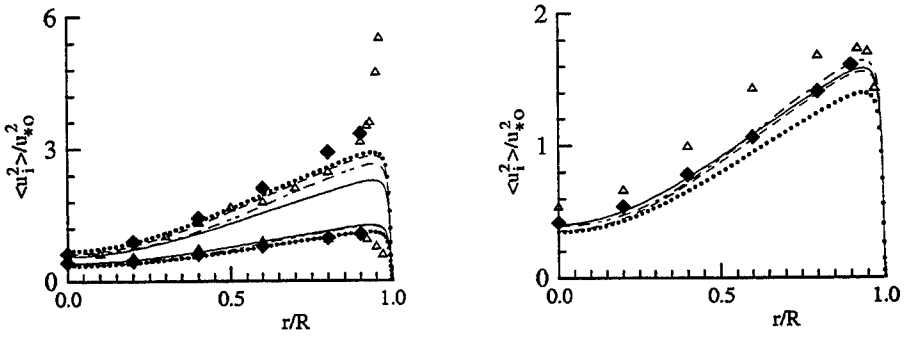

FIGURE 7. Turbulent kinetic energy components in a stationary pipe flow at $Re = 4 \times 10^4$ a) $< u^2 > /u_{*o}^2$ (upper), $< v^2 > /u_{*o}^2$ (lower); b) $< w^2 > /u_{*o}^2$. Notation is inn Figure 3, ($\triangle$) correspond to experimental data of Laufer (1954).

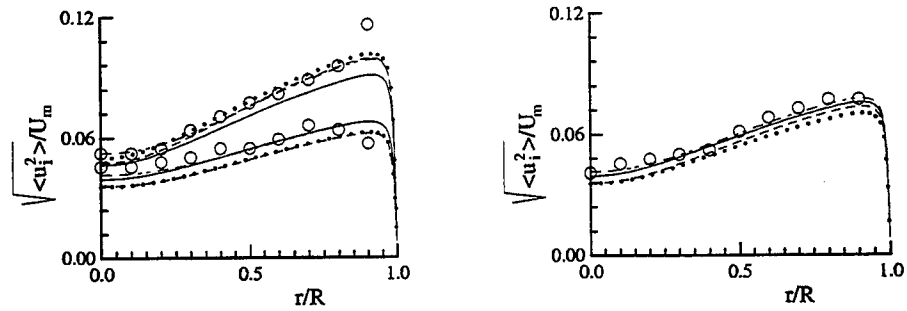

FIGURE 8. Turbulent kinetic energy components in a stationary pipe flow at $Re = 2 \times 10^4$ a) $\sqrt{< u^2 >}/U_m$ (upper), $\sqrt{< v^2 >}/U_m$ (lower); b) $\sqrt{< w^2 >}/U_m$ (see notation in Figure g3).

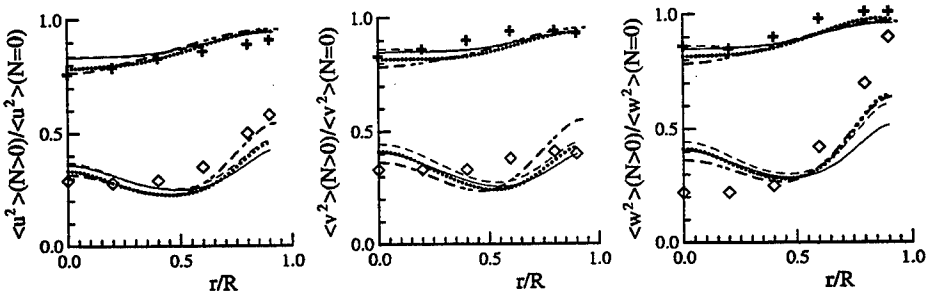

FIGURE 9. Effect of rotation on the turbulent kinetic energy components ($Re = 4 \times 10^4$: see notation in Figure 3).

could be predicted better, contribute less than $< u^2 >$ to the turbulent kinetic energy near a wall.

At $Re = 2 \times 10^4$, the partition of the turbulent kinetic energy between components is shown in Fig. 8. The Q model gives the best agreement with the experimental data. Wall corrections are again necessary only in the region ($0.8 \leq r/R \leq 1$). It seems that the size of this region is not significantly influenced by Reynolds number, at least for Re values in the range considered here. In rotating flow all three components are significantly overpredicted (not shown here) as in the case of the turbulent kinetic energy.

The influence of rotation on profiles of turbulent kinetic energy components at $Re =$

4×10^4 is shown in Fig. 9. It is seen that the Q model describes the change in the $< u^2 >$ profile with increasing rotation very well, and does not need an additional wall correction. Also, the SSG model describes the core of a flow well, whereas the LRR and the LSSG models overpredict the value of the normalized axial component in the core but underpredict it in the near-wall area. Profiles of $< v^2 >$ and $< w^2 >$ at $N = 0.15$ are better described in the flow core by the LSSG and LRR models. At this value of N no model needs wall corrections. At $N = 0.6$ results obtained by different models are comparable. All models overpredict the core values of $< w^2 >$ but underpredict in the near-wall region, though they show qualitatively correct behavior in the latter region. In this case LRR gives worse agreement with the experimental data. As for calculations of $< v^2 >$ at $N = 0.6$, it is difficult to choose which model gives the best results. All profiles are comparable and in satisfactory agreement with the experiments. Problems observed in the near-wall region can be corrected, at least in some degree (Kurbatskii & Poroseva, 1999), by choosing a turbulent diffusion model more suitable to the flow. However, the cause of the strong overprediction of $< w^2 >$ in the core of the flow is not clear at the moment.

4. Conclusions and future plans

Being the simplest, the IP pressure-strain model is widely used in practical applications. However, as we have seen, this model is too simple to describe complex physics in a pipe flow. The simplicity in such a case is actually a disadvantage, to compensate for which the RSTE model should include additional wall corrections, such as damping functions or the elliptic relaxation scheme. This makes the final model more complex, not necessarily more physical or cheaper than more refined basic approaches to pressure-strain correlation modeling.

The other four pressure-strain models tested in the present study capture the physics of the pipe flow significantly better. Profiles of the mean velocity components, calculated without wall corrections, are in good agreement with the experimental data. The models give results close to each other, but at $Re = 2 \times 10^4$ the circumferential mean velocity profiles calculated by the Q model are rather far from the experimental data. With increasing Reynolds number, the difference between profiles calculated with the different models becomes negligible.

Practically no model needs additional corrections for the $< uv >$ shear stress at high Reynolds number ($Re = 4 \times 10^4$). Disagreement between calculations and experiments observed for $< uv >$ in the near-wall region of rotating pipe flow at $N = 0.6$ can be reduced significantly by choosing a more adequate model for the turbulent diffusion, as was shown by Kurbatskii & Poroseva (1999). The popular DH model does not correctly describe the third-order moments anywhere in a pipe flow. The influence of these moments, which appear in the exact turbulent diffusion terms, is significant, especially in the near-wall region. The tensor-invariant HL model was recommended by Kurbatskii & Poroseva (1999): it will be applied in the future to simulate a pipe flow at low Reynolds number, to clarify in more detail the role of the turbulent diffusion model in such a flow. It is expected that predictions ofthe effect of rotation on the second-order statistics at $Re = 2 \times 10^4$ (which are all overpredicted) will also be improved in this way.

The prediction of the turbulent kinetic energy and its partition between components near a wall in a stationary pipe flow is not strongly influenced by the turbulent diffusion model. Therefore, all models need additional wall corrections for the turbulent kinetic

energy, and especially for its axial component, in the region $0.8 \leq r/R \leq 1$ approx. It seems that the size of this region is not much influenced by Reynolds number, at least in the range of values considered here. The radial component needs less correction and the circumferential one needs only minor corrections, if any. Any wall modifications applied to a turbulence model should reflect the observed anisotropy.

In general, the LRR model still seems to miss some important physics. This results mostly in poor predictions of the turbulent kinetic energy and its axial component in a stationary pipe flow. The SSG fails at $N = 1$, predicting flow relaminarization, which is in complete disagreement with the experiments. Other models also predict flow relaminarization, but at least at higher values of the rotation number. The Q model gives better results for turbulent kinetic energy in a stationary pipe flow at both Reynolds numbers, and with increasing rotation at $Re = 4 \times 10^4$. Also, it better describes the partition of the turbulent kinetic energy between its components at $Re = 2 \times 10^4$. However, the circumferential mean velocity profiles calculated with the Q model are in poorer agreement with the experimental data than the profiles obtained with the other models. Note however that unlike the other models tested here, the Q model formulation used in this work is incomplete, in the sense that only the transport equation for the Q–tensor incorporates the new structure tensors. The Q-model formulation for the dissipative process that was used here does not include those tensors, even though there is good reason to expect a significant effect of turbulence structure on the dissipative process. Work by the structure-based modeling group at Stanford to include structure information in the transport equation for a second turbulence scale is currently in progress. A full evaluation of the potential of the structure-based model will become possible once this work is completed: therefore the results reported here for the Q model are preliminary. Finally, the LSSG is the recommended choice for practical calculations at the moment. The model provides a reasonable balance between complexity and quality of performance at all Reynolds and rotation numbers considered here.

The influence of Reynolds and rotation numbers is similar. With increases in either parameter, predictions without additional wall corrections in the pressure-strain models improve significantly.

Acknowledgments

The author is grateful to Mr. C. A. Langer for fruitful discussions on the topic of the study, the whole group of Prof. W. C. Reynolds for collaboration in research and the Center of Turbulence Research for their support and hospitality.

REFERENCES

DALY, B. J. & HARLOW, F. H. 1970 Transport equations in turbulence. *Phys. Fluids* **13**, 2634-2649.

DURBIN, P. A. 1991 Near-wall turbulence closure modeling without "damping functions". *Theor. and Comp. Fluid Dyn.* **3**, 1-13.

GATSKI, T. B. & SPEZIALE, C. G. 1993 On explicit algebraical stress models for complex turbulent flows. *J. Fluid Mech.* **254**, 59-78.

GIBSON, M. M. & LAUNDER, B. E. 1978 Ground effects on pressure fluctuations in the atmospheric boundary layer. *J. Fluid Mech.* **86**, 491-511.

HANJALIĆ, K. & LAUNDER, B. E. 1972 A Reynolds stress model of turbulence and its application to thin shear flows. *J. Fluid Mech.* **52**, 609-638.

IMAO, S., ITOH, M. & HARADA, T. 1996 Turbulent characteristics of the flow in an axially rotating pipe. *Int. J. Heat and Fluid Flow* **17**, 444-451.

KASSINOS, S. C., LANGER, C. A., HAIRE, S. L. & REYNOLDS, W. C. 2000 Structure–based turbulence modeling for wall–bounded flows. *Int. J. Heat and Fluid Flow* **21**, 599-605.

KASSINOS, S. C., REYNOLDS, W. C. AND ROGERS, M. M. 2001 One-point turbulence structure tensors.*J. Fluid Mech.* **428**, 213-248.

KIKUYAMA, K. *et al.* 1983 Flow in an axially rotating pipe (a calculation of flow in the saturated region). *Bull. JSME* **26**, 506-513.

KURBATSKII, A. F. & POROSEVA, S. V. 1999 Modelling turbulent diffusion in a rotating cylindrical pipe flow. *Int. J. Heat and Fluid Flow* **20**, 341-348.

LAUFER, J. 1954 The structure of turbulence in fully developed pipe flow. *NASA* Report 1174.

LAUNDER, B. E., REECE, G. J. & RODI, W. 1975 Progress in development of a Reynolds–stress turbulent closure. *J. Fluid Mech.*, **68**, 537-566.

NISHIBORI, K., KIKUYAMA, K., & MURAKAMI M. 1987 Laminarization of turbulent flow in the inlet region of an axially rotating pipe. *Bull. JSME* **30**, 255-262.

POROSEVA, S. V., KASSINOS, S. C., LANGER, C. A. AND REYNOLDS, W. C. 2000 Computation of a turbulent flow in a rotating pipe using structure-based model. *Annual Research Briefs*, Center for Turbulence Research, NASA-Ames/Stanford Univ., 279-290.

POROSEVA, S., KASSINOS, S., LANGER, C. & REYNOLDS, W. C. 2001 Computation of a turbulent flow in a rotating pipe using the structure-based model. *Proc. 2nd Int. Sympo. on Turbulence and Shear Flow Phenomena* (Stockholm, Sweden), **III**, 149-154.

SO, R.M.C. & YOO, G.J. 1986 On the modeling of low-Reynolds-number turbulence. *NASA* CR 3994.

SPEZIALE, C. G., SARKAR, S. & GATSKI, T. B. 1991 Modeling the pressure-strain correlation of turbulence: an invariant dynamical system approach. *J. Fluid Mech.* **227**, 245-272.

ZAETS, P. G., SAFAROV, N. A. & SAFAROV R. A. 1985 Experimental study of the behavior of turbulence characteristics in a pipe rotating around its axis (in Russian). *Modern Problems of Continuous Medium Mechanics*, Moscow Physics and Technics Institute, 136-142.

APPENDIX
Roster

NAME/TERM		AREA OF RESEARCH
POSTDOCTORAL FELLOWS		
BOTELLA, Dr. Olivier 9/98-8/01	(Ph.D. Engineering, 1997, University of Nice, France)	Numerical methods
CHA, Dr. Chong 4/00-present	(Ph.D. Mechanical Engineering, 2000, University of Washington)	Turbulent combustion
DARVE, Dr. Eric 9/99-8/01	(Ph.D. Mathematics, 1999, Univ. Paris 6, France)	Computational biology
DUBIEF, Dr. Yves 5/01-present	(Ph.D. Fluid Mechanics, 2000, Institute National Polytechnique de Grenoble, France)	LES of turbulent flows
DUCHAMP DE LAGENESTE, Dr. Laurent 2/00-present	(Ph.D. Fluid Mechanics, 1999, Ecole Central de Lyon, France)	LES for premixed combustion
FAVIER, Dr. Valerie 10/00-present	(Ph.D. Combustion, 2000, Inst. National Sciences Appliquees de Rouen, France)	Cardiovascular mechanics
GULLBRAND, Dr. Jessica 1/00-present	(Ph.D. Mechanical Engineering, 1999, Lund Institute of Technology, Sweden)	Large eddy simulation
IDOWU, Dr. Olusola 10/00-present	(Ph.D. Applied Mathematics, 2000, Univ. of Newcastle, UK)	Protoplanetary accretion disks
LIN, Dr. Hao 8/01-present	(Ph.D. Mechanical Engineering, 2001, UC Berkeley)	Protoplanetary disks
POROSEVA, Dr. Svetlana 8/99-8/01	(Ph.D. Physics, Aerophysics, & Aerodynamics, 1996, Novosibirsk State University, Russia)	Structure based modeling
SCHLUTER, Dr. Jorg 10/00-present	(Ph.D. Physics, Fluid Mechanics, 2000, CERFACS, France)	Turbulent combustion
STEMMER, Dr. Christian 8/01-present	(Ph.D. Aerospace Engineering, 2000, Univ.of Stuttgart, Germany)	Hypersonic flows

NAME/TERM		AREA OF RESEARCH
TALLEY, Dr. Sharon 1/01-present	(Ph.D. Biology, 1999, University of Utah	Biological fluid mechanics
TROUILLET, Dr. Phillipe 3/00-present	(Ph.D. Mechanical Engineering, 2000, University of Poitiers, France)	Turbulent combustion
UMURHAN, Dr. Matt 9/98-8/01	(Ph.D. Astronomy, 1998, Columbia University)	Protoplanetary disks
SR. RESEARCH ASSOC.		
WANG, Dr. Meng 9/92-present	(Ph.D. Mech. Engr., 1989, University of Colorado)	Aerodynamic noise
FATICA, Dr. Massimiliano 10/95-present	(Ph.D. Fluid Mechanics, 1995, Univ. of Rome, Italy)	Parallel computing
RESEARCH ASSOCIATES		
APTE, Sourabh 9/00-present	(Ph.D. Engineering, 2000, Pennsylvania State University)	Large eddy simulation
IACCARINO, Gianluca 4/98-present	(Masters Aeronautical Engineering, 1994, University of Naples, Italy)	Turbulence modeling
MARTIN, Dr. Maria Pino 8/00-8/01	(Ph.D. Aerospace Eng., 1999, University of Minnesota)	Hypersonic flows
CONSTANTINESCU, Dr. George 11/99-present	(Ph.D. Environmental Eng. 1998, University of Iowa)	LES for complex geometries
PITSCH, Dr. Heinz 4/99-present	(Ph.D. Mechanical Eng., 1998, RWTH-Aachen, Germany)	Turbulent combustion
SR. VISITING FELLOWS		
FEDOTOV, Dr. Sergei 8/01-10/01	Univ. Manchester Inst. of Science and Technology, U.K.	Turbulent combustion
FREUND, Dr. Jonathan 7/01-8/01	UCLA	Jet aeroacoustics
GARCIA, Dr. Javier 7/01-10/01	Polytechnic University of Madrid, Spain	LES of particle laden flows
GOROKHOVSKI, Dr. Mikhail 8/01-9/01	University of Rouen, France	Turbulent dispersion in LES
MAJUMDAR, Dr. Sekhar 6/01-present	National Aerospace Laboratories Bangalore, India	RANS methods for complex geometry

NAME/TERM		AREA OF RESEARCH
MOHAMMADI, Prof. Bijan 11/00	University of Montpellier, France	Large eddy simulation
OBERLACK, Dr. Martin 8/01-9/01	Inst. Tech. Mech. RWTH-Aachen	Large eddy simulation modeling
PATANKAR, Dr. Neelesh 8/01-9/01	Northwestern University	DNS of fluid particle motion
WU, Dr. Xuesong 4/01-10/01	Imperial College, UK	Hydrodynamic instability
SR. RESEARCH FELLOWS		
JIMENEZ, Prof. Javier 1987-present	University of Madrid, Spain	Wall turbulence
KOUMOUTSAKOS, Dr. Petros 8/94-present	(Ph.D. Aeronautics & Applied Mathematics, 1992, California Institute of Technology)	Turbulence physics Control and optimization
YAGLOM, Prof. Akiva 7/95-present		Writing of 2nd edition of "Statistical Fluid Mechanics"
VISITING RESEARCHERS		
KOTSALIS, Evangelos 7/01-10/01	Swiss Federal Institute of Technology, Switzerland	Molecular dynamics simulation
DEL ALAMO, Juan Carlos 7/01-9/01	University of Madrid, Spain	Large eddy simulation
GRADUATE STUDENTS		
HAN, Donghee 1/01-3/01	(Stanford University)	Turbulent combustion
DESHPANDE, Ajit Avinah	(Stanford University)	Turbulence modeling of flow
HAMMOND, Edward Percy 7/1-9/30	(Stanford University)	Biological DNS
RAY, Prasun 7/1-9/30	(Stanford University)	Simulation of fuel cells
SHARMA, Vivek Kumar 7/1-12/31	(Stanford University)	Turbulent modeling
MOULY-AIGROT, Bertrand Pierre 1/01-12/31	(Stanford University)	Molecular simulations

2001 ADVISORY COMMITTEE

Prof. Ron F. Blackwelder (Chair)
University of Southern California

Dr. David E. Crow, Sr. VP Eng. Tech.
United Technologies-Pratt & Whitney

Dr. Marvin E. Goldstein, Chief Scientist
NASA Glenn Research Center

Prof. Brian Launder
University of Manchester

Dr. Sid Leibovich
Cornell University

Dr. Spiro Lekoudis
Office of Naval Research

Prof. Phil Marcus
University of California at Berkeley

Prof. Richard A. Matzner, Dir. Center for Relativity
U of Texas at Austin

Dr. Charles Smith
NASA Marshall Space Flight Center

Dr. Julian Tishkoff
Air Force Office of Scientific Research

Prof. Forman Williams
University of California

Dr. Pat Purtell (Observer)
Office of Naval Research

Dr. Thomas Beutner (observer)
AFOSR/NA

2001 STEERING COMMITTEE

Prof. Paul A. Durbin
Mechanical Engineering, Stanford University

Prof. Sanjiva K. Lele
Mechanical Engineering Aeoronautics &
Astronautics, Stanford University

Prof. Javier Jiménez
Sr. Research Fellow, Center for Turbulence Research,
Professor, University of Madrid

Dr. Nagi N. Mansour
Deputy Director, Center for Turbulence Research
NASA Ames Research Center

Prof. Parviz Moin
Director, Center for Turbulence Research
Professor, Mechanical Engineering, Stanford.
Sr. Staff Scientist, NASA Ames Research Center

Prof. Norbert Peters
Mechanical Engineering, Stanford University

Prof. William C. Reynolds
Program Coordinator, Center for Turbulence Research
Professor, Mechanical Engineering, Stanford.
Sr. Staff Scientist,
NASA Ames Research Center

Dr. Karim Shariff
Research Scientist, NASA Ames Research Center